HANDBOOK FOR MAP VOLUME 20

Edited by
S. A. Bowhill
Belva Edwards

(NASA-CR-176262) MIDDLE ATMOSPHERE PROGRAM. HANDBOOK FOR MAP, VOLUME 20 (International Council of Scientific Unions) 519 p

N87-10419
THRU
N87-10525
Unclas
CSCL 04A
G3/42 44000

ICSU

International Council of Scientific Unions

SCOSTEP

Scientific Committee on Solar-Terrestrial Physics
K. D. Cole, President
J. G. Roederer, Vice President
C. H. Liu, Scientific Secretary

MAP ORGANIZATION

MIDDLE ATMOSPHERE PROGRAM STEERING COMMITTEE
S. A. Bowhill, SCOSTEP, Chairman
K. Labitzke, COSPAR, Vice Chairman
C. H. Liu, SCOSTEP, Secretary

H. S. Ahluwalia, IUPAP
R. D. Bojkov, WMO
A. D. Danilov, COSPAR
J. C. Gille, COSPAR
I. Hirota, IUGG/IAMAP
A. H. Manson, SCOSTEP
L. R. Megill, IUGG/IAGA
T. Nagata, SCAR
R. G. Roper, IAMAP
P. C. Simon, IAU
J. Taubenheim, IUGG/IAGA
T. E. VanZandt, URSI
R. A. Vincent, URSI

MAP STANDING COMMITTEES
Data-Management -- G. Hartmann and I. Hirota, Co-Chairmen
Dynamics Calendar -- T. E. VanZandt, Chairman
Publications -- C. F. Sechrist, Jr., Chairman

MAP STUDY GROUPS
MSG-5 Ions and Aerosols, F. Arnold and M. P. McCormick, Co-Chairmen
MSG-8 Atmospheric Chemistry, G. Witt, Chairman
MSG-9 Measurement of Middle Atmosphere Parameters by Long Duration Balloon Flights, J. E. Blamont, Chairman

APPROVED MAP PROJECTS

	Coordinator
AMA:	T. Hirasawa
ATMAP:	J. M. Forbes
CAMP:	G. Witt
CLIMAT:	J. M. Russell
DYNAMICS:	K. Labitzke
GLOBMET:	R. G. Roper
GLOBUS:	J. P. Pommereau
GOSSA:	M. P. McCormick
GRATMAP:	D. C. Fritts
MAC-Epsilon:	E. V. Thrane
MAC-SINE:	E. V. Thrane
MAE:	R. A. Goldberg
MASH:	A. O'Neill
MSTRAC:	P. K. Rastogi
NIEO:	S. Kato
OZMAP:	D. F. Heath
SSIM:	P. C. Simon
WINE:	U. von Zahn

MAP REGIONAL CONSULTATIVE GROUP

Europe M. L. Chanin, Chairman

M I D D L E

A T M O S P H E R E

P R O G R A M

HANDBOOK FOR MAP

Volume 20

Papers presented at the
URSI/SCOSTEP Workshop on
Technical and Scientific Aspects
of MST Radar
October 21-25, 1985

Edited by

S. A. Bowhill
Belva Edwards

June 1986

Published for the ICSU Scientific Committee on Solar-Terrestrial Physics (SCOSTEP) with financial assistance from the National Aeronautics and Space Administration under the 1986 Middle Atmosphere Program Management contract and Unesco Subvention 1986-1987.

Copies available from SCOSTEP Secretariat, University of Illinois, 1406 W. Green Street, Urbana, Illinois 61801

FOREWORD

The Third Workshop on Technical and Scientific Aspects of MST (mesosphere-stratosphere-troposphere) radar was held in Aguadilla, Puerto Rico, on October 21-15, 1985. This was the first time that the Workshop was held outside the continental United States; the previous Workshops (in May 1983 and May 1984) were held in Urbana, Illinois. My Co-Organizer, Dr. C. H. Liu, and I are extremely grateful to the staff of the Arecibo Observatory of Cornell University for arranging and supporting a week of very intensive technical activities. We would particularly like to thank the Director of the Arecibo Observatory, Dr. Tor Hagfors, for the courteous and sympathetic reception he accorded to the participants; and also Dr. Jurgen Rottger for his unstinting efforts in the Workshop organization.

The MST radar technique for studying the dynamics of the middle atmosphere continues to take bold strides. Particularly noteworthy is the extent to which the technique is beginning to be used operationally for the measurement and prediction of tropospheric weather. It will be interesting to see the extent to which ST radars will supplant or complement balloon measurments of wind and temperature during the coming years.

The subject of gravity waves and turbulence continues to be a dominant topic; nearly one quarter of this volume is devoted to scientific and methodological papers in this area. Now that we are learning more about the phenomenon of gravity-wave saturation, and are beginning to measure momentum fluxes, many previously obscure features of mesospheric gravity waves are beginning to be understood. One clear lack in present measurements is the absence of networks of MST radars at a suitable spacing for the determination of horizontal wavelengths of gravity waves.

Many examples are given in this volume of intercomparison between MST radars and other techniques. It is fair to say that none of these comparisons cast serious doubt on MST radar measurements of winds and waves that are now part of the literature.

Technical aspects of the design of MST radar systems continued to be a major preoccupation in this Workshop as new radars are planned, and as existing radars are moved to new locations, where the parameters of the installation or environment are different.

There is no doubt that development and exploitation of the MST radar technique is one of the major contributions of the Middle Atmosphere Program. As we move into the period of MAC (Middle Atmosphere Cooperation), it will continue to be used by many scientists in developing an improved understanding of stratospheric and mesospheric processes.

THIRD WORKSHOP ON TECHNICAL AND SCIENTIFIC ASPECTS OF MST RADAR
Aguadilla, Puerto Rico
October 21-25, 1985

CONTENTS

1.1.1 ON THE POTENTIAL USE OF RADAR-DERIVED INFORMATION IN OPERATIONAL NUMERICAL WEATHER PREDICTION

Ronald D. McPherson

National Meteorological Center
Washington, D. C. 20233

HISTORICAL PERSPECTIVE OF OPERATIONAL NUMERICAL WEATHER PREDICTION

Operational numerical weather prediction has historically been concerned with the prediction of atmospheric flow patterns and associated sensible "weather", which have characteristic length scales of 2000 km and greater, and periods longer than a day. The physical basis for this approach was established in the late 1940s and early 1950s, and rests upon the approximate balance between the forces associated with the equator-to-pole gradient of pressure and the earth's rotation. Mathematically, numerical weather prediction is posed as an initial value problem. Its solution thus depends on specifying the state of the atmosphere at the initial time of the forecast period, providing a mathematical "model" of the physical laws which govern the evolution of the atmosphere, and access to sufficient computational power to advance the model solution forward in time.

For the quasi-horizontal, quasi-balanced flows with relatively large length and time scale which have been the principal focus of operational numerical weather prediction, the initial state specification was provided at the beginning of the operation NWP era by balloon-borne measurements of temperatures and wind as functions of pressure. The measurements were taken at locations mostly in populous areas of the Northern Hemisphere, with an average distance between locations of 300-500 km. Soundings were obtained generally twice per day. From these measurements were derived digital representations of the three-dimensional mass distribution of the atmosphere at a given time. Such representations served as the initial conditions for early prediction models.

During the years since the beginning of operational numerical weather prediction in 1955, the data base has expanded, especially from satellite-based observing systems. Atmospheric models have steadily grown in realism, and improved in accuracy. In parallel, the necessary computing technology has advanced to enable the improvements in modeling. Nevertheless, the object of numerical weather prediction has remained the same: the forecasting of large-scale atmospheric flow patterns and associated precipitation. The data base for this operation, while expanded, remains concentrated on sampling the slowly evolving flow patterns twice per day. Such a data base cannot profit very much from radar-derived information, where one of the principal advantages lies in frequent temporal sampling. Indeed, radar measurements have played virtually no role in numerical weather prediction thus far.

However, it is widely known that many important precipitation events occur on a much smaller space and time scale than the flow pattern in which they are imbedded. Such events are poorly predicted by present operational NWP methods. This is manifest in the long-term performance records of operational NWP centers: forecasts can be readily demonstrated. No such increase is apparent with respect to numerical predictions of precipitation.

EXTENSION OF OPERATIONAL NWP METHODOLOGY TO SMALLER TIME AND SPACE SCALES

In recent years, major advances have occurred in understanding the physical processes associated with many smaller-scale major precipitation events coupled with advances in the numerical modeling of those processes. A

growing consensus has resulted that an extension of operational NWP to smaller scales is feasible, and in view of the deficiency in the skill of precipitation forecasts, is highly desirable as well. To be successful, however, the recent advances in modeling must be accompanied by an appropriate enhancement of the observing system, and of course, more powerful computers. In an agreeable conjunction of circumstances, modern computing and observing technologies appear able to produce the required enhancements. In the latter, radar technology will evidently play a major role.

This may be illustrated by an examination of the requirements likely to be placed on an augmented observing system by numerical weather prediction. Such requirements cannot be specified with any accuracy very far in advance because the frontier of our knowledge advances by a sequence of creative imbalances. Thus, the recent advances in modeling have resulted in an imbalance between models and observations, and efforts are being made to redress the imbalance by enhancing the observing system. After information from the improved observing system has been studied, it may be that deficiencies in the models will be revealed, and the modelers will respond. Thus the process is a dynamic one which may result in frequent revision of the requirements. Nevertheless, we may attempt some estimates.

One of the most important conceptual advances in recent years is the recognition that major precipitation events, especially those in the warm season, are usually associated with organized convective systems. Examination of cloud imagery from geostationary satellites has revealed some of the characteristics of these systems. They appear with a wide spectrum of characteristic dimensions, ranging from a few hundred kilometers to almost synoptic scale (>2000 km). It is difficult, and perhaps misleading, to assign one number as a characteristic horizontal length, but for this discussion perhaps 1000 km will serve. The convective systems generally occupy most of the troposphere, so we may assign a characteristic vertical dimension of about 10 km. Sequences of satellite images, plus surface-based observations, show a typical life cycle of perhaps 12 hours; occasionally, a system will persist longer, but even so, often displays a diurnal variation in intensity. Thus we may take 12 hours as a characteristic time dimension.

If we require that our observing system must sample the phenomenon of interest at least 10 times per characteristic dimension, then the observing network suitable for accurately describing the "typical" convective system as outlined in the previous paragraph must have the following characteristics:

Horizontal resolution	100 km
Vertical resolution	$\sim$1 km*
Temporal resolution	$\sim$1 hr

*The vertical resolution should, of course, be substantially higher in the planetary boundary layer.

By contrast with the existing large-scale observing network, where observations are required only twice per day, the mesoscale observing system is required to sample once per hour. It is in this connection that radar-based observations will play a major role.

To summarize our estimates of the requirements likely to be levied on a new observing system for mesoscale meteorology, observations of wind and temperature are required with horizontal resolution of approximately 100 km, and vertical resolution of at least 1 km in the free atmosphere and perhaps an order of magnitude greater in the boundary layer. Atmosphere moisture measurements are also required, but with greater spatial resolution in view of the notoriously inhomogeneous character of moisture fields.

In addition, it is important that the mesoscale model of the atmosphere should know where and at what rate the real atmosphere is precipitating at the initial time. This requires knowledge of the horizontal and vertical distribution of precipitation, as well as the precipitation rate.

POTENTIAL OBSERVING SYSTEMS FOR OPERATIONAL NUMERICAL WEATHER PREDICTION ON THE MESOSCALE

Several observing systems developed in recent years offer potential application to the mesoscale numerical weather prediction problem. Summarized in the list below are systems which have not been used or fully exploited in operational meteorology.

Temperature

1. Thermodynamic Profiler: This is an experimental six-channel radiometer, based at the surface and pointed upward. It derives profiles of temperature from infrared radiation emitted from relatively deep atmospheric layers. It thus has relatively coarse vertical resolution and is adversely affected by precipitation at the observing site. Soundings can be produced each hour, and the integrated measurements (e.g., heights of standard isobaric surfaces) are quite accurate. The greatest accuracy is found in the lower levels. Scanning is not possible, so horizontal resolution is limited.

2. VAS (VISSR Atmospheric Sounder): This is an infrared radiometer on the Geostationary Orbiting Earth Satellite. Temperatures are derived from upwelling radiation, in the same way as with the thermodynamic profiler. VAS has the advantage of scanning, and thus offers good horizontal resolution. It also offers high frequency soundings in time. The soundings are most accurate in the higher atmosphere. VAS soundings suffer from coarse vertical resolution, and are not available in cloudy areas.

Wind

3. Wind Profiler: This is a clear-air Doppler radar, surface-based, with two orthogonal beams pointing upward at 15° from the zenith. Wind profiles can be produced each hour or even more frequently, from about 500 m above the ground into the lower atmosphere. The profiles have acceptable vertical resolution above the boundary layer. Scanning is not possible, so horizontal resolution depends on the spacing between instrument sites. Preliminary estimates suggest that the wind measurements are of acceptable accuracy.

4. Doppler Surveillance Radar: The National Weather Service has embarked on a program (NEXRAD) to install new weather surveillance radars at approximately 160 sites in the US. It will be possible to derive winds from the radar measurements when precipitating clouds, or other targets such as insects, are present. The accuracy is good, vertical resolution is good, and the data may supplement the wind profiler in the boundary layer. Winds are not available under all conditions; in particular, clear air in the cold season will be void of data from this source.

5. Automated Aircraft Data: Modern wide-bodied commercial jet aircraft are being equipped with communication devices which relay temperatures and winds measured by the aircraft's sensors and inertial navigation systems to the ground. Observations of wind and temperature will be available at roughly 100-km intervals in level flight, and 10 mb intervals on ascent and descent. Slant profiles will therefore be available in the vicinity of major airports. The accuracy of the winds obtained from this source is good, but the temperatures are less accurate.

Moisture

6. Moisture Profiler: A two-channel radiometer has been developed to provide frequent, accurate measurements of the total water content of the atmosphere above the radiometer. Profiles are not available. No scanning is done, so horizontal resolution is determined by the distance between observing sites.

7. VAS: Frequent estimates of total water content can also be determined from the VAS instrument. Scanning is done, however, so the horizontal resolution is quite good.

It is clear from this brief summary that no single component listed above satisfies all the requirements of the data base for operational mesoscale numerical weather prediction. Instead, the requisite observing system will be a composite of all the above elements, plus the existing network which is part of the synoptic scale observing system.

The cornerstone of the network is likely to be the wind profiling radar. Because of the accuracy and frequency of the radar wind observations, it will be possible to estimate not only the wind field at any one time, but also its tendency, with considerable accuracy. The former is extremely important, indeed vital, to mesoscale prediction; the latter is important because it can be used through the hydrodynamic equations to enhance the vertical resolution of the coarsely resolved temperature profiles, thus indirectly enhancing the accuracy of the prediction.

CONCLUDING REMARKS

The National Meteorological Center is convinced that a mesoscale observing system, with elements as described above, will be a reality within a few years. It thus becomes a matter of some importance to devise a four-dimensional data assimilation system capable of intelligently treating data from these various sources. The Center has committed substantial resources to this development project, and recognizing the long lead time necessary in such endeavors, work is already underway. Experiments with simulated observations will begin in 1987. Read data experiments will begin with the availability of wind profiler data from a 30-station demonstration network in 1989. As NEXRAD installations proceed, efforts will be made to incorporate wind data from this source, also.

D2-47
12 P.

1.1.2 A THEORY FOR THE RETRIEVAL OF VIRTUAL TEMPERATURE FROM WINDS, RADIANCES AND THE EQUATIONS OF FLUID DYNAMICS

Tzvi Gal-Chen

School of Meteorology, University of Oklahoma
Norman, Oklahoma 73019

ABSTRACT

A technique to deduce the virtual temperature from the combined use of the equations of fluid dynamics, observed wind and observed radiances is described. The wind information could come e.g., from ground-based sensitive very high frequency (VHF) Doppler radars and/or from space-borne Doppler lidars. The radiometers are also assumed to be either space-borne and/or ground-based. From traditional radiometric techniques the vertical structure of the temperature can be estimated only crudely. While it has been known for quite some time (GAL-CHEN, 1978; HANE and SCOTT, 1978) that the virtual temperature could be deduced from wind information only, such techniques had to assume the infallibility of certain diagnostic relations. The proposed technique is an extension of the Gal-Chen technique. It is assumed that due to modeling uncertainties the equations of fluid dynamics are satisfied only in the least square sense. The retrieved temperature, however, is constrained to reproduce the observed radiances. It is shown that the combined use of the three sources of information (wind, radiances and fluid dynamical equations) can result in a unique determination of the vertical temperature structure with spatial and temporal resolution comparable to that of the observed wind.

1. INTRODUCTION

A few years ago, GAL-CHEN (1978) and HANE and SCOTT (1978) noted that if sufficiently accurate measurements of the wind and its time history could be obtained from Doppler radars, this information would, in principle, define also the thermodynamic structure. In essence, this is done by requiring that the data will also satisfy the momentum equations in the least square sense. This has reduced the problem to a classical calculus of variation problem (COURANT and HILBERT, 1953). The form of the momentum equations assumed in these studies is quite general and is, in principle, applicable to small meso- and large-scale atmospheric motions. While not immediately obvious, when the approximations appropriate to large-scale atmospheric flows are employed, the above variational formulation is reduced to solving a classical balance equation (HALTINER and WILLIAMS, 1980) of obtaining the geopotential from the wind.

GAL-CHEN and KROPFLI (1984), ROUX et al. (1984) and HANE and RAY (1985) have tested the practical utility of the above-mentioned variational formulation on a variety of observed small-scale phenomena; planetary boundary layer (PBL) convection in the Gal-Chen and Kropfli case; severe storms for the Hane and Ray case, and a tropical squall line for the Roux et al. case. In all, the three case studies of temperature and pressure are deduced from observed Doppler radars wind. Satisfactory agreement with *in situ* thermodynamic observations is reported in all three cases.

As GAGE and BALSLEY (1978) point out, sensitive Doppler radars can be used to obtain mesoscale wind profiles under all weather conditions. The vertical resolution is up to 100 m. The time resolution is about 1 hour and the horizontal resolution is determined by the average distance between the profilers. Comparable resolution is not obtainable from radiometric measurements of the atmosphere either from the ground or from satellites. The purpose of this paper is to extend and modify the GAL-CHEN (1978) technique to satisfy the following requirements:

(a) The horizontal momentum equations are satisfied in the least square sense (to be defined further below).
(b) The hydrostatic constraint is satisfied exactly.
(c) The thermodynamic equation is satisfied in the least square sense.
(d) The radiative transfer equation at various frequencies is satisfied exactly.
(e) Given wind and radiances as input, virtual temperatures should be obtained as an output. The retrieved temperature should have horizontal and vertical resolution compared to that of the observed wind.

In this paper only the theory is developed. The practical utility remains to be checked. This should be done first by simulation studies and then by examining real data. The task is vast and difficult and I hope that the theory developed here will stimulate other researchers to check its practical utility and to seek even better ways to estimate the virtual temperature.

The technique discussed in this paper has some similarities to the techniques considered by KUO and ANTHES (1985) and by BRUMMER et al. (1984). However, it also has some potentially important differences. These include inter alia:

(a) Lateral boundary conditions for the temperature are obtained directly from the wind data rather than prescribed from a 12-hour forecast as in Kuo and Anthes or, as in the Brummer et al. case, prescribed from a vertically smoothed temperature profile obtained by pure radiometric techniques.
(b) In both the Kuo and Anthes and Brummer et al. techniques, the horizontal divergence equation is used; as a weak constraint in the Brummer case and as a diagnostic equation for the geopotential in the Kuo and Anthes case. In our case, attempt is made to satisfy, albeit in the least square sense, all the prognostic equations relevant to describing mesoscale motions.
(c) The Kuo and Anthes approach does not utilize the information contained in the radiances. It is assumed that in nature the divergence equation is satisfied exactly. This is not true even if the wind measurements are error free. In the Brummer technique, a temperature profile is sought that will, on the one hand, satisfy the divergence equation as close as possible, and on the other hand, is also not too far from the smooth temperature profile retrieved from radiometric data. Our technique, however, demands that the retrieved temperature satisfy the radiative transfer equation, augmented by additional dynamical constraints. Unlike the pure radiometric techniques, the above set is mathematically well posed and no a priori smoothing or statistical constraints need to be imposed on the retrieved temperature.

2. MODELING ASSUMPTIONS

Governing equations. The governing hydrostatic primitive equations in Cartesian x, y, z coordinates may be written as:

Continuity equation,

$$D\rho/Dt + \rho\nabla\cdot\underset{\sim}{u} = 0 \qquad (1)$$

Horizontal momentum equations,

$$Du/Dt = -(1/\rho)\partial p/\partial x + F_1 + fv \tag{2}$$

$$Dv/Dt = -(1/\rho)\partial p/\partial y + F_2 - fu \tag{3}$$

Here D/Dt is a symbol for total derivative

$$D/Dt = \partial/\partial t + u\partial/\partial x + v\partial/\partial y + w\partial/\partial z \tag{4}$$

f is the Coriolis parameter ($f = 2\Omega\sin\phi$; Ω is the earth angular velocity and ϕ is the latitude). For convenience we are displaying the equations using Cartesian coordinates. Nevertheless, the extension of our ideas to spherical coordinates is obvious and all our subsequent discussions (conclusions) are valid for spherical geometry. The hydrostatic equation is given vis.,

$$\partial p/\partial z = -\rho g \tag{5}$$

An approximate form of the thermodynamic equation neglecting the contribution of moisture to the density ρ and to the heat capacity (under constant pressure) C_p is

$$C_p\, DT/Dt - (1/\rho)Dp/Dt = S_h \tag{6}$$

The heat capacity under constant pressure is given vis. $C_p = (7/2)R$ with R the gas constant for dry air. The equation for conservation of water vapor is

$$Dq/Dt = S_v \tag{7}$$

The equation of state is

$$p = \rho R T_v \tag{8}$$

Here u is the three-dimensional wind vector $\underset{\sim}{u} = (u, v, w)$. u is the horizontal velocity in the x direction; v is the velocity in the y direction and w is the velocity in the vertical direction, z. The density of dry air is denoted by ρ; p is the pressure; g is the acceleration of gravity; F_1 and F_2 are symbols for turbulent friction forces (of dimension Newton/kg) which in this study we assume that they can be either measured directly or parameterized based on wind observations. T is a symbol for temperature; p is the pressure. T_v is the virtual temperature defined vis.

$$T_v - T = 0.61\, qT \tag{9}$$

Here q is the water vapor mixing ratio (expressed in 10^{-3}g/(kg of dry air)). The symbol S_h is for sources (or sinks) of heat energy. Since in this study we are limiting ourselves to relatively short time scales (0-12 hours), radiative processes are presumed to be of secondary importance (SMAGORINSKY, 1974) and the major source of heating in the free atmosphere is due to precipitation. The major heating source in the planetary boundary layer (PBL) is assumed to be fluxes of sensible heat. S_v is a symbol for sources or sinks of water vapor and in accordance with our previous presumption that the major contributor to S_v in the free atmosphere is the removal of vapor by precipitation. In the PBL, the major source is evaporation from the ground.

The nature of the data and/or the parameterizations. Our major assumptions about the nature of the observed data or the parameterizations employed are as follows:

(a) Horizontal motions can be measured by means of powerful Doppler radars (frequency range is 50-900 MHz). The measurements have accuracy of ± 1 ms^{-1}; are such that all motions with time scales with less than 1 hour have been filtered and are possible under all weather conditions (LITTLE, 1982).

(b) Vertical motions with scales described in (a) can be either deduced from the horizontal motions (using the mass continuity equation) or else can be measured directly by Doppler radars (NASTROM et al., 1985). To be useful for predictions of synoptic scale motions, the accuracy of the deduced (or measured) vertical motions must be of the order of $\pm$ 1 cms^{-1} (HALTINER and WILLIAMS, 1980).

(c) Remote sensing of temperature and moisture profiles using ground-based and/or space platforms renders some useful information under almost all weather conditions (WESTWATER et al., 1985). (This is true only if the infrared channels are augmented by additional channels from the microwave. Otherwise, contamination from clouds may be severe. Furthermore, microwave measurements are contaminated under the presence of heavy rain.) The temperature and moisture retrieved from these measurements typically have poor vertical resolution. As a result, the retrieved profiles have an accuracy of no better than $\pm$ 3°C for temperature and $\pm$ 5 g/kg for the moisture.

(d) At the minimum, it is assumed that the measurements described in (a)-(c) are available in at least three spatial locations to be able to define a triangle. The satisfaction of this requirement would enable calculations of horizontal gradients. It must be borne in mind that the distance between the stations also determine the smallest scales that can be resolved by such a network. Thus, even though the horizontal wind measurements described e.g., in (a) may contain spatial scales of motions smaller than the distance between the stations, the computed horizontal gradients cannot properly resolve this information.

(e) As is customary in numerical weather prediction (NWP) models (HALTINER and WILLIAMS, 1980), we assume that all motions and processes with spatial and temporal scales that cannot be resolved by the network can either be "parameterized" in terms of what is observed or measured directly. For instance, F_1 and F_2 (in (2) and (3)) which are turbulent friction terms may be estimated from single Doppler radar data (KROPFLI, 1984). Alternatively, one may attempt to parameterize it in terms of the larger scale winds. (The simplest parameterization is to set $F_1 = F_2 = 0$.) Another example is the precipitation rate and the vertical distribution of latent heat release which may be evaluated using conventional radars (DOVIAK, 1981) or from satellite data (ATLAS and THIELE, 1981) or parameterized (e.g., ignored).

3. ALGORITHM DEVELOPMENTS

Deduction of horizontal virtual temperature gradients. Taking into account our assumption (a) and (b) in the previous section, we may write the horizontal momentum equations (2) and (3) as:

$$(1/\rho)\nabla_H P = \underset{\sim}{G} \tag{10}$$

Here, $\underset{\sim}{G} \equiv (G_1, G_2)$ is a given two-dimensional vector function ($G_1 = -Du/Dt + fv + F_1$; $G_2 = -Dv/Dt - fu + F_2$) which, in principle, can be computed from the observed wind; ∇_H is the two-dimensional gradient operator. Differentiating (10) with respect to z and using hydrostatic (5), and the equation of state (8) one gets

$$(1/\rho)\nabla_H P \partial \ln T_v/\partial z + g\nabla_H \ln T_v = \partial \underset{\sim}{G}/\partial z.$$

Taking it into account (10)

$$\underset{\sim}{G}\partial \ln T_v/\partial z + g\nabla_H \ln T_V = \partial \underset{\sim}{G}/\partial z \qquad (11)$$

(11) can be considered as a generalization of the thermal wind relation in z coordinates. In fact, for $\underset{\sim}{G} = (fv;-fu)$ the thermal wind is reproduced.

Equation (11) expresses horizontal and vertical temperature gradients in terms of observed quantities (i.e., winds and its derivatives). Together with other relations to be used further below, it can be used to infer the vertical structure. Nevertheless, it is also useful to consider several approximations of (11). First consider the ratio (denoted by R_a) of $g\nabla_H \ln T_V$ to $\underset{\sim}{G}\partial \ln T_v/\partial z$. Traditional scale analysis considers (e.g., PEDLOSKY, 1979, pp. 1-10) dictates that the order of magnitude of the above-mentioned ratio is given by

$$R_a = \frac{g\delta^h T/L}{O(\underset{\sim}{G})\Gamma}$$

Here, $\delta^h T$ is a typical horizontal temperature difference over a typical length scale L and Γ is the lapse rate ($\Gamma \equiv -\partial T_v/\partial z$). We shall now try to obtain for baroclinic weather systems a lower bound of R_a. We know that Γ can hardly exceed the dry adiabatic lapse (g/C_p). Furthermore,

$$\text{Max}|\underset{\sim}{G}| = \text{Max}(U/\tau,\ U^2/L,\ fU)$$

Here, U is a typical velocity associated with the scale L, f is the Coriolis parameter, and τ is a typical time scale. Thus, overall

$$\text{Min}(R_a) = \frac{(\delta^h T/L)C_p}{\max(U/\tau, U^2/L, fU)}$$

For large-scale flows in the middle latitudes, $L \sim 10^6$ m, $U \sim 10$ ms^{-1}, $f \sim 10^{-4}$ s^{-1}, $O(\underset{\sim}{G}) \sim fU$. Also, a modest estimate of the large scale temperature gradient in a baroclinic flow is 3 deg/1000 km; in addition, $C_p = 1004$ Jdeg^{-1}kg^{-1}, thus $\text{Min}(R_a) = O(3)$. This means that in the l.h.s. of (11), the contribution of the terms associated with the horizontal temperature gradient typically dominate that associated with the vertical temperature gradient. The net result is

$$g\nabla_H \ln T_v \simeq \partial \underset{\sim}{G}/\partial z \qquad (11)'$$

For the geostrophic case, G = (fv,-fu) and (11)' is recognized as an approximate form of the thermal wind relation (e.g., HESS, 1959, p. 191). As long as significant baroclinicity exists, the approximation (11)' continues to be valid for mesoscale flows with $L \sim 10^5$ m, $U \sim 10$ ms^{-1}, $|\underset{\sim}{G}| \sim U^2/L$ and $\delta^h T/L = 0.3$ deg/100 km.

Another useful form of (11) can be utilized if one recognizes that the l.h.s. of (11) is actually $g\nabla_H \ln T_v)_p$. Here the operator $\nabla_H)_p$ is the horizontal gradient in x, y, p, t space (p is held constant). To see why this is so, note (HESS, 1959, pp. 260-264) that

$$\nabla_H T)_z = \nabla_H T)_p + (\partial T/\partial P)\nabla_H P$$

Using hydrostatic (5) and the chain rule, we obtain

$$\partial T/\partial P = -(1/\rho g)\partial T/\partial z$$

We also know from (10) that, $(1/\rho)\nabla_H P = \underset{\sim}{G}$ thus, overall,

$$g\nabla_H T_v)_z = g\nabla_H T_v)_p - \underset{\sim}{G}\partial T_v/\partial z$$

The net result is

$$g\nabla_H \ln T)_p = \partial \underset{\sim}{G}/\partial z \qquad (11)''$$

(11)" is an exact expression to calculate horizontal temperature gradients; nevertheless, to utilize it, its r.h.s. must be known at selected p levels. This requires knowledge of the pressure as a function of z. Typically, in the absence of rawinsonde, this is accomplished by utilizing a crude first guess of temperature from the radiometers, together with hydrostatic (5) and the equation of state (8). This results in a crude first guess of the pressure (typically $\pm$ 10 mb). Equipped with this information, one can interpolate $\partial \underset{\sim}{G}/\partial z$ which is observed in x, y, z, t space to an x, y, p, t coordinate. In practice, this is accomplished by interpolating to those z which correspond to constant p levels. Setting aside for the purpose of this discussion the standard errors associated with interpolations, there is an error associated with the fact that the pressure is inaccurately known; consequently, the z's associated with the constant p levels are inaccurately known.

We will now proceed to evaluate the above-mentioned errors. From hydrostatic we know that

$$\partial z/\partial \ln p = -RT_v/g$$

Integrating from sea level to some specified height (assuming for convenience p (sea level) $\sim$ 1000 mb) we get

$$z = (R\overline{T}_v/g)\ln(p/1000)$$

Here $\overline{T}_v$ is some vertically averaged temperature in the interval (o,z) and p is the pressure at level z. In the lower troposphere $\ln(p/1000) = O(1)$ and $R\overline{T}_v/g = O(8\text{ km})$ (see e.g., HESS, 1959, pp. 75-77). Assuming a worst case scenario that the errors in estimating $\overline{T}_v$ and T_v strictly from radiometric data are the same, we obtain for δz (the error in z) that,

$$\delta z = (R\,\delta\overline{T}_v/g)O(1)$$

Taking $\delta T_v \sim 3°K$ we obtain $\delta z \sim 100$ m. Now from (11)" and Taylor expansion

$$\delta(\partial \underset{\sim}{G}/\partial z) \sim \delta z\, \partial^2 \underset{\sim}{G}/\partial z^2 \qquad (12)$$

Furthermore, for Rossby number not too large from unity (essentially corresponding to large and mesoscale motion) $\underset{\sim}{G} = O(fU)$ thus,

$$\partial^2 G/\partial z^2 = O(fU/D^2) \qquad (13)$$

Here D is a typical vertical scale over which significant variation of $\partial^2 u/\partial z^2$ are occurring. For the troposphere, D $\sim$ 5 km, $f \sim 10^{-4}\ s^{-1}$, $U \sim 10\ ms^{-1}$, $T \sim 273°K$. Also as discussed above, $\delta z \sim 100$ m. Substituting the above results in (12) and (13) and also taking into account (11)" we obtain

$$\delta\nabla_H T)_p \sim O(10^{-2}\text{deg/100 km}) \qquad (14)$$

$\delta\nabla_H T)_p$ in (14) is an estimate of the error in the evaluation of the horizontal temperature gradient in p coordinates due to interpolation errors from x, y, z, t space to x, y, p, t space. As discussed above, these errors

are the result of our inaccurate knowledge of p. The error appears to be quite acceptable. Nevertheless, it should be remembered that our error estimate is quite sensitive to the choice of D, the vertical scale. At any rate, the algorithm to be described further utilizes (11) which is the exact form in x, y, z, t space rather than the approximate form (11)' or the form (11)" which is exact but requires interpolation to x, y, p, t space.

Deduction of vertical virtual temperature gradients. So far we have shown how to find horizontal virtual temperature gradients. To find the vertical temperature gradients we will have to use the thermodynamic equation (6). A difficulty arises because while $T_v \simeq T$ to within 1% (HESS, 1959, p. 44) the contribution of the moisture to the horizontal virtual temperature gradient at the lower troposphere could be comparable to that of the horizontal temperature gradients. To overcome this difficulty we will now derive an alternative form of (6) containing only gradients of the virtual temperature. We start by noting that the continuity equation (1) and the equation of state (8) imply that

$$-(1/\rho)Dp/Dt = -RDT_v/Dt + RT_v \mathrm{div}\cdot\underset{\sim}{u}$$

This enables us to rewrite (6) as

$$C_p DT/Dt - RDT_v/Dt + RT_v \mathrm{div}\cdot\underset{\sim}{u} = S_h \tag{15}$$

From the definition of virtual temperature (9) we obtain

$$DT/Dt = DT_v/Dt - 0.61\, qDT/Dt - 0.61\, (Dq/Dt)T \tag{16}$$

Now, under all meteorological conditions $q \sim 10^{-2}$ and less. Thus, the second term ot the r.h.s. of (16) is always negligible compared to the first term. Under conditions of strong moisture gradient (e.g., dry lines) the third term may be important and is therefore retained. However, in the third term, we may substitute T_v for T. Utilizing the above approximations we may substitute (16) in (15)' taking also into account the moisture equation (7) and the fact that $C_p - C_v = R$ to obtain

$$C_v DT_v/Dt - RT_v \mathrm{div}\cdot\underset{\sim}{u} - 0.61\, C_p S_v T_v = S_h \tag{17}$$

We next substitute (11) in (17) replacing the horizontal temperature gradient in (17) by $(T_v/g)\partial\underset{\sim}{G}/\partial z - (\underset{\sim}{G}/g)\partial T_v/\partial z$. The net result is

$$C_v(\partial \ln T_v/\partial t + \tilde{w}\partial \ln T_v/\partial z) = F - S_h/T_v \tag{18}$$

Here F is a symbol for presumably observed quantities, i.e.,

$$F = 1/g(\underset{\sim H}{u}\cdot\partial\underset{\sim}{G}/\partial z) + R\,\mathrm{div}\cdot\underset{\sim}{u} - 0.61\, C_p S_v \tag{19}$$

$\tilde{w}$ is the modified vertical velocity given by

$$\tilde{w} = w + (\underset{\sim H}{u}\cdot\underset{\sim}{G})/g \tag{20}$$

The horizontal velocity vector is denoted by $\underset{\sim H}{u}$ [$\underset{\sim H}{u} = (u,v)$].

The next step is to obtain explicit expressions for $\partial \ln T_v/\partial z$ which do not contain temperature tendencies. This is accomplished by applying the vector operator $g\nabla_H + \underset{\sim}{G}\partial/\partial z$ on both sides of (18). The result using (11) and calculus rules of the sort f'g = (gf)' - g'f are terms like

$$\partial/\partial t(g\nabla_H \ln T_v) + \underset{\sim}{G}\partial/\partial t(\partial \ln T_v/\partial z) = (g\nabla_H + \underset{\sim}{G}\partial/\partial z)\partial \ln T_v/\partial t$$

$$g\tilde{w}\partial/\partial z(\nabla_H \ln T_v) + g(\nabla_H \tilde{w})\partial \ln T_v/\partial z = g\nabla_H(\tilde{w}\partial \ln T_v)/\partial z$$

$$\underset{\sim}{G}\tilde{w}\partial/\partial z(\partial \ln T_v/\partial z) + \underset{\sim}{G}(\partial \tilde{w}/\partial z)\partial \ln T_v/\partial z = \underset{\sim}{G}\partial/\partial z(\tilde{w}\partial \ln T_v/\partial z)$$

Furthermore, from calculus

$$\underset{\sim}{G}\partial/\partial t(\partial \ln T_v/\partial z) = \partial/\partial t(\underset{\sim}{G}\partial \ln T_v/\partial z) - (\partial G/\partial t)(\partial \ln T_v/\partial z)$$

Thus,

$$(g\nabla_H = \underset{\sim}{G}\partial/\partial z)\partial \ln T_v/\partial t = \partial/\partial t(g\nabla_H + \underset{\sim}{G}\partial/\partial z)\ln T_v$$

$$- (\partial \underset{\sim}{G}/\partial t)\partial \ln T_v/\partial z$$

Using (11),

$$(g\nabla_H + \underset{\sim}{G}\partial/\partial z)\partial \ln T_v/\partial t = \partial^2 \underset{\sim}{G}/(\partial z \partial t) - (\partial \underset{\sim}{G}/\partial t)\partial \ln T_v/\partial z$$

Similarly,

$$(g\nabla_H + \underset{\sim}{G}\frac{\partial}{\partial z})\tilde{w}\cdot\frac{\partial \ln T_v}{\partial z} = g(\nabla_H \tilde{w})\frac{\partial \ln T_v}{\partial z} + \underset{\sim}{G}\frac{\partial \tilde{w}}{\partial z}\cdot\frac{\partial \ln T_v}{\partial z} + \tilde{w}\frac{\partial^2 \underset{\sim}{G}}{\partial z^2} - \tilde{w}(\partial \underset{\sim}{G}/\partial z)\frac{\partial \ln T_v}{\partial z}$$

Also utilizing (11)

$$(g\nabla_H + \underset{\sim}{G}\partial/\partial z)\frac{S_h}{T_v} = \frac{1}{T_v}(g\nabla_H + \underset{\sim}{G}\partial/\partial z)S_h - (S_H/T_v)\partial \underset{\sim}{G}/\partial z$$

Overall, the net results are two separate estimates for the vertical temperature gradient, namely

$$C_v(g\nabla_H \tilde{w} + \underset{\sim}{G}\partial \tilde{w}/\partial z - \partial \underset{\sim}{G}/\partial t - \tilde{w}(\partial \underset{\sim}{G}/\partial z)\frac{\partial \ln T_v}{\partial z} = \underset{\sim}{H} \tag{21}$$

where $\underset{\sim}{H}$ is given by

$$\underset{\sim}{H} = (g\nabla_H + \underset{\sim}{G}\partial/\partial z)F - (S_h/T_v)\partial \underset{\sim}{G}/\partial z + (1/T_v)(g\nabla_H + \underset{\sim}{G}\partial/\partial z)S_h \tag{22}$$

Here F is given by (19). Since we have assumed that a first guess of T_v is available from the radiometers and is accurate to within $\pm$ 3°K it is permissible to substitute this first guess in the r.h.s. of (22). The net result is that $\underset{\sim}{H}$ is an observed vector function.

It is now useful to put together the forms of the horizontal and vertical virtual temperature gradients and their dependence on the observed winds. They are:

The generalized thermal wind relation (11) rewritten here as

$$(g\nabla_H + \underset{\sim}{G}\partial/\partial z)\ln T_v = \partial \underset{\sim}{G}/\partial z \tag{23}$$

Equations for vertical temperature gradient (21) rewritten as

$$\underset{\sim}{A}\partial \ln T_v/\partial z = \underset{\sim}{H} \tag{24}$$

Here $\underset{\sim}{G}$ are the horizontal accelerations (with a minus sign), namely

$$\underset{\sim}{G} = (-Du/Dt + fv + F_1;\ -Dv/Dt - fu + F_2) \tag{25}$$

The term H is given by (22) and from (21)

$$\underset{\sim}{A} = C_v(g\nabla_H \tilde{w} + \underset{\sim}{G}\partial \tilde{w}/\partial z - \partial \underset{\sim}{G}/\partial t - \tilde{w}(\partial \underset{\sim}{G}/\partial z) \tag{26}$$

We close this section by noting that considerable simplifications of the expressions for $\underset{\sim}{A}$, $\underset{\sim}{H}$, and F may be realized if either the approximation (11)' is used or pressure coordinates are utilized. In that latter case (11)" may be employed. While we have shown that the above approximations are for the most part reasonable, we prefer the use of the more exact forms because the numerical solution of (23) and (24) does not become easier when (23) is replaced by (11)' or (11)" and approximate forms for $\underset{\sim}{A}$ and $\underset{\sim}{H}$ are utilized.

Retrieval of the virtual temperature from the wind and radiances. Relations (23) and (24) contain information about spatial gradients of the virtual temperature. From this, as is discussed e.g., in GAL-CHEN (1978), a second-order three-dimensional Poisson-like partial differential equation for T_v may be obtained. To be solved in a limited domain, the boundary conditions (BC) need to be prescribed. GAL-CHEN (1978) has shown that Neumann-type boundary conditions (i.e., conditions on the virtual temperature gradient in the direction of the normal to the boundary) may be obtained from the observed wind (essentially from the components of $\underset{\sim}{H}$ and $\underset{\sim}{G}$ in the direction of the normal). Such a procedure appears to be better than using Dirichlet-type BC which require the specification of the virtual temperature itself on the boundaries. In the absence of radiosonde information, Dirichlet-type BC are usually known very crudely (either from radiometric data or from a guess from a larger scale model).

Regardless of what type of BC are used, the use of (23) and (24) may not be optimal because it does not utilize the radiances from the infrared and microwave channels. Also, retrieval techniques based solely on (23) and (24) tacitly assume that the formulation of the dynamical equation (1)-(7) are infallible, i.e., that the retrieval errors of the virtual temperature would be attributed solely to observational uncertainties about the wind.

We shall now proceed to develop a formulation which incorporates the observed radiances into the retrieval procedure. We start by noting that the radiative transfer equation may be reduced often to a Fredholm intergral equation of the first kind (e.g., WESTWATER and STRAND, 1972), namely,

$$\int_0^\infty B_\nu(T)K(\nu,z)dz = \tilde{I}_\nu \tag{27}$$

Here, ν is the frequency, $B_\nu(T)$ is the flanck function, K are the weights and $\tilde{I}_\nu$ are observed radiances. The surface temperature contributions are included in the r.h.s. of (27). These contributions can be determined from the "window channel" measurements for space-borne radiometers and from the "big bang" cosmic background of 2.9°K for ground-based observations. For a well mixed gas, the function $K(\nu,z)$ is known except perhaps for a small temperature dependence. Traditional methods of determination of vertical temperature profile rely on solving (27) for various channels (frequencies) having different weights $K(\nu,z)$. Thus, the contributions from different height layers can be varied and a degree of height resolution can be achieved. Extensive research (e.g., CHESTERS et al., 1982) have demonstrated the limitations of such inversion techniques. In essence, the kernel $K(\nu,z)$ acts as a vertical smoother (low pass filter). As a result, the retrieved temperature profile has a poor vertical resolution (at least in the troposphere). However, if (27) is combined with (23) and (24) the problem of vertical resolution is eliminated. In essence, the large vertical scales may be determined from (27) and the smaller vertical scales, which cannot be resolved by (27) would be determined from (23) and (24).

Before we proceed with further mathematical developments of the idea outlined above, we note that (27) has been formulated for temperatures while (23) and (24) are valid for virtual temperature gradients. Furthermore, as has been noted before, the moisture contributions to the gradient may be

important. To express (27) in terms of the virtual temperature, observe that a Taylor expansion of $B_\nu(T_v)$ around T_ν taking into account (9) and the smallness of the virtual temperature correction would result in

$$B_\nu(T_v) = B_\nu(T) + (\partial B_\nu/\partial T)0.61\ qT \tag{28}$$

Now, the second term in the r.h.s. of (28) while small compared to the first, may not be neglected if we desire at least $\pm$ 1°K accuracy for temperature retrievals; nevertheless, we may substitute the radiometers first guess about the moisture and temperature in the second term. To justify this approximation, let us denote by $\delta()$ the first guess retrieval errors. We may recall that $\delta q = \pm 6\ gkg^{-1}$ and $\delta T = \pm 3°K$. We also know that, $T \sim 300°K$ and (for the lower troposphere) $q \sim 10\ gkg^{-1}$. Therefore, substituting the radiometers first guess in the second term of the r.h.s. of (28) would result in virtual temperature error δT_v of the order

$$\delta T_v = 0.61\ q\delta T + 061\ T\delta q$$

Taking into account the order of magnitude of the various terms, the error is at most $\pm$ 1°K. Furthermore, the contribution of this error to the radiances [$\tilde{I}_\nu$ in (27)] is further reduced due to the averaging implied. Overall, we may substitute (28) in (27) approximating the second term in the r.h.s. of (28) by the radiometers first guess with the net result

$$\int_o^\infty B_\nu(T_v)K(\nu,z) = I_\nu \tag{29}$$

where the moisture correction to the radiances $\tilde{I}_\nu$ have been absorbed in the term I_ν.

The general retrieval algorithm may now be formulated as follows: Find a T_v such that

$$\iiint[(g\nabla_H + \tilde{G}\partial/\partial z)\ln T_v - \partial\tilde{G}/\partial z]^2 + (\tilde{A}\partial \ln T_v/\partial z - \tilde{H})^2 = \text{Min} \tag{30a}$$

subject to the constraint that

$$\int_o^\infty B_\nu(T_v)K(\nu,z)dz = I_\nu \tag{30b}$$

This is a familiar calculus of variation problem (COURANT and HILBERT, 1953, Vol. 1, pp. 164-274) whose solution will not be discussed here. We note, however, that (30-a,b) attempts to satisfy the dynamical equations in the least square sense while enforcing the retrieved virtual temperature to satisfy everywhere the radiative transfer equation.

A potential weakness of the retrieval algorithm is that the terms $\tilde{A}$ and $\tilde{H}$ involves calculating higher order derivative terms in both space and time. The estimate of such terms from the observed wind and its time history may be "noisy". To alleviate this problem one may use the Kalman filter approach (GHIL et al., 1980) where observations at more than two (or three) time levels are used to improve the estimate obtained from the solution of (30-a,b). Detailed examinations of the terms involved in (30-a,b) reveal that for the most part only two time levels are required. The calculation of $\tilde{A}$ (equation 26) requires knowledge of $\partial\tilde{G}/\partial t$. Since $\tilde{G}$ is acceleration, this requires knowledge of the wind at three time levels. Nevertheless, $\partial\tilde{G}/\partial t$ would be dropped out if we utilize pressure coordinates and relation (11)" or use the approximate form (11)'. As noted earlier (11)" is exact but the use of pressure as a vertical coordinate requires some a'priori knowledge of the pressure distribution.

REFERENCES

Atlas, D., and O. W. Theile (1981), Precipitation Measurements from Space. Workshop Report, NASA Goddard Space Flight Center, available from NASA Goddard Laboratory for Atmospheres, Greenbelt, MD 20071.

Brummer, R., R. Bleck, and M. A. Shapiro (1984), The potential use of atmospheric profilers in the short-range prediction, Proc. Second Int. Symp. Nowcasting, 3-7 Sept., Norrkoping, Sweden, ESA SP-208, European Space Agency, Paris, 209-212.

Chesters, D., L. W. Uccellini, and A. Mostek (1982). VISSR Atmospheric Sounder (VAS) simulation experiment for a severe storm environment, Mon. Wea. Rev., 110, 198-206.

Courant, R., and D. Hilbert (1953), Methods of Mathematical Physics, 1, Interscience, 561 pp.

Doviak, R. J. (1981), A survey of radar rain measurement techniques, in Precipitation Measurements from Space. Workshop Report, edited by D. Atlas and O. W. Thiele, NASA Goddard, D-105-D121, available from NASA Goddard Laboratory for Atmospheres, Greenbelt, MD 20771.

Gage, K. S., and B. B. Balsley (1978), Doppler radar probing of the clear atmosphere, Bull. Am. Meteorol. Soc., 59, 1074-1093.

Gal-Chen, T. (1978), A method for the initialization of the anelastic equations: Implications for matching models with observations, Mon. Wea. Rev., 106, 587-696.

Gal-Chen, T., and R. A. Kropfli (1984), Buoyancy and pressure perturbations derived from dual-Doppler radar observations of the planetary boundary layer: Applications for matching models with observations, J. Atmos. Sci., 41, 3007-3020.

Ghil, M., S. Cohn, J. Tavantzis, K. Bube, and E. Isaacson (1980), Application of estimation theory to numerical weather prediction, Seminar 1980 Data Assimilation Methods, September 15-19, 1980, published by the European Centre for Medium Range Weather Forecasting, Reading, UK, 249-334.

Hane, C.E., and B. Scott (1978), Temperature and pressure perturbations within convective clouds derived from detailed air motion information, Preliminary testing, Mon. Wea. Rev., 106, 654-661.

Hane, C. E., and P. S. Ray (1985), Pressure and buoyancy fields derived from Doppler radar data in tornadic thunderstorms, J. Atmos. Sci., 42 18-35.

Haltiner, G. J., and R. T. Williams (1980), Numerical Prediction and Dynamic Meteorology, Wiley, 477 pp.

Hess, S. L. (1959), Introduction to Theoretical Meteorology, Holt, Rhinehart and Winston, 362 pp.

Kropfli, R. A., (1984), Turbulence measurements from particulate scatter in the optically clear unstable boundary layer using single Doppler radar, Preprints 22nd Conf. on Radar Meteorology, Zurich, Switzerland, Am. Meteorol. Soc., 495-500.

Kuo, Y.-H., and R. A. Anthes (1985), Calculations of geopotential and temperature fields from an array of nearby continuous wind observations, J. Atmos. Oceanic Tech., 2, 22-34.

Little, C. G. (1982), Ground-based remote sensing for meteorological nowcasting, in Nowcasting, edited by K. A. Browning, Academic Press, 65-85.

Nastrom, G. P., W. L. Ecklund, and K. S. Gage (1985), Direct measurements of large scale vertical velocities using clear-air Doppler radars, Mon. Wea. Rev., 113, 708-718.

Roux, F., J. Testud, M. Payen, and B. Pinty (1984), West African squall line thermodynamics structure retrieved from dual-Doppler radar observations, J. Atmos. Sci., 41, 3104-3121.

Smagorinsky, J. (1974), Global atmospheric modeling and the numerical simulation of climate, in Weather Modification, edited by W. N. Hess, Wiley, 631-686.

Pedlosky, J. (1979), Geophysical Fluid Dynamics, Springer, 624 pp.
Westwater, E. R., and O. N. Strand (1972), Inversion techniques, in Remote Sensing of the Troposphere, edited by V. E. Derr, National Oceanic and Atmospheric Administration, USA Superintendent of Documents, USA Government Printing Office, Washington, D. C., 16-1-16-13.
Westwater, E. R., W. Zhenhui, N. C. Grody, and L. M. McMillin (1985), Remote sensing of temperature profiles from a combination of observations from the satellite-based microwave sounding unit and the ground-based profiler, J. Atmos. Oceanic Tech., 2, 97-109.

1.2.1 EXAMPLES OF MESOSCALE STRUCTURES AND SHORT-TERM WIND VARIATIONS DETECTED BY VHF DOPPLER RADAR

G. S. Forbes

Department of Meteorology
The Pennsylvania State University
University Park, PA 16802

INTRODUCTION

The first of three wind profilers planned for operation in central and western Pennsylvania began full-time, high-quality operation during July 1985. It is located about 20 km south-southeast of University Park and operates at 50 MHz. Another 50-MHz radar and a 400-MHz radar are to be installed over the next few months, to complete a mesoscale triangle with sides of 120-160 km.

During the period since early July, a number of weather systems have passed over the wind profiler. Those accompanied by thunderstorms caused data losses either because the Department computer system lost power or because power went out at the profiler site. A backup power supply and an automatic re-start program will be added to the profiler system to minimize such future losses. Data have normally been averaged over a one-hour period, although there have been some investigations of shorter-period averaging. In each case, preliminary examinations reveal that the profiler winds are indicative of meteorological phenomena. The only occasions of bad or missing data are obtained when airplane noise is occasionally experienced and when the returned power is nearly at the noise level, at the upper few gates, where a consensus wind cannot be determined. Winds are being examined in high-resolution (close range) mode and low-resolution (far range) mode. Range gates are separated by about 290 m in the former and about 870 m in the latter. For the types of examples presented in this paper, with emphasis on mesoscale variations, illustrations below are normally taken from the high-resolution data.

SUMMARY OF ANALYSIS SCHEME DEVELOPMENT

Before the first Penn State profiler began operation, much effort was put into the development of analysis and display schemes. These were first tested on data obtained on tape from the Fleming radar of the Wave Propagation Laboratory. Some of these techniques are illustrated with Penn State data in the sections that follow. Among the schemes developed are:

- Power spectra displays
- Tabulations of wind components, returned power, consensus statistics
- Displays of u and v component vertical profiles
- Time-height section displays of u, v, velocity vectors, wind speed, wind direction, returned power
- Time series displays of u, v, wind speed, wind direction at a selected level
- Tabulations of vertical wind shear and component normal to the shear vector
- Tabulations and profile displays of temperature gradient, temperature advection, stability gradient, and stability advection
- Hodograph displays

In the temperature gradient, temperature advection, stability gradient, and stability advection calculations, it has been assumed, as a first approximation, that the vertical shear of the wind is in geostrophic (i.e., thermal wind) balance, even though the individual winds themselves may have an ageostrophic component. The idea of computing the shear vector at various

levels and the wind components normal to these shear vectors is that (1) many atmospheric banded features are oriented along the shear vector and (2) these features are steered by the normal component of the mean wind in the layer.

CONFLUENCE ZONE ALONG WEST SIDE OF WARM CONVEYOR BELT

On 27 August 1985, at about 1400 GMT, a sharp wind shift occurred at the 8-9 km levels (Figure 1). The wind shift was accompanied by the passage of a narrow band of cirrus clouds that marked the western edge of a warm conveyor belt which was only partially filled with clouds. There was also a marked decrease in wind speed at this time. While satellite imagery showed a near discontinuity at this time, conventional upper-air analyses (Figure 2) did not indicate that a wind shift would be expected over Pennsylvania. In fact, a much more marked wind shift was evident across central Ohio. Knowledge of the profiler wind would have allowed for a better interpretation of the hints of a trough axis near Buffalo, New York, by allowing for a diagnosis that the main part of the trough was negatively tilted (from near Buffalo to central Pennsylvania) and was "lifting out" rapidly toward the northeast, leaving behind the southern, positively tilted portion of the trough from central Ohio to Tennessee and Louisiana. This shearing of the trough became apparent on the next upper-air charts 12 hours later.

TAIL OF COMMA CLOUD

The extreme southern end of the tail of a comma cloud pattern passed over the profiler at about 1000 GMT on 19 August 1985. Its approach was accompanied by a weak trough (backing) in the wind field, and a sudden clockwise shift (veering) of the wind at its rear edge (Figure 3). The comma was accompanied by a wind speed maximum. The data suggest that the trough line was nearly vertical from surface to upper troposphere.

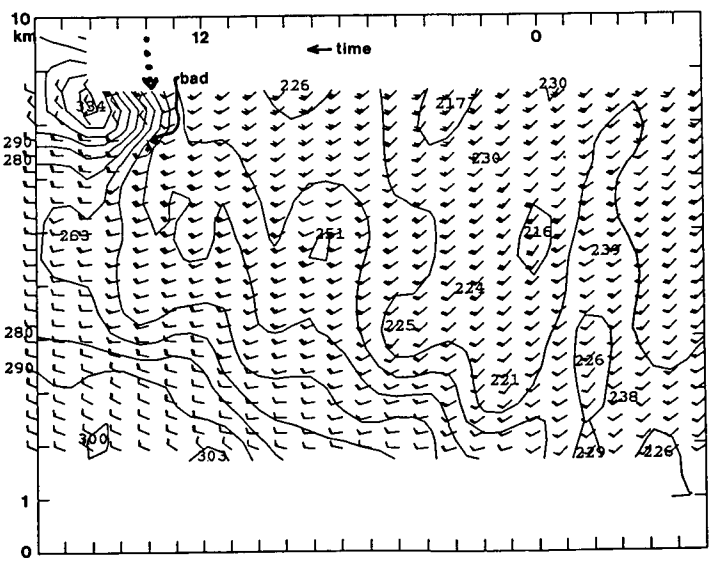

Figure 1. Time-height section of hourly wind vectors (one barb equals 5 m/s) and isopleths of wind direction from 1800 GMT on 26 August 1985 (right) to 1800 GMT on 27 August 1985 (left). Dots indicate cloud band.

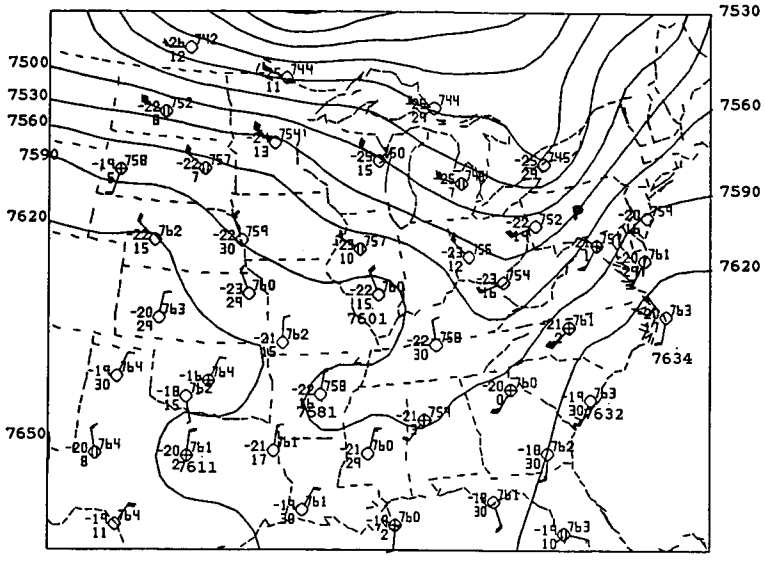

Figure 2. Upper-air chart of the 400 m surface at 1200 GMT on 27 August 1985. Winds are in knots, and a flag is approximately 5 m/s.

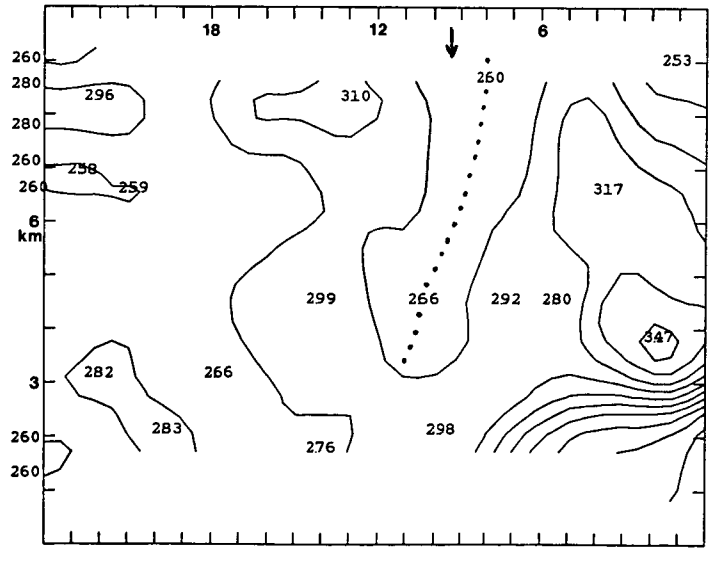

Figure 3. Isopleths of wind direction from 0000 GMT on 19 August 1985 (right) and hourly to 0000 GMT on 20 August 1985. Trough line is shown by dots, and center of comma cloud tail by arrow.

MINOR TROUGH AND CLOUD BAND

During the morning hours of 19 September 1985 an unexpected thin patch of clouds drifted across central Pennsylvania. These accompanied a rather dramatic pattern of wind shifts shown in Figure 4. The clouds occurred near the axis of a minor short wave trough at the 3-5 km levels from about 0500-1300 GMT, marked by a shift of the winds from N or NW to almost westerly before veering back to north. There was no reason to expect this trough, based upon the previous 0000 GMT upper-air charts (Figure 5).

Some other types of displays are illustrated in Figures 6-9. Figure 6 is a vertical profile of geostrophic temperature advection at 0600 GMT on 19 September. Note that veering and backing of the winds indicate warm/cold advection by the geostrophic wind. Figure 7 is a hodograph of the low-resolution (far range) winds at this time. Figure 8 shows an overlay of three vertical profiles of the v component of the wind at 0000, 0600, and 1200 GMT on 19 September 1985. Figure 9 is a time series of the u component of the winds at 5.12 km MSL from 0000 to 1800 GMT on 19 September 1985. Each of these displays reveals that the temporal and spatial variations of the wind are rather systematic and contain little apparent noise.

JET STREAM AND WARM CONVEYOR BELT

The rear edge of a warm conveyor belt cloud pattern passed over the profiler at about 1200 GMT on 20 August 1985. Wind speeds were high within the conveyor belt (Figure 10), in excess of 25 m/s at the 8-km level, and decreased rapidly as the west edge of the cloud pattern passed. Wind directions also began to veer abruptly aloft (Figure 11) as the edge of the clouds passed.

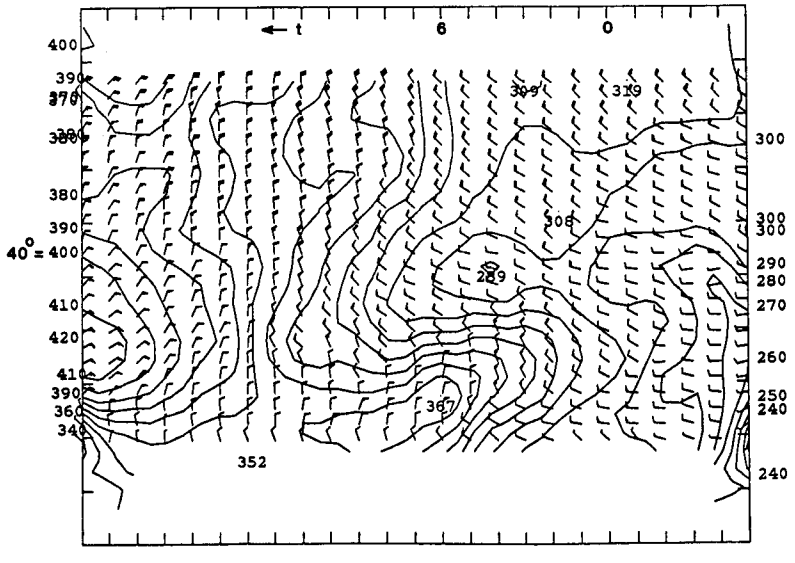

Figure 4. Time-height section of hourly wind vectors and isopleths of wind direction from 1900 GMT on 18 September 1985 (right) to 2900 GMT on 19 September 1985. Vertical scale is 0-10 km at 1-km intervals.

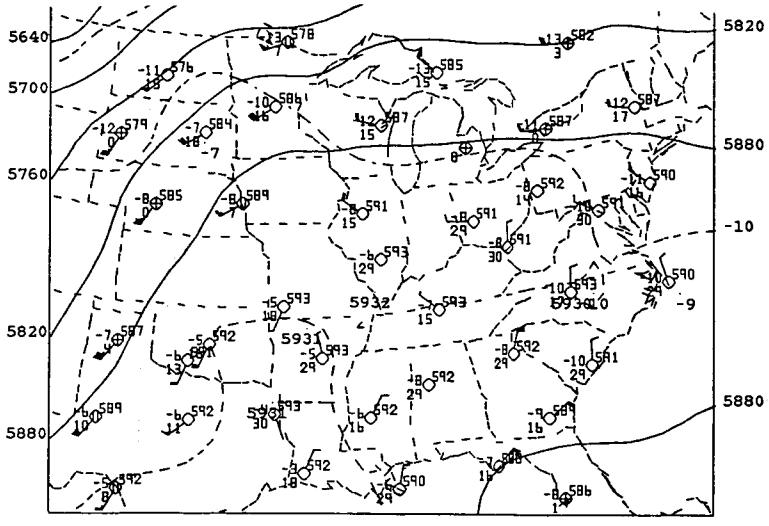

Figure 5. Upper-air chart of the 500-mb surface at 0000 GMT on 19 September 1985.

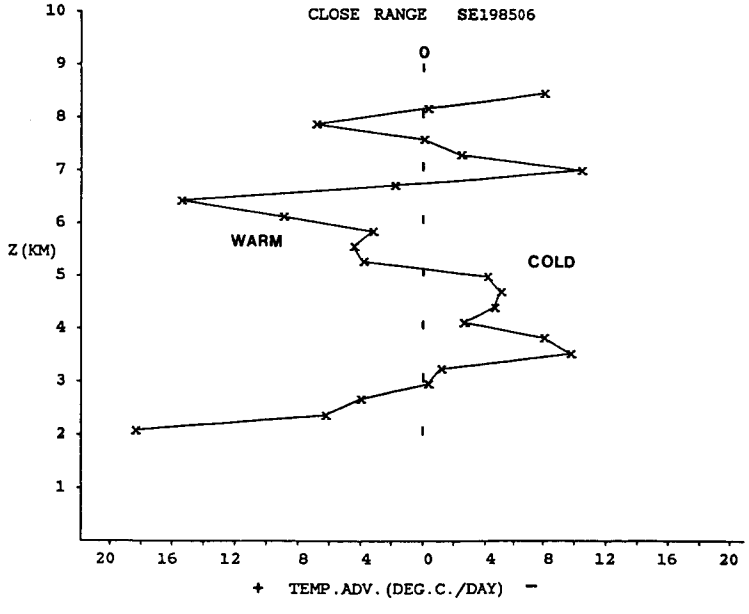

Figure 6. Vertical profile of geostrophic temperature advection at 0600 GMT on 19 September 1985.

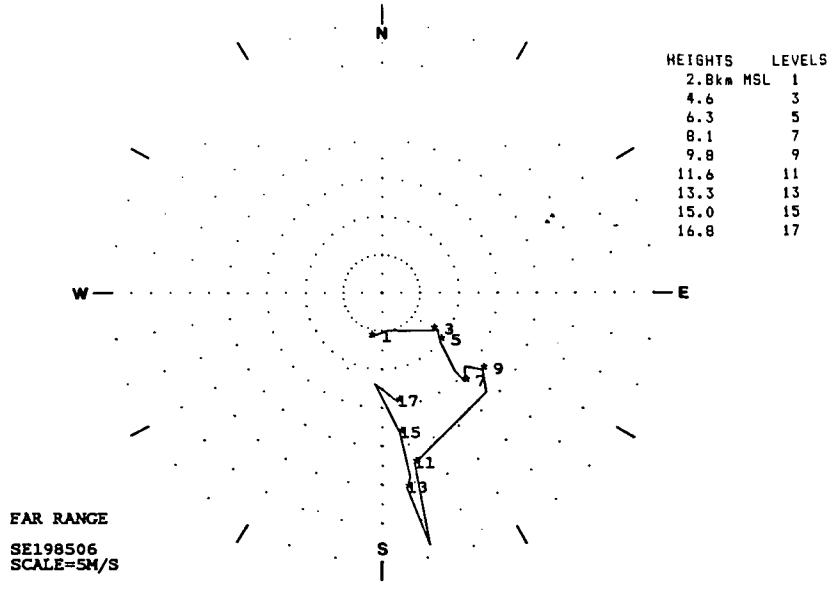

Figure 7. Hodograph of the low-resolution (far range) winds at 0600 GMT on 19 September 1985.

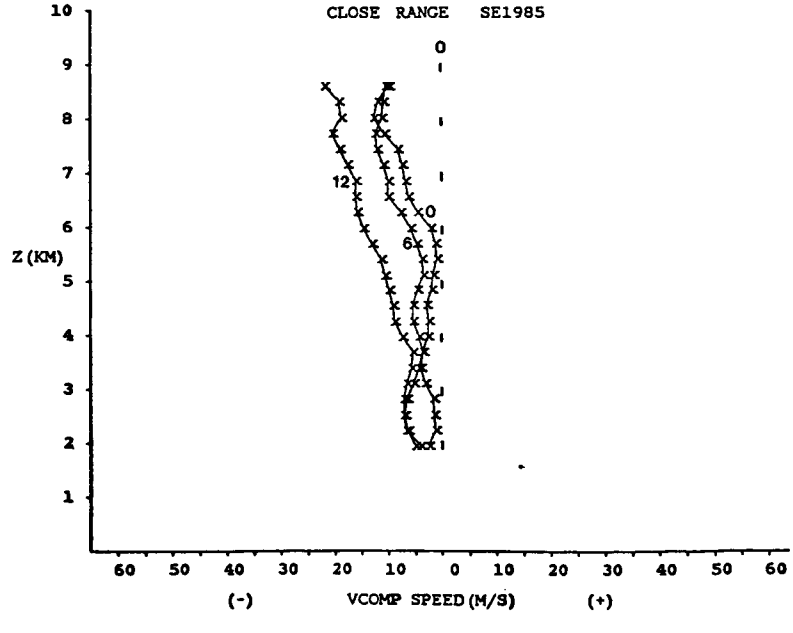

Figure 8. Sequence of vertical profiles of the v (north-south) component of the wind at 0000, 0600, and 1200 GMT on 19 September 1985.

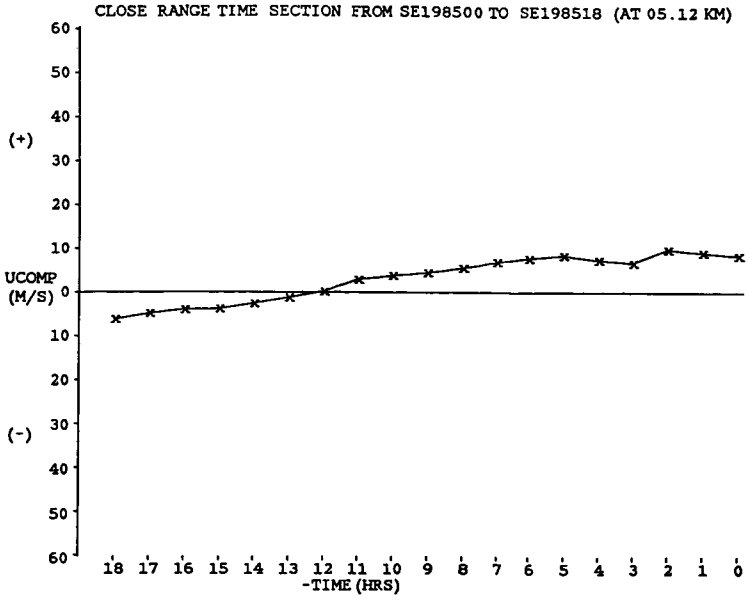

Figure 9. Time series of the u (east-west) component of the wind at 5.12 km MSL from 0000 GMT (right) to 1800 GMT (left) on 19 September 1985.

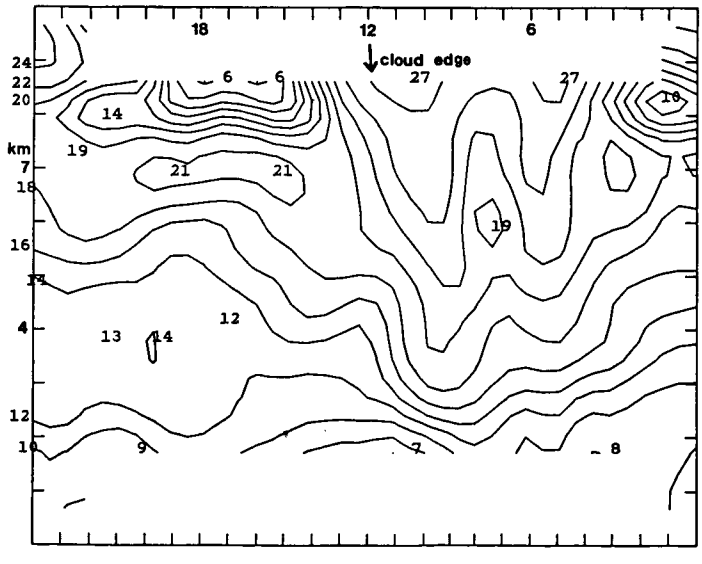

Figure 10. Time-height section of the wind speed (m/s) from 0000 GMT 20 August 1985 (right) to 0000 GMT 21 August 1985 (left).

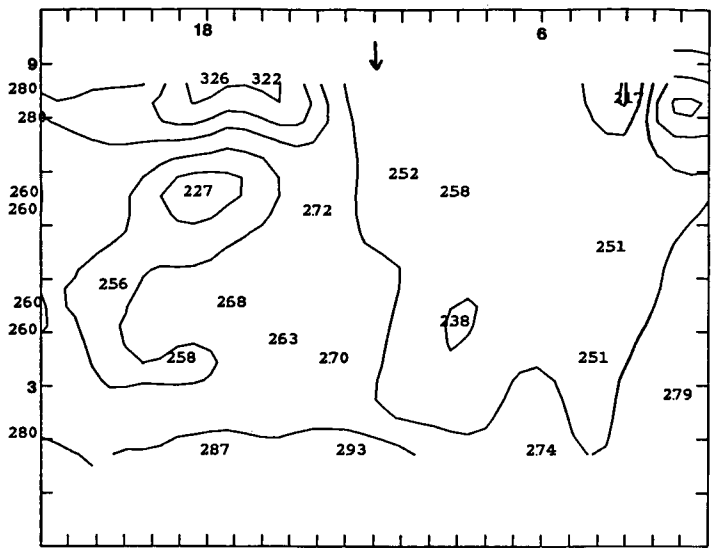

Figure 11. Time-height section of the wind direction from 0000 GMT 20 August to 0000 GMT 21 August 1985.

COUPLED UPPER AND LOWER JET STREAK CIRCULATIONS

The exit region of an upper-tropospheric jet streak began to affect the profiler about 1100 GMT on 1 September and apparently had maximum impact at low elevations at about 1600 GMT. While there was little speed increase at the 2.5-km level, there was a marked backing of the flow to a direction from the southwest (Figure 12), becoming almost normal to the prevailing flow in this region to the west side of the trough axis. There had also been a previous jet streak, which passed over the profiler at about 0600 GMT on 1 September (Figure 13). The flank of the secondary streak passed the profiler at about 1900 GMT.

The response of low-level winds to upper-tropospheric jet streaks has been discussed by UCCELLINI and JOHNSON (1979). Briefly, at low levels beneath the exit region of an upper-tropospheric jet streak there is an indirect vertical circulation and a transverse flow toward the cold side of the jet. In this case, the transverse flow was from the southwest since the jet stream was from the northwest.

UNEXPECTEDLY SHARP RIDGE AXIS

Figure 14 shows a rather rapidly evolving pattern of wind directions, even if the noise in the upper left is ignored. The winds progressively evolved from easterly to southeasterly at elevations below about 5 km MSL. At about 6 km, it can be deduced that the high-pressure center passed just to the north of the profiler, allowing winds to retain an easterly component throughout the period and to shift from ENE to ESE (compare to Figure 15, the 500 mb chart).

DIURNAL OSCILLATIONS/TRAVELLING MESOSCALE RIDGES

Pronounced wind variations have been observed during a quiescent period dominated by a quasi-stationary ridge axis located several hundred kilometers southwest of the profiler. Without cloud patterns to supply some independent mesoscale data, interpretation of the variations has been difficult. A good

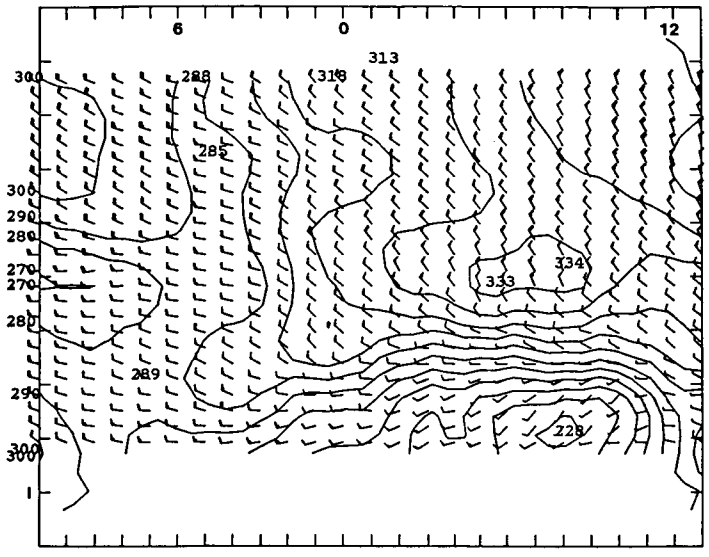

Figure 12. Time-height section of wind vector and wind directions from 0000 GMT on 1 September to 1100 GMT on 2 September 1985.

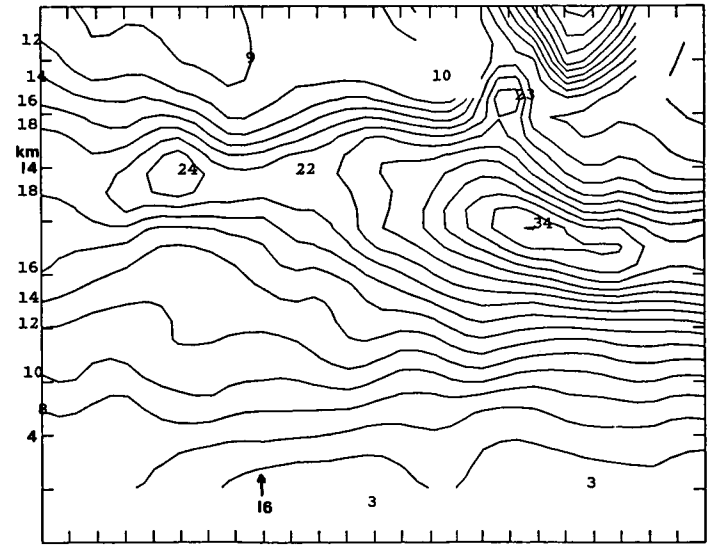

Figure 13. Far-range (low resolution) time-height section of wind speed from 0000 GMT on 1 September 1985 (right) to 0000 GMT on 2 September (left).

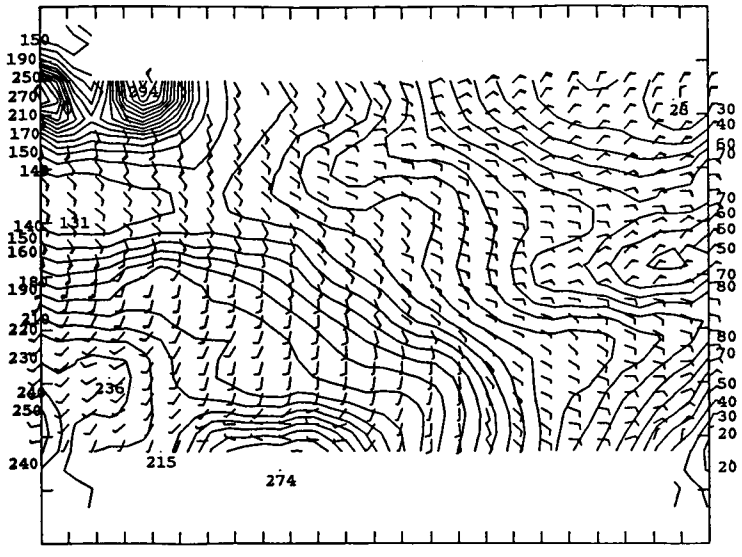

Figure 14. Time-height section of wind vectors and wind direction from 0000 GMT on 20 September 1985 to 0000 GMT on 21 September 1985.

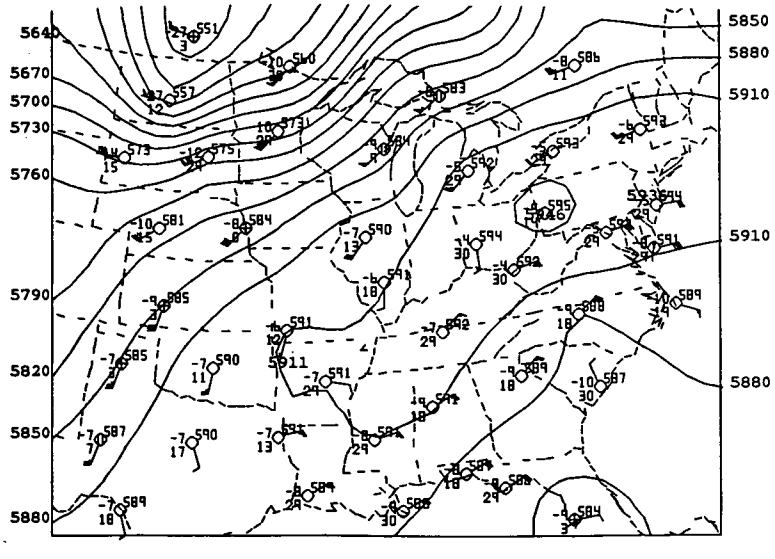

Figure 15. Upper-air chart of the 500-mb surface at 1200 GMT on 20 September 1985. Notice the high pressure system centered near Pittsburgh, PA.

example is the north/west/north pattern at about 3 km on Figure 16, with apparent period of about 18-19 hours. This is approximately the period of an inertial oscillation at the latitude of the profiler (about 41.5°N). It is, of course, well known that there is an oscillation of the wind induced by the diurnal mixing cycle (BLACKADAR, 1957), wherein winds that are subgeostrophic at the top of the boundary layer in late afternoon undergo an inertial oscillation during the nighttime and become supergeostrophic at some time before sunrise. In the case of Figure 16, the geostrophic winds were from the northwest, such that the wind oscillation shown appears to have the proper phase. However, there may also have been some substructure within the ridge, with short-wavelength ridges or lobes travelling around its periphery. As these approached, winds would become more northerly, and then become more westerly as the mesoscale disturbance passed to the south of the profiler. Upper-air observations were inadequate to definitively resolve these features, if they did exist.

HIGH-TEMPORAL-RESOLUTION DATA

Figures 17 and 18 show about one hour of profiler winds comprised of about 2-minute averages. There is obvious noise in the 3 upper gates and the contamination from aircraft near 6 km in the sixth profile. Some eddy-like variations can be seen in the lowest three gates during the early minutes. Otherwise, the 2-minute-sampled winds are quite steady. These winds were measured during a meteorologically quiescent period, which suggests that (1) random fluctuations may not pose a problem for short-term measurements, and (2) the potential exists for accurate measurement of short-term variations when mesoscale features are present. Research on this topic and on the application of VHF Doppler radar for nowcasting and very-short-term forecasting will continue.

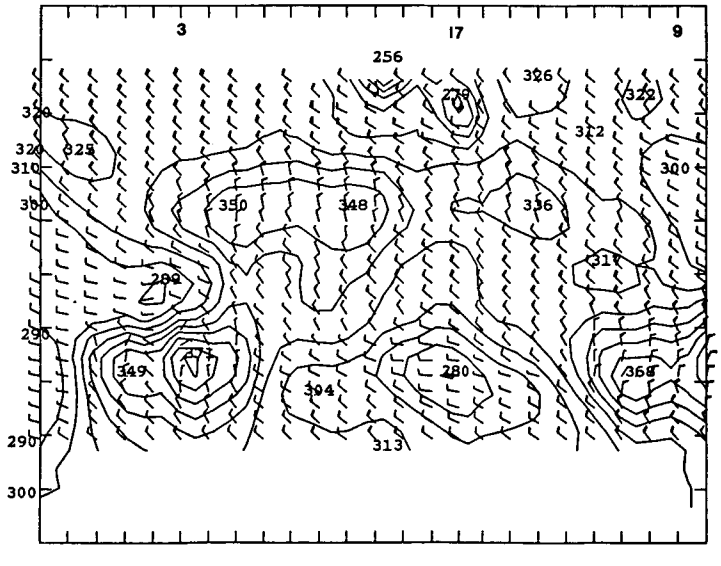

Figure 16. Time-height section showing oscillations in the wind direction during the period from 0800 GMT on 7 September to 0800 GMT on 8 September 1985.

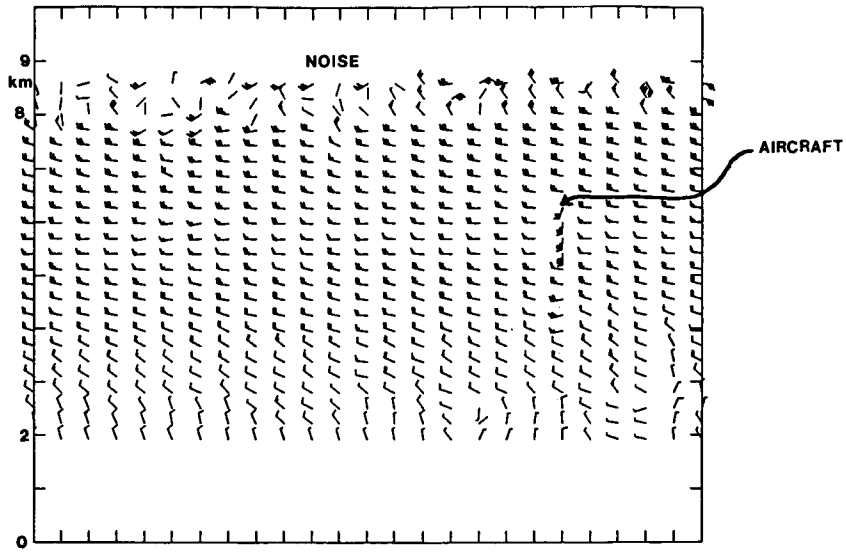

Figure 17. Time-height section of winds at about 2-minute intervals beginning about 0000 GMT on 12 September 1985.

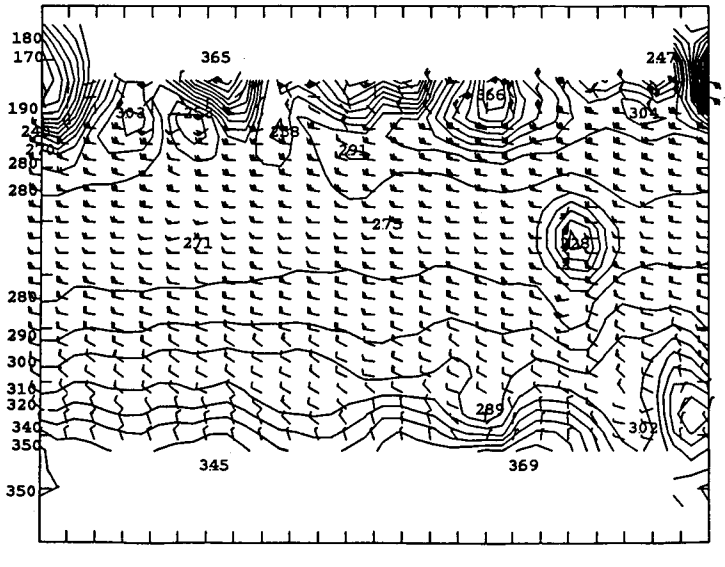

Figure 18. Time-height section of wind direction at 2-minute intervals beginning about 0000 GMT on 12 September 1985.

ACKNOWLEDGEMENTS

Art Person, Paul Neiman, Cathy Carlson, Scott Williams, John Cahir, Dennis Thomson, Chris Fairall, Bob Peters and others have contributed directly or indirectly to this research effort. The instrumentation acquisition and deployment has been supported by D.O.D. University Research Instrumentation Grant AFOSR-83-0275, and The Pennsylvania State University, which provided almost 30% of the funds. This research has been sponsored by the Air Force Geophysics Laboratory under contract F19628-85-K-0011.

REFERENCES

Blackadar, A. K. (1975), Boundary layer wind maxima and their significance for the growth of nocturnal inversions, Bull. Am. Meteorol. Soc., 38, 283-290.

Uccellini, L. W., and D. R. Johnson (1979), The coupling of upper- and lower-tropospheric jet streaks and implications for the development of severe convective storms, Mon. Wea. Rev., 107, 682-703.

1.2.2 WIND PROFILER DATA IN A MESOSCALE EXPERIMENT FROM A METEOROLOGICAL PERSPECTIVE

Edward J. Zipser

National Center for Atmospheric Research*
Boulder, Colorado 80307

John Augustine and John Cunning

Weather Research Program, Environmental Sciences Group
NOAA, Boulder, Colorado 80303

During May and June of 1985, the Oklahoma-Kansas Preliminary Regional Experiment for STORM-Central (OK PRE-STORM) was carried out, with the major objectives of learning more about mesoscale convective systems (MCSs) and gaining experience in the use of new sensing systems and measurement strategies that will improve the design of STORM-Central. Three 50-MHz wind profilers were deployed in a triangular array with sides about 275 km (Figure 1). There will be great interest in learning whatever we can from the profiler data from these sites, especially in relation to mesoscale weather systems. It is far too soon to report any results of this effort, for it has barely begun. The purpose of this paper is to show some examples of the data, some of the surrounding "conventional" data, to discuss some of the issues important to meteorologists in evaluating the contribution of the profiler data.

We concentrate on the case of 10-11 June 1985, featuring a major squall line system which crossed the dense observing network from northwest to southeast, passing the Liberal site about 2230 GMT/10 June, the McPherson site about 0100 GMT/11 June, and Wichita about 0300 GMT/11 June. Radar and satellite data show that the system was growing rapidly when it passed Liberal, and was large and mature when it passed through McPherson and Wichita. Figure 2 gives the radar depiction of the system during this stage, with the McPherson site in the intense convective echoes near the leading edge at 01 GMT and in the stratiform precipitation at 03 GMT.

Figure 3 (Liberal) and Figure 4 (McPherson) show the profiler wind data for a 9-hour period encompassing the squall line passage at each site. (Ignore obvious noisy data, which is not the subject of discussion here; the two systems have different antenna systems and sizes, different processing algorithms, and were passed by different parts of the storm system.) Both systems were unable to function during the 60-90 minutes of most intense thunderstorms. However, both clearly captured the major wind features ahead of and, more interestingly, in the mesoscale stratiform precipitation region which forms the rear half of the system. These include the northerly winds at low levels, the increased southerly component in the upper troposphere (mostly obscured by noise at McPherson) and a midlevel "jet" of inflow from the rear, sloping downward from northeast to southeast (upward with time). The same features are observed at nearby radiosonde sites, with Wichita chosen for illustration (Figure 5). It is appropriate to compare times at Wichita with those 2 hours earlier at McPherson to account for the later passage over Wichita.

The increased time resolution of the profiler data is extremely important in mesoscale research. One well-known problem is the difficulty of covering the lowest kilometer -- in this case as in others, the wind structure here is

*The National Center for Atmospheric Research is supported by the National Science Foundation.

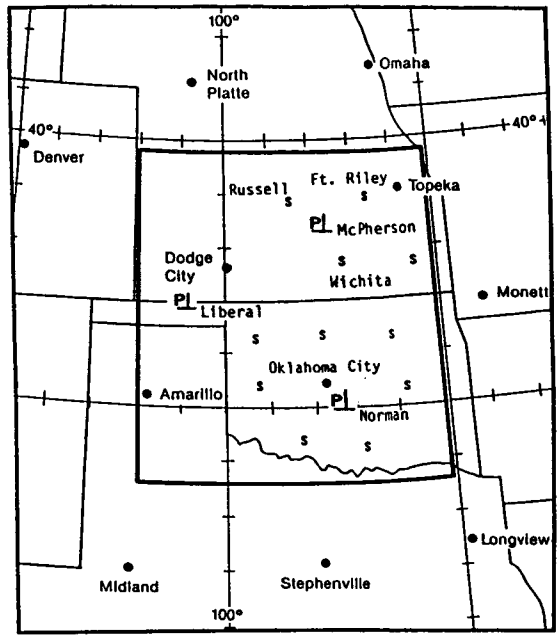

Figure 1. Location map for the wind profiler network in OK PRE-STORM, marked by "P" at Liberal, McPherson, and Norman. National Weather Service rawinsonde sites are given by black dots, and supplemental sites by "S"; those surrounding the McPherson site are named.

crucial to understanding the system. It is encouraging that the profiler appears to be defining the midlevel jet in a disturbed region; it will be important to establish reliability of the profiler data in the anvil outflow region nearer the tropopause, in view of the large area covered.

ACKNOWLEDGMENTS

We appreciate the efforts of Robert Ortiz in processing the data, Dave Jorgensen and Irv Watson in preparing the radar data, and Adrian Marroquin and Boba Stankov for graphics assistance. Thanks are due the NOAA Aeronomy Laboratory and the Radian Corporation for supplying samples of preliminary data on short notice.

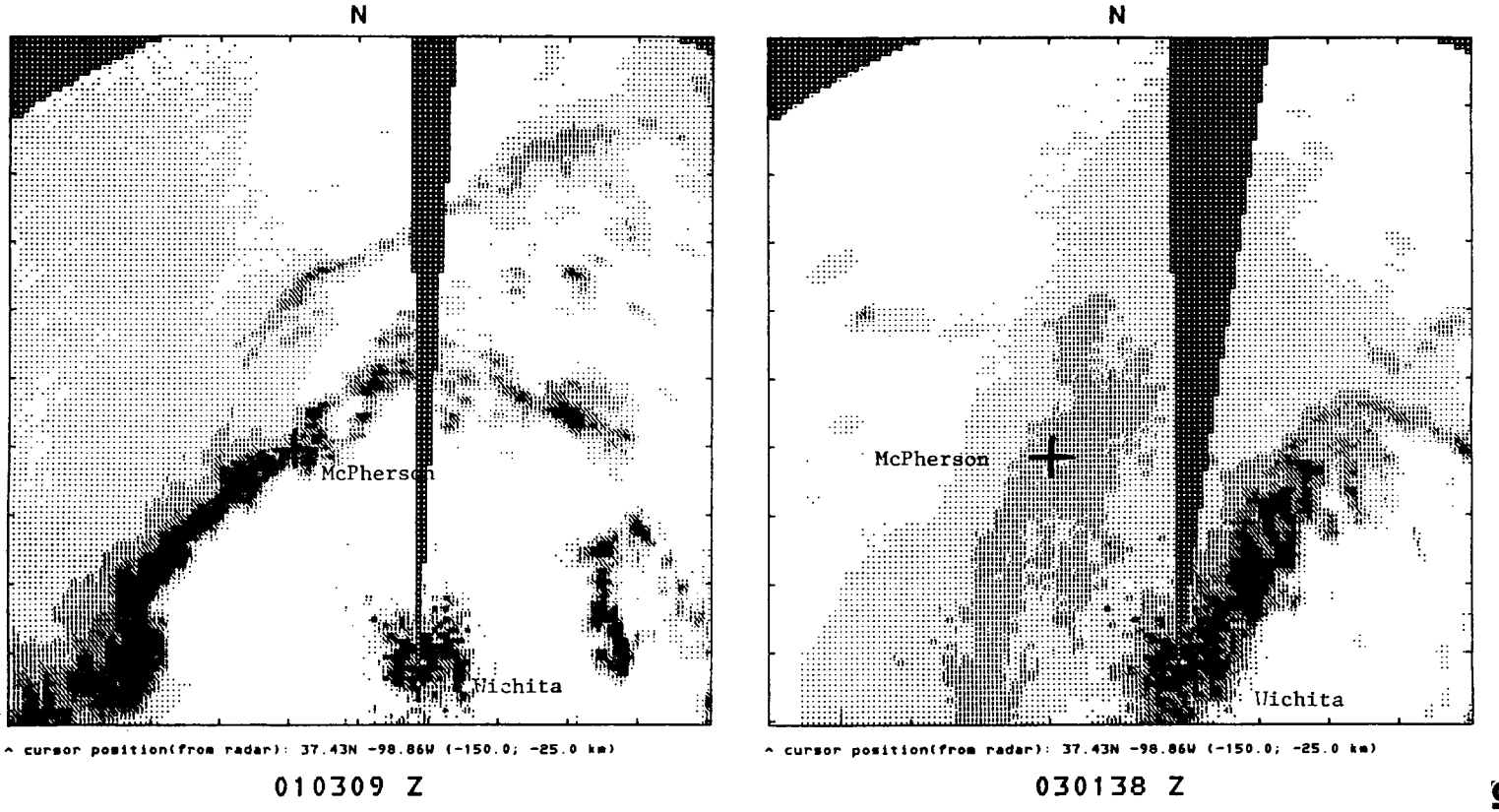

Figure 2. Digitized reflectivity display for the Wichita radar, located in the center of the ground clutter near the bottom of each frame. Each frame covers 256 x 256 km; the cross locates the McPherson site about 100 km northwest of Wichita. Lightest shading is above an 18 dBZ threshold; then at 30, 40, and 50 dBZ thresholds.

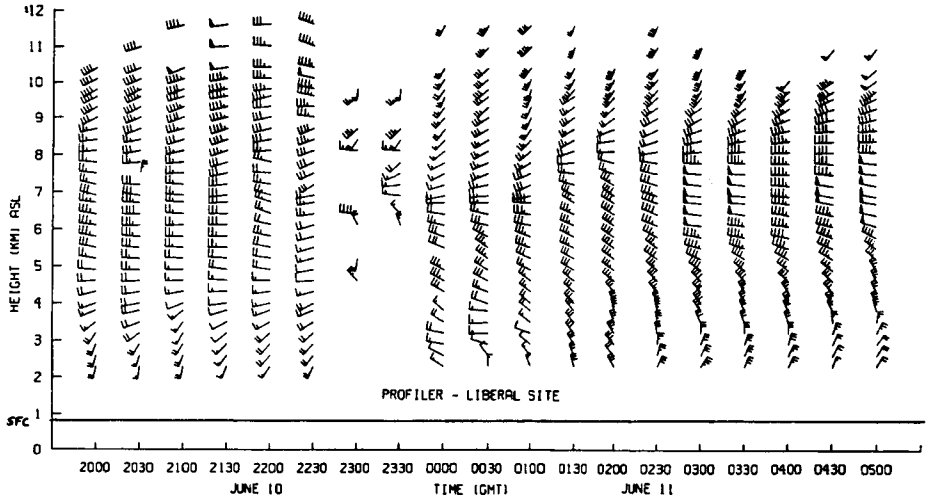

Figure 3. Time-height cross section of the Liberal wind profiler data. Each full barb is 5 m s^{-1}, each half-barb 2.5 m s^{-1}, and each flag 25 m s^{-1}.

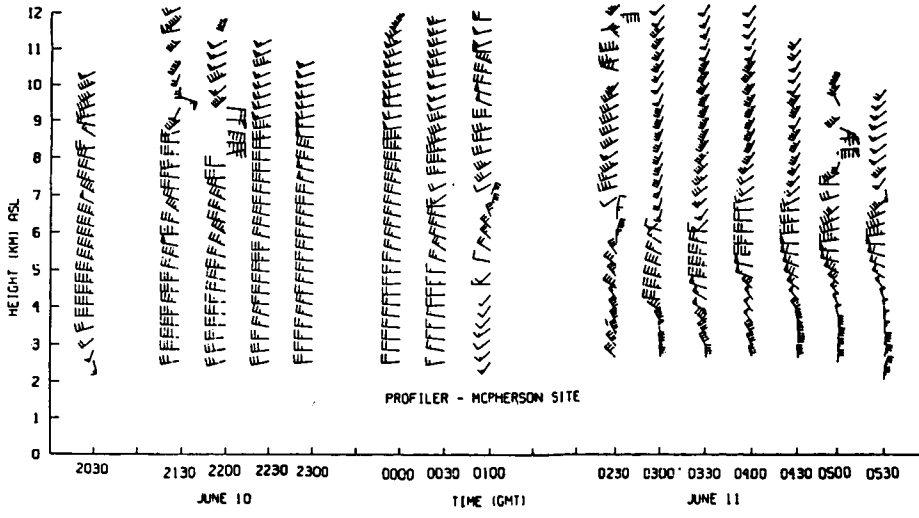

Figure 4. Time-height cross section of the Wichita radiosonde wind data. Legend for winds as in Figure 3.

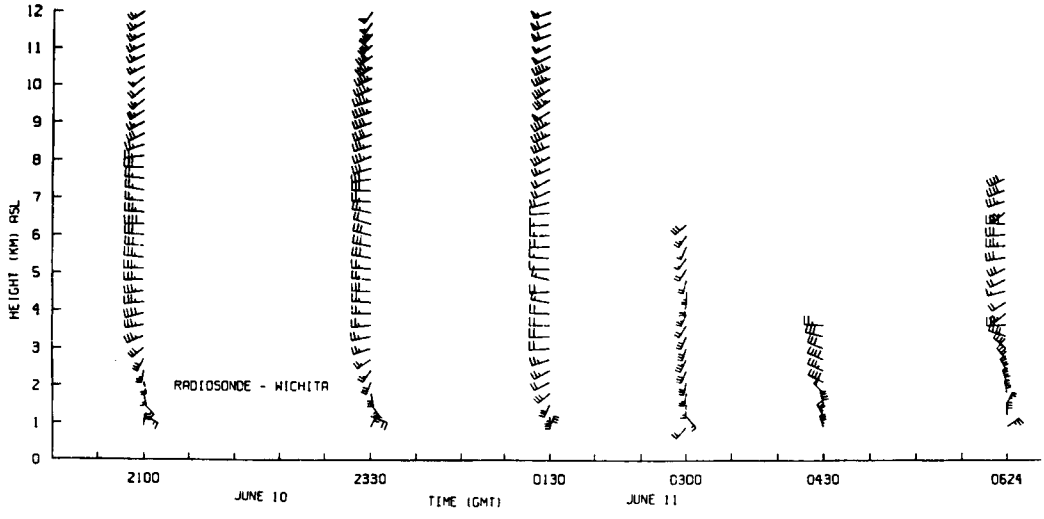

Figure 5. Time-height cross section of the Wichita radiosonde wind data. Legend for winds as in Figure 3.

1.2.3 OBSERVATIONS OF MESOSCALE VERTICAL VELOCITIES AROUND FRONTAL ZONES

T. S. Dennis, M. F. Larsen

Department of Physics
Clemson University
Clemson, South Carolina 29631

J. Rottger*

Arecibo Observatory
Box 995
Arecibo, Puerto Rico 00612

INTRODUCTION

We have analyzed vertical velocity and reflectivity data obtained with a VHF Doppler radar over a 15-day period in October and November of 1981 (DENNIS, 1985). Standard radiosonde data and surface observations have been used to locate two occluded fronts, two warm fronts, and a cold front that passed the radar site. These fronts are also evident in the radar reflectivity data.

Most studies of the vertical circulation patterns associated with mesoscale systems have used precipitation and cloud formations as tracers. Unlike other observational techniques, the VHF radar permits the continuous measurement of the three-dimensional air velocity vector in time and height from a fixed location. With the beam in a vertically pointing position, signals are scattered from turbulent variations in the refractive index with half the scale of the radar wavelength and by regions with sudden changes in the refractive index associated with horizontally stratified layers. Generally, the strongest echoes occur at the maximum in the vertical gradient of refractivity, usually at the base of a temperature inversion, such as the tropopause.

VHF radars can also be used to locate atmospheric fronts, which are characterized by static stability, large horizontal temperature gradients, large vorticities, and vertical wind shears (LARSEN and ROTTGER, 1982, 1983, 1984). Since these radars are not restricted to clear-air observations, they can provide the velocity field data needed to study wave motions associated with fronts and to compare the actual vertical circulation to theoretical predictions. These radars can provide data on the horizontal and vertical components of the wind with vertical resolution of approximately 150 to 300 meters and temporal resolution of about 1 minute.

DESCRIPTION OF THE DATA SET

The SOUSY VHF radar is located near Bad Lauterberg, West Germany, and is operated by the Max-Planck Institute. It is a pulsed coherent radar operating at a wavelength of 5.6 meters. From 1600 GMT on October 28 through 1400 GMT on November 12, 1981, the radar wind profiler was operated in the spaced antenna mode using 196 Yagi antennas for transmission and three arrays of 32 Yagi antennas for each reception. The spaced antenna technique uses vertically pointing transmitters and thus detects echoes with a higher signal-to-noise ratio than could be achieved with off-vertical beams. The applied average transmitter power for this experiment was 20 kW with a height resolution of

*On leave from Max-Planck-Institut fur Aeronomie, Katlenburg-Lindau, West Germany.

150 to 300 m and an effective antenna aperture of 2500 mB2. The height range is limited to 3.6 to 21.67 km due to the signal-to-noise levels. Approximately one minute is required for each profile, but the radar was not run continuously in order to reduce the amount of raw data. Throughout the period, data were taken for at least 12 minutes on the hour, but there were also two periods of continuous data taken so that five 12-minute averages per hour were available for a detailed view of approximately 30 hours beginning at 1600 GMT on October 28 and of approximately 24 hours beginning at 1500 GMT on November 4.

POTENTIAL TEMPERATURES AND RADAR REFLECTIVITIES

Potential temperatures and reflectivities are shown in Figures 1 and 2 with contours at 5-K and 3-dB intervals, respectively. The tropopause heights recorded by the radiosonde, represented as solid dots in each graph, agree with the levels indicated by the grouping of the potential temperature contours and by the higher reflectivity levels in these areas.

Frontal systems cause a packing in the potential temperature contour lines. The contours sloping downward from left to right represent warm fronts with upper-level effects occurring first while those sloping upward represent cold fronts. The use of radiosonde potential temperature contours only give the approximate location of frontal zones due to the poor time resolution. There are many unexplained deviations in the contours that may be the result of changes in the slopes of fronts or perhaps small fronts not established in the data analysis. By comparing the potential temperature contour groupings to breaks in the reflectivity contours, the location of frontal zones are more accurately established. The major disturbances include an occlusion, a warm front followed by a cold front, on October 29 and another occlusion on October 31; a warm front that arrives at the surface on November 3; a surface cold frontal passage on November 4; and a warm front that passed the surface on November 12. There are also two upper-level fronts that cause distinctive breaks in the reflectivity contours. The warm front on November 7 and 8

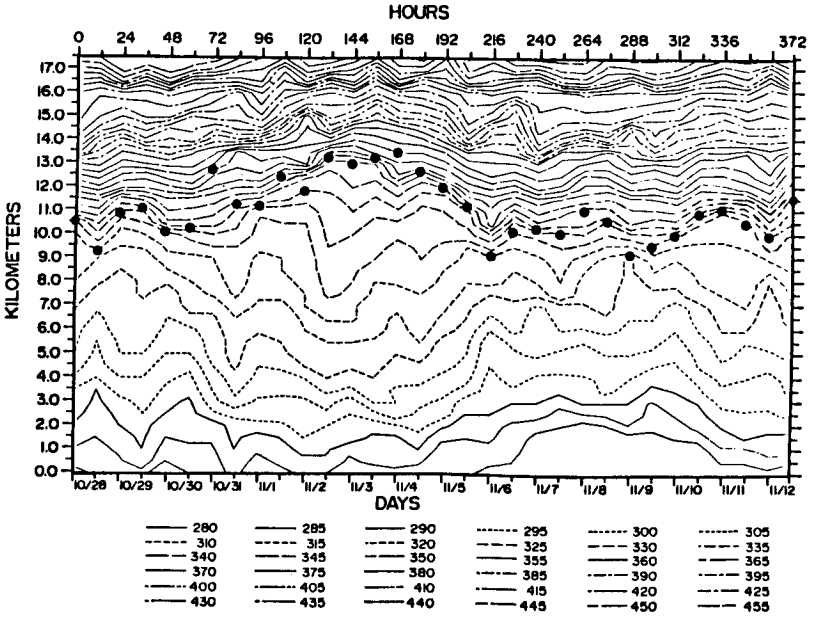

Figure 1. Potential temperature (K) with contours as indicated.

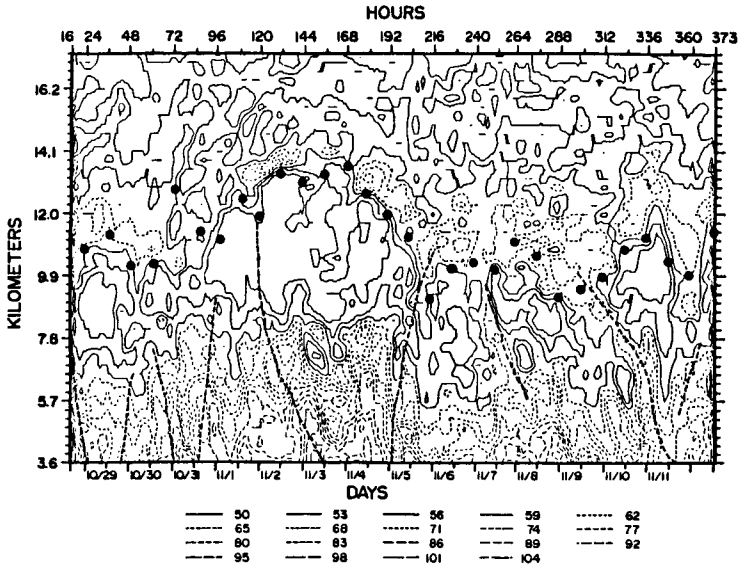

Figure 2. Radar reflectivity (dB) with contours as indicated.

stretches from 10 km down to 6 km, and the cold front on November 11 and 12 reaches up from 5 km to 8 km. These fronts have been sketched as dotted lines in Figure 2.

Beginning around October 30, the tropopause began to rise rapidly. There may even have been a separation of the lower tropopause as seen in the splitting of the potential temperature contour lines. The disturbance near the tropopause was present through November 4 and peaked around November 2. This phenomenon has all the characteristics of a tropopause fold, although the potential vorticity cross section will have to be calculated for confirmation.

VERTICAL VELOCITIES

The vertical velocities measured by the radar are contoured at 2-cm/s intervals with upward velocities graphed in Figure 3 and downward velocities graphed in Figure 4. The established fronts are drawn as dotted lines and the radiosonde tropopause levels are shown as solid dots. The most striking feature of these two graphs is the vertical stratification of the vertical velocities. Some regions are dominated by vertically stratified waves of upward velocities reaching to the top of the tropopause, while similar waves of downward velocity dominate other regions.

OCCLUSION

The occlusion on October 31 partially overlaps the less occluded front of October 29 and may cause variations in the normal occluded circulation patterns. There are waves of strong downward flow in the pockets between the warm and cold fronts, where a zone of rising air was expected to be found. The downward flow becomes more intense at lower levels in the occlusions with velocities reaching 26 cm/s at 3.6 km on October 29 and 40 cm/s at 4 km on October 31. A column of strong subsidence reaches 26 cm/s on October 30 between the two occluded fronts, which is expected of air beneath a cold frontal zone and beneath an approaching warm frontal zone.

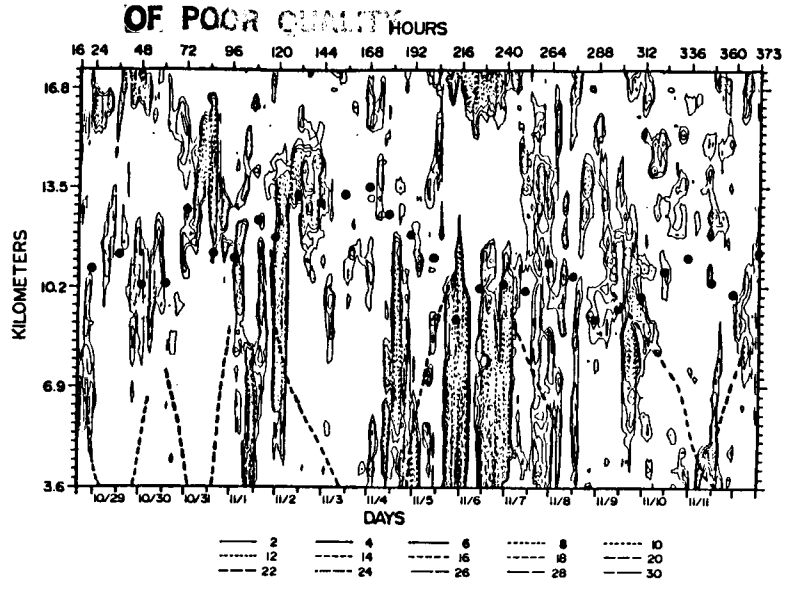

Figure 3. Upward velocity (cm/s) with hourly profiles and contours as indicated.

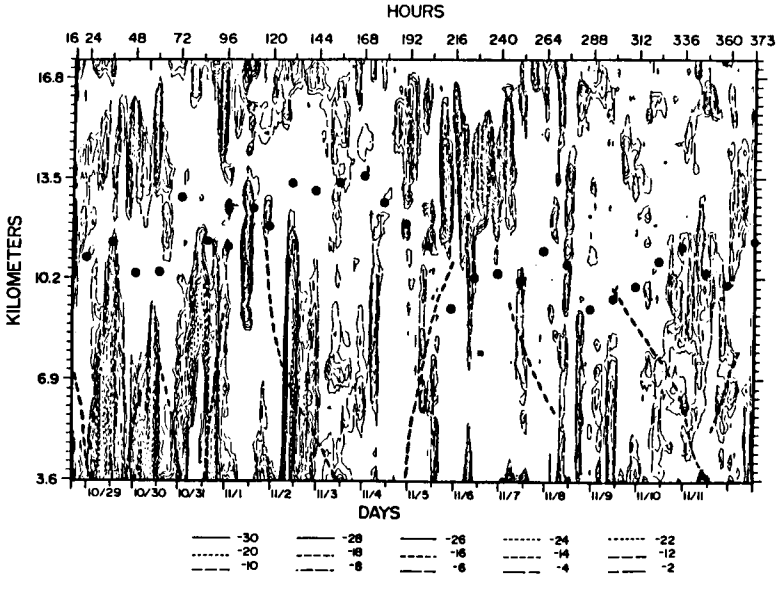

Figure 4. Downward velocity (cm/s) with hourly profiles and contours as indicated.

The occluded front is characterized by banded regions of subsiding air. There are several areas with strong downward velocity throughout the entire pocket of the occluded front at all levels of the troposphere. Two of these columns of air begin in the stratosphere around 1400 GMT and 1800 GMT on October 29. There are also cells of rising air alternating with cells of subsidence above the cold front. These cells frequently contain velocities up to 26 cm/s. The dominating downward flow in the occluded pocket, especially above the cold front, is an unexpected feature but could be caused by the complex circulation around the occluded frontal zone. The frequent intrusions of air across the tropopause is also an unexpected feature of the occlusion.

TROPOPAUSE FOLD

On November 2, the upward thrust of a column of air with wind speeds up to 16 cm/s seems to be the source of the tropopause rise. This region of rising air may be caused by the associated warm front. Immediately following this column of rising air is a strong downward flow of air which begins around 12 km just behind the warm front. This stratified region continues downward across the frontal zone where vertical wind speeds intensify up to 30 cm/s. The warm frontal zone may be the almost vertical boundary between the stratified columns of rising and subsiding air, but, when drawn in Figures 3 and 4 as derived from the reflectivity and potential temperature contours, the frontal zone appears to be located in the column of rising air at upper levels.

COLD FRONT

The cold front on November 4 and November 5 causes four or five columns of rising air, where the last two columns may be associated with the large warm front beginning on November 9 or with the upper-level front beginning on November 7. The first column arrives eight or nine hours before the cold front arrives at the surface, extends about ten or eleven hours past the surface arrival, and has upward velocities up to 12 cm/s. There are also smaller columns of rising and subsiding air on both sides of the major column.

The second column of air has stronger velocities than the first column and begins about 23 hours after the cold front begins at the surface. This column is beneath the cold frontal zone and has strong upward velocities at lower levels up to 20 cm/s and upper-level velocities of only 15 cm/s.

The third column begins about five hours after the second column ends and almost 40 hours after the surface frontal passage. Similar to the second column, the highest velocities are in the lower regions of the column. Velocities up to 20 cm/s are found in the lower levels compared to 10 cm/s in the upper levels. The upper-level warm front on November 7 extends into this column of air at about 9 km and thus influences the associated velocity patterns.

The fourth column of air begins about eight hours after the previous column ends and almost 70 hours after the initial cold front arrives at the surface. Even though the positive velocities in this region only approach 8 cm/s, the column stretches through the tropopause and into the stratosphere. The potential temperature contours in Figure 1 do not show any fluctuations caused by the passage of air through this region. The upper-level warm front extends through this column of air and may be the major influence in the vertical velocities in this region.

There are small columns of subsiding air between these columns of rising air, but none of these regions have the spatial extent of the first four columns. The downward velocities occur above and below the cold front and have velocities up to 30 cm/s in a region beneath 4 km on November 7. Unfortu-

nately, there are only 25 hours of continuous data associated with this frontal passage. Only the first column of rising air can be examined with these data.

"RAINBANDS"

With 12-minute velocity averages, the cold front on November 4 and November 5 can also be examined in more detail. The velocity data from 1500 GMT on November 4 through 1536 GMT on November 5 are graphed in Figures 5 and 6 with upward velocities and downward velocities, respectively, contoured at 2 cm/s intervals. The location of the cold front is sketched in the contours. This view of the cold front covers only the first of the five major columns of upward velocity pictured in Figure 3. The most striking feature is the banded structure of upward velocity that appears as only one column in the hourly data. The columns seem to decrease in height as the front moves through the area, but it is not clear how far beneath the front these columns extend. Areas of downward velocity are between these columns, while other downward bands extend across the front or are located beneath the front. One band of upward velocity around 1000 GMT on November 5 rises through the tropopause. Especially noticeable is the area of rising air towards the end of the data set. One region of rising air has velocities up to 35 cm/s centered around an intense cell near 10 km. Another cell of intense rising air lies below the cold front and possibly stretches across the front.

The detailed view of the cold frontal system in Figures 5 and 6 shows that even the large columns of rising air are composed of smaller, stratified regions. The vertical velocity structure around the cold front supports the rainband model shown in Figure 7 by HOBBS et al. (1980). The banded structure in Figure 3 contains a column in the warm region and columns straddling the frontal zone, as does the rainband model, but the horizontal dimensions of the columns in Figure 3 are much larger than those of the rainband model. The entire horizontal scale of the rainband structure is only about 175 km, compared to 300 km and 200 km for the first two columns of rising air for the

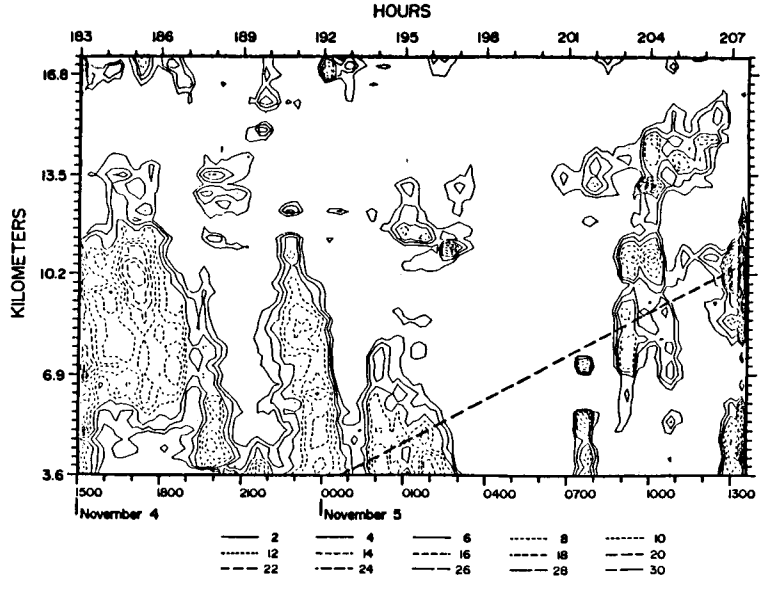

Figure 5. Upward velocity (cm/s) for the cold front with 12-minute profiles and with contours as indicated.

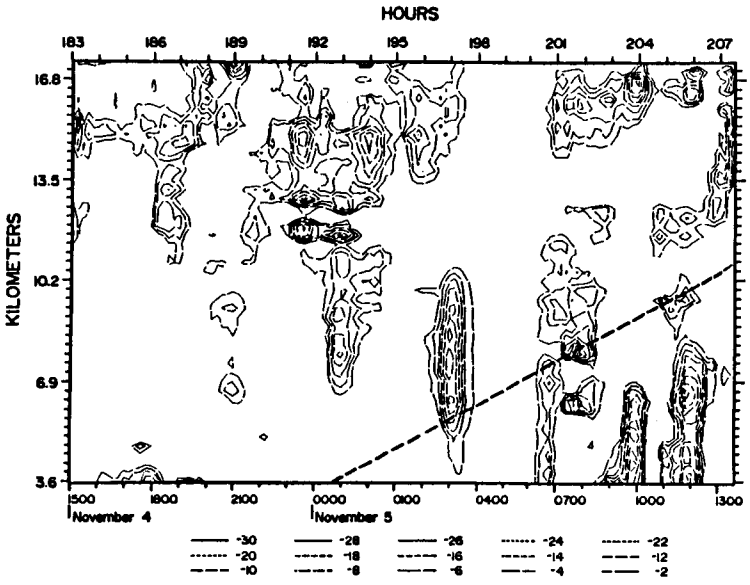

Figure 6. Downward velocity (cm/s) for the cold front with 12-minute profiles and with contours as indicated.

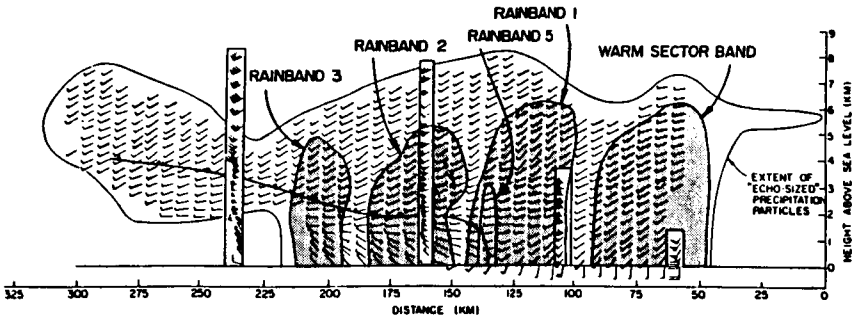

Figure 7. Rainband structure of a cross section perpendicular to a surface cold front.

analyzed cold front in Figure 3. The first column is in the warm section of the cold front in Figure 3, and stretches across the frontal zone. Since this column is also stratified into smaller columns, as seen in Figure 5, the rainbands in Figure 7 are probably associated with this region of the cold front.

The simulation of a cold front by HSIE et al. (1984) shown in Figure 8 has a vertically banded structure 600 km in front of the surface cold frontal zone and vertical bands above the frontal zone, but there are no bands stretching across the frontal zone or located beneath the zone. The vertical columns in Figures 3, 4, 5, and 6 are located in front of the surface frontal zone and behind the zone. The banded structure in Figure 8 is supported by the experimental results, but the model fails to simulate bands beneath and behind the frontal zone.

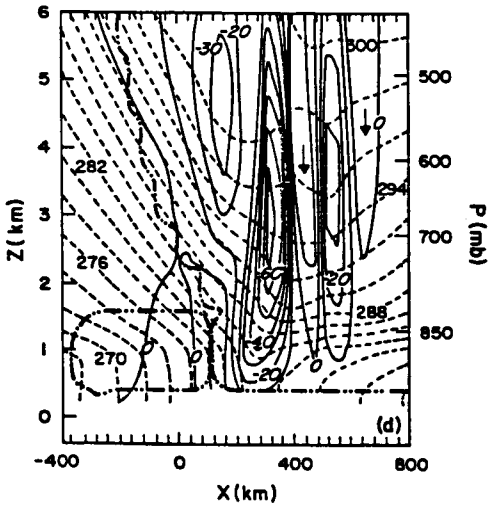

Figure 8. Cross section of the moist model of a cold front at 78 h.

WARM FRONT

The large warm front extending over November 9, 10, 11, and 12 has similar features to the other warm fronts studied in this data set. A column of rising air on November 11 is directly over a strong flow of downward velocities. The upward velocities approach 14 cm/s, but the downward velocities reach 30 cm/s. There are large areas of weak subsidence above the front, but there is a strong column of downward velocities on November 12. The upper-level cold front of November 11 also influences the velocity structure in this region, but it is not possible to determine the extent of this influence.

CONCLUSION

Vertical velocity data and reflectivity data from the SOUSY VHF radar were analyzed for a 15-day period in October and November of 1981. The analysis supports the use of the VHF radar as an effective tool for locating the tropopause and upper-level fronts and provides a detailed observation of the vertical circulation around frontal systems.

The tropopause levels recorded by the radiosonde and those calculated from the potential temperature contours and temperature contours correspond well to the levels determined from the radar reflectivities. Likewise, the frontal

systems, established from the potential temperature contours, the weather maps, and the temperature, pressure, and refractivity data, are identifiable in the reflectivity data as well. These results support the findings of LARSEN and ROTTGER (1982, 1983, 1984) on the effectiveness of the VHF radar. The analysis of the vertical velocity data reveals the stratification of rising and subsiding air columns around frontal zones. In regions of strong velocity the stratification is intensified.

Circulation patterns around the warm fronts show rising air, especially at the upper levels of the frontal zones. There is some stratification around warm fronts, but the circulation is not as strong as the velocity near the cold fronts. The overall patterns around the cold and the warm fronts were expected results. The vertical circulation associated with the two occlusions, however, contains much stronger velocities and a larger area of subsidence in the pockets than was expected. These results indicate that occluded fronts may play a more important role in mesoscale dynamics than was previously believed.

The vertical circulation pattern near the tropopause folding event consists of two vertically stratified columns of air moving in opposite directions stretching below it. There is also a region of upward velocity above the event that extends into the stratosphere. The tropopause is lifted nearly 3 km at one point during the event and is effectively displaced for over four days. Analysis of the associated potential vorticity is necessary to determine whether a tropopause folding event actually occurred.

ACKNOWLEDGEMENT

TSD and MFL were supported by the Air Force Office of Scientific Research under grant AFOSR-85-2016 while this work was carried out.

REFERENCES

Dennis, T. S. (1985), Observations of mesoscale vertical velocities around frontal zones, M.S. thesis, Department of Physics, Clemson, University.

Hobbs, P. V., T. J. Matejka, P. H. Herzegh, J. D. Locatelli, and R. A. Houze, Jr. (1980), The mesoscale and microscale structure and organization of clouds and precipitation in mid-latitude cyclones. Part I: A case study of a cold front, J. Atmos. Sci., 37, 568-596.

Hsie, E.-Y, R. A. Anthes, and D. Keyser (1984), Numerical simulation of frontogenesis in a moist atmosphere, J. Atmos. Sci., 41, 2581-2594.

Larsen, M. F., and J. Rottger (1982), VHF and UHF Doppler radars as tools for synoptic research, Bull Am. Meteorol. Soc., 63, 996-1008.

Larsen, M. F., and J. Rottger (1983), Comparison of tropopause height and frontal boundary locations based on radar and radiosonde data, Geophys. Res. Lett., 10, 325-328.

Larsen, M. F., and J. Rottger (1984), Observations of frontal zone structures with a VHF Doppler radar and radiosondes, 22nd Conf. Radar Meteorol., 489-493.

1.2.4 COMPARISON OF VERTICAL VELOCITIES ANALYZED BY A NUMERICAL MODEL AND MEASURED BY A VHF WIND PROFILER

M. F. Larsen[1], J. Rottger[2,3], and T. S. Dennis[1]

[1]Department of Physics and Astronomy
Clemson University
Clemson, South Carolina 29631

[2]Arecibo Observatory
P.O. Box 995
Arecibo, Puerto Rico 00612

1. INTRODUCTION

The use of wind profilers for measuring vertical velocities in the troposphere and lower stratosphere is potentially of great interest for verification of forecasts, diagnosis of mesoscale circulations, and studies of wave motions. The studies of profiler vertical velocities to date (ECKLUND et al., 1981; LARSEN and ROTTGER, 1982; NASTROM et al., 1985; DENNIS et al., 1986) have shown that the observed patterns of ascent and subsidence are reasonable when compared to the synoptic conditions. However, difficulties arise when a direct verification of the profiler vertical winds is sought. Since no other technique can measure the vertical velocities over the same height range and with the same claimed accuracy as the profilers, direct comparisons are impossible. The only alternative is to compare the measurements to analyzed vertical velocity fields.

In this paper, we will compare vertical velocity measurements made with the SOUSY VHF radar over a period of 11 days at the beginning of November 1981 to the analyzed vertical velocities produced by the European Centre for Medium-range Weather Forecasting (ECMWF) model for grid points near the radar site.

2. PREVIOUS STUDIES

A number of studies have compared the overall characteristics of the measured vertical velocity fields to the synoptic conditions (e.g., ECKLUND et al., 1981, 1982; LARSEN and ROTTGER, 1982; NASTROM et al., 1985; DENNIS et al., 1986) and have found the expected trends. Thus, upward velocities were generally on the warm side of the front and downward velocities on the cold side. Also, the variability in the vertical velocities was found to increase in connection with flow over nearby mountains, as opposed to prevailing winds coming from the direction of flatter terrain.

Only one study that we are aware of has compared the measured vertical velocities to the analyzed vertical velocity fields (NASTROM et al., 1985). NASTROM et al. (1985) used measurements made with the VHF radar located at Platteville, Colorado, and a temporary installation of three VHF radars located in the Rhone Delta in connection with ALPEX. Radiosonde data were the basic input to the analysis scheme which used the quasi-geostrophic omega equation, the kinematic method, and the adiabatic method to calculate the vertical velocity expected at the radar sites. The conclusion of the study was that the measured velocities were generally many times larger, and sometimes an order of magnitude larger, than the calculated values, although there was general agreement between the measured and calculated directions. Perhaps the

[3]On leave from the Max-Planck-Institut fur Aeronomie, Katlenburg-Lindau, West Germany.

difference in the magnitudes is not surprising because the radar measurements are most likely associated with a smaller spatial scale than the vertical velocity analysis. However, we will show that better agreement is possible when a more sophisticated analysis scheme is used.

3. DESCRIPTION OF THE DATA SET

The radar data consists of vertical velocity measurements made with the SOUSY VHF radar located in the Harz Mountains near Bad Lauterberg, West Germany. Data used in the comparison cover the period from November 1-11, 1981, and have a height resolution of 300 m above 3 km. The radar was operated for 12 min beginning on the hour. A vertical wind profile was produced every minute while the radar was operating, and 12 values were averaged to produce an hourly wind profile. Only a few hours of data were missing during the 11-day period.

The ECMWF data consists of analyzed vertical velocities at the 6 grid points nearest the radar site. The model analysis uses the 12-hour model integration as the initial guess and updates the analyzed field once every 6 hours based on the standard meteorological observations, including radiosonde data, pilot reports, satellite cloud motions, etc. (DELL'OSSO, 1984). The analysis scheme is a normal mode initialization procedure which includes the divergent motions associated with those gravity wave modes allowed by the dynamics of the model. Vertical velocity data were available at all the standard levels up to 70 mb.

4. MODEL AND RADAR COMPARISON

The synoptic situation during the 11-day period of the comparison has been described in much greater detail by DENNIS et al. (1986) in this volume. However, Figure 1 shows the radar reflectivities for the period with the location of the frontal zones indicated by dashed lines. The location of the fronts was determined by analyzing a combination of the surface and upper air maps, the potential temperature cross sections, and the radar reflectivities.

Figure 2 shows the comparison of the radar vertical velocities and the analyzed vertical velocities at nine standard levels from 700 to 70 mb. The radar data are the barbed wire and the model analysis is indicated by the solid line. The "hourly" radar data were averaged over a period from three hours before to three hours after the model analysis time in order to decrease the smaller time scale variations in the radar data.

The comparison shows that the amplitude of the radar and model velocities are close in magnitude. The analysis used here produced vertical velocities 3 or 4 times larger than the velocities produced in the analysis used by NASTROM et al. (1985). The overall trends in both sets of velocities are the same, but there are short periods when the variability is larger and there are more significant discrepancies. A comparison between Figures 1 and 2 shows that periods when the disagreement is most pronounced are associated with times of frontal passages. Finally, the variance of the vertical velocities can be seen by inspection to decrease in both the radar and model data above the tropopause.

5. CONCLUSION

Our comparison of analyzed model vertical velocities and vertical velocities measured with a VHF wind profiler have shown good agreement in both the overall magnitude and general direction. The most prominent discrepancies occur at times of frontal passages. An earlier study by NASTROM et al. (1985) which used a cruder analysis scheme did not find such good agreement with

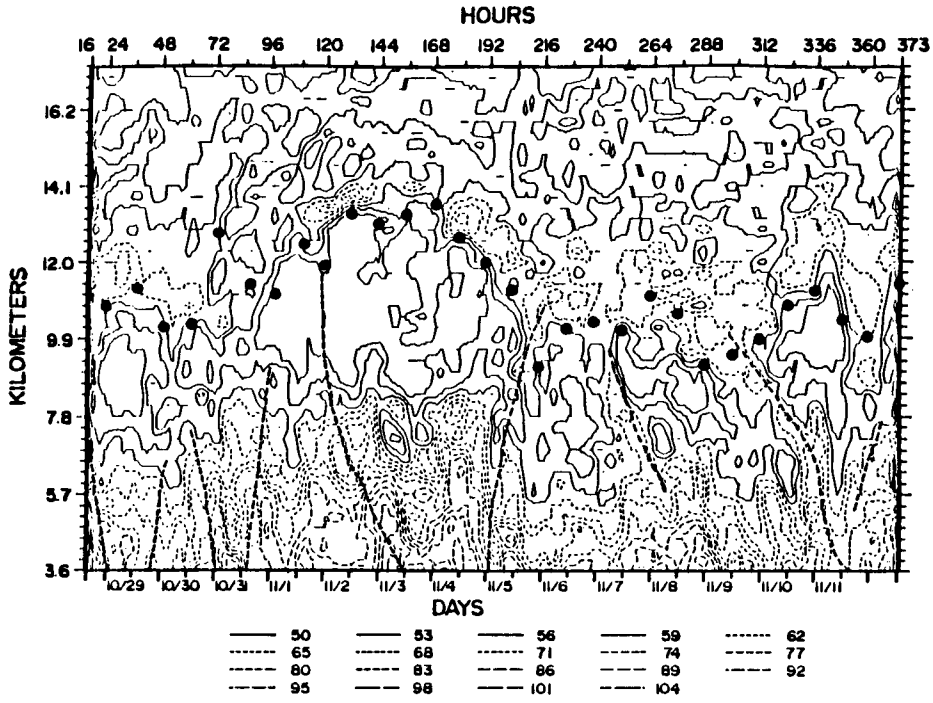

Figure 1.

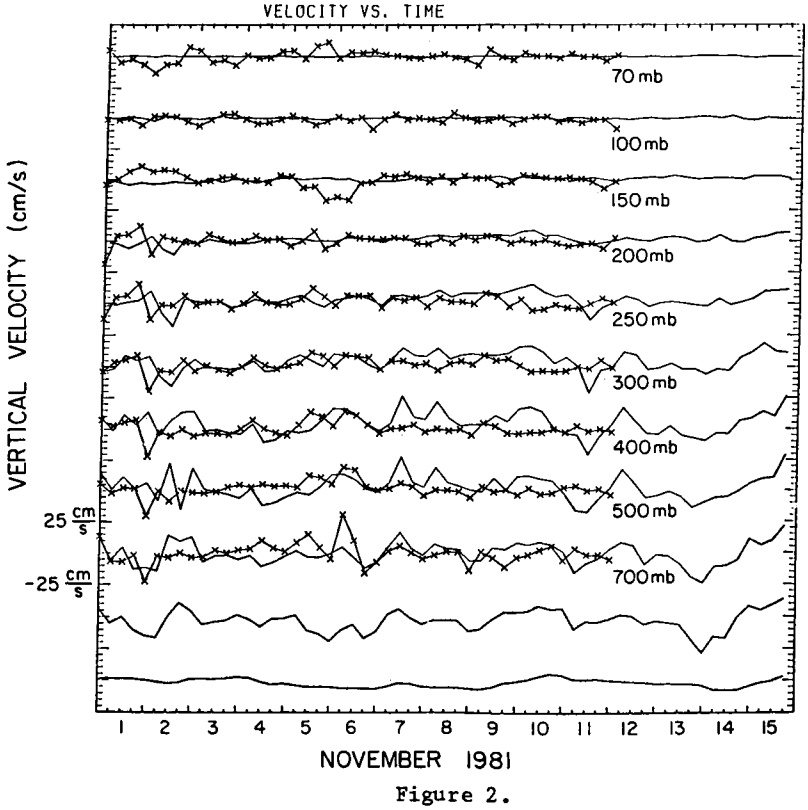

Figure 2.

respect to the amplitudes. The implication is that the more sophisticated normal mode analysis used by ECMWF preserves more of the divergence in the analyzed fields and this leads to an improved estimate of the vertical velocities.

ACKNOWLEDGMENTS

MFL and TSD were supported by the Air Force Office of Scientific Research under grant AFOSR-85-2016 while this work was carried out.

REFERENCES

Dell'Osso, L. (1984), High-resolution experiments with the ECMWF model: A case study, Mon. Wea. Rev. 112, 1853-1883.

Dennis, T. S., M. F. Larsen, and J. Rottger (1986), Observations of mesoscale vertical velocities around frontal zones, this volume.

Ecklund, W. L., K. S. Gage, and A. C. Riddle (1981), Gravity wave activity in vertical winds observed by the Poker Flat MST radar, Geophys. Res. Lett., 8, 285-288.

Ecklund, W. L., B. B. Balsley, R. G. Strauch, and J. L. Green (1982), Vertical wind variability observed by VHF radar in the lee of the Colorado Rockies, Mon. Wea. Rev., 110, 1451-1457.

Larsen, M. F., and J. Rottger (1982), VHF and UHF Doppler radars as tools for synoptic research, Bull. Am. Meteorol. Soc., 63, 996-1008.

Nastrom, G. D., W. L. Ecklund, and K. S. Gage (1985), Direct measurement of large-scale vertical velocities using clear-air Doppler radars, Mon. Wea. Rev., 113, 708-718.

1.2.5 MEASUREMENTS OF PRECIPITATING ATMOSPHERE BY THE MU RADAR

Koichiro Wakasugi[1], Shoichiro Fukao[2,3], and Susumu Kato[3]

[1]Department of Electrical Engineering, Kyoto Institute of Technology
Kyoto 606, Japan
[2]Department of Electrical Engineering, Kyoto University, Kyoto 606, Japan
[3]Radio Atmospheric Science Center, Kyoto University, Kyoto 611, Japan

INTRODUCTION

Although MST radars make it possible to study the dynamics of the middle atmosphere (BALSLEY and GAGE, 1980), simultaneous observations of the troposphere are also important, since various dynamical processes in the middle atmosphere originate with meteorological phenomena in that region.

Sensitive VHF Doppler radars have the capability to detect echoes from precipitation particles as well as refractive index irregularities. We have used the middle and upper (MU) atmosphere radar at Shigaraki, Japan for tropospheric observations of precipitating atmosphere (FUKAO et al., 1985a). We have detected precipitation motions simultaneously with the ambient air motion (FUKAO et al., 1985b), and shown the capabilities of the MU radar in investigating mesoscale structures of meteorological phenomena such as air and precipitation motions within a cold frontal system (WAKASUGI et al., 1985a). More recently, a direct method for deducing the drop size distribution of precipitation particles was developed using Doppler spectra of the MU radar (WAKASUGI et al., 1985b). This method is free from errors inherent in conventional measurements using microwave Doppler spectra.

In the present paper, we will discuss the capabilities of the MU radar for studies of the precipitating atmosphere. Meteorological microwave radar (i.e., non-MST radar) data are also utilized for monitoring vertical and horizontal structures of precipitation.

DOPPLER SPECTRA FROM THE PRECIPITATING ATMOSPHERE

Figure 1 shows typical altitude variations of Doppler spectra obtained in the vertical direction during periods with and without perceivable precipitation on the surface (FUKAO et al., 1985b). The rainfall rates at Kinose, 6.9 km north of the MU radar, provided by the Japan Meteorological Agency, is 1 and 0 mm h^{-1} in the respective periods. The rain is considered to be a weak stratiform type.

Of the two spectral components in Figure 1(a), the minor one with large positive (downward) Doppler shift does not exist while no precipitation is observed, whereas the major one with near zero Doppler shift persistently appears irrespective of the precipitation.

The vertical speed of the minor component is about 7 ms^{-1} above 5 km, while it is less than 2 ms^{-1} above 6 km. The fairly large change with altitude near 5-6 km is quite certain because the minor component is clearly separated from the major one below 8.5 km. The minor component merges in the major one above 9 km. The half-power spectral width varies by more than 3 times in the vicinity of 5-6 km, and is roughly constant elsewhere, i.e., 0.8 and 2.7 ms^{-1} above and below the melting layer, respectively. These features, which are consistent with those of precipitation particles observed with meteorological Doppler radars (DOVIAK and ZRNIC', 1984), indicates that the minor component of the MU radar echo originates from precipitation particles, i.e., snowflakes above the melting layer and raindrops below it.

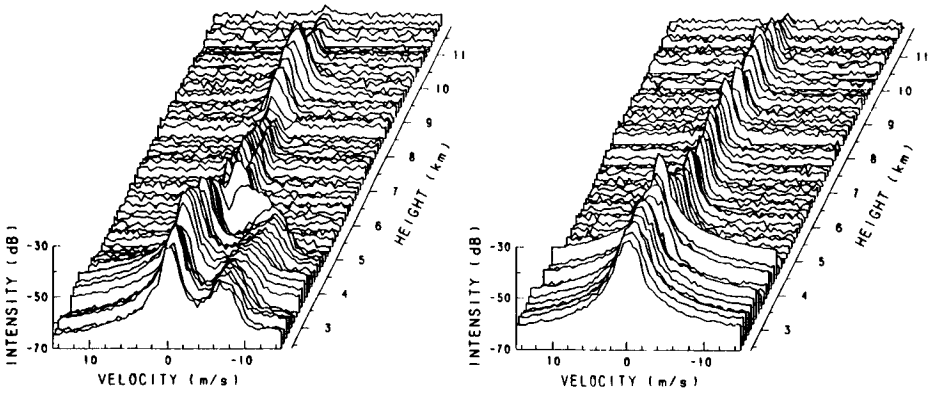

Figure 1. Doppler spectra versus altitude obtained in the vertical direction. The observational periods are (a) 0845-0851 LT and (b) 0750-0756 LT on 22 August 1984. The power is in decibels with an arbitrary reference level. Downward motions are positive in this figure.

RADAR OBSERVATION OF A COLD FRONT

The three-dimensional motions of both air and precipitation particles can be deduced when two off-vertical beams are used in addition to the vertical one. Therefore, a modified VAD technique is used for the present observations (WAKASUGI et al., 1985a).

The observations were made on 19-20 June 1984, during a period of a cold front moving southeastward. Figure 1 shows the horizontal radar reflectivity patterns observed with the Miyama microwave radar (5260 MHz). Several rainbands, which moved with the front, were several tens kilometers wide. These rainbands can be attributed to wide cold-frontal rainbands as described by HOBBS et al. (1980).

Figure 3 shows a time-altitude section of airflow perpendicular to the front. The horizontal component is the relative speed of the front which is assumed to move, on average, at a speed of 5.5 ms^{-1} toward 150° azimuth (see Figure 2). For the vertical component, the figure shows that upward motions are predominant during most of the observation. A relatively strong updraft is observed around 17, 21 LT on June 19 before the frontal passage. A deep strong updraft, associated with the leading edge of the cold front, begins at 03 LT on June 20 at the lowest level of data. The lifted air then ascends and reaches above an altitude of 10 km at 05 LT. Upward velocities in the region are 2.0

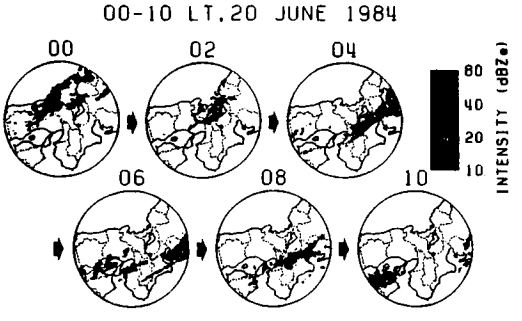

Figure 2. Radar reflectivity patterns with the Miyama radar. The dot is the location of the MU radar at Shigaraki. The circle diameter is 400 km.

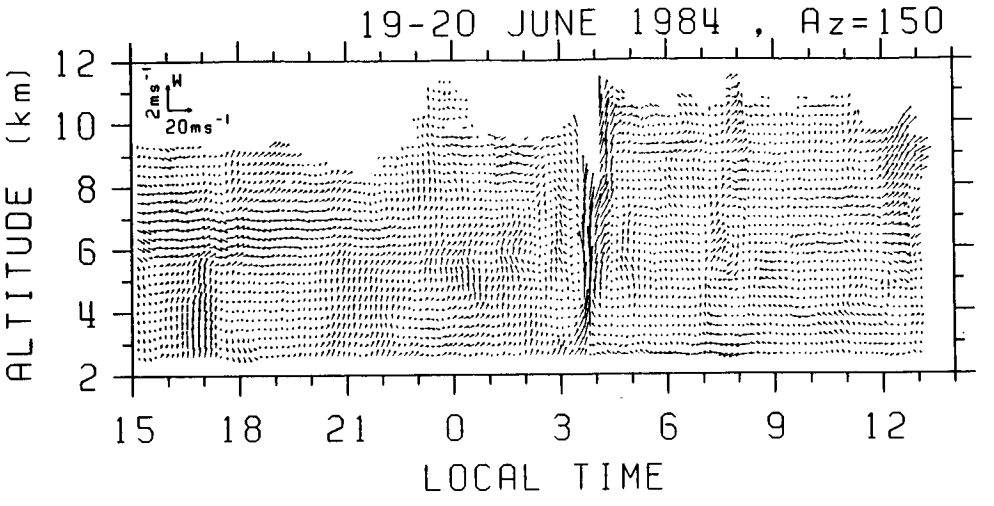

Figure 3. Vertical and transverse airflow relative to a cold front. Time resolution is ten minutes. The vertical and horizontal speed scales are indicated in the upper right-hand corner.

ms^{-1}. For the horizontal component, the figure shows that air flows into the cold front region at low levels both from ahead and behind the front.

DROP SIZE ESTIMATION FROM DOPPLER SPECTRA

Measurements of the size distribution of precipitation are important in studies of the growth of precipitation and cloud modeling. In this section, we will show a direct method in deriving parameters of N(D) from the VHF Doppler radar spectra (WAKASUGI et al., 1985b).

In the presence of the mean (up- or downdraft) velocity w, the Doppler spectrum S_o can then be written as $S_o(V) = P_1 S_1(v-w) * S_2(v) + P_2 S_2(v-w)$ where upward speeds are positive. P_1 and P_2 are the echo powers associated with precipitation and refractive index irregularities. The asterisk denotes the convolution operation between S_1 and S_2. We have assumed that S_1 is of Gaussian form, and S_2 of exponential drop size distribution with parameter N_o and Λ.

Figure 4 shows examples of the 10-min average Doppler spectra obtained with the vertical beam during the frontal passage. Although the exponential function well approximates the size distributions during the observation, least squares fit errors sometimes decrease when a truncated N(D) was used. Figure 4 also shows the temporal variations of the estimated parameters N_o, Λ and the liquid water content M. Temporal variations are characterized by a sudden decrease of N_o and Λ with the passage of the front at 0400 LT. This corresponds to narrow size distribution of particles changing into much broader distribution. However, the Doppler spectra of the precipitation before the passage is wider than that observed after the passage. This is attributed to the broadening due to turbulence and confirms that the information of spectral broadening of the air component is essential to estimate precipitation particle parameters accurately (HAUSER and AMAYENC, 1981).

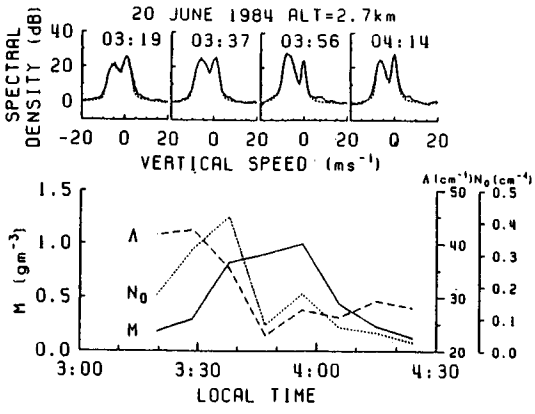

Figure 4. Temporal variations of observed spectra and the estimated parameters N_o, Λ and M during the frontal passage. Upward motions are positive.

RADAR CALIBRATION USING PRECIPITATION ECHO

Finally, we will proceed to the calibration of radar sensitivity. A direct calibration of the MST-type radars is difficult because the large aperture antenna of MST radars can only be pointed to a limited number of directions near the zenith. For the present observation, we have used the radar reflectivity factor Z obtained by the Miyama meteorological radar to calibrate the MU radar sensitivity.

The MU radar reflectivity factor is first calculated with an unknown constant which is proportional to the sensitivity, and then, this constant is determined by equalizing the two reflectivity factors. This method can be used for the calibration of other MST radars especially when the microwave radar is reliably calibrated, and both radars illuminate the same precipitating volume. However, the resolution volume of the Miyama radar is about 500 times larger than that of the MU radar over Shigaraki. Therefore, we conclude that the accuracy is expected to within 5 decibels for our case. The MU radar reflectivity factor is also estimated from the signal-to-noise ratio of the precipitation component following the procedure proposed by VANZANDT et al.(1978). The estimates generally coincide with that of the Miyama radar.

REFERENCES

Balsley, B. B., and K. S. Gage (1980), The MST radar technique: Potential for middle atmospheric studies, Pure Appl. Geophys., 118, 452-493.

Doviak, R. J., and D. S. Zrnic' (1984), Doppler Radar and Weather Observations, 458 pp, Academic Press, New York.

Fukao, S., K. Wakasugi, T. Sato, T. Tsuda, I. Kimura, N. Takeuchi, M. Matsuo, and S. Kato (1985a), Simultaneous observation of precipitating atmosphere by VHF band and C/Ku band radars, Radio Sci., 20, 622-630.

Fukao, S., K. Wakasugi, T. Sato, S. Morimoto, T. Tsuda, I. Hirota, I. Kimura, and S. Kato (1985b), Direct measurement of air and precipitation particle motion by VHF Doppler radar, Nature, in press.

Hauser, D., and P. Amayenc (1981), A new method for deducing hydrometeor-size distribution and vertical air motions from Doppler radar measurements at vertical incidence, J. Appl. Meteorol., 20, 547-555.

Hobbs, P. V., T. J. Matejka, P. H. Herzegh, J. D. Locatelli, and R. A. Houze, Jr. (1980), The mesoscale and microscale structure and organization of clouds and precipitation in midlatitude cyclones. I: A case study of a cold front, J. Atmos. Sci., 37, 568-596.

VanZandt, T. E., J. L. Green, K. S. Gage, and W. L. Clark (1978), Vertical profiles of refractivity turbulence structure constant: Comparison of observations by the Sunset radar with a new theoretical model, Radio Sci., 13, 819-829.

Wakasugi, K., S. Fukao, S. Kato, A. Mizutani, and M. Matsuo (1985a), Air and precipitation particle motions within a cold front measured by the MU VHF radar, Radio Sci., 20, 1233-1240.

Wakasugi, K., A. Mizutani, M. Matsuo, S. Fukao, and S. Kato (1985b), Drop-size distribution and vertical air velocities directly derived from VHF Doppler radar spectra, in preparation.

1.3.1 THE REAL-TIME USE OF WIND PROFILERS IN NOWCASTING

Tracy Lorraine Smith and Thomas W. Schlatter

ERL/PROFS, National Oceanic and Atmospheric Administration
Boulder, CO 80303

I. INTRODUCTION

The Program for Regional Observing and Forecasting Services (PROFS) has been using wind profile data in experimental forecast applications for over two years, mostly in the form of real-time color displays on the PROFS forecast workstation. The most ambitious test of the workstation to date, the 1985 PROFS Real-Time Experiment (RT-85), ran from 15 May-23 August, 1985. This paper describes the use of wind profiler products during this and previous experiments.

Data from the experimental profiler network in Colorado (Figure 1) and from the PRE-STORM profiler in Oklahoma reach PROFS via ERL's Wave Propagation Laboratory, which operates the network. The data are in the form of hourly averages. Arriving data frequently contain errors whose origins range from interference by aircraft in the beams to highway truck traffic. Most of the irregularities are apparent through visual inspection of profiler wind observations plotted on a time-height cross section, but this method of quality control is inadequate if the intended uses of the data involve numerical calculations.

With the advent of the STORM program and plans for the Profiler Hub (a facility for collection, quality control, and archival of all profiler data), PROFS has been assigned responsibility for developing automated quality control procedures for profiler wind observations. At present, the quality control is rudimentary, including only a check for excessive vertical shear. The vertical check is limited in that it can recognize only two consecutive bad data points. Because as many as eight or ten vertically adjacent profiler wind observations have been in error in some cases, a more stringent quality control is needed. PROFS is refining the vertical quality control procedures and adding tests for temporal and horizontal consistency.

II. PROFILER DATA ON THE PROFS WORKSTATION

Several products on the PROFS forecast workstation utilize profiler data. Most popular with the forecasters is the time-height cross section of wind observations from a particular profiler site. This 12-hour time series has time increasing to the left to allow spatial interpretation of the data through the principle of time-space conversion. Different modes of operation (different pulse lengths and pulse repetition intervals) are color-coded on the screen. Longer pulses at longer intervals allow probing higher in the atmosphere, but at decreased vertical resolution. The utility of this display during a PROFS' Spring 1984 forecasting exercise has been discussed by GAGE and SCHLATTER (1984). In particular, with the increased spatial and temporal resolution of tropospheric data over Colorado, forecasters became adept at tracking short waves moving across the state and in detecting short-term changes in their amplitude, including the formation of closed circulations.

Another display, added during RT-85, is a quasi-three-dimensional depiction of wind profiles from all four Colorado sites projected onto a regional map. Winds are color-coded as in the time-height cross section. This is an hourly product that can be animated.

The Profiler Station Plot is a plot of the winds at all profiler stations for one level, developed for overlay on a satellite image.

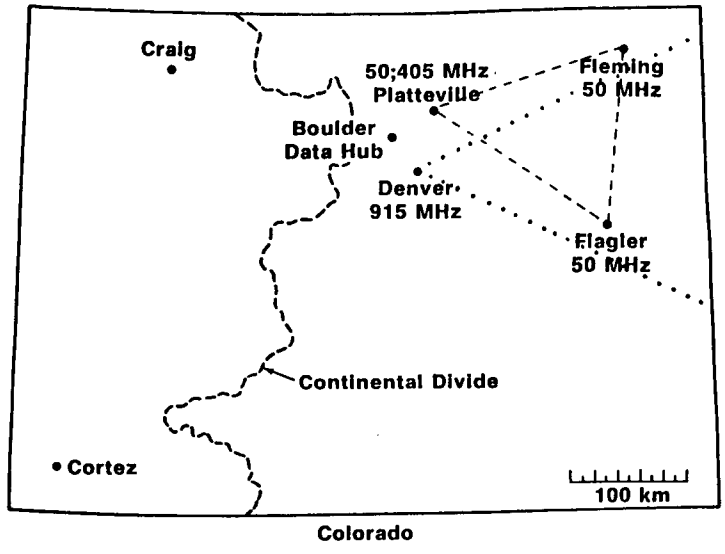

Figure 1. The Colorado profiler network overlayed with the kinematic analysis areas. The profiler triangle is in dashed lines; the RAOB triangle is denoted by dotted lines.

Smooth temperature and moisture profiles derived from a six-channel radiometer (HOGG et al., 1983) supplement measurements by the wind profiler. Accurate estimates of the geopotential height and total precipitable water have been obtained from these profiles, and several color displays are based upon them, but they will not be discussed further here.

Profiler data provide input to the Mesoscale Analysis and Prediction System (MAPS) and the Kinematic Analysis Model (KAM). MAPS is a mesoscale analysis/short-range forecasting system, utilizing data from rawinsondes, VAS soundings, aircraft reports, and wind and temperature profiles (BENJAMIN et al., 1985). MAPS will provide upper-level guidance to PROFS forecasters in the form of frequent analyses and 12-hour wind forecasts over the contiguous United States and adjacent areas.

The Kinematic Analysis Model, which was brought to PROFS from Purdue University, calculates vertical profiles of vorticity, divergence, and vertical velocity. The computer code was originally written for use with RAOB data in prediction of Great Lakes snowstorms (AGEE, 1983). KAM uses data from a triangle formed by three sounding stations. At each station, the u and v components of the wind are expanded in a first-order Taylor's series

$$u_n = u_o + \left(\frac{\partial u}{\partial x}\right)_o (x_n - x_o) + \left(\frac{\partial u}{\partial y}\right)_o (y_n - y_o)$$

$$v_n = v_o + \left(\frac{\partial v}{\partial x}\right)_o (x_n - x_o) + \left(\frac{\partial v}{\partial y}\right)_o (y_n - y_o) \qquad n = 1,2,3$$

where the zero subscript refers to the middle of the triangle. These are six equations in six unknowns, u_o, v_o, and their partial derivatives. Once the

equations are solved, the vertical component of vorticity and the horizontal divergence can be calculated. Pressure data, required to determine the vertical velocities, are unavailable from the profiling system. As an expedient, the pressure/height correspondence for the closest RAOB is calculated and applied to the profiler data heights to get a good approximation of the actual pressure. If the RAOB data are missing, the radiometric profile at Denver is used (HOGG et al., 1983). The vertical velocity can be derived by integrating the boundary conditions. At present, the vertical velocity is assumed to be zero at the lowest level, about 1500 meters above the ground. This is a shortcoming, particularly in summer, because it is known that most of the convergence which initiates thunderstorms occurs in the first kilometer above ground. We will attempt to remedy the situation by using PROFS' surface mesonet data in specification of the lower boundary conditions.

Another liability in the computation of kinematic quantities from three profiler sites is the data availability. If any of the three instruments is inoperative or transmitting unreliable data, then the analysis cannot be run -- an annoying situation which arose on some of the more interesting days last summer. Improved automatic quality control of the data will help to solve this problem.

III. PROFILERS IN USE: AN RT-85 CASE STUDY

The Kinematic Analysis Model was first used extensively with profiler data during RT-85. Two consecutive days, 1 and 2 August, provide an interesting comparison of synoptic vs mesoscale influences. In the following paragraphs, we refer to profiles of convergence and vertical velocity computed from soundings made at the vertices of two triangles. The small triangle (Figure 1) includes the profiling sites at Platteville, Flagler, and Fleming, Colorado. The large triangle (western portion shown in Figure 1) includes the rawinsonde sites at Denver, Colorado, North Platte, Nebraska, and Dodge City, Kansas.

On the afternoon of 1 August, a typical flow pattern existed over the Colorado Rockies. In Figure 2, a broad band of clouds depicts a weak flow of warm and very moist air extending from the Mexican border north-northeastward to Colorado. At 500 mb, a trough of cool air lies to the northwest over Washington and Oregon. Profiles of convergence and vertical velocity from the large and small triangles (Figures 3 and 4, respectively) show similar patterns -- slight divergence and subsidence at all levels. Although very little convective activity occurred inside either triangle, strong convection occurred to the west: the Cheyenne, Wyoming, hailstorm and flash flood caused fatalities between 0200 and 0400 GMT 2 August; another cluster of thunderstorms caused excessive rainfall and hail south of Denver.

By 2 August, the trough aloft had moved east to the northern Rockies (Figure 5), and the flow over Colorado had become more westerly, although still moist. The early evening profiles from the large triangle (Figure 6) show very weak divergence in the lower troposphere and weak convergence above 500 mb. The vertical velocity is correspondingly weak, mostly downward. A much different situation exists within the small triangle (Figure 7), with moderate convergence aloft and rising motion. Thunderstorms developed during the afternoon and moved into the triangle by early evening. They dropped hail both outside the triangle -- on the foothills northwest of Platteville -- and inside. Near the western corner of the triangle, hail up to 2 cm in diameter lay in drifts along the roadside.

The correspondence between profiles of vertical velocity and thunderstorm activity is by no means perfect, in part, because the 50-MHz profilers cannot obtain measurements close to the ground and because surface wind observations are not yet being used. We expect to remedy the latter problem soon.

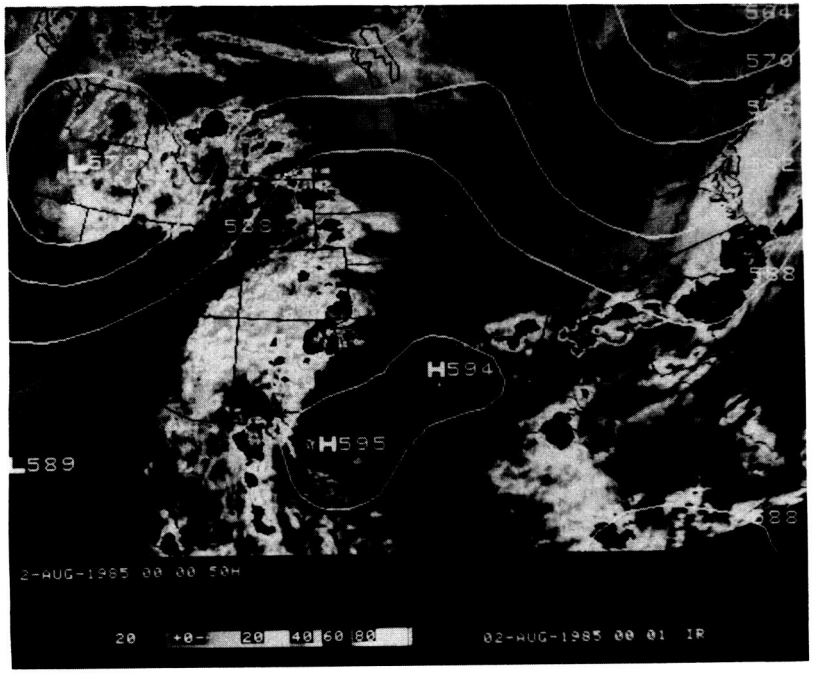

Figure 2. GOES IR image for 00:00Z, 2 August 1985, overlayed with corresponding 500 mb height analysis.

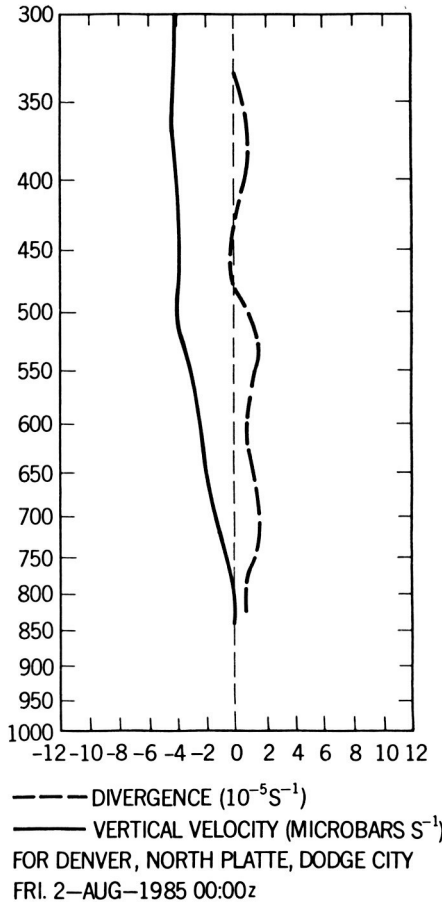

Figure 3. Kinematic Analysis Model output at 00:00Z, 2 August 1985, for the RAOB triangle. Rising motion is denoted by vertical velocity values to the right of the zero line.

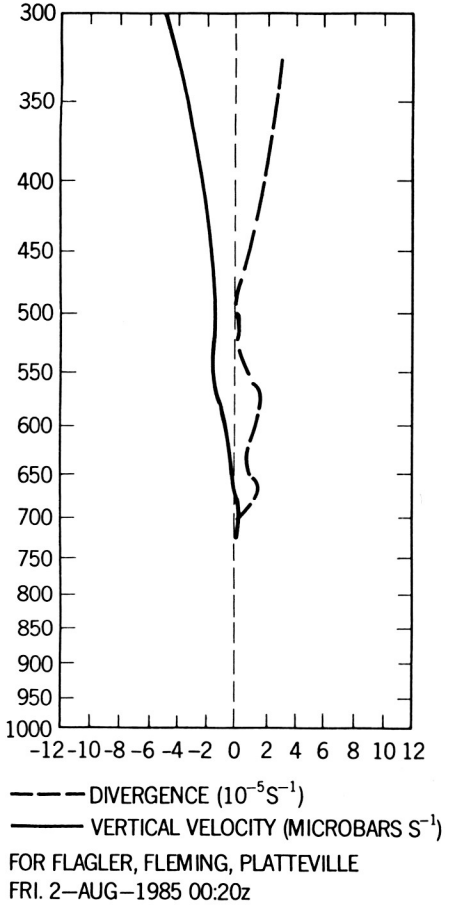

Figure 4. Kinematic Analysis Model output at 00:20Z, 2 August 1985, for the profiler triangle.

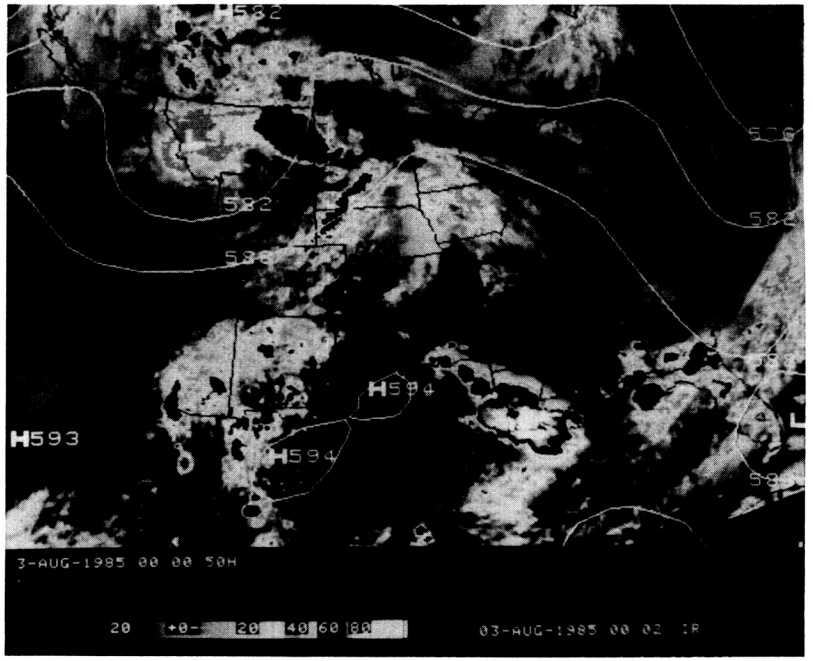

Figure 5. GOES IR image for 00:00Z, 3 August 1985, overlayed with corresponding 500 mb height analysis.

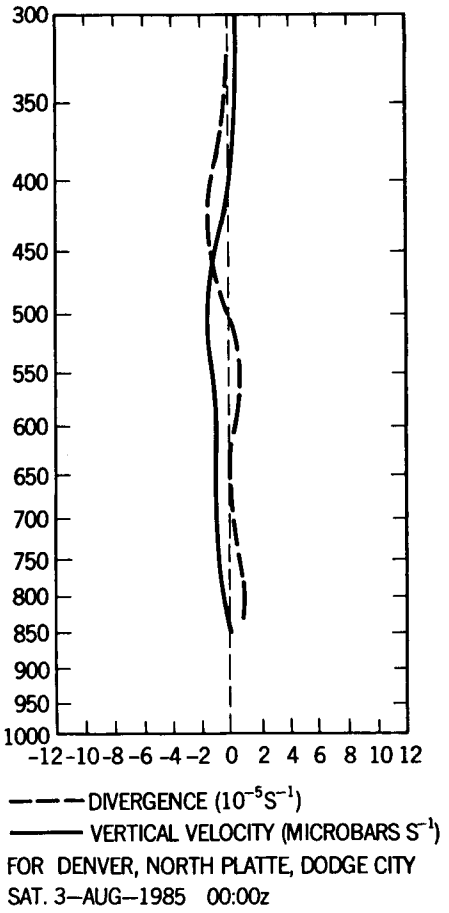

Figure 6. Kinematic Analysis Model output at 00:00Z, 3 August 1985, for the RAOB triangle.

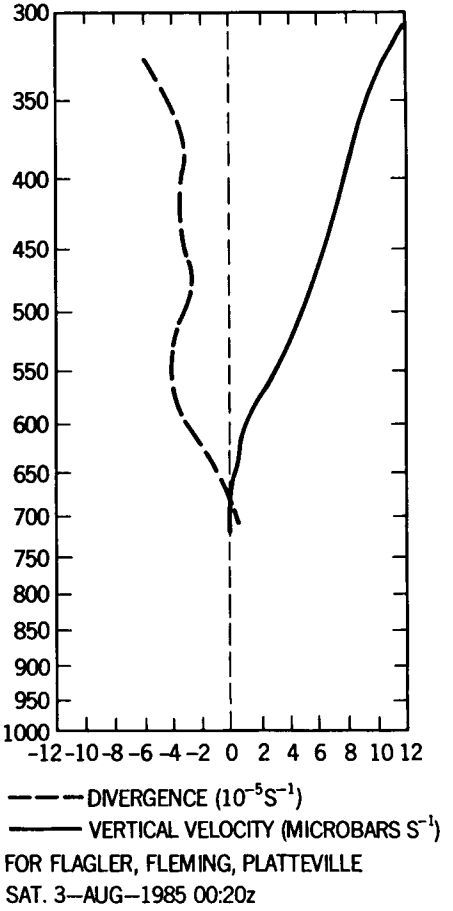

Figure 7. Kinematic Analysis Model output at 00:20Z, 3 August 1985, for the profiler triangle.

IV. FUTURE WORK

Applications of the profiler winds are continuing to be discovered and developed. BLECK et al. (1984) have developed a method for using the profiler winds to put better vertical resolution into the radiometric profiles of temperature. The radiometer is capable only of smooth profiles because the radiation it measures emanates from thick layers. Any sharp kinks in the temperature profile such as a frontal inversion are undetectable. Using variational calculus and the profiler wind data, Bleck and his colleagues expect to build such details back into the temperature profile. In an operational setting, this technique could be used to upgrade the quality of radiometric or satellite soundings.

Visiting forecasters who operate the PROFS workstation often recommend extensions to existing products. One useful suggestion is a time series of divergence, vorticity, and vertical velocity at a given level. We are also adding the capability of making an hourly product of the kinematic fields, so that it can be loaded for animation, to give the observer a dynamic view of the temporal changes.

If we can trust the early indications, profiler data displayed in a great variety of ways will prove to be a boon to very-short-range forecasting. PROFS will be continuing its application of profiler data to the problems of forecasting during its next cool-season exercise in early 1986.

ACKNOWLEDGMENTS

The authors wish to thank the NOAA Wave Propagation Laboratory for supplying PROFS with data from the profiling system. Nita Fullerton helped prepare the manuscript. Joe Wakefield and Stan Benjamin assisted with critical reviews.

REFERENCES

Agee, E. M. (1983), Implementation of a kinematic analysis routine at NOAA-ERL/PROFS, 7 pp. (unpublished manuscript). Copies available through PROFS, R/E23, 325 Broadway, Boulder CO, 80303.

Benjamin, S. G., R. S. Lieberman, T. W. Schlatter, R. G. Rasmussen (1985), Preliminary tests of a regional objective analysis and short-range numerical forecasting system, Preprint, 7th Conf. Numerical Weather Prediction, June 17-20, Montreal, P.Q., Canada, Am. Meteorol. Soc., Boston, MA, 440-443.

Bleck, R., R. Brummer, and M. Shapiro (1984), Enhancement of remotely sensed temperature fields by wind observations from a VHF radar network, Mon. Wea. Rev., 112, 1795-1803.

Gage, K. S., and T. W. Schlatter (1984), VHF/UHF radar and its application to nowcasting, Proc. Second Int. Symp. Nowcasting, 3-7 September, Norrkoping, Sweden, ESA SP-208, European Space Agency, Paris, 193-200.

Hogg, D. C., M. T. Decker, F. O. Guiraud, K. B. Earnshaw, D. A. Merritt, K. P. Moran, W. B. Sweezy, R. G. Strauch, E. R. Westwater, and C. G. Little (1983), An automatic profiler of the temperature, wind, and humidity in the troposphere, J. Climate Appl. Meteorol., 22, 807-831.

1.4.1 THE INFLUENCE OF VELOCITY VARIABILITY ON THE DETERMINATION OF WIND PROFILES

Jurgen Rottger*

AX-208 300

Arecibo Observatory
Box 995
Arecibo, Puerto Rico

High sensitivity radars allow the determination of velocity estimates at time resolutions down to one minute or better. Because of the variability introduced to the mean wind due to turbulence and waves, the high resolution profiles may not be too useful for forecasting applications, although they yield the most realistic estimate of the instantaneous wind profile. Figure 1 shows profiles of wind speed and direction, vertical velocity and echo power, which were deduced in real-time on 23 August 1981 with the spaced antenna drift mode of the SOUSY-VHF-Radar (ROTTGER, 1984). Whereas these profiles were measured within 1 minute, the operating routine allowed the selection of variable (longer) measuring periods, and one has to search for the optimum duration of the data averaging period.

Figure 2 shows a high time resolution wind vector diagram which gives an idea of the temporal variability (from ROTTGER, 1981a). The data were obtained with the spaced antenna technique, which allows a good estimate of the horizontal wind without having to correct for the vertical velocity component. The wind vectors of Figure 2 specifically indicate a quasi-periodic variation in direction. This is assumed to be due to gravity waves since also the vertical velocity (Figure 2b) shows periodical variations with the same period.

In addition to the variability due to waves we have to regard the variability due to turbulence as well as the variability introduced to the analysis due to statistical variations of echo power and correlation time. We have applied very stringent selection criteria, allowing only 5% of the latter "instrumental" or "analysis" effects diluting the data when deducing the distributions of wind speed and direction (Figure 3). These results indicate that the meteorological variability (due to waves and turbulence) can still be up to several 10% of the centre value, even at these fairly low wind velocities. Less stringent criteria allow a display of the total profile but introduce larger "analysis" variability (see Figures 4 and 5 of ROTTGER and CZECHOWSKY, 1980).

The selection or quality criteria (for the spaced antenna method: the relative difference between time lags around the spaced antenna triangle, the amplitude of the cross correlation maximum and the signal-to-noise ratio) can be used to weight the significance of velocity estimates when deducing a mean profile. In all our analyses only median values were used instead of mean values, since this procedure disregards large singular deviations which may occur due to analysis or meteorological effects (e.g., at 9:22 UT above 21 km in Figure 2). We also use half the difference between the upper and lower quartile instead of the variance. If the selection criteria did discard all data in one range gate, a spline function was used to interpolate these data. This procedure yielded mean wind velocities, which are shown in the profiles of Figure 4 and the time series of Figure 5. The consistency of these spaced-antenna VHF radar results with the radiosonde data allows us to be convinced that the method, which is only briefly outlined in this note, is quite suitable for wind profiling applications.

*On leave from Max-Planck-Institut fur Aeronomie, Katlenburg-Lindau, West Germany.

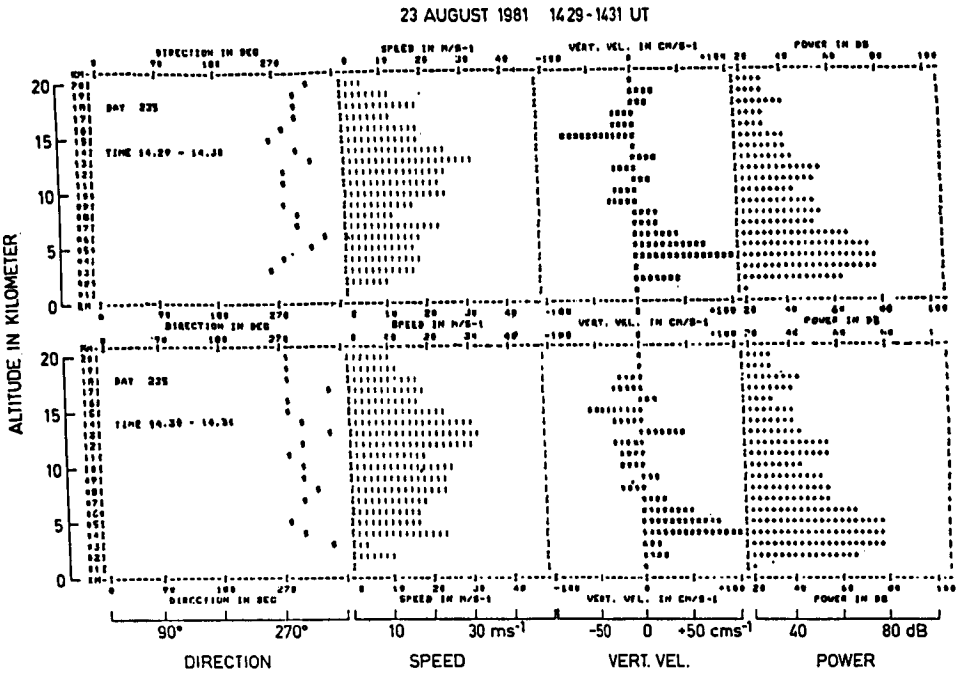

Figure 1. First real-time velocity and power (reflectivity) profiles recorded at intervals of 1 minute with the spaced antenna drift mode of the SOUSY-VHF-Radar: instantaneous wind direction and speed, and vertical velocity. The power profile allows an immediate determination of the tropopause height (here 10 km), defined by an intermediate power increase larger than 10 dB (ROTTGER, 1984).

The averaging time period T_v, to obtain a mean velocity profile, should be determined by the characteristic time scale τ_v of the velocity fluctuations. The time scale τ_v can be deduced form the time lag τ at which the autocovariance function of the velocity time series has fallen to a specified (absolute) value. In order to reduce the statistical variations due to turbulence, waves and analysis uncertainties, the averaging time T_v must be larger than the characteristic time τ_v. The latter can be deduced in real-time allowing to select also the velocity averaging period T_v in real time. Since a short time τ_v can be due to highly turbulent fluctuations, their large rms variations have to be smoothed out by averaging over a sufficiently large number of samples. Typical averaging time periods are between 5 and 30 minutes (Figure 5).

On the other hand, we also have to use as good a height resolution as possible, because serious velocity errors can occur when applying too coarse a height resolution. As was shown by SATO and FUKAO (1982), the wind velocity is considerably biased (of the order of 10 ms^{-1} for resolution of 3 km) when the wind shear is large and the echo power profile has strong gradients within the resolution volume. An appropriate height resolution appears to be 150-300 m.

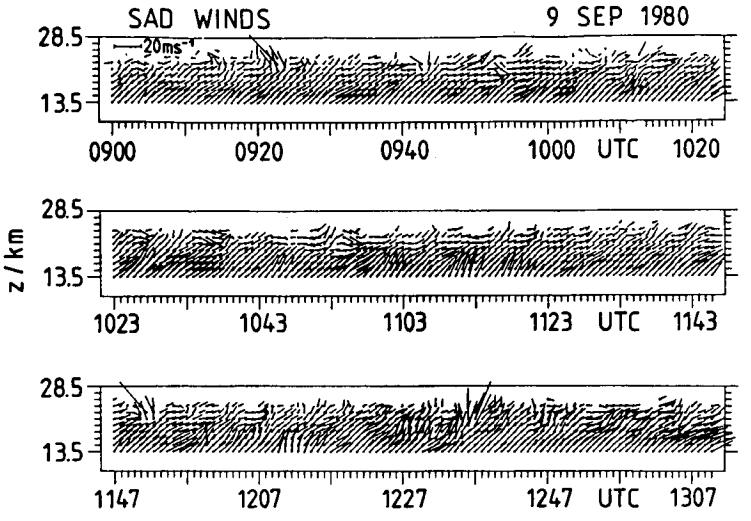

a)

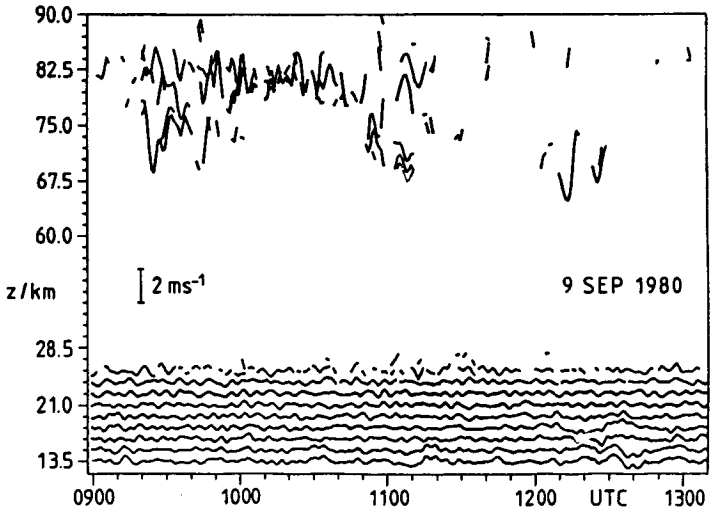

b)

Figure 2. Vector field of horizontal velocity component (a) and corresponding time series of vertical velocity (ROTTGER, 1981a).

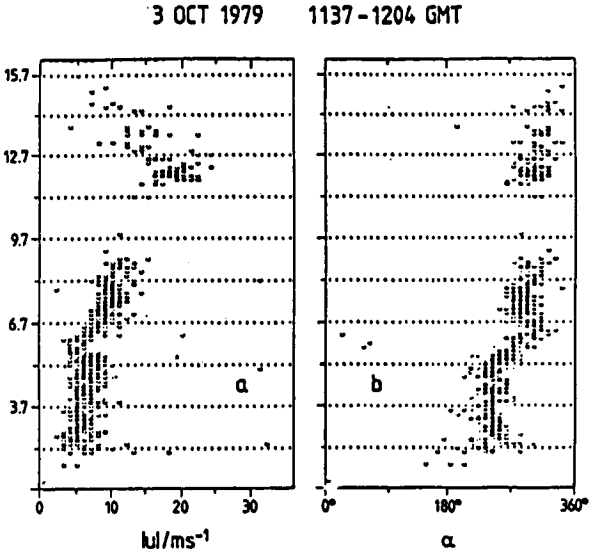

Figure 3. Meteorological variability of wind speed $|u|$ and direction α, measured with the spaced antenna method (ROTTGER and CZECHOWSKY, 1980).

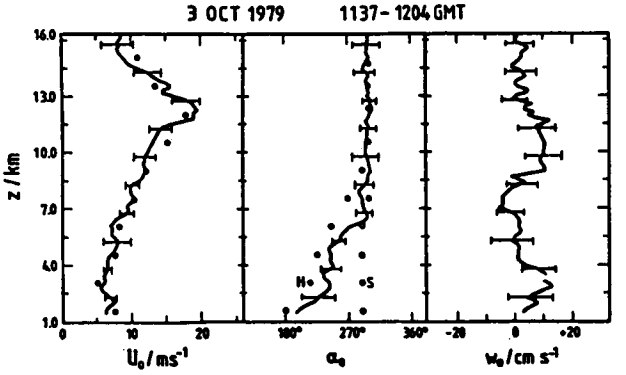

Figure 4. Mean profiles of wind speed U_0, direction and vertical velocity W_0. Circles are radiosonde data, north and south of the radar location (ROTTGER, 1981b).

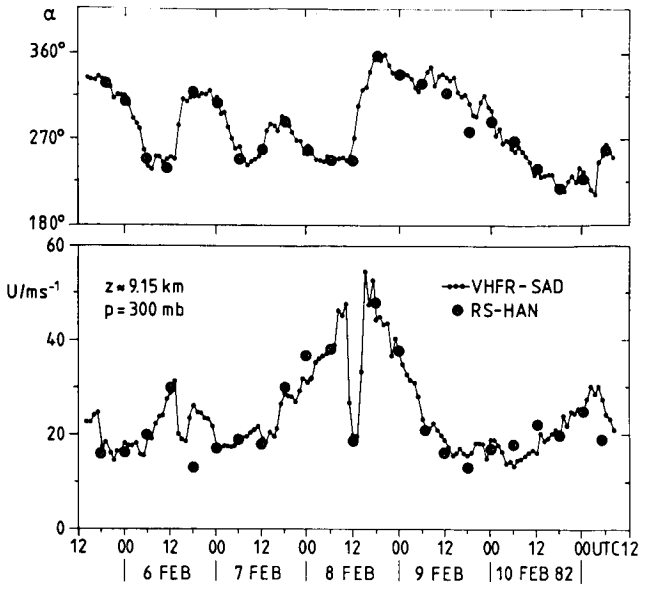

Figure 5. Wind speed U and direction α measured during 12 minutes every hour with the spaced antenna method and radiosonde data (ROTTGER, 1983).

REFERENCES

Rottger, J. (1981a), Wind variability in the stratosphere deduced from spaced antenna VHF radar measurements, Preprint 20th AMS Conf. Radar Meteorol., November 1981, Boston, MA, 22-29.

Rottger, J. (1981b), Investigations of lower and middle atmosphere dynamics with spaced antenna drifts radars, J. Atmos. Terr. Phys., 43, 277-292.

Rottger, J. (1983), The correlation of winds measured with a spaced antenna VHF radar and radiosondes, Preprint 21st AMS Conf. Radar Meteorol., September 1983, Edmonton, Canada, 97-99.

Rottger, J. (1984), The potential of VHF radars for meteorological applications, Polarfront, 11, No. 41, 6-11.

Rottger, J., and P. Czechowsky (1980), Tropospheric and stratospheric wind measurements with the spaced antenna drifts technique and the Doppler beam swinging technique using a VHF radar, Preprint 19th AMS Conf. Radar Meteorol., April 1980, Miami, FL, 577-584.

Sato, T., and S. Fukao (1982), Altitude smearing due to instrumental resolution in MST radar measurements, Geophys. Res. Lett., 9, 72-75.

1.4.2 PERFORMANCE CHARACTERISTICS OF WIND PROFILING RADARS

R. G. Strauch, A. S. Frisch, B. L. Weber

NOAA/ERL/WPL
325 Broadway
Boulder, CO 80303

INTRODUCTION

Doppler radars used to measure winds in the troposphere and lower stratosphere for weather analysis and forecasting are lower-sensitivity versions of MST (mesosphere-stratosphere-troposphere) radars widely used for research. We have used the term "wind profiler" to denote these radars because measurements of vertical profiles of horizontal and vertical wind are their primary function. It is clear that wind profilers will be in widespread use within five years: procurement of a network of 30 wind profilers is underway (CHADWICK, 1986). The Wave Propagation Laboratory (WPL) has operated a small research network of radar wind profilers in Colorado for about two and one-half years (STRAUCH et al., 1985). Table 1 lists the transmitted power and antenna aperture for these radars. Data archiving procedures have been in place for about one year, and we are able to use this data base to evaluate the performance of the radars.

Table 1. WPL wind profilers (1985)

Site	Wavelength (m)	Average Power (W)	Antenna area (M^2)
Stapleton Airport	0.3	450	100
Platteville, CO	0.74	400	54
Platteville, CO	6.02	400	10,000
Fleming, CO	6.02	400	2,500
Flagler, CO	6.02	400	2,500

One of the prime concerns of potential wind profiler users is how often and how long wind measurements are lacking at a given height. Since these "outages" constitute an important part of the "performance" of the wind profilers, they are calculated at three radar frequencies, 50-, 405-, and 915-MHz, (wavelengths of 6-, 0.74-, and 0.33-m) at monthly intervals to determine both the number of outages at each frequency and annual variations in outages. This study on the monthly performance of the wind profilers (i.e., measurement or no measurements at various heights) is based on the more recent archived data from the Colorado Wind Profiler network. It does not consider the accuracy of the wind measurements.

RADAR SENSITIVITY COMPARISONS

The three radars operated with pulse widths of 3- and 9-μs. (The 405- and 915-MHz radars also have a 1-μs pulse mode.) We can compare the sensitivities of the various radars and their modes using the meteorological equation.

First, when we compare pulse widths for the same radar, we find relative sensitivity is proportional to $[\Delta R \bar{P}_t \sqrt{T_o}]$ where ΔR is the range resolution P_t is the average transmitted power and T_o is the observation time. For our radars the 9-μm mode is more sensitive than the 3-μs mode as shown below:

50 MHz, + 6.4 dB
405 MHz, + 7.3 dB
915 MHz, + 7.1 dB

These relative sensitivity values are important for evaluating the performance of a given radar with different pulse widths.

Second, when we compare the three radars and assume scattering from homogeneous, isotropic turbulence in the optically clear atmosphere with the radar half-wavelength in the inertial subrange, then relative sensitivity is proportional to

$$\frac{\bar{P}_t A_e \Delta R \sqrt{T_o}\, \lambda^{1/6}}{(T_{op})\, L}$$

where A_e is the effective antenna aperture, λ is the radar wavelength, T_{op} is the system noise temperature and L is the total loss (rf losses and receiver losses). For the 9-μs pulse mode, the 50-MHz radar is 6.5 dB more sensitive than the 405-MHz radar. These numbers are important in comparing the performances of the different radars.

PROFILER OUTAGES

Figure 1 shows an example of the outage in hourly-averaged wind profiles for the 3- and 9- s modes of the 405-MHz radar. Each vertical dash represents available data for that height and hour; no symbol is printed if data are not available. The periods that show no data at all heights are due to equipment failures including loss of power, loss of telephone transmission, etc.; these outages are not included in the statistics. The 9-μs mode shows fewer outages below 10 km than does the 3-μs mode because the sensitivity of the 9-μs mode is about 7 dB greater. Where both modes show outages the scattering is too weak to detect. Since there is no signal the "depth of fade" is unknown. If the loss of signal is related to an increase in the inner scale of turbulence, the fade could be very large and increased radar sensitivity could yield little reduction of outages. If the loss of signal is related to weak scattering where the fade is on the lower tail of a normal distribution, then the reduction of outage with increased sensitivity can be inferred.

One of the statistics used to measure the performance of the profilers is the percent of time that the profiler was "down" at each height (no wind data, given that the radar is operating) for three or more consecutive hours. Samples of these down-time statistics for January 1985 at the three frequencies are shown in Figures 2-4. The 50-MHz profiler at Fleming (Figure 2) had no outages to 6 km in either the 3- or 9-μs mode, and none until almost 14 km in the 9-μs mode. In comparison, the 405-MHz (Figure 3) Profiler had outages starting at 6 km in the 3- s mode, and at 9 km in the 9-μs mode; the 915-MHz Profiler (Figure 4) had outages starting at a little over 5 km in the 3-μs mode and at 6 km in the 9-μs mode. All radars are in the same geographical area and all radars have about the same sensitivity increase for the 9-μs pulse mode relative to the 3-μs pulse mode (the 50-MHz radar has the least sensitivity increase). However, the 50-MHz radar has a 6-7 km increase in height coverage for the 9-μs mode compared to the 3-μs pulse mode whereas the 915-MHz radar and 405-MHz do no show nearly as much increase. This difference in performance indicates a frequency-dependent profile of backscattering cross section.

To evaluate the height performance of the profilers and determine whether this frequency-dependent difference in height performance for the two modes was consistent, the lowest height where the probability of an outage for three or more consecutive hours reached 0.1 was calculated based on monthly statistics. These heights for the two modes are shown in Figures 5-7. The 915-MHz Profiler consistently shows the smallest height difference for the two modes (Figure 5).

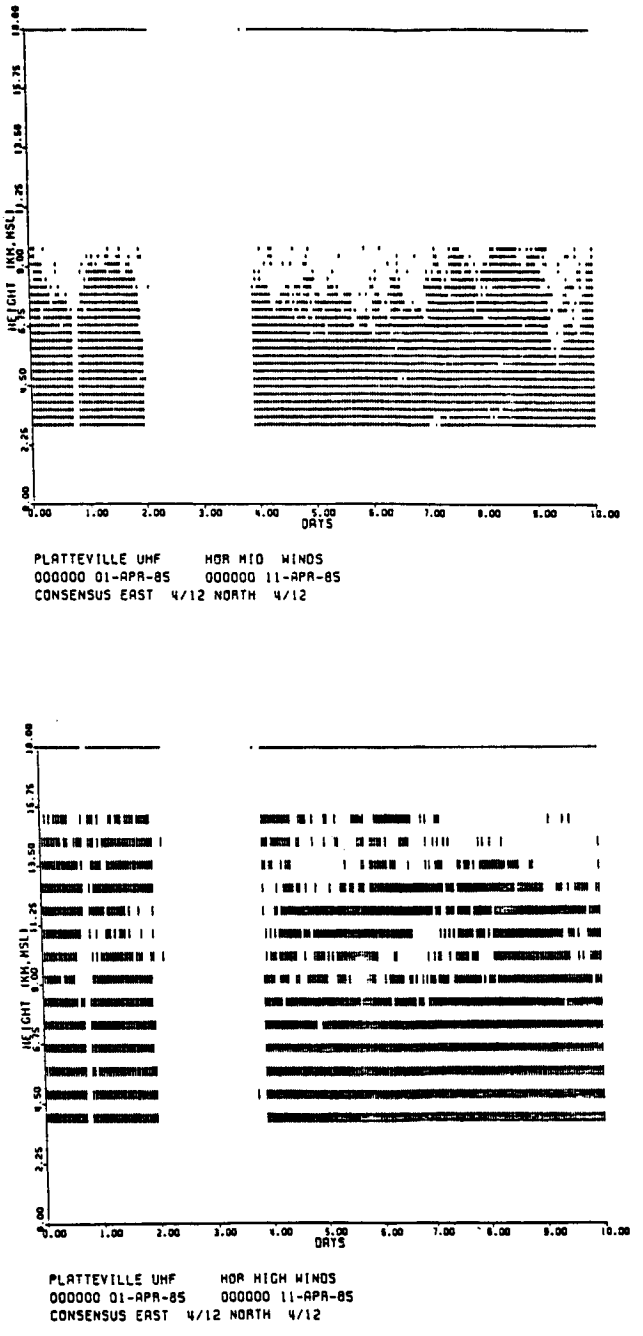

Figure 1. Height-time display of 3- (top) and 9-μs (bottom) modes for Platteville 405-MHz wind profiler. Vertical dashes indicate that there was a wind measurement at that time and height.

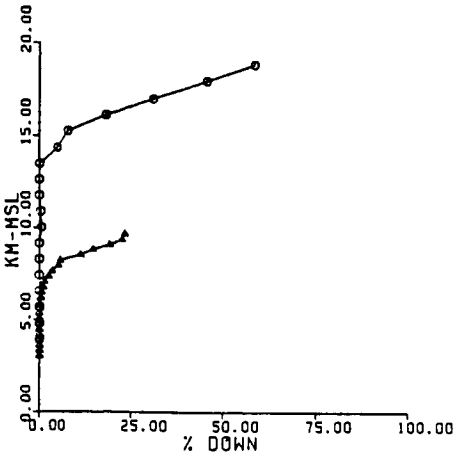

Figure 2. Probability that an outage will last 3 or more consecutive hours vs height at 50 MHz for the 3-μs (triangles) and 9-μs (circles) modes based on January 1985 statistics.

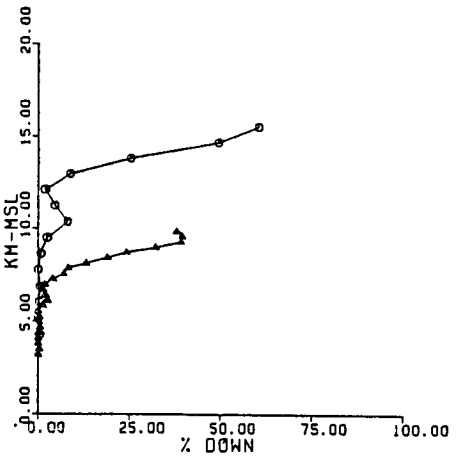

Figure 3. Probability that an outage will last 3 or more consecutive hours vs height at 405 MHz for the 3-μs (triangles) and 9-μs (circles) modes based on January 1985 statistics.

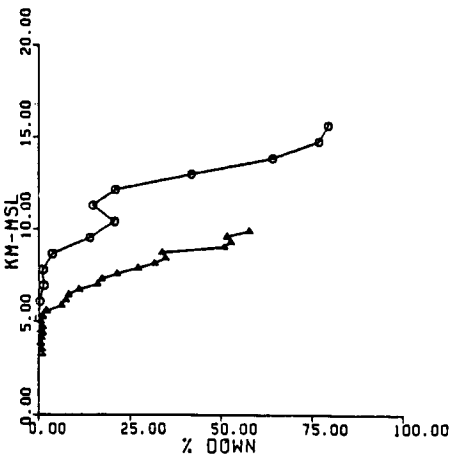

Figure 4. Probability that an outage will last 3 or more consecutive hours vs height at 915 MHz for the 3-μs (triangles) and 9-μs (circles) modes based on January 1985 statistics.

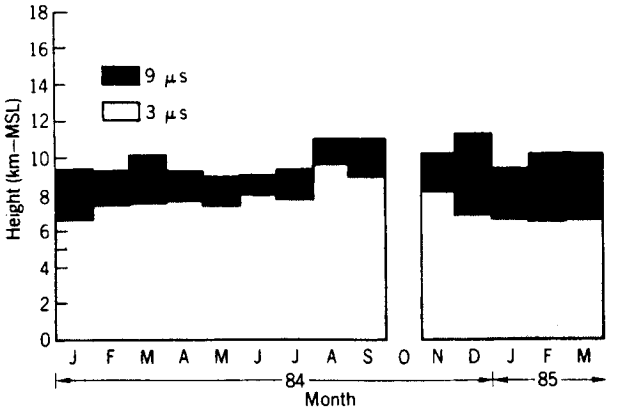

Figure 5. Lowest height where the probability of an outage for ≥ 3 consecutive hours is 0.1 for the 3- and 9-μs modes (915 MHz).

(The radar did not operate with a 9-μs pulse width in October 1984.) Note that the difference in height resolution for the two modes is about 900 m; therefore an increase of about 500 m would occur in the data even if there were no actual height increase. The actual height difference for the 915-MHz Profiler for the summer of 1984 is therefore very small. The height difference for the 50-MHz radar (Figure 6) shows a small height increase for the 9-μs mode for the summer of 1984 and 6-7 km for other months. Preliminary analyses of summer data for 1985 also shows a 6-7 km difference. The 405-MHz radar started operating in January 1985, and its height coverage and the difference between the two pulse widths falls between the other two radars (Figure 7).

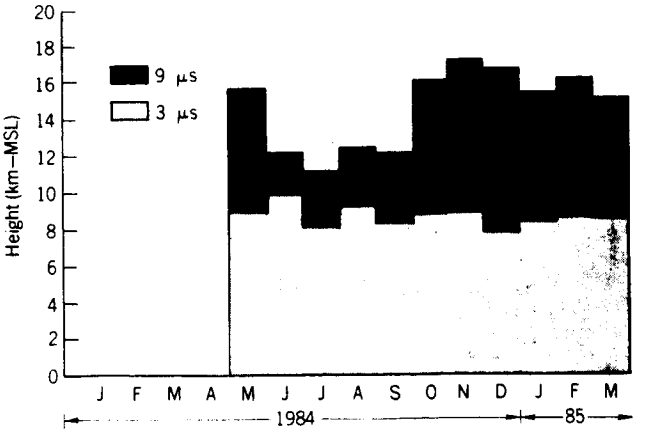

Figure 6. Lowest height where the probability of an outage for ≥3 consecutive hours is 0.1 for the 3- and 9-μs modes (50 MHz).

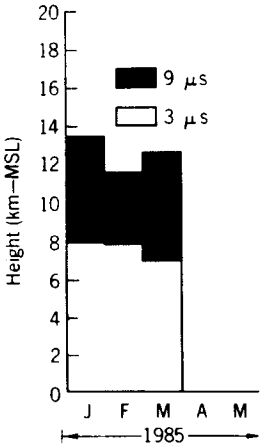

Figure 7. Lowest height where the probability of an outage for ≥ 3 consecutive hours is 0.1 for the 3- and 9-μs modes (405 MHz).

CONCLUSIONS

The height performance of radar wind profilers at upper-tropospheric and lower-stratospheric altitudes is important because the radar sensitivity required to measure winds at these altitudes is a major factor in determining the cost of the profiler. The profilers must reach these altitudes to provide the wind data needed for synoptic meteorology and commercial aviation. The specification of performance of a wind profiler must be a statistical specification because of the variability of backscatter cross section; if a profiler is required to measure winds to height H with height resolution of ΔH in time T under all meteorological conditions, the cost would be prohibitive for H, ΔH, and T needed for operational applications.

The upper-tropospheric/lower-stratospheric performance of wind profilers operating at 50-, 405-, and 915-MHz has been evaluated according to statistical criteria. The results of the evaluation indicate a wavelength-dependent backscatter cross section profile that favors longer wavelength radars for upper tropospheric wind measurement. For years it has been noted that 10-cm wavelength radars are not very useful clear-air radars above the boundary layer. The 33-cm (915-MHz) radar (with less sensitivity than that of a 10-cm wavelength meteorological Doppler radar) has dramatically different performance in that it can measure winds routinely to 9-10 km MSL. However, the 915-MHz radar has a much lower increase in height coverage when the sensitivity is increased compared to the height increase found with lower frequency radars. Both the fact that the 915-MHz radar can measure winds to much greater altitude than 3-GHz radars with equal sensitivity, and the fact that increased sensitivity with the 915-MHz radar does not produce the same increase in height coverage that is found with lower frequency radars, support the concept of a frequency-dependent backscatter cross section that is related to the increase in the length of the inner scale of turbulence as height increases, or that the wavelength dependence in theory of scattering is incomplete. The 405-MHz radar, with sensitivity equivalent to the 915-MHz radar, was able to obtain wind data to about 3 km greater altitude. The 50-MHz radar, with 6-7 dB more sensitivity than the UHF radars was able to measure winds to 15-16 km except during the summer months of 1984. (Summer data from 1985 show measurement capability to 16 km.) In case studies it has been noted that the 50-MHz profiler has marginal sensitivity for some meteorological conditions; a 3-dB increase in sensitivity should be sufficient to satisfy most requirements.

The 405-MHz radars being procured for a 30-station network (CHADWICK, 1986) will be about 9 dB more sensitive than the 405-MHz radar used in this study. The performance of these network radars would exceed that of the 50-MHz radar used in this study if the backscatter cross section is not frequency dependent. However, the data from this study indicate a frequency dependence that may limit the increased height coverage due to increased sensitivity, so a conservative statement regarding the upper altitude performance of the network radars is that they will clearly exceed the performance of the 405-MHz radar analyzed here and should be able to measure wind profiles to greater than 14 km MSL using statistical criteria similar to those used here.

REFERENCES

Chadwick, R. B. (1986), Wind profiler demonstration system, this volume.

Strauch, R. G., D. A. Merritt, K. P. Moran, K. B. Earnshaw, and D. W. van de Kamp (1985), The Colorado wind-profiling network, J. Atmos. Oceanic Technol., 1, 37-49.

1.4.3 A LOOK AT PROFILER PERFORMANCE

Edwin Kessler, Michael Eilts

National Severe Storms Laboratory, NOAA
Norman, OK 73069

NM 48481

Kevin Thomas

Cooperative Institute for Mesoscale Meteorological Studies
Norman, OK 73019

?
Ø9473 598

INTRODUCTION

Since about 1974, Doppler radars operating in UHF and VHF ranges have been used increasingly to study atmospheric winds. Historically, large systems capable of obtaining data from high altitudes have focused attention on the mesosphere and stratosphere, rather than on the troposphere (MST) wherein abides most of the weather considered by most meteorologists. Excellent histories and exposition of the technology involved have been given by GAGE and BALSLEY (1978) and BALSLEY and GAGE (1982). Perhaps the most recent comprehensive collection of MST studies is the HANDBOOK FOR MAP (Middle Atmosphere Program) Volume 9 (BOWHILL and EDWARDS, 1983).

Refinement of smaller systems with down-to-earth capabilities has stimulated investigation of their application to meteorological problems as evidenced by the existence of the session on forecasting applications at this Workshop. The prospect that vertical profiling radars would provide accurate wind information frequently and automatically is very intriguing to meteorologists at a time when data processing and communicating capabilities are advancing rapidly with commensurate development of numerical meteorological models. One scenario, for example, envisages that a network of wind profiling radars, substantially denser than the present day rawinsonde system but no more expensive, would transmit wind data as often as hourly to a central station, where a grand numerical model would fuse kinematic details with thermodynamic data gathered from weather satellites and perhaps a few ground-based thermodynamic profilers, and produce a weather outlook updated hourly. No weather system 100 km in size or larger would escape detection with this network; incipient storm triggers would be incorporated into the forecasts, and we would only very rarely be much surprised by weather developments.

Since this session includes papers by experts who indicate practical approaches to this meteorological utopia (see especially the outline of mathematical synthesis of diverse data given by Gal-Chen, this volume), we do not dwell on this further here. Rather, we address some questions the meteorologist must logically ask first, viz., what is the actual performance capability of these systems, how accurate is the wind data of interest to meteorologists, and from what altitudes in the troposphere are the data reliably obtained?

LITERATURE ON ACCURACY OF WIND FINDING BY PROFILING RADARS IN THE TROPOSPHERE

CLARK et al. (1985) cite 11 references that present some analysis of the accuracy with which wind profiling radars measure the winds. The findings of these studies are summarized in Table 1 and our list of references includes their sources. From these papers we have drawn the following conclusions:

a. There is a remarkable paucity of solid tests. Most tests involve one or more of the following limitations: check data unfortunately distant in time and/or space; too few cases to be definitive; winds too light to be definitive; test conducted in region where winds are quite variable.

Table 1. Profiler winds compared with winds by rawinsonde and other means.

Radar Location	Frequency	Beam-Width	Author	Date	Rawinsonde site & distance	Radar Method	Results
1. Sunset, Colo.	40 MHz	7.1° E-W 14.2° N-S	Green et al.	1975	Denver, 55 km	2 beams, 30° from vert.	About 65 wind measurements but unclear how many soundings involved. E-W radar wind and rawinsonde winds correlated 0.84. stand. dev. of diff ~5 ms^{-1}.
2. Sunset, Colo.	40 MHz	Presumably as in (1).	Warnock et al.	1978	Tabernash 33 km	2 beam method; compare winds with soundings whose balloons pass within 25 km.	Five cases; correlation 0.96 with winds above 4 km MSL. Some differences up to 5 ms^{-1}. Could be due to spatial separation.
3. Sunset, Colo.	40 MHz	Presumably as in (1).	Green et al.	1980	-	Winds by radar and NCAR aircraft compared.	On a day with Queenair, winds less than 5 m/sec; some differences were about as large, but reasonable agreement in profile shapes. On windy Feb. day with Sabreliner, almost all data (dis)agreed within 5-10 ms^{-1}. Data 4-6 km MSL only.
4. Sunset, Colo. Platteville	40 MHz 50 MHz	4.8° 2.5°	Clark et al.	1985	-	5 beams: one vertical, 2 E-W, 2 N-S	More consistent data on horizontal winds follow correction for vertical winds. Vertical winds more a problem in mountainous areas than on plains.
5. Chatanika, Alaska	1290 MHz	0.6°	Balsley et al.	1977	Fairbanks 5 km	VAD	Agreement to within 1-2 ms^{-1}.
6. Poker Flat, Alaska	50 MHz	2.0° az 4.0° el	Ecklund et al.	1977	2 km	143° component measured at different heights with beam fixed in elevation.	Two weather balloons, one was two hours different in time. Soundings and radar winds agreed to ~2 m/sec. Winds ranged from 1-14 m/sec.

Radar Location	Frequency	Beam-Width	Author	Date	Rawinsonde site & distance	Radar Method	Results
7. Max Planck Inst. for Aeronomy	53.5 MHz	3.5°	Rottger et al.	1978	Hannover 90 km	Measurements at vertical incidence and 12.5° off zenith.	Fair agreement (3 ms^{-1}) between radar and rawinsonde winds in one case. No winds below 1 km from radar. But max. rawinsonde wind only 6 ms^{-1}.
8. Arecibo	430 MHz	0.17°	Farley et al.	1979	San Juan 75 km	VAD scanning 22.5° intervals	Agreement w/San Juan generally to 3 ms^{-1}. Large variations in both ff and dd faithfully mirrored. Measurement above 5 km MSL; strong zero shift returns at low altitudes. Data scaled by hand; reference to need to develop criteria to deal with clutter echoes and complex atmos. echoes with multiple spectral peaks.
9. Arecibo	430 MHz	0.17°	Fukao et al.	1982	San Juan 75 km	Wind components measured along beam directed 15° from zenith, in meridional and azimuthal directions, each for 30 minutes.	Standard deviation of differences between radar and rawinsonde components was under 5 m/sec, ascribed to rawinsonde errors & temporal and spatial variability of winds. Rather faithful match vertical irregularities in Arecibo and San Juan profilers. Winds up to 30 ms^{-1}.
10. Platteville, Colo.	50 MHz	2°	Ecklund et al.	1979	Denver	2 beams, 15° from vertical	2 comparisons. Differences generally <5 ms^{-1} except one at 8 km >20 ms^{-1}. Only heights above 4 km agl.
11. Kwajalein	410 MHz	1.06°	Crane	1980	-	Compared with Jimsphere tracked with same radar.	Agreement to ~ 1 ms^{-1}.
12. Jicamarca	50 MHz	0.5°	Fukao et al.	1981	Lima 30 km	2 beams, 3.45° from vertical	Four cases; radar data offset 10-15 ms^{-1} from Lima data 20 km away. Reason for discrepancies unclear. Note that any systematic error must be greatly amplified in calculations because of small zenith angle.

b. In a few cases (5, 8, 9, 11) with radar beams quite narrow (~1° or less), results are excellent, differences with other reported winds being indisputably within the range of uncertainty attributable to the other wind-finding method.
c. Almost all of the test data concern VHF. There are only three papers treating results in the 400-MHz region, and these apply to unusual and markedly superior equipment, not of the economical type being recommended for development and deployment in a meteorological network.
d. The typical deviation of radar-measured and comparison winds is near 5 m s^{-1}. This is not small enough to give ease but not so large that it cannot be largely explained by spatial and temporal separations in the data acquired.
e. There are not enough data for us to be confident about possible systematic differences between true winds and data gathered with VHF radars of the type proposed for meteorological use. It appears, however, that bias, if it exists, is not greater than about 2 m s^{-1}.
f. Study (4) in Table 1 is persuasive in its indication that vertical velocity contaminates the indications of horizontal winds at the Sunset site and in its suggestions of means to reduce such contamination greatly with multibeam systems. This paper, in a milieu of other meteorological inputs, is also persuasive in its evidence for a substantially smaller magnitude and persistence of vertical velocities in the plains than in the Rocky Mountains.
g. Data collected by the 50-MHz systems deployed for weather studies are in the layer between about 2 km AGL and 17 km.

As we interpret these data to reach our conclusions, we should refer to studies of wind variability and of rawinsonde accuracy; rawinsondes represent usual means for measuring and studying winds. During 1968, during the NSSL spring program of observations, paired soundings were released within five minutes of each other at two sites and tracked with independent tracking systems within a few hundred feet of each other on the ground. Seven pairs at each site produced comparative wind data. The standard deviation of wind speed differences near Fort Sill, Oklahoma, was 1.43 m s^{-1}, and near the television antenna for WKY north of Oklahoma City it was 2.55 m s^{-1}; standard deviations of directional differences were 6.00 and 7.68 degrees, respectively. Since the balloons were launched in fair weather, it is estimated that practically all the differences are attributable to properties of the procedures and equipment used to gather the data. In particular, the larger value given for the WKY site probably reflects some difficulties there that were especially noticeable (BARNES et al., 1971). Also in 1968, at 10-station rawinsonde network near the National Severe Storms Laboratory in Norman, with station spacing ranging from 25 to 132 km and average spacing of 39 km, provided 573 soundings appropriate for study of wind structure, of which 104 soundings were made during periods devoid of local storms (BARNES and LILLY, 1975). The rms vector wind difference measured at the 46 km distance significant for the current study was less than 3 m s^{-1} at each of the altitudes examined -- 1500, 3000, and 5700 m MSL.

Finally, there is the study of HOEHNE (1980) who found 3.1 m s^{-1} to be the standard deviation of the difference between wind speeds measured with separate tracking systems that tracked pairs of sondes suspended from single balloons. Hoehne's value seems large in view of the results from the NSSL data described above.

Clearly, work remains to define both the wind-profiling performance envelope of the 50-MHz and 405-MHz systems proposed for meteorological use, and the spatial variability of actual winds.

50-MHz PROFILER IN OKLAHOMA

In a project involving cooperation between the Wave Propagation Laboratory in Boulder, Colorado, and the National Severe Storms Laboratory, a 2-beam 50-MHz profiler was installed during Spring 1985 at Great Plains Apiaries, 34°58'N x 97°31'W. This is in Section 21, Township 6 North, Range 3 West, McClain County, Oklahoma, 46 km south of the Oklahoma City Weather Service Forecast Office, where rawinsonde data are obtained twice daily. It is a region of rolling hills with slopes averaging near 2°; and valley bottoms are about 35 meters below hilltops about 2 km apart. The radar is at an elevation of 330 meters MSL and surrounding hilltops are typically 355 meters MSL. In order to minimize displacement of earth during installation and subsequent erosion problems, the 50-m-square dipole arrays were oriented along azimuths 11.3° and 101.3°, referenced to true north, with Earth's surface at the site tilted upward 2.1° toward azimuth 11.3°. The dipoles oriented toward 11.3° project a beam toward azimuth 109.4° and elevation angle 75.4°; and the dipoles oriented toward 101.3° project a beam toward 191.3° and elevation angle 73.4°. The two-way beamwidths are about 5° to half power. The radar was placed "on the air" about May 10th with software applicable to installations on a level surface; software properly accounting for the tilted terrain and beam angles given above was installed on July 15th. Data collected before the revised software was installed can be corrected.

The radar operates automatically, with data transmissions hourly to computers at the Wave Propagation Laboratory in Boulder, Colorado, and at the University of Oklahoma in Norman. The archival data are represented in Table 2. The winds are drived from a composite of up to 12 determinations during the previous hour; the computer selects contributions to the composite on the basis of a sufficiently large signal-to-noise ratio; processing details and other information have been presented by STRAUCH et al. (1985). Details on the Doppler spectra are available but must be requested specifically. A dedicated line will facilitate more comprehensive recording and in-depth study of the Oklahoma data.

SOME COMPARISONS INVOLVING DATA FROM THE OKLAHOMA 50-MHz PROFILER

We have compared rawinsonde data acquired at Oklahoma City on 39 occasions from August 8 to September 8, 1985, and on 11 occasions from October 1 to October 8, 1985, with profiler data acquired at the same times (within one hour of 00 Z and 12 Z). (Obviously erroneous data in both sets, such as the point indicated in Table 2 were excluded.) A majority of the soundings in the first set are characterized by light winds and weak shear throughout the troposphere. The second set is marked by substantially stronger winds and vertical shear.

Vertical interpolation is necessary for comparison of the rawinsonde data with profiler data. Data from one sensor were linearly interpolated to the height of the data from the other sensor. This interpolation is a source of error in the comparison; its magnitude is surely small because of the small vertical separation between data (290 m for the short pulse and 870 m for the long pulse). At the higher heights the long pulse data are sometimes sparse, with larger interpolation errors.

The root-mean-square (rms) average difference for the 39 comparisons of the first set, for both the u (positive to the east) and the v (positive to the north) wind components are listed in Table 3a. The average rms differences of the components are about 2.5 m s^{-1} for the rawinsonde/short pulse comparison, 3.5 m s^{-1} for the rawinsonde/long pulse comparison, and 1.5 m s^{-1} for the long pulse/short pulse comparison. The rms vector differences are the square roots of the sum of squares of the average rms differences.

C-2

Table 2.

SITE: OKLAHOMA
DATE: 85 5 23
TIME: 23 0 0
NPRO: 12 NTDA: 350 NOSP: 13 PULW: 3.67 PRPR: 238.00
MAX HOR VEL: 62.87
FIRST HT (AGL): 1.64
NUMBER OF HEIGHTS: 24
DELTA HEIGHT (KM): .29
POWER ANTENNA: EW

GATE	SPEED	DIRECT	HEIGHT	#E	#N	POWER
1	-999.00	-999.0	1.97	2	12	-999.0
2	5.37	301.5	2.26	9	12	48.3
3	7.57	297.5	2.54	12	12	58.9
4	7.88	303.6	2.83	12	12	69.4
5	7.42	307.2	3.12	12	12	72.0
6	7.84	322.9	3.41	12	12	65.6
7	6.17	338.4	3.70	12	12	57.2
8	5.45	343.3	3.99	12	12	52.3
9	4.88	323.7	4.28	12	12	49.1
10	6.80	304.3	4.57	12	12	46.5
11	8.12	299.9	4.86	12	12	45.5
12	5.65	300.4	5.14	12	11	48.5
13	4.60	294.8	5.43	12	11	48.2
14	3.89	294.3	5.72	12	11	42.7
15	3.27	293.4	6.01	11	10	36.1
16	5.46	302.1	6.30	11	9	35.2
17	9.74	302.0	6.59	11	10	38.0
18	10.34	299.2	6.88	12	11	38.0
19	10.84	294.2	7.17	12	10	35.7
20	11.43	293.2	7.46	10	9	31.3
21	11.22	292.2	7.74	9	7	29.2
22	13.54	287.7	8.03	8	6	25.0
23	13.61	288.7	8.32	8	5	23.6
24	2.25	314.5	8.61	5	5	34.8

SITE: OKLAHOMA
DATE: 85 5 23
TIME: 23 0 0
NPRO: 12 NTDA: 124 NOSP: 22 PULW: 9.67 PRPR: 672.00
MAX HOR VEL: 62.85
FIRST HT (AGL): 2.65
NUMBER OF HEIGHTS: 18
DELTA HEIGHT (KM): .87
POWER ANTENNA: EW

GATE	SPEED	DIRECT	HEIGHT	#E	#N	POWER
1	7.22	310.7	2.98	12	12	65.8
2	7.35	317.8	3.84	12	12	66.9
3	6.70	314.4	4.71	12	11	61.8
4	5.85	305.8	5.58	11	10	54.1
5	6.20	309.1	6.44	11	12	46.2
6	7.59	301.9	7.31	11	12	42.3
7	7.83	294.1	8.18	10	12	37.8
8	8.82	287.3	9.05	9	9	32.0
9	6.36	291.2	9.91	9	8	28.6
10	11.75	294.6	10.78	8	10	25.9
11	20.44	289.1	11.65	8	10	24.6
12	19.53	292.0	12.51	8	10	24.8
13	19.65	287.5	13.38	7	7	23.4
14	18.03	285.5	14.25	5	7	20.6
15	10.49	291.9	15.11	6	8	23.2
16	11.79	303.7	15.98	7	4	21.7
17	10.82	279.2	16.85	5	5	19.9
18	-999.00	-999.0	17.71	5	3	27.4

Table 3a. Average RMS difference of the u and v wind components for 39 comparisons during August 8 - September 8, 1985.

Comparison	Average RMS difference		RMS vector wind difference ms^{-1}
	u	v	
Rawinsonde/short pulse	2.55	2.44	3.5
Rawinsonde/long pulse	4.15	2.93	5.1
Long pulse/short pulse	1.73	1.17	2.1

Table 3b. Average RMS difference of the u and v wind components for 11 cases during October 1-8, 1985.

Comparison	Average RMS difference		RMS vector wind difference ms^{-1}
	u	v	
Rawinsonde/short pulse	2.8	2.3	3.6
Rawinsonde/long pulse	4.3	3.3	5.4
Long pulse/short pulse	3.1	1.5	3.4

In order to learn if the average rms differences include a systematic bias, we also computed the mean wind speed at all the points for which comparative data existed (approximately 400 from each sensor). These mean winds for the first set of data are listed in Table 4a. Note that the average profiler winds, both with long pulse and short pulse, are smaller than the mean winds estimated by rawinsonde. In the rawinsonde/short pulse comparison the difference between the mean wind estimates is 1.9 m s^{-1}; the speed of the short pulse winds averages 74.3% of the rawinsonde winds. Similarly, the long pulse winds average 71.9% of the rawinsonde winds or 2.5 m s^{-1} less than corresponding rawinsonde winds.

The findings from the August 8 - September 8 period are reinforced in the October data, represented in Tables 3a and 4a. The October period was one of substantially stronger winds, as shown by the u component listed in Table 4a.

All in all, these comparisons of rawinsonde and profiler data indicate a bias toward zero in the profiler winds. More comparisons with other sensors as well as in-depth analysis of Doppler spectral data with collocated profiler and rawinsonde should be informative. It will be particularly important to determine whether the rawinsonde/profiler differences represent a constant offset or a percentage bias.

It should be noted that the average differences discussed here are compounded of rather widely different situations. Thus, Figure 1a shows a case with marked systematic differences between wind speeds at the rawinsonde and

Table 4a. Mean wind speeds for the three comparisons in Table 3a.

Sensor	Mean Wind	Sensor	Mean Wind	Difference
Rawinsonde	7.24 m s^{-1}	short pulse	5.38 m s^{-1}	1.86 m s^{-1}
Rawinsonde	8.94	long pulse	6.43	2.51
Long pulse	5.22	short pulse	5.11	0.11

Table 4b. Mean wind speeds for the three comparisons in Table 3b.

Sensor	Mean Wind (u comp.)	Sensor	Mean Wind (u comp.)	Difference of means
Rawinsonde	14.2	short pulse	12.8	1.4
Rawinsonde	18.1	long pulse	15.2	2.9
Long pulse	15.5	short pulse	13.4	2.1

profiler sites, but 1b shows that wind directions reported on the same occasion agree quite well. On another date, shown in Figure 2a and 2b, rawinsonde and profiler wind speeds are in remarkable agreement except in the layer from 7.5 to 11 km, where differences are up to about 15 m s^{-1}, while directions are in close agreement except differences up to about 60° in the layer from 3 to 6 km! We certainly must identify the reason(s) for such features since they represent very large deviations in implied kinetic energy and are correspondingly significant for forecasting; such interesting characteristics are present in practically every sounding pair.

POSSIBLE EXPLANATIONS FOR DISCREPANCIES IN OKLAHOMA DATA

The following possible sources of differences noted above are: ground clutter contamination; interference from stray electromagnetic transmissions during oil field operations, rawinsonde errors, spatial and temporal variability of the wind, hardware and software discrepancies in the profiler radar; backscatter from edges of the main beam and from sidelobes, and contamination by vertical velocities associated with standing and/or migratory waves. At this writing we are just beginning to investigate these possibilities and to look for others.

The authors believe that the differences presented are significantly larger than can be explained by spatial variability of the wind. We plan to evaluate this definitively during Spring 1986 with aid of a rawinsonde unit at the radar site.

The sometime differences between profiler indications on long and short pulse illustrated in Figure 3 may be relatable to nonlinear vertical distributions of wind shear interactive with the different pulse lengths.

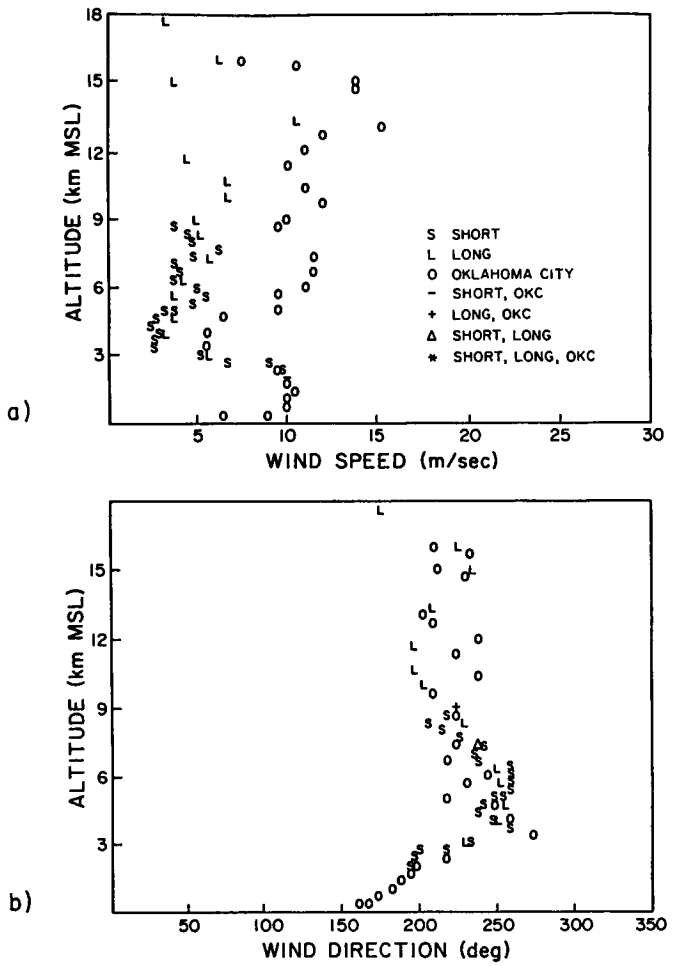

Figure 1. Wind speed (top) and direction (bottom) measured by rawinsonde (O) and Oklahoma profiler (other symbols) on 13 August 1985, 00 GMT. Abscissae show wind speed in increments of 5 m s^{-1} and direction in increments of 50°, respectively. Ordinates show heights MSL in km.

Concerning variations of reflectivity with elevation angle, it has been noted that since VHF reflectivity declines with increasing zenith angle, the measured velocities are biased low by the more reflective patches that have smaller radial velocities in the more elevated portions of the beam. Although formulations by DOVIAK and ZRNIC' (1984) show this effect to be negligible at zenith angles larger than about 8° (Figure 4), consideration of sidelobes may alter first impressions. A useful experiment in this regard would involve addition of switchable phase shifters to the profiler antenna system and study of backscattered power from a beam scanned in elevation.

GENERAL CONCLUSIONS

Highly accurate wind finding is confirmed for radars with narrow beams, especially when VAD scanning is employed. Systematic differences up to 2 m

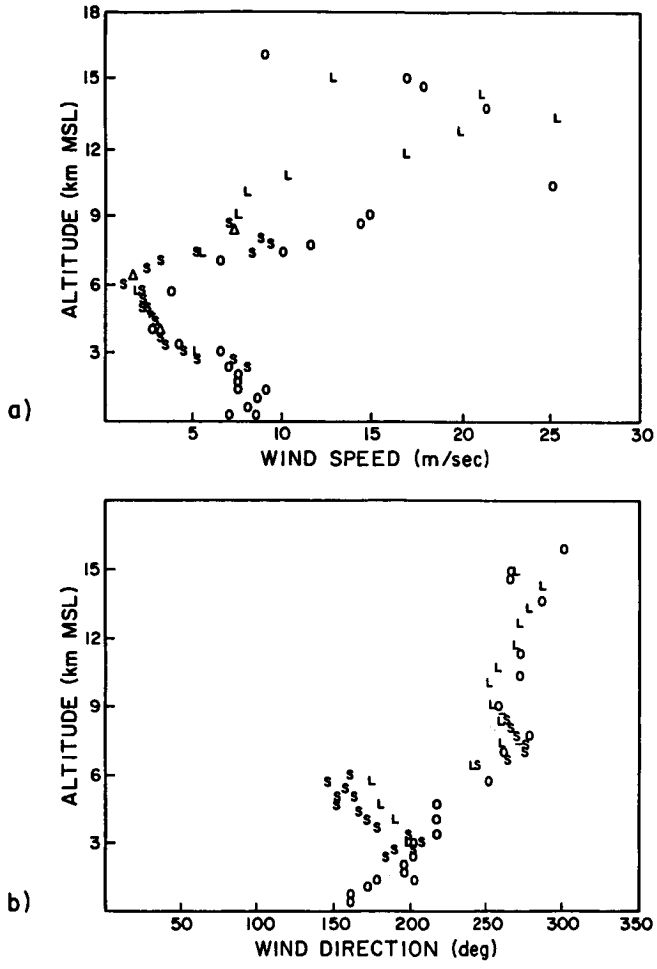

Figure 2. Same as Figure 1, except 19 August 1985, 00 GMT.

s^{-1} between wind data from rawinsondes and profilers of the inexpensive type recommended for widespread use, average random variations up to 5 m s^{-1} between wind data from these sensors, and occasional differences up to 15 m s^{-1}, are not well explained in much of the data reported so far. This is not reason to be discouraged, however, because confidence in the basic profiler method is well founded (KOSCIELNY et al., 1984), and the studies that leave us with concerns, including this one, are insufficiently definitive. We are stimulated to concentrate our efforts toward quantifying the differences in observations by profilers and other sensors, and then seeking their causes, so that large variances can be understood and data of known and acceptable accuracy can be produced routinely. We can be confident that a much better situation will develop as we direct our resources strongly to this problem.

SUMMARY

The Workshop provided a valuable exchange of information among meteorologists and engineers. Clearly, advances in communicating, data processing, and

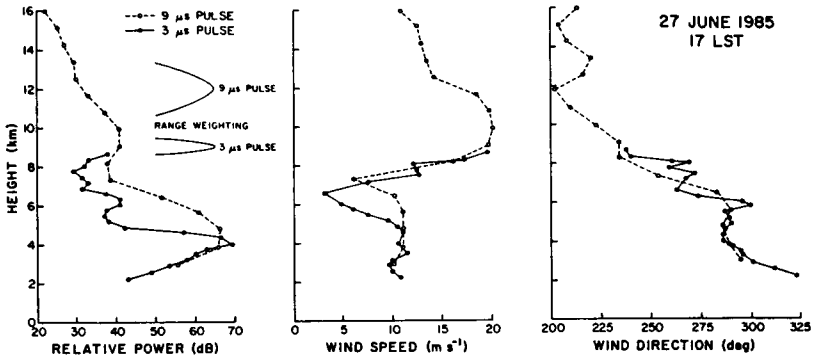

Figure 3. Vertical variations of reflectivity in a layer with vertical wind shear produce differences between the winds measured with short pulse and long pulse. Ordinates show heights in kilometers. Abscissae left to right are relative power, wind speed, and wind direction measured by the 50-kHz profiler in Oklahoma.

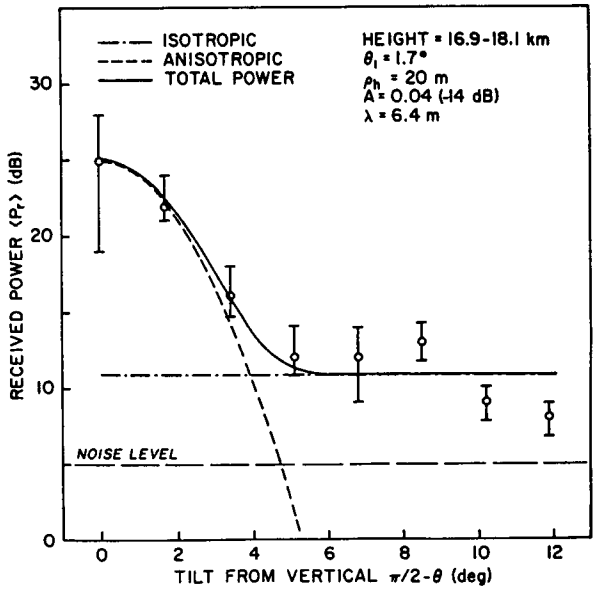

Figure 4. Reflectivity vs zenith angle based on data gathered by Rottger and a model by DOVIAK and ZRNIC' (1984).

mathematical modeling of meteorological phenomena have brought the meteorological community to the threshold of effective use of kinematic and thermodynamic data gathered more frequently and on a finer grid than heretofore. Such additional data provided routinely should lead to improved models and to improved forecasts of precipitation and other weather variables.

Conference papers demonstrate a wide range of interesting studies ongoing with profilers, but the performance envelope of wind profiling radars needs better definition. In particular, further address is needed toward questions concerning possible bias in profiler wind data, measurement of winds in the planetary boundary layer, and the accuracy of wind estimates in relation to the time period over which averages are calculated.

In view of great interest in boundary layer parameters and their importance to interpretation of individual profiler data, as well as to forecasting with network data, it is urged that profiler programs identify and implement means for providing boundary layer data, especially on wind and precipitation, at profiler radar sites.

The meteorological community is interested in prospects for studying lightning and precipitation processes with VHF and UHF profiler radars because Doppler signatures of meteors and of the air motion itself may be apparent simultaneously.

ACKNOWLEDGMENTS

We thank S. L. Barnes, R. J. Doviak, R. G. Strauch, and D. S. Zrnic' for good advice and for some substantial contributions to this paper. The Oklahoma profiler was installed by engineering students at Oklahoma University with guidance and assistance of N. Abshire of the Wave Propagation Laboratory, which provided the instrument. R. Castaldo and J. Windes of OU have maintained the Oklahoma profiler since its installation, and E. Walker of OU has been principal investigator on the contract arranged to install and maintain this facility in Oklahoma.

REFERENCES

Balsley, B. B., N. Cianos, D. T. Farley, and M. J. Baron (1977), Winds derived from radar measurements in the arctic troposphere and stratosphere, J. Appl. Meteorol., 16, 1235-1239.

Balsley, B. B., and K. S. Gage (1982), On the use of radars for operational wind profiling, Bull. Am. Meteorol. Soc., 63, 1009-1018.

Barnes, S. L., J. H. Henderson, and R. J. Ketchum (1971), Rawinsonde observation and processing techniques at the National Severe Storms Laboratory, NOAA Tech. Memo. ERL NSSL-53, 244-246.

Barnes, S. L., and D. K. Lilly (1975), Covariance analysis of severe storm environments, Preprints, Ninth Conf. on Severe Local Storms, Oct. 21-23, 1975, Am. Meteorol. Soc., Boston, MA, 301-306.

Bowhill, S. A., and B. Edwards (1983), Middle Atmosphere Program, Handbook for MAP, Vol. 9, SCOSTEP Secretariat, Univ. Illinois, Urbana-Champaign.

Clark, W. L., J. L. Green, and J. M. Warnock (1985), Estimating meteorological wind vector components from monostatic Doppler radar measurements: A case study, Radio Sci. (in press).

Crane, R. K. (1980), Radar measurements of wind at Kwajalein, Radio Sci., 15, 383-394.

Doviak, R. J., and D. S. Zrnic' (1984), Reflection and scatter formula for anisotropically turbulent air, Radio Sci., 19, 325-326.

Ecklund, W. L., D. A. Carter, and K. S. Gage (1977), Sounding of the lower atmosphere with a portable 50 MHz coherent radar, J. Geophys. Res., 82, 4969-4971.

Ecklund, W. L., D. L. Carter, and B. B. Balsley (1979), Continuous measurements of upper atmospheric winds and turbulence using a VHF Doppler radar: Preliminary results, J. Atmos. Terr. Phys., 41, 983-944.

Farley, D. T., B. B. Balsley, W. E. Swartz, and C. LaHoz (1979), Tropical winds measured by the Arecibo radar, J. Appl. Meteorol., 18, 227-230.

Fukao, S., A. Aoki, K. Wakasugi, T. Tsuda, S. Kato, and D. A. Fleisch (1981), Some further results on the lower stratospheric winds and waves over Jicamarca, J. Atmos. Terr. Phys., 43, 649-661.

Fukao, S., T. Sato, N. Yamasaki, R. M. Harper, and S. Kato (1982), Winds measured by a UHF Doppler radar and rawinsondes: Comparisons made on twenty-six days (August-September 1977) at Arecibo, Puerto Rico, J. Appl. Meteorol., 21, 1357-1363.

Gage, K. S., and B. B. Balsley (1978), Doppler radar probing of the clear atmosphere, Bull. Am. Meteorol. Soc., 59, 1074-1093.

Green, J. L., J. M. Warnock, R. M. Winkler, and T. E. VanZandt (1975), Studies of winds in the upper troposphere with a sensitive VHF radar, Geophys. Res. Lett., 2, 19-21.

Green, J. L., K. S. Gage, W. L. Clark, T. E. VanZandt, and P. H. Hildebrand (1980), Joint instrumented aircraft and VHF Doppler radar measurements of wind near Boulder, Colorado, Preprints, 19th Conf. on Radar Meteorology, April 15-18, Miami Beach, FL, 624-628.

Hoehne, W. E. (1980), Precision of National Weather Service upper air measurements, NOAA Tech. Memo NWS, T&DE-16.

Koscielny, A. J., R. J. Doviak, and D. S. Zrnic' (1984), An evaluation of the accuracy of some radar wind profiling techniques, J. Atmos. and Oceanic Tech., 1, 309-320.

Rottger, J., J. Klostermeyer, P. Czechowsky, R. Ruster, and G. Schmidt (1978), Remote sensing of the atmosphere by VHF radar experiments, Naturwiss., 65, 285-296.

Strauch, R. G., D. A. Merritt, and K. P. Moran (1985), Radar wind profilers in the Colorado network, NOAA Tech. Memo., ERL WPL-120.

Warnock, J. M., T. E. VanZandt, J. L. Green, and R. H. Winkler (1978), Comparisons between wind profiles measured by Doppler radar and by rawinsonde balloons, Geophys. Res. Lett., 5, 109-112.

D12-47

2.1.1 HARDWARE REQUIREMENTS: A NEW GENERATION PARTIAL REFLECTION RADAR FOR STUDIES OF THE EQUATORIAL MESOSPHERE

R. A. Vincent

Physics Department
University of Adelaide
Adelaide, South Australia 5001

A new partial reflection radar is being developed for operation at the proposed Equatorial Observatory. The system is being designed to make maximum use of recent advances in solid-state technology in order to minimize the power requirements. In particular, it is planned to use a solid-state transmitter in place of the tube transmitters previously used in PR systems. Solid-state transmitters have the advantages that they do not need high voltage supplies, they do not require cathode heaters with a corresponding saving in power consumption and parts are readily available and inexpensive; the cost of high voltage vacuum tubes is becoming prohibitive. It should be possible to achieve 25 kW peak powers with recently announced fast switching transistors. Since high mean powers are desirable for obtaining good signal-to-noise ratios, it is also planned to phase code the transmitted pulses and decode after coherent integration.

All decoding and signal processing will be carried out in dedicated microprocessors before the signals are passed to a microcomputer for on-line analysis. Recent tests have shown that an Olivetti M24 micro (an IBM compatible) running an 8-MHz clock with a 8087 coprocessor can analyze data at least as fast as the minicomputers presently being used with the Adelaide PR radar and at a significantly lower cost. The processed winds data will be stored in nonvolatile CMOS RAM modules; about 0.5 to 1 Mbyte is required to store one week's information.

By using solid state, a modularized construction and keeping the use of moving parts to a minimum (i.e. no tape or disk drives) the system will be more rugged and compact than previous systems and will be significantly more power efficient. These are important considerations when the system will be used in a hot and humid environment.

2.1.2 NEED FOR A SUBTROPICAL WIND PROFILING SYSTEM

J. Rottger[1], M. F. Larsen[2], H. M. Ierkic[1], and T. Hagfors[3]

[1]Arecibo Observatory, Arecibo, Puerto Rico
[2]Clemson University, Clemson, South Carolina
[3]NAIC, Ithaca, New York

INTRODUCTION

The purpose of this paper is to point out the need for, and the benefit that can be derived from, a national wind profiling facility located in the subtropics. At present no such facility exists. There are several advantages associated with a low-latitude location. The first is that wave motions and large-scale circulations unique to the tropics can be studied. The second is that the relatively steady mean flows in the subtropical belt may provide a "cleaner" environment for studies of waves common at all latitudes. Examples will be given below. We suggest the Arecibo Observatory as an ideal site for a wind profiling facility since the land and much of the computing, technical, and scientific support is already available.

LARGE-SCALE WAVES

The Arecibo Observatory in Puerto Rico is located at 18°N and has a subtropical climate. Large-scale disturbances affecting the island are typically associated with waves in the easterlies. The ITCZ (Intertropical Convergence Zone) is usually considerably south of Arecibo but does reach that far north on occasion. Hurricanes and tropical storms sometimes track across or very near the island.

An example of the research topics that a wind profiler system at Arecibo could be used to investigate is the observation of quasi-inertial waves. SATO and WOODMAN (1982) obtained radar data in the upper troposphere and lower stratosphere over a period of 48 hours. Their analysis indicated a long period wave in the lower stratosphere with amplitude of several m/s. Further analysis of the same data set by MAEKAWA et al. (1984) has shown that the intrinsic wave period is very near the inertial period, although the earth-fixed period is nearly twice as long. The wave behavior is particularly evident between 14 and 20 km altitude. A graduate student at Cornell (C. R. Cornish) is just finishing his analysis of a 6-day data set obtained in May 1982. Again there were wind perturbations with a period very near the inertial period for the latitude of Arecibo. The preliminary results indicate that the waves are generated near the height of the subtropical jet and propagate upward into the lower stratosphere. The wave is dissipated significantly by the time it reaches an altitude of 20 km due to its short vertical wavelength of the order of 1 km. Amplitudes of 3-5 m/s are significant in the lower stratosphere, and the dissipation of the waves implies that there is a redistribution of energy and momentum so as to decrease the subtropical jet maximum. The wind profiler array, together with radiosonde data from the region, would provide information about the intermittency of the waves, the dependence of wave amplitude on the wind speed maximum or local shear, and the effect of wave dissipation on the flow at higher altitudes.

The observations of CADET and TEITELBAUM (1979) and BARAT (1983) indicate that quasi-inertial waves are strongly affected by the mean flow when the wind speeds increase. The steady easterly flows in the subtropical regions provide a good "laboratory" for studying the interaction of waves and the background medium under conditions that are less complicated than those typically found at midlatitudes.

EFFECTS OF TROPICAL CONVECTION AND LOCAL HEATING

Other topics of interest would include the dynamics of locally generated tides as first observed by WALLACE and HARTRANFT (1969) and WALLACE and TADD (1974). They noted that the tidal motions in the lower stratosphere in the Caribbean were not migrating tides but appeared to be generated by local surface heating. To our knowledge, still very little is known about such an effect. Data could also be provided to support land/sea breeze studies and modeling. Land/sea breezes have been reviewed extensively by ATKINSON (1981) who points out the connection between this type of circulation and the development of local convection.

A great deal was learned about the dynamics of waves in the easterlies in the GATE experiment (NCAR, 1977). However, further observations can still be useful for the purpose of better defining the interaction between large and small scales and for improving our understanding of the effect of the environment on clouds. Also, measurements of vertical velocity fields within developing clouds can be used to improve parameterizations of the effects of clouds on their environment (ANTHES, 1983). Vertical velocity measurements will not be possible once heavy precipitation develops since even the echoes at the relatively long wavelength of 6 m will then be dominated by the precipitation. Cloud studies will be particularly effective if they are carried out with the VHF radar in conjunction with other instrumentation to determine temperature and moisture fields. On a longer time scale, a climatology of the vertical velocity can be developed in order to improve our understanding of the dynamics responsible for the vertical velocity fields in the subtropics.

Dr. Joanne Simpson of GLAS (Goddard Laboratory for Atmospheric Sciences) has indicated (private communication, 1984) that observations of the horizontal winds and vertical velocity fields prior to the development of cumulus over the island would be valuable input to and for comparison with a numerical cloud model that Dr. Simpson has developed at GLAS. Dr. Bruce Albrecht of the Pennsylvania State University has pointed out (private communication, 1984) that our understanding of how convection develops could be improved significantly if the Penn State portable 0.5-cm radar was brought to Puerto Rico for the purpose of observing clouds and the dynamic environment in which they develop in conjunction with the profiler measurements. The wind profiler data could be used to study land/sea breezes and for comparisons with models such as the one developed by Dr. Roger Pielke of Colorado State University.

TURBULENT PROCESSES

Recently, there has been considerable controversy about the underlying dynamics responsible for mesoscale kinetic energy spectra. There appears to be agreement about the spectral slope of the energy spectrum of the horizontal wind (BALSLEY and CARTER, 1982; LARSEN et al., 1982; NASTROM and GAGE, 1983; LILLY and PETERSEN, 1983). A number of observations have shown the slope to follow a $k^{-5/3}$ power law from some undetermined small-wavelength or low-frequency limit out to scales as large as 500-1000 km and periods out to 12 hours. There is little doubt that the motions are not three-dimensional at such large scales, at least not in the sense required for a Kolmogoroff inertial subrange. The competing interpretations argue that the observations indicate either a two-dimensional turbulent process (GAGE, 1979; LILLY, 1983) or that it is a manifestation of a universal spectrum of gravity waves similar to what is observed in the oceans (VANZANDT, 1982).

Analysis by LARSEN et al. (1985) of several of the 3 to 8 hour time series of velocity obtained earlier at Arecibo has shown an instance of a strong spectral peak near the Brunt-Vaisala period during a period of active convection. The spectrum a few hours later shows an enhancement of the energy at lower

frequencies. This example is far from conclusive, but it is suggestive of a two-dimensional turbulent process in which energy cascades from smaller to larger scales. More extensive observations during and following periods of convection are needed to determine whether the effect is repeatable. It is possible that the enhancement of low frequency power is associated with an unrelated process. Simultaneous frequency and vertical wave number spectra of the horizontal and vertical velocities would also help to resolve the problem of the interpretation of mesoscale kinetic energy spectra since the predictions of the universal gravity-wave spectrum theory, in particular, could then be tested.

In addition, the VHF array can provide information about the frequency of occurrence and spatial distribution of turbulent layers in the lower stratosphere. The theoretical analysis of WOODMAN and RASTOGI (1984), based on earlier Arecibo 430-MHz observations, has already shown that vertical transport by turbulence is a much more important process than had been thought earlier. The crucial parameters determining the magnitude of the transport are the frequency of occurrence and distribution of widths of the layers, information that the radar can provide. Also, the relationship between the layers and waves in the medium is still an open question, although it appears that the layers occur at certain phases of the long-period, near-inertial waves seen in the lower stratosphere. Dr. P. K. Rastogi of Case Western Reserve University is interested in obtaining more statistics on the intermittency, width, and height of occurrence of turbulent layers in the lower stratosphere in order to refine a model of turbulent transport due to such layers.

VERTICAL MOMENTUM FLUXES

At present there is great interest in upward momentum fluxes due to gravity waves (VINCENT and REID, 1983) since it is believed that gravity waves breaking in the mesosphere account for the momentum sources needed to explain the general circulation of that region (LINDZEN, 1983; LINDZEN and FORBES, 1983). The wind profiling array at Arecibo could be used to study both the momentum fluxes out of the troposphere and their variation with height in the mesosphere. The antenna array will probably not be sensitive enough to detect turbulent scatter from the mesosphere directly, but it should be possible to use it as a meteor radar (S. K. Avery, private communication). Whenever detection of turbulence in the mesosphere is required, the 430-MHz facility may be applied.

METEOR RADAR

In addition to studying the momentum fluxes in the mesosphere, an important research topic, it is also important to obtain a better climatology of the mesospheric circulation above Arecibo. The data could be used to calculate momentum fluxes and accelerations of the mean flow due to gravity waves (S. K. Avery, private communication, 1984) and to study tidal characteristics at those altitudes.

CONCLUSION

The research topics described above are only representative, but they indicate the unique characteristics of the subtropical region as a site for a wind profiling system.

REFERENCES

Anthes, R. A. (1983), Numerical models, in The National STORM Program: Scientific and Technological Bases and Major Objectives, edited by R. A. Anthes, UCAR, Boulder, Colorado.

Atkinson, B. W. (1981), Meso-scale Atmospheric Circulations, Academic Press, New York, 495 pp.

Balsley, B. B., and D. A. Carter (1982), The spectrum of atmospheric velocity fluctuations at 8 km and 86 km, Geophys. Res. Lett., 9, 465-468.

Barat, J. (1983), The fine structure of the stratospheric flow revealed by differential sounding, J. Atmos. Sci., 40, 2451-2466.

Cadet, D., and H. Teitelbaum (1979), Observational evidence of internal inertia-gravity waves in the tropical stratosphere, J. Atmos. Sci., 36, 892-907.

Gage, K. S. (1979), Evidence for a $k^{-5/3}$ law inertial range in mesoscale turbulence, J. Atmos. Sci. 36, 1950-1954.

Larsen, M. F., M. C. Kelley, and K. S. Gage (1982), Turbulence spectra in the upper troposphere and lower stratosphere at periods between 2 hours and 40 days, J. Atmos. Sci., 39, 1035-1041.

Larsen, M. F., R. F. Woodman, T. Sato, and M. K. Davis (1985), Power spectra of vertical velocities in the troposphere and lower stratosphere observed at Arecibo, Puerto Rico, submitted to J. Atmos. Sci..

Lilly, D. K. (1983), Stratified turbulence and the mesoscale variability of the atmosphere, J. Atmos. Sci., 40, 749-761.

Lilly, D. K., and E. L. Petersen (1983), Aircraft measurements of atmospheric kinetic energy spectra, Tellus, 35A, 379-382.

Lindzen, R. S. (1983), Turbulence and stress owing to gravity wave and tidal breakdown, J. Geophys. Res., 86, 9707-9714.

Lindzen, R. S., and J. Forbes (1983), Turbulence originating from convectively stable internal waves, J. Geophys. Res., 88, 6549-6553.

Maekawa, Y., S. Fukao, T. Sato, S. Kato, and R. F. Woodman (1984), Internal inertia-gravity waves in the tropical lower stratosphere observed by the Arecibo radar, submitted to J. Atmos. Sci..

Nastrom, G. D., and K. S. Gage (1983), A first look at wavenumber spectra from GASP data, Tellus, 35A, 383-388.

NCAR (1977), Report of the U. S. Gate Central Program Workshop, 25 July-12 August, NCAR, Boulder, Colorado.

Sato, T., and R. F. Woodman (1982), Fine altitude resolution radar observations of upper tropospheric and lower stratospheric winds and waves, J. Atmos. Sci., 39, 2539-2545.

VanZandt, T. E. (1982), A universal spectrum of buoyancy waves in the atmosphere, Geophys. Res. Lett., 9, 575-578.

Vincent, R. A., and I. M. Reid (1983), HF Doppler measurements of mesospheric gravity wave momentum fluxes, J. Atmos. Sci., 40, 1321-1333.

Wallace, J. M., and F. R. Hartranft (1969), Diurnal variations, surface to 30 kilometers, Mon. Wea. Rev., 97, 446-455.

Wallace, J. M., and R. F. Tadd (1974), Some further results concerning the vertical structure of atmospheric tidal motions within the lowest 30 kilometers, Mon. Wea. Rev., 102, 795-803.

Woodman, R. F., and P. K. Rastogi (1984), Evaluation of effective eddy diffusive coefficients using radar observations of turbulence in the stratosphere, Geophys. Res. Lett., 11, 243-246.

3.0 GRAVITY WAVES IN THE MIDDLE ATMOSPHERE: RECENT PROGRESS AND NEEDED STUDIES

David C. Fritts

Geophysical Institute
and
Department of Physics
University of Alaska
Fairbanks, Alaska 99775-0800

INTRODUCTION

The recent recognition of the important role played by gravity waves in the large-scale circulation and thermal structure of the mesosphere and lower thermosphere (HOUGHTON, 1978; LINDZEN, 1981) has stimulated considerable research on their properties and their middle atmosphere effects. For example, these studies have begun to provide important information on gravity wave scales, propagation, filtering, and the processes responsible for saturation and turbulent diffusion. There remain, however, many areas in which our current understanding of middle atmosphere gravity waves is deficient. The purposes of this paper are to review the progress that has been made to date and to suggest areas in which additional studies are most needed.

Major motivations for studies of gravity waves in the middle atmosphere, of course, are the roles of such motions in providing both a drag on the large-scale flow and a turbulent diffusion that acts on the heat and constituent distributions as well as the need to incorporate these effects in dynamical, chemical, and radiative models of these regions. In the mesosphere and lower thermosphere, gravity-wave drag results in a reversal of the vertical shear of the zonal mean wind, driving a strong mean meridional circulation and a reversal of the mean meridional temperature gradient near the mesopause. The effects of gravity-wave drag in the stratosphere, while not as significant as at higher levels, appear to be important nevertheless in maintaining the large-scale circulation of this region. Likewise, turbulent diffusion due to gravity wave saturation contributes significantly to maintenance of the heat and constituent distributions in the mesosphere and lower thermosphere and may be important in the stratosphere as well. The theory and observations relating to gravity-wave saturation were reviewed by FRITTS (1984).

RECENT PROGRESS IN GRAVITY-WAVE STUDIES

A number of studies in the last few years have addressed various aspects of gravity-wave propagation, saturation, and effects in the middle atmosphere. As a result, we are beginning to understand in more detail the role of gravity waves in middle atmosphere dynamics. Several studies have examined gravity-wave scales and phase speeds, yielding an indication of those wave motions that are likely to be most important in the middle atmosphere (VINCENT and REID; 1983; SMITH and FRITTS, 1983; MEEK et al., 1985a). Typical motions were found to have horizontal wavelengths that range from $\sim$ 10 to 10^3 km, observed periods of $\sim$ 10 to 10^3 min, and phase speeds of $\sim$ 10 to 10^2 ms^{-1}. In most cases, these values were associated with wave motions having vertical scales $\gtrsim$ 10 km due to resolution constraints of the various observing systems. There is also evidence, however, of motions with much smaller vertical scales, and likely much smaller horizontal scales and phase speeds as well, from high-resolution rocket, radar, and balloon soundings of the stratosphere, mesosphere, and lower thermosphere (PHILBRICK et al., 1983; FRITTS et al., 1985; SATO and WOODMAN, 1982a; BARAT, 1983; and others).

Other studies have examined the mechanisms responsible for gravity-wave saturation in the middle atmosphere and the amplitude limits implied by these mechanisms. The dominant saturation mechanisms appear to be convective and dynamical instabilities, with nonlinear wave-wave interactions contributing, perhaps, at small vertical scales (FRITTS and RASTOGI, 1985). These wave field instabilities seem to limit wave amplitudes, as assumed by HODGES (1967) and LINDZEN (1981), but to amplitudes somewhat smaller than monochromatic saturation values due to wave superposition (ORLANSKI and CERASOLI, 1981; FRITTS, 1985). Indeed, the amplitude limits imposed by saturation appear now to account for the shape of the vertical wave number spectrum of gravity-wave motions (DEWAN and GOOD, 1985; SMITH et al., 1985) and thus may explain the apparent universality of the atmospheric motion spectrum (VANZANDT, 1982). These studies have also shown the gravity-wave spectrum to be saturated throughout the lower and middle atmosphere, with a characteristic vertical scale and energy that increase with height (SMITH et al., 1985).

We are also beginning to understand the processes responsible for turbulence production and turbulent diffusion. These are the convective and dynamical instabilities mentioned above, and they appear, in many instances at least, to result in the generation of strong, local turbulence at preferred locations within the wavefield (SATO and WOODMAN, 1982b; BALSLEY et al., 1983; BARAT, 1983; COT and BARAT, 1985; FRITTS et al., 1985). The convective instability is thought to predominate for high-frequency wave motions (with $\omega >> f$) while the dynamical instability appears more likely for low-frequency motions (with $\omega \sim f$). In either case, the wave motion is believed to be most unstable where T_z' is a minimum rather than where u_z' is a maximum (FRITTS and RASTOGI, 1985). The resulting distribution of turbulence throughout the wave field appears to result in a large turbulent Prandtl number (JUSTUS, 1967) and a reduction of the effective turbulent diffusion of heat and constituents due to gravity-wave saturation (FRITTS and DUNKERTON, 1985; STROBEL et al., 1985).

Finally, recent studies have begun to address the distributions of gravity wave energies and momentum fluxes with height and time. Studies of the former by MEEK et al. (1985b) and VINCENT and FRITTS (1986) suggest significant seasonal variations as well as short-term fluctuations. The seasonal variations of gravity-wave energies correlate well both with variations in the turbulent diffusion of H_2O inferred from SME O_3 fluctuations (THOMAS et al., 1984) and with observed seasonal variations of turbulence intensities (Vincent, private communication, 1985). Short-term fluctuations appear to correlate with variations in the mean winds at lower levels.

Observational studies of gravity-wave momentum fluxes by VINCENT and REID (1983), REID (1984), and FRITTS and VINCENT (1985) have provided estimates of zonal accelerations due to gravity-wave drag ~ -50 $ms^{-1}day^{-1}$, largely consistent with expectations based on the observed zonal wind structure (HOLTON, 1983). In addition, the latter studies have found considerable variability of the momentum flux due to high-frequency gravity waves with time-of-day, suggesting a modulation of this flux by tidal motions. A model of the modulation and of its implications for mean flow accelerations and tidal measurements was proposed by FRITTS and VINCENT (1985). This study also found the majority ($\sim$ 70%) of the gravity-wave momentum flux and flux divergence to be associated with motions with periods $<$ 1 hr, suggesting that the dominant flux is due to motions with small horizontal scales as well (VINCENT and REID, 1983).

NEEDED STUDIES

The gravity-wave studies described above have contributed substantially to our knowledge of the role of such motions in middle atmosphere dynamics. However, there remains a great deal that is unknown or poorly known concerning gravity-wave propagation, saturation, and effects in the middle atmosphere.

The purpose of this section is to highlight several areas in which our knowledge is particularly limited.

As noted above, some attention has focused on the dominant gravity-wave scales in the middle atmosphere, but the identified motions number only ~ 100. And because these studies were performed at only a few locations, the results may not be representative of the global gravity-wave distribution. Most observational facilities are located in or near mountainous terrain, which might bias wavelength and/or phase speed distributions. Preliminary motion spectra in the equatorial Pacific, for example, exhibit a somewhat different character than those obtained over significant topography (BALSLEY, personal communication, 1985).

The character of the gravity-wave spectrum will have a major influence on the response of the middle atmosphere, however, and should serve to motivate additional studies of this sort, hopefully representing a more diverse global coverage than is presently available. An indication of the geographic variability of gravity-wave sources and of the middle atmosphere response is provided by the model studies of MIYAHARA et al. (1985), which show considerable variability in the gravity-wave momentum flux extending to upper levels due to localized regions of convective activity. And this is in a model that does not resolve what are now thought to be the dominant temporal and spatial scales (FRITTS, 1984). Presumably, smaller spatial scales would produce even more localized middle atmosphere effects.

Other areas of major uncertainty are the causes and effects of variability of the gravity-wave spectrum. Variability imposed by planetary-wave motions were examined by DUNKERTON and BUTCHART (1984), HOLTON (1984), SCHOEBERL and STROBEL (1984), and MIYAHARA et al. (1985). Observational studies have likewise provided evidence of considerable variability of gravity-wave energies, momentum fluxes, and turbulent diffusion (REID, 1984; THOMAS et al., 1984; MEEK et al., 1985b; VINCENT and FRITTS, 1986; FRITTS and VINCENT, 1985; FRITTS et al., 1985). Yet our knowledge of these processes remains primitive due to the extremely limited observations. Of particular importance, perhaps, are observations addressing the variability due to gravity-wave sources and filtering, as these appear to operate on the planetary-wave scales of relevance to the middle atmosphere circulation and structure.

Another area requiring additional study is the generation and subsequent evolution of turbulence resulting from gravity-wave saturation. Again, while preliminary studies of the mechanisms responsible for turbulence generation have been performed, we know little about either the primary products of turbulence decay (secondary gravity waves, 2-D turbulence, or heat), and thus their role in middle atmosphere dynamics, or the role of such turbulence in the diffusion of heat and constituents.

Finally, our understanding of the role of nonzonally propagating gravity waves is very limited. Most numerical and observational studies to date have considered primarily zonal propagation in zonal flows. Yet there is no reason to suppose that meridionally propagating motions are not equally important. Indeed, studies by SMITH and FRITTS (1983), MEEK et al. (1985a), and VINCENT and FRITTS (1986) indicate that meridional propagation may be preferred, perhaps due to zonal filtering by large zonal winds.

Thus, there are numerous valuable studies remaining to be done which may keep us all busy for quite some time.

REFERENCES

Balsley, B. B., W. L. Ecklund, and D. C. Fritts (1983), VHF echoes from the high-latitude mesosphere and lower thermosphere: observations and interpretations, J. Atmos. Sci., 40, 2451-2466.

Barat, J. (1983), The fine structure of the stratospheric flow revealed by differential sounding, J. Geophys. Res., 88, 5219-5228.

Cot, C., and J. Barat (1985), Wave-turbulence interaction in the stratosphere: A case study, submitted to J. Geophys. Res..

Dewan, E. M., and R. E. Good (1985), Saturation and the "universal" spectrum for vertical profiles of horizontal scalar winds in the atmosphere, submitted to J. Geophys. Res..

Dunkerton, T. J. and B. Butchart (1984), Propagation and selective transmission of internal gravity waves in a sudden warming, J. Atmos. Sci., 41, 1443-1460.

Fritts, D. C. (1984), Gravity wave saturation in the middle atmosphere: A review of theory and observations, Rev. Geophys. Space Phys., 22, 275-308.

Fritts, D. C. (1985), A numerical study of gravity wave saturation: Nonlinear and multiple wave effects, J. Atmos. Sci., 42, in press.

Fritts, D. C., and T. J. Dunkerton (1985), Fluxes of heat and constituents due to convectively unstable gravity waves, J. Atmos. Sci., 42, in press.

Fritts, D. C., and P. K. Rastogi (1985), Convective and dynamical instabilities due to gravity wave motions in the lower and middle atmosphere: Theory and observations, Radio Sci., in press.

Fritts, D. C., S. A. Smith, B. B. Balsley, and C. R. Philbrick (1985), Evidence of gravity wave saturation and local turbulence production in the summer mesosphere and lower thermosphere during the STATE experiment, submitted to J. Geophys. Res..

Fritts, D. C., and R. A. Vincent (1985), Mesospheric momentum flux studies at Adelaide, Australia: Observations and a gravity wave/tidal interaction model, submitted to J. Atmos. Sci..

Hodges, R. R., Jr. (1967), Generation of turbulence in the upper atmosphere by internal gravity waves, J. Geophys. Res., 72, 3455-3458.

Holton, J. R. (1983), The influence of gravity wave breaking on the general circulation of the middle atmosphere, J. Atmos. Sci., 40, 2497-2507.

Holton, J. R. (1984), The generation of mesospheric planetary waves by zonally asymmetric gravity wave breaking, J. Atmos. Sci., 41, 3427-3430.

Houghton, J. T. (1978), The stratosphere and mesosphere, Q. J. Roy. Meteorol. Soc., 104, 1-29.

Justus, C. G. (1967), The eddy diffusivities, energy balance parameters, and heating rate of atmospheric turbulence, J. Geophys. Res., 72, 1035-1039.

Lindzen, R. S. (1981), Turbulence and stress due to gravity wave and tidal breakdown, J. Geophys. Res., 86, 9707-9714.

Meek, C. E., I. M. Reid, and A. H. Manson (1985a), Observations of mesospheric wind velocities. I. Gravity wave horizontal scales and phase velocities determined from spaced wind observations, Radio Sci., in press.

Meek, C. E., I. M. Reid and A. H. Manson (1985b), Observations of mesospheric wind velocities. II. Cross sections of power spectral density for 48-8h, 8-1h, 1h-10 min over 60-110 km for 1981, Radio Sci., in press.

Miyahara, S., T. Hayashi, and J. D. Mahlman (1985), Interactions between gravity waves and planetary scale flow simulated by the GFDL "SKYHI" model, submitted to J. Atmos. Sci..

Orlanski, I., and C. P. Cerasoli (1981), Energy transfer among internal gravity modes: weak and strong interactions, J. Geophys. Res., 86, 4103-4124.

Philbrick, C. R., K. U. Grossmann, R. Hennig, G. Lange, D. Krankowsky, D. Offermann, F. J. Schmidlin, and U. von Zahn (1983), Vertical density and temperature structure over Northern Europe, Adv. Space Res., 2, 121-124.

Reid, I. M. (1984), Radar studies of atmospheric gravity waves, Ph. D. Thesis, University of Adelaide, Australia, 300 p..

Sato, T., and R. F. Woodman (1982a), Fine altitude resolution radar observations of upper-tropospheric and lower-stratospheric winds and waves, J. Atmos. Sci., 39, 2539-2545.

Sato, T., and R. F. Woodman (1982b), Fine altitude resolution observations of stratospheric turbulence layers by the Arecibo 430 MHz radar, J. Atmos. Sci., 39, 2546-2552.

Schoeberl, M. R., and D. F. Strobel (1984), Nonzonal gravity wave breaking in the winter mesosphere, Dynamics of the Middle Atmosphere, edited by J. R. Holton and T. Matsuno, 45-64.

Smith, S. A., and D. C. Fritts (1983), Estimations of gravity wave motions, momentum fluxes and induced mean flow accelerations in the winter mesosphere over Poker Flat, Alaska, Proc. 21st Conf. Radar Meteorol., Edmonton, 104-110.

Smith, S. A., D. C. Fritts, and T. E. VanZandt (1985), Evidence of a saturated gravity wave spectrum throughout the atmosphere, submitted to Geophys. Res. Lett..

Strobel, D. F., J. P. Apruzese, and M. R. Schoeberl (1985), Energy balance constraints on gravity wave induced eddy diffusion in the mesosphere and lower thermosphere, submitted.

Thomas, R. J., C. A. Barth, and S. Solomon (1984), Seasonal variations of ozone in the upper mesosphere and gravity waves, Geophys. Res. Lett., 11, 673-676.

VanZandt, T. E. (1982), A universal spectrum of buoyancy waves in the atmosphere, Geophys. Res. Lett., 9, 575-578.

Vincent, R. A., and I. M. Reid (1983), HF Doppler measurements of mesospheric gravity wave momentum fluxes, J. Atmos. Sci., 40, 1321-1333.

Vincent, R. A. and D. C. Fritts (1986), The morphology of gravity waves in the mesosphere and lower thermosphere at Adelaide, Australia, submitted to J. Atmos. Sci.

TOPIC 3 SUMMARY: GRAVITY WAVES AND TURBULENCE

Papers presented in this session revealed that we have made considerable progress in understanding a number of important problems concerning gravity wave and turbulence processes in the lower and middle atmosphere since the last MST workshop. Advances were made in understanding the spectral description of the motion field, including the effects of anisotropy and Doppler shifting on gravity-wave spectra, the mechanisms leading to saturation and their effects on wave amplitudes and turbulence intensities, and the causes of the apparent universality of the gravity-wave spectrum and the variation of this spectrum with height. Other studies revealed significant variability of gravity-wave and turbulence parameters and effects, on small to large (annual) temporal scales, associated with changing forcing conditions or propagation environments. Of particular significance in this regard were annual climatologies of gravity-wave energy and turbulence intensity in the mesosphere suggesting a reduction of turbulent diffusion during equinoxes. Evidence was also provided that the more dynamically significant gravity-wave motions (in terms of energy and momentum transports) are those with small horizontal wavelengths (< 200 km) and high intrinsic frequencies. Finally, a number of studies addressed characteristic gravity-wave and turbulence parameters and their variability as well as various means to distinguish between gravity-wave and turbulence motions.

Despite recent progress in understanding gravity-wave and turbulence processes, there remains much that is not known about these motions, their variability, and their effects in the lower and middle atmosphere. Particularly important in this regard are studies (both case studies and climatologies) that address gravity-wave sources, including the dominant temporal and spatial scales and phase speeds, and their long- and short-term variability.

It is important to examine, with whatever systems are available, the climatologies and variability of gravity-wave energy and momentum fluxes and the role of turbulence in the diffusion of heat and constituents throughout the atmosphere. A major factor in the annual climatologies of gravity waves and turbulence in the mesosphere, and one requiring considerable study, is the filtering of the gravity-wave spectrum by local mean winds at lower levels, which causes significant modulations in the energy and momentum fluxes (and in the associated turbulent diffusivities) at higher levels.

The momentum flux divergence due to gravity waves is also likely to be important in the upper troposphere and stratosphere, though the magnitude is expected to be much smaller on average than in the mesosphere and contributions due to various sources may be very localized. This requires high-resolution observations capable of inferring these contributions in a wide range of conditions and locations. It is also important to exercise care in estimating the momentum flux due to mountain waves as these motions are nearly stationary and may not be able to be studied using the dualbeam technique on short time scales.

In addition, further studies are required of the mechanisms and effects of gravity-wave saturation and of the evolution of the motion spectrum by processes other than gravity-wave filtering. With a little luck, our progress in understanding these motions in the next two years will be as significant as in the last two!

3.1.1 A MODEL FOR GRAVITY-WAVE SPECTRA OBSERVED BY DOPPLER SOUNDING SYSTEMS

T. E. VanZandt

18899 NJ-920944

Aeronomy Laboratory
National Oceanic and Atmospheric Administration
Boulder, Colorado 80303

It has been proposed that mesoscale fluctuations of wind and temperature in the free atmosphere are due to internal gravity (buoyancy) waves (VANZANDT, 1982). Critical tests of this hypothesis must involve the comparison of models based on the theory of gravity waves with suitable measurements. The MST radar technique is particularly attractive for this purpose, because it can measure several independent power spectra simultaneously. However, because of the complexities of the geometry of the MST radar experiment, which measures the radial velocity as a function of radial range and time, and the particular geometry of buoyancy waves, the relation between the observed spectra and the usual description of buoyancy wave spectra is not simple.

In this paper a model for MST radar spectra is developed following the formalism presented by PINKEL (1981). Expressions for the one-dimensional spectra of radial velocity versus frequency and versus radial wave number are presented. Their dependence on the parameters of the gravity-wave spectrum and on the experimental parameters, radar zenith angle χ and averaging time T_{av}, are described and the conditions for critical tests of the gravity-wave hypothesis are discussed (VANZANDT, 1985). SMITH et al. (1985) compare the model spectra with spectra observed in the Arctic summer mesosphere by the Poker Flat radar.

This model applies to any monostatic Doppler sounding system, including MST radar, Doppler lidar and Doppler sonar in the atmosphere, and Doppler sonar in the ocean.

REFERENCES

Pinkel, R. (1981), On the use of Doppler sonar for internal wave measurments, Deep-Sea Res., 28A, 269-289.

Smith, S. A., D. C. Fritts, and T. E. VanZandt (1985), Comparison of mesospheric wind spectra with a gravity-wave model, Radio Sci., 20, 1331-1338.

VanZandt, T. E. (1982), A universal spectrum of buoyancy waves in the atmosphere, Geophys. Res. Lett., 9, 575-578.

VanZandt, T. E. (1985), a model for gravity wave spectra observed by Doppler sounding systems, Radio Sci., 20, 1323-1330.

3.1.2 HALF-DAY AND FOUR-DAY WAVES IN THE STRATOSPHERE

Jurgen Rottger*

Arecibo Observatory
P.O. Box 995
Arecibo, Puerto Rico 00612

Further analysis of spaced-antenna measurements of 3-dimensional velocity in the stratosphere (ROTTGER, 1981) was performed over a period of 10 days and compared with meteorological observations.

A quasi-four-day wave in the lower stratosphere can be shown to originate in planetary wave/synoptic scale disturbances in the troposphere. Its phase propagates downwards and its amplitude decreases strongly with height in the lower stratosphere. The wave features are most pronounced in the meridional wind component, but they show up also in the vertical component (Figure 1).

A 12-h oscillation with downward phase progression and about 1.5 ms^{-1} velocity amplitude is also detected in the meridional component above 18 km, but there is no comparable feature seen in the troposphere.

REFERENCE

Rottger, J. (1981), Wind variability in the stratosphere deduced from spaced antenna VHF radar measurements, Proc. 20 AMS Conf. Radar Meteorol., Boston/MA.

*On leave from Max-Planck-Institut fur Aeronomie, Katlenburg-Lindau, West Germany.

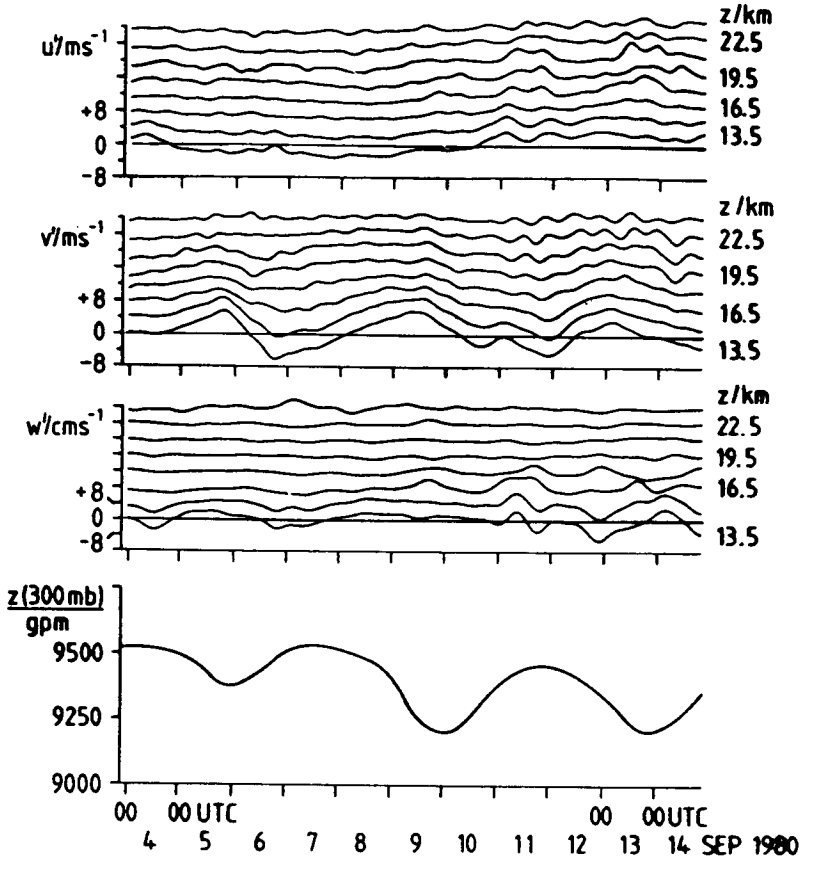

Figure 1. Time series of velocity deviations u, m, w from the mean velocities over the period 4-14 Sept. 1980, and height of the 300 mb level.

3.1.3 TROPOSPHERIC TURBULENCE PARAMETERS MEASURED BY USING THE MU RADAR

Toru Sato[1], Hiromasa Matsumoto[2], Shoichiro Fukao[2], and Susumu Kato[1]

[1]Radio Atmospheric Science Center
Kyoto University, Uji 611, Japan

[2]Department of Electrical Engineering
Kyoto University, Kyoto 606, Japan

INTRODUCTION

The spectral width of the Doppler radar echo has been used to estimate the atmospheric turbulence parameters (CUNNOLD, 1975; SATO and WOODMAN, 1982; HOCKING, 1983a), because it is directly related to the kinetic energy contained in the turbulence. However, sufficient care must be taken in deriving the turbulence parameters since the measured spectral width can be easily affected by undesired factors such as beam broadening, shear broadening, and the temporal variation of the wind field (SATO and WOODMAN, 1982; HOCKING, 1983b).

Here we examine these factors in the case of the MU radar observation of the upper troposphere, and present preliminary results obtained so far.

METHOD AND DATA

The MU radar has a relatively broad antenna beam among existing radars (see FUKAO, et al., 1985 for details of the system), thus suffers mainly from the beam broadening effect. The shear broadening does not cause any trouble because the antenna beam can be pointed to the zenith. It is even possible to estimate the strength of the shear inside the turbulent layers by comparing the spectral width in the vertical and off-vertical directions. The temporal variation of the wind field may add to some error, but it is not the major factor since the time resolution is as good as 1 min. The magnitude of rms fluctuation within 1 min is estimated to be about 0.2 m/s based on the record-to-record valiability of the radial wind velocity.

In order to estimate and correct the effect of the beam broadening, it is important to measure the horizontal wind accurately. We used five antenna beams in the present observation; one pointing vertically, and remaining four toward north, east, south, and west at a zenith angle of 10°. The zonal and meridional wind components derived from the line-of-sight velocity in these directions are used to correct the beam broadening effect.

The solid line in Figure 1 shows the result of a numerical simulation which relates the true and observed spectral width σ and the horizontal wind velocity V_h. The broken line shows the case where the antenna beam pattern is approximated by a Gaussian. In this case, the effect of the beam broadening is expressed simply as

$$\sigma_{obs}^2 = \sigma_{true}^2 + C^2 V_h^2 \qquad (1)$$

where $C = 0.044$ is a constant determined for the MU radar antenna. Thus, it can be easily removed if the horizontal wind velocity is known. This approximation is used in the following. The spectral width and the mean Doppler shift are determined by fitting a Gaussian to the observed spectra.

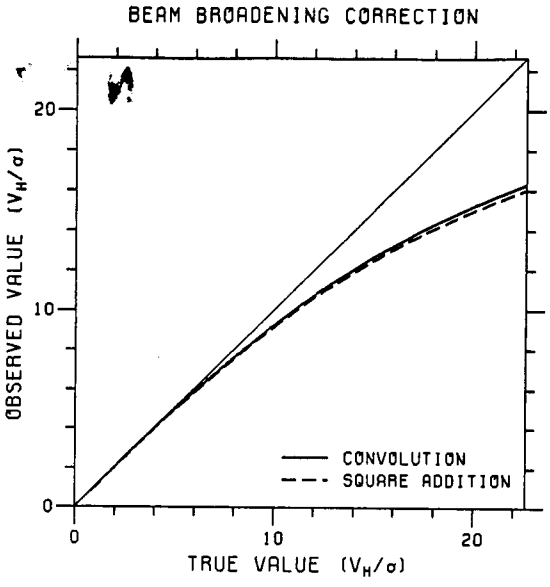

Figure 1. Numerical calculation showing the effect of the beam broadening.

After subtracting the beam broadening effect, the energy dissipation rate k and the eddy thermal diffusivity k_h can be estimated as (SATO and WOODMAN, 1982; HOCKING, 1983b)

$$\varepsilon = 0.49\,\sigma^3 k_o \tag{2}$$

$$k_h = \varepsilon / 3\omega_b^2 \tag{3}$$

where $k_o = \omega_b/\sigma$ is the outer scale wave number of the turbulence (WEINSTOCK, 1981), and ω_b is the Brunt-Vaisala frequency.

The data were taken for four days in July, 1985, when the stratospheric jet was weak. The time and height resolutions are 1 min and 150 m, respectively, and the height range in which the meaningful data are obtained was 4.8-16 km.

RESULTS

Figure 2 shows a 24-hour mean observed spectral width at 5 beam directions and the beam broadening factor obtained from the horizontal wind velocity. An interesting feature is that no appreciable difference exists between the spectral width in the vertical and off-vertical directions, which means that no shear broadening effect is observed. This is probably due to the convective structure of the troposphere where large shear cannot last for a long duration over a large vertical dimension.

Figure 3 is the resultant 24-hour mean profiles of the derived parameters. The Brunt-Vaisala frequency is estimated from nine temperature profiles obtained by rawinsondes launched at Hamamatsu, about 150 km east of the MU radar. The values are slightly larger than those obtained at Arecibo, Puerto Rico (SATO and WOODMAN, 1982).

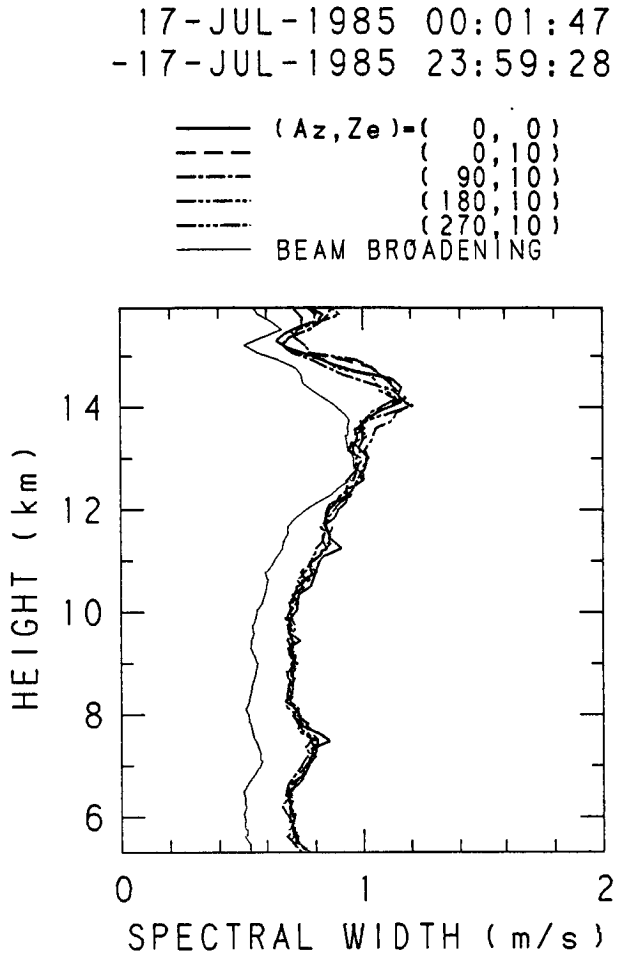

Figure 2. Observed spectral width at 5 beam directions, and the beam broadening factor estimated from the horizontal wind.

The fairly large outer scale of turbulence, which is close to the height resolution of 150 m, seems to be consistent with the macroscopic behavior of the layers found in the time-height variability of the echo power structure. However, the turbulence parameters obtained here must be treated with care, because the temperature profiles observed by rawinsondes do not reflect local structures, although the radar itself has a high resolution.

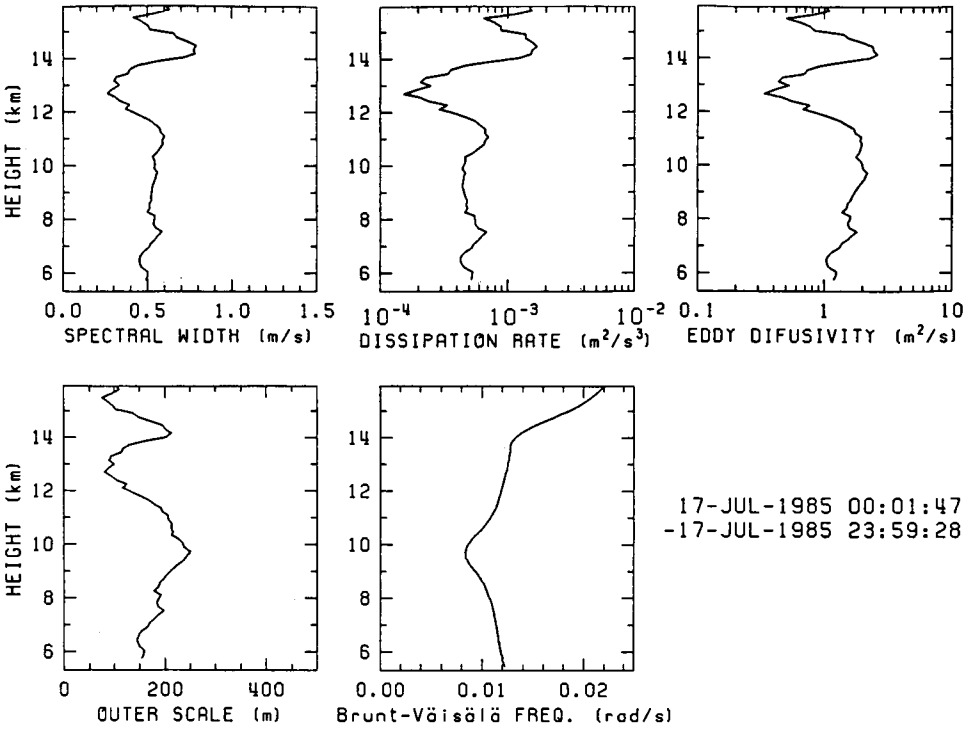

Figure 3. A 24-hour mean profile of the corrected spectral width, the energy dissipation rate, the eddy thermal diffusivity, the outer scale of turbulence, and the Brunt-Vaisala frequency.

REFERENCES

Cunnold, D. M. (1975), J. Atmos. Sci., 32, 2191-2199.
Fukao, S., T. Sato, T. Tsuda, S. Kato, K. Wakasugi, and T. Makihira (1985), Radio Sci., 20, 1169-1176.
Hocking, W. K. (1983a), J. Atmos. Terr. Phys., 45, 103-114.
Hocking, W. K. (1983b), J. Atmos. Terr. Phys., 45, 89-102.
Sato, T., and R. F. Woodman (1982), J. Atmos. Sci., 39, 2546-2552.
Weinstock, J. (1981), J. Atmos. Sci., 38, 880-883.

3.1.4 SIMULTANEOUS VHF AND UHF RADAR OBSERVATION OF THE MESOSPHERE AT ARECIBO DURING A SOLAR FLARE: A CHECK ON THE GRADIENT-MIXING HYPOTHESIS

P. K. Rastogi, J. D. Mathews

Electrical Engineering and Applied Physics Department
Case Western Reserve University
Cleveland, Ohio 44106

and

J. Rottger

Arecibo Observatory
P.O. Box 995
Arecibo, Puerto Rico 00612

INTRODUCTION

The physical mechanism responsible for backward scattering of radio waves from the middle atmosphere depend on the microstructure of small-scale refractivity fluctuations in the vicinity of the Bragg scale, and the spatial distribution (or morphology) of this microstructure within the scattering volume. The electromagnetic part of the scattering process now appears to be reasonably well understood. Characterization of refractivity microstructure, however, is only possible in a statistical sense through simplified models for turbulent gradient-mixing of passive scalars. Such models were originally applied to early tropospheric radio propagation experiments (see e.g. BOLGIANO, 1968), and with slight modification form the basis for the MST radar technique (ROTTGER, 1984). Radar experiments at multiple wavelengths can provide useful information on the refractivity microstructure and its dependence on scales associated with turbulence (BOLGIANO, 1963; RASTOGI and MATHEWS, 1984). Such experiments are feasible only at select facilities.

In this paper, we discuss the results of a two wavelength (VHF and UHF) mesosphere experiment performed at the Arecibo Observatory on January 5, 1981. The 46.8-MHz VHF radar (3.21 m Bragg scale) was operated by the Max-Planck-Institut fur Aeronomie (MPI) to provide spectral measurements of signals scattered from refractivity fluctuations due to turbulence (ROTTGER et al., 1983). Other physical parameters such as radial velocities (V_r), scattered signal power (P_s), and Doppler spread (W_s) due to turbulence can be derived from signal spectra. The 430-MHz UHF radar (0.36 m Bragg scale) was used for D-region electron-density (N) measurements using the incoherent scatter technique with a comparable height resolution (MATHEWS, 1984). The radars were pointed symmetrically about the vertical with a beam spacing of 5.5 degree in the meridional plane. Occurrence of a type 4 solar flare during the experiment produced enhanced D-region electron-density gradients. This was a unique circumstance that provided the possibility of testing the basic premises of the turbulent gradient-mixing hypothesis.

The behavior of physical parameters derived from the VHF experiment is analyzed in the next section. We focus on the evolution of a strong layer of turbulence at 71 km immediately after the flare onset. It is argued that the turbulent layer existed prior to the onset of flare, but was rendered visible through enhanced electron-density gradients established after the onset. Incoherent-scatter electron-density measurements described in Section 3 clearly show substantial enhancement of D-region ionization after the flare. In Section 4, we briefly outline the turbulent gradient-mixing hypothesis. The VHF and UHF observation are then used to show that the development of the layer at 71 km is almost entirely due to enhanced gradients.

VHF OBSERVATIONS DURING THE FLARE

Details of the MPI VHF experiment at Arecibo and the salient results for the December-January 1981 period have been reported by ROTTGER et al. (1983). We review the observations for January 5, 1981, and present the results of further analyses.

Figure 1 shows contours of constant received signal power as a function of height and time. The ST region from 9 to 27 km shows several thin persistent layers. The mesospheric signals are weaker in comparison, but layers in the vicinity of 65, 71, 73, and 77 km can be distinctly seen. The layer at 71 km appears suddenly after 12:16 AST, coincident with the occurrence of the flare, but vestiges of it could be seen even earlier. A weak (1-2 dB) but abrupt enhancement of received signal power at this time occurs at all heights, and is probably due to enhanced solar radio emission seen through a secondary lobe of the antenna radiation pattern (ROTTGER, 1983). Details of flare occurrence are shown in Figure 2.

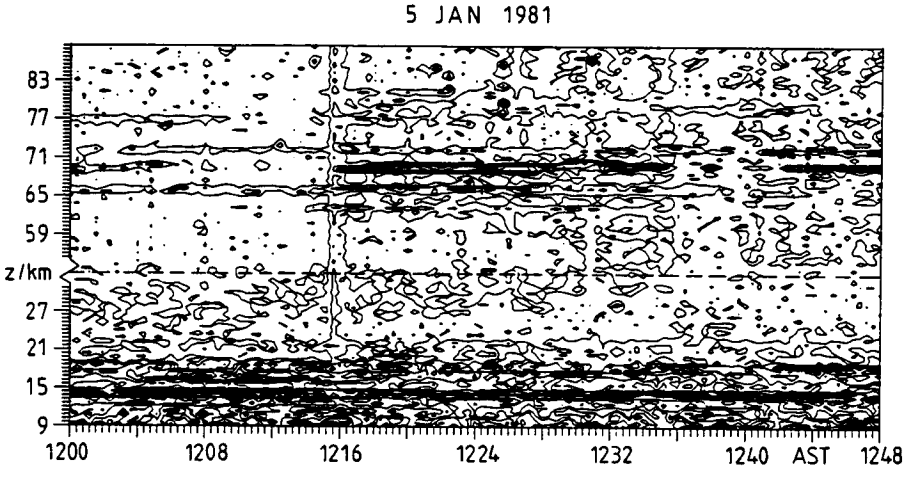

Figure 1. Contour plots of the total received signal power ($P_s + P_n$) at 2 dB increments as a function of height Z and time in AST (UT - 4 hr) for the MPI VHF experiment at Arecibo. Noise enhancement at 12:16 hr AST and subsequent development of the echoing region at 71 km is attributed to the occurrence of a Type 4 Solar Flare. (ROTTGER et al., 1983).

Figure 3 shows the linearly scaled spectra of the received signal and profiles of the noise power P_n, signal power P_s, radial velocity V_r, and Doppler spread W_s in the mesosphere just before and just after the flare onset. A new layer with a near 10 dB enhancement in P_s appears to form at 71 km, but the weak layers at 68 and 73 km do not show any significant variation in the signal power. Enhancement of incoming ionizing radiations (Lyman Alpha and hard X-rays) during the flare cannot produce turbulence, but it can amplify the refractivity structure within an already turbulent layer by creating steeper gradients in the ambient electron densities.

The intensity of turbulence within a layer of thickness L is characterized by the parameter ε denoting the rate at which energy is dissipated per unit mass by turbulence. ε can be related to overturning by buoyancy of the largest eddies (of size L) within the layer. Mean background wind shear produces a

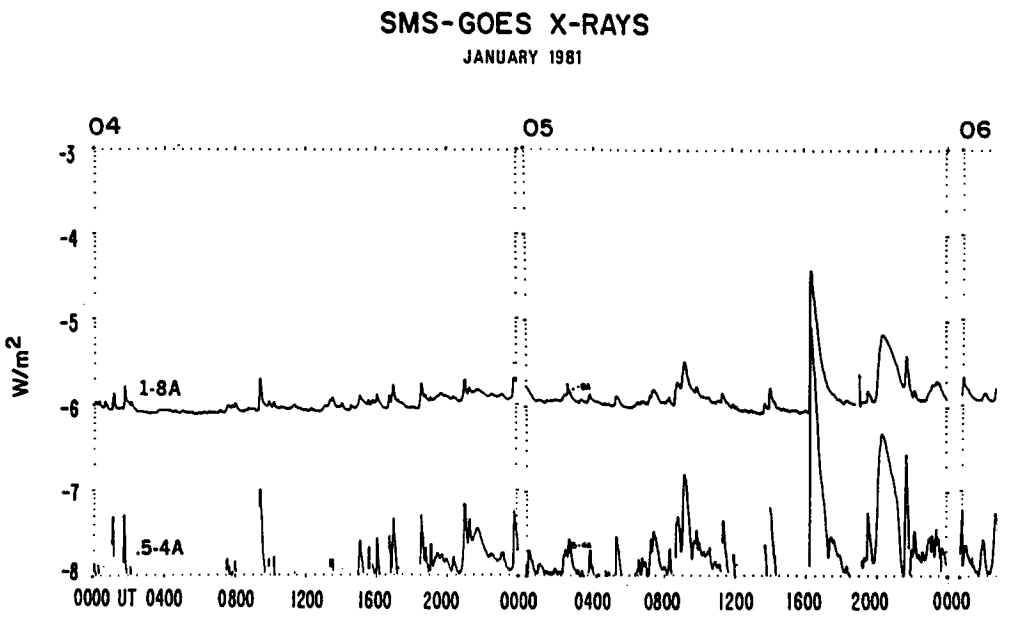

Figure 2. Solar X-ray fluxes in the 1-8 A band (upper) and 0.5-4 A band (lower) recorded by the SMS GOES satellite for January 4-5, 1981. A Type 4 solar flare occurred at 16:13 hr UT (12:13 hr AST) on January 5. It reached a maximum at 16:16:30 hr UT and lasted for 11 min. (Solar-Geophysical Data Comprehensive Reports, No. 443 pt II, July 1981, NOAA).

velocity differential across the layer which is mixed by eddies of successively smaller sizes. The velocity profile in the vicinity of the layer is slightly deformed to maintain a supply of energy to the layer at the rate ε. Details of this process have been considered by LINDEN (1979) and ROTTGER (1981). The distribution of turbulent velocity fluctuations across the layer is mapped into the Doppler spectrum of the scattered signal, and the Doppler spread W_s is linearly related to ε. A small contribution to W_s due to wind shear is negligible for radar pointing directions close to vertical (SATO, 1981).

Figure 4 shows the time evolution of received signal power P_s and Doppler spread W_s in the vicinity of the 71-km layer. At 70.8 km, estimates of W_s (without any noise correction) are slightly less than 1.5 m/s for noise alone. The statistical variation in this parameter is about 0.2 m/s and remains at about the same level for time intervals 11:30-12:15 AST and 12:15-13:00 AST. We conclude, therefore, that the average energy dissipation parameter $\langle\varepsilon\rangle$ remains reasonably constant before, during and after the occurrence of the flare.

ELECTRON-DENSITY MEASUREMENTS

Profiles of electron densities obtained with the incoherent-scatter technique are shown in Figure 5. The time resolution for these measurements is typically 10 min and height resolution is typically 0.5 km. The profiles have been rescaled from total signal power profiles that are smoothed and filtered to remove the effect of external interference. A typical uncertainty in electron-density measurements is of the order of 10 electrons cm^{-3}. The

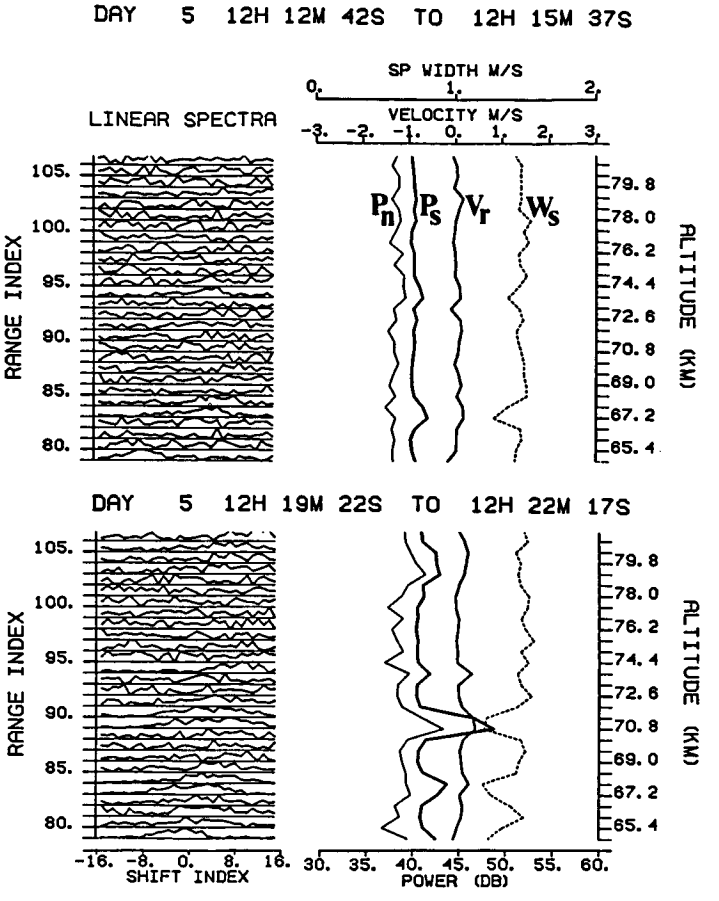

Figure 3. Received signal spectra in the mesosphere, linearly rescaled for each height, are shown on the left for the VHF experiment. Derived parameters P_n, P_s, V_r, and W_s (see text) are shown in the right panels. Top two panels cover the period just before the flare reached its peak. The two lower panels are after the flare peak. Appearance of the layer at 71 km is discussed in the text.

profiles are not obtained at equal time spacing. The actual averaging intervals are tabulated in Figure 5. Profiles 1 and 2 correspond to periods just before and just after the flare onset. Profiles 3 to 5 are for successively later periods. At a height of 71 km, electron density abruptly increases from $\sim$80 cm^{-3} to $\sim$700 cm^{-3} during the first 10 min of the flare, and then gradually decays back to $\sim$100 cm^{-3} over the next half hour. Electron-density gradients dN/dZ in the vicinity of the layer show a local maximum, and a similar pattern of enhancement after the flare onset.

DISCUSSION OF TURBULENT GRADIENT MIXING

The local gradients dN/dZ in electron density N (any passive scalar in general) are mixed by turbulence, producing a spatial power spectrum of fluctuations in N. The scattered signal is obtained as a component of this

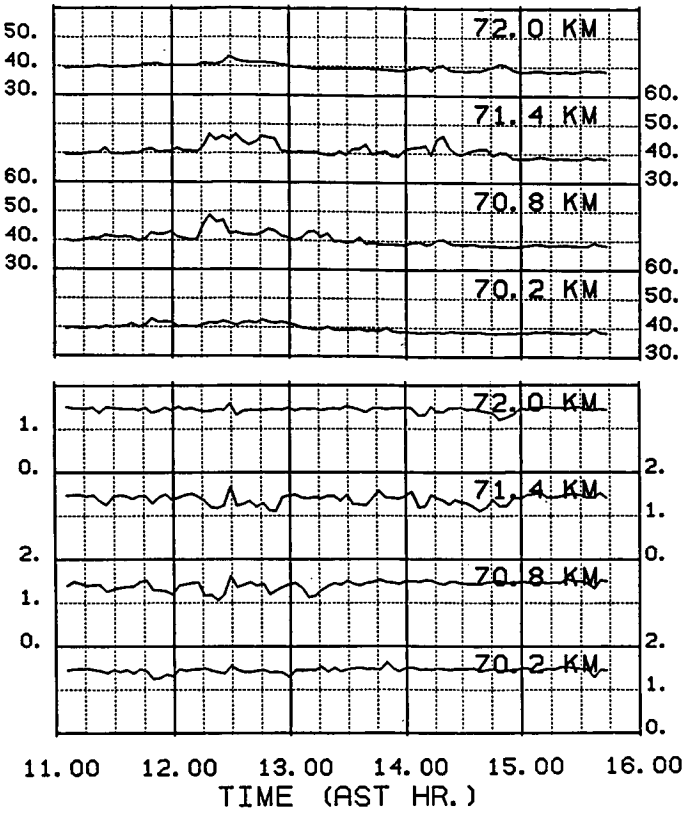

Figure 4. Time variation of total received signal power $P_s + P_n$ (top panel) and Doppler spread W_{s+n} without noise correction (bottom panel). Flare occurs at about 12:15 hr AST. The statistical variation in W_{s+n} is about the same over 11:30-12:15 hr as over 12:15-13:00 for the 70.8 km altitude. For this altitude $P_s + P_n$ jumps by about 9 dB at 12:15 hr.

spatial fluctuation spectrum evaluated at the Bragg wave number. It follows that the scattered signal power P_s would depend on $[dN/dZ]^2$. The energy spectrum of velocity fluctuations that mix the scalar gradient has several (two or more) cutoff scales associated with it. The smallest of these scales depends on the energy dissipation parameter ϵ. The exact wave number dependence of the energy spectrum, hence the wavelength dependence of P_s is decided by the location of Bragg scale in relation to the cutoff scales. RASTOGI and BOWHILL (1976a,b) discuss wavelength dependence of P_s from dimensional considerations. BOLGIANO (1968) and others have pointed out that potential concentrations of the passive scalars should be considered in mixing theories. HOCKING (1983) has derived improved relations for wavelength dependence of P_s in the mesosphere for inertial range turbulence. For discussion of experiments at Arecibo we consider only the $[dN/dZ]^2$ term, since no information can be obtained on wavelength dependence.

On the basis of earlier discussion, we assume that the turbulent layer at 70.8 km has constant thickness L and constant energy dissipation parameter

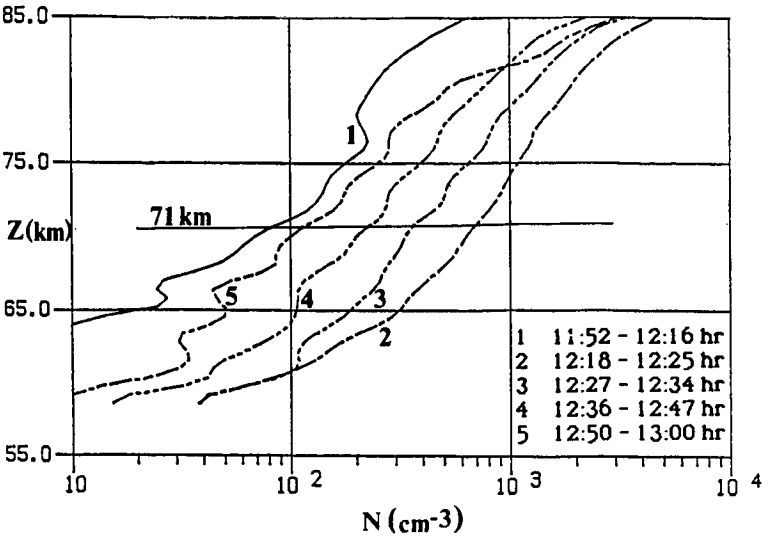

Figure 5. Time evolution of electron-density profiles on January 5, 1981, using the incoherent-scatter technique at 430 MHz. The averaging time corresponding to each profile is shown in the table. For the entire time interval shown, the solar zenith angle remained within 41.0 to 41.6 degrees.

ε for about 0.5 hr before and 0.5 hr after the flare onset. We will consider the following form for the signal power:

$$P_s = A\ F(\varepsilon, L, f_o)\ [dN/dZ]^2 + B$$

where A is a constant, F contains the dependence on ε, layer thickness L, and radar frequency f_o. B is an additive correction term that may be important in more exact formulations using potential quantities. We will assume that B=0.

Figure 6 shows the time variation of the total signal power at 70.8 km in the VHF experiment, and electron-density gradients at 2-km scale derived from the UHF experiment. Suppose that at two closely spaced times t_1 and t_2 signal powers are P_1 and P_2, and gradients are $[dN/dZ]_1$ and $[dN/dZ]_2$. If all other parameters are constant and B=0, then the ratio R given by:

$$R = [P_2\ dB - P_1\ dB]\ /\ \log_{10}\{[dN/dZ]_1\ /\ [dN/dZ]_2\}^2$$

should be 10. In applying this test to data of Figure 6, we face the problem that the power and gradients have disparate time scales. This problem can be circumvented by considering transitions in gradients (labeled 1 to 4) and using appropriate values of P_s. The noise level is reasonable constant at 40 dB. For transition 1, we find that R = 8. Transition 2 has only a small change in gradient associated with it, so we combine it with 3. These two transitions give R = 8.7. Transition 4 cannot be used, as a decrease in gradient is associated with enhancement in power. This suggests that the assumption of constant ε and L may have become untenable for intervals exceeding 1 hr.

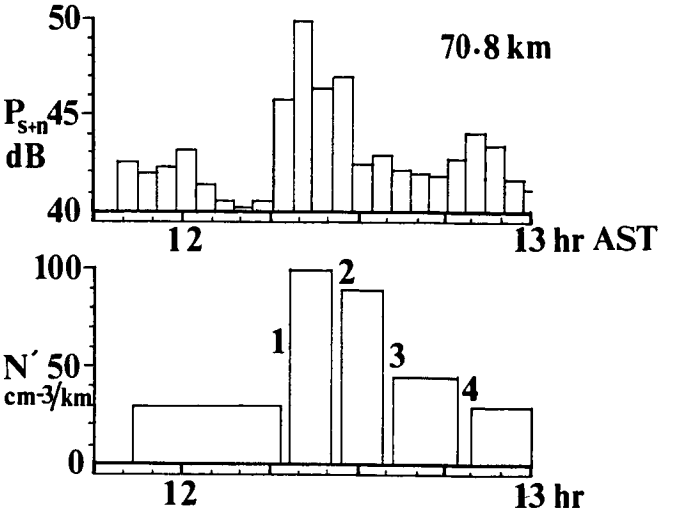

Figure 6. Time variation of the total VHF received signal power P_{s+n} for the 71-km layer at 3 min intervals (upper panel), and the electron-density gradients obtained with the incoherent-scatter method with variable averaging intervals as shown (lower panel). Gradients are obtained with a 2-km scale. Labels 1-4 in the lower panel indicate transitions in gradients that are referred to in the text.

We note that the value of R found in the two cases are both less than and close to 10. This suggests that the assumptions made in our analysis hold reasonably well, and that enhanced electron-density gradients associated with the flare were the principal reason for the layer seen at 70.8 km. A value of R>10 is physically unrealistic as it does not allow dependence on other parameters. The deficit from R=10 can be attributed to following plausible reasons: (a) variability in ϵ, L, (b) local gradients steeper than average gradients, and (c) non-zero additive terms derived from mixing of potential scalars. In view of intermittent nature of turbulence, we expect (a) to be most significant.

ACKNOWLEDGMENT

This work was supported by the National Science Foundation through Grants ATM 8418977 and ATM 8313153. We thank Dr. T. E. VanZandt for useful comments.

REFERENCES

Bolagiano, R. Jr. (1963), The role of radio wave scattering in the study of atmospheric microstructure, in Electromagnetic Scattering, edited by M. Kerker, 261-267, MacMillan, New York.

Bolgiano, R. Jr. (1968), The general theory of turbulence - turbulence in the atmosphere, in Winds and Turbulence in Stratosphere, Mesosphere, and Ionosphere, edited by K. Rawer, 371-400, North Holland, Amsterdam.

Hocking, W. K. (1983), The relationship between strength of turbulence and backscattered radar power at HF and VHF, Handbook for MAP, 9, edited by S. A. Bowhill and B. Edwards, 289-301, SCOSTEP Secretariat, Urbana, Illinois.

Linden, P. F. (1979), Mixing in stratified fluids, Geophys. Astrophys. Fluid Dyn., 13, 3-23.

Mathews, J. D. (1984), Incoherent scatter radar studies of the mesosphere, Handbook for MAP, 13, edited by R. A. Vincent, 135-154, SCOSTEP Secretariat, Urbana, Illinois.

Rastogi, P. K., and S. A. Bowhill (1976a), Radio wave scattering from the mesosphere 2. Evidence for intermittent mesospheric turbulence, J. Atmos. Terr. Phys., 38, 399-411.

Rastogi, P. K. and S. A. Bowhill (1976b), Radio wave scattering from the mesosphere 2. Evidence for intermittent mesospheric turbulence, J. Atmos. Terr. Phys., 38, 449-462.

Rastogi, P. K. and J. D. Mathews (1984), Usefulness of multifrequency MST radar measurements, Handbook for MAP, 14, edited by S. A. Bowhill and B. Edwards, SCOSTEP Secretariat, Urbana, Illinois.

Rottger, J. (1981), The dynamics of stratospheric and mesospheric fine structure investigated with an MST VHF radar, Handbook for MAP, 2, edited by S. K. Avery, 341-349, SCOSTEP Secretariat, Urbana, Illinois.

Rottger, J. (1983), Origin of refractive index fluctuations in the mesosphere as opposed to the stratosphere and troposphere, Handbook for MAP, 9, edited by S. A. Bowhill and B. Edwards, 143-144, SCOSTEP Secretariat, Urbana, Illinois.

Rottger, J. (1984), The MST radar technique, Handbook for MAP, 13, edited by R. A. Vincent, 187-232, SCOSTEP Secretariat, Urbana, Illinois.

Rottger, J., P. Czechowsky, R. Ruster, and G. Schmidt (1983), VHF radar observations of wind velocities at the Arecibo Observatory, J. Geophys., 52, 34-39.

Sato, T. (1981), Coherent radar measurements of the middle atmosphere and design concepts of the MU radar, Ph. D. Thesis, Kyoto University, Japan.

D19-46
7P.

3.1.5 EVIDENCE OF ATMOSPHERIC GRAVITY WAVE PERTURBATIONS OF THE BRUNT-VAISALA FREQUENCY IN THE ATMOSPHERE

R. E. Good, R. W. Beland, J. H. Brown, and E. M. Dewan

Air Force Geophysics Laboratory
Hanscom AFB
Bedford, MA 01731

A series of high altitude, medium resolution, measurements of temperature, pressure and turbulence have been performed by the Air Force Geophysics Laboratory. These measurements were conducted using the VIZ Manufacturing Co. microsondes with attached AFGL micro-thermal probes measuring the temperature structure coefficient C_T (BROWN et al., 1982). A typical atmospheric temperature measurement is shown in Figure 1. Several small temperature inversions are evident in the troposphere. The stratosphere is marked with numerous fluctuations in the temperature profile. Microsondes provide temperature and pressure measurements every 4 seconds up to a maximum altitude of 30 km (MSL). Since the average ascent rate is 5 m/s, the altitude interval between the measurement reports is 20 m. The potential temperature is calculated from the temperature and pressure from the definition (COLE, 1970):

$$\theta = T \left| \frac{1000}{P} \right|^{R/C_p}$$

where T is the temperature in Kelvins with a resolution of 0.1 K and P is pressure in millibars, R is the ideal gas constant and C_p is the specific heat of air at constant pressure. This equation defines the potential temperature for adiabatic displacements relative to the 1000 mb level. The nominal ratio of R to C_p has the value 0.286.

The Brunt-Vaisala frequency squared, N^2, is defined by

$$N^2 = \frac{g}{\theta} \frac{d\theta}{dz}$$

A problem of computing the Brunt-Vaisala frequency from the microsonde data is thus one of numerical differentiation. Some smoothing of the data is essential due to the tendency that numerical differentiation has in amplifying high frequencies, and hence, noise. Such filtering reduces the spatial resolution of N^2. However, the competing interests of maximizing resolution while minimizing noise must be balanced. The filtering adopted here has two steps. The first filter is a simple 5-point moving average filter. Smoothed potential temperature ($\bar{\theta}$) is computed by:

$$\bar{\theta}_j = \sum_{k=-2}^{+2} \theta_{j-k}/S$$

The transfer function of this filter is:

$$A(k) = \frac{1}{5} \frac{\sin(5k/2)}{\sin(k/2)}$$

The transfer function is displayed in Figure 2. This is a simple low-pass filtering scheme that reduces the vertical resolution of the data from 20 m to approximately 50 m (one half the wavelength of the first null in the transfer function). The sidelobes of this filter are significant. After a differencing, these lobes are much larger than the main peak due to the fact that differentiation corresponds to multiplication by k in the Fourier domain. To overcome this sidelobe problem, a second-stage filter is employed. This stage is a 13-point least squares parabola, i.e., the previous and succeeding 6 points are used to smooth the center of the data. The transfer function of this parabolic filter is also shown in Figure 2. This too is a form of a low-pass filter which reduces the resolution of the data to approximately 75 m.

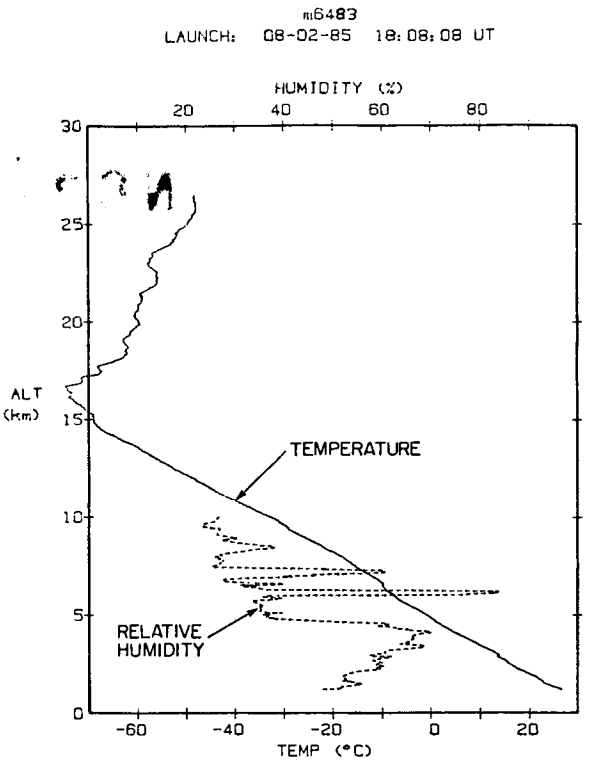

Figure 1. Microsonde temperature profile, Flight M6483 on August 3, 1985 at noon local time, using a standard rod thermistor.

The useful feature of this two-stage filter is that the parabolic sidelobes tend to cancel the moving average sidelobes. This cancellation holds only for certain combinations of orders of the parabola and moving average. The net two-stage transfer function is shown in Figure 2. The potential temperature is smoothed in this two-stage fashion. A further useful feature of the second-stage parabolic filter is that the filter form is a polynomial which is easily differentiated. The transfer function of this differentiating filter is shown in Figure 2. The spatial resolution of the differentiator is approximately 100 m. This is the method of determining the vertical potential temperature gradient; the least squares parabola is differentiated after the first smoothing with the moving average. The Brunt-Vaisala frequency is then calculated using this derivative and the two-stage smoothed potential temperature. The actual derivative can be considered as having occurring over dz of about 300 m. Shorter wavelengths are attenuated.

A typical Brunt-Vaisala frequency squared profile is shown in Figure 3. Depending upon the atmospheric boundary layer conditions, there may exist static instability conditions as indicated when the Brunt-Vaisala frequency is negative. Above 5 km altitude, the Brunt-Vaisala frequency averages to around 0.01 sec^{-1}, while in the stratosphere, the frequency was about 0.025 sec^{-1}. The wave-like structure apparent throughout the atmosphere exhibits different

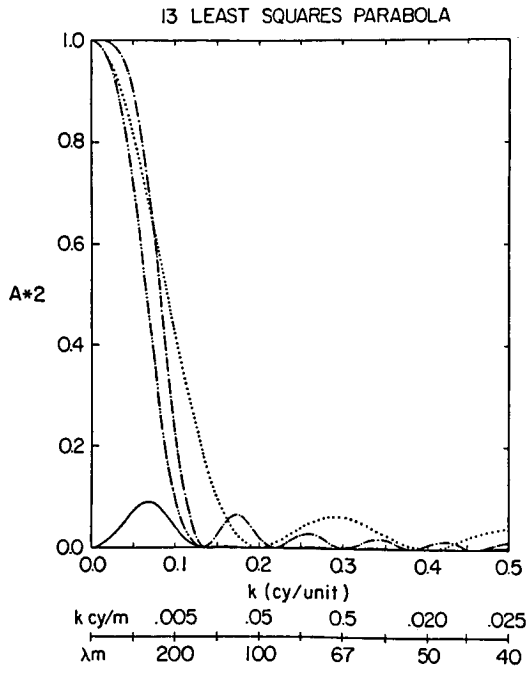

Figure 2. Numerical filters used in smoothing and differentiation. Data initially smoothed with 5-point moving average (– – –), then fitted with a 13-point parabola (–·–·–·–·–·–). These are combined as shown by the (–··–··–··–··–) curve. Differentiation of the combined the 5-pt and 13-pt parabola (————) yields the Brunt-Vaisala frequency.

characteristic scales in the troposphere and the stratosphere. An examination of Figure 3 indicates a visual periodicity of 1 to 3 km in the stratosphere and less than 1 km in the troposphere. The Brunt-Vaisala frequency transition between the troposphere and the stratosphere generally occurs over a 1- to 4-km altitude region.

A power density spectra was obtained of the Brunt-Vaisala frequency squared to examine possible periodicities in the wave-like structures. The procedure applied was to use the Blackman-Tukey approach of (1) de-trending the data by removing a mean, (2) obtaining the truncated autocorrelation, (3) Hamming the autocorrelation and then (4) computing the power spectral density (PSD) of N^2, § $(rad/s)^4/(cy/m)$, as a function of wave number, k (cy/m). Note that no pre-whitening and subsequent post-darkening is applied. The reason for not doing this is that we are interested only in the low frequencies. Furthermore, the data have been extensively smoothed which avoids aliasing errors in the PSD. We have also used a minimum entropy method linear predictor with 20 and 40 coefficients. The 20 coefficients are used to obtain smooth PSD plots to examine the envelope. The 40 coefficients are used to identify specific wave number contributions.

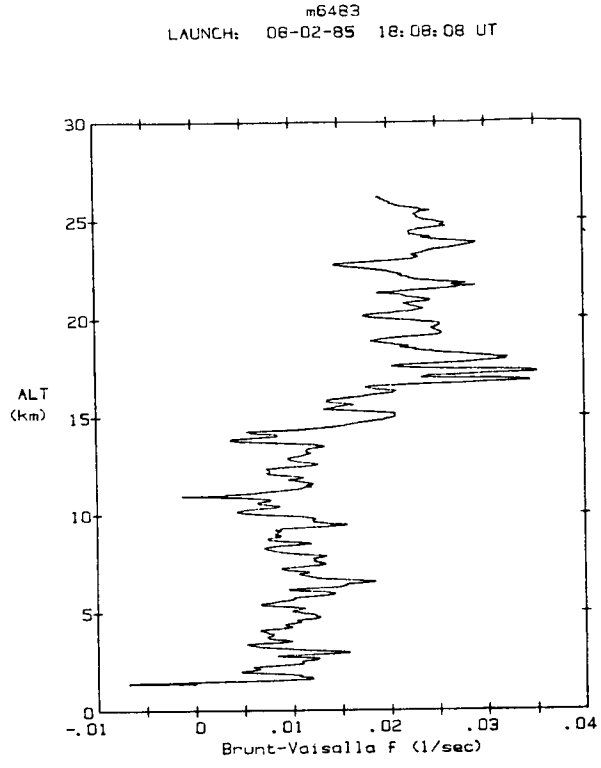

Figure 3. Calculated Brunt-Vaisala frequency, Flight M6483.

Figures 4a and 4b represent the PSD of the vertical spatial profile of the squared Brunt-Vaisala frequency for the microsonde flights shown in Figure 3. The stratospheric region is defined as being between 17 km to 27 km and the troposphere is defined as between 2.5 and 14 km. The spectral envelope is one of constant PSD to the maximum wave number, k*. The PSD decreases as the wave number increases from k* to the filter cutoff, $k_f = 1/200\ m^{-1}$. A detailed look at the spectrum shows 2-4 identifiable peaks. This is interpreted as indicating a narrow selection of gravity waves in the stratosphere and not a continuous array of wavelengths. This can be visualized in Figure 5 which is an expanded graph of the Brunt-Vaisala data.

Finally, we have combined the spectra from four soundings (M5309, M6472, M6474, and M6483) and obtain an average PSD for the troposphere and the stratosphere shown in Figure 5. Shown here is the fact that the spectra can be considered to have a -1 slope between 4 km and the 300-m wavelength of the filter. The stratosphere amplitude is about an order of magnitude larger than the troposphere amplitude.

FRITTS (1984) and WEINSTOCK (1984) have indicated that gravity-wave saturation should occur simultaneously with the existence of convective instability regardless of whether or not the saturation mechanism is due to Kelvin-Helmholtz instability, nonlinear wave interactions, or direct

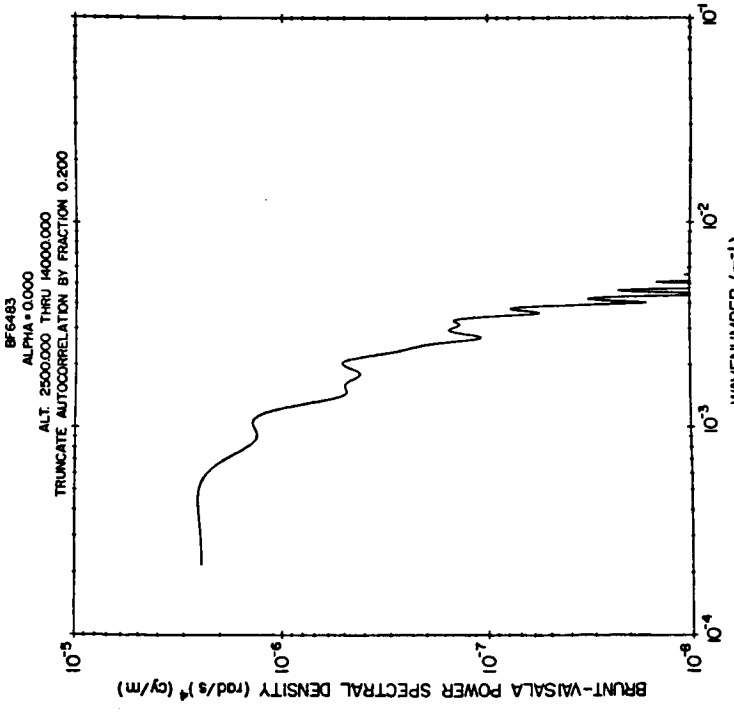

Figure 4a. Power spectral density of tropospheric Brunt-Vaisala frequency squared (Flight M6483) for the altitude region between 2.5 and 14 km.

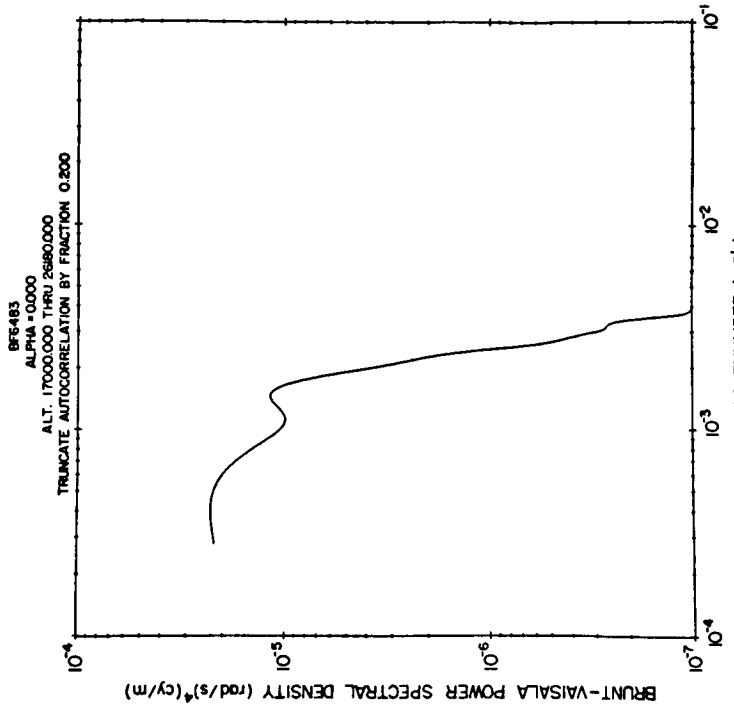

Figure 4b. Power spectral density of stratospheric Brunt-Vaisala frequency squared (Flight M6483) for the altitude region between 17 and 27 km.

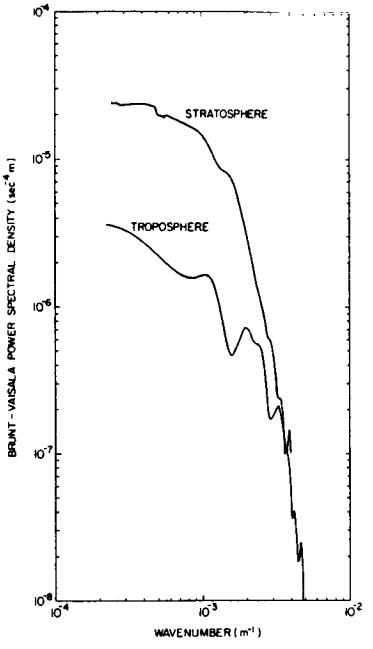

Figure 5. Comparison of the power spectral density of the stratosphere and troposphere. Each curve represents the linear average of four PSDs obtained from flights M6483, M5309, M6472, M7474 from July 31 to August 3, 1985.

convective instability. The fact that we do not see convective instabilities above the boundary layer (as indicated by negative Brunt-Vaisala frequencies), may be due to the following reasons. First, the instability produces turbulence at scales less than 100 m and have been filtered out of this presentation. This is consistent with the detailed turbulent layer measurements of BARAT and BERTIN (1984). Second, the microsonde thermistor rod has a long time constant ($t \sim 15$ seconds at 25 km, 7.8 sec at 15 km) and is unable to accurately respond to the presence of 20- to 40- m thick regions exhibiting adiabatic lapse rates. We are presently conducting experiments using both bead and rod thermistors. The hope is that the bead thermistor, while having errors in absolute temperature, will indicate the small-scale regions of adiabatic lapse rate owing to their fast time constant ($t \sim .3$ second).

The source of the wave-like structure is assumed to be gravity waves. DEWAN and GOOD (1985) have suggested that gravity waves grow in amplitude during passage up through the atmosphere. However, a maximum growth is reached when the saturation conditions occur. The saturation instability leads to the production of turbulence. The spectra of vertical profile of horizontal winds observed in the stratosphere has been shown by DEWAN and GOOD (1985) and SMITH et al. (1985) to exhibit a -3 slope for all wavelengths greater than the dominate wavelength, k*. The question that needs to be answered is, What is the mechanism for producing the wave-like structure in the Brunt-Vaisala frequency? An explanation is that the gravity waves themselves alter the Brunt-Vaisala frequency in the atmosphere. HODGES (1967) estimates the density and temperature perturbations of a gravity wave. It can be shown that the squared Brunt-Vaisala power density spectrum under gravity-wave saturation hypothesis will have a slope of -1.

Thus, the temperature changes that can be produced by a gravity wave are small unless nonlinear effects are occurring. Such nonlinear interactions can occur and themselves limit the growth of gravity waves. FRITTS (1984) has shown that these nonlinear interactions can produce a gravity-wave spectrum similar to the saturation theory.

CONCLUSIONS

Spectral analysis of atmospheric Brunt-Vaisala frequencies reveal spectra similar to the velocity spectra of DEWAN et al. (1984), DANIELS (1982), and ENDLICH and SINGLETON (1969). The Brunt-Vaisala spectra indicate existence of separate, distinguishable wave modes.

REFERENCES

Barat, J., and F. Bertin (1984), Simultaneous measurements of temperature and velocity fluctuations within clear air turbulence layers: Analysis of the estimate of dissipation rate by remote sensing techniques, J. Atmos. Sci., 41, 1613-1619.

Brown, J. H., R. E. Good, P. M. Bench, and G. Faucher (1982), Sonde experiments for comparative measurements of optical turbulence, AFGL-TR-82-0079.

Cole, F. (1970), Introduction to Meteorology, John Wiley & Sons, N.Y.

Daniels, G. (1982), Terrestrial environment (climatic) criteria guidelines for use in aerospace vehicle development, 1982 Revision NASA Tech. Memo, NASA TM-82473.

Dewan, E. M., N. Grossbard, A. F. Quesada, and R. E. Good (1984), Spectral analysis of 10 m resolution scaler velocity profiles in the stratosphere, Geophys. Res. Lett., 11, 80-83 and 624.

Dewan, E. M., and R. E. Good (1985), Saturation and the universal spectrum for vertical profiles of horizontal scaler winds in the atmosphere, submitted to J. Geophys. Res..

Endlich, R. M., and R. C. Singleton (1969), Spectral analysis of detailed vertical wind speed profiles, J. Atmos. Sci., 26.

Fritts, D. C. (1984), Gravity wave saturation in the middle atmosphere: A review of theory and observations, Rev. Geophys. Space Phys., 22, 275-308.

Hodges, R. R., Jr. (1967), Generation of turbulence in the upper atmosphere by internal gravity waves, J. Geophys. Res., 72, 3455-3458.

Smith, S., D. C. Fritts, and T. E. VanZandt (1985), Evidence of a saturation spectrum of atmospheric gravity waves, submitted to Geophys. Res. Lett..

Weinstock, J. (1984), Gravity wave saturation and eddy diffusion in the middle atmosphere, J. Atmos. Terr. Phys., 46, 1069-1082.

3.1.6 ATMOSPHERIC WAVES AND THE NATURE OF BUOYANCY TURBULENCE IN THE CONTEXT OF THE WAVES VS 2D-TURBULENCE DEBATE

Edmond M. Dewan

Air Force Geophysics Laboratory
Optical Physics Division
Hanscom AFB, MA 01731

INTRODUCTION

An interesting question is "How does one empirically distinguish between velocity fluctuations due to turbulence and those due to waves?" The subject is more interesting at present because there is a controversy between those who interpret such velocity fluctuations as being due to 2-D turbulence (GAGE, 1979; LILLY, 1983) vs those who attribute them to waves (VANZANDT, 1982; DEWAN, 1979). Is there a way to determine by means of experiment which view is correct, or when one or the other is more appropriate? Unfortunately, the power spectral density (PSD) does not help very much with this problem.

The goal of this and the companion paper to follow is to address this problem. It will, however, be necessary to first discuss the physical differences between waves and turbulence. One of the main purposes of this paper is to display certain new theoretical ideas on the subject of buoyancy range turbulence in this context. The companion paper presents a proposed empirical test to distinguish between 2-D turbulence and gravity waves.

WAVES VS TURBULENCE

Inertial range turbulence (IRT) involves an energy cascade or, to put it another way, strong mode interactions. The PSD has a $k^{-5/3}$ dependence where k is the wave number. IRT also involves strong mixing and it is isotropic. The cascade was vividly described by TENNEKES and LUMLEY (1972) in terms of a 3-D vortex stretching interaction between scales. RICHARDSON (1972) used poetry for the same purpose.

In contrast, buoyancy range turbulence is not isotropic but is strongly affected by buoyancy. It was described by Bolgiano (1959) who gave a $k^{-11/5}$ dependence for the spectrum, and by LUMLEY (1964) who gave k^{-3} for the dependence. There were other prominent contributors as well, but, the main point is that this work led to a particular length scale known as the buoyancy length $l_B = (\epsilon/N_B^3)^{1/2}$ where ϵ is the dissipation rate and N_B the buoyancy frequency. This scale separates IRT from BRT according to these early authors. As we shall see, this is indeed correct, but a slight extension of this concept leads to a scale which separates waves from BRT.

Table 1 summarizes some basic differences between waves and turbulence. A particularly useful distinction involves the interaction time between modes. BRT can be best regarded as a field of wave modes which interact so strongly that a given mode dies within one period or so of oscillation. In contrast, the fluctuations which can properly be called waves oscillate for very many periods and do so in a linear fashion i.e., without significant mode interaction.

INTERACTION TIME AND THE BRT/WAVE SEPARATION SCALE

While there is very little interaction between waves, Phillips and others have shown that under certain resonant conditions (PHILLIPS, 1977) there is indeed some interaction. He has shown (PHILLIPS, 1960) that the interaction time, T_i, is to a certain approximation,

$$T_i \tilde{=} (k_1 v_1 k_2 v_2)^{-1/2} \tag{1}$$

where k_i and v_i refer to the wave numbers and particle velocities of components of a resonant triad of interacting waves. If one ignores constants of order unity and if we let k and v refer to the primary wave, then we can, for our purposes, use the approximation

$$T_i \tilde{=} (kv)^{-1} \tag{2}$$

The dispersion relation for an incompressible buoyancy wave is simply

$$T_w = (N_B \cos \theta)^{-1} \tag{3}$$

where T_w is the wave period, θ is the angle between the wave vector k, and the horizontal. In this paper, we shall ignore factors of 2.

In view of the above discussion, we shall characterize waves by

$$T_i << T_w \tag{4}$$

and BRT by the reverse of this inequality. It follows that the boundary between the two regimes is given by $T_i = T_w$. From this it follows that at the boundary

$$(N_B \cos \theta) = (kv) \tag{5}$$

from (2) and (3).

It is useful to eliminate v from (5). For this purpose we consider the case where $\theta = 0$. As will be shown below, this leads to the transitional scale that separates horizontally propagating waves and IRT. We next assume that at this scale all the energy of this borderline wave with velocity v is fed into the IRT cascade and that the energy emerges from the small scale end of that cascade in the form of ε, i.e., dissipation. With this in mind, and using the definition that a borderline wave dumps all of its energy in one period, we obtain

$$\varepsilon = \frac{v^2}{T_w} \tag{6}$$

This is used in Equation (5) to eliminate v and hence

$$N_B = k_B \left(\frac{\varepsilon}{N_B}\right)^{1/2} \tag{7}$$

or

$$k_B = (N^3/\varepsilon)^{1/3} \tag{8}$$

an equation which has what may be a surprisingly familiar look to it. It is, of course, the inverse of the well-known buoyancy length, but it appears in a novel context. At first it seems to contradict the assertion that this length separates IRT and BRT; however, the seeming contradiction will soon be resolved below.

To address the above paradox, we now turn to the general case where θ is allowed to be arbitrary. In this case, the borderline condition which is given by $T_w = T_i$ leads to

$$k_B = (N_B{}^3 \cos^3 \theta/\varepsilon')^{1/2} \tag{9}$$

where ε has been replaced by ε' in anticipation of the discussion to follow. For BRT we claim that the clearest physical description is that it consists of a cascade of strongly interacting waves of large amplitude. This cascade resembles IRT in the sense that, for the most part, the flow of energy is down the scale. (The subharmonic instability is a good candidate for the mechanism of interaction). Now an interesting observation is that, as θ is increased, T_w is also increased (in accordance with the dispersion relation). This means that for any T_i one can find a T_w such that $T_i = T_w$. In principle, as θ goes to 90°, T_w goes to ∞. It is these waves where $\theta > 0$ but where $T_w < T_i$ which are not proper waves in the usual sense but are, rather, the strongly interacting buoyant modes which constitute what is designated at BRT.

As promised, we now discuss ε'. In BRT, there are two additional ways for energy to be dissipated in contrast to IRT which has only ε. These are, namely, ε_{PE} which is the dissipation rate of potential energy brought about by mixing in the stratified fluid, and ε_{RAD} which is due to the radiation of energy in the form of gravity waves that are generated by a certain amount of "up scale" energy flow caused by mode interactions. Thus,

$$\varepsilon' = \varepsilon_{PE} + \varepsilon_{RAD} + \varepsilon \tag{10}$$

Unfortunately, the numerical values of ε_{RAD} and ε_{PE} are not known. As can be seen from Equation (9), BRT can exist for wavelengths ranging from the usual "buoyancy length border" or, the outer scale of IRT, to scales that are boundless for θ close to 90°. The very large wavelengths and associated long periods correspond to nearly horizontal particle motion as can be seen from the incompressibility condition $\vec{k} \cdot \vec{v} = 0$. In other words, as θ is increased, $\vec{k}$ becomes more vertical, the period lengthens, and particle motion becomes horizontal. Thus, the question arises, "Does this type of BRT represent what is usually called 2D-turbulence?" The answer seems to be "no" for the following reason. The 2D-turbulence in the literature involves a cascade in the direction of small to large scale, which is to say, a reverse cascade. BRT does not seem to fit this description.

We leave as an unanswered question "Where does 2-D turbulence fit as strongly interacting buoyancy-affected modes such that

$$k < (N_B^3 \cos^3\theta/\varepsilon')^{1/2}$$

Equation (11), in principle, could lead to an empirical test between BRT and waves. Further discussion will be given in the companion paper.

Table I

Physical distinctions between waves and turbulence

Waves	Turbulence
1. Linear Superposition	1. NonLinear "Promiscuous" Mode-Interaction ("Cascade" in k-space)
2. No Fluid Mixing	2. Fluid Mixing (Dispersion)
3. Wave Pattern is Global (In Space & Time	3. Eddies are Local (In Space & Time)
Propagation	No Propagation
Lasts many periods	Decays in about one period
Coherence	Incoherence
4. Obeys Dispersion Relation	4. No Dispersion Relation

REFERENCES

Bolgiano, R. (1959), Turbulent spectra in a stably stratified atmosphere, J. Geophys. Res., 64, 2226-2229.

Dewan, E. M. (1979), Stratospheric wave spectra resembling turbulence, Science, 204, 832-835.

Gage, K. S. (1979), Evidence for a $k^{5/3}$ law inertial range in mesoscale two-dimensional turbulence, J. Atmos. Sci., 36, 1950-1954.

Lilly, D. K. (1983), Stratified turbulence and the mesoscale variability of the atmosphere, J. Atmos. Sci., 40, 749-761.

Lumley, J. L. (1964), The spectrum of nearly inertial turbulence in a stably stratified fluid, J. Atmos. Sci., 21, 99-102.

Phillips, O. M. (1977), The Dynamics of the Upper Ocean, 2nd edition, 336 pp., Cambridge University Press, New York.

Phillips, O. M. (1960), On the dynamics of unsteady gravity waves of finite amplitude, J. Fluid Mech., 9, 193-217.

Richardson, L. E. (1972), Weather Prediction by Numerical Process, MIT Press, Cambridge, MA, Chap. 8.

Tennekes, H. and J. L. Lumley (1972), A First Course in Turbulence, 300 pp., MIT Press, Cambridge, MA.

VanZandt, T. E. (1982), A universal spectrum of buoyancy waves in the atmosphere, Geophys. Res. Lett., 9, 575-578.

3.1.7 A PROPOSED EXPERIMENTAL TEST TO DISTINGUISH WAVES FROM 2-D TURBULENCE

Edmond M. Dewan

Air Force Geophysics Laboratory
Optical Physics Division
Hanscom AFB, MA 01731

While the companion paper on buoyancy range turbulence given here leads to a unique scale, k_B, that allows one to differentiate between waves and turbulence for the special case of $\theta = 0$ (i.e., horizontally propagating waves), it does not seem to lead to a practical empirical distinction for the general situation. This is due to the fact that, as θ is increased, one has the ever-increasing presence of BRT for longer wavelengths (see Figure 1 below). The fact that the numerical values of ε' are not yet available compounds the difficulty. In addition, it does not appear possible to encompass true 2-D turbulence in the above picture. We are thus driven to a test which circumvents all these difficulties.

Our proposed test is based on the idea shown in Table 1 (of the companion paper) that waves are coherent and propagate while in turbulence we have the opposite situation. In particular, our test is suggested by the following quotation from MULLER (1984), on the nature of such turbulence: "The turbulence in each horizontal plane is independent from the turbulence in the other planes." If this statement were to be taken literally, it would imply that the temporal coherence between horizontal speeds, separated only in altitude, would be zero. Any vertical separation would be enough to destroy coherence. Naturally, in the real world, one would be forced to take into account the effects of viscosity; that is to say, a specific finite vertical separation would be needed to destroy coherence. In order to estimate this distance, L, one can use (see PRANDTL, 1952, P. 107)

$$L = C(\nu/S)^{1/2} \tag{1}$$

where ν is the kinematic viscosity, S is the shear scale, and C is a constant of order unity. Thus, if the coherence were very close to zero for vertical separations somewhat larger than L, then this would constitute strong evidence for two-dimensional turbulence and against other types of fluctuations such as gravity waves or three-dimensional turbulence over that frequency range. Numerically, L is of the order of 10 m in the troposphere and stratosphere. If however, ν in Equation (1) is replaced by turbulent eddy viscosity, then L would be increased by something like an order of magnitude. If C = 5, we would have something like 500 m. Perhaps, then, L = 1 km would be a safe value.

In view of the practical importance we will now present some of the mathematical details of the above test (see BENDAT and PIERSOL, 1971, 335-339). The coherence γ_{xy}^2 between two time series x and y is defined by

$$\gamma_{xy}^2 \equiv \frac{|\phi_{xy}(f_m)|^2}{\phi_x(f_m)\phi_y(fm)} \tag{2}$$

Here the x and y time series are obtained at N discrete times separated by the sampling time interval Δt. The frequencies f_m are given by

$$f_m = \frac{m}{N\Delta t} \quad , \quad (m=0,1\ldots\frac{N}{2}) \tag{3}$$

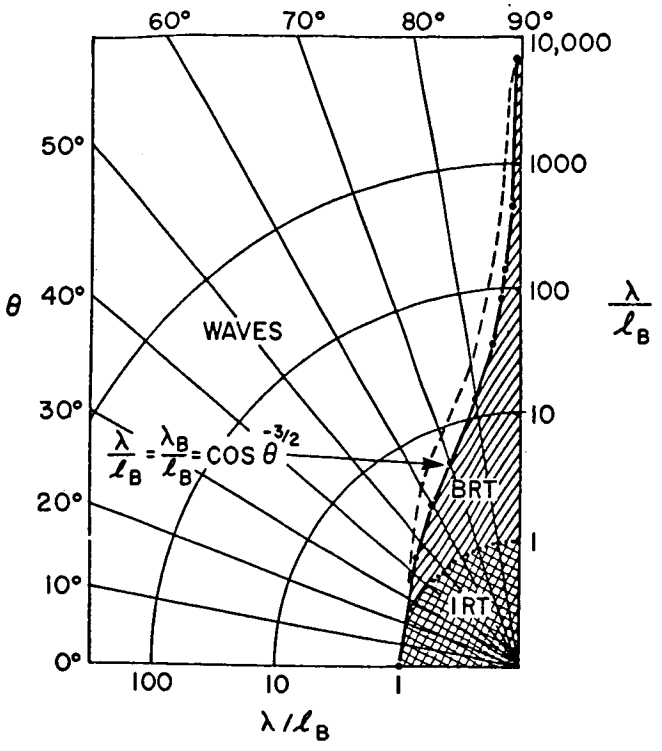

Figure 1. A polar plot of λ/ℓ_B as a function of θ • $\lambda_B \equiv k_B^{-1}$, $\ell_B \equiv (\frac{\varepsilon}{N_B^3})^{1/2}$. Regions of turbulence and waves are indicated. Note that here we take $\lambda_B = (N_B^3 \cos^3 \theta/\varepsilon)^{1/2}$ but to be strictly correct $\lambda_B = (N_B^3 \cos^3 \theta/\varepsilon')^{1/2}$. ($\varepsilon'$ is unknown). Note that BRT can extend to long wavelengths in the vertical direction when θ approaches 90°.

The cross spectrum, $\phi_{xy}(f_m)$ is defined by

$$\phi_{xy}(f_m) \equiv \frac{2\Delta t}{N} |X^*(f_m) Y(f_m)| \tag{4}$$

where

$$X(f_m) \equiv \sum X_n \exp[-j \frac{2\pi nm}{N}] \tag{5}$$

and this would be computed by means of the "fast Fourier transform" and then smoothed by means of standard windowing and averaging methods as described by BENDAT and PIERSOL [1971]. The $Y(f_m)$ is related to y by the same relation. X_m^* is the complex conjugate of X_m. The PSD, $\phi_x(f_m)$, is obtained from (4) by setting y = x and using only the x series. A similar thing is done to obtain ϕ_y. In other words,

$$\phi_x(f_m) = \frac{2\Delta t}{N}|X_m {}^* X_m| \qquad (6)$$

and similarly for ϕ_y.

At the meeting, we shall discuss the caveats associated with this test, and perhaps we can arrive at that time at a numerical specification of coherence which will satisfy most people in regard to a definitive test between waves and 2-D turbulence.

As a final remark, it should be pointed out that a certain amount of care is needed in order to avoid artifact when calculating the coherence. In particular, a single unsmoothed data set would automatically lead to a value of unity for γ_{xy}^2. In this way, an enthusiast for the gravity-wave interpretation would unwittingly delude himself into thinking that he had proven his case. To circumvent this artifact the procedure is to (a) calculate ϕ_{xy}, ϕ_x, and ϕ_y on a significantly large number of data records, or (b) to use appropriate smoothing. Bendat and Piersol point this out on p. 339 of their book in Section 6.6.

REFERENCES

Bendat, J. S., and A. G. Piersol (1971), Random Data, John Wiley, New York.

Muller, P. (1984), Small scale vortical motions, in Internal Gravity Waves and Small Scale Turbulence, edited by P. Muller et al., 249-264, Hawaiian Institute of Geophysics.

Prandtl, L. (1952), Essentials of Fluid Dynamics, Hafner, New York.

3.2.1 PROPAGATING TIDES IN THE MESOSPHERE

S. A. Bowhill and K. O. Merewether

Aeronomy Laboratory
Department of Electrical and Computer Engineering
University of Illinois
Urbana, Illinois

A preliminary search has begun for evidence of tides in the 1-hr average line-of-sight mesospheric velocity data from the Urbana radar in the period 1978-1982, inclusive. Since the Urbana antenna has only a single pointing direction, 1.6 deg away from vertical toward the southeast, observations are restricted to the southeasterly component of those velocities. Since observations are only available for a fraction of a day due to the absence of nighttime ionization in the Urbana mesosphere, it was decided to adopt an unusual procedure in the search; namely, to perform a Fourier analysis in the vertical direction and look for rotation in phase of vectors representing spatial frequency components. Propagating tidal modes would then show as vectors with a net rotation corresponding to their downward phase velocity.

Figures 1 and 2 show 5-year monthly averages of hourly mean horizontal velocities inferred from the Urbana data. Consistent diurnal variation is seen for a number of months. These data were analyzed for vertical spatial periods of 3, 4.5, 6, 9, 12, and 24 km. When plotted as a function of time of day, many of the phasors tended to show a net rotation; for example, Figures 3 and 4 show data for January and June at a period of 24 km.

The sense of rotation of a spinning vector in the complex plane can be determined objectively by computing the signed area swept out by the vector in moving from point to point. This calculation, performed on two separate components, indicated downward motion in 8 out of 12 months for the 9-km component and in 11 out of 12 months for the 24-km component. A comparison of the magnitudes of the 6 modes showed that the primary component was the 24-km component, a result confirmed by the tidal models of Forbes.

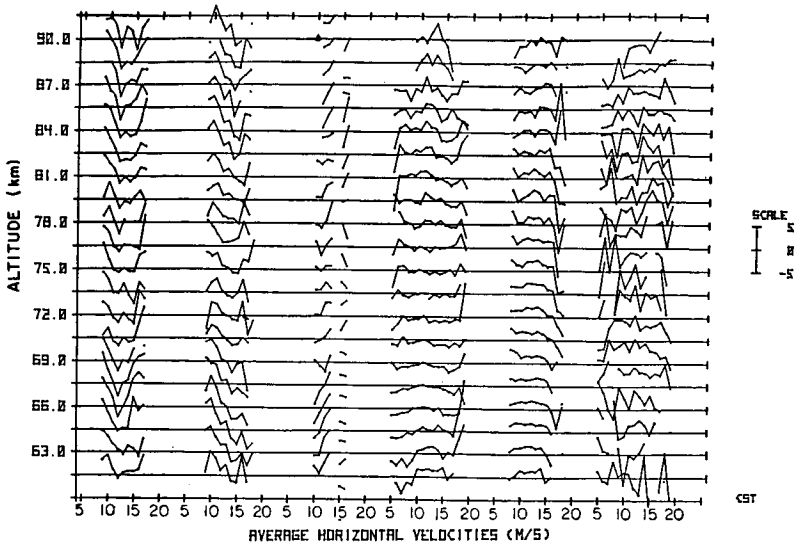

Figure 1. Average northwesterly horizontal velocity for the months January through June (1979 - 1982 average).

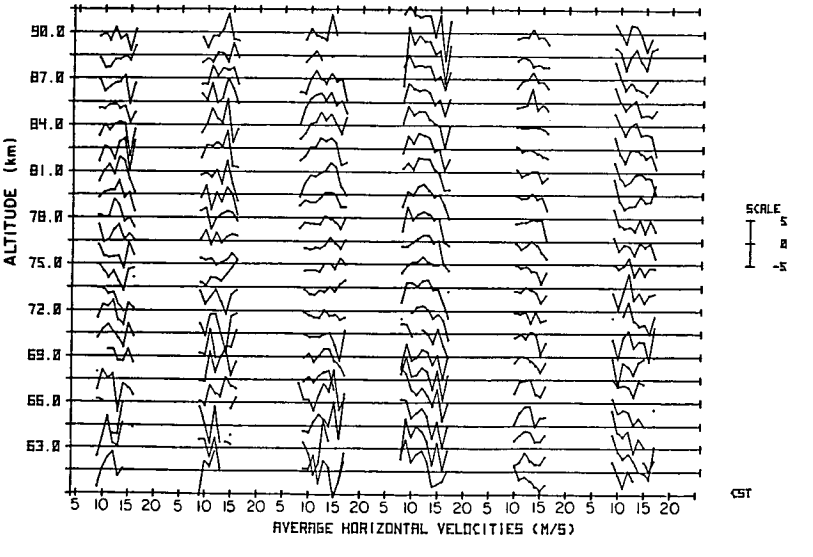

Figure 2. Average northwesterly horizontal velocity for the months July through December (1979 - 1982 average).

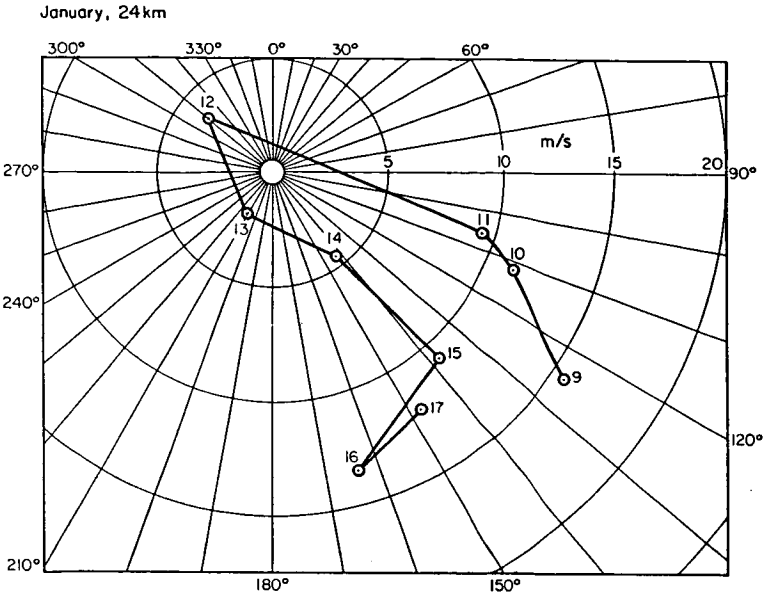

Figure 3. Phasor for the 24-km vertical wavelength in the hourly mean northwesterly horizontal velocity, for 09 through 17 local time, January 1979 - 1982.

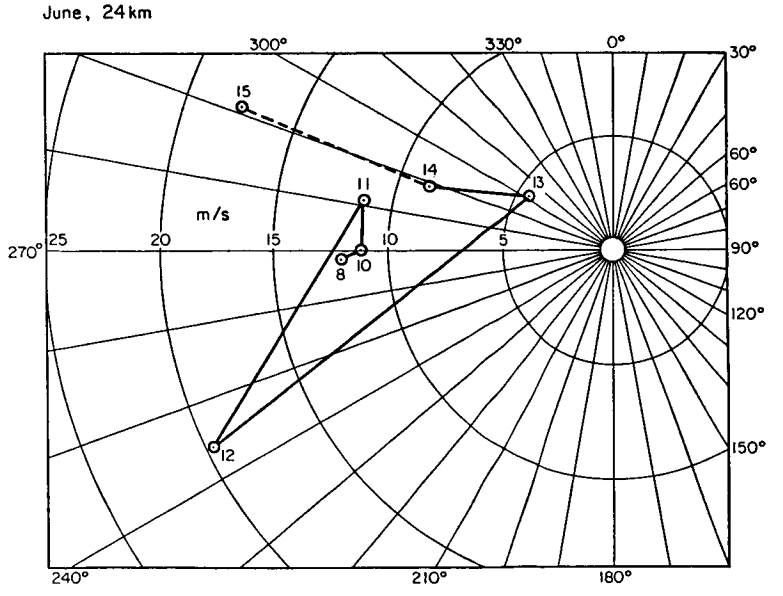

Figure 4. Same as Figure 3, but for 08 through 15 local time, June 1979 - 1982.

3.2.2 GRAVITY WAVES IN SEVERE WEATHER

S. A. Bowhill and S. Gnanalingam

Aeronomy Laboratory
Department of Electrical and Computer Engineering
University of Illinois
Urbana, Illinois

During 1983, the Urbana radar operated essentially every day gathering stratospheric and mesospheric gravity-wave data, for two hours centered around local noon. This paper presents some preliminary analyses of those data.

Figure 1 shows plots of the noon gravity-wave amplitude for April - December 1983, derived by subtracting the hourly mean for each day and averaging the residual minute-by-minute data. Considerable variability is seen from day to day and with season in both the stratosphere and mesosphere. Stratospheric data have been revised using the Tukey algorithm (BOWHILL and GNANALINGAM, 1986).

Annual average climatology is shown in Figure 2 between the stratosphere and mesosphere. On average, the rms gravity-wave velocity is about 15x larger in the mesosphere than in the stratosphere.

Figure 3 shows the relationship between the stratospheric and mesospheric gravity-wave amplitudes on a daily basis. Correlation between them is fairly strong, indicating that much of the variation in mesospheric wave amplitude is produced by gravity waves propagating from the stratosphere.

With a view to determining the role of severe weather in producing gravity waves, two tests were made. In the first, the wind speed measured at two nearby radiosonde stations, Peoria and Salem, was correlated with the stratosphere gravity-wave intensity at Urbana. Figures 4 and 5 show the results for May and August 1983. Although the gravity-wave intensity fluctuated greatly from day to day, there is little if any correlation with the stratospheric wind speed. This suggests that orographic forcing is not a factor in generating gravity waves in Urbana.

On the other hand, Figure 6 shows a scatter plot of gravity-wave intensity vs the heights of the highest cloud tops associated with precipitation within 100 miles of Urbana. A clear correlation is found between cloud top heights exceeding 20,000 ft and an increased gravity-wave amplitude in the stratosphere.

Two examples are now shown of the correlation of gravity-wave intensity with radar summary charts. Figure 7 shows a set of summary charts for May 7, 1983, with strong convective activity centered over Urbana starting at 1235 CST. Figure 8 shows an explosive growth of stratospheric gravity waves shortly following 1230 CST, suggesting that convective activity was the cause of the gravity waves seen.

On the other hand, Figure 9 shows summary charts for September 9, 1983, with no convective activity within about 1000 km of Urbana, but Figure 10 shows strong wave activity in the upper stratosphere. It is noticeable that there is a strong wind shear between 12 and 13.5 km, evidenced by the change in mean level of the line-of-sight velocity measurements. The fact that the Urbana antenna is tilted at an angle of 1.6 deg to the southeast suggests the existence of a strong shear in the southeasterly velocity just above 12 km, and this is probably responsible for the generation of the gravity waves seen at altitudes up to 22.5 km.

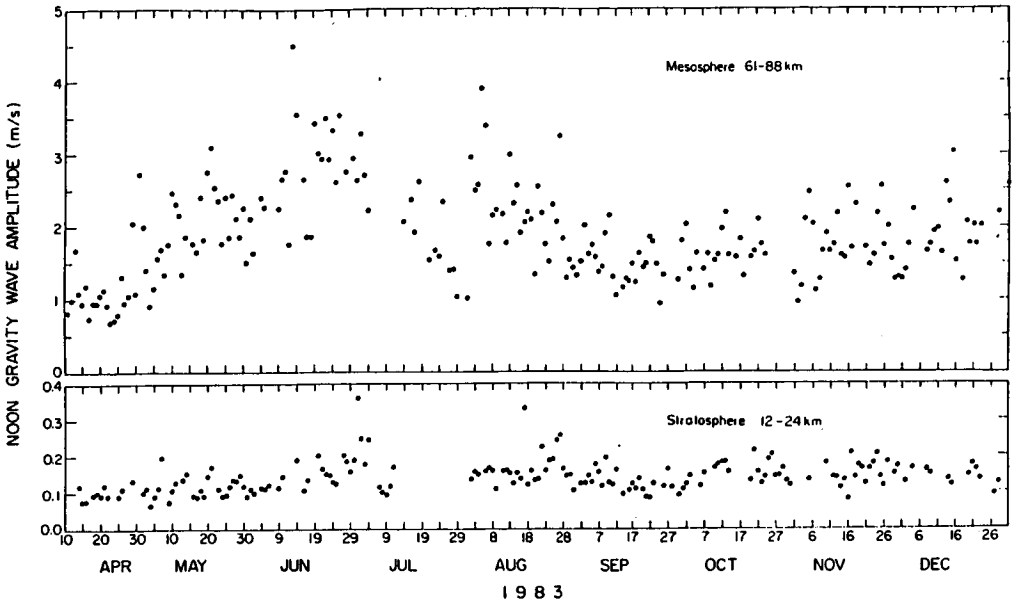

Figure 1. Daily variation of noon gravity-wave amplitude in the mesosphere and stratosphere.

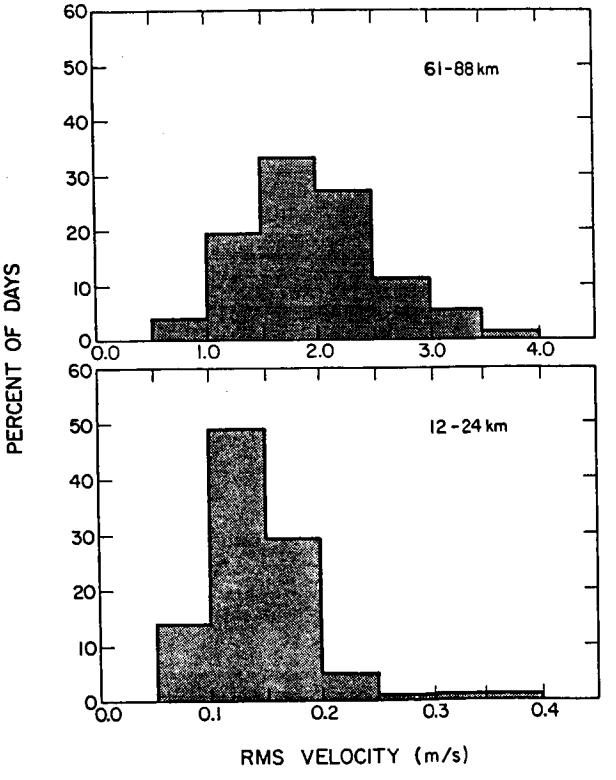

Figure 2. Annual average climatology for the the stratospheric and mesospheric vertical gravity-wave velocity, periods less than 1 hour.

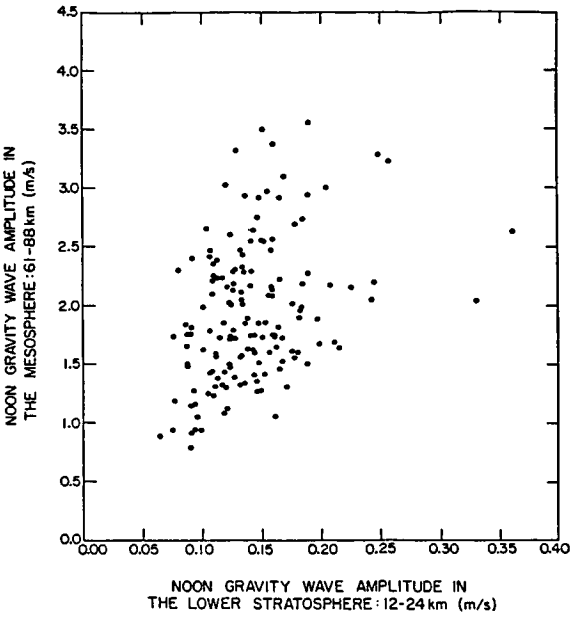

Figure 3. Scatter diagram illustrating the correlation between gravity-wave activity in the lower stratosphere and mesosphere.

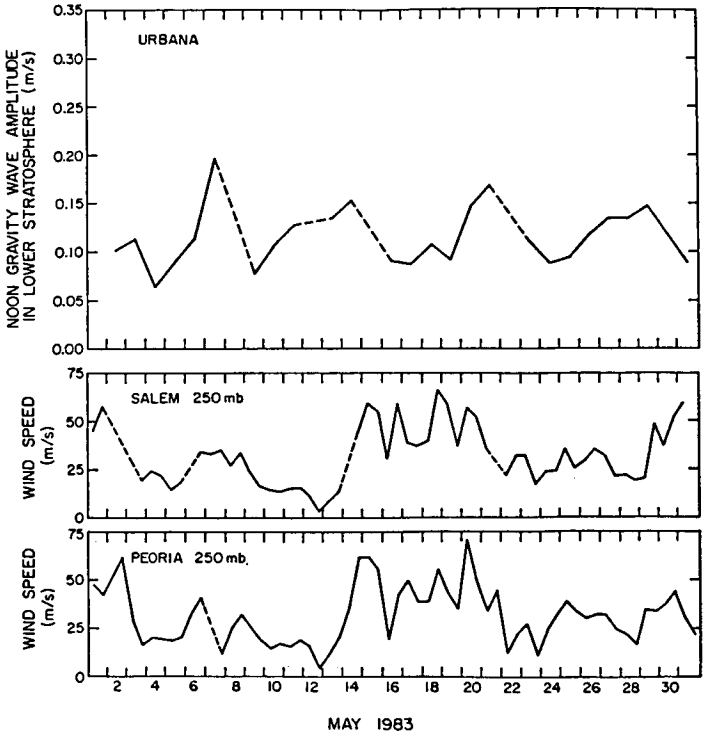

Figure 4. Relationship between stratospheric gravity-wave amplitude and wind speed: May, 1983.

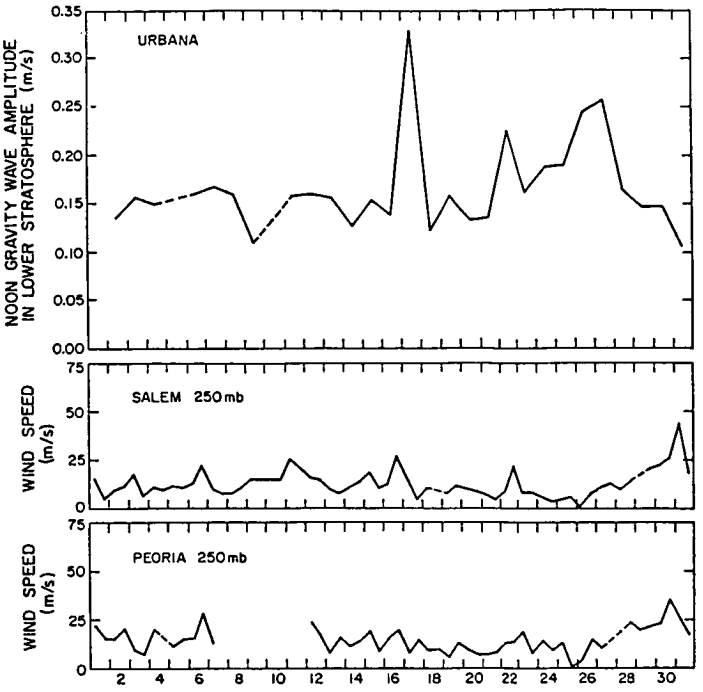

Figure 5. Relationship between stratospheric gravity-wave amplitude and wind speed: August 1983.

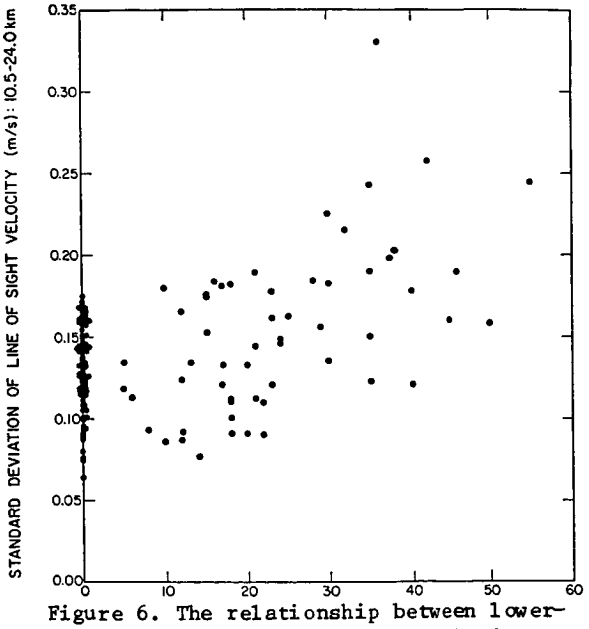

Figure 6. The relationship between lower-stratospheric gravity-wave velocity and highest cloud-top height within 100 miles of Urbana (thousands of feet).

MAY 07, 1983

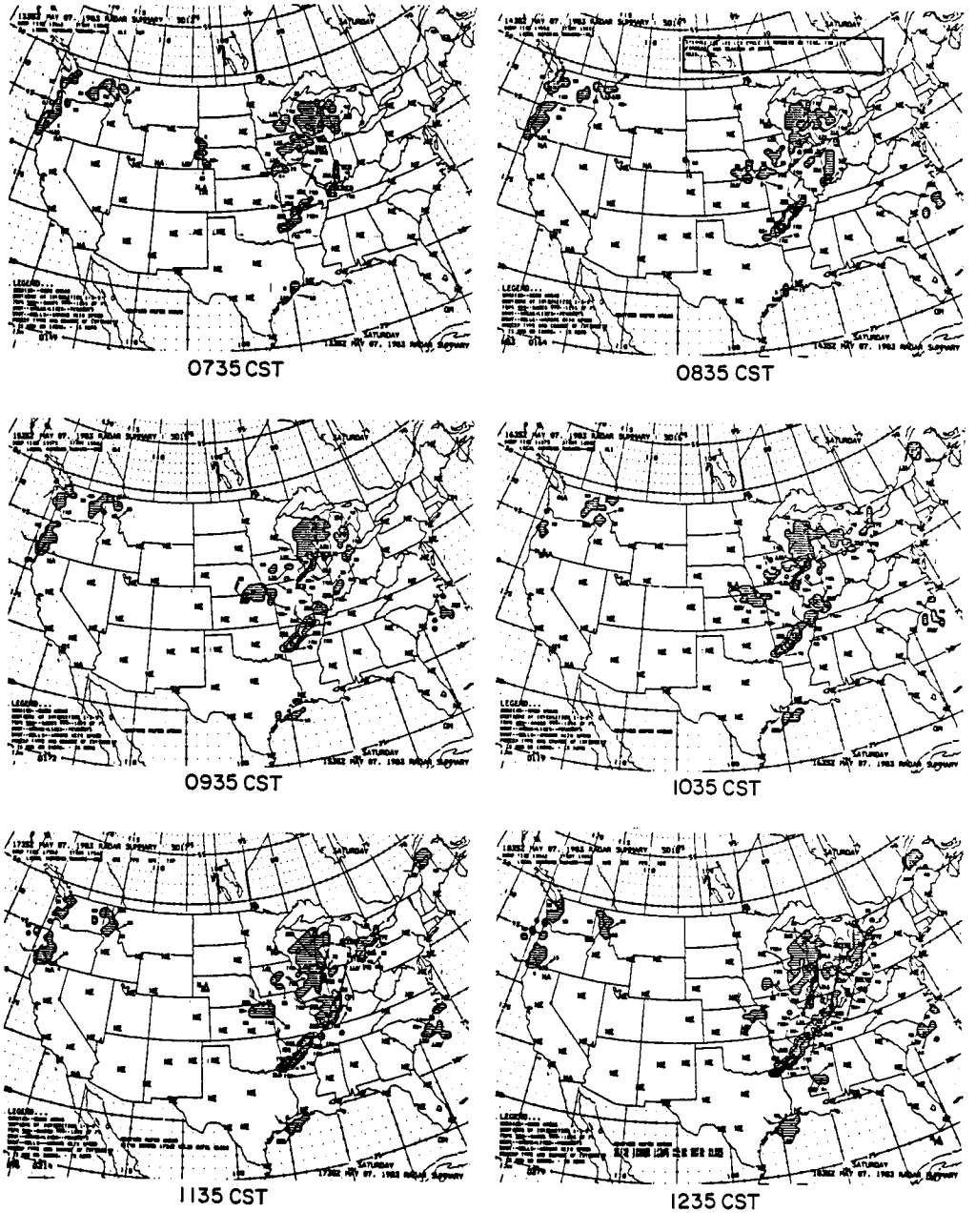

Figure 7. Radar summary chart showing strong convective activity over Urbana at 1235 CST on May 7, 1983.

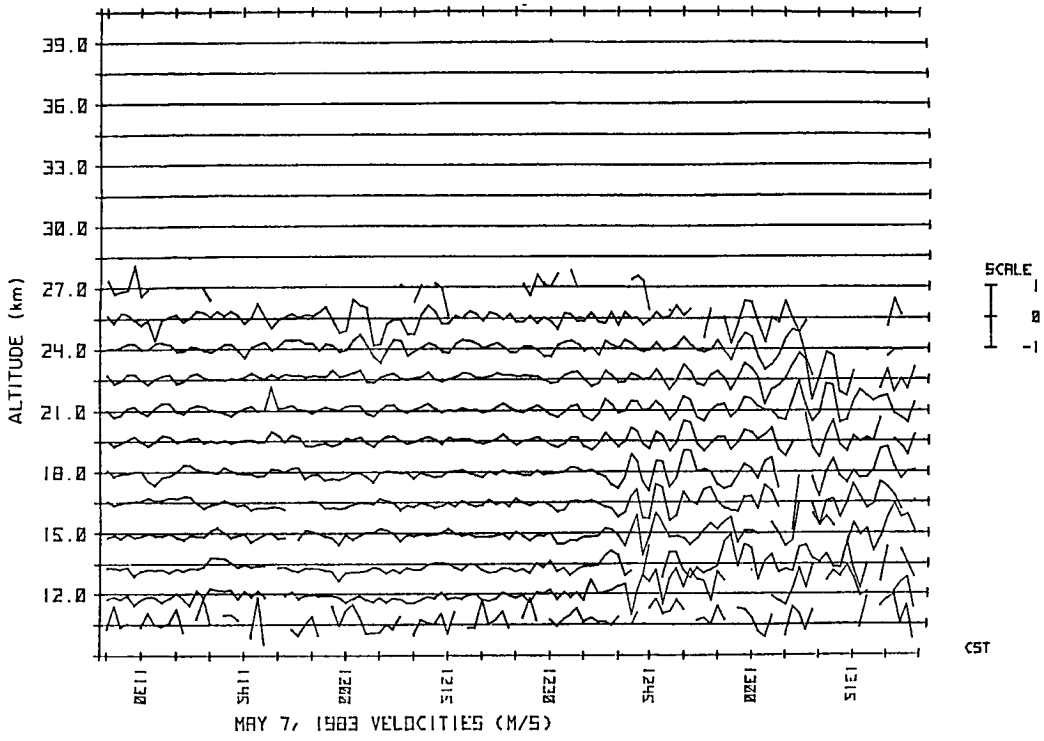

Figure 8. Vertical velocity plot over Urbana on May 7, 1983, showing an explosive growth of gravity waves at 1235 CST.

SEPTEMBER 09, 1983

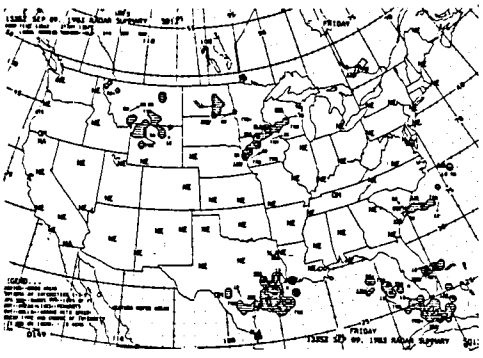

0735 CST

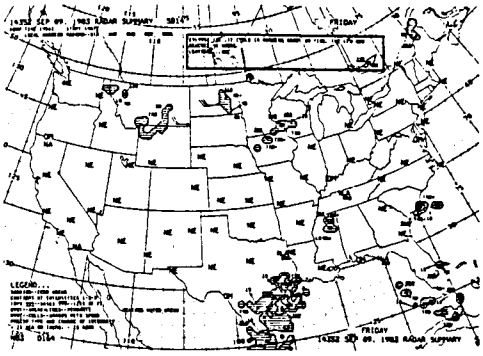

0835 CST

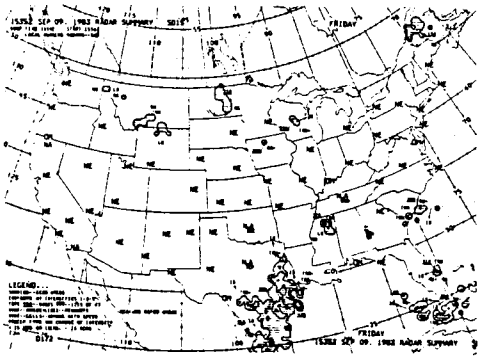

0935 CST

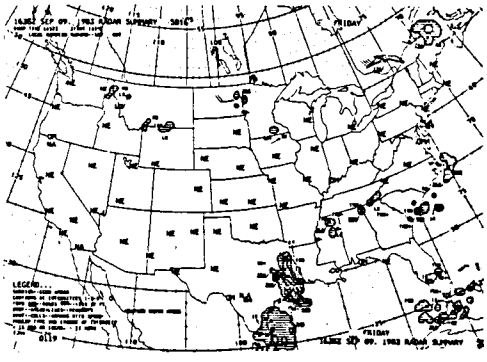

1035 CST

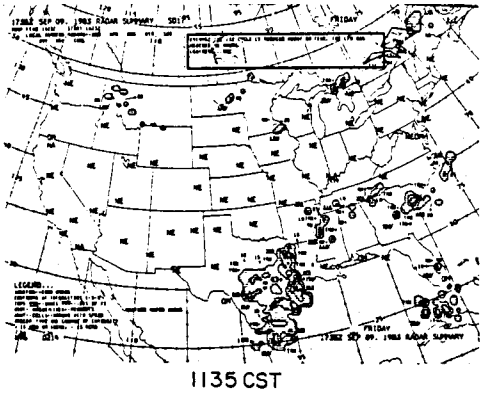

1135 CST

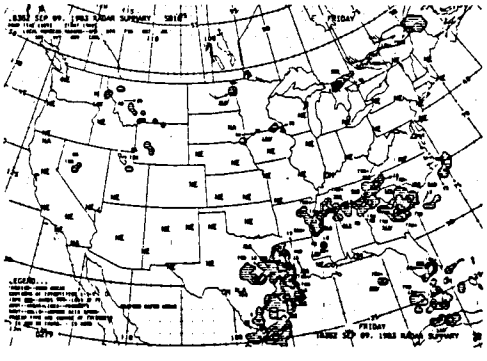

1235 CST

Figure 9. Radar summary charts showing lack of convective activity over Urbana on September 9, 1983.

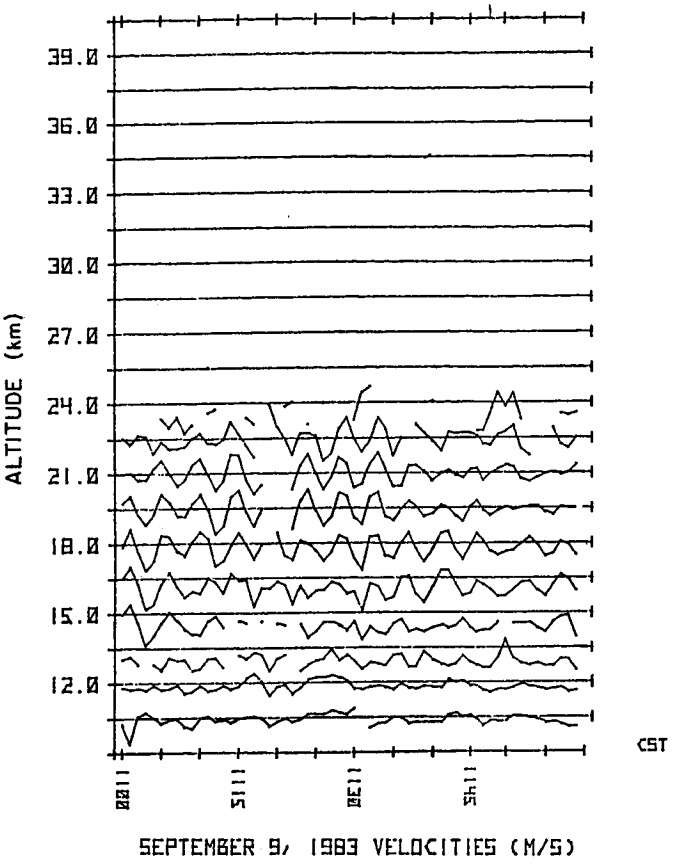

Figure 10. Strong gravity-wave activity over Urbana on September 9, 1983.

Reference

S. A. Bowhill, and S. Gnanalingam (1986), The Tukey algorithm for enhancing MST radar data, this volume.

3.2.3 SIMULTANEOUS ROCKET AND MST RADAR OBSERVATION OF AN INTERNAL GRAVITY WAVE BREAKING IN THE MESOSPHERE

Steven A. Smith* and David C. Fritts

Department of Physics, Geophysical Institute
University of Alaska
Fairbanks, AK 99701

Ben B. Balsley

Aeronomy Laboratory
National Oceanic and Atmospheric Administration
Boulder, CO 80303

C. Russell Philbrick

Air Force Geophysics Laboratory
Hanscom AFB, MA 01731

INTRODUCTION

In June, 1983, the STATE (Structure and Atmospheric Turbulence Environment) rocket and Poker Flat MST radar campaign was conducted to measure the interaction between turbulence, electron density and electron density gradient that has produced unusually strong MST radar echoes from the summer mesosphere over Poker Flat, Alaska (PHILBRICK et al., 1984). During the campaign, the Poker Flat MST radar was operating with a spatial resolution of 300 m and a time resolution of 1 1/2 to 3 minutes to obtain radial wind velocities along a vertical beam and two oblique beams directed 15° off-zenith and toward azimuths of 334°E (the 'north' beam) and 64°E (the 'east' beam). Several rocket salvos were launched consisting of passive spheres, electron density probes and accelerometers. In this paper, we present the analysis of radar wind measurements and a concurrent wind and temperature profile obtained from a rocket probe carrying a three-axis accelerometer. The two data sets provide a fairly complete (and in some cases, redundant) picture of the breaking (or more correctly, the saturation) of a large-amplitude, low-frequency, long-wavelength internal gravity wave. The data show that small-scale turbulence and small-scale wave intensity is greatest at those altitudes where the large-scale wave-induced temperature lapse rate is most negative or most nearly unstable, but the wind shear due to the large-scale wave is a minimum.

A brief review of linear gravity-wave theory will be presented in the next section as an aid to the identification of the gravity-wave signature in the radar and rocket data. A more complete review of gravity-wave saturation theory can be found in FRITTS (1984). Analysis of the time and height cross sections of wind speed and turbulence intensity observed by the Poker Flat MST radar will follow. Then, the vertical profile of temperature and winds measured by a rocket probe will be examined. Finally, the use of the independent but complimentary data sets provided by the rocket and the radar will be discussed and implications for theories of wave saturation will be presented.

*Currently at the Cooperative Institute for Research in Environmental Sciences (CIRES), University of Colorado, Boulder, CO.

ABBREVIATED GRAVITY-WAVE THEORY

Application of the linear perturbation method to the equations of motion, continuity and thermodynamic energy produces gravity-wave solutions with waves of the form $e^{z/2H} e^{-i(kx + mz - kct)}$ where H is the density scale height, k ($= 2\pi/\lambda_x$) and m ($= 2\pi/\lambda_z$) are horizontal and vertical wave numbers, c ($= w/k$) is horizontal phase speed and x, z and t represent horizontal and vertical distances and time. For simplicity, it is assumed that the wave is propagating in the x direction. The $e^{z/2H}$ factor maintains a constant energy flux for waves propagating vertically through the atmosphere with density decreasing exponentially with height. Mean quantities will be denoted by overbars, perturbation quantities will be primed and subscripts (except on λ) will represent derivatives with respect to the subscript.

Substituting solutions of this form in the equations yields a dispersion relation

$$m = \frac{N}{\bar{u}-c} \tag{1}$$

where N is the Brunt-Vaisala frequency defined by $N^2 = \frac{g}{\theta}\frac{\partial\theta}{\partial z}$ (g is the acceleration due to gravity and θ is potential temperature) and $\bar{u}$ is the mean horizontal wind in the direction of wave propagation. This is a simplified dispersion relation obtained by assuming an intrinsic frequency, w ($= k(\bar{u}-c)$), far from the inertial frequency, f, and from N, or $f << w << N$, assuming that the waves are hydrostatic (i.e., $k << m$) and also by neglecting vertical shear of the horizontal wind and neglecting terms of the order of $1/4H^2$ which implies that $\lambda_z < 4\pi H \sim 90$ km. The approximate dispersion relation yields an estimate of $\bar{u}-c$ from measurements of N and vertical wavelength.

Since radars and rockets measure two orthogonal, horizontal wind components and temperature, relations between these variables are needed to concisely identify a gravity wave. A relation between horizontal and vertical velocity perturbations comes from the continuity equation

$$u' = -\frac{m}{k} w' \tag{2}$$

u' and v' (the transverse wind component) are related by

$$v' = \frac{if}{w} u' \tag{3}$$

which comes from solution of the horizontal component equations of motion. This relation demonstrates that as w approaches f, the transverse wave perturbation component increases and the perturbation velocity vector traces out an ellipse. Such elliptical waves are known as inertio- or rotary-gravity waves.

Finally, from the thermodynamic energy equation relations for temperature perturbations are obtained:

$$\theta' = -i\frac{u'\bar{\theta}_z}{N} \qquad T' = -i\frac{u'\bar{T}_z}{N} \tag{4}$$

With these relations for temperature variables, a saturation limit on wave amplitude can be obtained. When, $(\bar{\theta} + \theta')_z < 0$ or $\theta_z' \leq -\bar{\theta}_z$ the atmosphere is convectively unstable. Taking derivatives gives

$$\frac{mu'}{N}\bar{\theta}_z \leq -\bar{\theta}_z \tag{5}$$

substituting for $m = N/\bar{u}-c$ we obtain

$$|u'| \geq |\bar{u} - c| \tag{6}$$

Thus, whenever the wave perturbation velocity exceeds the intrinsic wave phase speed, convective instabilities are initiated in that portion of the wave field where $\theta_z' \leq -\bar{\theta}_z$ which also corresponds to that point in the wave field where u' is maximum in the direction of wave propagation. Thus, the wave breaks down where the velocity perturbation is a maximum and the shear is a minimum. In the case of rotary waves, there is a shear of the transverse component at the point where u' is maximum. This transverse shear contributes to lowering the local Richardson number and instabilities can develop at amplitudes smaller than $\bar{u}-c$ (FRITTS and RASTOGI, 1985).

From the above discussion, a possible scenario for a propagating wave is that it will grow in proportion to $e^{z/2H}$ as it ascends until it reaches the saturation amplitude of $\bar{u}-c$. At that height, turbulence will be produced by instabilities, which will prevent the wave from growing further and hence the wave amplitude will be fixed at the saturation amplitude. This scenario was originally proposed by HODGES (1967).

Wave structure will be determined using the above relations and different aspects of the data. From both the rocket and radar measurements of the horizontal winds, the direction of wave propagation can be obtained. Both radar and rocket data yield estimates of the vertical wavelength and thus approximate intrinsic phase speeds from equation 1. Then it is possible to check the saturation condition with equation 6. The rocket probe provides an additional check on the saturation condition since θ' and θ_z' can be observed.

POKER FLAT MST RADAR DATA

The horizontal winds observed by the Poker Flat radar near the mesopause on June 15, 1983, are shown in Figure 1. The plotted vectors are computed from 15-minute averages of the oblique, radial winds that have been converted to horizontal by assuming the vertical wind is zero for a 15-minute average. Notice also, that only measurements at locations where the signal was significantly above the noise floor were used in the averages. Thus, it is possible to see two regions of strong signal propagating downward with time near 1400 and 2100 AST (Alaska Standard Time) which are separated by a blank region of no signal. This blank region implies either that the 3 m (radar half wavelength) component of turbulence was weak or that the electron-density gradient was weak or both.

The wind pattern in the latter half of the day reveals the presence of an inertio-gravity wave since the wind vectors rotate clockwise with time at any given height and also rotate clockwise with height at any given time. This is the sense of rotation corresponding to an upward propagating wave with $c > \bar{u}$ or a downward propagating wave with $c < \bar{u}$ in the Northern Hemisphere. Estimates of $\bar{u}$ by direct observation and $\bar{u} - c$ from equation 1 reveal that $c > \bar{u}$, implying upward energy propagation.

A quantitative picture of the wave came from least squares fitting of sine curves to the time series of radial velocities measured at each height in each beam is shown in Figure 2. These fits gave the amplitude and phase (or time of maximum) and the best fit period of the wave. The period was found to be 7 hrs. Combining the phase and amplitude parameters from the two orthogonal beams revealed the fact that the rotating wind vector traced out an ellipse with a maximum amplitude of 38 m/s horizontal with the major axis of the ellipse along a line from 50° to 230°. In principle, knowledge of the time of

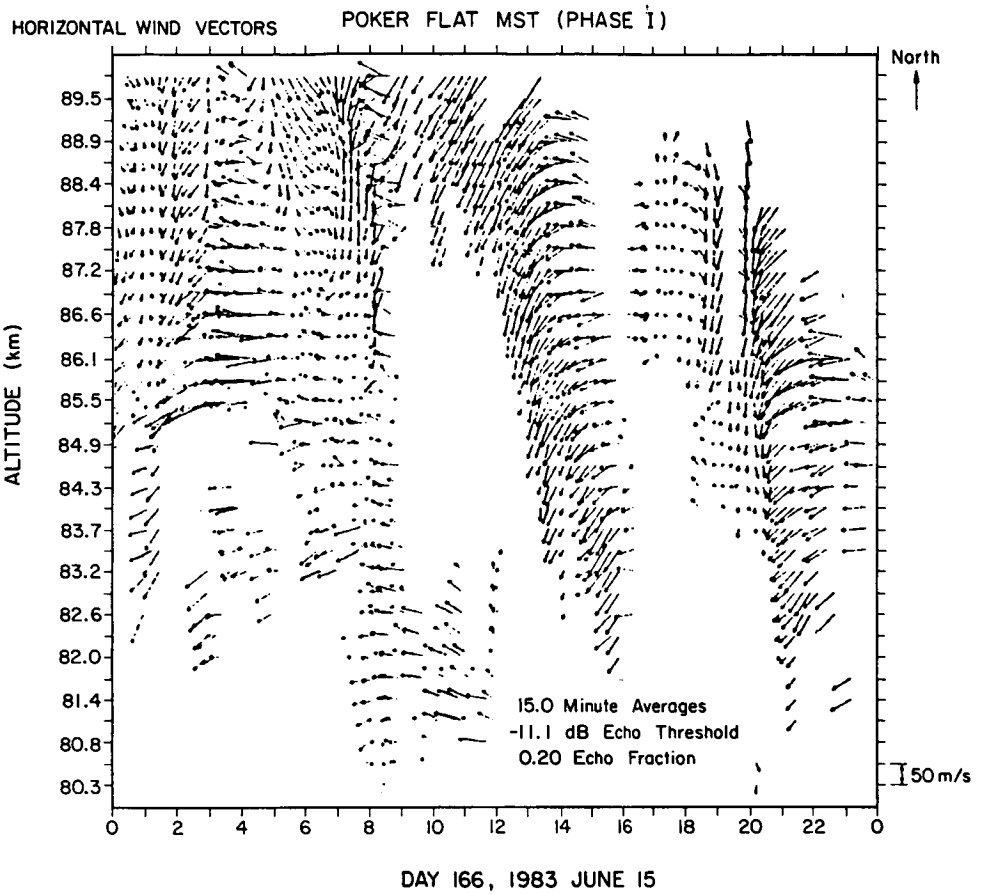

Figure 1. Time-height cross section of horizontal winds estimated from Poker Flat MST radar data. Blank spaces occur where the return signal was too weak to yield reliable wind estimates.

maximum vertical velocity would determine the direction of wave propagation but during the STATE campaign the Poker Flat MST radar's Doppler velocity resolution was insufficient to reliably measure the small vertical velocity component of this wave. The propagation direction was determined through use of the rocket data as will be mentioned below.

Measurement of the change of phase with height, apparent in Figure 2, led to an estimate of 19 km for the vertical wavelength of this wave. With our estimate for N of 0.03 rad/s from the rocket-measured temperature profile and the observed value for m, $\bar{u}$-c is found to be 90 m/s using the approximate dispersion relation. This implies that the wave amplitude is at about 40% of the saturation amplitude. Thus, it appears that this wave is not large enough, by itself, to produce the turbulent mixing of the electron-density gradient to which the MST radar is sensitive. However, the wave amplitude, shown in Figure 3, is not growing exponentially with height, implying that some of the wave energy is being dissipated in the 82-89 km region.

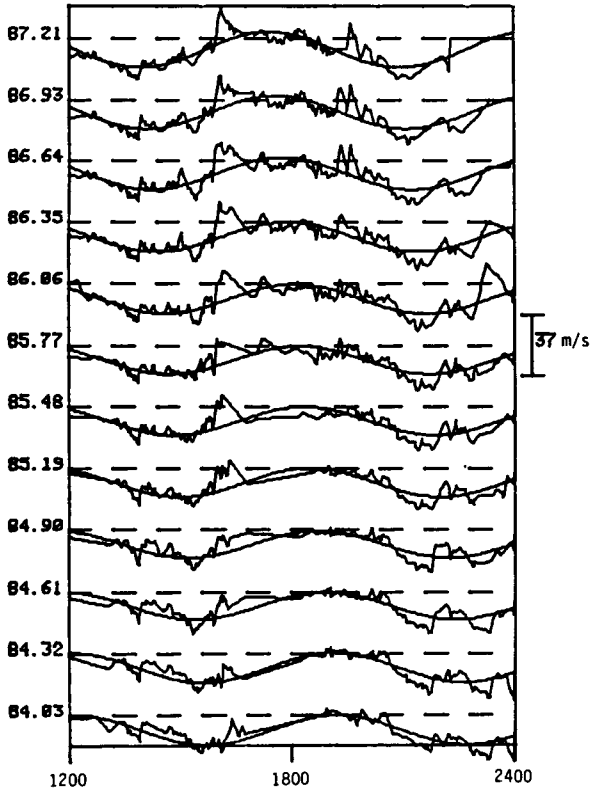

Figure 2. Time series of wind speeds measured along the east beam on June 15, 1983. Times are in Alaska Standard Time (local meridian time).

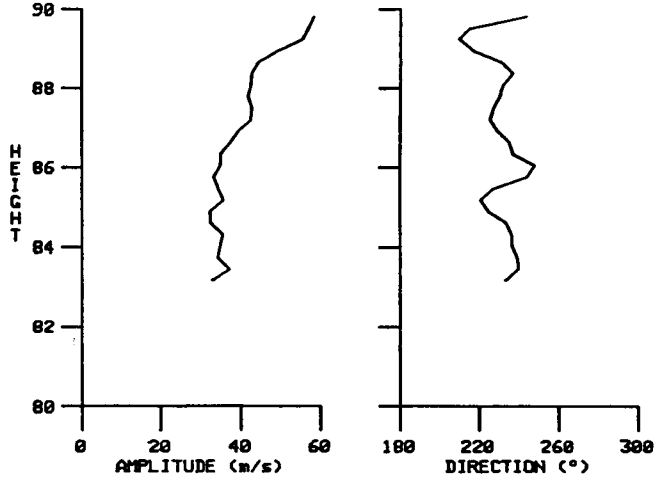

Figure 3. Estimated horizontal amplitude (u') and propagation direction profiles for the 7-hr wave.

NIKE-HYDAC ROCKET DATA

At 2051 AST on June 15, 1983, a Nike-Hydac rocket boosted an instrumented sphere to an altitude of about 75 km. The sphere continued in free flight to an altitude of 130 km. Data were obtained from both the upleg and downleg flights providing a continuous profile of winds and temperature from 75 to 130 km. The one instrument in the sphere relevant to this study was a 3-axis accelerometer used to measure accelerations due to density changes and changes in the winds. The temperature profile was obtained through integration of the measured density profile.

The resultant meosphere/lower thermosphere temperature profile is shown in Figure 4. There is a deep temperature minimum of 130°K at the summer mesopause near 86 km. The wind component profiles obtained from the accelerometers appear in Figure 5. Again, the presence of an inertio-gravity can be inferred from the wind data since the wind vector rotates clockwise with height above about 90 km.

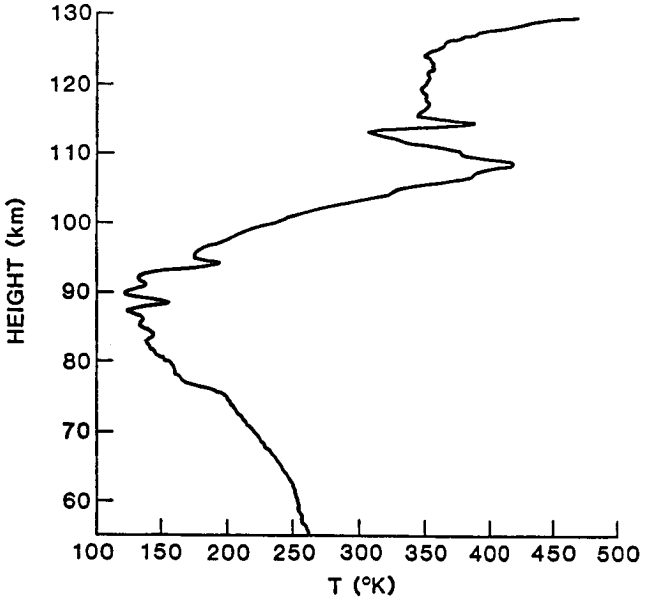

Figure 4. Temperature profile obtained by accelerometer sphere at 2055 AST, June 15, 1983. Note the cold summer mesopause with a temperature of 130°K near 86 km.

Before attempting to fit sine waves to the temperature and wind profiles, the data were differenced to remove linear trends such as the steady increase of temperature with height in the lower thermosphere. The differenced profiles appear in Figure 6. Fits were only made to the data above 85 km to avoid any influence the notch at the mesopause might have on wave amplitude or phase.

The best fit vertical wavelength was found to be 30 km. Combining the wave amplitudes and phases from the wind data led to the conclusion that a wave with an amplitude of 82 m/s was propagating towards 6° or 186°, with the maximum velocity occurring at 92 km. The propagation direction can be

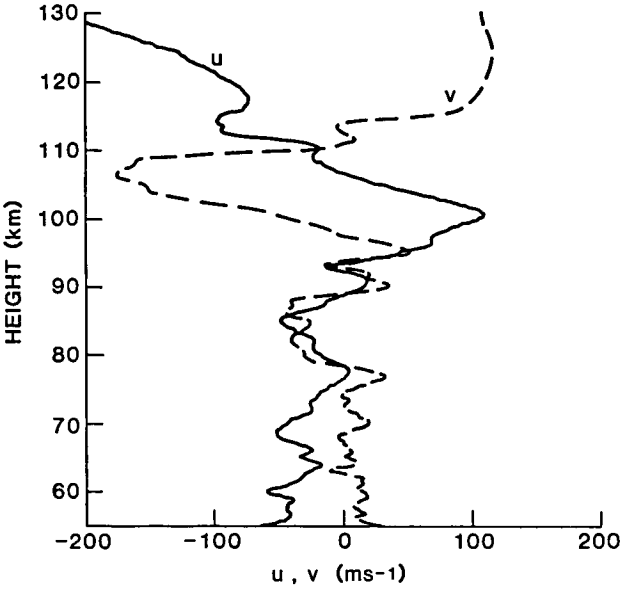

Figure 5. Wind profiles from the accelerometer sphere flight at 2055 AST, June 15, 1983. U is the zonal and V the meridional wind component.

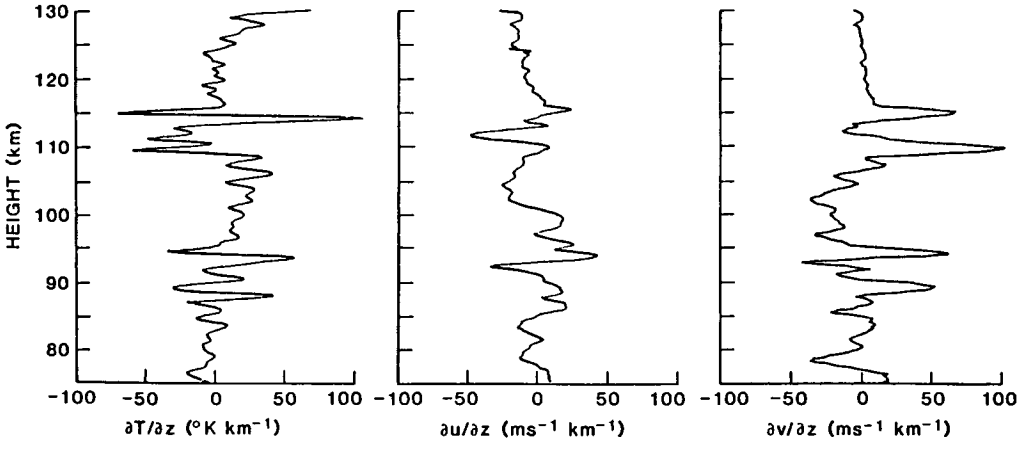

Figure 6. Differenced data from the profiles of Figures 4 and 5. Note the large variance in all three profiles at heights of 85 and 115 km.

determined through use of the temperature data and the fact that the most negative temperature gradient will occur at the height at which the perturbation velocity is in the direction of propagation. This occurred at 85 km where the wind vector is directed towards 295°. Thus, the two direction estimates from the rocket data bracket the direction inferred from the radar data. Uncertainties in the rocket data, principally the uncertainty introduced when removing the linear trend in the velocity profiles without actually knowing the mean wind profile, produce large uncertainties in the wave direction. However, the location of the most negative temperature gradient coincides with a wave velocity maximum in the radar data directed towards 230°. This fact and the nearly constant propagation direction profile in Figure 3 suggest that 230° is the most probable direction of wave propagation.

The wave amplitude and $\bar{u}$-c inferred from the vertical wavelength imply the wave is near 75% of saturation amplitude. The percentage of saturation amplitude from the velocity estimates agrees rather well with the degree of saturation from the temperature measurements. The ratio of the perturbation temperature lapse rate to that of the mean plus adiabatic lapse rate gives a figure of 73% of saturation amplitude. The analysis by FRITTS and RASTOGI (1985) yields a saturation amplitude of 0.82 ($\bar{u}$ - c) due to the transverse shear of the wave and the corresponding decrease in the local Richardson number. Thus, this wave was very near saturation at upper heights. This seems to contradict the radar data that suggested the wave was at only 40% of saturation amplitude. However, the radar data are centered near 85 km while the wave parameters from the rocket data were computed for the region from 85 to 130 km. The wave amplitude increase with height is consistent with the radar data in Figure 3.

Another discrepancy between the two data sets is the vertical wavelength of 19 km from the radar data and 30 km from the rocket data. This difference is to be expected since the steep temperature gradient above the mesopause and larger values of N act to suppress vertical motion and lead to a compression of vertical wavelenghts relative to the less steep gradients and smaller values of N in the thermosphere as can be seen from the approximate dispersion relation (equation 1).

The wave parameters are summarized in Table I along with 95% confidence limits from the least squares fitting of sine waves. The larger values of $\bar{u}$ - c, in Table I come from use of a more complete dispersion relation than equation 1, which has been used in the preceding paragraphs.

DISCUSSION

Analysis has shown that both the rocket payload and the radar were observing the same low-frequency (7 hr period), long-wavelength (19-30 km), large-amplitude (.4 - .8 of saturation amplitude) inertio-gravity wave. Both data sets also exhibit manifestations of wave saturation or breaking.

The variance of the difference profiles of Figure 6 is much greater at heights of 85 and 115 km than elsewhere and this is true for all three profiles. These heights are also the heights at which the wave-induced temperature perturbation lapse rate is most negative and the atmosphere is most nearly unstable. The increased variance appears to be due to the presence of smaller scale wave activity.

The radar data show that the regions of greatest S/N coincide with the locations of the most unstable lapse rate and of the maximum velocity perturbation in the direction of wave propagation as can be seen in Figure 7. The contours are of S/N averaged over both oblique beams. The solid lines mark

Table I

Large-scale wave characteristics on June 15, 1983

	Radar data	Rocket data
Data window	1200-2400 AST 82 - 89 km	2055 AST 85 - 130 km
Period	7 hr	
λ_z	19 km	30 km
u'	38 $\pm$ 5 m/s	82 $\pm$ 9 m/s
T'		59 $\pm$ 5°
T' (using u' and polarization relations)	20°	69°
propagation dir.	230 $\pm$ 10°	186 or 295 $\pm$ 55°
assumed N	0.03 rad/s	0.023 rad/s
$\bar{U} - c$	121 m/s	110 m/s
c	151 m/s	
$u' / \bar{U} - c$	0.26	0.75
$T_z' / (\bar{T}_z + g/c_p)$		0.73
u' / v'	1.48	1.98
intrinsic period using $\bar{U} - c$ using u'/v'	 8.74 hr 9 hr	 6.67 hr

the location of the most negative temperature gradient determined from the rocket temperature data (to be at 85.4 km at 2055 AST) and the vertical phase speed estimated from the radar data. Clearly, the largest radar signal strengths (and presumably the largest 3 m turbulence intensity) come from regions determined by the near saturation of the inertio-gravity wave. Recall that the single wave by itself was not large enough to saturate and produce turbulence, but FRITTS (1985) reported a numerical simulation demonstrating that a superposition of waves can lead to saturation, even though none of the waves possess saturation amplitude independently. Thus, gravity-wave saturation near the mesopause involves a broad spectrum of internal gravity waves.

This phenomenon of largest S/N appearing where the wave field is most nearly unstable and also where the perturbation velocity vector is in the direction of wave propagation allowed the determination of wave parameters for a 3-hr period wave on June 17, for which temperature measurements were not available.

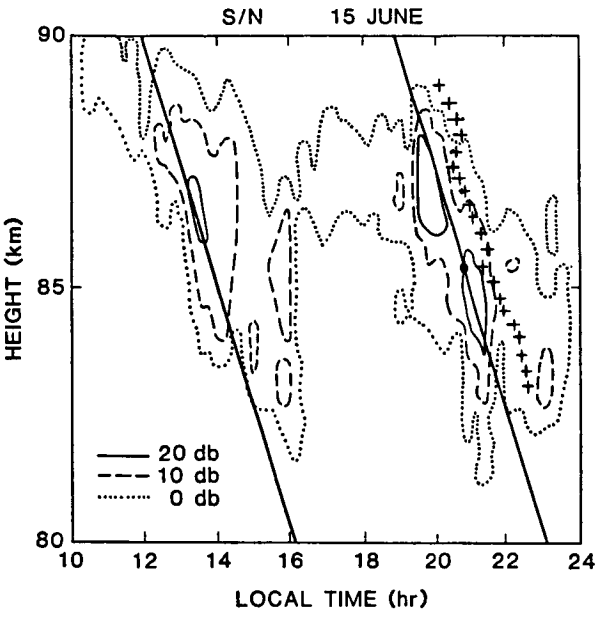

Figure 7. Contours of S/N averaged over both oblique radar beams. Crosses are locations of the maximum amplitude of the 7-hr inertio-gravity wave. Dot at 85 km is location of most unstable lapse rate from rocket data and solid line indicates motion of that lapse rate with the phase speed of the 7-hr wave.

Both of these cases imply that the regions of intense mixing of the electron-density gradient are closely coupled to the saturation of large-scale inertio-gravity waves. The scenario developed by BALSLEY et al. (1983) of gravity waves being vertically compressed as they approach the summer mesopause and thus approaching instability thresholds, holds for the inertio-gravity waves observed during STATE.

This study has benefited tremendously from the combined data sets obtained by rocket and MST radar. Future analysis of mesospheric dynamics and chemistry should involve different, yet complimentary data-acquisition methods, i.e., the radar provides a time history of winds while rockets provide a more extensive height profile of winds and temperature. Substituting a lidar for the rocket measurements would permit acquisition of a very complete picture of gravity-wave dynamics.

ACKNOWLEDGEMENTS

This work was supported by Air Force Office of Scientific Research (AFSC) under Grant AFOSR-82-0125. The preparation of this manuscript was expeditiously completed by the staff at CIRES.

REFERENCES

Balsley, B. B., W. L. Ecklund, and D. C. Fritts (1983), VHF echoes from the high-latitude mesosphere and lower thermosphere: Observations and interpretations, J. Atmo. Sci., 40, 2452-2466.

Fritts, D. C. (1984), Gravity wave saturation in the middle atmosphere: A review of theory and observations, Rev. Geophys. Space Phys., 22, 275-308.

Fritts, D. C. (1985), A numerical study of gravity wave saturation: Nonlinear and multiple-wave effects, J. Atmo. Sci., in press.

Fritts, D. C., and P. K. Rastogi (1985), Convective and dynamical instabilities due to gravity wave motions in the lower and middle atmosphere: Theory and observations, Radio Sci., 20, 1247-1278.

Hodges, R. R., Jr. (1967), Generation of turbulence in the upper atmosphere by internal gravity waves, J. Geophys. Res., 72, 3455-3458.

Philbrick, C. R., D. P. Sipler, B. B. Balsley, and J. C. Ulwick (1984), The STATE experiment - Mesospheric dynamics, in Adv. in Space Research, 4, 6, 129-132.

3.2.4 OBSERVATIONS OF THUNDER WITH THE ARECIBO VHF RADAR

D. N. Holden and M. F. Larsen

Department of Physics and Astronomy
Clemson University
Clemson, SC 29634-1911

ABSTRACT

An experiment was carried out at the Arecibo Observatory in Puerto Rico in August 1985 to study Doppler velocities in a thunderstorm environment with a beam pointed 2.5° off-vertical. We have detected two types of echoes associated with lightning. The first is associated with scattering from the lightning channel itself and has characteristics similar to those observed previously with meteorological radars. The second appears to be due to scattering from the turbulence organized by phase fronts of an acoustic wave generated by lightning. The observation described here is consistent with a wave traveling at a velocity near the speed of sound and having a vertical phase velocity component of 40 m/s.

INTRODUCTION

A number of investigators, including LIGDA (1950), ATLAS (1958), HOLMES et al. (1980) and MAZUR et al. (1984), have observed transient echoes associated with lightning at shorter wavelengths typical of meteorological radars (e.g., S band). These transient echoes are generally attributed to scattering from the plasma in the lightning channel itself, as described by DAWSON (1972). The plasma is expected to move with the surrounding air, and, indeed, the transient echoes at S band (MAZUR et al., 1984) and our observations at UHF have mean Doppler shifts typical of the air motions inside a cloud and the spectral widths are in agreement with the broadening expected due to the effects of atmospheric turbulence.

ROTTGER (1981), GAGE et al. (1978), and FUKAO et al. (1985) have already shown that both the precipitation echoes and the "clear air" echoes due to scattering by turbulent variations in the refractive index can be detected at wavelengths near 6 m. The relative contributions of the two scattering mechanisms depend on the radar wavelength, the intensity of the turbulence, and the intensity of the precipitation, but usually it is not difficult to separate the effects since the precipitation and air motions will be different, except for the smallest droplets.

There have been very few observations of Doppler velocities in a thunderstorm environment at wavelengths longer than a few tens of centimeters. Exceptions include the experiments of LARSEN et al. (1982) at UHF and those of ROTTGER (1981), GAGE et al. (1978), and FUKAO et al. (1985) at VHF. In most of the experiments, the coherent integration has been sufficiently long to exclude the observation of effects on a time scale comparable to the scale of lightning or acoustic waves. In August 1985, we carried out an experiment with the new VHF radar located at the Arecibo Observatory in Puerto Rico in which the raw pulse-to-pulse data were recorded for later analysis. The observations show what we believe is the first detection of acoustic waves generated by lightning.

DESCRIPTION OF THE DATA

The VHF radar with a frequency of 46.8 MHz and UHF radar with a frequency of 430 MHz were operated on five separate afternoons in August 1985. We will focus on the VHF radar data for the afternoons of August 4th and August 7th.

The VHF transmitter operates at 50 kW peak power. The system uses the 300-m diameter dish, of which the Yagi feed at the focus illuminates 200 m for an effective beamwidth of less than 2°. The beam was pointed at 2.5° zenith angle in this experiment and operated in one of two data-taking modes. The first used a 1-μsec pulse length and coherent integration online to give an effective sampling time of 92 msec. The second mode used a 2-μsec pulse length and an interpulse period of 750 μsec. The raw data were then recorded on magnetic tape in this mode, so that the IPP and sampling interval were the same, or we could coherently integrate off line to produce a smaller Nyquist frequency if desired.

An electric field change meter and two tipping-bucket rain gauges were also installed at the site and operated in conjunction with the radar measurements. The field change meter was used to determine the time of occurrence of lightning, as well as a qualitative estimate of the distance of the discharge from the radar.

DOPPLER SPECTRA

Figure 1 shows an example of Doppler spectra over a range of heights obtained with Mode I when a thunderstorm was overhead. The heights in range gates 48 through 81 show a contribution primarily from the "clear air" scatter. These spectra are wider than the spectra observed in a nonconvective environment. The upper heights, e.g., gates 82 to 95, show spectra that are broadened to such an extent that it is difficult to discern a peak. The power profile at the right of Figure 1 shows that these heights are characterized by high rather than low power levels.

The maximum unambiguous velocity using Mode I was ± 8.7 m/s. The lightning-associated spectra have widths which are of the order of the spectral window since the power is essentially constant across the window. A possible explanation is that the mean Doppler velocity is much greater than the maximum resolvable velocity. We expect that the spectral width would scale in some way with the mean velocity and would account for these observations. Although a large velocity would cause aliasing, the aliasing itself would not account for the increase in the width of the spectra. We infer that lightning was present in the beam when only some of the range gates show the broad spectra, as in Figure 1.

An example of the spectra obtained using Mode II is shown in Figure 2. The increased time resolution made it possible to attain much larger unambiguous velocity determinations. We found no evidence of lightning in the beam on the days when data were taken with Mode II. However, the electric field change data did show evidence of more distant lightning discharges. Figure 2 shows such spectra recorded at the same time as a more distant discharge. Of particular interest are the features with velocities near ± 30 m/s in gates 19 to 23 which appear only for the time required to produce the spectra (less than 4 sec). The change in sign of the vertical Doppler shift between gates 20 and 21 could be attributable to vertical phase variation in the wave or to the geometrical relation between the observing angle of the radar and the location of the source, as we will show in the next section.

INTERPRETATION OF MEASURED VELOCITIES

The signals measured at VHF will have a component due to the scattering from the lightning channel itself, a component due to the backscatter from refractive index variations, and a component due to the scatter from liquid or frozen droplets. The first does not appear to affect the observations on August 4th, based both on the characteristics of the spectra and the electric field change records which did not indicate any lightning nearby. It is

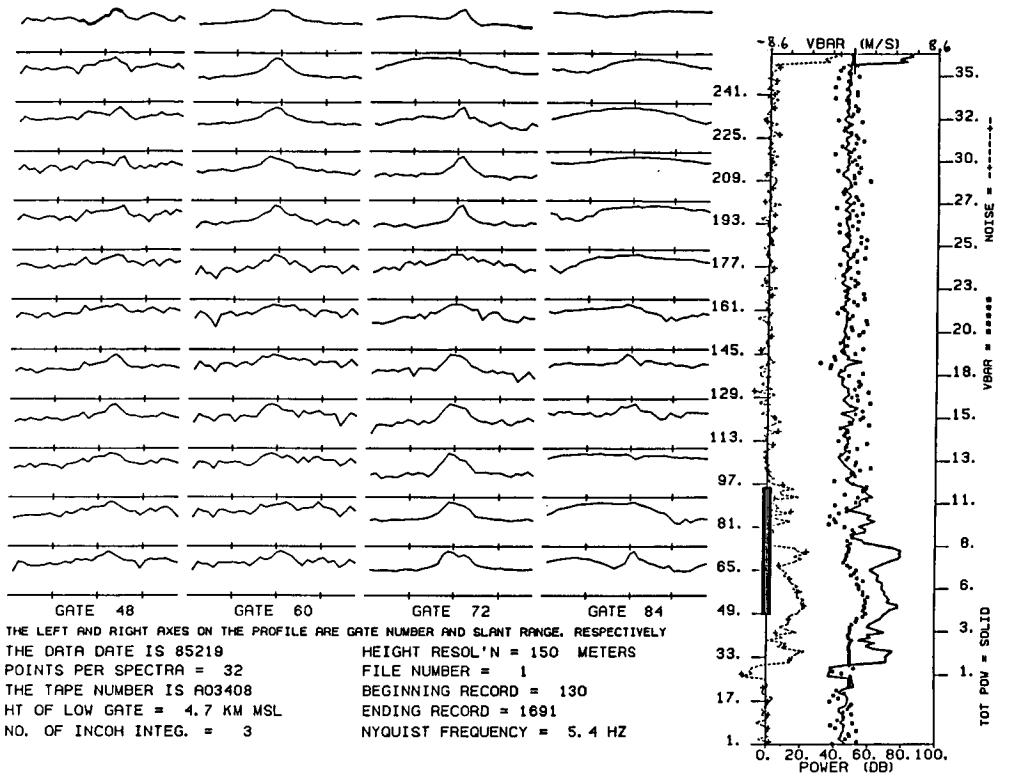

Figure 1. VHF Doppler spectra integrated for nine seconds, with spectra plotted for gates 44 through 91 and a height profile of mean velocity, total power, and noise level for 256 gates. Positive Doppler velocity (toward the radar) is to the right of center, each spectra is scaled to its own peak. Note the large variance in the upper gates (above 90) as compared with the lower ones.

unreasonable to expect that either solid or liquid precipitation will travel at velocities close to 40 m/s since terminal velocities, even for hail, are less than 20 m/s (PRUPPACHER and KLETT, 1980) and would be only downward directed; further, no precipitation was recorded by the rain gauges.

Vertical motions of 40 m/s inside the cloud cannot be excluded absolutely but appear unlikely. It would be easier to explain the observed velocities as being due to the vertical projection of a near-horizontal acoustic phase velocity. However, it cannot be that we are scattering from 3-m acoustic waves, because in that case only waves propagating parallel to the radar beam contribute to the backscatter. Also, a wavelength of 3 m is not consistent with the wave properties derived below. A possible explanation is that 3-m irregularities are acting as a tracer of the motion of the acoustic front.

The observations can be interpreted in terms of the dispersion relation for acoustic-gravity waves (YEH and LIU, 1974).

$$k_h^2 \, (1 - \omega_b^2/\omega) + k_z^2 = k_o^2 \, (1 - \omega_a^2/\omega^2).$$

The behavior will be complicated by the background temperature gradients and

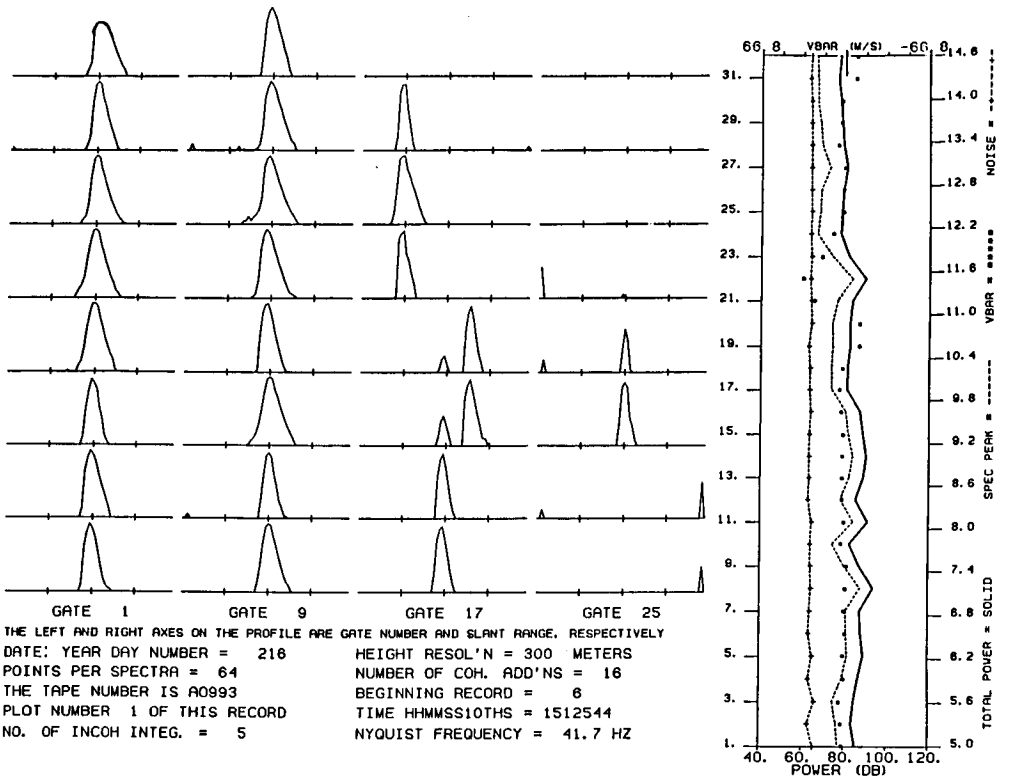

Figure 2. VHF Doppler spectra taken in mode II (see text). Note the large Doppler shift in gates 19 through 23. The spectra are integrated for 3.8 seconds, the anomalous echoes did not appear in the previous spectra nor in the next. The time of these spectra is coincident with a lightning discharge as indicated by an electric field change meter.

other effects not accounted for in this simple form of the dispersion relation. Here, $k_o = \omega/c_o$, $\omega_a = c_o/2H$ is the acoustic cut-off frequency, and ω_b is the Brunt-Vaisala frequency. The local speed of sound is c_o, the scale height is H, and k_h and k_z are the horizontal and vertical wave number components, respectively. The background parameters were calculated from the San Juan radiosonde data closest to the time of the observations.

We can only look at the behavior of the wave solutions in certain limits since we do not know the horizontal wave number. The first limit corresponds to a horizontal wave number that is much smaller than the vertical wave number which we calculate from the power profile to be $k_z = 2\pi/2400$ m. The solution for the wave period then gives a value of $\tau = 7.9$ s, which is on the acoustic branch of the dispersion relation. The total phase velocity is close to the speed of sound as determined from the sounding and has a large horizontal component.

If we assume that the horizontal and vertical wave numbers are comparable in magnitude, one solution corresponds to a period of 7.3 min which is in the gravity regime, the other solution corresponds to a period of 5.6 s which is also on the acoustic branch. However, the phase velocity of the gravity wave is much less than the observed velocity, and the observation could only be

explained if the mean air motion over the pulse volume was of the order of 30-40 m/s.

A point source at some distance laterally will produce an acoustic wave that is propagating more or less horizontally above the vertically pointing radar. A wave traveling at the speed of sound (∿300 m/s) can produce a vertical component of the phase velocity of ∿30-40 m/s if it enters the pulse volume at a large zenith angle, say 85°. Also, there would be upward and downward velocity components above and below the height corresponding to the height of the source. Figure 3 shows the geometry of a single source, displaced horizontally 6 km and downward 0.2 km. The downward displacement accounts for the larger upward velocities observed in the upper range gates. The temperature profile to the right indicates an inversion at an altitude of around 11 km. The inversion may have provided some ducting of the acoustic wave which would explain the appearance of the anomalous echoes in only a few gates.

CONCLUSION

Experiments carried out with the 46.8-MHz Arecibo radar during August 1985, have shown that there is a component in backscattered signals produced in connection with lightning events that are not observed at shorter wavelengths, e.g., S band. There are many unknowns in the analysis of these new echoes, as detailed above, but is plausible that the echoes are due to scattering from refractive index variations associated with acoustic waves generated by

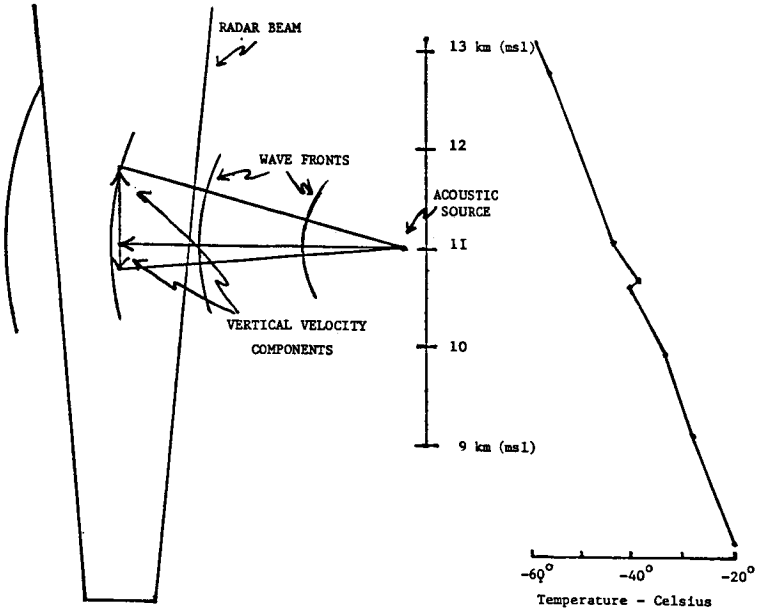

Figure 3. Schematic representation of lightning produced acoustic wave as measured by vertically pointing VHF Doppler radar. The distance from the source is estimated to be 6 kilometers, horizontally, where the angles have been enlarged for the sake of clarity. The temperature profile on the right is taken from the San Juan radiosonde. Note the inversion that occurs at approximately 11 km msl.

lightning. The data taken when lightning was some distance from the radar shows a pattern of positive and negative velocities with amplitudes on the order of 20-40 m/s. The observations can be explained if the velocity is the line-of-sight component of the acoustic phase velocity traced by 3-m irregularities and the source was some 6 km away. The data taken when lightning is in the beam are more difficult to interpret, partly because in that particular data-taking mode, a smaller value for the maximum unambiguous velocity resulted in aliasing of the Doppler spectra. We cannot rule out that acoustic waves were responsible for these echoes, as well.

REFERENCES

Atlas, D. (1958), Radar lightning echoes and atmospherics in vertical cross-section, in Recent Advances in Atmospheric Electricity, edited by L. G. Smith, 441-459, Pergamon, New York.

Dawson, G. A. (1972), Radar as a diagnostic tool for lightning, J. Geophys. Res., 77, 4518-4527.

Fukao, S., K. Wakasugi, T. Sato, S. Morimoto, T. Tsuda, I. Hirota, I. Kimura, and S. Kato (1985), Direct measurement of air and precipitation particle motion by VHF Doppler radar, June, 1985 issue of Nature.

Gage, K. S., J. L. Green, and T. E. VanZandt (1978), Application of the VHF pulsed Doppler radar to cloud physics research, Preprint volume, Conf. on Cloud Physics and Atmospheric Electricity, July 31 - August 4, 1978, Issaquah, Wash., Am. Meteorol. Soc., Boston, MA, 394-401.

Holmes, C. R., E. W. Szymanski, S. J. Szynmanski, and C. B. Moore (1980), Radar and acoustic study of lightning, J. Geophys. Res., 85, 7517-7532.

Larsen, M. F., W. E. Swartz, and R. F. Woodman (1982), Gravity-wave generation by thunderstorms observed with a vertically-pointing 430 MHz radar, Geophys. Res. Lett., 9, 571-574.

Ligda, M. G. H. (1950), Lightning detection by radar, Bull. Am. Meteorol. Soc., 31, 279-283.

Mazur, V., D. S. Zrnic, and W. D. Rust (1984), Lightning and precipitation velocity determined with a vertically looking radar, Preprints, 22nd Conf. on Radar Meteorology, Sept. 10-13, Zurich Switzerland.

Pruppacher, H. R., and J. D. Klett (1980), Microphysics of Clouds and Precipitation, D. Riedel Publishing Co.

Rottger, J. (1981), Development of refractivity structures during anticlyclonic weather conditions, Preprint volume, Nineteenth Conf. on Radar Meteorology, April 15-18, 1980, Miami, FL, Am. Meteorol. Soc., Boston, MA, 593-598.

Yeh, K. C., and C. H. Liu (1974), Acoustic-gravity waves in the upper atmosphere, Rev. Geophys. Space Phys., 12, 193-216.

3.2.5 THE PROUST RADAR: FIRST RESULTS

F. Bertin, A. Cremieu, M. Glass, M. Massebeuf, and M. Petitdidier

CNET/CRPE
4 Av. de Neptune
94107 St Maur des Fosses, France

Two campaigns took place in 1984 with the PROUST Radar operating in a bistatic mode, the transmitting antenna pointing at the vertical and the receiving one, 1° off the vertical axis. The antenna beam intersection covers an altitude range between 3 and 9 km. A complete description of the radar characteristics can be found in BERTIN et al. (1986). The first of these campaigns are analysed here.

1. LEE WAVES OBSERVATION DURING AN "AUTAN WIND" SITUATION.

The "Autan" wind is a strong southeasterly wind observed in the southwest of France, generated by a typical synoptic situation: high pressure over Scandinavia associated with low pressure over Spain. Radiosonde measurements yield a horizontal wind contribution of at most 0.2 m/s along the radar line-of-sight. The dashed line in Figure 1b gives the observed vertical wind profile, and the vertical line, the estimated horizontal wind contribution. The observed wind can be regarded as mainly due to the vertical component. Over the whole range of observed altitude, a downward wind is detected with an amplitude that decreases from 1.2 m/s (at 3 km) to 0.25 m/s (at 7.2 km). The horizontal bars give the error on the vertical wind, inferred from the Doppler shift estimation. This profile shape might be interpreted as due to the interaction between "Autan" wind and "Massif Central" topography. In order to test this assumption, the lee wave model of QUENEY (1948) is used (Figure 1a). This model gives a downward vertical wind above St Santin up to 7 km. For comparison, this theoretical wind profile is also plotted in Figure 1b. A good agreement is found between observation and theory, the systematic difference between the two profiles being probably due to the horizontal wind contribution.

2. OBSERVATION OF WAVE - TURBULENCE INTERACTION IN A STORMY WARM FRONT

On June 6th, 1984, a stormy warm front was crossing over St Santin. The echo power profiles associated with this front show an intense turbulence observed both on the refractive index (signal-to-noise ratio) and on the vertical wind fluctuations (spectral broadening). Figure 2 shows the spatio-temporal evolution of the radar echo intensity and Doppler shift in the altitude range 3-10 km. In each gate, the echo power (S/N ratio expressed in dB) is scaled according to a dashed code. The Doppler shift is scaled in m/s on the vertical axis, while the local time is scaled in hours on the horizontal axis. The contribution of the horizontal wind is, in this experiment, never greater than 0.1 m/s. The mean value of the Doppler shift gives evidence of a global upward wind of about 1 m/s during the front crossing. Associated with this global upward movement, a very active turbulence gives rise to the observed radar echoes.

2.1 Estimation of the energy dissipation rate. For the strongest echoes (occurring in gates n° 6 and 7), a spectral broadening of about 0.5 m/s is observed. It is noteworthy that the spectral broadening due to the deformations introduced by the antenna beam geometry (and detailed in SPIZZICHINO, 1975) is estimated to be never greater than 0.1 m/s. In these conditions, the observed spectral widths give an estimation of the rms value of the turbulent wind fluctuations w' along the vertical. The energy dissipation rate ε can be easily inferred from w' by using the following expression

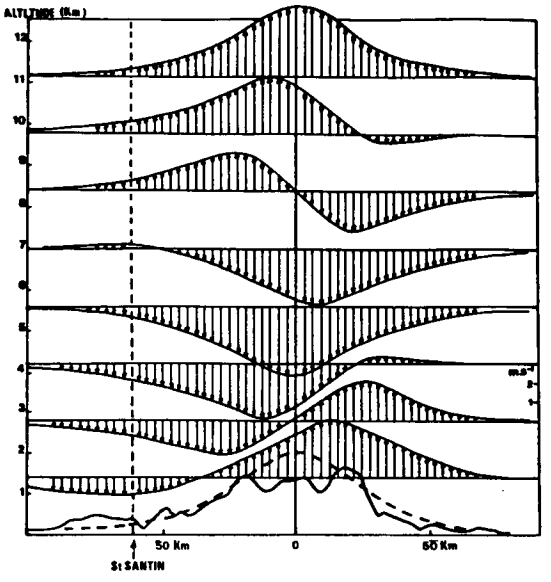

Figure 1a. Vertical velocity field and streamlines over the "Massif Central", modelised by a symetrical shape.

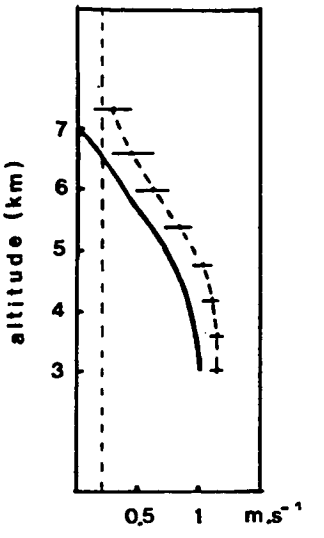

Figure 1b. Vertical wind profile (observed and theoretical).

proposed by WEINSTOCK (1981).

$$\varepsilon = 0.4\ \overline{w'^2}\,\omega_B \qquad (1)$$

where ω_B is the Brunt-Vaisala frequency.

Figure 3 shows the Brunt-Vaisala period (BVP) profile, obtained from radiosonde data. Finally, relation (1) yields an energy dissipation rate value in the range

$$1.10^{-3} < \varepsilon < 2.10^{-3}\ m^2 s^{-3}$$

for the strongest echoes observed in gate n°7. This is a typical value for a very active turbulence (LILLY et al., 1974).

2.2 Waves and turbulence. Besides the global upward movement of the air along the front, oscillations are observed in the vertical wind intensity, period and amplitude of which vary versus altitude. In gates n°8 to 10, oscillations with a range period of 8-9 minutes are clearly observed, while a 3-minute period appears in gates n°6 and 7 just after the strong intensification of the turbulent activity mentioned above. Comparison between these periods and the BVP profile plotted in Figure 3 exhibits a striking agreement. This observation is consistent with theoretical studies on gravity waves generated by turbulence in stratified fluids. WEINSTOCK (1978, 1981) has shown that, in a stratified atmosphere, the time evolution of the vertical velocity spectrum implies the emission of gravity waves, generated by the vertical motion of the air particles, with a frequency ω_K given by:

$$\omega_K = \omega_B \frac{K_H}{K} \qquad (2)$$

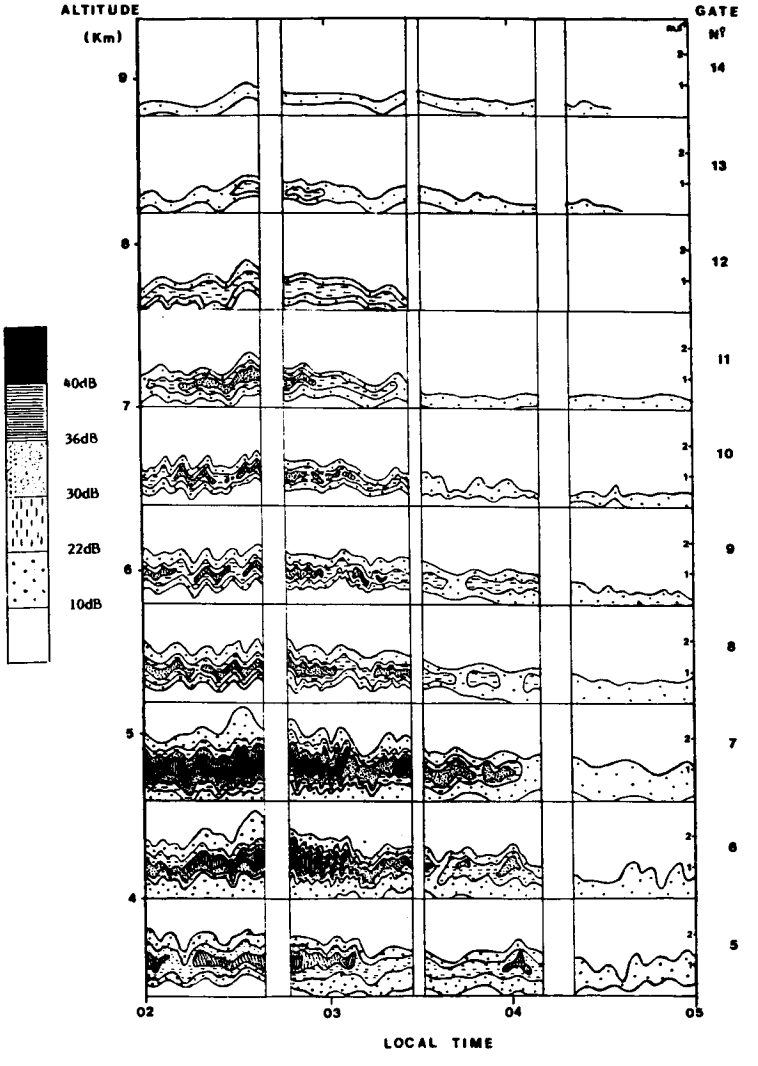

Figure 2. Spatio-temporal evolution of the radar echo power on June 6, 1984.

where K is the wave number and K_H its horizontal component. The good correlation between BV and observed frequency seems to indicate that the wave propagation is mainly horizontal. These propagation characteristics are also found by METAIS (1984) with a numerical model.

CONCLUSION

The first results analysed above show the capability of the PROUST Radar to measure the turbulent parameters and study the turbulence-wave interaction. In its present configuration (bistatic mode and 600 m vertical resolution), it has been necessary to make some assumptions that are known not to be truly fulfilled: homogeneous turbulence and constant vertical wind intensity over a 600-m thickness. It is clear that a more detailed study of the interaction

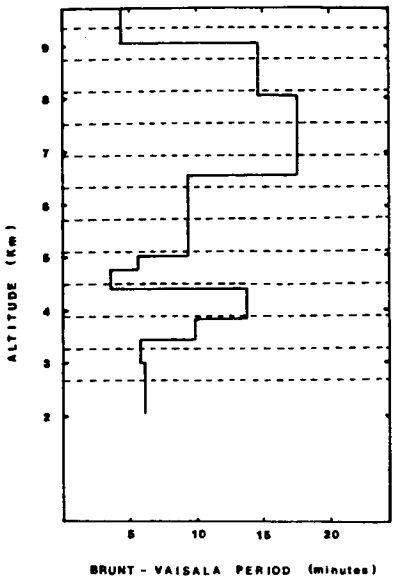

Figure 3.

between wave and turbulence will be possible with the next version of PROUST Radar (30-m altitude resolution and monostatic mode) that will soon be achieved.

REFERENCES

Bertin, F., M. Glass, R. Ney, and M. Petitdidier (1986), The PROUST Radar, this volume.

Lilly, D. K., D. E. Waco, and S. I. Adelfang (1974), Stratospheric mixing estimated from high-altitude turbulence measurements, J. Appl. Meteorol., 13, 488-493.

Metais, O. (1985), Direct numerical simulation of stratified turbulence, 5th Symp. on Turb. Shear Flows.

Queney, P. (1975), The problem of airflow over a mountains: a summary of theoretical studies, Bull. Am. Meteorol. Soc., 29, 16-26.

Spizzichino, A. (1975), Spectral broadening of acoustic and radio waves scattered by atmospheric turbulence in the case of radar and sodar experiments, Ann. Geophys., 31, 433-445.

Weinstock, J. (1978), On the theory of turbulence in the buoyancy subrange of stratified flows, J. Atmos. Sci. 35, 635-659.

Weinstock, J. (1981), Vertical turbulence diffusivity for weak or strong stable stratification, J. Geophys. Res., 86, 9925-9928.

3.2.6 SIMULTANEOUS FINE STRUCTURE OBSERVATION OF WIND AND TEMPERATURE PROFILES BY THE ARECIBO 430-MHz RADAR AND IN SITU MEASUREMENTS

D. Thomas[1], F. Bertin[1], M. Petitdidier[1]
H. Teitelbaum[2], and R. F. Woodman[3]

[1]CNET/CRPE 4 AV. de Neptune 94107 St. Maur des Fosses, France
[2]LMD Ecole Polytechnique, 91128 Palaiseau, France
[3]Instituto Geofisico del Peru, Apartado 3747, Lima 100, Peru

INTRODUCTION

The study of the interaction between waves and turbulence in the troposphere and lower stratosphere requires continuous fine structure observation of both wind and temperature profiles. The radar technics (ST radars) allow a continuous observation of wind profiles with a vertical resolution of at least 150 m, while balloon-borne measurements of temperature and wind are potentially able to provide a spatial resolution as short as 0.1 m along the balloon trajectory. The use of balloon-borne technics, concurrently with radar observations, is necessary to understand the generation mechanisms of turbulence and to improve our knowledge about the radar measurement physics FRITTS et al., 1984; THOMAS et al., 1985).

EXPERIMENT

A simultaneous campaign of balloon and radar measurements took place on March 14-16th, 1984, above the Arecibo 430-MHz radar. This radar was operating with a vertical resolution of 150 m following two antenna beam directions: 15° from the zenith, respectively, in the N-S and E-W directions (WOODMAN, 1980). The balloons (5-m diameter) were equipped with sonic anemometers (accuracy of 0.05 m/s) and temperature sensors (accuracy of 0.1 K). The vertical velocity of the balloons was of about 4 m/s. One of the three balloons, launched during this campaign, flew only 3 km apart the radar beam in the altitude range 14-15 km (Figure 1).

RESULTS

We analyse here the main results concerning the comparison between the flight and simultaneous radar measurements obtained on March 15, 1984.

1) The radar return power profile (S/N ratio in dB) exhibits maxima which are generally well correlated with step-like structures in the potential temperature profile (Figure 2). These structures are generally considered as the consequence of the mixing processes induced by the turbulence.

2) A good correlation appears in the altitude range 12.5 - 19 km between wind shears induced by a wave structure observed in the meridional wind and the radar echo power maxima. This wave structure is characterized by a vertical wavelength of about 2.5 km, and a period in the range 30-40 hours. These characteristics are deduced from the twice daily rawinsonde data launched from the San Juan Airport by the National Weather Service (ROE, 1981).

CONCLUSION

These results have pointed out an example of the interaction between wave and turbulence in the upper troposphere and lower stratosphere. Turbulent layers are observed at locations where wind shears related to an internal inertia-gravity wave are maxima. Wind and turbulence radar measurements will allow to obtain the temporal variation of this interaction and to estimate the amount of kinetic energy dissipated by this wave. A comparison between the

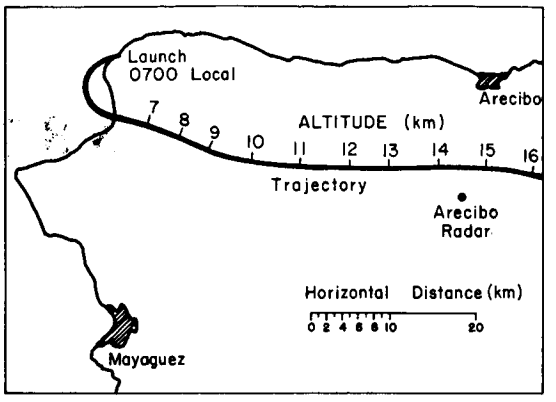

Figure 1. Balloon trajectory.

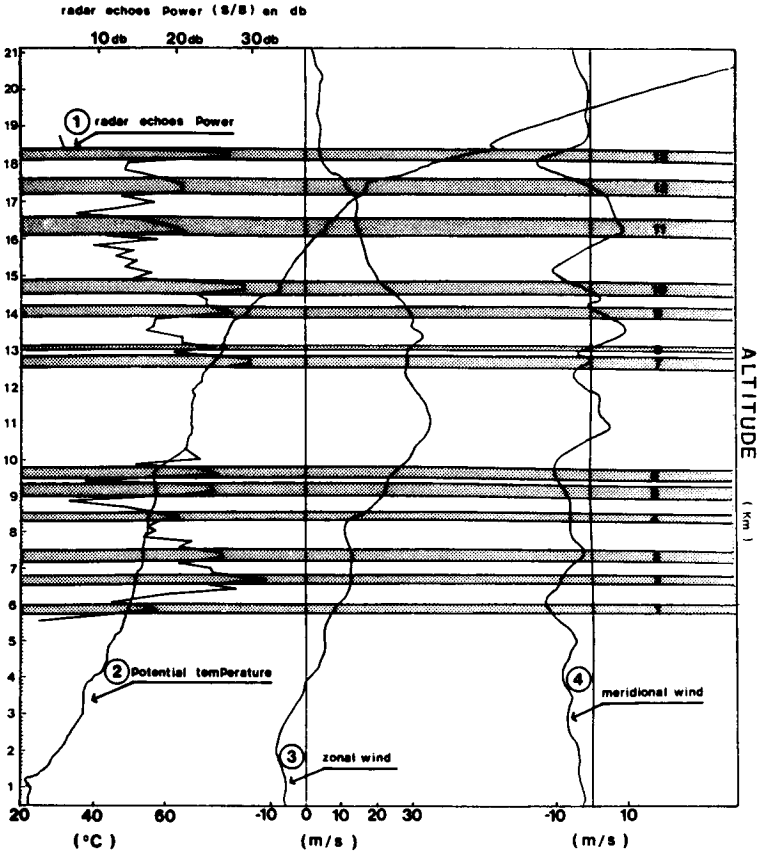

Figure 2. Radar echo power (1) ; Potential temperature profile deduced from balloon experiment (2) ; Zonal wind (3) and meridional wind (4) profiles measured with the Arecibo radar. Dotted area, numbered from 1 to 13, correspond to maximum echo power and are interpreted in terms of turbulent layers.

energy dissipation rate deduced from the velocity variance and the spectral width of the radar echoes is now in progress.

ACKNOWLEDGMENTS

We are grateful to H. Ovarlez and H. Cabritta from Laboratoire de Meteorologie Dynamique (France) who built the balloon payloads and took care of the launching and data acquisition in Puerto Rico. The Arecibo Observatory is part of the National Astronomy and Ionosphere Center, which is operated by Cornell University under contract with the National Science Foundation. The Weather Service Forecast Office (Isla Verde International Airport, San Juan, Puerto Rico) provided us rawinsonde data.

REFERENCES

Fritts, D. C., M. A. Geller, B. B. Balsley, M. L. Chanin, I. Hirota, J. R. Holton, S. Kato, R. S. Lindzen, M. R. Schoeberl, R. A. Vincent, and R. F. Woodman (1984), Research status and recommendations from the Alaska Workshop on gravity waves and turbulence in the middle atmosphere, Bull. Am. Meteorol. Soc., 65, 149.

Roe, J. M. (1981), Climatology of wind at San Juan, Informal report to the Arecibo Observatory.

Thomas, D., F. Bertin, M. Petitdidier, H. Teitelbaum, R. F. Woodman (1985), Simultaneous fine structure observation of wind and temperature profiles by the Arecibo 430 MHz radar and in situ measurements, Proceedings of the 7th ESA symposium on European Rocket and Balloon Programmes.

Woodman, R. F. (1980), Height altitude resolution stratospheric measurements with the Arecibo 430-MHz radar, Radio Sci., 15, 417.

3.2.7 COMPARISON BETWEEN S.T. RADAR AND IN SITU BALLOON MEASUREMENTS

F. Dalaudier[1], J. Barat[1], F. Bertin[2], E. Brun[3], M. Crochet[3], and F. Cuq[3]

[1]Service d'Aeronomie du CNRS, BP3-91370 Verrieres-le Buisson, France
[2]CNET/CRPE 4 Avenue de Neptune 94107, St Maur des Fosses, France
[3]LSEET UA 705, Universite de Toulon, France

A campaign for simultaneous in situ and remote observation of both troposphere and stratosphere took place near Aire-sur-l'Adour (in southeastern France) on May 4, 1984. The aim of this campaign was a better understanding of the physics of radar echoes. The backscattered signal obtained with an ST radar both at the vertical and 15° off vertical is compared with the velocity and temperature measurements made in the same region (about 10 km north of the radar site) by balloon-borne ionic anemometers and temperature sensors.

Radar Description	Balloon Characteristics
Frequency: 47.8 MHz (λ = 6.3 m)	Diameter: 20 m
Antenna: coaxial collinear, 2560 m^2	Ascending velocity: 3 to 5 m/s
Beamwidth: 8.8°	Ionic anemometer, accuracy: 0.02 m/s
Range resolutions: 300, 750, 2400 m	Temperature sensor, accuracy: 0.01 K
Duty cycle: 0.5 to 1%	Balloon trajectory: given in Figure 1

The detailed analysis of the results obtained is not yet achieved. We present here some preliminary results.

1. RADAR RESULTS

Typical examples of radar power return are given in Figure 2, in oblique (Figure 2a) and vertical (Figure 2b) directions. The vertical line at -10 dB corresponds to the limit of detectability. The signal-to-noise ratio is 5 to 10 dB stronger in the vertical than in the oblique direction. An enhancement of the radar power return is observed in the lower stratosphere both in oblique and vertical directions, but in the latter direction, the enhancement is affected by a temporal variability.

2. BALLOON RESULTS

A comparison between velocity and temperature variance profiles is given in Figure 3 and suggests the following comments:

- As a general rule, the velocity variance is much smaller in the stratosphere than in the troposphere because of the hydrostatic stability in the former. On the other hand, temperature variance is far greater in the stratosphere than in the troposphere. This is the consequence of the atmospheric stratification.
- Six turbulent layers (labelled from 1 to 6 in Figure 3) are clearly observed both in velocity and temperature profiles.
- In the stratosphere, maxima in temperature variance are not always associated with maxima in velocity variance. In these regions, the temperature fluctuations are not compatible with the classical turbulence theory, although they contribute to the radar power return.

The temperature gradient profile obtained from the balloon-borne temperature sensors (Figure 4a) exhibits a rather complex structure in the stratosphere: very strong gradients may arise in very thin layers (few meters width). The horizontal extent of these thin layers is not known but, as a general rule, it is observed (Figure 4b) that in regions where the mean

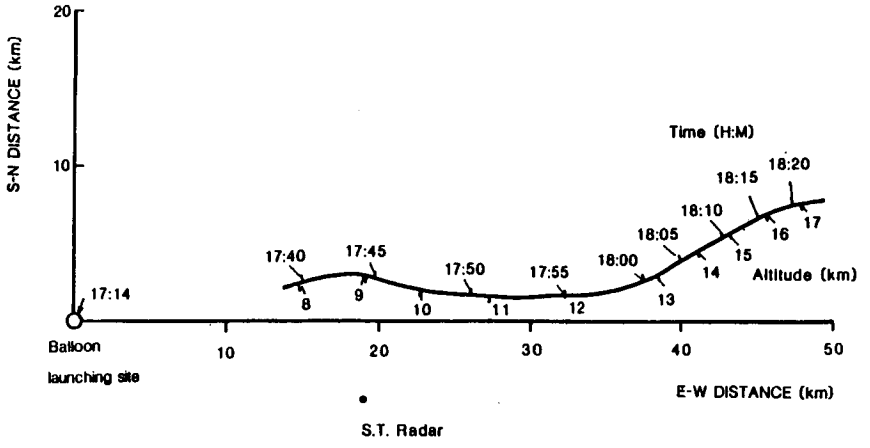

Figure 1. Balloon trajectory.

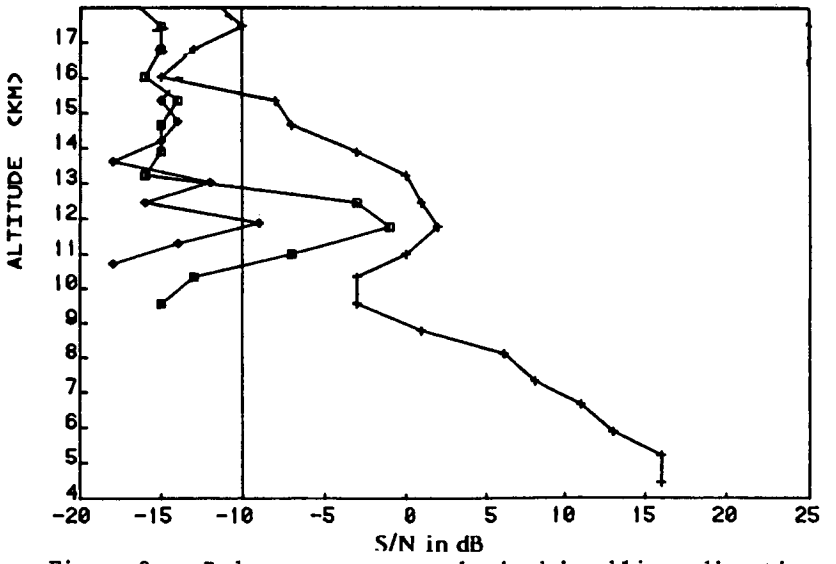

Figure 2a. Radar power return obtained in oblique direction for three range resolution: 2400 m (++), 750 m (□□), and 300 m (◆).

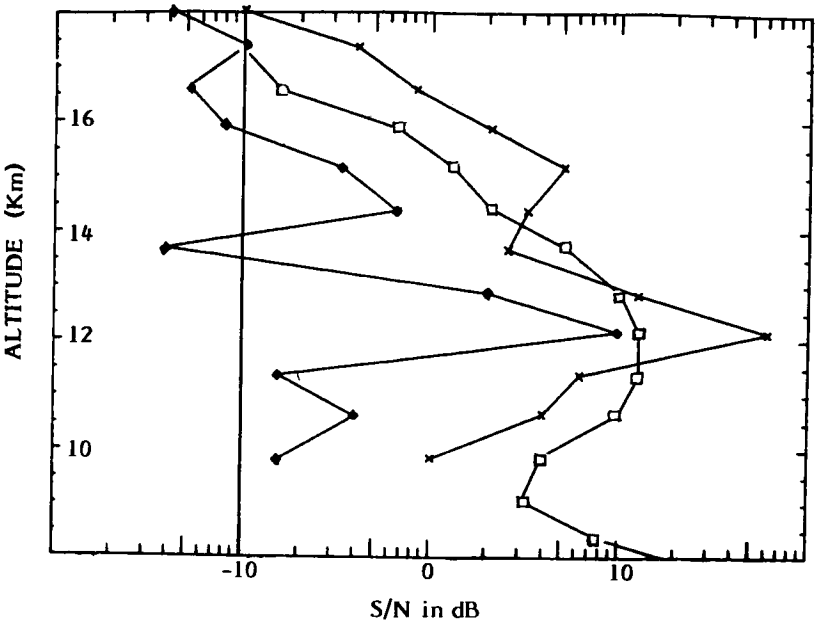

Figure 2b. Radar power return obtained at the vertical for three range resolutions: 2400 m (□□), 750 m (××), and 300 m (◆).

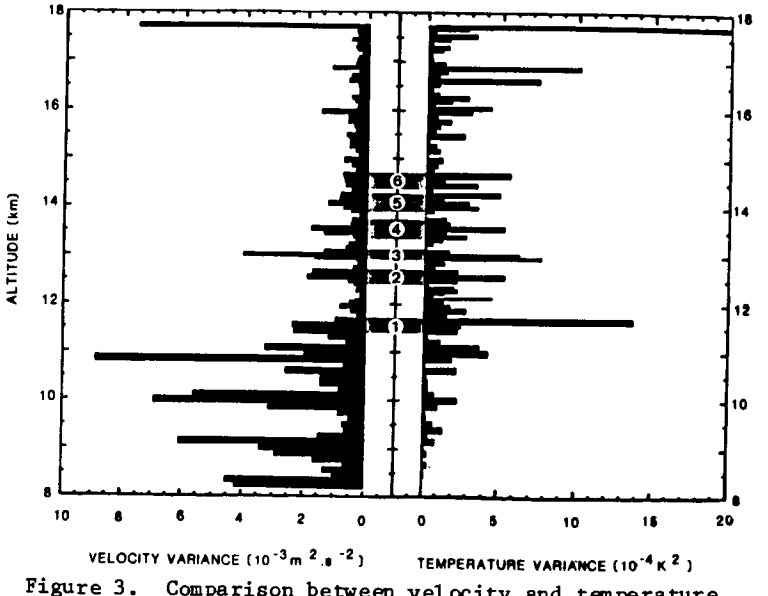

Figure 3. Comparison between velocity and temperature variances. Six turbulent layers are observed.

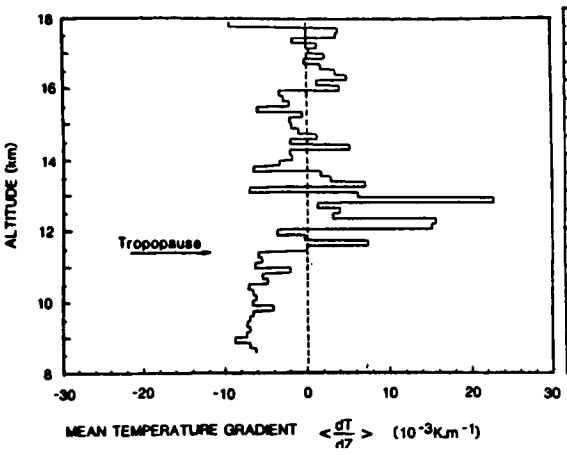

Figure 4a. Mean temperature gradient (over 150 m) profile.

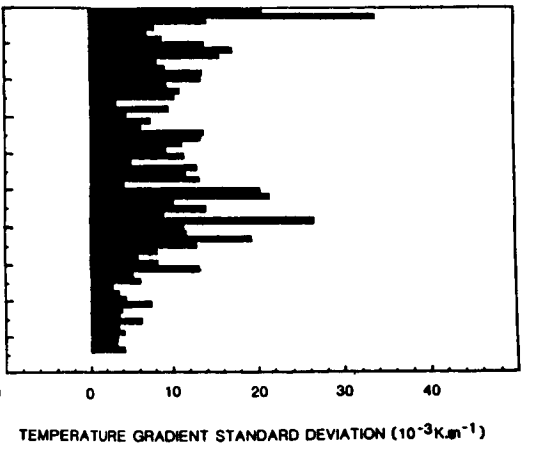

Figure 4b. Temperature gradient standard deviation (over 150 m).

gradient (over 150 m) is highly positive, the standard deviation of the local gradients is important, its value being of the same order as the mean gradient itself.

3. COMPARISON BETWEEN RADAR BALLOON RESULTS

3.1 Oblique direction. The theoretical radar reflectivity $\eta(k)$ and the C_n^2 parameter have been estimated (under the classical quasi-isotropy assumption) from the temperature fluctuation spectra computed in successive 30-m width layers. The amplitude of the spectra for the value $k_o = 4\pi/\lambda$ gives, after integration through the appropriate radar weighting function, an estimation of (k) and C_n^2. The following expressions (OTTERSTEN 1969) are used:

$$\eta(k) = 5/3\ (\pi/8)\ k_o S_n(k)$$

$$\eta(k) = 0.38\ C_n^2 \lambda^{-1/3}$$

In (1), $S_n(k_o)$ is the normalized one-dimensional spectrum of turbulence, while in equation (2), a k spectrum is assumed.

The $\eta(k)$ profile so obtained is compared in Figure 5 with the radar results. For this comparison, the $\eta(k)$ values calculated from balloon measurements are systematically divided by ten. It can be seen on this figure that radar and balloon $\eta(k)$ profiles exhibit a remarkably similar shape. This good general agreement confirms that the radar echo power is strongly correlated with the amplitude of the temperature fluctuation spectra. However, as shown in Section 2, the assumption used in equations (1) and (2), (isotropy of the turbulent field and spectra in $k^{-5/3}$) for calculating the radar reflectivity, are certainly not always fulfilled. This discrepancy with respect to the classical theory may explain the systematic difference between the η values respectively calculated from radar and balloon-borne measurements.

In fact, the one-dimensional spectrum $S_n(k)$ of temperature fluctuations along the balloon trajectory is an integral in the Fourier space and in a plane perpendicular to the k_o vector. Note that all these contributions are coming

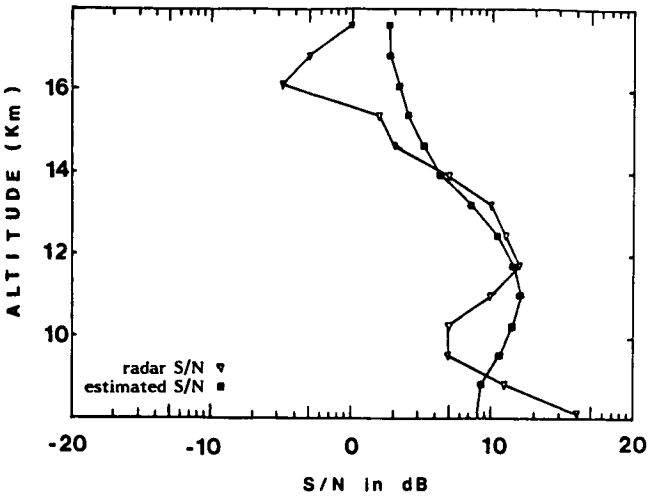

Figure 5. Comparison between oblique power return of the radar and in situ estimation of radar reflectivity from equation 1.

from k vectors greater or equal to k_o. On the other hand, the radar samples the three-dimensional spectrum $\phi(k)$ at the particular mode k_o in the radar radial direction. So, the observed difference between radar and balloon estimation of $\eta(k)$ could be the consequence of the three-dimensional spectrum anisotropy for k values greater than k_o i.e., for wavelength $\lambda < 3$ m. However, this assumed small-scale anisotropy is in contradiction with turbulent fields generally observed that appear to be quasi-isotropic for scales smaller than 10 m (BARAT and BERTIN, 1984). Consequently, the above assumed small-scale anisotropy could be associated with the nonturbulent fine structure of the temperature profiles observed in stratified fluids. This hypothesis is supported by the balloon observation of strong increase of the temperature gradient variance in highly stratified regions (see Figure 4b).

3.2 Vertical direction. The observed radar signal is 5 to 10 dB stronger at the vertical than in the oblique direction but is affected by a greater variability. The intensification of the echo power at the vertical is generally interpreted as the result of a partial reflection on stable layers in the stratosphere. The particular thermal structure of the stratosphere observed in Figure 4a and 4b may explain the two main characteristics of the vertical radar return power profile:

- spatial stability of the enhanced echoes which occur in regions where the mean temperature gradient exhibits maxima
- temporal variability of these enhancements which could be explained by a limited spatial extent of the thin layers where the strongest gradients occur.

An estimation of the radar reflection coefficient (GAGE and BALSLEY, 1980) computed from the temperature gradient profile is given in Figure 6. In this estimation, the contribution of the individual layers have been incoherently added in the radar resolution range. The shape of this profile is in general agreement with the radar vertical profiles of signal-over-noise ratio. This result, obtained with simultaneous measurements, confirms the strong correlation between mean stratification and strengthening of radar vertical echo power already mentioned by GREEN et al. (1980). Moreover, the detailed temperature profile shows that these regions of strong stratification are also regions of highly layered temperature gradient (see Figure 4b), leading to an increase of reflection coefficient in the vertical direction.

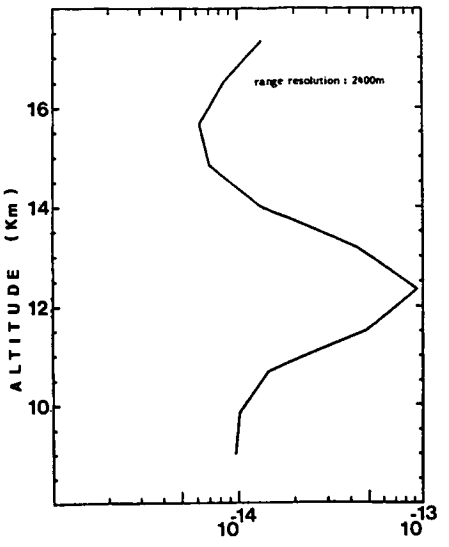

Figure 6. Estimation of the radar vertical reflection coefficient from the temperature gradient profile.

CONCLUSION

In situ measurements clearly indicate that the temperature fluctuations are not always consistent with the standard turbulent theory. Nevertheless, the assumptions generally made (isotropy and turbulent field in k) and the classical formulation so derived for radar reflectivity (equations 1 and 2) are able to reproduce the shape of the radar return power profiles in oblique directions. Another significant result is the confirmation of the role played by the atmospheric stratification in the vertical echo power. It is important to develop these simultaneous in situ and remote experiments for a better description of the dynamical and thermal structure of the atmosphere and for a better understanding of the mechanisms governing clear-air radar reflectivity.

REFERENCES

Barat, J., and F. Bertin (1984), Simultaneous measurements of temperature and velocity fluctuations within clear air turbulence layers: analysis of the estimate of dissipation rate by remote sensing techniques, J. Atmos. Sci., 41, 1613.

Gage, K. S., and B. B. Balsley (1980), On the scattering and reflection mechanisms contributing to clear air echoes from troposphere and stratosphere, Radio Sci., 15, 243.

Green, J. L., and K. S. Gage (1980), Observation of stable layers in the troposphere and stratosphere using VHF radars, Radio Sci. 15, 399.

Ottersten H. (1969), Atmospheric structure and radar backscattering in clear air, Radio Sci. 4, 1179.

3.3.1 A STATISTICAL MODEL TO ESTIMATE REFRACTIVITY TURBULENCE STRUCTURE CONSTANT C_n^2 IN THE FREE ATMOSPHERE

J. M. Warnock and T. E. VanZandt

Aeronomy Laboratory
National Oceanic and Atmospheric Administration
Boulder, Colorado 80303

INTRODUCTION

A computer program has been tested and documented (WARNOCK and VANZANDT, 1985) that estimates mean values of C_n^2 in the stable free atmosphere from standard National Weather Service balloon data or an equivalent data set. The program is based on the statistical model for the occurrence of turbulence developed by VANZANDT et al. (1981). Height profiles of the estimated C_n^2 agree well with profiles measured by the Sunset radar with a height resolution of about 1 km. The program also estimates the energy dissipation rate ε, but because of the lack of suitable observations of ε, the model for ε has not yet been evaluated sufficiently to be used in routine applications.

MODEL

There is considerable evidence that in the free atmosphere there are many thin horizontally stratified turbulent layers embedded in the large-scale laminar flow. They are thought to be due to local dynamic shear instabilities in regions where the large-scale flow itself is stable (BRETHERTON, 1969; ROSENBERG and DEWAN, 1974; WOODMAN, 1980; BARAT, 1982; VANZANDT, 1983; GOSSARD et al., 1984). The value of the Richardson number, Ri, describes the stability of the flow; it is defined as the ratio of the static stability, N^2, to the square of the vector wind shear, S, i.e., $Ri = N^2/S^2$ where N is the Brunt-Vaisala frequency. In most regions Ri is greater than its critical value, which is usually taken to be 1/4, and the flow is dynamically stable.

In the model, we make the following basic assumptions consistent with the above scenario: (1) the fine structure in N^2 and S^2 is horizontally stratified and is superimposed on their large-scale mean vertical profiles. This leads to fine structure in Ri; (2) turbulence occurs where the local small-scale value of $Ri \leq 1/4$, so that thin horizontally stratified turbulent layers are formed. Because the fine structure is not observed directly, we estimate the occurrence of turbulence indirectly by using a statistical approach. We parameterize the fine structure of S^2 and N^2, and therefore, Ri, in terms of the large-scale observable data. Because the fine structure is thought to be due to a spectrum of gravity waves (VANZANDT, 1982), the parameterization equations are consistent with gravity-wave theory. The thickness of these layers is usually a few tens of meters.

COMPARISONS WITH RADAR DATA

Vertical profiles of model C_n^2 have been compared with profiles measured by both radar and optical remote sensors. VANZANDT et al. (1978, 1981) found good agreement between profiles measured by the well-calibrated ST Sunset radar and an earlier version of the model; furthermore, they found that the model correctly tracked rapid changes of C_n^2 measured during the passage of a jet stream over the radar site. GAGE et al. (1978) found satisfactory agreement between an earlier version of the model and profiles measured at four different radar sites operating at UHF and VHF. More recently, GREEN et al. (1984) compared model profiles of C_n^2 measured simultaneously by the Sunset radar and by the double star scintillometer operated by Jean Vernin of the Universite de Nice. Excellent agreement was found between the radar and

model profiles; however, at times the scintillometer measurements were less than both the radar and model values.

In all of the above comparisons the model C_n^2 profile was derived from a single balloon sounding. WARNOCK et al. (1985) conducted an observing campaign during both the winter and summer of 1982; they compared the model and radar measurements of the minimum, median, and maximum of 12 winter profiles and 22 summer profiles. The model profiles agreed well with the data in both magnitude and variability; futhermore, the calculations gave insight into the meteorological conditions responsible for the C_n^2 variability.

REFERENCES

Barat, J. (1982), Some characteristics of clear-air turbulence in the middle stratosphere, J. Atmos. Sci., 39, 2553-2564.

Bretherton, E. P. (1969), Waves and turbulence in stably stratified fluids, Radio Sci., 4, 1279-1287.

Gage, K. S., T. E. VanZandt, and J. L. Green (1978), Vertical profiles of C_n^2 in the free atmosphere: Comparison of model calculations with observations, Proc. 18th Conf. on Radar Meteorology, Atlanta, GA, 80-87.

Gossard, E. E., R. B. Chadwick, T. R. Detman, and J. Gaynor (1984), Capability of surface-based clear-air Doppler radar for monitoring meteorological structure of elevated layers, J. Climatol. Appl. Meteorol., 23, 350-362.

Green, J. L., J. Vernin, T. E. VanZandt, W. L. Clark, and J. M. Warnock (1984), A comparison of optical and radar measurements of C_n^2 height profiles, Preprint Vol., 22nd Conf. on Radar Meteorology, Zurich, Switzerland, Am. Meteorol. Soc., 470-475.

Rosenberg, N. W., and E. M. Dewan (1974), Stratospheric turbulence and vertical effective diffusion coefficients, Proc. Third Conf. on the Climatic Impact Assessment Program, edited by A. J. Broderick and T. M. Hardy, Report No. DOT-TSC-OST-74-15, 91-101.

VanZandt, T. E., J. L. Green, K. S. Gage, and W. L. Clark (1978), Vertical profiles of refractivity turbulence structure constant: Comparison of observations by the Sunset radar with a new model, Radio Sci., 13, 819-829.

VanZandt, T. E., K. S. Gage, and J. M. Warnock (1981), An improved model for the calculation of profiles of C_n^2 and in the free atmosphere from background profiles of wind, temperature, and humidity, Preprint Vol., 20th Conf. on Radar Meteorology, Boston, MA, 129-135.

VanZandt, T. E. (1982), A universal spectrum of buoyancy waves in the atmosphere, Geophys. Res. Lett., 9, 575-578.

VanZandt, T. E. (1983), Existence of a persistent background of turbulence, Handbook for MAP, 9, edited by S. A. Bowhill and B. Edwards, 256-261.

Warnock, J. M., and T. E. VanZandt (1985), A statistical model to estimate refractivity turbulence structure constant C_n^2 in the free atmosphere, NOAA Tech. Memo, NOAA/ERL, Boulder, Colorado.

Warnock, J. M., T. E. VanZandt, and J. L. Green (1985), A statistical model to estimate mean values of parameters of turbulence in the free atmosphere, Preprint Vol., Seventh Symposium on Turbulence and Diffusion, Boulder, CO, Am. Meteorol. Soc., Boston.

Woodman, R. F. (1980), High-altitude resolution stratospheric measurements with the Arecibo 430 MHz radar, Radio Sci., 15, 417-422.

3.3.2 DETERMINATION OF THE BRUNT-VAISALA FREQUENCY FROM VERTICAL VELOCITY SPECTRA

Jurgen Rottger*

Arecibo Observatory
P.O. Box 995
Arecibo, Puerto Rico

Recent work on the spectra of vertical velocity oscillations due to gravity waves in the troposphere, stratosphere and the mesosphere has revealed a typical feature which we call the "Brunt-Vaisala cutoff". Several observers (RASTOGI, 1975; ROTTGER, 1980a,b; ECKLUND et al., 1985) noticed a spectral peak near the Brunt-Vaisala frequency. This peak often is characterized by a very steep slope at the high frequency part, but a fairly shallow slope towards lower frequencies. Some example spectra of stratosphere observations are shown in Figure 1. This distinct spectral shape (most clear at the upper height 22.5 km) can be explained by the fact that the vertical velocity amplitudes of atmospheric gravity waves increase with frequency up to their natural cutoff at the Brunt-Vaisala frequency. ROTTGER and IERKIC (1985) showed that this peak around the 4-6 min period is very definitely due to gravity waves. VANZANDT (1982) suggested that the total spectra of vertical velocity variations is a manifestation of a universal spectrum of gravity waves.

RASTOGI (1975) found that the upper cutoff frequency of his mesospheric observations is consistent with the Brunt-Vaisala frequency deduced from model temperature profiles. ROTTGER (1980 a,b) compared the cutoff directly with the profiles of the Brunt-Vaisala frequency deduced from radiosonde temperature profiles of the troposphere and stratosphere. The spectrum-contour plot of Figure 2 shows a typical example, indicating the consistency of the cutoff with the Brunt-Vaisala frequency.

The observed spectral shape (Figure 1) almost exactly resembles the model spectra (Figure 3, vertical = 0°) of SCHEFFLER and LIU (1985), when one disregards here the low-frequency cutoff at the inertial frequency in the model. It was pointed out by FRITTS (1984) and VANZANDT, LIU and GAGE (personal communications, 1985) that Doppler shifts can substantially distort the spectra. LIU and SCHEFFLER (personal communication, 1985) recently did some model computations and showed that the spectral energy is redistributed through the spectrum due to a Doppler shift. Although Liu and Scheffler used the Boussinesq approximation in their simplified calculations to determine this effect of the Doppler shift, it is reasonably evident that it will also be revealed in the full wave solutions. The Doppler shift is most pronounced for just those waves with frequencies very close to the Brunt-Vaisala frequency.

We assume that the distribution of gravity-wave phase velocities is isotropic in azimuth with respect to the wind velocity (within a suitable observation period). Then about one quarter of the waves are shifted to higher frequencies, one quarter to lower frequencies and two quarters are not very little shifted because their phase velocities are (exact or almost) perpendicular to the wind velocity. The effect is that the spectrum is well smeared out, but the peak at the Brunt-Vaisala frequency still remains unshifted (due to the perpendicular waves) although it becomes less distinguishable from the spread-out background spectrum. Another effect, wave steepening due to amplitude growth of gravity waves can also have an influence on the spectral shape. It was pointed out by WEINSTOCK (1985) that the wave

*On leave from Max-Planck-Institut fur Aeronomie, Katlenburg-Lindau, West Germany.

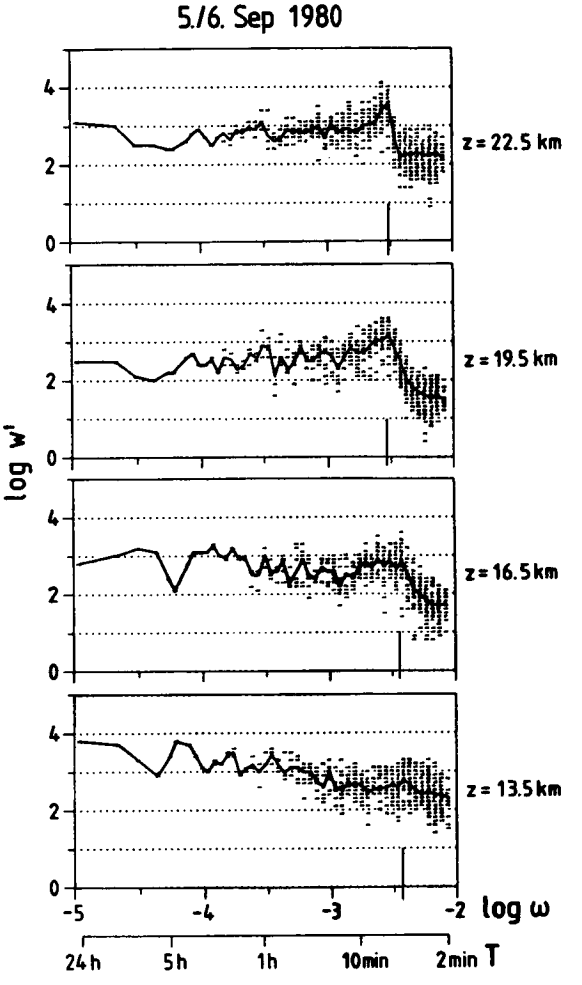

Figure 1. Power spectrum of vertical velocity, measured with the SOUSY VHF Radar (see ROTTGER, 1981, for details). The large tickmarks on the log scale indicate the position of the spectral peak, which is supposed to be at the Brunt-Vaisala frequency.

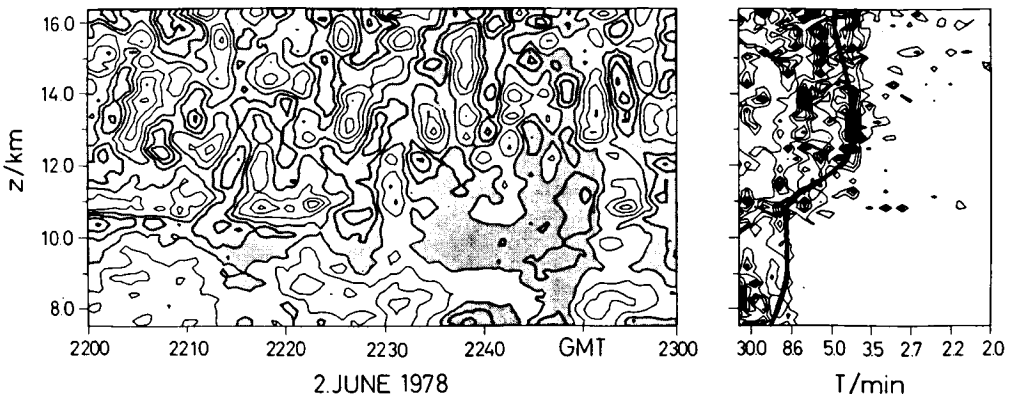

Figure 2. Contour plot of vertical velocity and spectral density (right-hand side). The continuous curve indicates the profile of the Brunt-Vaisala frequency deduced from radiosonde temperature profiles (from ROTTGER, 1980a).

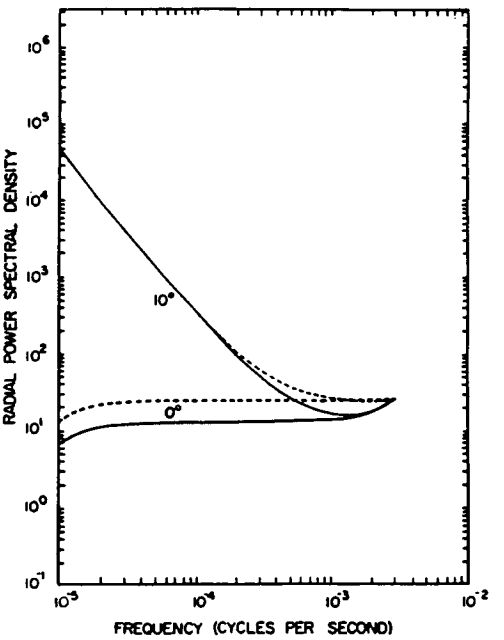

Figure 3. Frequency spectra of gravity wave velocities for 0° (vertical) and 10° zenith angle. The dashed curves are for the Boussinesq solution and the continuous curves are for the full gravity wave solution (from SCHEFFLER and LIU, 1985).

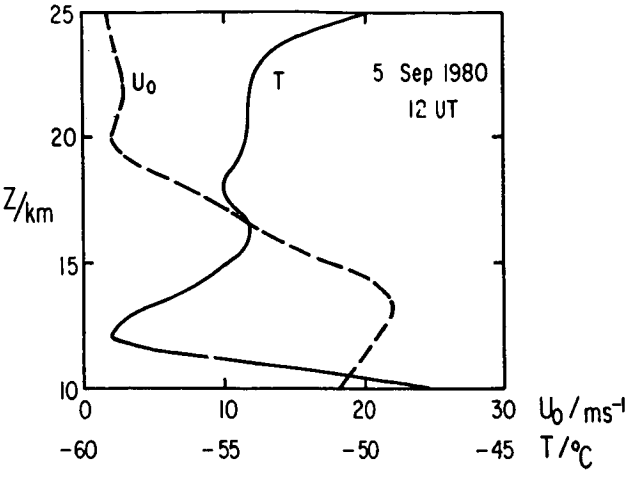

Figure 4. Radiosonde profiles of wind speed U_o and temperature T measured at a time in the interval 5/6 Sept. 1980, when the spectra of Figure 1 were obtained.

velocity steepens before it breaks. The steepening is because of harmonics which also tend the spectrum to be shifted towards higher frequencies. A cut-off above the Brunt-Vaisala frequency, however, is still apparent.

This effect may have influenced the velocity spectra observed by ECKLUND et al. (1985) during disturbed conditions (high wind), but their spectral power increased conspicuously, which may be attributed to spill-over from the horizontal velocities through a wide antenna beam width or sidelobes. The spread-out expected without the power increase can be noticed in the spectra of heights 13.5 km and 16.5 km in Figure 1, where a substantial amount of spectral energy if found at periods of a few minutes, i.e., at frequencies higher than the Brunt-Vaisala frequency. (This is particularly evident when one compares the spectra of different heights.)

Figure 4 shows the profiles of the mean wind U_o and temperature T. We notice a wind maximum of 22 ms^{-1} at 13 km, and a gradual decay of the wind velocity down to a few ms^{-1} at 20 km. It was found by ROTTGER and IERKIC (1985) that the gravity waves at the 4-6 min period have phase velocities of about 40 ms^{-1} and horizontal wavelengths of about 10 km. A wind velocity of 20 ms^{-1} can consequently yield a Doppler shift towards higher or lower frequencies by up to almost a factor of two. The low wind velocity of a few ms^{-1} above 18 km has only a negligible influence on the spectral shape. This effect of cutoff-steepening during low-wind velocities is clearly noticed when comparing Figures 1 and 4. The peak near the Brunt-Vaisala frequency is rather seen at z = 13.5 km, but it gets more salient with height. It is also shifted towards lower frequencies with height. Since a Doppler shift only widens but does not shift the peak, this frequency shift can be attributed only to a change of the Brunt-Vaisala frequency itself, which is equivalent to a change of the vertical temperature gradient. This is quite apparent in Figure 4, where we notice a highly stable temperature profile, i.e., a large Brunt-Vaisala frequency, between 12 km and 16 km, and a lower-stability profile, i.e., lower Brunt-Vaisala frequency, above 16 km.

We thus regard the measurement of the frequency of the peak in a vertical velocity spectrum to yield most directly the Brunt-Vaisala frequency from MST-radar measurements. Knowing the Brunt-Vaisala-frequency profile, one can deduce the potential temperature profile, if one has a calibration temperature at one height. However, even the uncalibrated profile will be quite useful, e.g., to determine fronts (defined by temperature inversions) and the tropopause height. It has to be noted, however, that this method fails for super-adiabatic lapse rates when the Brunt-Vaisala frequency is imaginary. Examples can be found in the spectral plots published by ROTTGER (1980b). The application of this method will also be difficult when the wind velocity is too high, causing the Doppler effect to smear out the total spectrum and blur the Brunt-Vaisala cutoff. A similar deficiency will also appear if the gravity-wave distribution has a maximum in wind direction.

REFERENCES

Fritts, D. C. (1984), Gravity wave saturation in the middle atmosphere: A review of theory and observations, Rev. Geophys. Space Phys., 22, 275-308.

Ecklund, W. L., B. B. Balsley, D. A. Carter, A. C. Riddle, M. Crochet, and R. Garello (1985), Observations of vertical motions in the troposphere and lower stratosphere using three closely-spaced ST-radars, Radio Sci., 20, 1196-1206.

Rastogi, P. K. (1975), Remote sensing of the mesosphere using the Jicamarca incoherent-scatter radar, Aeronomy Report No. 68, Dept. Elec. Eng., Univ. Illinois, Urbana, IL.

Rottger, J. (1980a), Structure and dynamics of the stratosphere and mesosphere revealed by VHF radar investigations, Pageoph, 118, 494-527.

Rottger, J. (1980b), Development of refractivity structures during anticyclonic weather conditions, Preprint Volume, 19th AMS Conf. Radar Meteorol., Miami, FL, 593-598.

Rottger, J. (1981), Wind variability in the stratosphere deduced from spaced antenna VHF radar measurements, Preprint Volume, 20th AMS Conf. Radar Meteorol., Boston, MA, 22-29.

Rottger, J., and H. M. Ierkic (1985), Postset beam steering and interferometer application of VHF radars to study winds, waves, and turbulence in the lower and middle atmosphere, Radio Sci., 20, 1461-1480.

Scheffler, A. O., and C. H. Liu (1985), On observation of gravity wave spectra in the atmosphere using MST radars, Radio Sci., 20, 1309-1322.

VanZandt, T. E. (1982), A universal spectrum of buoyancy waves in the atmosphere, Geophys. Res. Lett., 9, 575-578.

Weinstock, J. (1985), Finite amplitude gravity waves: Harmonics, advective steepening and breaking, Manuscript, Aeronomy Lab., NOAA/Boulder, CO.

D31-46
6 P.

3.3.3 THE USE OF THE EXPERIMENTALLY DEDUCED BRUNT-VAISALA FREQUENCY AND TURBULENT VELOCITY FLUCTUATIONS TO ESTIMATE THE EDDY DIFFUSION COEFFICIENT

Jurgen Rottger*

Arecibo Observatory
P.O. Box 995
Arecibo, Puerto Rico

The determination of the turbulent energy dissipation rate or the eddy diffusion coefficient from radar observations can be done through the turbulence refractive index structure constant, deduced from calibrated echo power measurements, or through the turbulent velocity fluctuations, deduced from the echo spectrum width. Besides the radar parameters, power and spectrum width, the first approach needs knowledge of profiles of temperature (and electron density in the mesosphere) and the fraction of the radar volume filled with turbulence, and the latter approach needs knowledge of the temperature profile, namely, the Brunt-Vaisala frequency. HOCKING (1985b) has recently reviewed these techniques. WEINSTOCK (1981a) has shown that the energy dissipation rate is of turbulence in the stable free atmosphere:

$$\varepsilon = 0.4 \cdot \langle W^2 \rangle \cdot \omega_B. \qquad (1)$$

The mean squared velocity $\langle W^2 \rangle$ can be directly reduced from the width of the radar power spectrum, provided that the effects of wind shear and beam width broadening are negligible. It is shown by ROTTGER (1985a) that also the Brunt-Vaisala frequency ω_B can be estimated from radar observations. Thus, the energy dissipation rate ε can be directly deduced from radar data without the need of any supplementary data or assumptions. The eddy diffusion coefficient K, similarly is given by radar observations (e.g. WEINSTOCK, 1981b).

$$K = \frac{0.8\varepsilon}{\omega_B^2} = 0.32 \langle W^2 \rangle / \omega_B \qquad (2)$$

The factor of 0.8 in Equation (2) is not well known yet, however.

Mesospheric data were taken during an ATMAP campaign, in November 1981, with the SOUSY VHF Radar at the Arecibo Observatory using an average power of 6 kW on 46.8 MHz and a height resolution of 1.2 km, applying an 8-bit complementary code. The main dish of the Observatory was used as an antenna yielding a half-power beam width of 1.7°. The beam was pointed 2.3° off the zenith such that a quasi-vertical velocity was measured, allowing to investigate short-period gravity waves. The beam was kept fixed at the E- or N- direction for about one hour, such that also the mean horizontal wind could be measured.

Figure 1 shows the average horizontal velocity profiles, and Figure 2 shows the spectra of the quasi-vertical velocity variations deduced from velocity time series (see ROTTGER, 1985a). We notice fairly low horizontal velocities smaller than 20 ms^{-1}, and we also notice a clear cutoff of the spectra at periods of a few minutes. Following the arguments of ROTTGER (1985a), we assume that this cutoff is at the Brunt-Vaisala frequency. Since the mean wind velocities were fairly low, only a small Doppler shift did result and the spectra mostly indicate a clear cutoff. This is also seen in the spectra intensity plots of Figure 3. To accentuate the consistency of the cutoff with height and time, the spectra intensities are normalized separately for each hour and altitude. The cutoff deduced from Figure 3, which is assumed to be consistent with the Brunt-Vaisala frequency ω_B, is shown in Figure 4.

*On leave from Max-Planck-Institut fur Aeronomie, Katlenburg-Lindau, West Germany.

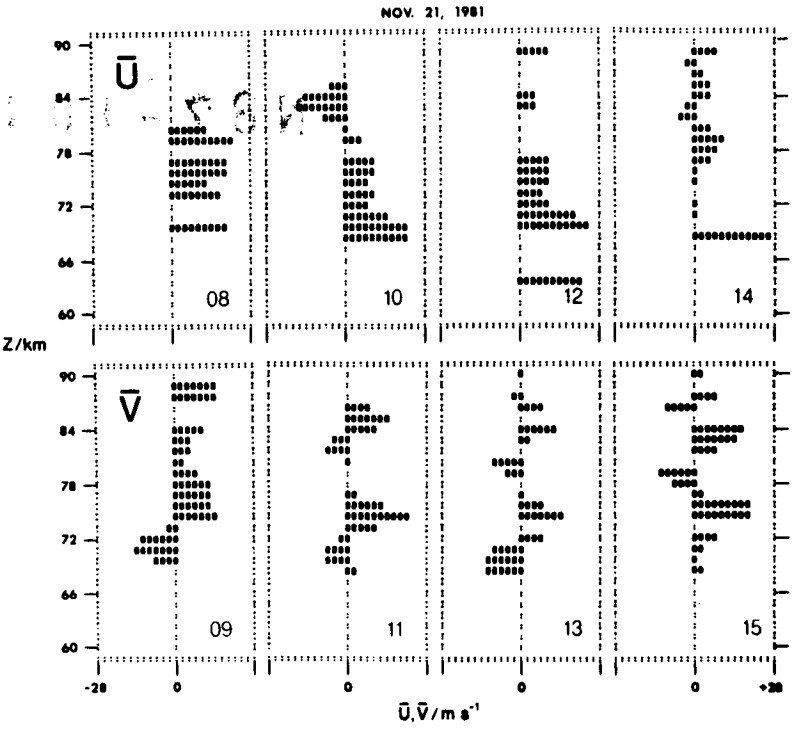

Figure 1. Average profiles of zonal (U) and meridional (V) winds in the mesosphere. Time (numbers) is AST.

This is an average over 8 hours of mesospheric observations from 08 to 16 UT. Since we have not observed an apparent anisotropy of the wave phenomena, i.e., the E- and N-beam spectra were not significantly different, data of all 8 hours were combined in Figure 4 to yield the average ω_B. We clearly see a significant increase of the average ω_B with height above 77 km. This increase is expected to be an indication of the mesopause, which we estimate from these data to be around 80 km. Furthermore, we can deduce the profiles of mean square wave velocity $\langle \tilde{w}^2 \rangle$ from the velocity time series, and the mean square turbulent velocity $\langle w^2 \rangle$ from the spectral widths (average over 50 s). The latter deduction can be done without applying corrections, since beam width and wind shear broadening effects are estimated to be small (see HOCKING, 1985b).

Since the mean square wave velocity $\langle \tilde{w}^2 \rangle$ is about constant with height and does not follow the exponential increase (continuous curve in Figure 4), we assume that the waves were dissipated (see also ROTTGER, 1985b). This is consistent with other mesospheric observations (e.g., FRITTS et al., 1984). If we assume that the gravity waves are dissipated into turbulence, we would assume an increase in the energy dissipation rate. This quantity can be deduced from the mean square turbulent velocity and the Brunt-Vaisala frequency profiles (see Equation (1)). The energy dissipation rate is proportional to the eddy diffusion coefficient, which is shown in Figure 5. It apparently has a maximum between 70 and 78 km, where the wave velocity stays almost constant. Above 78 km, the eddy diffusion coefficient is small and constant. This is

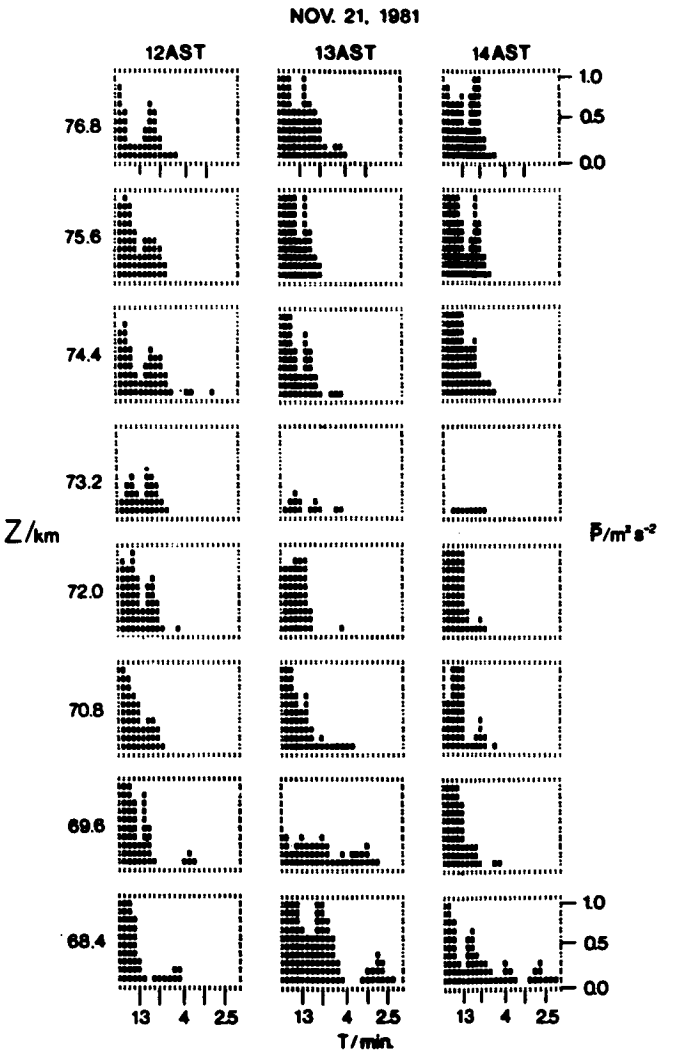

Figure 2. Spectra of quasi-vertical velocity, averaged over 54 minutes. P = 1 m^2 s^{-2} corresponds to a power density of 3.2 · 10^3 m^2 s^{-2} /Hz.

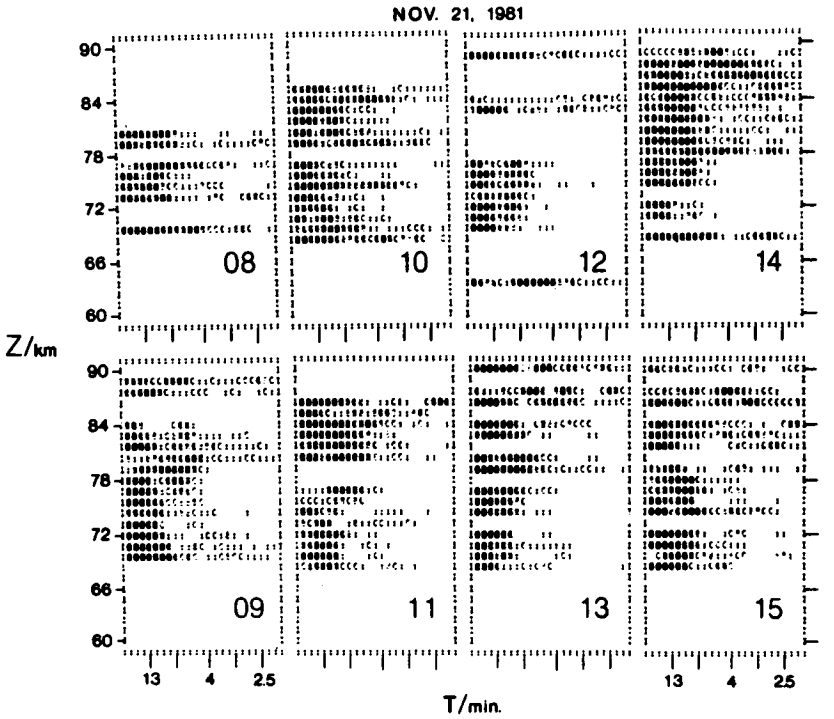

Figure 3. Spectra intensity plots. Time is in AST; even hours with beam at 2.3° zenith angle to the east and odd hours to the north.

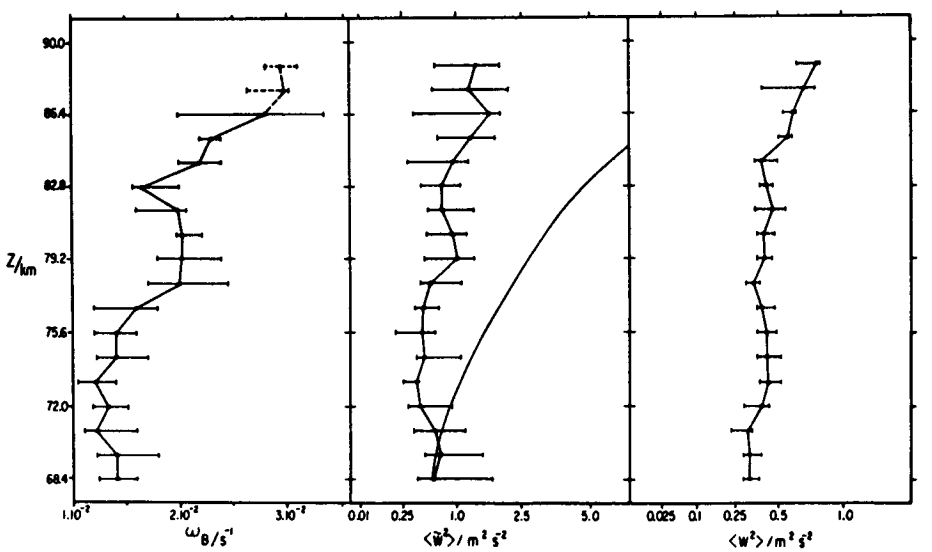

Figure 4. Profiles of average (8 hours) estimate of Brunt-Vaisala frequency ω_B, mean square wave velocity $\langle \tilde{W}^2 \rangle$ and mean square turbulent velocity $\langle W^2 \rangle$. The continuous curve in the middle diagrams indicates the exponential increase.

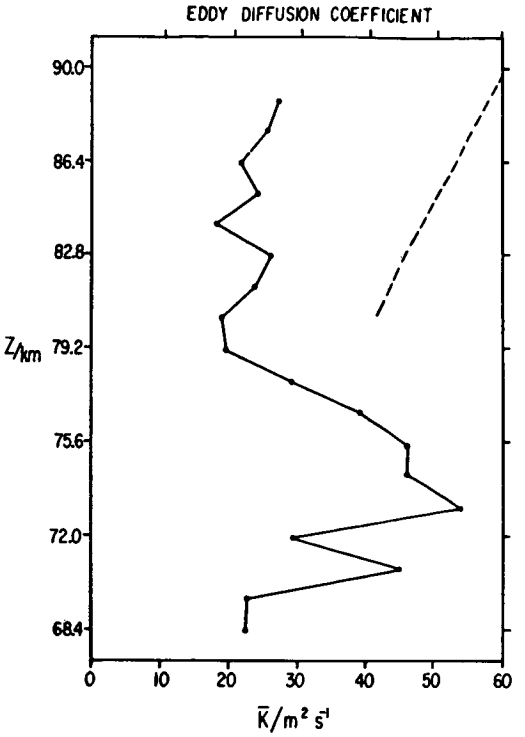

Figure 5. Profile of mean eddy diffusion coefficient (solid line) deduced from Figure 4. The dashed lines is from HOCKING (1985).

quite consistent with the observation that the mean wave velocity again starts to increase with height above 78 km.

In Figure 5, also the mean eddy diffusion coefficient (dashed line) from HOCKING (1985a) is included for heights above 80 km. It is about a factor of 2 larger than our values and it appears to be in the minimum of the mean values given by HOCKING (1985a). Since our data are averages over one day only, they, however, may not be representative for an average energy dissipation rate but also large variations around mean values may occur. Since we are fairly confident on the exact and well-defined deduction of the spectrum width, a Brunt-Vaisala frequency 2 times smaller than our deducted ω_B would be necessary to increase the eddy diffusion coefficient K. Such a low Brunt-Vaisala frequency ($\sim 10^{-2}$ Hz) cannot be found from our spectra. We therefore conclude that our profile of K is the most exact estimate available from radar observations.

REFERENCES

Fritts, D. C., M. A. Geller, B. B. Balsley, M. L. Chanin, I. Hirota, J. R. Holton, S. Kato, R. S. Lindzen, M. R. Schoeberl, R. A. Vincent, and R. F. Woodman (1984), Research status and recommendations from the Alaska Workshop on gravity waves and turbulence in the middle atmosphere, Bull. Am. Meteorol. Soc., 65, 149-159.

Hocking, W. K. (1985a), Turbulence in the altitude region 80-120 km, Handbook for MAP, 16, 290-304.
Hocking, W. K. (1985b), Measurement of turbulent energy dissipation rate in the middle atmosphere by radar techniques - a review, Radio Sci., 20, 1403-1422.
Rottger, J. (1985a), Determination of the Brunt-Vaisala frequency from vertical velocity spectra, this volume.
Rottger, J. (1985b), The relation of gravity waves and turbulence in the mesosphere, this volume.
Weinstock, J. (1981a), Energy dissipation rates of turbulence in the stable free atmosphere, J. Atmos. Sci., 38, 880-883.
Weinstock, J. (1981b), Vertical turbulence diffusivity for weak or strong stable stratifications, J. Geophys. Res., 86, 9025-9928.

3.3,4 THE RELATION OF GRAVITY WAVES AND TURBULENCE IN THE MESOSPHERE

Jurgen Rottger*

Arecibo Observatory
P.O. Box 995
Arecibo, Puerto Rico

Gravity-wave saturation in the middle atmosphere is widely assumed to be due to the increase of wave amplitude or from the encountering of a critical level such that convective and/or shear instability limits the wave growth (e.g., FRITTS, 1984). The growth of wave amplitude first results in a steepening of wave velocities, i.e., in the generation of harmonics before the wave eventually breaks into turbulence and gets saturated. As pointed out by WEINSTOCK (1985), the saturation of the wave is accompanied by a near adiabatic lapse rate and turbulence.

VHF MST radars with suitable sensitivity can detect turbulence in the mesosphere if the electron density and its vertical gradient is sufficiently strong. It is unquestionable from many experiments that the radar-detected turbulence is intermittent in space and time. Figure 1 shows an example of layers of mesospheric echoes detected with the SOUSY VHF Radar at the Arecibo Observatory (ROTTGER et al., 1981; CZECHOWSKY et al., 1984). A clear feature in this figure is the splitting into several, periodically arranged layers. Many authors have reported an apparent downward progression of such structures, which is not readily apparent in Figure 1, however. These discrete layers can be due to turbulence or due to very persistent steep electron-density gradients. We cannot imagine that the latter can endure in the daylight ionosphere if they were not controlled by some kind of neutral atmosphere effect. It is often observed that long-period atmospheric gravity waves or tides can give rise to turbulence layer generation (e.g., FRITTS et al., 1986). The layers then should move downward which we do not observe. It is also reported that layers occur preferably in strong wind shear regions (e.g., RUSTER, 1984). Figure 2 shows the simultaneously measured mean wind profiles. These indicate a downward moving shear (trace the zero-crossings, particularly in the meridional component), which is likely to be due to the diurnal tide. Since the shear moves downward, we have to exclude that the observed height-stationary turbulence layers of Figure 1 have to do with the tidal variation of velocity or temperature.

We also cannot believe that these fairly thin and persistent layers (better to be called sheets or laminae because of their narrowness) are generated by short-period gravity waves. A common explanation is that gravity wave breaking causes turbulence (e.g., FRITTS and RASTOGI, 1985) which we should see in our records. Figures 3a and 3b show time series of spectra-intensity plots for different altitudes. The intensity is printed in an absolute reflectivity scale, such that the height and time dependence of turbulence intensity (assuming no substantial electron-density profile change), spectral width and mean radial (= almost vertical at 2.3° zenith angle) velocity can be identified. We notice quite a substantial wave activity at many different periods from 4 minutes upwards. If wave breaking would occur, we should see an increase of intensity and spectrum width at certain phases of these oscillations. Except occasionally in some upper heights, where some intensity bursts are apparent (above 78 km in Figure 3b), we cannot clearly detect such phenomena. The intermittency in space and time of the turbulence

*On leave from Max-Planck-Institut fur Aeronomie, Katlenburg-Lindau, West Germany.

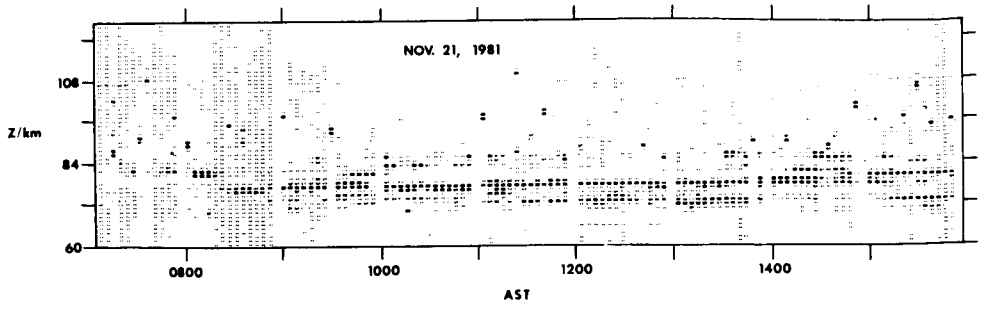

Figure 1. Height-time-intensity plot of mesospheric VHF-radar echoes detected at the Arecibo Observatory. The antenna pointed at 2.3° zenith angle, during even hours towards last and during odd hours towards north (see ROTTGER, 1985).

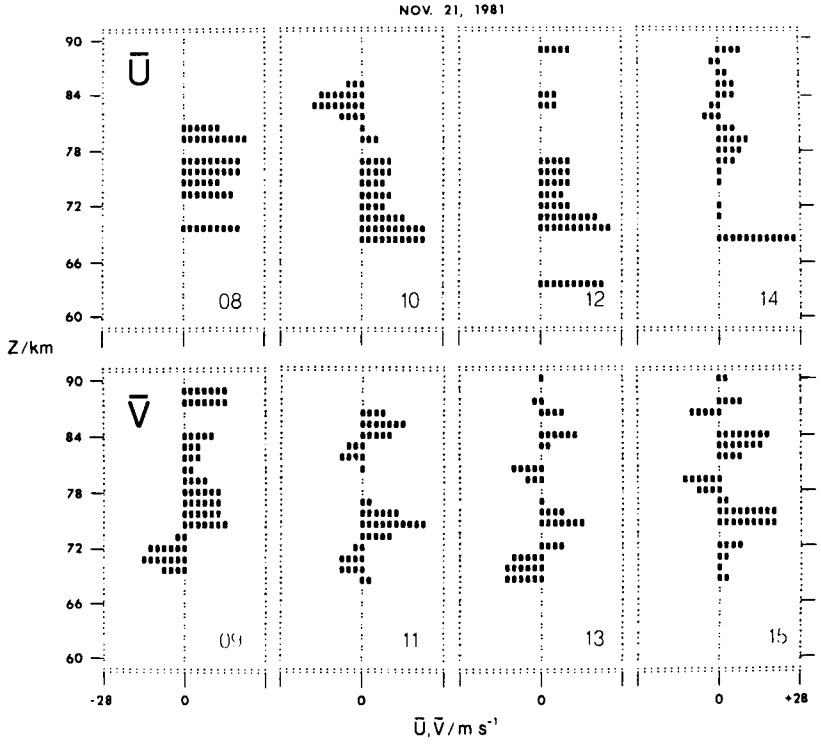

Figure 2. Profiles of zonal (U) and meridional (V) component of the mean wind, measured over periods of 54 min. The numbers denote time in AST.

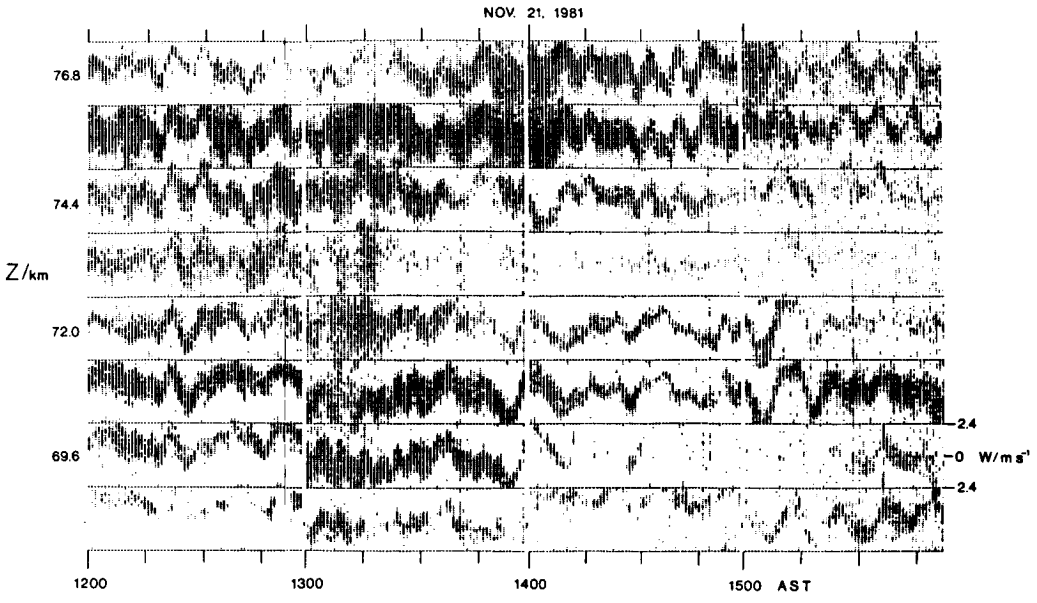

Figure 3a. Intensity plots of spectra (see the layered structure of turbulence in Figure 1).

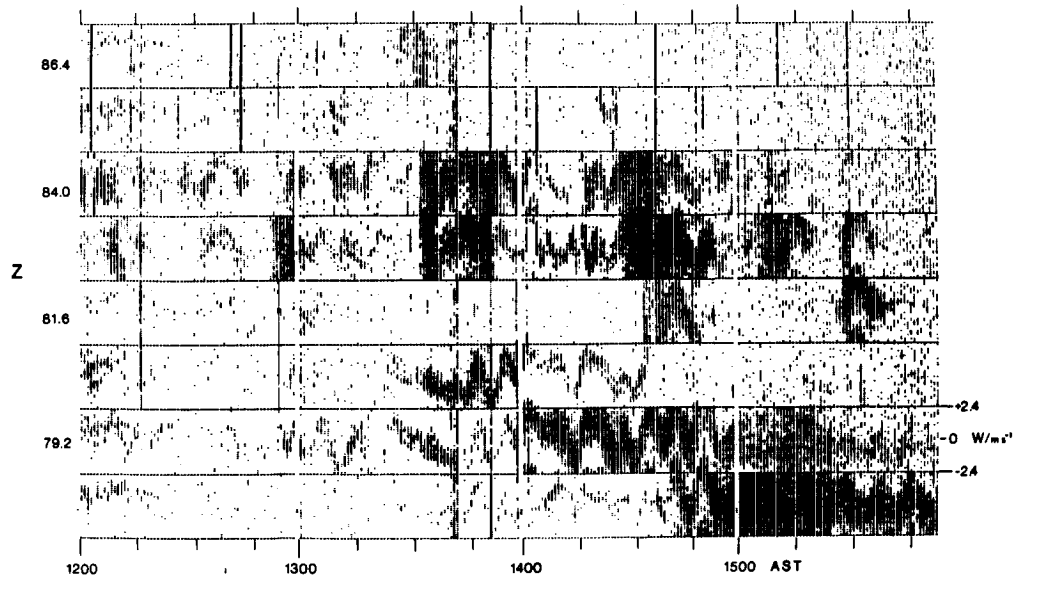

Figure 3b. Intensity plots of spectra (see the layered structure of turbulence in Figure 1).

echoes appears in the majority of times and heights not related to these short-period gravity waves. When carefully viewing the velocity oscillations, we, however, often find clear indications of a nonsinusoidal variation. This indicates a nonlinear steepening effect (WEINSTOCK, 1985), which transfers energy from the fundamental into harmonics -- in our case mostly without leading to breaking into turbulence. Another peculiar effect is seen sometimes, when a high-frequency wave is superimposed on a low-frequency wave oscillation (e.g., at 69.6 km after 13 AST). KLOSTERMEYER (1984) has explained similar observations at thermospheric heights to be due to parametric instabilities.

There is apparently no distinct amplitude growth of these wave oscillations (e.g., fairly clearly seen from 12-13 AST between 69.6 km and 76.8 km, as well as in Figure 4 of ROTTGER, 1985). We, therefore, have to imply a saturation process if we assume that these are vertically propagating waves. Since in our case study we seldom observe a clear indication for wave breaking into turbulence, we have to invoke other dissipation effects which limit the wave growth, such as energy transfer into higher harmonics (nonlinear steepening), parametric instabilities, radiative dampening or dissipation due to kinematic viscosity and heat conduction. We also could assume that the observed short-period gravity waves are locally generated or guided in wave ducts, since most of the oscillations are confined to height ranges of a few kilometers only.

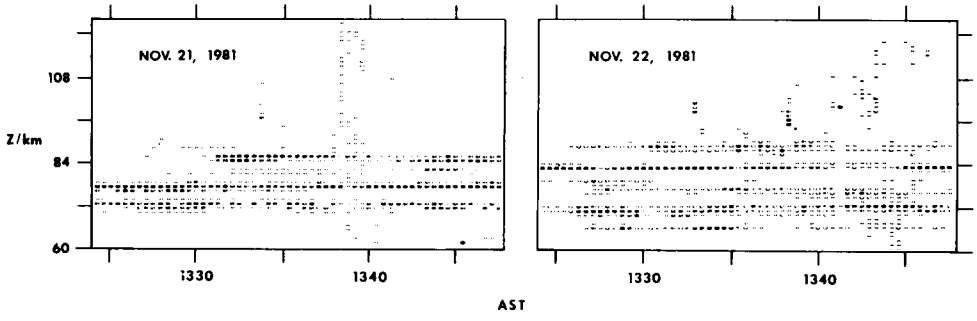

Figure 4. Height-time-intensity plots of mesospheric VHF-radar echoes detected at the same time on two different days.

Since we cannot prove that the mesospheric turbulence layers (Figure 1) are generated by the simultaneously existing short-period gravity waves (Figure 3), we have to invoke other generation mechanisms than wave breaking. Possible mechanisms like lateral convection (ROTTGER, 1980a), quasi-geostrophic flows at mesoscales (LILLY, 1983) or vortical modes of motion as seen in the ocean (MULLER and PUJALET, 1984) could be candidates. We are inclined to see a connection of these layers or laminae with very-long-period internal waves because of the periodicity in their vertical structure and their long mean persistency (see Figure 5, which shows their appearance at two time periods separated by 24 hours). ROTTGER (1980b) had proposed that such structures are due the modulation of the mean temperature and wind profiles by internal waves. The superposition of random or short-term wave-induced wind and temperature fluctuations with the background profile, modulated by very-long-period waves (quasi-inertia waves) then would yield the observed effects, namely could explain the vertical periodicity, the long-term mean persistency as well as some short-term variability of their intensity. Note that this phenomenon does not need the short-term gravity waves to break into turbulence, rather than to add a small shear of temperature variation to the background profile

modulated by long-period waves (which cannot be detected with the radars), to lead to very thin laminae where the Richardson number is smaller than its critical value to initiate turbulence.

REFERENCES

Czechowsky, P., G. Schmidt, and R. Ruster (1984), The mobile SOUSY Doppler radar: Technical design and first results, Radio Sci., 19, 441-450.

Fritts, D. C. (1984), Gravity wave saturation in the middle atmosphere: A review of theory and observations, Rev. Geophys. Space Phys., 22, 275-308.

Fritts, D. C., and P. K. Rastogi (1985), Convective and dynamical instabilities due to gravity wave motions in the lower and middle atmosphere: Theory and observations, Radio Sci., 20, 1247-1277.

Fritts, D. C., S. A. Smith, B. B. Balsley, and C. R. Philbrick (1986), Evidence for gravity wave saturation and local turbulence production in the summer mesosphere and lower thermosphere during the STATE experiment, Radio Sci., to appear.

Lilly, D. K. (1983), Stratified turbulence and the mesoscale variability of the atmosphere, J. Atmos. Sci., 40, 749-761.

Muller, P., and R. Pujalet (1984), editors, Internal Gravity Waves and Small-Scale Turbulence, Proc. Hawaiian Winter Workshop, University of Hawaii at Monoa.

Rottger, J. (1980a), Structure and dynamics of the stratosphere and mesosphere revealed by VHF radar investigations, Pageoph., 118, 494-527.

Rottger, J. (1980b), The dynamics of stratospheric and mesospheric find structure investigated with an MST VHF Radar, Handbook for MAP, 2, 341-350.

Rottger, J. (1985), The use of the experimentally deduced Brunt-Vaisala frequency and turbulent velocity fluctuations to estimate the eddy diffusion coefficient, this volume.

Rottger, J., P. Czechowsky, and G. Schmidt (1981), First low-power VHF radar observations of tropospheric, stratospheric, and mesospheric winds and turbulence at the Arecibo Observatory, J. Atmos. Terr. Phys., 43, 789-800.

Ruster, R. (1984), Winds and waves in the middle atmosphere as observed by ground-based radars, Adv. Space Res., 4, 3-18.

Weinstock, J. (1985), Finite amplitude gravity waves: Harmonics, advective steepening and breaking, manuscript, Aeronomy Laboratory, NOAA-Boulder, CO.

3.3.5 CAN STOCHASTIC, DISSIPATIVE WAVE FIELDS BE TREATED AS RANDOM WALK GENERATORS?

J. Weinstock

Aeronomy Laboratory
NOAA, Boulder, CO 80303

A suggestion by MEEK et al. (1985) that the gravity wave field be viewed as stochastic, with significant nonlinearities, is applied to calculate diffusivities.

In a talk given in Boulder, REID (personal communication, 1985) described the mesospheric wave field to be predominantly stochastic in character. In fact, a recent paper by MEEK et al. (1985) quoted the BRISCOE (1975) description of the ocean wave field as "...an intermittent stochastic process with significant... nonlinearities", and suggested that this view should be adopted in atmospheric studies. Others have noted the random character of the gravity wave field as well (e.g., Vincent, Balsley).

If the Meek et al. point of view is adopted -- and account is taken that the gravity wave field is often dissipative -- then one might be able to apply the stochastic methods of turbulence transport theory to the gravity wave field. That is, the wave field may be viewed as causing a random walk (of air parcels) in the manner of turbulence: an irreversible process. However, since the waves are not as dissipative or random as turbulence, the random walk can only be an approximation -- an approximation that improves with increasing dissipation and randomness.

Aside from this uncertainty, there is the obvious difference that the wave field "eddies" (which we picture as dissipating gravity waves) are strongly influenced by stratification whereas the neutral turbulence eddies are not. This difference can be accounted for in expressions of turbulent diffusion by replacement of turbulent eddies with gravity wave Fourier components. The question that remains is whether or not such a stochastic wave model is significant for diffusion in the mesosphere.

The purpose of our article is to calculate the diffusivity for that stochastic model and compare with previous diffusivity estimates. We do this for an idealized case in which the wind velocity changes but slowly, and for which saturation is the principal mechanism by which wave energy is lost. A related calculation was given in a very brief way (WEINSTOCK, 1976), but the approximations were not fully justified, nor were the physical pre-suppositions clearly explained. The observations of MEEK et al. (1985) have clarified the pre-suppositions for us, and provided a rationalization and improvement of the approximations employed.

The derivation begins with the diffusivity tensor $\underset{\approx}{D}$ of a stochastic, dissipating velocity field given by TAYLOR (1921) as

$$\underset{\approx}{D} = \lim_{t\to\infty} < (\underset{\sim}{x}_t - \underset{\sim}{x})^2 > /2t$$

$$\underset{\approx}{D} = \int_0^\infty dt \langle \underset{\sim}{v}'(\underset{\sim}{x}, t')\underset{\sim}{v}'(\underset{\sim}{x} + \underset{\sim}{x}_t, t' + t)\rangle \qquad (1)$$

$$\equiv \int_0^\infty dt \left\{\frac{1}{L^2}\int_0^L dx_1 \int_0^L dx_2 \frac{1}{T}\int_0^T dt' \, \underset{\sim}{v}'(\underset{\sim}{x}, t')\underset{\sim}{v}'(\underset{\sim}{x}_t, t + t')\right\}$$

where $\underset{\sim}{v}'(\underset{\sim}{x}, t')$ is the velocity fluctuation at point $\underset{\sim}{x}$ at time t', $\underset{\sim}{x}_t$ is the

position a particle will be at time t + t' given that the particle was previously at point $\underset{\sim}{x}$ at time t' (the orbit of a particle in the combined velocity field of mean flow and waves), the angular brackets denote an average over time t' and over horizontal spatial coordinates x_1 and x_2, L is the length scale of the spatial average and T is the time scale of the time average. The time scale T is taken to be much larger than largest gravity wave period $2\pi/\omega (T >> 2\pi/\omega)$, and L is much larger than the largest wavelength under consideration. Equation (1) also occurs in the theory of Brownian motion.

For a spectrum of gravity waves, the (stochastic) velocity fluctuation can be represented by

$$\underset{\sim}{v}'(\underset{\sim}{x}, t') = \sum_{\underset{\sim}{k}_1} \underset{\sim}{v}_{\underset{\sim}{k}_1} \exp(i\underset{\sim}{k}_1 \cdot \underset{\sim}{x} + i\omega_1 t')$$

$$\underset{\sim}{v}'(\underset{\sim}{x}_t, t+t') = \sum_{\underset{\sim}{k}_2} \underset{\sim}{v}_{\underset{\sim}{k}_2} \exp[i\underset{\sim}{k}_2 \cdot \underset{\sim}{x}_t + i\omega_2 (t + t')], \tag{2}$$

where $\underset{\sim}{k}_1$ is the wave vector of a wave fluctuation, $\underset{\sim}{v}_{\underset{\sim}{k}_1}$ its amplitude, and ω_1 its frequency. Note that $\langle (\underset{\sim}{v}')^2 \rangle = \Sigma \underset{\sim}{v}_{\underset{\sim}{k}_1} \underset{\sim}{v}_{\underset{\sim}{k}_1}^*$, where the asterisk denotes the complex conjugate, and we use $\underset{\sim}{v}(-\underset{\sim}{k}_1) = \underset{\sim}{v}^*_{\underset{\sim}{k}_1}$ to ensure that (2) is real.

Substitution of (2) and (1), it is found in a detailed derivation that D_{zz}, the vertical diffusivity is given by

$$D_{zz} \approx \sum_{\underset{\sim}{k}} \frac{\langle w_{\underset{\sim}{k}} w_{\underset{\sim}{k}}^* \rangle}{\gamma k_z H \omega} \tag{3}$$

where $w_{\underset{\sim}{k}}$ is the vertical component of wave velocity $\underset{\sim}{v}_{\underset{\sim}{k}}$, and ω is the frequency of wave $\underset{\sim}{k}$. This equation was derived for a saturated wave field, and dissipation was required for its derivation.

To generalize (3) to the case of a not completely saturated wave field, it can be shown that H need be replaced by h_o in (3)

$$D_{zz} \approx \sum_{\underset{\sim}{k}} \frac{\langle w_{\underset{\sim}{k}} w_{\underset{\sim}{k}}^* \rangle}{\gamma k_z h_o \omega}, \tag{4}$$

where h_o is the "dissipation length" of the wave field, i.e., the length over which the wave energy decay e-folds owing to saturation.

Whether or not this "stochastic wave" model of diffusion is useful for the atmosphere we are not sure. Perhaps it may be useful as an upper bound -- the more dissipative the waves, the more justified its application. Numerically, the model gives values of D_{zz} in conformity with chemical model estimates (e.g., VINCENT, 1984), but whether this is more than a coincidence, we do not know. It is a straightforward way in which to apply the suggestion of Meek et al. to the problem of diffusivity.

REFERENCES

Briscoe, M. G. (1975), Introduction to a collection of papers on oceanic internal waves, J. Geophys. Res., 80, 289.

Fisz, M. (1963), Probability Theory and Mathematical Statistics, John Wiley & Sons, Inc., New York, Chap. 4.

Meek, C. E., I. M. Reid, and A. H. Manson (1985), Observations of mesospheric wind velocities, I. Report No. 1, Atmospherics Dynamics Group, Univ. of Saskatchewan, Saskatoon, Saskatchewan.

Taylor, G. I. (1921), Diffusion by continuous movements, Proc. London Math Soc., 20, 196-212.

Vincent, R. A. (1984), Gravity-wave motions in the mesosphere, J. Atmos. Terr. Phys., 46, 119-128.

Weinstock, J. (1976), Nonlinear theory of acoustic-gravity waves: Saturation and enhanced diffusion, J. Geophys. Res., 81, 633-652.

3.4.1 OBSERVATIONS AND A MODEL OF GRAVITY-WAVE VARIABILITY IN THE MIDDLE ATMOSPHERE

David C. Fritts

Geophysical Institute and Department of Physics,
University of Alaska
Fairbanks, AK

and

Robert A. Vincent

Department of Physics
University of Adelaide
Adelaide, S. Australia

I. Introduction

The recent recognition of the important role of gravity waves in middle atmosphere dynamics has stimulated renewed interest in their propagation and effects. The most significant effect, perhaps, is the drag that results from a vertical divergence of the gravity-wave momentum flux due to wave saturation. Initial studies of this momentum flux and divergence were performed by VINCENT and REID (1983) and REID (1984). The purpose of this note is to report on a more recent study that addressed the gravity-wave momentum flux, and its variability in space and time, in detail.

II. DATA PRESENTATION AND DISCUSSION

As in the studies cited above, the data used in this study were collected with the HF radar in Adelaide, Australia. The system capabilities and momentum flux measurement technique were described by VINCENT and REID (1983).

A major goal of the present study was to determine what portion of the gravity-wave frequency spectrum accounted for the majority of the momentum flux and divergence, as this has important implications for the middle atmosphere response. It was found that $\sim 70\%$ of the total flux and divergence was due to wave motions with observed periods < 1 hr, consistent with expectations based on the shape of the observed gravity-wave spectrum (FRITTS, 1984). This dominance of the momentum flux and divergence by high-frequency motions implies a potential for the modulation of those quantities by large-amplitude motions at lower frequencies.

A second, striking aspect of the velocity and momentum flux data is its dramatic diurnal variability, particularly at certain levels. This variability is illustrated with the momentum flux, computed in 8-hr blocks, in Figure 1. Note the large negative values occurring at 0000 local time at upper levels and the phase lag at lower levels. As indicated above, the dominant contributions here are due to waves with periods < 1 hr. The variability with height and time of the mean square velocity in the west beam and the momentum flux, averaged over the 3-day period, are illustrated in Figure 2. Note here the rapid growth of wave amplitude (and momentum flux) below 90 km during the 8-hr period centered at 0000 local time.

We have performed a detailed analysis of the various tidal motions present during this data interval and have determined that variations in the zonal wind profile imposed by the diurnal tidal motion likely are responsible for the modulation of the gravity-wave amplitudes and momentum fluxes. The modulation appears to proceed as follows. For most of each 24-hr period, the tidal winds

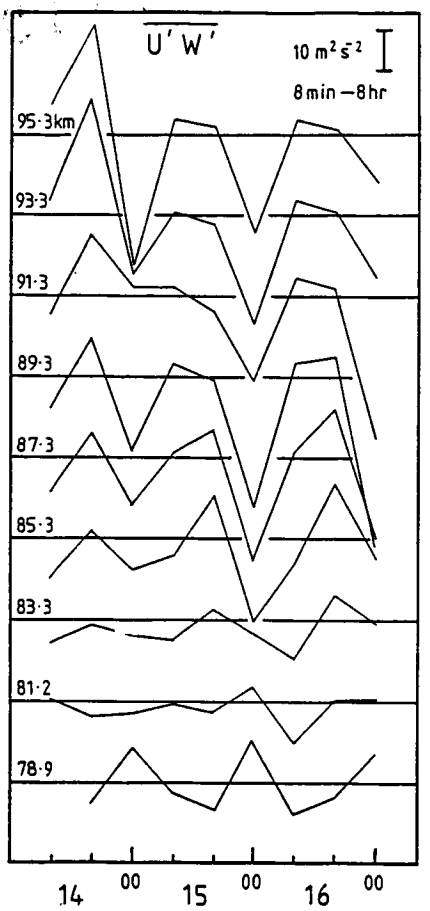

Figure 1. Momentum flux estimates in 8-hr blocks as a function of height for 14-16 June. Note the large diurnal modulation at upper levels and the phase lag at lower levels. Large negative values occur preferentially near 0000 local time.

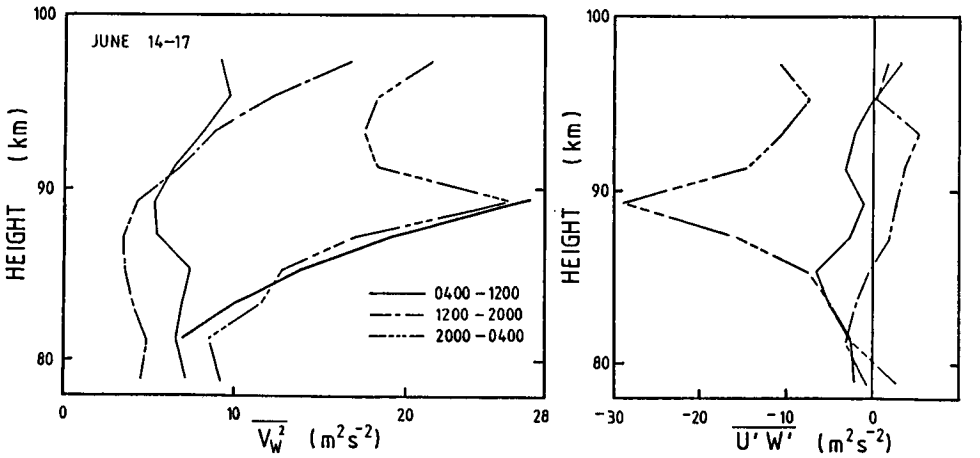

Figure 2. West mean square velocity and momentum flux profiles for 8-hr intervals averaged over the final three days of the observation period.

do not alter substantially the zonal wind shears, which are normally negative, causing a gradual reduction in $\bar{u} - c$ (for westward propagating gravity waves) and a gradual constriction of the momentum flux due to such waves, as shown schematically in Figure 3a. These are the dominant gravity waves as evidenced by the momentum flux data presented by VINCENT and FRITTS (1985). During the interval centered at 0000 local time, however, the tidal winds during this 3-day period acted to reverse (make positive) the vertical shear of the zonal "mean" wind, producing an environment in which high-frequency easterly wave motions experience a considerable increase of $\bar{u} - c$ with height. Because the amplitude needed for saturation scales as $\bar{u} - c$, these waves now propagate upward largely without saturating, resulting in am amplitude and momentum flux as shown in Figure 2 (see Figure 3b). Near 90 km, however, the waves again encounter an adverse shear, causing a rapid amplitude reduction and a large momentum flux divergence.

The implications of this tidal modulation of the high-frequency momentum fluxes are illustrated in Figure 4. The diurnal tidal amplitude at 90 km is shown in Figure 4a and reaches a maximum near 0000 local time, at which time the momentum flux and flux divergence below and at 90 km achieve large values. The strong diurnal variation of the momentum flux divergence results in large, temporarily localized zonal flow accelerations which may themselves alter the

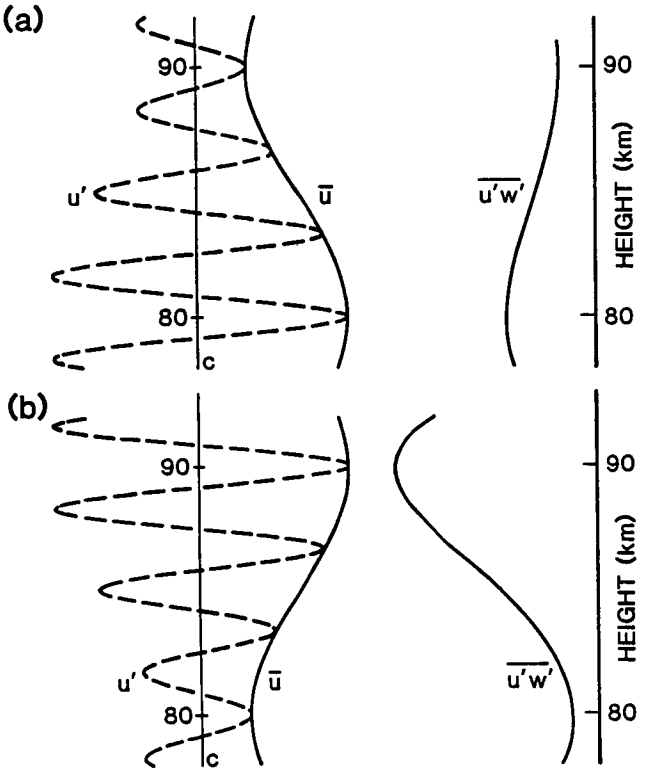

Figure 3. Schematic of saturated gravity-wave amplitude and momentum flux in an environment with $\bar{u}$-c decreasing (a) and increasing (b). Note that the implied zonal drag is very large above 90 km in the lower figure.

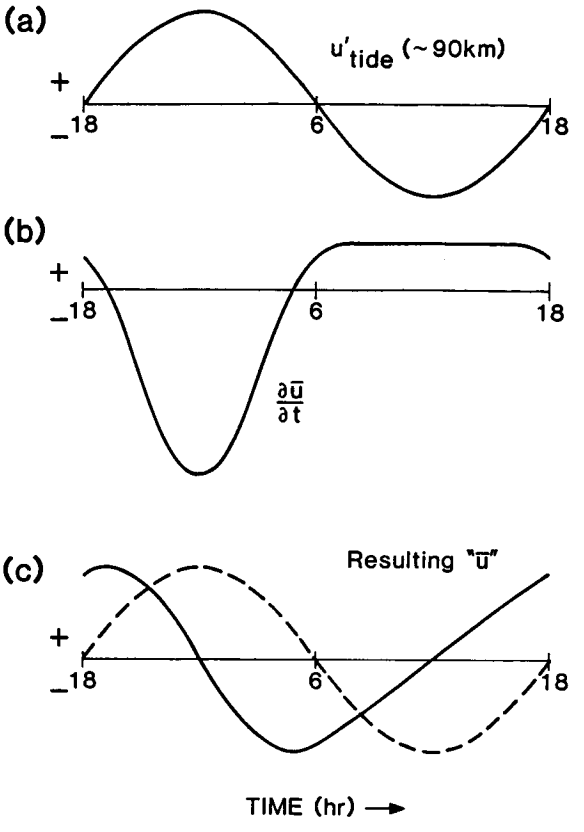

Figure 4. Schematic illustrating the effects of a diurnally varying zonal drag on the inferred tidal structure. The results are an altered amplitude and an advanced phase of the apparent tidal motion.

tidal structures or at least our ability to infer the tidal amplitudes and phases. This mechanism suggests an advance of the phase of the diurnal tidal motion during periods of particularly large diurnal tidal amplitudes, consistent with tidal observations made during this period. This mechanism may also be expected to contribute to the variability of tides and other low-frequency components of the motion spectrum at other locations.

REFERENCES

Fritts, D. C. (1984), Gravity wave saturation in the middle atmosphere: A review of theory and observations, Rev. Geophys. Space Phys., 22, 275-308.

Reid, I. M. (1984), Radar studies of atmospheric gravity waves, Ph.D. Thesis, Univ. of Adelaide, Australia, 300 p.

Vincent, R. A., and I. M. Reid (1983), HF Doppler measurements of mesospheric gravity wave momentum fluxes, J. Atmos. Sci., 40, 1321-1333.

Vincent, R. A., and D. C. Fritts (1985), Gravity wave motions and momentum fluxes in the middle atmosphere at Adelaide, Australia, Handbook for MAP, Vol. 18, 299-301, SCOSTEP Secretariat, Dep. Elec. Computer Eng., Univ. IL, Urbana.

3.5.1 CLIMATOLOGY OF GRAVITY WAVES OVER POKER FLAT, ALASKA FOR 1983

Ben B. Balsley

Aeronomy Laboratory
National Oceanic and Atmospheric Administration
Boulder, Colorado 80303

and

Rene Garello

E.N.S.T.Br., Z.I. de Kernevent
Plouzane B. P. 856
29279 Brest-Cedex, France

An analysis of short-period wind fluctuations over Poker Flat, Alaska, obtained using the Poker Flat MST Radar is presented in Figure 1. Results are shown for the troposphere and lower stratosphere as well as for the upper mesosphere and lower thermosphere. Contours depict various levels of wind variance (m^2s^{-2}). These results pertain only to wind fluctuation periods lying between one and six hours. These particular fluctuations are generally considered to arise primarily from atmospheric gravity waves. Insofar as this is true, the figure thus describes a general climatology of gravity waves at high latitudes.

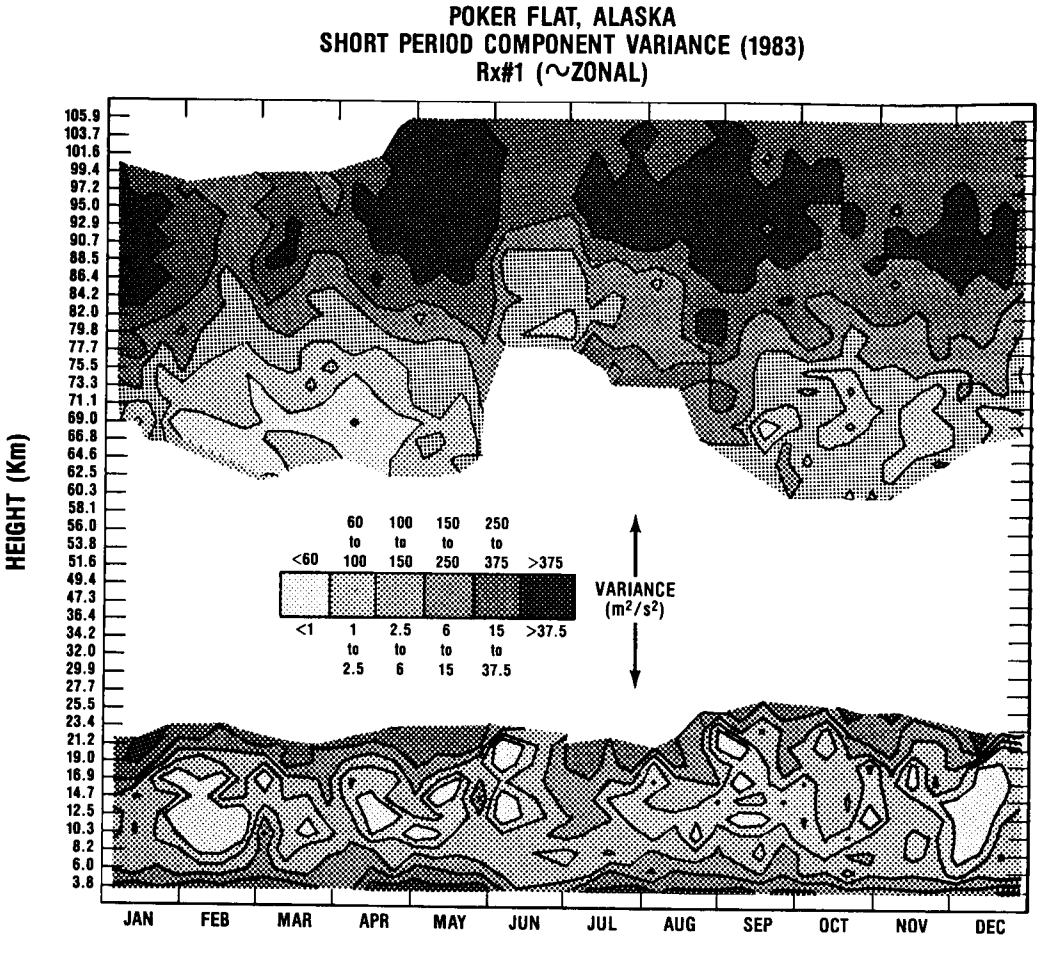

Figure 1. Showing the variance of short-period wind fluctuations versus height time for 1983. Note that blank regions correspond to regions of no data.

3.5.2 CLIMATOLOGY OF TROPOSPHERIC VERTICAL VELOCITY SPECTRA

W. L. Ecklund, K. S. Gage, B. B. Balsley, and D. A. Carter

Aeronomy Laboratory
NOAA
Boulder, Colorado 80303

In this brief report, we show vertical velocity power spectra obtained from Poker Flat, Alaska; Platteville, Colorado; Rhone Delta, France; and Ponape, East Caroline Islands using 50-MHz clear-air radars with vertical beams. The spectra were obtained by analyzing the quietest periods from the one-minute-resolution time series for each site. The lengths of available vertical records ranged from as long as 6 months at Poker Flat to about 1 month at Platteville.

The quiet-time vertical velocity spectra are shown in Figure 1. Spectral period ranging from 2 minutes to 4 hours is shown on the abscissa and power spectral density is given on the ordinate. The Brunt-Vaisala (B-V) periods (determined from nearby sounding balloons) are indicated by the arrows. All spectra (except the one from Platteville) exhibit a peak at periods slightly longer than the B-V period, are flat at longer periods, and fall rapidly at periods less than the B-V period. This behavior is expected for a spectrum of internal waves and is very similar to what is observed in the ocean (ERIKSEN, 1978). The spectral amplitudes in Figure 1 vary by only a factor of 2 or 3 about the mean, and show that under quiet conditions vertical velocity spectra from the troposphere are very similar at widely different locations.

Preliminary spectra from Liberal, Kansas and Christmas Island, Kiribati are indicated by hatched areas in Figure 1. These spectra were obtained from time series covering only 1 or 2 days and cannot be taken as being representative of quiet periods. It should be noted, however, that the shapes and amplitudes of the spectra from these two sites are similar to the spectra from the four other sites displayed in Figure 1.

REFERENCE

Eriksen, C. C. (1978), Measurements and models of fine structure, internal gravity waves, and wave breaking in the deep ocean, J. Geophys. Res., 83, 2989-3009.

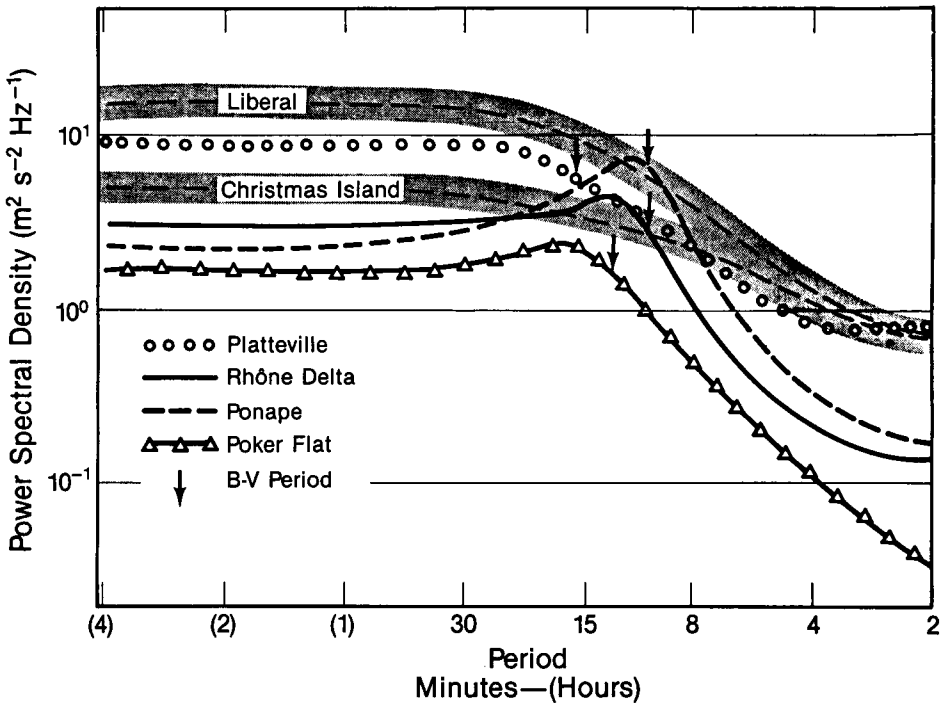
Liberal
Christmas Island
Platteville
Rhône Delta
Ponape
Poker Flat
B-V Period
Power Spectral Density (m² s⁻² Hz⁻¹)
10¹
10⁰
10⁻¹
(4)
(2)
(1)
30
15
8
4
2
Period
Minutes—(Hours)

Figure 1.

3.5.3 MESOSPHERIC GRAVITY-WAVE CLIMATOLOGY AT ADELAIDE

R. A. Vincent

Physics Department
University of Adelaide
Adelaide, South Australia, 5001

The MF Adelaide partial-reflection radar has been operating continuously since November 1983. This has enabled a climatology of gravity-wave activity to be constructed for the mesosphere. In accordance with recommendations of the GRATMAP Steering Committee, the data have been analysed for a 'medium-period' range of 1 to 8 hr and a longer period range between 8 and 24 hr, covering the inertio-period waves. The tidal motions have been filtered out prior to analysis.

For the data analysed so far (Nov 1983 - Dec 1984), a number of interesting features have emerged. Firstly, the wave activity at heights above 80 km shows a small semiannual variation with season with the activity being strongest in summer and winter. At heights below 80 km however, there is a similar but more marked variation with the weakest amplitudes occurring at the time of the changeovers in the prevailing circulation. If breaking gravity waves are responsible for much of the turbulence in the mesosphere, then the periods March-April and September-October might also be expected to be periods of weak turbulence. These predictions appear to be supported by direct observations of turbulence dissipation rates (HOCKING, private communication).

Another important feature of the gravity waves is that the wave field appears to be partially polarized. The meridional amplitudes are larger than the zonal amplitudes, especially in winter, and there is a small but finite $\overline{u'v'}$ the sign of which changes with season. By calculating the "Stokes parameters" for the gravity-wave field, in analogy to a partially polarized electromagnetic wave field, it is found that the degree of polarization is about 15% in summer and 30% in winter. The polarized component is found to propagate in the opposite direction to the background flow in the stratosphere which suggests that the polarization arises through directional filtering of the waves as they propagate up from below.

3.5.4 HORIZONTAL WIND PERTURBATIONS AND THEIR RELATION TO TRANSIENT INTERNAL GRAVITY WAVES

A. Ebel

Institut fur Geophysik und Meteorolgie
Universitat Zu Koeln, Koeln 41, D-5000
Federal Republic of Germany

A. H. Manson and C. E. Meek

Physics Department
University of Saskatchewan
Saskatoon, Saskatchewan, S7N OWO Canada

ABSTRACT

Horizontal winds as measured with the Saskatoon MF radar exhibit wind fluctuations which have preferred directions toward north or south in the period range 0-60 min at heights between about 60 and 110 km. Longer period perturbations ($\sim$ 1-6 h) tend to have an additional maximum of direction frequencies in the E-W sector. The polarization effect analysed for more than 6 years shows regular changes with season.

The main features of the seasonal variations of the direction distributions can be explained by directional filtering of vertically propagating nonstationary gravity waves and appropriate changes of the wave source strength and position in the troposphere. The N-S polarization of the gravity-wave field appears to result in meridional wind reversals with height above the mesopause.

1. Introduction

A statistical study (over height and season) of wind perturbation directions, measured by the MF radar at Saskatoon (52°N, 107°W) is made. The direction (mod π) of maximum perturbation is found from σ_N, σ_E, and ρ_{NE}. The variance as a function of direction is an ellipse, and the axial ratio in conjunction with the number of wind values used defines a significance level (by comparison with randomly generated sequences), viz. the probability that the perturbations are not isotropic. The two kinds of perturbations used are those within an hour (WH) with respect to the hourly mean, and differences of consecutive hourly means (HD) occurring during a day -- the periods are approximately $\lesssim$ 1 hr, and $\sim$ 1-6 hr, respectively (data gaps within the hour cause some smearing of the period ranges).

On the assumption that these directed perturbations are a result of gravity waves (GW) propagating in the direction of maximum perturbation, an attempt is made to duplicate their measured total and seasonal characteristics with a combination of background wind filtering and (possibly) anisotropic GW direction distributions incident on the mesosphere from below.

2. DATA

Figure 1 shows the total (over height and month) histograms (number per 10° direction box) for the HD and WH perturbations with no applied confidence level (solid line) and all data falling below 80% confidence (dashed line). As expected, the theoretically more isotropic ellipses are distributed more

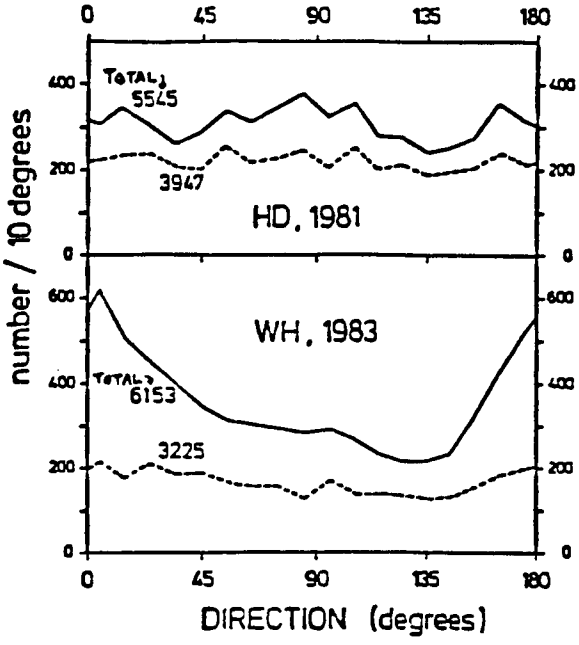

Figure 1. Histograms of ellipse tilt angle directions for long (HD) and short (WH) period wind perturbations at all heights (60–110 km): all data (solid line), and data below 80% confidence level (dashed line).

uniformly in direction. Also, the HD and WH data have different features; the former having peaks in N-S and E-W and the latter one peak at $\sim 10°$ E of N. Figures 2a and 2b show monthly % occurrence histograms for two years (these have been smoothed by a 1,1,1 filter before contouring). The HD data show that the E-W peak occurs mainly in the winter, whereas the N-S peak is present most of the year. The WH data show that N-S perturbations are more likely in the summer. Both types tend towards flatter distributions at the equinoxes.

Figures 3a and 3b divide the data into three height regions (the confidence limit had to be discarded in order to obtain sufficient data quantity).

3. MODELS

Five background wind filters are considered (Figure 4) by superposition of troposphere and stratosphere/lower mesosphere wind conditions. Except in model A, winds are assumed to vary from 0 to the maximum speed in each region. Model A assumes a minimum speed of 20 m/s (e.g., for tropospherically generated waves). Model A' (not shown) is the same as model A except that the minimum speed is 0 m/s. The hatched areas in this figure indicates forbidden phase velocities (the smallest circle excludes quasi-stationary waves in all models).

Three GW direction distributions are used: isotropic, predominantly E-W [$1 + \cos^4 (\phi - 90°)$], and northward biased [1 for $\phi = 90° - 270°$, and

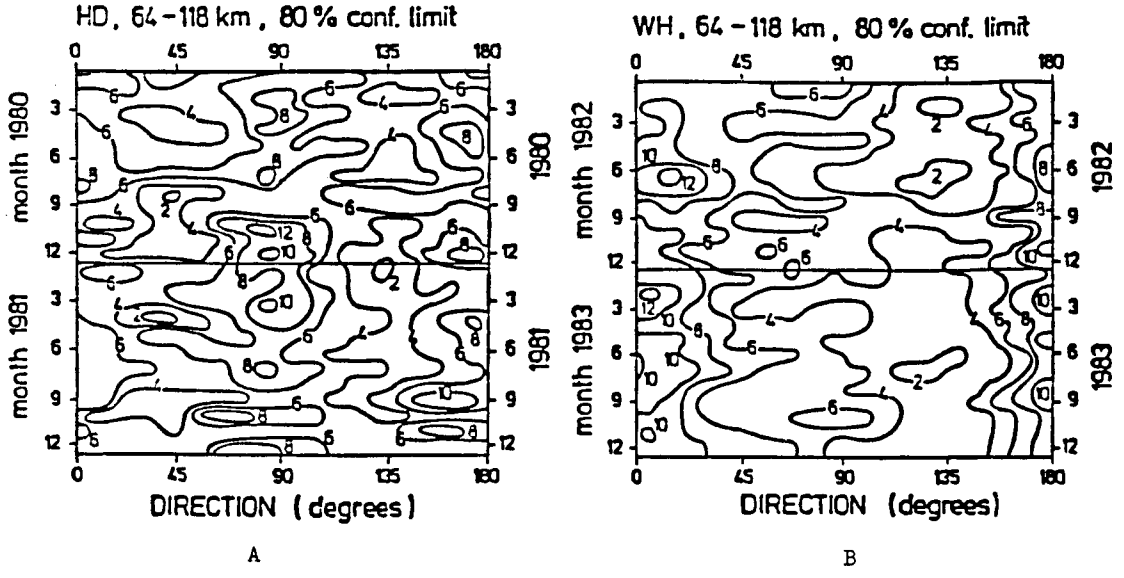

Figure 2. Smoothed monthly percentage (per 10° box) histograms over two years: long period (A) and short period (B). The nominal height range given corresponds to actual heights 60-110 km.

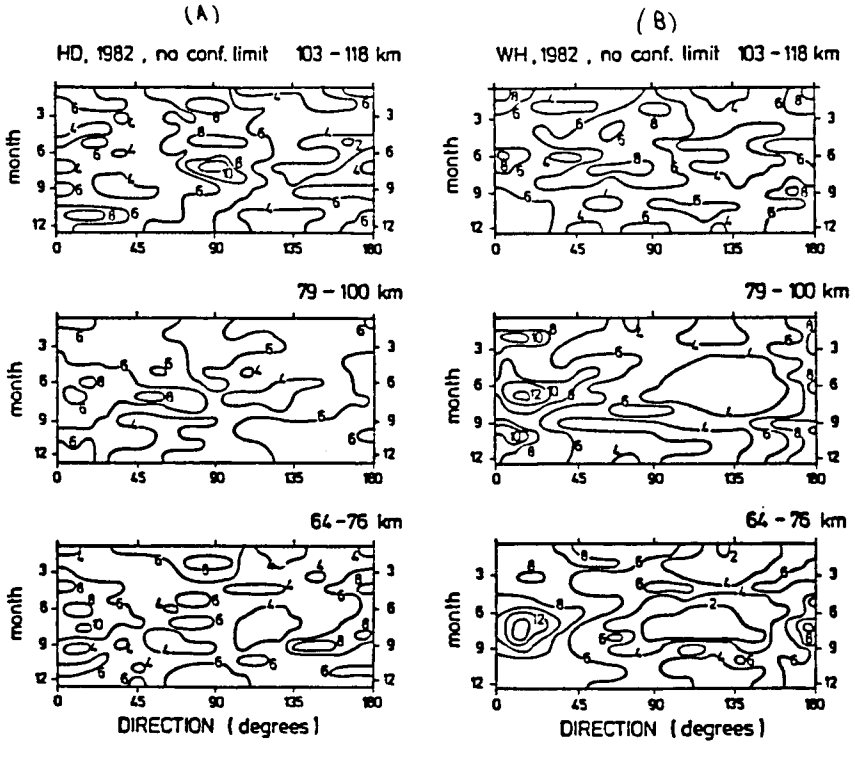

Figure 3. Height variation of direction distributions.

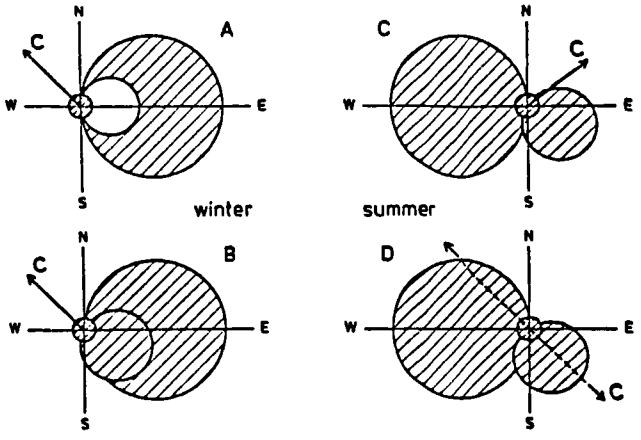

Figure 4. Model filters based on background seasonal wind characteristics. Maximum troposphere speed is 25 m/s; maximum stratosphere/lower mesosphere speed is 50 m/s; minimum wind speed (A only) is 20 m/s. Shaded areas indicate forbidden propagation for gravity waves.

1 + 0.3cos (ϕ) otherwise]. The last might simulate an increased northward flux created by thunderstorms and tornadoes in the summer. The phase speed distribution is Gaussian:

$$G(c) = \exp(c^2/2\sigma_c^2)$$

where σ_c is 30 m/s.

Predicted direction distributions created by combinations of filter and source assumptions are shown in Figure 5.

CONCLUSIONS

In such a short paper, it is impossible to discuss the results fully, but the following points may be made. For the WH data, it appears that filtering action by the predominant northwesterlies in the troposphere could be the cause of the bias towards NE perturbations in the mesosphere; also the fact that this bias is strongest in summer indicates an increase in N-S propagating waves, possibly due to thunderstorms or tornadoes. The HD data peak in the E-W direction is not easily explainable, unless the incident GW distribution has an E-W bias at these longer periods.

Wind Filter (see Fig. 4)	GW distrib. (N ↑, E →)	Curve
A'	⊙	1a
A	⊙	1b
A	⊙	2
B	⊙	3
C	⊙	4
C	⊙	5
D	⊙	6
C	⊙	7

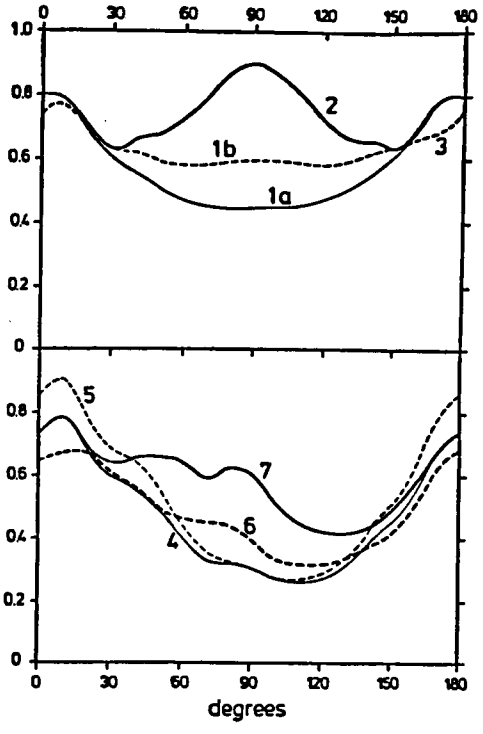

Figure 5. Theoretical direction distributions produced by combinations of different filter and GW direction distributions shown in the table (see text).

3.6.1 POSSIBILITY OF MEASURING GRAVITY-WAVE MOMENTUM FLUX BY SINGLE BEAM OBSERVATION OF MST RADAR

C. H. Liu

Department of Electrical and Computer Engineering
University of Illinois at Urbana-Champaign
Urbana, IL 61801

VINCENT and REID (1983) proposed a technique to measure gravity-wave momentum fluxes in the atmosphere by MST radars using two or more radar beams. Since the vertical momentum fluxes are assumed to be due to gravity waves, it appears possible to make use of the dispersion and polarization relations for gravity waves in extracting useful information from the radar data. In particular, for an oblique radar beam, information about both the vertical and the horizontal velocities associated with the waves are contained in the measured Doppler data. Therefore, it should be possible to extract both V_z and V_h from a single beam observational configuration. In this paper, we propose a procedure to perform such an analysis. The basic assumptions are: the measured velocity fluctuations are due to gravity waves and a separable model gravity-wave spectrum of the Garrett-Munk type that is statistically homogeneous in the horizontal plane. Analytical expressions can be derived that relate the observed velocity fluctuations to the wave momentum flux at each range gate. In practice, the uncertainties related to the model parameters and measurement accuracy will affect the results.

Let us consider an MST radar configuration. For an oblique beam, the radial velocity contains information of both $\vec{v}_h$ and v_z. The polarization relations (SCHEFFLER and LIU, 1985)

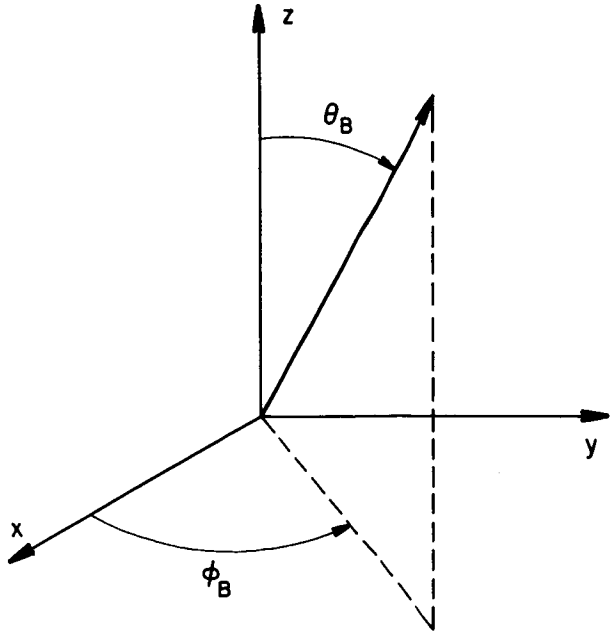

$$R_x = -\left(\frac{\omega_b^2-\omega^2}{\omega^2-\omega_i^2}\right)\left(\frac{k_x+i\frac{\omega_i}{\omega}k_y}{k_z}\right)R_z$$

$$R_y = -\left(\frac{\omega_b^2-\omega^2}{\omega^2-\omega_i^2}\right)\left(\frac{k_y-i\frac{\omega_i}{\omega}k_x}{k_z}\right)R_z$$

$$\therefore\ R_xR_z^*+R_yR_z^* = -\left(\frac{\omega_b^2-\omega^2}{\omega^2-\omega_i^2}\right)\frac{(k_x+k_y)-i\frac{\omega_i}{\omega}(k_x-k_y)}{k_z}|R_z|^2 \qquad (1)$$

On the other hand, the polarization for the observed radial velocity is given by

$$R_{0_b} = R_x\cos\phi_B\sin\theta_B+R_y\sin\phi_B\sin\theta_B+R_z\cos\theta_B \qquad (2)$$

From (1) to (2), we obtain

$$R_xR_z^*+R_yR_z^* = f(\vec{k},\omega,\phi_B)|R_{0_b}|^2$$

where

$$f = \frac{\left(\frac{\omega^2-\omega_i^2}{\omega_b^2-\omega^2}\right)k_hk_z\left[\cos\phi+\sin\phi-i\frac{\omega_i}{\omega}(\cos\phi-\sin\phi)\right]}{\left[k_h\cos(\phi-\phi_B)\sin\theta_B+\frac{\omega^2-\omega_i^2}{\omega_b^2-\omega^2}k_z\cos\theta_B\right]^2+\frac{\omega_i^2}{\omega^2}k_h\sin^2\theta_B\sin(\phi-\phi_B)} \qquad (3)$$

Spectral representation of the velocities can be written as a Fourier-Stieltjes integral:

$$v_x = \int R_x(\vec{k},\omega)\,e^{i(\vec{k}\cdot\vec{r}-\omega t)}\,d\nu(\vec{k},\omega)$$

$$v_y = \int R_y(\vec{k},\omega)\,e^{i(\vec{k}\cdot\vec{r}-\omega t)}\,d\nu(\vec{k},\omega)$$

$$v_z = \int R_z(\vec{k},\omega)\,e^{i(\vec{k}\cdot\vec{r}-\omega t)}\,d\nu(\vec{k},\omega)$$

$$v_{0_b} = \int R_{0_b}(\vec{k},\omega)\,e^{i(\vec{k}\cdot\vec{r}-\omega t)}\,d\nu(\vec{k},\omega)$$

Therefore

$$\langle v_xv_z\rangle + \langle v_yv_z\rangle = \int (R_xR_z^*+R_yR_z^*)E(\vec{k},\omega)d\vec{k}\,d\omega$$

$$= \int f(\vec{k},\omega)\,|R_{0_b}|^2\,E(\vec{k},\omega)\,d\vec{k}\,d\omega. \qquad (4)$$

where the relation

$$\langle dv(\vec{k}_1,\omega_1)\,dv(\vec{k}_2,\omega_2)\rangle = E(\vec{k}_1,\omega_1)\;\delta(\vec{k}_1-\vec{k}_2)\,\delta(\omega_1-\omega_2)\,d\vec{k}_1 d\vec{k}_2 d\omega_1 d\omega_2$$

has been used.

On the other hand, we have

$$\langle v_{0_b}{}^2\rangle = \int |R_{0_b}|^2\, E(\vec{k},\omega)\,d\vec{k}\,d\omega$$

$$|R_{0_b}|^2 = \left[\left(\frac{\omega_b{}^2-\omega^2}{\omega^2-\omega_i{}^2}\right)^{1/2}\frac{k_h}{k}\cos(\phi-\phi_B)\sin\theta_B - \left(\frac{\omega^2-\omega_i{}^2}{\omega_b{}^2-\omega^2}\right)^{1/2}\frac{k_z}{k}\cos\theta_B\right]^2$$

$$+\left(\frac{\omega_b{}^2-\omega^2}{\omega^2-\omega_i{}^2}\right)\frac{k_h{}^2}{k^2}\left(\frac{\omega_i}{\omega}\right)^2\sin^2(\phi-\phi_B)\sin^2\theta_B \qquad (5)$$

Procedure proposed for computing the momentum flux:

1. Assume a model spectrum $E(\vec{k},\omega)$ with several parameters, including possible anisotropy.
2. Fit the theoretical spectrum $E_{0_b}(\omega)$ to the observed radial velocity spectrum to determine the best set of parameters for the model. This determines the model.
3. Use this model, compute through equations (4) and (5)

Discussion:

1. This procedure assumes the spectral shape remains approximately the same at different heights and they are due to gravity waves.
2. The spectral fitting procedure depends on how sensitive is the spectrum due to changes of model parameters. This should be studied.
3. It is expected noise in observed spectra due to the uncertainties related to the model parameters and measurement inaccuracy may greatly affect the results.
4. In principle, the procedure should also apply to cases with Doppler shift. However, unless one has information about the background wind vector, the model may contain too many parameters for realistic spectral fitting.

REFERENCES

Scheffler, A. O., and C. H. Liu (1985), On observation of gravity wave spectrum in the atmosphere by using MST radars, Radio Sci., 20, 1309-1322.

Vincent, R. A., and I. M. Reid (1983), HF Doppler measurements of mesospheric gravity wave momentum fluxes, J. Atmos. Sci., 40, 1321-1333.

3.6.2 PRELIMINARY ESTIMATES OF VERTICAL MOMENTUM FLUX

G. D. Nastrom

Control Data Corporation
Minneapolis, MN 55440

and

J. L. Green

NOAA, Aeronomy Laboratory
Boulder, CO 80303

INTRODUCTION

The capability of ST radars to provide direct measurements of the momentum flux presents an opportunity for major advances in atmospheric science. Some of the issues, needs, and techniques surrounding the measurement of momentum flux are discussed by FRITTS (1984) and SCHOEBERL (1984), among others. The vertical momentum flux was first measured using the two-beam technique by VINCENT and REID (1983), who used mesospheric observations. They also presented the body force due to the vertical divergence of the vertical momentum flux. CORNISH and LARSEN (1984) examined the vertical momentum flux at 14.5 km over Arecibo, but did not look into the momentum flux divergence. It appears that no other results from the troposphere and stratosphere are available.

The purpose of this paper is to present preliminary results of momentum flux and momentum flux divergence calculations made using data from the Sunset radar. In an attempt to illustrate changing conditions, we present results from a day when the background wind speeds aloft changed abruptly.

DESCRIPTION OF THE EXPERIMENT

The Sunset radar (GREEN et al., 1985) is located in a narrow mountain canyon 15 km west of Boulder, Colorado, and is just east of the Continental Divide. The array antenna of this VHF (ST) pulsed Doppler radar can be steered in the east-west or north-south vertical plane. During the experiment reported here, five antenna beam positions were used: vertical and 15° to the east, west, north, and south. Three consecutive observations were made at each beam position at 90-second intervals and then the beam was moved. A full cycle could thus be made each 20 minutes. The relative locations of the radar volumes are illustrated in Figure 1.

The synoptic situation early in the day chosen, January 28, 1985, was characterized by light winds throughout the height region sampled by the radar (from about 4 to 14 km). After about 15 UT, a weak jet stream sagged southward with winds at 10 km over the radar increasing from 10 m/s to over 30 m/s by 18 UT. Winds at all levels above 4 km were primarily from the west; surface wind data were not available.

The method of VINCENT and REID (1983) was used for this calculation. The vertical momentum flux, $\overline{u'w'}$ or $\overline{v'w'}$, is found from

$$\overline{u'w'}(z) = \left[\overline{V^2(\theta,R)} - \overline{V^2(-\theta,R)}\right] / (2 \sin 2\theta)$$

where V is the radial velocity, θ is the antenna beam angle, R is the range and z is the altitude. Altitudes from 4 to 14 km were sampled at 1-km intervals. Decreasing signal-to-noise sometimes rendered the upper level useless.

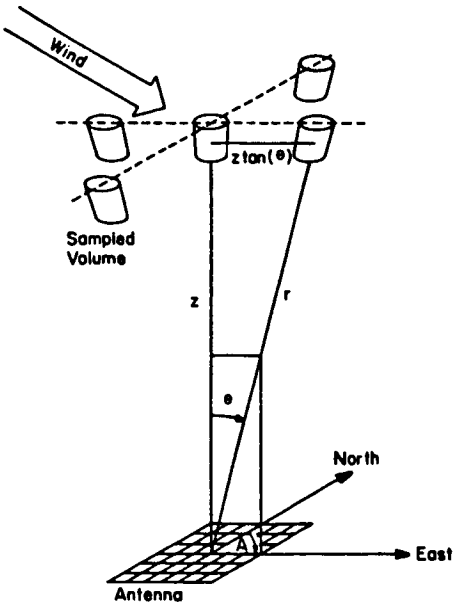

Figure 1. Schematic depiction of the radar beams positions at Sunset.

The calculation was made at a given height only if all beam positions were sampled every cycle during a full hour. Averaging periods of one hour and three hours were used; as the results are similar except that the three-hourly values are obviously smoothed, we have chosen to present the one-hour results in order to capture as much detail of the effects of transients as possible.

Figure 2 shows the hourly momentum flux from 00-18 UT. Values for the meridional component $\overline{v'w'}$ are typically a few tens of cm^2/s^2 from about 00-09 UT, and then increase in magnitude to on the order of a m^2/s^2 after 09 UT. The most notable event is found below 5 km at 10-12 UT, when $\overline{v'w'}$ reached over -20 m^2/s^2. The values for the zonal component $\overline{u'w'}$ are usually less than a few m^2/s^2 before 09 UT, although a few magnitudes exceed 10 m^2/s^2. These results can be compared with the aircraft measurements given by LILLY and KENNEDY (1973). They report horizontally averaged momentum flux values of about 8 dynes/cm^2 (which corresponds with 2 m^2/s^2 for mean density of 5 x 10^{-4} g/cm^3); although their traces of integrated momentum flux show large variability, indicating local values range far from the mean. At 10-12 UT a maximum is found in $\overline{u'w'}$ at the same location where a minimum was found in $\overline{v'w'}$. After 12 UT the values of $\overline{u'w'}$ generally exceed 10 m^2/s^2 above 8 km, with a local minimum found at 11 km at 18 UT.

Figure 3 shows the vertical flux divergence of meridional and zonal momentum. These results were computed from the data in Figure 2 by taking differences across layers 1 km apart. No smoothing has been applied in an effort to preserve as much detail in the results as possible. The units used, 10^{-3} m/s^2, correspond to 3.6 m/s/hour (e.g., the contour labelled $10x10^{-3}$ m/s^2 is the same as 36 m/s/hour). In Figure 3, the large values of zonal and meridional momentum flux divergence occur near 6 km at 10-12 UT. Otherwise, the meridional values are nearly all less than about 3 units. Alternating periods of large zonal values are found above 10 km at 14-18 UT. After about 11 UT, the contours of zero zonal momentum flux divergence slope

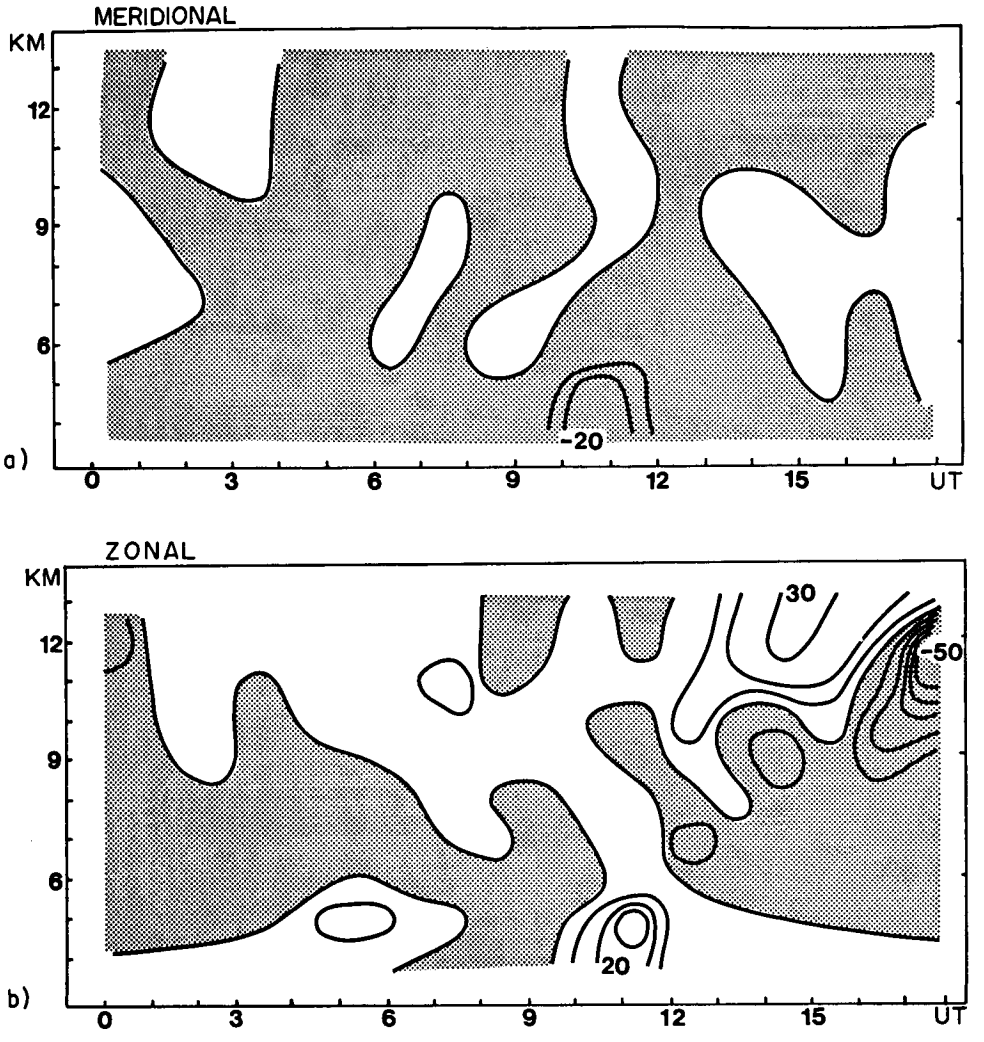

Figure 2. Time-height section of the vertical momentum flux at Sunset on January 18, 1985. Units: m^2/s^2. (a) meridional (b) zonal.

upward to the right, while at the same time the contours of zero meridional flux slope downward to the right. The significance of this pattern, if any, is not yet clear.

CONCLUSION

We have presented preliminary results of the momentum flux and flux divergence during a transient episode, as a jet stream moved over the radar. The zonal and meridional momentum flux and flux divergences displayed remarkable continuity with altitude in time, increasing in intensity as lee waves and other gravity-wave activity developed while the jet stream approached. The momentum flux values observed compare favorably with aircraft measurements made over similar topography, at least during the early part of the day. The accelerations due to the momentum flux divergence seem rather large at first

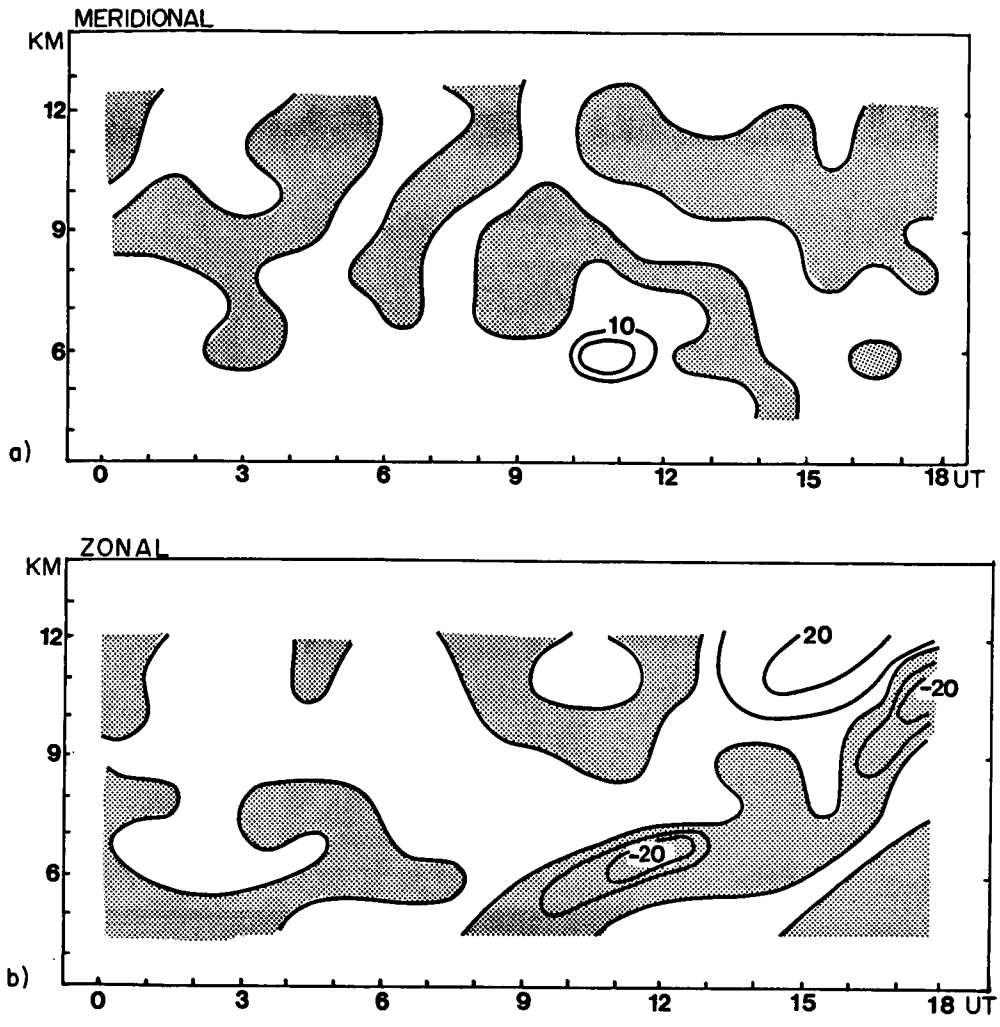

Figure 3. Time-height section of the vertical divergence of the vertical momentum flux at Sunset on January 28, 1985. Units: 10^{-3} m/s^2. (a) meridional (b) zonal.

glance, especially for the late part of the day. However, we note that there may be compensating forces due to effects not considered here, such as transverse circulations or, likely more important, scales of motion too small to be resolved by these data.

REFERENCES

Cornish, C. R., and M. F. Larsen (1984), Use of the VAD technique and measurements of momentum flux in the stratosphere at Arecibo, Handbook for MAP, 14, 208-210.

Fritts, D. C. (1984), Momentum flux measurements; techniques and needs, Handbook for MAP, 14, 216-218.

Green, J. L., J. M. Warnock, W. L. Clark, and T. E. VanZandt (1985), Recent results at the Sunset Radar, Handbook for MAP, this volume.

Lilly, D. K., and P. J. Kennedy (1973), Observations of a stationary mountain wave and its associated momentum flux and energy dissipation, J. Atmos. Sci., 30, 1135-1152.

Schoeberl, M. R. (1984), Techniques for the study of gravity waves and turbulence, Handbook for MAP, 14, 179-182.

Vincent, R. A., and I. M. Reid (1983), HF Doppler measurements of mesospheric gravity wave momentum fluxes, J. Atmos. Sci., 40, 1321-1333.

3.7.1 EFFECTS OF ANISOTROPY ON THE FREQUENCY SPECTRUM OF GRAVITY WAVES OBSERVED BY MST RADAR

C. H. Liu

Department of Electrical and Computer Engineering
University of Illinois at Urbana-Champaign
Urbana, IL 61801

In the investigation of gravity waves using MST radar data, model gravity-wave spectra have been used. In these model spectra, one usually assumes azimuthal symmetry. The effect of spectral anisotropy on the observed spectrum is studied in this paper. It will be shown that for a general Garrett-Munk-type spectrum, the anisotropy does not affect the frequency spectrum observed by the vertically beamed radar. For the oblique beam, however, the observed frequency spectrum is changed.

Let us consider a general gravity wave spectrum including azimuthal anisotropy:

$$E(\vec{k},\omega) = \frac{1}{4\pi k_h} E_0 A(k_z) B(\omega) F(\phi) \delta[k_h - (\frac{\omega^2-\omega_i^2}{\omega_b^2-\omega^2})^{1/2} |k_z|] \tag{1}$$

Next, let us consider the following two parameter model of anisotropy:

$$F(\phi) = 1+a \cos 2(\phi-\phi_0) \tag{2}$$

Then it can be shown that the observed spectrum is given by (SCHEFFLER and LIU, 1985),

$$E_{0_b}(\omega) = E_0 H(\omega) \cdot B(\omega) \tag{3}$$

where

$$H(\omega) = \frac{\omega^2-\omega_i^2}{\omega_b^2-\omega_i^2} \cos^2\theta_B + \frac{\omega_b^2-\omega^2}{\omega_b^2-\omega_i^2} \sin^2\theta_B [1-\frac{1}{2}(1-\omega_i^2/\omega^2)(1-\frac{a}{2}\cos 2(\phi_B-\phi_0))] \tag{4}$$

θ_B: zenith angle of radar beam, ϕ_B: azimuth angle of radar beam. The effects of anisotropy are included in (4). It is possible to determine a and ϕ_0 of the anisotropy model in the following manner.

For any $\theta_B \neq 0$, take three beam measurements at $\phi_{B1}=0°$, $\phi_{B2}=90°$ and $\phi_{B3}=45°$.

Let

$$A = \langle v_{0_{b1}}^2 \rangle - \langle v_{0_{b2}}^2 \rangle \tag{5}$$

$$B = 1/2 [\langle v_{0_{b1}}^2 \rangle + \langle v_{0_{b2}}^2 \rangle] \tag{6}$$

$$C = \langle v_{0_{b3}}^2 \rangle - B \tag{7}$$

where $\langle v_{0_{bj}}^2 \rangle$ is the variance of observed velocity fluctuation along the j-th beam position.

Then we have

$$\phi_0 = 1/2 \tan^{-1} \left(\frac{2C}{A}\right) \tag{8}$$

$$a = \frac{3A}{E_0 \cos 2\phi_0 \sin^2 \theta_B} \tag{9}$$

E_0, the total power associated with the wave spectrum, can be determined from the spectrum, or additional vertical beam measurement.

We note from equation (4), for vertical beam, $\theta_B = 0°$, the anisotropy does not affect the observed spectrum. The two parameter anisotropy model, equation (2) is a rather simple one. It does, however, contain some of the most important features of an anisotropic spectrum. Therefore, the results in (3) and (4) are expected to present some of the important effects on observed gravity-wave spectrum due to anisotropy.

REFERENCE

Scheffler, A. O., and C. H. Liu (1985), On observation of gravity wave spectrum in the atmosphere by using MST radar, Radio Sci., 20, 1309-1322.

3.7.2 THE FREQUENCY SPECTRUM OF C_n^2 FROM MST RADAR DATA

G. D. Nastrom

Control Data Corporation
Minneapolis, MN 55440

INTRODUCTION

In a recent study (NASTROM et al., 1986), the variability of the refractivity turbulence structure constant, C_n^2, was examined using observations from the ST/MST radars at Poker Flat, Alaska, and Platteville, Colorado. Variations of C^2 with height, season, and weather conditions were examined. Also, the autocorrelation function and the frequency distribution of C_n^2 were studied, and it was shown that C_n^2 follows a log-normal frequency distribution. The interested reader is referred to that paper for details. One of the more tentative results given in that paper is a first look at the spectrum of log C_n^2 as a function of frequency at Poker Flat. This spectrum, shown in Figure 1, appears to obey a power law relation with frequency, $P(F) \sim F^k$, with k near -5/3 at periods between about 4 hours and 6 days, and with k near -1 at shorter periods. Power law behavior of a spectrum often helps us to infer the underlying dynamics which give rise to this spectrum, and it is thus of some concern to establish further confidence in the spectral shape. For example, is the shape displayed in Figure 1 representative of other altitudes or locations, and does it change with season or background weather conditions. The purpose of this contribution is to address these questions.

SPECTRAL ANALYSIS RESULTS

Figure 2 shows the spectra of C_n^2 in the troposphere at Poker Flat (8.2 km) and Platteville (7.3 km) over the range of periods from about 9 minutes to 24 hours. These results are based on a larger data set than that used in Figure 1 as indicated by N in the figure. N is the number of 9-hour or 36-hour data segments used to estimate the spectrum. The lag correlation method was used. The lines with slopes -5/3 and -1 have been added at the same coordinates as in Figure 1 to aid comparison. At both stations in Figure 2, the spectral shape is approximately the same as in Figure 1, with a change in slope found near the 2-4 hour period. The spectral amplitude at Platteville is higher than that at Poker Flat at periods less than about 2 hours. Note that all spectra show a markedly decreased slope at periods less than about 15 minutes. As discussed by NASTROM et al. (1986), this behavior may be due to noise or aliasing, or may arise from reduced spectral fidelity due to occasional gaps in the data (BAER and TRIBBIA, 1976).

Figure 3 shows the spectra at Poker Flat at 12.5 km for periods from about 9 minutes to 6 hours for summer (May-August) and winter (October-April). There is no obvious change with season, except that the spectral amplitude appears slightly higher in summer than in winter.

The results in Figures 1-3 strongly suggest that the shape of the spectrum of log C_n^2 is fairly universal, and shows little dependence on season, location, or across the tropopause. As a check on possible synoptic weather dependence, the mean spectrum was formed for the 97 cases when the background wind speed near the tropopause was in excess of 21 m/s^{-1}. The results, not shown, are nearly identical to the winter results in Figure 3 and show that strong background wind does not distort the spectrum.

The -1 slope region of the spectrum was not anticipated, and warrants further attention. Current theories of gravity wave motions and quasi-two-

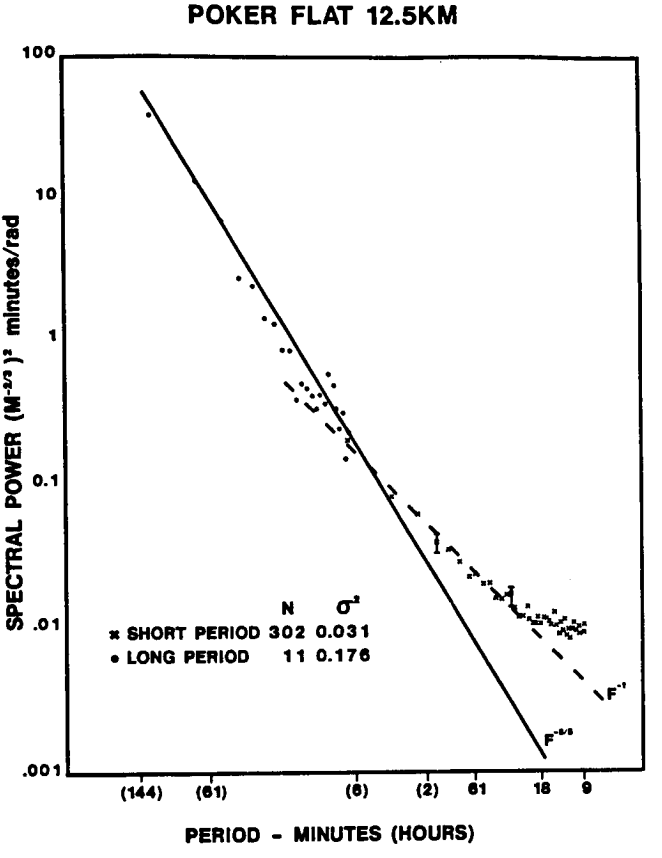

Figure 1. The variance power spectrum of log C_n^2 at 12.5 km at Poker Flat (NASTROM et al., 1985).

dimensional turbulence do not predict a -1 slope region. However, due to its robust statistical character and firm observational basis, it cannot be ignored. Beside the present results, a -1 slope region was noted by BALSLEY and CARTER (1982) in the spectrum of radial velocities. Also, a -1 slope region was found by NASTROM and GAGE (1983) in the wave number spectrum of winds encountered by airplanes during and immediately after encounters with moderate turbulence. HARRINGTON and HEDDINGHAUS (1974) noted a -1 slope in winds near the surface at periods below about 2 hours. Finally, the spectrum of ozone in the upper troposphere shows a -1 slope region at wavelengths less than about 100 km as found by NASTROM et al. (1985), and as shown in detail in Figure 4. These results are based on data collected during GASP from aircraft and represent the average spectrum over N flight segments, where N is given in the figure. Mean ozone values less than 150 ppbv or so are typical of the troposphere.

DISCUSSION

In summary, the shape of the frequency spectrum of log C_n^2 is fairly universal; showing a -5/3 slope region at long periods and a -1 slope region at periods below 4 hours or so. Other meteorological data have also shown a -1

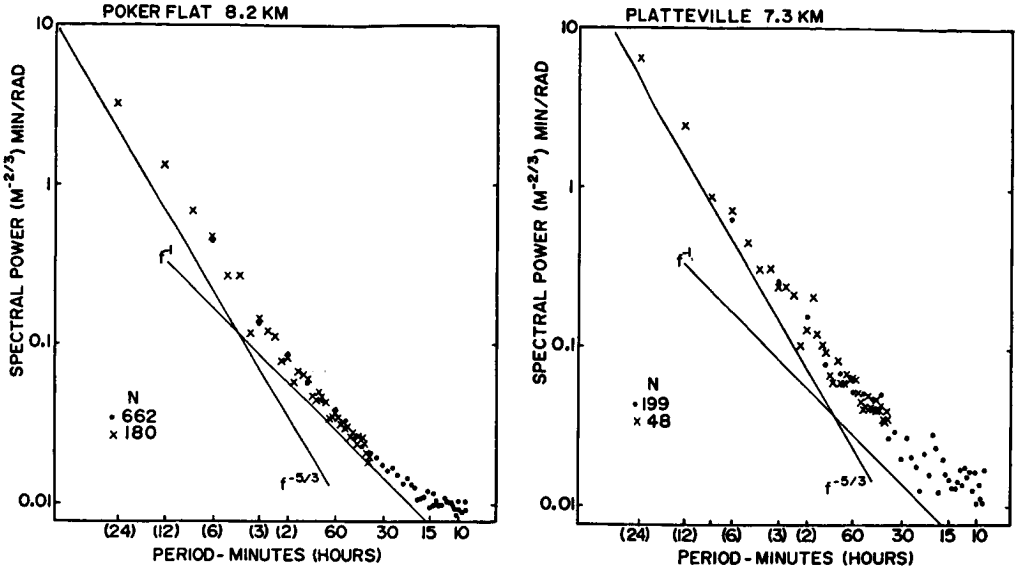

Figure 2. Power spectrum of log C_n^2 (a) Poker Flat at 8.2 km, (b) Platteville at 7.3 km.

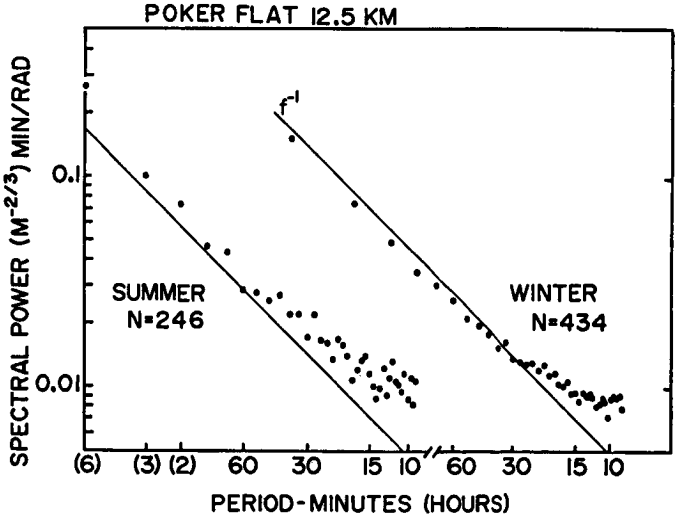

Figure 3. Power spectrum of log C_n^2 at 12.5 km at Poker Flat during summer (May-August) and winter (October-April), over the range of periods from about 9 minutes to 6 hours.

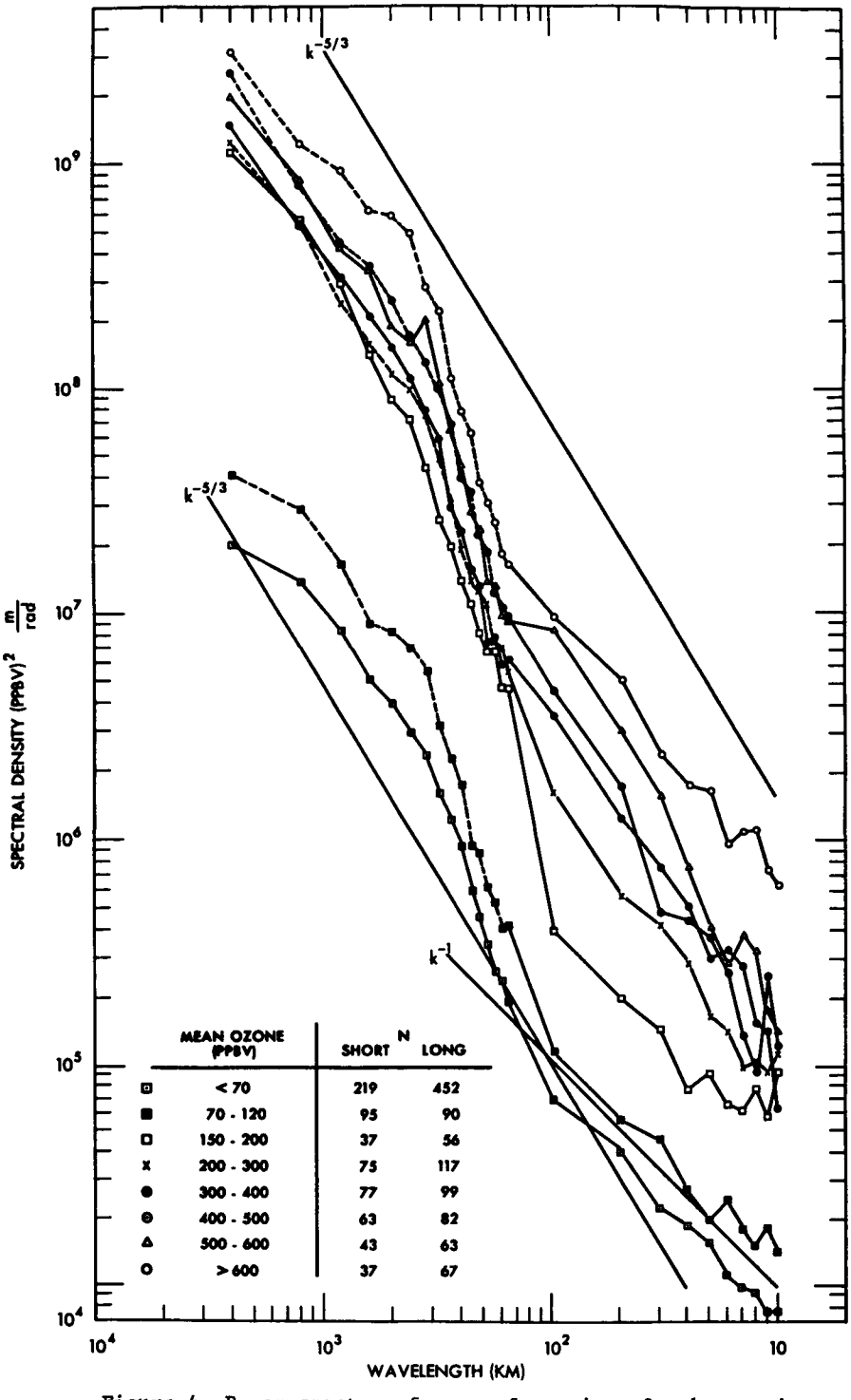

Figure 4. Power spectra of ozone from aircraft observations made during GASP, grouped according to the mean ozone along each flight segment.

slope region, indicating this signature is not specific to C_n^2. The -1 slope region is not anticipated by current theories. Important clues toward understanding it may be that it is associated with rather high levels of turbulence in the airplane wind data, and is the most apparent in ozone near the tropopause where folding processes may contribute significantly to the variance of ozone. LILLY (1983) predicted that two-dimensional decay spectra propagate in wave number space with the wave number and amplitude of the spectral peak following an approximately k^{-1} curve. When many such events are superposed, it is presumed that the net spectrum follows $k^{-5/3}$. However, it may turn out that when intense individual events are combined, as done here, the average spectrum retains a k^{-1} dependence. This issue will clearly require more attention in the future.

ACKNOWLEDGEMENTS

Discussions with Drs. K. S. Gage, W. L. Ecklund, and R. G. Strauch are gladly acknowledged. This work was supported by the Air Force Office of Scientific Research.

REFERENCES

Baer, F., and J. J. Tribbia (1976), Spectral fidelity of gappy data, Tellus, 28, 215-227.

Balsley, B. B., and D. A. Carter (1982), The spectrum of atmospheric velocity fluctuation at 8 km and 86 km, Geophys. Res. Lett., 9, 465-468.

Harrington, J. B., and T. R. Heddinghaus (1974), Determinism in mesoscale wind spectra at Columbia, Missouri, J. Atmos. Sci., 31, 727-737.

Lilly, D. K. (1983), Stratified turbulence and the mesoscale variability of the atmosphere, J. Atmos. Sci., 40, 749-761.

Nastrom, G. D., and K. S. Gage (1983), A first look at wavenumber spectra from GASP data, Tellus, 35A, 383-388.

Nastrom, G. D., K. S. Gage, and W. H. Jasperson (1985), Wavenumber spectra of ozone from GASP aircraft measurements, in Atmospheric Ozone, edited by C. S. Zerefos and A. Ghazi, D. Reidel, Boston, 580-584.

Nastrom, G. D., K. S. Gage, and W. L. Ecklund (1986), The variability of turbulence, 4 to 20 km, in Colorado and Alaska from MST radar observations, J. Geophys. Res., in press.

3.7.3. A STUDY OF GRAVITY-WAVE SPECTRA IN THE TROPOSPHERE AND STRATOSPHERE AT 5-MIN TO 5-DAY PERIODS WITH THE POKER FLAT MST RADAR

R. S. Bemra, P. K. Rastogi

18927

Electrical Engineering and Applied Physics Department
Case Western Reserve University
Cleveland, Ohio 44106

and

B. B. Balsley

Aeronomy Laboratory
National Oceanic and Atmospheric Administration
Boulder, Colorado 80303

1. INTRODUCTION

The wind field in the middle atmosphere can be decomposed into a continuum of spatial and temporal scales. At short time scales (of the order of 0.1-3 hr) the wind field is dominated by transient buoyancy waves with horizontal wavelengths of a few km to several hundred km. With recent improvements in the MST radar technique, it has become possible to measure, almost continuously, the velocity field at fixed altitudes for periods longer than a month (GAGE and BALSLEY, 1984; LARSEN et al., 1982). Instrumented aircrafts provide similar measurements along flight paths that are at least a few thousand km long (see e.g. LILLY and PETERSEN, 1983; NASTROM and GAGE, 1983).

Kinetic-energy spectra of the horizontal wind field obtained from several sets of such measurements show distinct power-law behaviors with frequency and wave number over wide range of scales extending to several days in time and several thousand km in the horizontal. A simple and direct scaling between the frequency and wave-number spectra exists under the Taylor Hypothesis, that the perturbations move with the mean horizontal wind without deformation (in a statistical sense). This makes possible first-order comparisons of frequency an wave-number spectra.

A mesoscale power-law behavior, $S(f) \sim f^{+n}$ or $S(k) \sim k^{+n}$ of the frequency (f) and the horizontal wave-number (k) spectra (S) has been reported in several studies with values of the spectral index (or slope) n in the vicinity of -5/3 (see e.g. GAGE, 1979; BALSLEY and CARTER 1982; NASTROM and GAGE, 1983, 1985). It has been suggested that the associated horizontal velocity perturbations in the atmosphere are either a manifestation of two-dimensional turbulence (GAGE and NASTROM, 1984) or of a universal cascade of buoyancy waves (VANZANDT, 1982).

In this paper, we present an analysis of frequency spectra at periods of about 5 days to 5 min from two 20-day sets of velocity measurements in the stratosphere and troposphere (ST) region obtained with the Poker Flat MST radar during January and June, 1984.

In Section 2, we outline a technique based on median filtering and averaged order statistics for automatic editing, smoothing and spectral analysis of velocity time series contaminated with spurious data points or outliers. The validity of this technique and its effects on the inferred spectral index has been tested through simulation. Spectra obtained with this technique are discussed in Section 3. The measured spectral indices show variability with season and height, especially across the tropopause. The discussion in Section 4 briefly outlines the need for obtaining better

climatologies of velocity spectra and for refinements of the existing theories to explain their behavior.

2. MEDIAN FILTERING, EDITING, SMOOTHING, AND SPECTRAL ANALYSIS OF VELOCITIES

MST radar provide measurements of radial velocity at selected ranges from spectral moments of the scattered signal. Spectra of the scattered signals are often contaminated with external interference, which produces spurious estimates of radial velocities. These spurious velocity values often occur as large, single or multiple spikes. Unless the spurious values, called outliers, can be successfully detected and removed, they would tend to introduce a whitening of high-frequency components in the velocity spectra. The velocity spectra are commonly obtained through discrete Fourier transform (DFT) of the uniformly sampled velocity time series using the fast Fourier transform (FFT) algorithm.

The spectrum S(f) is usually approximated by the time-averaged periodogram [P(f)], which is the squared magnitude of the Fourier transform. Periodogram provides only a distorted estimate of the spectrum. This distortion is most severe in the presence of trends or a slowly varying mean value component and arises due to aliasing of the autocorrelation function. Presence of a trend in the velocity data is likely to produce spectra with an inverse-square frequency dependence, or a spectral index n = -2. The simplest way to remove trends is to subtract the dc value from each segment of the velocity time series before spectral analysis. This has been done for the analysis described in this paper.

The spectral index (n) is obtained by a least-square error fit or regression of the form: $\log S(f) = n \log f + c$, where c is a constant. Equi-spaced frequency points tend to become clustered at high frequencies along the log f axis. This tends to bias n towards the high-frequency end, where the effect of outliers is likely to be most serious. To minimize this bias, it is necessary (i) to implement a scheme for locating outliers, and interpolating or smoothing through their locations and gaps; and (ii) to obtain the spectra of smoothed velocity time series in several bands of approximately equal width on the log f axis, with a proportionate number of points in each band.

Figure 1(a) shows the radial velocity time series at 10.3 km height for an off-vertical antenna. This series was sampled at 1-min intervals over 16.3 hr or 1000 min. Many outliers can be seen distinctly since they clearly do not belong with the rest of the data. If the velocity changes associated with the outliers are real, they would imply accelerations that cannot be justified on physical grounds. There also was a gap of about 5.5 hr near the middle. Figure 1(b) shows a filtered and interpolated time series that has been smoothed through a 30-min window, at 15-min intervals. The filtering and interpolation procedure is briefly outlined below.

Since some smoothing of time series is desirable, we prefer to look at all the N points within a smoothing window collectively. Suppose these points are sorted by their numerical values in an ascending or descending sequence. Outliers occur mostly near the top and the bottom of this sequence, whereas most of the valid data points tend to be clustered about the median. Median is a robust indicator of location with respect to outliers. If we reject x% of the highest and x% of the lowest points, and average over the remaining then this average will be almost unaffected by outliers. It is not necessary to sort (or order) all the N points. Sorting is needed for only x% of the highest and x% of the lowest values. Two types of errors can occur in this averaging scheme depending on N and x: a valid data point may be mistaken for an outlier, and an outlier may be mistaken as a valid data point. These errors are analogous to those encountered in transmission of signals over noisy

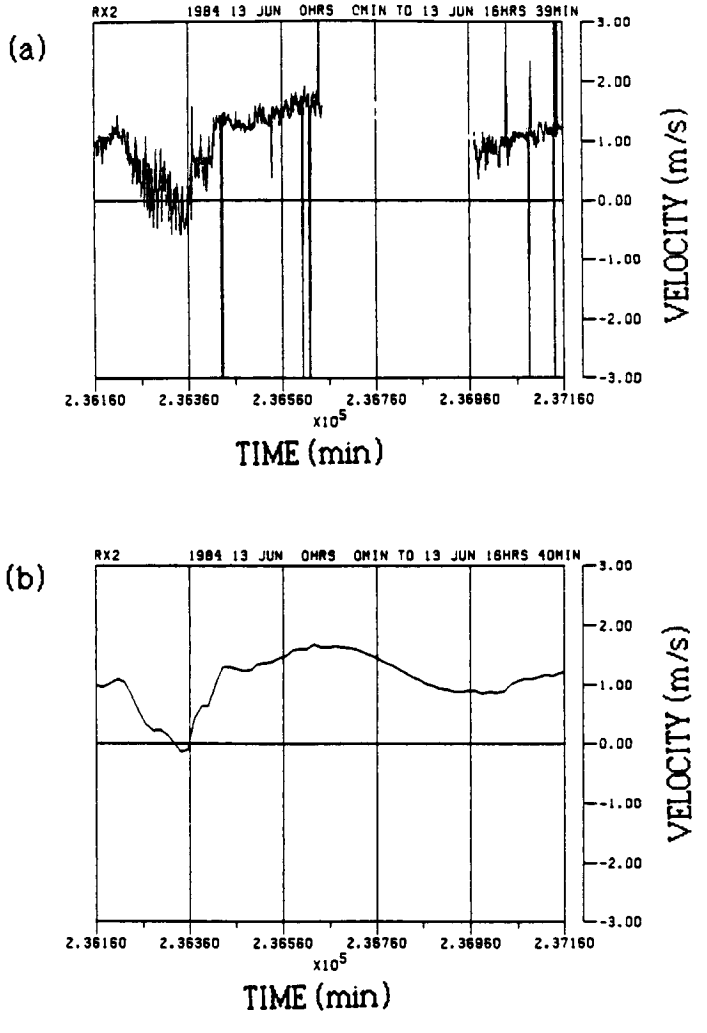

Figure 1. (a) Unedited time series of radial velocity for a 1000-min period observed with the Poker Flat MST radar, showing outliers and a 5.5-hr data gap. (b) Same time series after 30-min median filtering, smoothing, and interpolation with cubic splines. (Data for receiver 2, 13 June, 1984, 00 hr 00 min to 16 hr 39 min; Height 10.33 km.)

communication channels. Prior statistical information about data points and outliers (if available) can be used to minimize these errors. An alternative approach is to experiment with different values of rejection levels x. In the analysis of Poker Flat data we have found that for N = 30, rejection levels x = 7.5, 10 and 20% did not produce a significant effect on smoothed averages. A rejection level of 10% was used in subsequent analyses. For small values of N(<10) smoothing is not desirable, but median still provides reasonable outlier rejection. In many of the cases examined, the outlier-rejection schemes based on median and order statistics, perform as well as a human editor.

A few long gaps can be filled by interpolation of data smoothed through a median filter discussed above. We have used Cubic Splines (DEBOOR, 1978) as interpolating functions. To avoid instabilities in interpolation, it is recommended that the average slopes at the end points of each gap should be calculated separately and used to constrain the interpolated results. Most stable results are obtained by setting this slope to zero, e.g., by duplicating the end points in the gap.

Figure 2 shows a composite spectrum of meridional wind obtained from radial velocities measured along three pointing directions, one of which is close to vertical and two are 15 deg off vertical in two orthogonal planes. The spectrum was obtained from 20-day long, almost continuous velocity measurements with a 1-min time resolution. It covers a frequency range of over 3 decades for periods corresponding to 5 days–5 min and was obtained separately over three overlapping bands, each over a decade wide.

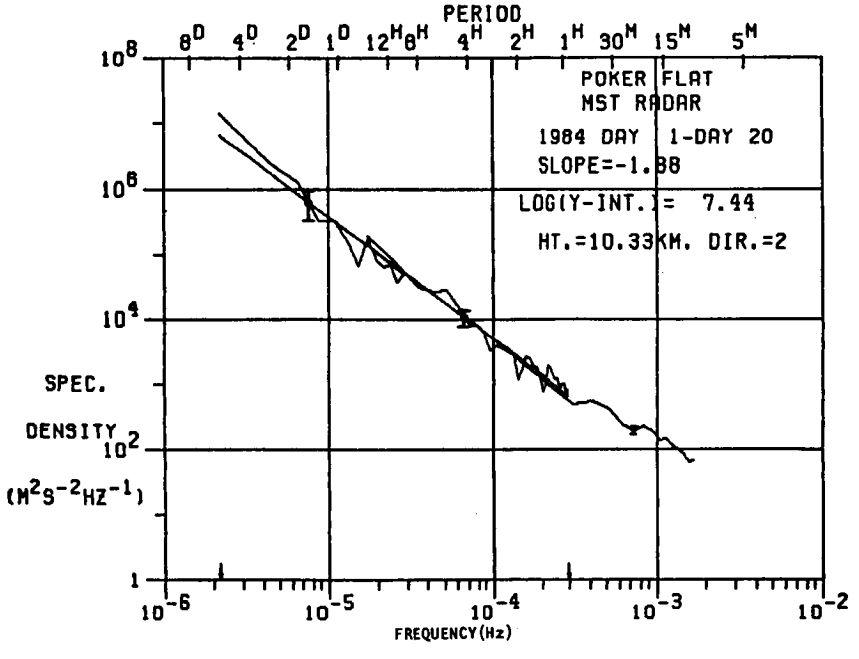

Figure 2. A composite spectrum of meridional winds obtained in three overlapping bands, each about 1 decade wide. Arrows show the frequency range (periods about 1 hr to 5 days) over which a spectral index was obtained through linear regression. Uncertainties in the spectrum estimates are also shown. (Data for January 1 to January 20, 1984.)

For the low and intermediate frequency bands, first the radial velocities were subjected to median filtering through a 30-min running window at 15-min intervals. The radial velocities were further smoothed for each frequency band, and decomposed into the three orthogonal velocity components: zonal, meridional and vertical. This decomposition is possible only for velocities smoothed over time scales of 1 hr or more. The spectrum was then computed as the averaged periodogram over each band. The number of periodograms averaged was 4 for the low and 15 for the intermediate frequency band.

For the high frequency band, the radial velocities cannot be resolved into orthogonal components due to the presence of short-period gravity waves. It is possible, however, to combine and rescale the spectra of radial velocities to obtain the spectra of the orthogonal components. The radial velocities were screened through a 5-point running median filter, with the output sampled at 2.5-min intervals. No attempt was made to interpolate through gaps. Approximately 80-90 periodograms obtained from short continuous segments were averaged over the entire 20-day period. The averaged periodograms of radial velocities were combined and rescaled to obtain the spectra of orthogonal velocity components.

The uncertainties in the estimation of the composite spectra are shown by the error bars for each frequency band (see e.g., BLACKMAN and TUKEY, 1958 or OPPENHEIM and SCHAFER, 1975) at one standard deviation level. The uncertainty is smallest at the highest frequencies due to the larger number of periodograms averaged in this band. In conventional methods of spectral analysis all the frequency points are equispaced, and the uncertainty in the spectrum magnitude is uniform throughout. The uncertainty in estimating the spectral index (n) through exponential regression (linear regression of log S(f) versus log f) is described in statistical texts (e.g., BROWNLEE, 1965). Through the use of composite spectra the uncertainty in spectral magnitude is considerably reduced at higher frequencies. Within an uncertainty of one standard deviation in spectral magnitude, composite spectra provide estimates of spectral index to within ± 0.1 over three decades and to within ± 0.15 over two decades. The composite spectra shown in Figure 2, show a distinct power-law behavior over three decades of frequency. In this example the spectral index obtained by regression (at 5 day - 1 hr periods) was -1.88. We have, however, tried to obtain additional confidence in the performance of analysis methods outlined above as follows.

The spectra and spectral slopes were also independently estimated by the correlation method. The results obtained by the two methods were almost identical and did not show any systematic differences. This indicates the effectiveness of trend removal used in the periodogram method in reducing distortions of spectra.

As an alternative check, time series for spectra with known spectral indices were synthesized as the sum of a large number of sinusoids in random phase. To these, random outlier values and data gaps were added with about the same statistics as in the original data. Median filtering and spectrum analysis of the synthesized time series recovered the spectral index to within 5% to 10% in all cases considered. We, therefore, conclude that the departures of spectral index from the 5/3rd shape as shown for example in Figure 2, are significant.

3. VARIATION OF SPECTRAL INDEX WITH HEIGHT AND SEASON

The composite spectra for several ST heights (8 - 23 km at 2.2 km step) and for all the three orthogonal velocity components are shown for 20 days of January, 1984 data in Figure 3. For clarity, the spectra for different heights

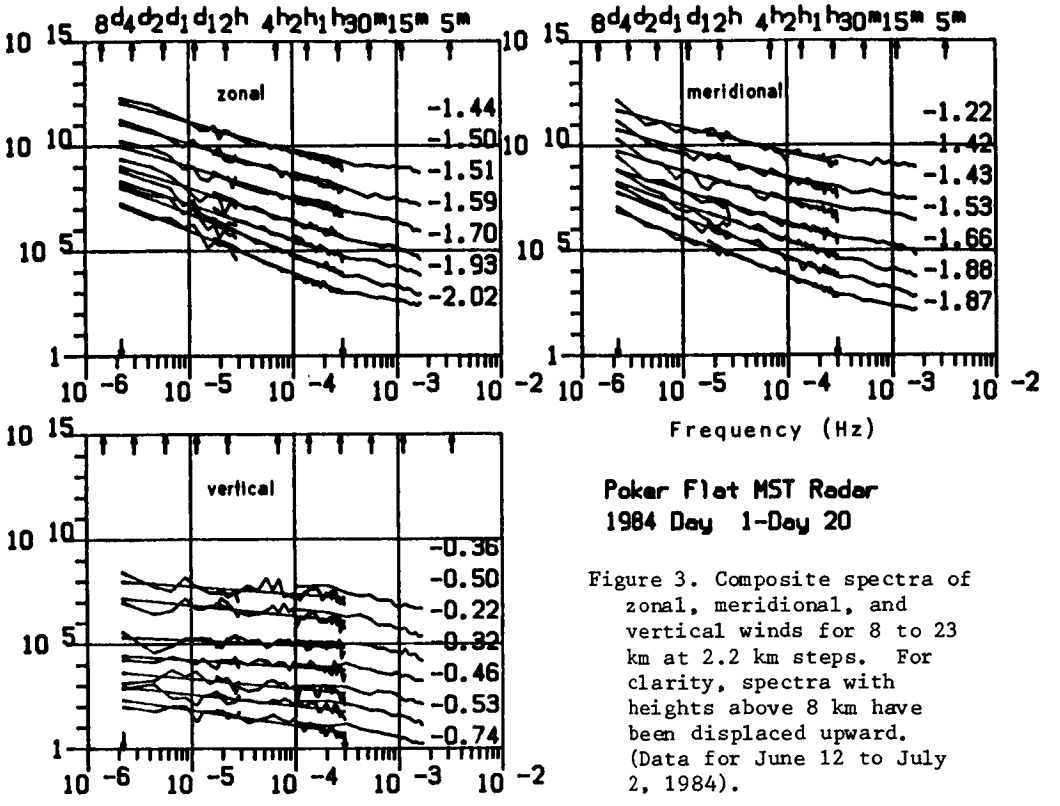

Figure 3. Composite spectra of zonal, meridional, and vertical winds for 8 to 23 km at 2.2 km steps. For clarity, spectra with heights above 8 km have been displaced upward. (Data for June 12 to July 2, 1984).

have been displaced upward by a constant amount. The behavior of zonal and meridional spectra is similar, with a power-law behavior extending to periods below 1 hr. The corresponding spectra for the vertical velocities are almost flat, with a hump between 3 hr and 24 hr at some altitudes. The spectral index for each height is also given. There is a weak indication of the presence of a semidiurnal (12 hr) tide in the spectra of the horizontal velocity components (see Figure 3, zonal).

Figure 4(a) shows the profiles of spectral index for each component for January, 1984. Figure 4(b) is a similar plot for June, 1984. The spectral index of the horizontal components reaches a minimum value of about -2 near the winter tropopause. A similar behavior is seen for June, 1984, except that the minimum value of spectral slope is about -1.4. The behavior of zonal and meridional spectral slopes is similar. The slope of zonal spectra appears, however, to be slightly steeper than that of the meridional spectra; the difference in their slopes is more pronounced during summer. The spectral index of vertical velocity is usually -0.5 to -1.0. Its height variation is much more erratic during winter.

Therefore, we conclude that the spectral index of about -5/3 for the horizontal velocities is exceptional. Indeed, the only case when it is close to this value is for 12-km altitude during January, just above the winter tropopause.

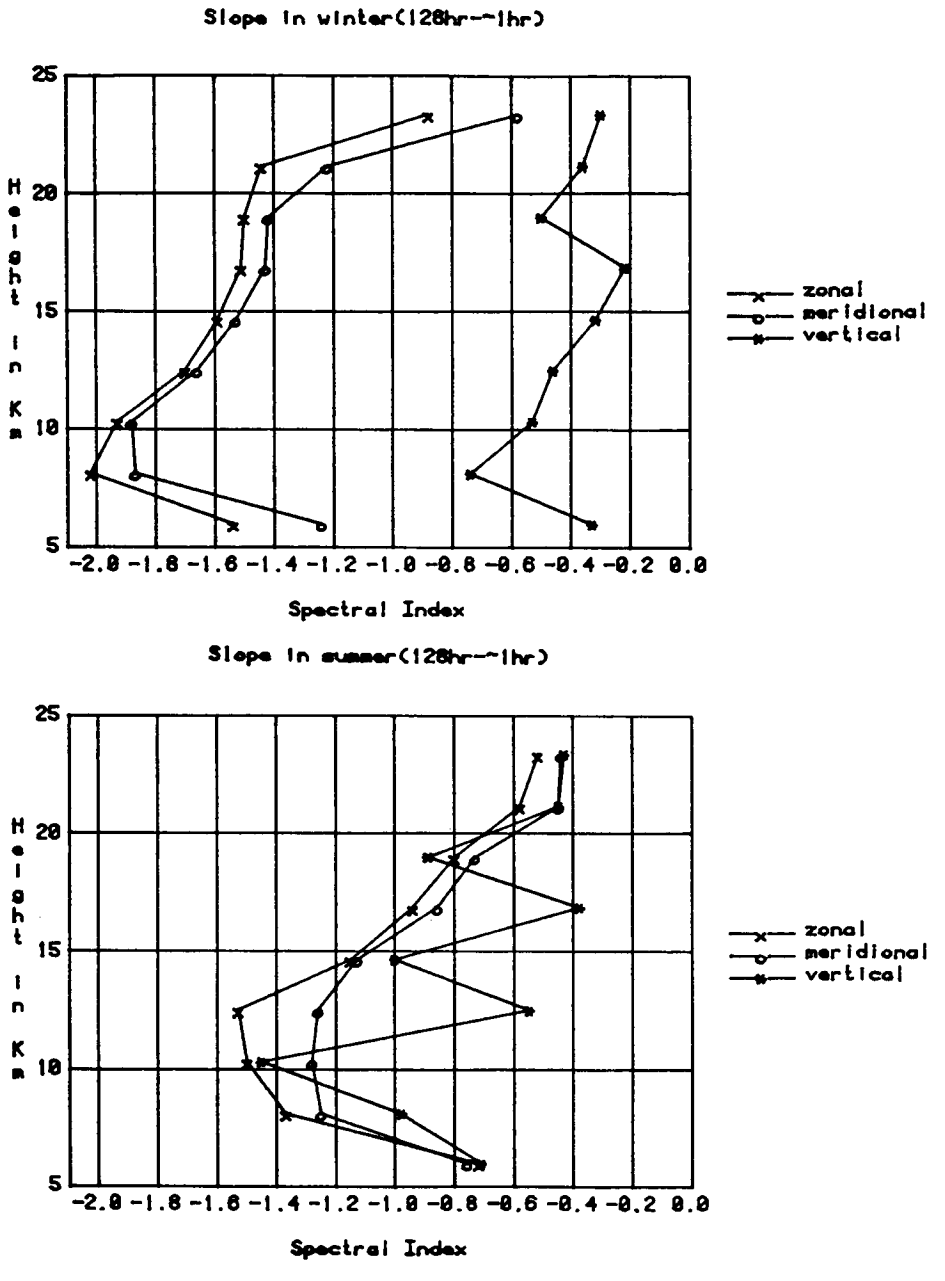

Figure 4. Spectral index of zonal, meridional, and vertical winds for 1-128 hr periods (a) January, 1984, and (b) June, 1984.

4. DISCUSSION

The analysis of velocity spectra described above shows that the spectral index of the horizontal velocity components varies with altitude and season. The spectral index tends to approach a minimum value in the vicinity of the tropopause. The altitude variation of spectral index is similar in winter and summer, except that the indices have higher values (less negative) in the summer. There does not seem to be a preferred tendency for a -5/3rd spectral slope, though this slope does occur in the 15–20 km range during winter. The variability of spectral index of horizontal velocities is also evident in the Poker Flat ST data analyzed by LARSEN et al. (1982). On the basis of the two-dimensional turbulence hypothesis, a spectral index of -5/3 is predicted for horizontal velocity spectra (GAGE, 1979). We conclude that the observations of spectral index reported here do not provide sufficient evidence for this hypothesis.

The time-scales considered in this analysis range from about 5 days to 1 hr. For a mean horizontal wind of 10 m/s that is typical for winter, the corresponding horizontal scales are 4500 km to 36 km. Mean winds during the summer are only about 2.5 m/s and the horizontal scales are smaller by a factor of 4. The steep slopes (-3) that have been reported in aircraft measurements for scales longer than about 1000 km (NASTROM and GAGE, 1985) have not been discerned in the spectra reported here. It is conceivable that the assumptions under which this simple scaling is possible are not valid at scales much longer than a day and 1000 km.

The spectral index of vertical velocities shown in Figure 4 is typically about -0.5 during winter. The average index is closer to -1 during summer. In both seasons, this index shows a large variability with values ranging from -1.4 to -0.2. LARSEN et al. (1985) have reported similar values of spectral index of vertical velocities measured at Arecibo with an average value of -1. Vertical wave number spectra obtained by KUO et al. (1985) using high-resolution data from the SOUSY radar show a similar behavior, with a distinct variation across the tropopause. According to LARSEN et al. (1985) an index of the order of 1/3 should be expected for a universal spectrum of buoyancy waves along the vertical direction provided that the horizontal spectra exhibit a -5/3 slope.

The universal buoyancy wave spectrum hypothesis (VANZANDT, 1982) attempts to seek relations between spectra of velocity components as functions of vertical and horizontal wave number. Though our observations do not appear to provide conclusive evidence for this hypothesis, they certainly suggest the need for a better climatology of horizontal and vertical velocity spectra and their comparison with improved models. SCHEFFLER and LIU (1985) and VANZANDT (1985) have proposed models for acoustic-gravity wave spectra of radial velocities, Doppler shifted by fluctuations in the background wind. There also is a need for improved radar experiments to provide measurements for valid comparisons with theoretical models.

Finally, it should be stressed that mesoscale spectra can possibly be influenced by several mechanisms viz. two-dimensional turbulence, a universal behavior attributed to buoyancy waves, and Doppler shifts of buoyancy waves through variable background winds. A clear-cut distinction between these mechanisms may not be readily possible, unless additional measurable parameters are introduced in theoretical models.

ACKNOWLEDGEMENT

This work supported under NSF Grant ATM-8313153. We thank Dr. T. E. VanZandt, Dr. M. F. Larsen and Dr. S. Smith for helpful discussions.

REFERENCES

Balsley, B. B., and D. A. Carter (1982), The spectrum of atmospheric velocity fluctuations at 8 km and 86 km, Geophys. Res. Lett., 4, 465-468.

Blackman, R. B., and J. W. Tukey (1985), The Measurement of Power Spectra, Dover Publication, New York.

Brownlee, K. A. (1965), Statistical theory and methodology in science and engineering, second edition, J. Wiley & Sons., New York, 590pp.

de Boor, C. (1978), A Practical Guide to Splines, Springer-Verlag, New York.

Gage, K. S. (1979), Evidence for a $k^{-5/3}$ law inertial range in mesoscale two-dimensional turbulence, J. Atmos. Sci., 36, 1950-1954.

Gage, K. S., and B. B. Balsley (1984), MST radar studies of wind and turbulence in the middle atmosphere, J. Atmos. Terr. Phys., 46, 739-753.

Gage, K. S., and G. D. Nastrom (1984), On the interpretation of the variance spectrum of velocity observed with ST/MST radars, 22nd Conf. on Radar Meteorol., Zurich, Switzerland, Am. Meteorol. Soc., Boston, 482-487.

Kuo, F. S., H. W. Shen, I. J. Fu, J. K. Chao, J. Roettger, and C. H. Liu (1985), Altitude dependence of vertical velocity spectra observed by VHF radar, Radio Sci., to appear.

Larsen, M. F., M. C. Kelley, and K. S. Gage (1982), Turbulence spectra in the upper troposphere and lower stratosphere at periods between 2 hours and 40 days, J. Atmos. Sci., 39, 1035-1041.

Larsen, M. F., R. F. Woodman, T. Sato, and M. K. Davis (1985), Power spectra of vertical velocities in the troposphere and lower stratosphere observed at Arecibo, Puerto Rico, submitted to J. Atmos. Sci..

Lilly, D. K., and E. L. Petersen (1983), Aircraft measurements of atmospheric kinetic energy spectra, Tellus, 35A, 379-382.

Nastrom, G. D., and K. S. Gage (1983), A first look at wave number spectra from GASP data, Tellus, 35A, 383-388.

Nastrom, G. D., and K. S. Gage (1985), A climatology of atmospheric wave number spectra of wind and temperature observed by commercial aircraft, J. Atmos. Sci., 42, 950-960.

Oppenheim, A. V., and R. W. Schafer (1975), Digital Signal Processing, Prentice-Hall Inc., Englewood Cliffs, N. J.

Scheffler, A. O., and C. H. Liu (1985), On observation of gravity wave spectra in the atmosphere by using MST radars, Radio Sci., 20, 1309-1322.

VanZandt, T. E. (1982), A universal spectrum of buoyancy waves in the atmosphere, Geophys. Res. Lett., 9, 575-578.

VanZandt, T. E. (1985), A model for gravity wave spectra observed by Doppler sounding systems, Radio Sci., 20, 1323-1330.

3.7.4 ON THE VARYING SLOPE OF VELOCITY SPECTRA

Jurgen Rottger*

Arecibo Observatory
P.O. Box 995
Arecibo, Puerto Rico

Spectra of zonal, meridional and vertical wind velocity, measured during a 24-hour period with the spaced-antenna technique indicate quite a variable slope as a function of height (Figure 1, from ROTTGER, 1981). It is found that the spectral slope (1h-24h) of all three components correlates with the mean horizontal wind velocity (Figure 2). A possible conclusion is that the frequency dependence of power density of horizontal and vertical fluctuation component apparently depends on the mean wind velocity. However, the vertical spectra at periods larger than about 1 hour can also be influenced by spillover (due to finite radar antenna beam width) from the horizontal fluctuation component or by a Doppler shift.

REFERENCES

Rottger, J. (1981), Wind variability in the stratosphere deduced from spaced antenna VHF measurements, Proc. 20 AMS Conf. Radar Meteorol., Boston, MA.

*On leave from Max-Planck-Institut fur Aeronomie, Katlenburg-Lindau, West Germany.

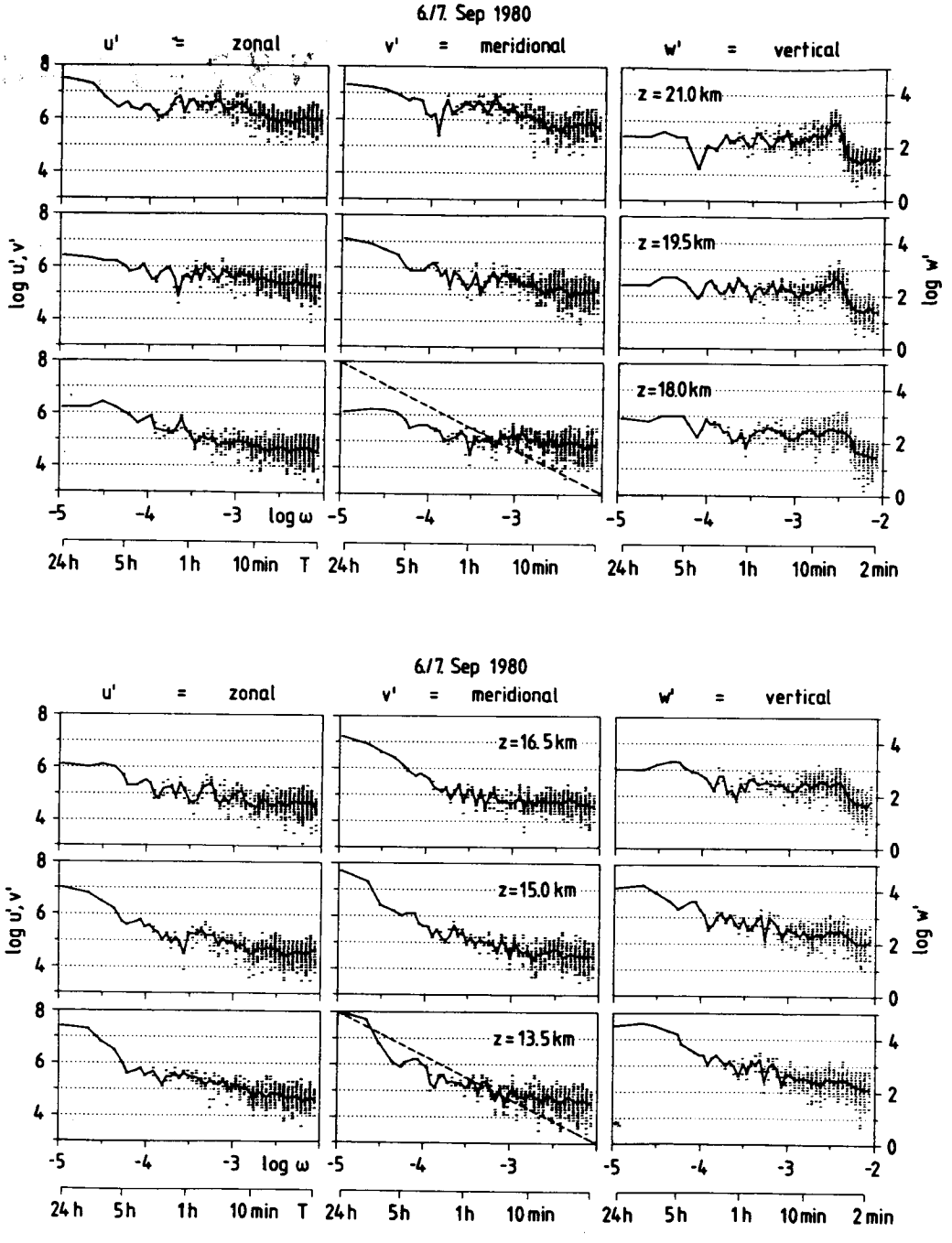

Figure 1. Power spectra of zonal (u), meridional (v) and vertical (w) velocity for a 24-hour period (from ROTTGER, 1981). The dashed lines give the m = -5/3 slope.

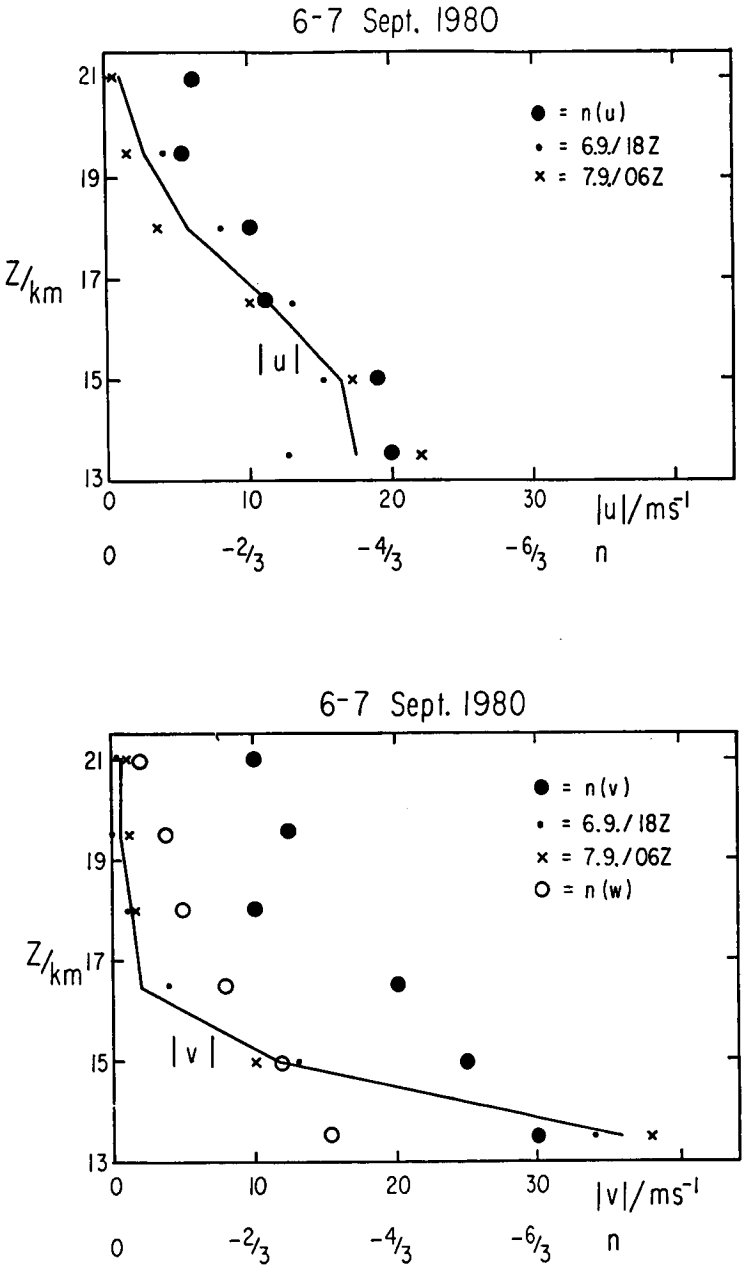

Figure 2. Absolute values of the mean horizontal wind components $|u|$ and $|v|$, compared with the spectral slope n of the zonal (u), meridional (v) and vertical (w) fluctuation component.

3.7.5 DOPPLER EFFECTS ON VELOCITY SPECTRA OBSERVED BY MST RADARS

A. O. Scheffler and C. H. Liu

Department of Electrical and Computer Engineering
University of Illinois
Urbana, IL 61801

1. INTRODUCTION

Recently, wind data from MST radars have been used to study the spectra of gravity waves in the atmosphere (SCHEFFLER and LIU, 1985; VANZANDT et al., 1985). Since MST radar measures the line-of-sight Doppler velocities, it senses the components of the wave-associated velocities along its beam directions. These components are related through the polarization relations which depend on the frequency and wave number of the wave. Therefore, the radar-observed velocity spectrum will be different from the original gravity-wave spectrum. Their relationship depends on the frequency and wave number of the wave as well as the propagation geometry. This relation can be used to interpret the observed data. It can also be used to test the assumption of gravity-wave spectrum (SCHEFFLER and LIU, 1985).

In deriving this relation, the background atmosphere has been assumed to be motionless. Obviously, the Doppler shift due to the background wind will change the shape of the gravity-wave power spectrum as well as its relation with the radar-observed spectrum. In this paper, we attempt to investigate these changes.

2. DOPPLER-SHIFTED FREQUENCY SPECTRUM

Let us first assume that the background wind is constant, blowing in the x-direction. In the rest frame coordinate of the atmosphere, the frequency Ω is related to the frequency ω of the laboratory frame through the relation

$$\Omega = \omega - k_h v_0 \cos\phi \tag{1}$$

where k_h is the horizontal wave number, v_0 is the wind speed and ϕ is the angle the horizontal wave vector $\vec{k}_h$ makes with the x-axis. Following the derivation in SCHEFFLER and LIU (1985), the frequency spectrum of the observed velocity fluctuations along a radar beam pointed at zenith angle θ_B can be written as

$$E_{0_b}(\omega) = \int_0^\infty \int_{-\infty}^{\infty} Q(\phi,\Omega) E(\vec{k},\Omega)\, \delta(\Omega-\omega+k_h v_0 \cos\phi)\, d\Omega d\vec{k} \tag{2}$$

where

$$Q(\phi,\Omega) = \frac{\Omega^2-\omega_i^2}{\omega_b^2-\omega_i^2}\cos^2\theta_B + \frac{\omega_b^2-\Omega^2}{\omega_b^2-\omega_i^2}\left[1-\left(1-\frac{\omega_i^2}{\Omega^2}\right)\sin^2(\phi-\phi_B)\right]\sin^2\theta_B \tag{3}$$

$E(\vec{k}, \Omega)$ is the power spectrum of the gravity wave in the rest frame (Lagrange frame). We further assume that the wave spectrum has the same form as that in the laboratory frame such that

$$E(\vec{k},\Omega) = \frac{E_0}{2\pi k_h} A(k_z) B(\Omega)\, \delta\left[k_h \pm \left(\frac{\omega^2-\omega_i^2}{\omega_b^2-\omega^2}\right)^{1/2} |k_z|\right] \tag{4}$$

where

$$A(k_z) = \frac{(t-1)k_z^{*t-1}}{(k_z^{*}+|k_z|)^t}$$

$$B(\Omega) = \frac{p-1}{\omega_1^{1-p} - \omega_b^{1-p}} \Omega^{-p} \qquad \omega_i \leq \Omega \leq \omega_b \tag{5}$$

Here, isotropy of the spectrum has been assumed. Equation (2), together with equations (3), (4), and (5), yields the observed frequency spectrum of the velocity fluctuation. We note that because of the two δ-functions, the original 4-fold integration in (2) is reduced to 2-fold which can be integrated numerically.

3. RESULTS

Figure 1 shows an example of numerical computation for the frequency spectrum. This is for the case where the radar beam is pointed vertically. The Doppler effect redistributes the wave energy so that the spectrum spreads out beyond the original limits (ω_i, ω_b). The level is depressed and a slope is introduced in the high frequency end of the spectrum. These effects become more apparent as the background wind speed v_u is increased. Figure 2 shows the result for an oblique radar beam with θ_B=10°. Again, the spectrum spreads out beyond ω_i and ω_B. The redistribution of energy due to the Doppler effect in this case makes the spectrum shallower. In a certain frequency range, the level can be higher than that for the case with no Doppler.

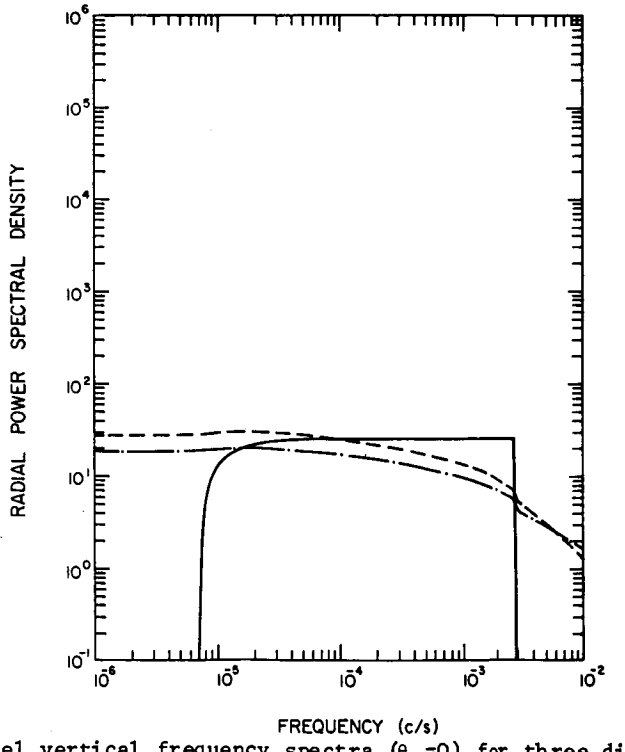

Figure 1. Model vertical frequency spectra (θ_B=0) for three different values of β, where $\beta = v_o k_z / \omega_b$. β=0 is solid curve, β=5 is dashed curve, β=10 is dotted and dashed. Other parameters are p=2, t=2.25, E_o=31 J/kg, f_i=7.2x10^{-6}Hz, and f_b=3.0x10^{-3}Hz. Typical values of k_z^* are of the order of 2πx10^{-4}m^{-1}.

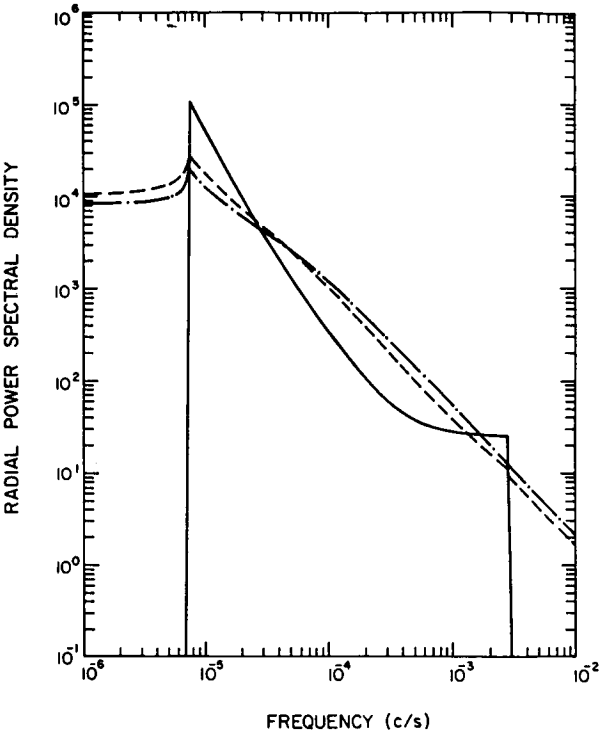

Figure 2. Same as Figure 1 except θ_B=10°.

4. CONCLUSIONS

The results show that the radar-observed frequency spectrum of velocity fluctuations due to gravity waves will be affected by the Doppler shift due to the background wind. The numerical results are for the case of isotropic gravity-wave spectrum in a constant background wind. The technique could be applied to the more general cases.

REFERENCES

Scheffler, A. O., and C. H. Liu (1985), On observation of gravity wave spectra in the atmosphere by using MST radar, Radio Sci., 20, 1309-1322.

VanZandt, T. E. (1985), A model for buoyancy wave spectra observed by Doppler sounding systems, Radio Sci., 20, 1323-1330.

3.7.6 OBSERVATIONS OF VERTICAL VELOCITY POWER SPECTRA WITH THE SOUSY VHF RADAR

M. F. Larsen[1], J. Rottger[2,3], D. N. Holden[1]

[1]Department of Physics and Astronomy
Clemson University
Clemson, SC 29631

[2]Arecibo Observatory
P. O. Box 995
Arecibo, PR 00612

1. INTRODUCTION

Recently LARSEN et al. (1985) have shown that the line-of-sight velocity power spectra measured at an oblique angle have a significant contribution from the vertical velocity out to periods close to 1 hr, in agreement with the earlier result of BALSLEY and CARTER (1982). The spectral slope of the inferred vertical velocity frequency spectrum was close to -1. The inferred vertical velocity vertical wave number spectrum had a slope that lay between -1 and -1.5. The frequency and vertical wave number spectra of the horizontal velocities had slopes in agreement with a number of earlier studies, namely -5/3 and -5/2, respectively.

In this study, we have used a data set taken with the SOUSY VHF radar from October 28 to November 13, 1981, to calculate the power spectrum of the vertical velocities directly from the vertical beam measurements. The spectral slopes for the frequency spectra have been determined out to periods of several days and have been found to have values near -1 in the troposphere and shallower slopes in the lower stratosphere. The value of -1 is in agreement with the value found by LARSEN et al. (1985) and BALSLEY and CARTER (1982) in the range from a few minutes to 1 hr.

2. DESCRIPTION OF THE DATA SET

From October 28 to November 13, 1981, the SOUSY VHF radar was operated in a mode that provided data for 12 min every hour on the hour. The radar was also operated continuously during three separate periods in the time span. Each profile consisted of a 1-μsec pulse sampled up to 4.5 km, and a 2-μsec pulse sampled from 3.0 km to 21.0 km. The signal-to-noise ratio was sufficiently good to determine the winds up to 18.0 km routinely.

Below 3.0 km, the 150-m resolution data were averaged to provide an effective height resolution of 300 m. Also, the profiles obtained over each 12-min interval every hour were averaged. Thus, the data set consists of one 12-min average profile every hour with height resolution of 300 m and covering the height range from 0.6 km to 18.0 km. Only six of the hourly profiles were missing, and they were replaced by linearly interpolated values.

3. FREQUENCY SPECTRA

The frequency spectra were calculated for the entire time series consisting of 360 points using the mixed radix transform developed by SINGLETON (1967). The spectra for all heights were then averaged to produce a single

[3]On leave from the Max-Planck-Institut fur Aeronomie, Katlenburg-Lindau, West Germany.

spectrum characteristic of the troposphere and lower stratosphere. The result is shown in Figure 1. The spectrum shows a characteristic power law close to -0.80.

Separate average spectra were also calculated for the troposphere only, for the height range around the tropopause, and for the lower stratosphere up to 18 km. The average tropospheric frequency spectrum is very similar in terms of power level and spectral slope to the average spectrum for the entire height range. However the spectra in the tropopause region and lower stratosphere both show a considerably shallower slope near -0.2. RASTOGI and BEMRA (1985) have found a similar result for the frequency spectra of the horizontal velocities based on data from the Poker Flat radar, namely that the spectral slope decreases near the tropopause.

4. INERTIAL WAVES

The vertical velocity/frequency spectrum in the tropopause region shows a very pronounced peak at a period near 14 hrs, close to the inertial period. Such a peak is not evident in either of the other two height ranges. The wave structure is clearly evident in the reflectivity data as well (not shown) and the phase propagation indicates a wave source in the vicinity of the tropopause.

Although the peak is close to the inertial period, the actual wave period must be slightly smaller since a purely inertial wave would not be propagating vertically. Also, there would be no vertical velocity perturbation associated with a wave characterized by the inertial period.

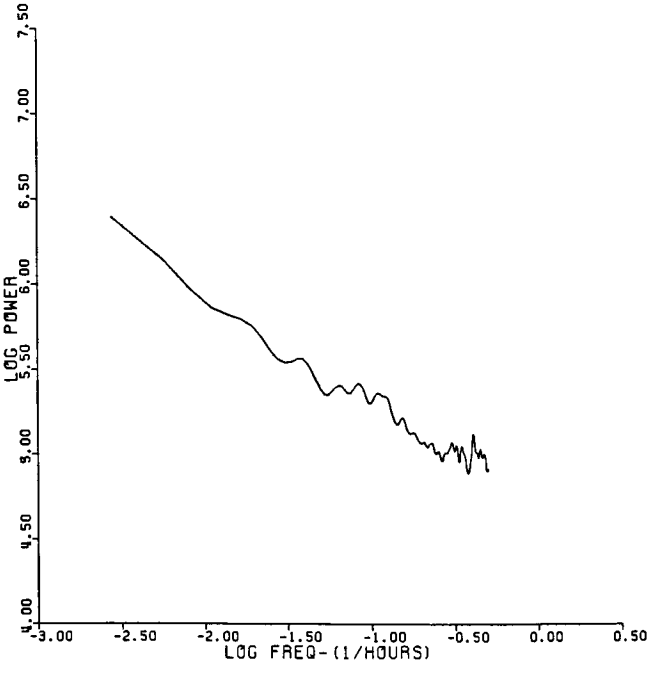

Figure 1. Average of log power spectrum for the atmosphere to 70 mb.

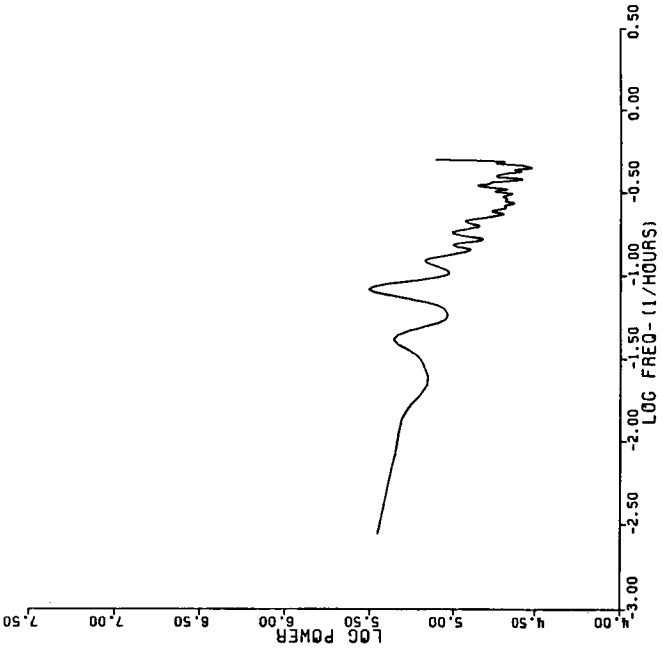

Figure 2. Average of log power spectrum for the troposphere to 230 mb.

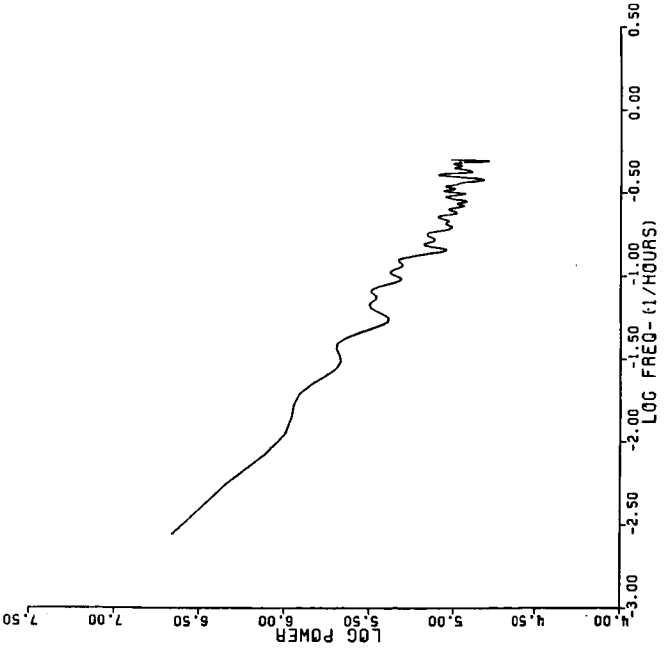

Figure 3. Average of log power spectrum around the tropopause at 230 mb.

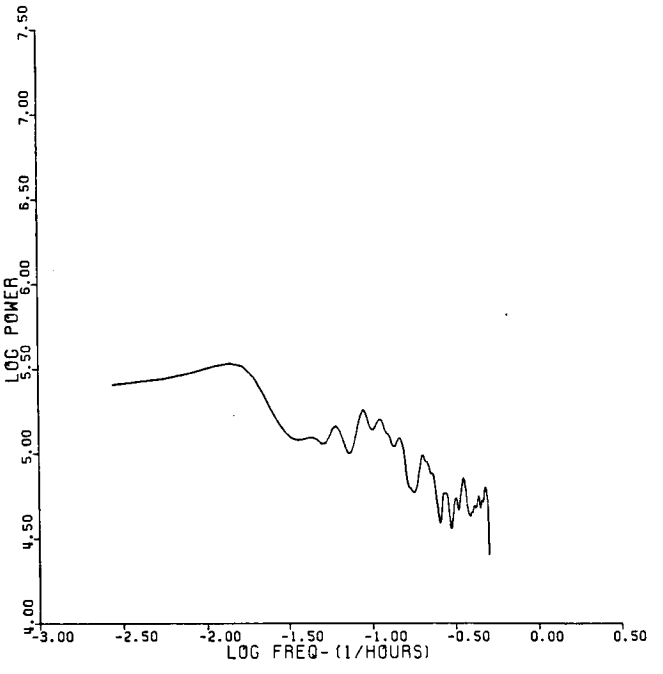

Figure 4. Average of log power spectrum for the stratosphere to 100 mb.

5. VERTICAL WAVE NUMBER SPECTRA

The 300-m height resolution of the data set is sufficient to produce meaningful vertical wave number spectra. The spectrum for each profile was calculated, and the average is shown in Figure 5. The spectral slope is close to -3/2 but much shallower than the slope of -5/2 expected from the GARRETT and MUNK (1975) predictions.

DISCUSSION

Our analysis of an extensive 15-day data set obtained with the SOUSY VHF radar has shown the slope of the vertical wave number spectrum of the vertical velocity to be close to -1.5, in agreement with the results of LARSEN et al. (1985) based on data from Arecibo, Puerto Rico. Also, the slope near -1 inferred by LARSEN et al. (1985) and BALSLEY and CARTER (1982) for the frequency spectrum of the vertical velocity at periods less than 1 hr has been shown to be characteristic of the vertical velocities in the troposphere out to periods of several days. However, the slope of the vertical velocity spectrum as a function of frequency is shallower near the tropopause and in the lower stratosphere.

There has been considerable discussion in the recent literature about the roles of gravity waves and two-dimensional turbulence in explaining the observed power spectra at scales characteristic of the mesoscale (GAGE, 1979; VANZANDT, 1982; LILLY, 1983; LARSEN et al., 1985). The observed vertical velocity spectral slopes may provide an impetus to further theoretical development of the various ideas. The observed slopes do not agree with the predictions of the GARRETT and MUNK (1975) spectrum which lead to a slope of

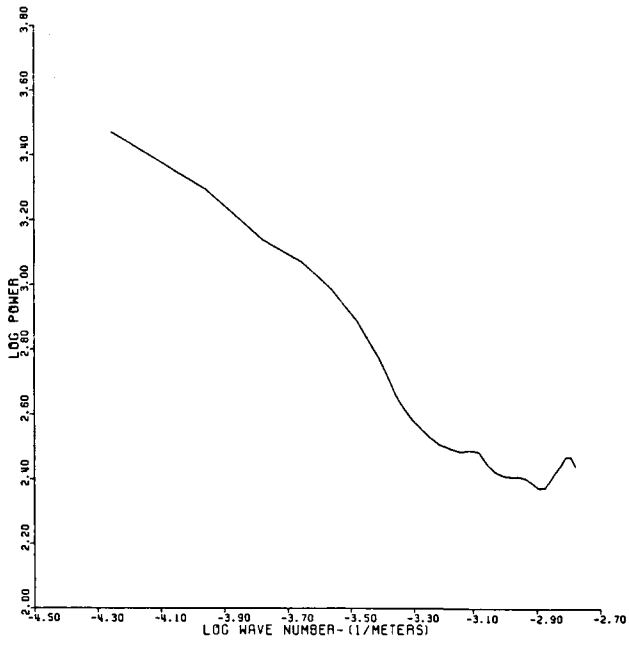

Figure 5. Average of log power spectrum for the atmosphere to 70 mb.

zero or +1/3 for the vertical velocity as a function of frequency and a slope of -5/2 for the vertical velocity as a function of vertical wave number. Since the theory for quasi-two-dimensional turbulence has not been developed sufficiently to include the effects of vertical velocities, no comparison can be made with the observations.

REFERENCES

Balsley, B. B., and D. A. Carter (1982), The spectrum of atmospheric velocity fluctuations at 8 km and 86 km, Geophys. Res. Lett., 9, 465-468.

Gage, K. S. (1979), Evidence for a $k^{-5/3}$ law inertial range in mesoscale two-dimensional turbulence, J. Atmos. Sci., 36, 1950-1954.

Garrett, C., and W. Munk (1975), Space-time scales of internal waves: A progress report, J. Geophys. Res., 80, 291-297.

Larsen, M. F., R. F. Woodman, T. Sato, and M. K. Davis (1985), Power spectra of vertical velocities in the troposphere and lower stratosphere observed at Arecibo, Puerto Rico, submitted to J. Atmos. Sci..

Lilly, D. K. (1983), Stratified turbulence and the mesoscale variability of the atmosphere, J. Atmos. Sci., 40, 749-761.

Rastogi, P. K., and R. S. Bemra (1985), Preliminary report on the analysis of 40 days of Poker Flat ST data for January and June 1984, Report WGR-85-3, Department of Electrical Engineering and Applied Physics, Case Western Reserve University, Cleveland, Ohio.

Singleton, R. C. (1967), On computing the fast Fourier transform, Commun, ACM, 10, 647-654.

VanZandt, T. E. (1982), A universal spectrum of buoyancy waves in the atmosphere, Geophys. Res. Lett., 9, 575-578.

3.7.7 MESOSPHERIC WAVE NUMBER SPECTRA FROM POKER FLAT MST RADAR MEASUREMENTS COMPARED WITH GRAVITY-WAVE MODEL

Steven A. Smith* and David C. Fritts

Geophysical Institute, Department of Physics
University of Alaska, Fairbanks, AK 99701

and

Thomas E. VanZandt

Aeronomy Laboratory
National Oceanic and Atmospheric Administration
Boulder, CO 80303

INTRODUCTION

This paper presents the results of a comparison of mesospheric wind fluctuation spectra computed from radial wind velocity estimates made by the Poker Flat MST radar with a gravity-wave model developed by VANZANDT (1982, 1985). The principal conclusion of this comparison is that gravity waves can account for 80% of the mesospheric power spectral density.

Two different hypotheses have been advanced in recent years to explain the origin and behavior of mesoscale (one to thousands of kilometers) wind fluctuations. One hypothesis is that these fluctuations are manifestations of two-dimensional (2D) turbulence (GAGE, 1979; LILLY, 1983). Two-dimensional turbulence consists of turbulent eddies with wind fluctuations constrained to occur primarily in a horizontal plane. The other hypothesis is that the observed wind fluctuations are due to a broad spectrum of gravity waves transporting momentum vertically (DEWAN, 1979; VANZANDT, 1982, 1985).

Both theories claim similar shapes for frequency and horizontal wave number spectra of horizontal wind fluctuations. Thus, observations that both frequency and horizontal wave number spectra follow power laws with an exponent of -5/3 cannot be used to determine what portion of the wind fluctuation energy spectrum is attributable to either type of motion.

There is a need to partition the spectrum between gravity waves and stratified, 2D turbulence in order to study the interaction of the fluctuations with the environment and to determine the horizontal and vertical transport of energy. For example, gravity waves are capable of vertical transport of energy and momentum and knowledge of gravity-wave flux at a given height would lead to estimates of mean flow drag, wave saturation and vertical transport of heat and chemical constituents at other altitudes.

Our approach to partitioning the spectrum has been to identify that part of the spectrum that is consistent with VANZANDT'S (1985) gravity-wave model as being due to gravity-wave motions. We have used vertical wave number (m) spectra to avoid the ambiguities mentioned earlier.

In the next section, a brief review of VanZandt's gravity-wave model formulation and the extension of that model to wind fluctuations along any oblique path will be presented. Then, spectra of vertical and oblique (15° off-zenith) radial winds measured near the summer mesopause by the Poker Flat

*Now at Cooperative Institute for Research in Environmental Sciences, University of Colorado, Boulder.

MST radar will be described. Finally, the comparison between the observations and the model will be made and the implication that gravity waves dominate the fluctuating wind field near the mesopause will be discussed.

MODEL WAVE NUMBER SPECTRA

VANZANDT (1985) transferred the successful oceanic internal gravity-wave model spectrum of GARRETT and MUNK (1972, 1975) to the atmosphere. In this model, the gravity-wave energy spectrum is assumed to be the product of two independent factors: a frequency spectrum and a wave number spectrum. Since the total energy spectrum is assumed to be separable, integration over frequency yields the wave number spectrum and vice versa. These simple manipulations are all that is needed for spectra of horizontal or vertical wind fluctuations since the model was formulated from such observations. However, extending the model to wind fluctuations along any oblique path requires further use of gravity-wave theory.

Velocity perturbations measured along an oblique ray will be a combination of horizontal and vertical perturbations. The ratio of horizontal to vertical velocity perturbations for gravity waves is determined by the gravity-wave dispersion relation, which in this formulation is obtained from a WKB solution of the wave equation. With the dispersion relation and the zenith angle of the sampling vector, a formula is derived for the measured wave perturbation in terms of the absolute amplitude and frequency of a wave. For a detailed model derivation, see VANZANDT (1985).

Though, as pointed out by VANZANDT (1982), there is evidence for a uniform wave amplitude over a wide range of observing sites and seasons, we avoid any uncertainty in the amplitude by using the ratio of spectra taken at different zenith angles. The absolute amplitude cancels out of the ratio. If the fluctuations are due to gravity waves, then the ratio should agree with the ratio predicted by the gravity-wave dispersion relation. Thus, we are not investigating the universality of the gravity-wave model but rather the application of the gravity-wave dispersion relation to the observed fluctuations.

It is important to note that Doppler shifting of the frequency spectrum has been neglected in the model formulation, since the gravity-wave dispersion relation used in the model assumes that the mean wind is zero. Doppler shifting should be considered in applying the model to frequency spectra. However, vertical wave number spectra are not affected by Doppler shifting because the velocity measurements along a beam are made nearly instantaneously and in a direction nearly orthogonal to the mean wind.

To apply the model to the data, the zenith angles of the radar beams, the slope of the horizontal velocity perturbations frequency spectra and the limits on the range of gravity-wave frequencies must be specified. The theoretical frequency limits are the inertial frequency, f, and the Brunt-Vaisala frequency, n. The approximate gravity-wave frequency spectra must be specified to permit integration over the frequency component of the total gravity-wave spectrum.

OBSERVED RADIAL WAVE NUMBER SPECTRA

Observations for this study are the radial wind velocities obtained by the Poker Flat MST radar from regions near the mesopause. Seasonal signal characteristics and radar system parameters are described in BALSLEY et al. (1983). We use high spatial resolution soundings (300 m) obtained during the STATE (STructure and Atmospheric Turbulence Environment) campaign in June 1983, and similar soundings obtained in July, 1984. In order to minimize cross talk,

the vertical and oblique transmitters were turned off during alternate sampling periods. The sampling periods were approximately 1.5 minutes long. Thus, oblique velocities were obtained over 1.5-minute periods separated by 1.5 minutes during which the vertical beam was operating.

Mesospheric wind velocities were obtained from a vertical beam and two oblique (15° off-zenith) beams and from heights of 82 to 88 km. The two orthogonal, oblique beams were directed towards azimuths of 64° and 334° east of north and will be referred to as the east and north beams. The vertical beam directly measured the vertical wind while each oblique beam measured the projection of the total wind vector along the beam. This projection of the wind vector was a composite of the vertical wind times cos 15° (=.97) plus the horizontal wind along the beam azimuth, times sin 15° (=.26). Since vertical sample volumes were approximately 20 km from the oblique sample volumes at mesopause heights, the measured vertical wind did not necessarily equal the vertical contribution to the oblique measurements. Instantaneous horizontal winds could not be unambiguously determined with this system unless it was assumed that the wind field was homogeneous and uniform over the region sampled by the three beams.

Before transforming the velocity measurements to wave number spectra, spurious points due to aircraft and meteors in sidelobes and other types of interference were removed. An empirical editing procedure was used similar to those described by CARTER (1983). The velocity time series from each beam and at each height was examined for accelerations greater than 3 times a running average of acceleration. Any points exceeding that limit were removed from further processing.

In order to compute ratios of oblique to vertical spectral densities over the greatest range of wave numbers, individual profiles were selected that continuously covered the greatest range of heights. This height range was limited by the vertical system which is about 10 dB less sensitive than the oblique system. The final range of heights was also determined by the number of resultant spectra with equal numbers of points that could be averaged together to improve the confidence level. Thus, the height range (and corresponding wave number range) selected was a compromise between the greatest range available and the range continuously sampled most frequently.

The linear trend of each selected profile was removed leaving fluctuations about the mean shear. Then the profiles were "prewhitened" by differencing data points from successive heights. A cosine window was applied to the differenced data to minimize power leakage across the spectra. The differenced data was then transformed to the wave number domain using an FFT (Fast Fourier Transform) routine. The real and imaginary coefficients were squared and added to obtain a power estimate at each wave number. Finally, the wave number spectra were adjusted to reverse the effect of the differencing and the cosine windowing and then normalized such that the integrated spectra were equal to the variances of the original profiles yielding power spectral densities.

Several power spectra were averaged together to narrow the confidence limits for the spectra. The averaging was done over the longest intervals for which vertical wind measurements over a sufficiently large and contiguous height interval were available. Since the radar echoes were not continuous in time, this averaging when signals were strong in the vertical beams means that our observed spectra are representative only of periods during which the intensity of 3-m scale-size, refractive index irregularities, which produce the backscattered radar echo, was greatest. The mesospheric irregularities are due to turbulent mixing of the electron-density gradient. Thus, the level of turbulence and/or the electron-density gradient was enhanced during the selected periods. Therefore, these spectra, obtained during periods of

enhanced radar signal strength, probably represent an upper limit to average power spectra in the summer mesosphere over Poker Flat.

Spectra from three such periods are shown in Figures 1-3. Each spectral curve is labelled by the beam from which the velocities were obtained, with the number of spectra in each average given in parentheses. The spectra are plotted versus vertical not radial wave number. This means that for the oblique data, the vertical wave number is the radial wave number divided by cos 15°, which represents a difference of 1.04 between radial and vertical wave numbers. We have computed 95% confidence intervals for the curve in each figure with the smallest number of averaged spectra using the degrees of freedom for a Bartlett spectral window and the procedure of JENKINS and WATTS (1968). Successive velocity profiles are not completely independent so the actual degrees of freedom are less than we have used and the confidence limits somewhat broader.

The spectra in the figures as well as additional spectra from July 1984, exhibit several points of similarity. The magnitudes of the oblique spectra are generally within a factor of 3 of each other and the spectral slopes from separate beams are approximately parallel. Indeed, an average of eight such spectra result in equal power spectral densities for the two oblique beams as shown in Figure 4. However, the slopes of the vertical power spectra are not as steep as the oblique spectra and we have sought an instrumental bias as an explanation for this discrepancy.

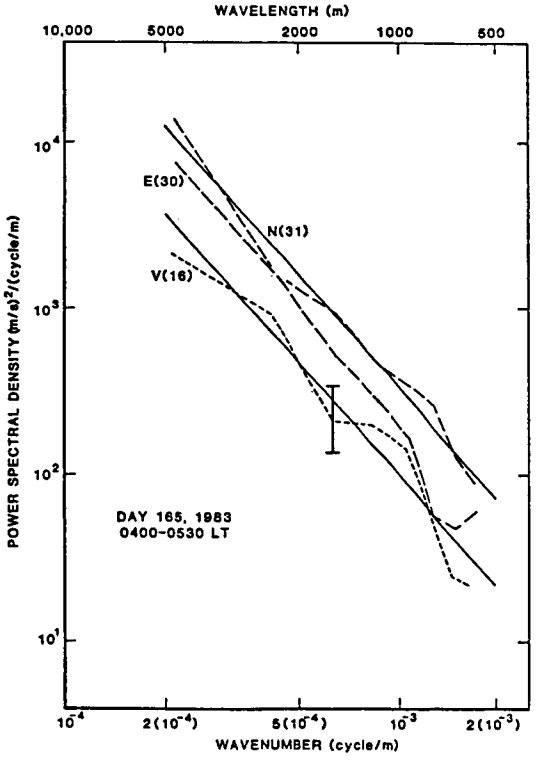

Figure 1. Vertical wave number spectra for Day 165 (June 14), 1983. Dashed lines are spectra computed from observations along East, North and Vertical beams. Each plotted spectrum is the average of the number of spectra in parentheses obtained between 0400 and 0530 local time. Solid lines are model curves.

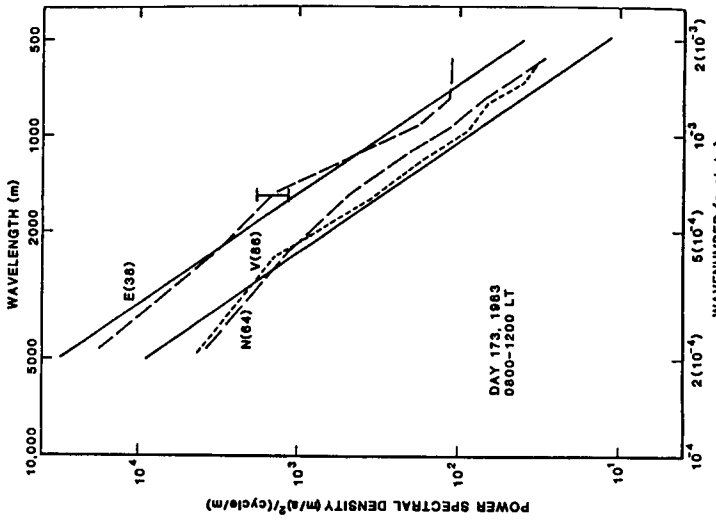

Figure 3. Same as Figure 1 but for Day 173 (June 22), 1983.

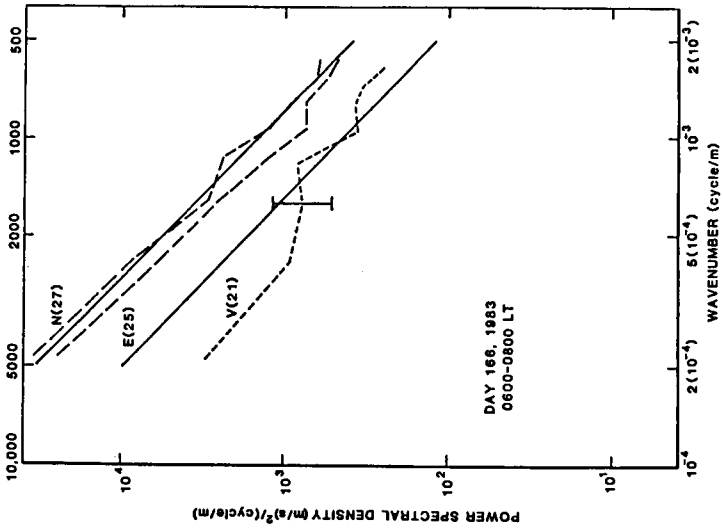

Figure 2. Same as Figure 1 but for Day 166 (June 15), 1983.

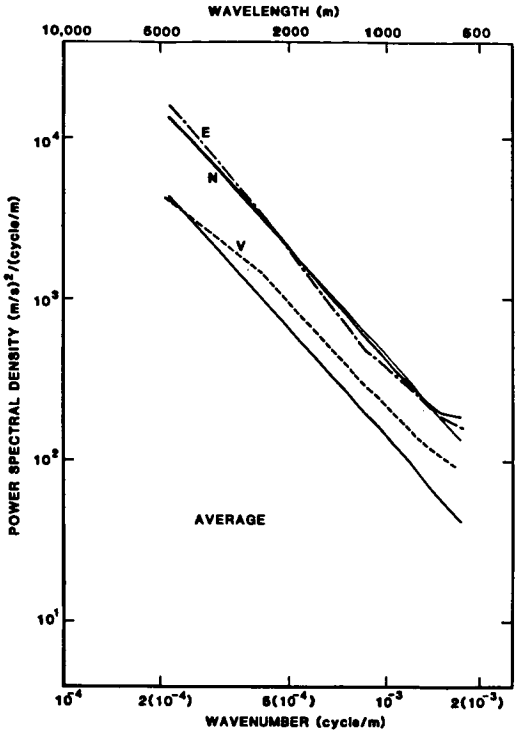

Figure 4. Vertical wave number spectra obtained by averaging all the spectra obtained over short periods in June 1983 and July 1984. The thin line through the East and North spectra is the model curve.

Research indicates that low resolution Doppler-shifted frequency spectra coupled with the clutter rejection scheme used at Poker Flat resulted in an increase in the magnitude of vertical velocity spectra by approximately a factor of 2. The computer at the Poker Flat MST radar samples the received signal, then performs coherent integration, accumulates 64 coherently integrated time series points at all heights and performs FFTs on those time series. This results in Doppler-shifted frequency or, equivalently, velocity spectra. In routine operation, the number of coherent integrations is set to cover the velocity range -35 to +35 m/s for oblique sampling and -4 to +4 m/s for the vertical velocities. Thus, spectral resolution is normally 1/8 m/s per spectral point on vertical spectra. During the STATE campaign, however, vertical velocities were obtained from spectra covering the range -36 to +36 m/s with 64 points for a resolution of about 1 m/s. The clutter rejection scheme used at Poker Flat consists of removing the mean of the 64-point time series gravity-wave dispersion relation, followed by a Hanning windowing of the time series before the FFT is computed. This procedure leaves a 3-point wide notch in the spectra at 0 m/s which is subsequently interpolated to restore some of the signal power at dc. This procedure does remove clutter signals but is also removes part of the signal power for velocities near zero. This effectively pushes near-zero velocities away from zero, increasing the variance of fluctuating vertical velocities and, therefore, artificially enhancing vertical power spectral density. When the spectral resolution is 1/8 m/s, as it usually is, this effect is not noticeable, but when the resolution is the

same as the limits of the measured vertical velocities, the power spectral density can be enhanced by a factor of two. This enhancement is apparent in Figure 4.

DISCUSSION

The thin solid lines in the Figures are the model spectra. The lines were placed as follows: first a straight line was fitted to the largest amplitude oblique spectra. Then, the model ratio was computed using N = 0.02 rad/s, f = 1.32 (10-4) rad/s (inertial period = 13.2 hrs for the latitude of Poker Flat) and a frequency spectral slope of -5/3. Finally the computed ratio was used to construct the expected vertical velocity spectra. The agreement between the observed and model vertical spectra is excellent for high wave numbers in Figures 1-3. The log (base 10) of the average observed ratio was 0.3 at the 10^{-3} cycle/m point (1 km wavelength), while the model predicted a log ratio of 0.53. There is also an indication of considerable day-to-day variability and anisotropy of the spectra in the east and north beams.

The agreement between the observed spectra and the gravity-wave model, while not perfect, does provide justification for a gravity-wave interpretation. With this comparison, we can begin to assess the relative contributions of gravity waves and 2D turbulence to the fluctuation spectra. Since 2D turbulence does not generate vertical motions, on average, the vertical velocity spectra are primarily due to gravity waves. Then that portion of the oblique spectra that agrees with the vertical spectra plus the log of the model ratio is probably contributed by gravity-wave motions. The excellent agreement shown in the figures suggests that most of the velocity fluctuations are gravity-wave motions and that there is little contribution from 2D turbulence. The observed vertical velocity spectra may be twice as great as the actual spectra due to data-acquisition processing and thus, the actual log of the ratio between the averages of the 8 sets of oblique and vertical spectra may be as great as 0.6. The difference between this ratio and the model-predicted log ratio of 0.53 suggests that a surplus of up to 17% of the probable gravity-wave spectral amplitude could be attributed to other processes such as 2D turbulence.

The fluctuation spectra exhibit azimuthal anisotropy that varies from day to day. For instance, in Figure 3, the north and vertical spectra are nearly equal, implying that the north beam is recording only vertical fluctuations while horizontal fluctuations are principally aligned east-west. With measurements in only two directions, determination of the exact shape of the azimuthal dependence is impossible. This anisotropy has an impact on the agreement between the model and the observations, but the difference cannot be quantified until similar measurements are made over a more complete set of azimuths.

The observed anisotropy can result from anisotropy in wave sources or from the selective transmission of gravity waves through an anisotropic wind field at lower levels. However, anisotropy argues against domination of the spectra by 2D turbulence since such turbulence should produce azimuthally isotropic, horizontal velocity fluctuations.

Isotropy is recovered when spectra are averaged for a sufficiently long period. The average east and north spectra in Figure 4 are approximately equal in contrast to the short-term averages presented in the other figures. These observations seem to suggest that the fluctuation spectrum is isotropic over long time scales but that large anisotropies can exist for brief periods. This long term isotropy is most likely not a consequence of 2D turbulence but due to a saturation amplitude limit to be discussed elsewhere.

ACKNOWLEDGEMENTS

Support provided by the Air Force Office of Scientific Research (AFSC) under grant AFOSR 82-0125.

REFERENCES

Balsley, B. B., W. L. Ecklund, and D. C. Fritts (1983), VHF echoes from the high-latitude mesosphere and lower thermosphere: observations and interpretations, J. Atmos. Sci., 40, 2451-2466.

Carter, D. A. (1983), Discrimination against interfering signals at the Poker Flat MST radar, MAP Handbook, 9, edited by S. A. Bowhill and B. Edwards, 120-121.

Dewan, E. M. (1979), Stratospheric wave spectra resembling turbulence, Science, 204, 832-835.

Gage, K. S. (1979), Evidence for a $k^{-5/3}$ law inertial range in mesoscale two-dimensional turbulence, J. Atmos. Sci., 36, 1950-1954.

Garrett, C., and W. Munk (1972), Space-time scales of internal waves, Geophys. Fluid Dyn., 2, 225-264.

Garrett, C., and W. Munk (1975), Space-time scales of internal waves: A progress report, J. Geophys. Res., 80, 291-297.

Jenkins, G. M., and D. G. Watts (1968), Spectral Analysis and its Applications, p. 252, Holden Day, San Francisco.

Lilly, D. K. (1983), Stratified turbulence and the mesoscale variability of the atmosphere, J. Atmos. Sci., 40, 749-761.

Muller, P., D. J. Olbers, and J. Willebrand (1978), The IWEX spectrum, J. Geophys. Res., 83, 479-500.

VanZandt, T. E. (1982), A universal spectrum of buoyancy waves in the atmosphere, Geophys. Res. Lett., 9, 575-578.

VanZandt, T. E. (1985), A model of gravity-wave spectra observed by Doppler sounding systems, Radio Sci., 20, 1323-1330.

3.7.8 EVIDENCE OF A SATURATED GRAVITY-WAVE SPECTRUM THROUGHOUT THE ATMOSPHERE

David C. Fritts and Steven A. Smith

Geophysical Institute and Department of Physics
University of Alaska
Fairbanks, AK

and

Thomas E. VanZandt

Aeronomy Laboratory, NOAA
Boulder, CO 80303

1. INTRODUCTION

A number of studies have addressed the frequency and wave number spectra of atmospheric motions over the past two decades and have revealed a surprising degree of consistency among different measurement techniques. This consistency in spectral shape and power has motivated two competing theories concerning the nature of atmospheric motions responsible for the spectral characteristics. One theory attributes atmospheric motions primarily to two-dimensional (essentially horizontal) turbulence (GAGE, 1979); the other identifies such motions with internal gravity waves (VANZANDT, 1982), analogous to the motion spectrum believed to exist in the oceans (GARRETT and MUNK, 1975).

In this paper, we adopt the view that the dominant mesoscale motions are due to internal gravity waves and show that previous and new vertical wave number spectra of horizontal winds are consistent with the notion of a saturation limit on wave amplitudes. We also propose that, at any height, only those vertical wave numbers $m > m_*$ are at saturation amplitudes, where m_* is the vertical wave number of the dominant energy-containing scale. Wave numbers $m < m_*$ are unsaturated, but experience growth with height due to the decrease of atmospheric density. The result is a saturated spectrum of gravity waves with both m_* decreasing and wave energy increasing with height. This saturation theory is consistent with a variety of atmospheric spectral observations and provides a basis for the notion of a "universal" spectrum of atmospheric gravity waves. It should be noted that the saturation spectrum argument has been advanced independently by DEWAN and GOOD (1985).

2. A SATURATED VERTICAL WAVE NUMBER SPECTRUM

Vertical wave number spectra of horizontal wind fluctuations from several sources that span the height range from the ground to 130 km are plotted in Figure 1. The curve labelled "troposphere" is smoothed data obtained with the use of Jimspheres by ENDLICH et al. (1969). This curve is an average of the spectra from six wind profiles, acquired at roughly 2-hr intervals, from which the average wind profile was subtracted, and has a slope at high wave numbers of ~ -2.5. The best fit curve of DEWAN et al. (1984) to their stratospheric spectra is displayed as the curve labelled "stratosphere". This curve follows an $m^{-2.7}$ power law (where m is vertical wave number) from a wave number of 10^{-3} to 5×10^{-2} cycles/m (corresponding to vertical wavelengths of 20 m to 1 km). The curve labelled "mesosphere" is the inferred horizontal velocity spectrum from the average of summer-time spectra obtained near the mesopause with the Poker Flat MST radar as discussed by SMITH et al. (1985). The slope of this velocity spectrum is -2.5. Finally, the thermospheric spectrum was obtained from winds measured between 85 and 130 km with a three-axis accelerometer sphere flown as part of the STATE campaign. This spectrum is of

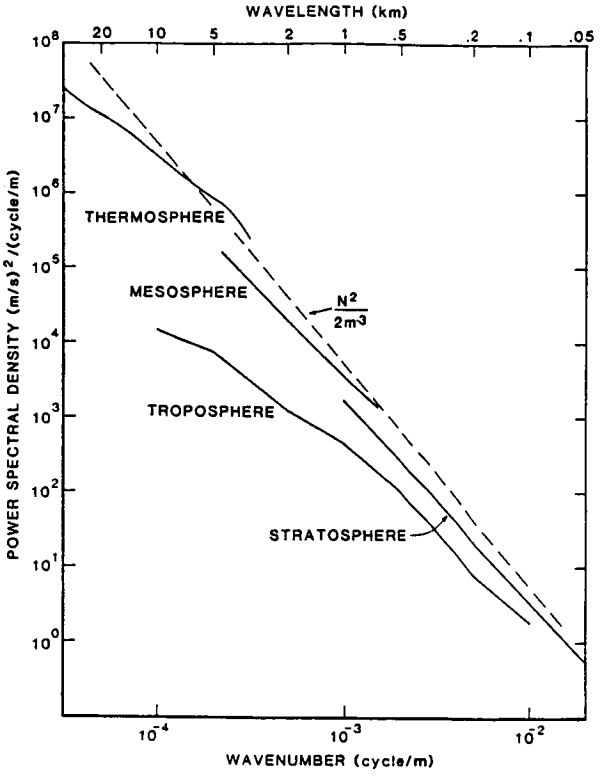

Figure 1. Vertical wave number spectra obtained in four regions of the atmosphere using a variety of different techniques. See text for details.

the scalar wind speed measured by the falling sphere and was smoothed by two passes of a three-point running average to increase the confidence level. It was not possible to remove the mean wind from this velocity data, however.

Figure 1 shows clearly that the spectral shape and the spectral power are very similar from the stratosphere to the lower thermosphere. This spectral similarity can be extended to the troposphere as well by scaling the spectra to a common value of the Brunt-Vaisala frequency, N. The data of DEWAN et al. (1984) and the radar and falling sphere data were obtained from regions with N $\sim$ 0.02 rad/s (a Brunt-Vaisala period near 5 min). However, a typical value of N in the troposphere is half that in the stratosphere. The linear saturation theory reviewed in the next section implies that spectral power should scale as N^2. Thus, an increase in the tropospheric data of ENDLICH et al. (1969) of $\sim$ 4 is required to permit its comparison with data obtained at greater heights.

Assuming that most of the spectral power is associated with vertically propagating gravity waves, the consistency of the scaled vertical wave number spectra with height clearly suggests that some process is acting to limit wave amplitudes, particularly at high vertical wave numbers, throughout the atmosphere. This is consistent with the suggestion, due to WEINSTOCK (1982), that gravity waves are saturated throughout much of the atmosphere.

3. LINEAR SATURATION THEORY

Linear saturation theory assumes that a monochromatic gravity wave will be limited to that amplitude at which the wave just reaches the point of convective instability, i.e., where

$$\theta_z = 0, \tag{1}$$

where θ is the potential temperature. This is equivalent to the condition (see FRITTS, 1984)

$$u' = c - \bar{u}, \tag{2}$$

where u' and u are the horizontal perturbation velocity and the mean flow in the direction of wave motion. This may be written, using the dispersion relation for gravity waves with intrinsic frequencies ω such that $f^2 << \omega^2 << N^2$, as

$$u' = N/m. \tag{3}$$

Thus, the power spectral density for horizontal velocity fluctuations inferred by assuming that each component of the gravity-wave spectrum is individually saturated is

$$E(m) = N^2/2m^3. \tag{4}$$

The third power of m is due to the wave number bandwidth corresponding to each component of the gravity-wave spectrum. This spectral power is shown for N = 0.02 rad/s with a dashed line in Figure 1.

The theoretical curve exceeds the power spectral densities observed throughout the atmosphere by about 2. We believe this difference may be attributed to the superposition of gravity waves in the atmosphere, which seems to restrict amplitudes to less than monochromatic saturation values (SMITH and FRITTS, 1983; MEEK et al., 1985), in good agreement with the observed power spectral densities. Recent numerical results by FRITTS (1985) suggest a similar reduction in the wave amplitudes required for saturation due to superposition.

4. VARIATION OF GRAVITY-WAVE SPECTRUM WITH HEIGHT

Both the data presented in Figure 1 and the form of the analytic gravity-wave spectrum used to fit successfully previous oceanic and atmospheric gravity-wave spectra (GARRETT and MUNK, 1975; VANZANDT, 1982) suggest that the gravity-wave spectrum at any height departs from a saturated spectrum at sufficiently small vertical wave numbers. Observational evidence of this departure is most evident in the tropospheric curve in Figure 1, but may be present in the thermospheric data as well. The departure in the analytic spectral description consistent with a saturated high wave number spectrum enters as a spectral break at a wave number m_* via a term of the form

$$(1 + m/m_*)^{-3}, \tag{5}$$

providing limiting slopes of -3 and 0 for high and low wave numbers, respectively.

The departure from a saturated spectrum at small vertical wave numbers in the lower atmosphere suggests that these motions are not excited at large amplitudes. As these motions propagate upward, however, they are expected to

grow with height due to the decrease in atmospheric density. The results of this process are a gravity-wave energy and a dominant vertical wavelength that increase with height, as noted in a number of previous studies.

A model of the proposed vertical wave number spectrum and its variation with height is presented in Figure 2. This spectrum assumes a vertical wave number dependence given by (5). At vertical wave numbers $m > m_*$, for which the spectrum is assumed saturated, the energy levels are the same at all heights. At smaller (unsaturated) wave numbers, however, the growth of wave amplitudes with height causes the dominant vertical scale (m_*^{-1}) to increase accordingly. This is shown with values of the dominant vertical wavelength ($\lambda_z = m_*^{-1}$) of 1, 5, and 20 km in the troposphere, stratosphere, and mesosphere, respectively.

Evidence of this behavior is provided by a variety of observations, including gravity-wave energies that increase with height (BALSLEY and CARTER, 1982; BALSLEY and GARELLO, 1985) and detailed gravity-wave studies in the stratosphere, mesosphere, and lower thermosphere showing gravity-wave scales that increase with height (SATO and WOODMAN, 1982; BARAT, 1983; SMITH and FRITTS, 1983; MEEK et al., 1985; FRITTS et al., 1985). We should expect, however, that the energy at low wave numbers, and hence m_*, will be considerably more variable than the energy at $m > m_*$, because the gravity-wave energy at $m < m_*$ is determined by the strenghts of various gravity-wave sources at lower levels, whereas that at $m > m_*$ is limited by saturation processes.

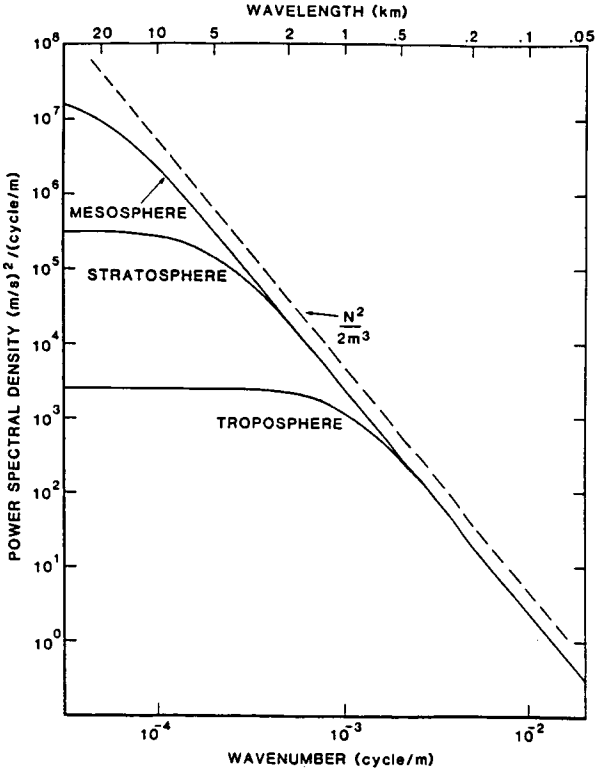

Figure 2. Model saturated gravity-wave spectrum scaled to a common N^2 at three different heights. Note the constant (saturated) energies for large wave numbers and the increase in the dominant vertical scale with height.

REFERENCES

Balsley, B. B., and D. A. Carter (1982), The spectrum of atmospheric velocity fluctuations at 8 and 86 km, Geophys. Res. Lett., 9, 465-468.

Balsley, B. B., and R. Garello (1985), The kinetic energy density in the troposphere, stratosphere and mesosphere: A preliminary study using the Poker Flat radar in Alaska, Radio Sci., 20, 1355-1362.

Barat, J. (1983), The fine structure of the stratospheric flow revealed by differential sounding, J. Geophys. Res., 88, 5219-5228.

Dewan, E. M., and R. E. Good (1985), Saturation and the "universal" spectrum for vertical profiles of horizontal scalar winds in the atmosphere, submitted to J. Geophys. Res.

Dewan, E. M., N. Grossbard, A. F. Quasada, and R. E. Good (1984), Good spectral analysis of 10 m resolution scalar velocity profiles in the stratosphere, Geophys. Res. Lett., 11, 80-83 and 624.

Endlich, R. M., R. C. Singleton, and J. W. Kaufman (1969), Spectral analysis of detailed vertical wind speed profiles, J. Atmos. Sci., 26, 1030-1041.

Fritts, D. C. (1984), Gravity wave saturation in the middle atmosphere: A review of theory and observations, Rev. Geophys. Space Phys., 22, 275-308.

Fritts, D. C. (1985), A numerical study of gravity wave saturation: Nonlinear and multiple wave effects, J. Atmos. Sci., in press.

Fritts, D. C., S. A. Smith, B. B. Balsley, and C. R. Philbrick (1985), Evidence of gravity wave saturation and local turbulence production in the summer mesosphere and lower thermosphere during the STATE experiment, submitted to J. Geophys. Res.

Gage, K. S. (1979), Evidence for $k^{-5/3}$ law inertial range in mesoscale two-dimensional turbulence, J. Atmos. Sci., 36, 1950-1954.

Garrett, C. J. R., and W. Munk (1975), Space-time scales of internal waves: A progress report, J. Geophys. Res., 80, 291-297.

Meek, C. E., I. M. Reid, and A. H. Manson (1985), Observations of mesospheric wind velocities, I. Gravity wave horizontal scales and phase velocities determined from spaced wind observations, Radio Sci., 20, 1363-1382.

Sato, T., and R. F. Woodman (1982), Fine altitude resolution radar observations of upper-tropospheric and lower-stratospheric winds and waves, J. Atmos. Sci., 39, 2539-2545.

Smith, S. A., and D. C. Fritts (1983), Estimation of gravity wave motions, momentum fluxes and induced mean flow accelerations in the winter mesosphere over Poker Flat, Alaska, Proc. 21st Conf. Radar Meteorol., Edmonton, Canada, 104-110.

Smith, S. A., D. C. Fritts, and T. E. VanZandt (1985), Comparison of mesospheric wind spectra with a gravity wave model, Radio Sci., 20, 1331-1338.

VanZandt, T. E. (1982), A universal spectrum of buoyancy waves in the atmosphere, Geophys. Res. Lett., 9, 575-578.

Weinstock, J. (1982), Nonlinear theory of gravity waves: Momentum deposition, generalized Rayleigh friction, and diffusion, J. Atmos. Sci., 39, 1698-1710.

4.0 INTERCOMPARISON AND CALIBRATION OF WIND AND WAVE MEASUREMENTS AT VARIOUS FREQUENCIES

R. A. Vincent

Physics Department, University of Adelaide
Adelaide, Australia 5001

INTRODUCTION

Radars are increasingly being used for determinations of the small-scale wave and turbulence fields of the atmosphere. It is important to understand as fully as possible the likely sources of error or bias in radar velocity determinations. This is especially true for the determination of wave and turbulence parameters which often rely on the measurement of first or 'second order' deviations from the prevailing wind and therefore require better precision and time resolution than is usually required for measurements of the mean winds alone. The intercomparison of velocity measurements made with different techniques (e.g., radar and balloon) can be expected to help determine not only the relative effectiveness of the different methods, but also the degree of reliability.

SYSTEMATIC AND RANDOM ERRORS IN RADAR WIND MEASUREMENTS

Systematic errors. In most respects, the more serious velocity errors are systematic in origin for the commonly used Doppler technique whereby the horizontal wind components are inferred by tilting the radar beam away from the zenith, systematic errors are most probably caused by the aspect sensitivity of the scattering irregularities. The effective pointing angle of the radar beam from the zenith is a product of the actual beam pattern and the angular dependence of the scattering, so if there is enhanced scattering from the zenith then the effective pointing angle of the radar beam will be less than the physical angle (e.g., ROTTGER and LARSEN, 1984). If such effects occur and are left uncorrected, then the net effect is to bias the wind speeds to low values. Recent multi-angle Doppler measurements made with the Kyoto MU radar show that aspect sensitivity problems are especially severe in the stratosphere (T. Tsuda, private communication) and that horizontal wind measurements are biased for pointing angles of less than 8-10°; these observations support the recommendations of the Second MST Workshop (VINCENT, 1984) that the optimum pointing angles are between 10° and 15°. However, when using large off-vertical angles care must be taken that any signal leakage through vertically pointing sidelobes are also accounted for (STRAUCH et al., 1984).

Radars provide a particularly powerful means of measuring vertical velocities (w) by observing the Doppler shifts of echoes received in vertically pointing beams. Because of the small magnitudes of w, however, care must be taken to remove any contamination due to the horizontal wind components. Contamination can arise in a number of ways (ROTTGER, 1984) and may be significant at VHF where specular reflections from tilted irregularities can be important. Special care must be taken in inferring vertical velocities when the transmitting and receiving antennas are separated, as would be the case in the SA experiment. Because of the geometry, the signals will be scattered at small angles to the vertical and the contamination will be significant, especially at low heights where the effect is most severe (May, private communication). ROTTGER (1984) has shown how interferometer measurements can be used, in principle, to correct observations of w.

The major source of systematic errors in the spaced antenna technique is likely to be the 'triangle-size effect'. If the receiving antenna size is too small compared with the average pattern size of the diffraction pattern, then

the velocities will tend to be underestimated. The factors which control the pattern size are discussed in VINCENT (1984) where recommendations are made for minimizing this effect, but more work needs to be done to understand its causes.

Random errors. DOVIAK et al. (1979) have discussed the factors which influence errors in Doppler measurements. The mean square error (σ_v^2) of a radial velocity (v_r) is given by

$$\sigma_v^2 = V_N^2 e^{(\pi\sigma_n)2} [(N/S)^2 + (\frac{2N}{S})(1-e^{-2(\pi\sigma_n)^2}) + \pi^{3/2}\sigma_n]/(2\pi^2 M) \quad (1)$$

where S/N is the signal-to-noise ratio, σ_n is the spectral width normalized to the Nyquist velocity, V_n, and M is the number of samples. For S/N > 10 dB the rms error is approximately

$$\sigma_v^2 \sim V_n^2 \sigma_n e^{(\pi\sigma_n)^2}/(2M\pi^{1/2}) \quad (2)$$

while at low S/N (<0 dB) the error is approximately

$$\sigma_v^2 \sim (N/S)^2 v_n^2/(2\pi^2 M) \quad (3)$$

For example, based on data taken with the MU radar, typical fractional errors in 90 s estimates of the horizontal wind component are about 0.07 in the lower troposphere (S/N $\sim$ 30 dB), about 0.13 in the upper troposphere (S/N -6 dB) and up to 0.25 in the lower stratosphere with S/N $\sim$ 6 dB.

Errors for the SA method are not so easy to evaluate, but MAY and BRIGGS (1985) have derived an expression for the random errors which is a particularly important development for this technique. The velocities are found using the time shifts to the maxima in the cross correlation functions (τ_{max}) and the times for the autocorrelation to fall to the value of the cross correlation at zero lag (τ_x) (BRIGGS, 1984). The respective errors are:

$$\sigma_{max} \sim 0.5\, \tau_{1/2}^{3/2}\, T^{-1}(1 - \rho_m^2)/\rho_m \quad (4)$$

$$\sigma \sim 0.5\, \tau_{1/2}^{5/2}\, T^{-1/2} \tau_x^{-1}(1 - \rho_x^2)/\rho_x \quad (5)$$

where $\tau_{1/2}$ is the mean fading time (proportional to the spectral width), T is the record length (proportional to M) and the correlation values (ρ_m, ρ_x) are evaluated before the effects of the noise are removed. In the mesosphere, for SA measurements made at MF with S/N $\sim$10 dB and fading times 2-5 s, May finds fractional errors in velocity of up to about 10%.

In the lower atmosphere, comparisons made with the Adelaide VHF radar operating in the spaced antenna mode with radiosonde winds made from a site 35 km away show rms differences of about 3 ms^{-1}.

ERRORS IN WAVE AND TURBULENCE MEASUREMENTS

Wave Fluxes. The random errors cited above give some idea about the averaging times which are required to achieve a desired level of accuracy in measuring gravity-wave parameters. Estimates of gravity-wave amplitudes vary, but balloon measurements suggest rms amplitudes of about 1-2 ms^{-1} for stratospheric inertio-gravity waves (e.g., BARAT, 1983). High resolution rocket smoke trail measurements also give rms amplitudes of about 1 to 2 ms^{-1}

in the lower to mid-stratosphere (DEWAN et al., 1984) with little or no geographic or seasonal variation. VHF radar measurements in the upper troposphere reported by BALSLEY and CARTER (1982) give similar amplitudes to those quoted above.

There are relatively few measurements of vertical wave amplitudes in the lower atmosphere, but unique constant-pressure balloon observations reported by MASSMAN (1981) for the Southern Hemisphere show differences between the upper tropical troposphere and the lower midlatitude stratosphere. Amplitudes were larger in the troposphere ($w' \sim 0.2$ ms^{-1}) than in the stratosphere ($w' \sim 0.1$ ms^{-1}). The intrinsic periods of the wave events observed by Massman ranged between 30 and 180 min, so using the gravity-wave dispersion relation, the corresponding rms horizontal amplitudes were also between 1 and 2 ms^{-1}. Overall, there appears to be relatively good agreement about wave amplitudes as observed by a variety of different techniques.

An important wave parameter is the vertical flux of horizontal momentum and particularly the zonal component, $\overline{u'w'}$. Radar estimates can be made by correlating u' and w' (e.g., SMITH and FRITTS, 1983) or by observing the mean square radial velocities along two radar beams offset at an angle θ to the zenith (VINCENT and REID, 1982) viz:

$$\overline{u'w'} \quad (\overline{v_1^2} - \overline{v_2^2})/(2 \sin 2\theta) \tag{6}$$

Because the difference of two quantities $\overline{v_1^2}$, $\overline{v_2^2}$ which are similar in magnitude is involved, the effects of random errors can be large. Approximately, the error is

$$\delta(\overline{u'w'}) \sim \overline{2u'\delta u'}/(\sin 2\theta) \tag{7}$$

In the mesosphere, for observations at an angle of, say, 10°, $u' \sim 3.5$ ms^{-1} (corresponding to a 20 ms^{-1} horizontal rms amplitude) and $\delta u' \sim 0.5$ ms^{-1} for a 4-min observation at 2 MHz so that to achieve an accuracy of ~ 1 m^2 s^{-2} requires about a 6-hr average. The only observations of $\overline{u'w'}$ so far for the mesosphere are radar measurements; typically, $\overline{u'w'} \sim 1$-5 ms^{-1} in magnitude. For the lower atmosphere, MASSMAN (1981) found from balloon measurements mean values of $\rho_0 \overline{u'w'}$ of about 0.04 Nm^{-2} in the upper troposphere and 0.02 Nm^{-2} in the stratosphere for freely propagating gravity waves. The respective values of $|\overline{u'w'}|$ are 0.18 and 0.06 m^{2}s^{-2}. To achieve accuracies of 0.01 m^{2}s^{-1} would require about 2 days of radar observations if an rms radial velocity of $u' \sim 0.25$ ms^{-1} and a comparable value for $\delta u'$ are assumed. These estimates are crude and may be overestimates of the averaging times required. REID (1981) found that mean square difference between Doppler velocities measured in the mesosphere over 3 days by two radar beams connected to independent receiving and digitizing systems was only 0.1 m^2 s^{-2}.

It should be noted that the radar technique of VINCENT and REID (1982) is not suitable for measuring the fluxes associated with topographic waves ($c = 0$). However, aircraft and balloon observations show the fluxes for stationary waves can be large in the troposphere and as PALMER et al. (1985) have noted, breaking mountain waves may be an important source of drag in the lower atmosphere. The momentum fluxes associated with these waves are found to be in the range 0.1 to 1 Nm^{-2}.

Turbulence Parameters. Radars can be used to estimate turbulence parameters such as eddy dissipation rates (ε) and diffusion coefficients (D), in a number of ways. However, the best way appears to be via measurements of the spectral width of the received signals, after the effects of shear and beam broadening, as well as "spikes" due to specular reflections, are taken into

account. These effects are relatively more important for wider beam radars and as the mean velocity of the background flow increases. HOCKING (1985) has recently summarized the various techniques and limitations of radar estimates of turbulence.

For example, the spectral width broadening due to turbulence, σ_t, is given by

$$\sigma_t^2 = \sigma_e^2 - \sigma_s^2$$

where σ_e and σ_s are the experimental (measured) and shear broadened width, respectively. Hocking points out that in many experimental situations σ_e and σ_s are similar in magnitude so that statistical fluctuations can cause negative values for σ_t^2; these should be taken into consideration along with the positive values, otherwise the estimates of ε will be biased too high. Often it may not be possible to obtain reliable estimates of σ_t^2 at all.

Indirect comparisons of radar measurements of ε in the lower atmosphere ($\sim$0.2 m^2s^{-1}) suggest they may be an order of magnitude greater than aircraft estimates (e.g., SATO and WOODMAN, 1982; Lilly et al., 1974). These discrepancies do not yet appear to have been resolved and it would be very desirable if simultaneous intercomparisons of balloon, radar and aircraft techniques were arranged.

TECHNIQUES FOR MEASURING HORIZONTAL WAVELENGTHS AND PHASE VELOCITIES

If the role played by gravity waves in the middle atmosphere is to be fully understood, then more measurements are required of horizontal scales (λ_x) and phase velocity (c) since these are amongst the least well-known gravity-wave parameters. A number of radar techniques have been devised but not yet widely applied. All methods measure the time for waves to pass between horizontally separated observing locations. The main differences between techniques depends on whether a single radar is used or a network. VINCENT and REID (1982) used a single radar to compare the wave motions observed in one beam with the motions measured in another, widely separated beam. Some assumptions have to be made in analyzing the results and there is the possibility of ambiguities for waves with λ_x less than the separation of the observed regions. ROTTGER (1984) has used an interferometric technique to compare the wave motions observed in a radar beam pointed in two directions close to the zenith. A network of spaced antenna stations (GRAVNET) has been used by MEEK et al. (1985) to study scales and velocities in the mesosphere and the results are similar to those found by VINCENT and REID (1982), while CARTER et al. (1984) used a network of three ST radars with vertically directed beams to investigate waves in the troposphere. An important finding of all these measurements is that monochromatic waves occur relatively infrequently and some way must be found of describing the rather random wave field which appears to be the norm in all regions of the atmosphere.

SUMMARY

Considerable progress has been made in applying MST radars to studies of wave and turbulence motions in the middle atmosphere. Where comparisons can be made between measurements made by different techniques, the results are in reasonable accord, taking into account the temporal and spatial separations often involved. The usual comparisons have been between radiosonde balloons and radar determinations of the prevailing wind, but before MST radar techniques can be fully exploited for wave and turbulence observations, it is necessary to understand the errors and limitations likely to be encountered. While the use of relations like equation (1) can give some indication of the likely errors involved in a single observation, it is essential that they be

checked by other means. For instance, one practical method would be to find the rms difference between velocities taken as closely spaced as possible in time or space. It is very important that further intercomparisons be made between as many different techniques as possible in order to test the basic assumptions which are inherent in any measurement of velocity. To this end, for example, the Kyoto and Adelaide atmospheric groups recently used the MU radar to make comparisons of velocities measured by the Doppler and SA methods. Multi-beam experiments were also made to test the assumption made in the "dual-beam" momentum flux techniques that the wave field is horizontally homogeneous. It is noted that most MST radar studies to date have been confined to observations of propagating waves. It would be an important development if these studies could be extended to investigations of orographic waves; joint experiments with balloons and aircraft are called for and the capability of radars to scan in azimuth and elevation needs to be exploited as well as the use of networks in order to measure such important properties as energy and momentum fluxes and wavelengths.

REFERENCES

Balsley, B. B., and D. A. Carter (1982), The spectrum of atmospheric velocity fluctuations at 8 km and 86 km, Geophys. Res. Lett., 9, 465-468.

Barat, J. (1983), The fine scale of stratospheric flow revealed by differential sounding, J. Geophys. Res., 88, 5219-5228.

Carter, D. A., B. B. Balsley, W. L. Ecklund, M. Crochet, A. C. Riddle, and R. Garello (1984), Tropospheric gravity waves observed by three closely spaced ST radars, Handbook for MAP vol 14, 219-228, SCOSTEP Secretariat, Dep. Elec. Computer Eng., Univ. IL, Urbana-Champaign.

Dewan, E. M. N. Grossbard, A. F. Quesada, and R. E. Good (1984), Correction, Geophys. Res. Lett., 11, 624.

Doviak, R. J., D. S. Zrnic', and D. S. Sirmans (1979), Doppler weather radar, Proc. IEEE, 67, 1522-1553.

Hocking, W. K. (1985), Measurements of turbulent energy dissipation rates in the middle atmosphere by radar techniques - A review, Radio Sci., 20, 1403-1422.

Lilly, D. K., D. E. Waco, and S. I. Adelfang (1974), Stratospheric mixing estimated from high-altitude turbulence measurements, J. Appl. Meteorol., 13, 488.

May, P., and B. H. Briggs (1985), Statistical errors in the spaced antenna technique, J. Atmos. Terr. Phys., submitted.

Massman, W. J. (1981), An investigation of gravity waves on a global scale using TWERLE data, J. Geophys. Res., 86, 4072-4082.

Meek, C., I. M. Reid, and A. H. Manson (1985), Observations of mesospheric wind velocities. I. Gravity wave horizontal scales and phase velocities determined from spaced wind observations, Radio Sci., 20, 1363-1382.

Palmer, T. N., G. J. Shutts, and R. Swinbank (1985), Alleviation of a systematic westerly bias in general circulation and numerical weather prediction models through an orographic gravity wave drag parameterization, to be submitted.

Reid, I. N. (1981), Radar studies of atmospheric gravity waves, Ph.D. thesis, University of Adelaide.

Rottger, J. (1984), Improvement of vertical velocity measurements, Handbook for MAP vol 14, 150-155, SCOSTEP Secretariat, Dep. Elec. Computer Eng., Univ. IL, Urbana-Champaign.

Rottger J., and M. F. Larsen (1984), Potential advantages of the spaced antenna method for operational wind profiling, Handbook for MAP vol 14, 134-138, SCOSTEP Secretariat, Dep. Elec. and Computer Eng., Univ. IL, Urbana-Champaign.

Sato, T., and R. F. Woodman (1982), Fine altitude resolution observations of stratospheric turbulent layers by the Arecibo 430 MHz radar, J. Atmos. Sci., 39, 2546.

Smith, S. A., and D. C. Fritts (1983), Estimation of gravity wave motions, momentum fluxes and induced mean flow accelerations in the winter mesosphere over Poker Flat, Alaska, Proc. 21st Conf. Radar Meteorol., Edmonton, Canada, 104-110.

Strauch, R. G., K. B. Earnshaw, D. A. Merritt, K. P. Moran, and D. W. van de Kamp (1984), Performance of the Colorado wind-profiling network, Handbook for MAP vol 14, 38-49, SCOSTEP Secretariat, Dep. Elec. Computer Eng., Univ. IL, Urbana-Champaign.

Vincent, R. A. (1984), Relationship of spaced antenna and Doppler techniques for velocity measurements, Handbook for MAP vol 14, 126-130, SCOSTEP Secretariat, Dep. Elec. Computer Eng., Univ. IL, Urbana-Champaign.

Vincent, R. A., and I. M. Reid (1982), HF Doppler measurements of mesospheric gravity wave momentum fluxes, J. Atmos. Sci., 40, 441.

SESSION SUMMARY AND RECOMMENDATIONS

The emphasis in this session was on velocity intercomparisons made not only between radars and radiosondes, but also between radars operating at different frequencies. There was general consensus that the agreement between radiosonde winds and the radar velocities whether measured by the Doppler or spaced antenna techniques was good. Typically, the rms differences were of the order of 3-5 ms^{-1}, which are generally within the limitations imposed by the spatial and temporal differences inherent in most of the comparisons made to date; even radiosonde packages flown on the same balloon give rms differences of about 3 ms^{-1}. Many comparisons have been of relatively short duration and it is desirable that more extensive series of evaluations be made so as to recognize and remove any sources of systematic bias which may be present in radar wind determinations. It was agreed that where feasible, special soundings be made in order to provide further intercomparisons that are as close in time and space as possible.

There was much discussion on the impact of random errors on radar measurements of wave turbulence parameters. In the lower atmosphere in particular, the random errors are likely to be of comparable magnitude to the wave amplitudes and there was general agreement that the errors in individual measurements needed to be assessed very carefully. Efforts should continue to find the optimum data reduction methods. Efforts should also continue to devise alternate techniques for measuring such important wave parameters as $\overline{u'w'}$. The dual-complementary-beam technique requires measurements from regions displaced horizontally in space but the best determinations will come from simultaneous measurements of u' and w' made in a common volume. Horizontally displaced receiving systems could be used to look at the same scattering volume from one or more angles other than backscatter. Such multistatic arrangements would not only allow more direct measurements of $\overline{u'w'}$ but also some of the assumptions of the dual-beam method to be tested.

Papers presented in this session gave further evidence of the ability of 50-MHz radars to make studies of precipitation during convective activity. There was much interest shown in this work which appears to provide opportunities for studies of cloud physics with low VHF radars.

Some of the most extensive discussions, both formal and informal, concerned the optimum frequency for clear-air wind profiling. To date, most ST radars have operated near 50 MHz, but now radars using frequencies near 400 MHz are being, or are about to be, evaluated. While a number of factors influence the choice of an operating frequency (including the availability of a suitable frequency band), concern was expressed that the effects of precipitation be taken into account when a choice is being made. Experience shows that the

precipitation and turbulence echoes can be separated at 50 MHz but, near 400 MHz the observed signals will be from water droplets rather than turbulence-induced refractive index fluctuations in nearly all precipitating systems. Precipitation, no matter how light, will therefore preclude direct vertical-beam, vertical wind measurements at the higher frequency. It probably does not matter about measurements in strong convection. However, the direct vertical wind data will be missing also in stratiform rain, which can be extensive in horizontal extent. The measured vertical velocities are important in order to convert correctly the off-vertical radial velocities to horizontal motions. It is not possible to infer vertical air motion from horizontal measurements for 3 beam systems (1 zenith beam) when the scattered signal is from water droplets. Indirect vertical velocity measurements would require different or additional pointing angles; however obtaining the vertical velocity from integration of the continuity equations may not be accurate enough anyway. Thus, one cannot expect to obtain vertical air motion in precipitation with UHF radars. Note that this is a problem in the lowest 4-6 km in stratiform precipitation; above this altitude, the fall speed of the particles and the uncertainty of the vertical velocity are comparable. The determination of network-type vertical velocities by objective analysis techniques is still possible but will be valid for the scale of the network spacing.

Concern was expressed that, before large-scale networks of wind-profiling radars be established, the relative merits of operating in either the lower VHF or lower UHF bands be fully assessed. It may well be that an intermediate frequency near, say, 200 MHz is optimum.

4.1.1 AN EVALUATION OF ERRORS OBSERVED IN THE MEASUREMENT OF LOW WIND VELOCITIES

S. R. Williams and D. W. Thomson

The Pennsylvania State University
Department of Meteorology
University Park, PA 16802

INTRODUCTION

Measurements of low wind velocities ($|V_H| \approx 0$ to 6 m/s) with a VHF wind profiler can be difficult if ground clutter, or other biases in the system dominate in altering the position of the perceived peak in the calculated power spectrum. A variety of methods for "ground clutter" suppression are used in profiler systems today (CORNISH, 1983). Typically, dc offsets are removed before the spectra are calculated. Several other techniques for editing are used for clutter suppression after the spectra are calculated. One of these methods called "zero suppression" takes the spectral value of a selectable number of points (N) on each side of 0 velocity (one point on either side, in this study) and sets them equal to the mean value of the points exterior to the specified N points on either side of 0. Our analysis done with the PSU VHF(1) radar, shows that this zero-suppression method can systematically bias horizontal winds (V_H) below 6 m/s. With the zero suppression, an artificial increase in absolute wind velocities occurs when the spectral peaks fall within the $\pm$ N points of the FFT (personal communication, Strauch, 1985). We have also established that the method artificially decreases the absolute wind velocities inferred from spectral peaks that are outside but near the suppressed region. In the remainder of this short report we show comparisons of wind profiles observed with and without zero suppression. The range of the biased velocities extends to about $\pm$ 6 m/s. Biases have been deduced to be as much as 2 m/s, but more commonly they are on the order of 1.0 m/s.

OBSERVATIONAL METHOD

In this study, comparative observations were made using only the high resolution (Δz = 270 m) mode. Nine separate first moment calculations were averaged together (STRAUCH et al., 1985) for each range gate (24 gates). In the standard observational sequence, 12 such velocity profiles are averaged together to create the reported hourly profile. To obtain the data for this study, the radar was shut off momentarily to manually switch the zero suppression from "ON" to "OFF". A 90-sec observation was then immediately taken after each such change in order to fairly compare the velocity profiles with and without zero suppression.

The first measurements were performed on August 12, 1985, when a single 90-sec observation with this suppression was immediately followed by an observation without it. This was made before we were strongly suspicious that such biases were of sufficient magnitude to be of substantial importance. By taking the first-moment calculations and plotting them as a function of height, one can readily show the bias introduced by the suppression (Figure 1). The corresponding power spectra (each of which is an average of 9 spectra) are shown in Figures 2a,b. The horizontal axis is scaled in FFT points, and the vertical axis represents the relative reflected power at each individual range gate. The topmost spectrum corresponds to the 8.60 km MSL range gate; the lowermost to 1.94 km MSL. The two hack marks indicated on each spectrum indicate the FFT points at which the velocity peaks first reached the noise level. In Figure 2a, the velocity peaks picked seem to lie just outside the suppressed area which can be seen as the "flat tops" near 0 velocity. Figure 2b shows the corresponding spectra evaluated without zero suppression. They

were taken approximately two minutes later. The "notch" evident at 0 velocity is a consequence of the dc removal.

Since typical magnitudes of velocity variations between two 90-sec observations can be as large as the bias seen in Figure 1, a single comparative observation as recorded on August 12 would not be statistically significant. Thus, following our initial observation of the possible bias, we waited for the appropriate weather conditions for a second "low velocity" day; it occurred on September 15, 1985. Data were recorded during two observation periods on September 15: labeled Period 1 (04:17 to 04:47 Z) and Period 2 (12:23 Z to 12:45 Z). In Period 1, six comparisons with and without zero suppression were taken. The average wind profiles for the component in each beam are plotted in Figures 3a,b. The histogram of absolute values for velocity differences (Figures 4a,b) show the average bias to be $\sim$ 1 m/s. During Period 2, although the velocities had changed appreciably, the bias still remained between 0.79 to 0.91 m/s on the average as seen in Figures 5 and 6.

A bias of f1 m/s in an absolute sense is small, but in relative terms this bias can easily be as much as 50 percent of the observed velocity. Furthermore, it could produce a substantial fraction of the rms error associated with the radar when its measurements are compared with conventional wind soundings. The error could be of particular significance when the radar is being used for estimating derived parameters such as temperature advections which are dependent upon the calculated vertical wind shear. On the other hand, referring back to Figures 2a,b, it can be seen that the present zero suppression can be helpful in the uppermost gates in which the signal-to-noise ratio is normally lower. Perhaps a gate-number-dependent zero-suppression technique should be applied which would take into account the number of each gate as well as the characteristics of each site's ground-clutter pattern and typical variations in S/N ratio, etc.

REFERENCES

Cornish, C. R. (1983), Parameterization of spectra, Handbook for MAP vol 9, 535-542, SCOSTEP Secretariat, Dep. Elec. Computer Eng., Univ. IL, Urbana-Champaign.

Strauch, R. G., D. A. Merritt, and K. P. Moran (1985), Radar wind profilers in the Colorado network, NOAA Tech. Memo. ERL WPL-120, March 1985.

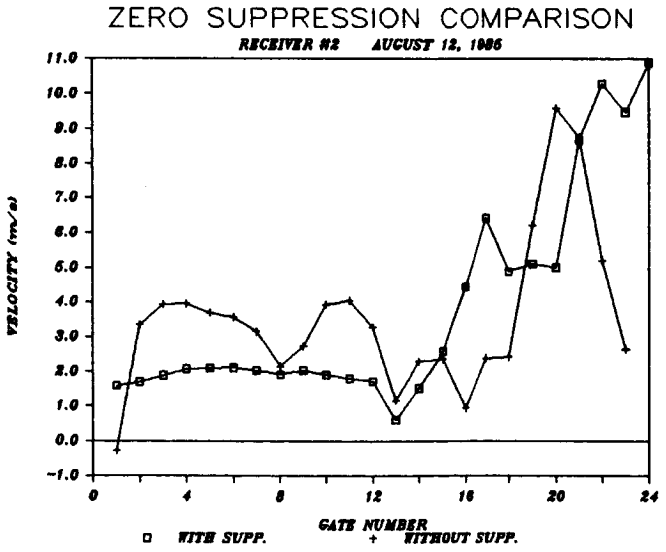

Figure 1.

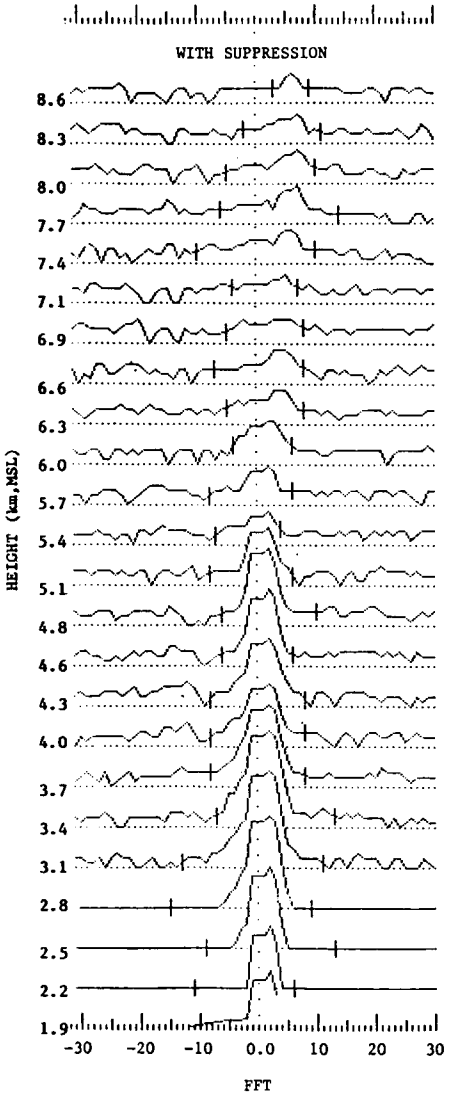

Figure 2a.

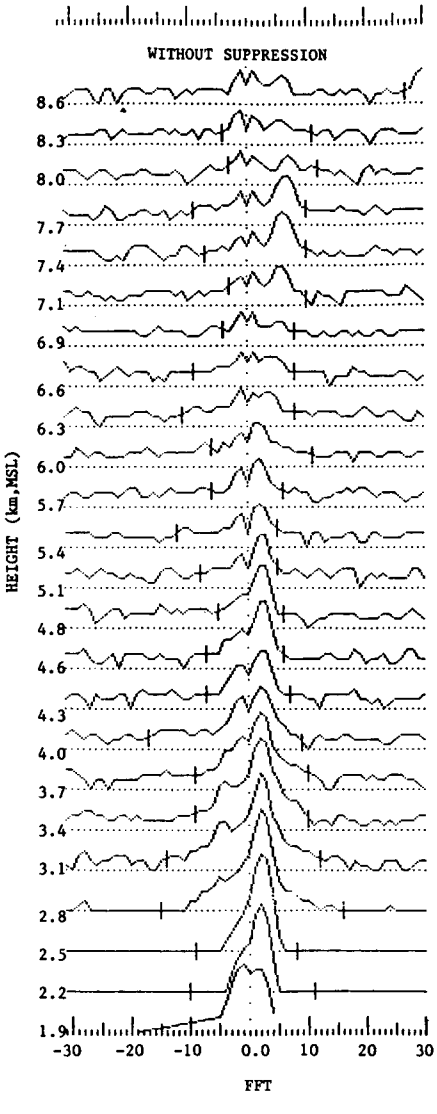

Figure 2b.

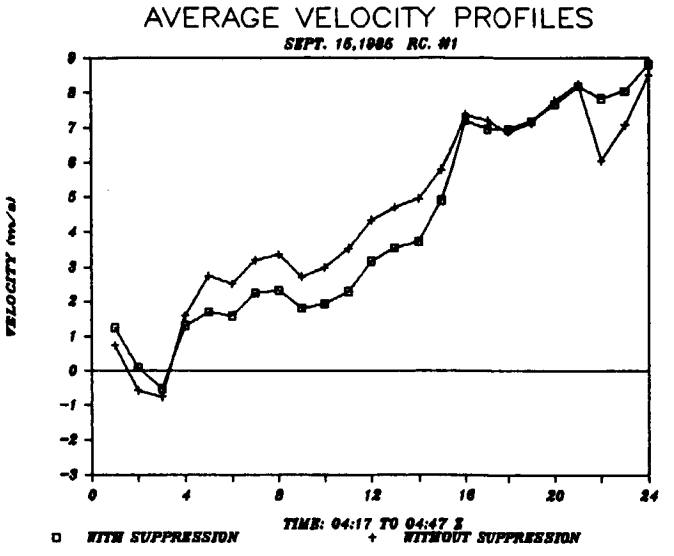

Figure 3a.

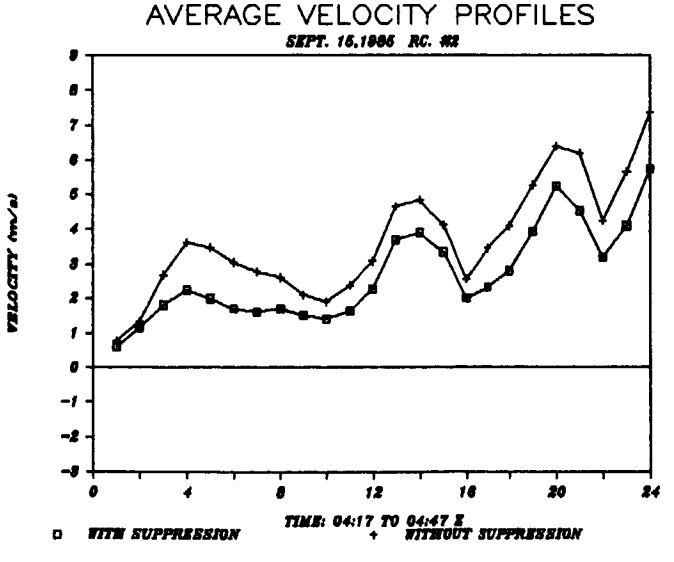

Figure 3b.

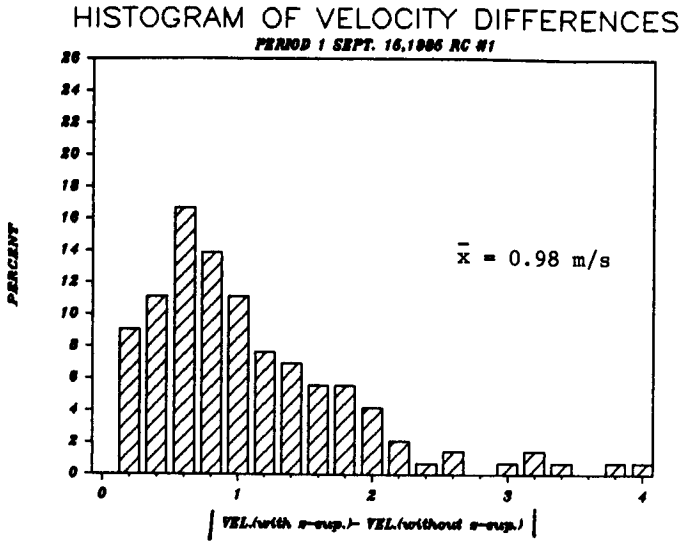

Figure 4a.

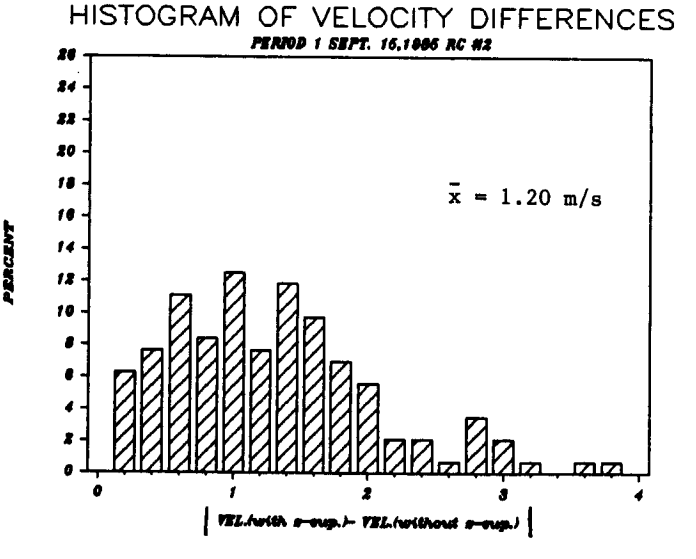

Figure 4b.

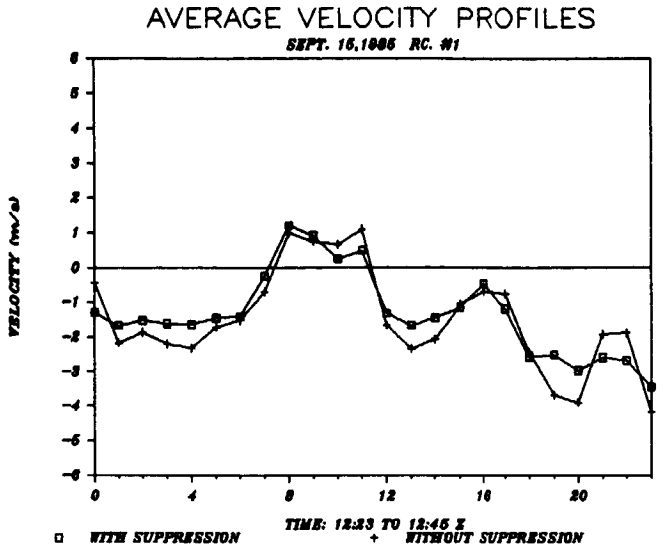

Figure 5a.

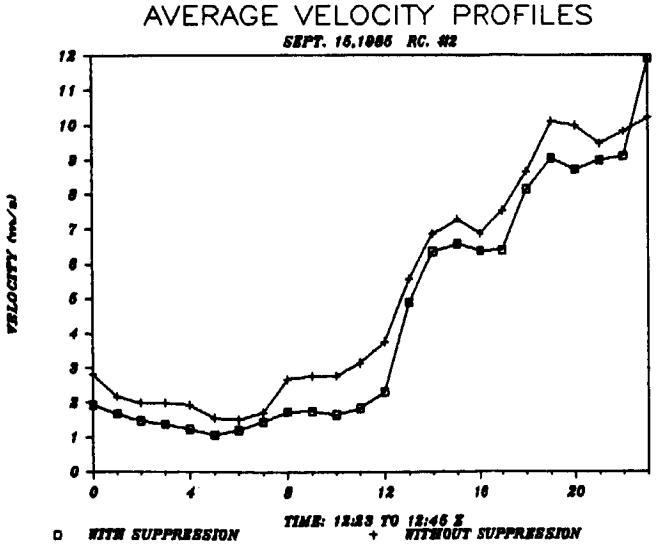

Figure 5b.

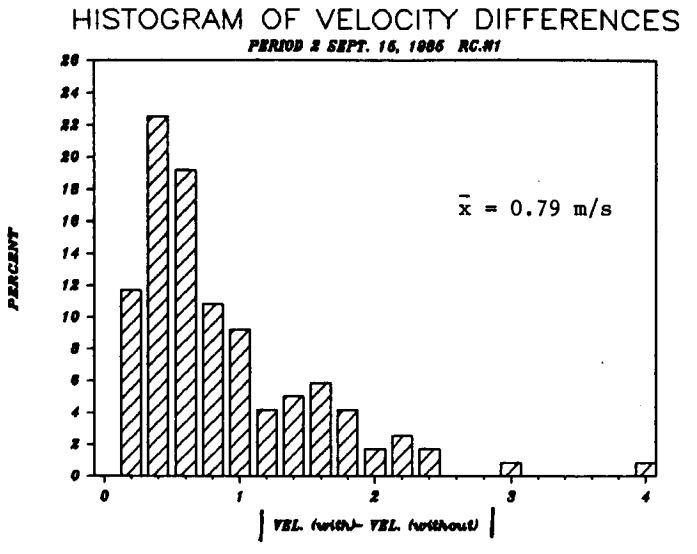

Figure 6a.

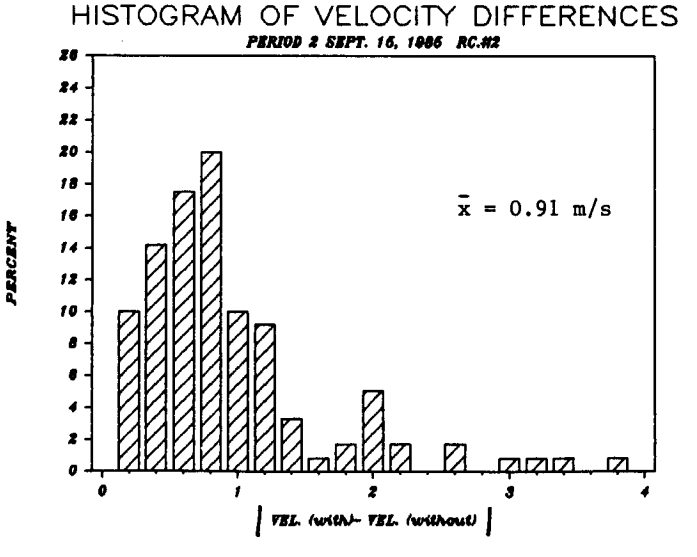

Figure 6b.

4.1.2 A COMPARISON OF VERTICAL VELOCITIES MEASURED FROM SPECULAR AND NONSPECULAR ECHOES BY A VHF RADAR

J. L. Green, W. L. Clark, J. M. Warnock

Aeronomy Laboratory
NOAA, Boulder, CO 80303

G. D. Nastrom

Control Data Corporation
Minneapolis, MN 55440

INTRODUCTION

One of the important and almost unique capabilities of the MST radar technique is the measurement of the vertical component of wind velocity. Measurements of vertical velocity are routinely made at many ST and MST radars both from scattering due to turbulence and quasi-specular reflection. Not only is the vertical velocity of great significance in itself, but as shown by CLARK et al. (1985), often the vertical velocity is required for accurate determinations of horizontal velocity.

However, for a number of years, there have been doubts about the accuracy of vertical velocities measured with quasi-specular reflections (GAGE and GREEN, 1978; ROTTGER, 1980, 1981). The concern has been that the layers producing the quasi-specular echoes might have small tilts as show in Figure 1a. Because of the quasi-specular reflection process, this hypothetical tilt would control the effective zenith angle of the radar antenna beam so that a small component of the horizontal velocity would be included in what was assumed to be a truly vertical beam. It is the purpose of the research reported here to test the hypothesis that there is an effect on the wind velocities measured on a vertical antenna beam due to a long-term tilting of the stable atmospheric layers that cause quasi-specular reflection.

Gravity waves have been observed to cause short-term tilting of turbulent layers (HOOKE and HARDY, 1975), and specularly reflecting layers (ECKLUND et al., 1981). In both cases, the effect was a wave-like deformation of atmospheric layers with a period of a few minutes. This geometry is shown in Figure 1b. Because of this influence of gravity waves, it was expected that there would be short-term variations in the vertical velocity.

EXPERIMENTAL METHOD

The Sunset radar (GREEN et al., 1986) was used for the experiments described here. This radar is located west of Boulder, CO, just 10 km from the Continental Divide as shown in Figure 2. Because of the mountain environment, there is frequent mountain lee wave activity above the radar. It was anticipated that the lee waves would exaggerate the tilting of the atmospheric layers causing a bias in the measured vertical velocities. It was also expected that the intense gravity wave associated with the mountain environment would increase the variance of the velocity measurements. The radial component of wind velocity was measured using five antenna beam positions, vertical and 15° from the vertical in the east, west, north and south. The geometry of the radar volumes is shown in Figure 3. An example of the radial velocity measured with the east and west slanted beams is shown in Figure 4. An estimate of the vertical component of wind velocity, W_{ew} can be derived from the two slant beams, assuming no gradients of horizontal velocity,

$$W_{ew} = (V_e + V_w)/\cos Z$$

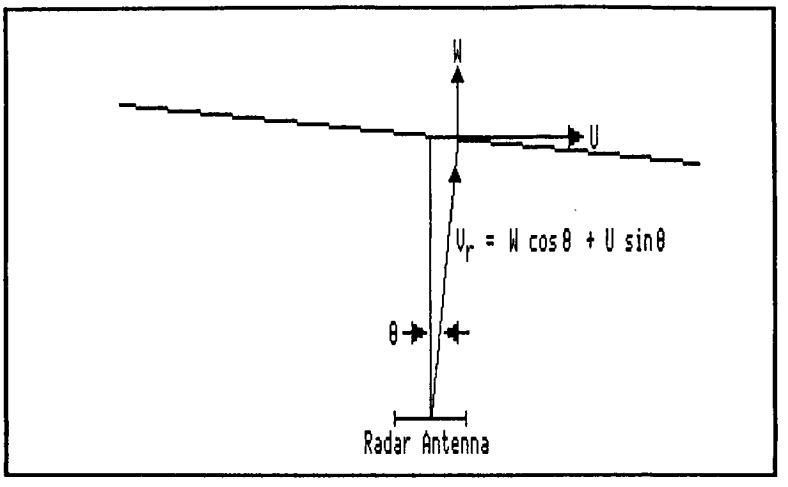

Figure 1a. Inclination of stable layer.

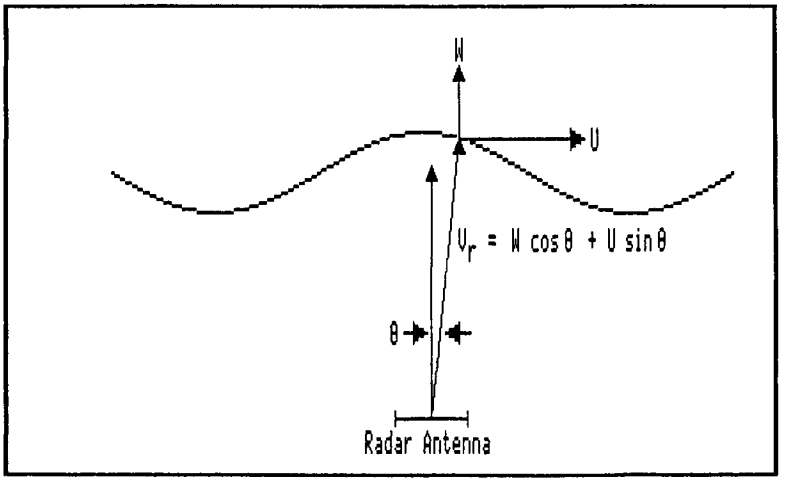

Figure 1b. Modulation of layers by gravity waves.

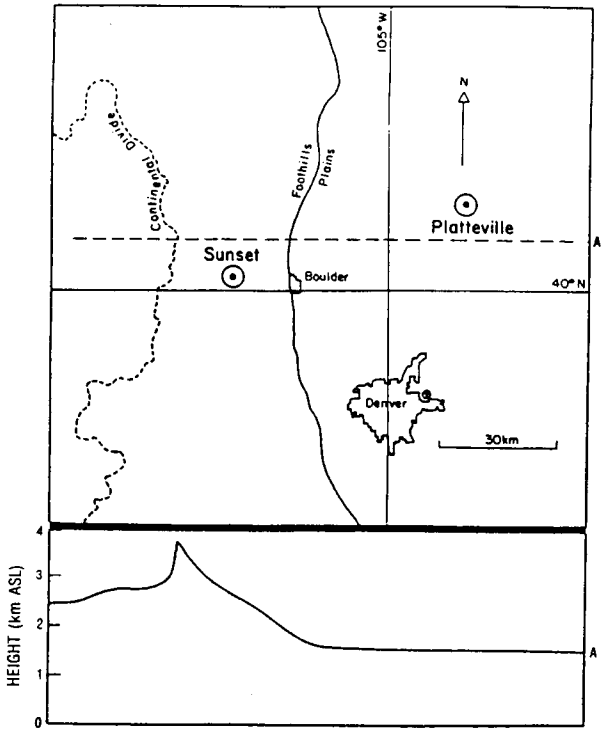

Figure 2. Location of Sunset radar.

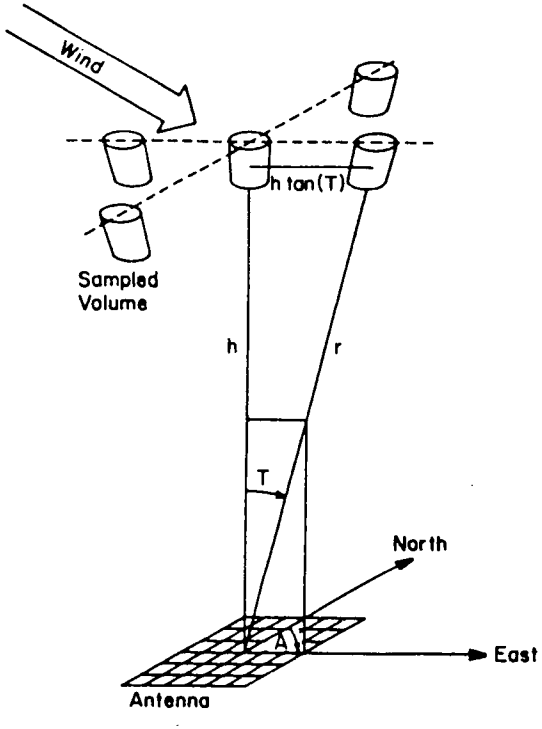

Figure 3. Antenna volume arrangement.

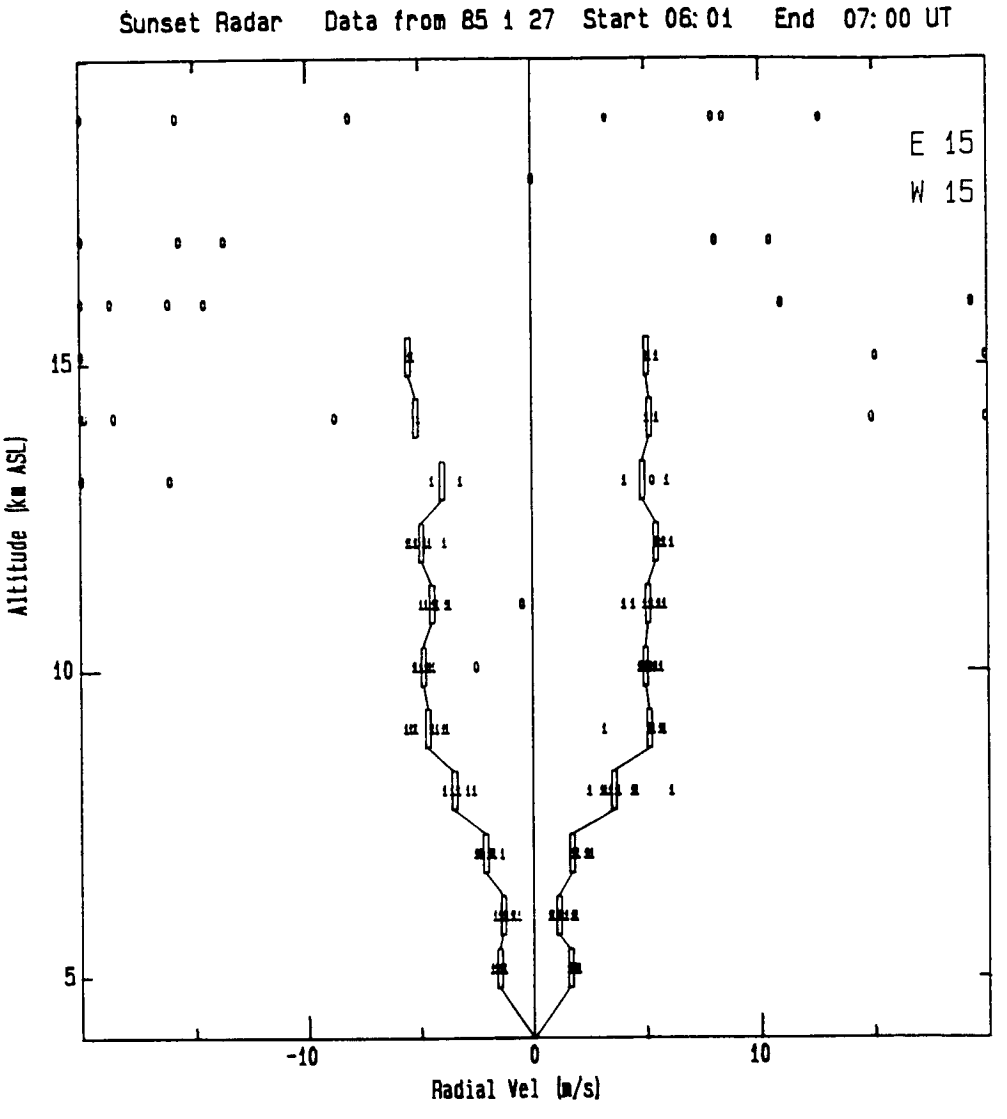

Figure 4. Example of radial velocity.

where Z is the angle from the zenith and V_e and V_w are the radial velocities measured on the antenna slanted to the east and west, respectively (VINCENT and REID, 1983). It has been established that echoes observed with antenna beams slanted away from the vertical are from turbulence scatter (VANZANDT et al., 1978). Therefore, W_{ew} can be always assumed to be measured from turbulence scatter. On the other hand, velocities measured with the vertical beam, W_{vert} can be from turbulence scatter or quasi-specular echoes, depending on the altitude and the time. Only the data from the antenna beam positions in the east-west vertical plane are presented here.

Figures 5-8 are XY plots comparing W_{vert} and W_{ew}. The range resolution was 1 km and the data were obtained from 5 - 15 km above sea level. The coordinates of each plotted point (W_{vert} and W_{ew}) were calculated from the medians of 9 - 12 individual radar records over one hour for each altitude and antenna beam direction. Only the measurements with valid data from the vertical beam and both slant beams are plotted. At a particular time and altitude, if the hourly median echo power from the vertical beam exceeded that of the slant beams by a factor of three, the data point was plotted as an "X" to signify that the echo from the vertical beam was quasi-specular, else it was plotted as an "O" to signify its origin in turbulence scatter. Each of these plots typically contains 24 hours of data. Before plotting, the entire data set was carefully hand-edited to eliminate echoes from aircraft.

To provide a measure of long-term bias, the median ($W_{vert} - W_{ew}$) for the cases when the echo on the vertical beam was quasi-specular, turbulence scatter and total cases inclusive are tabulated in the lower right-hand corner of each plot.

RESULTS

Figure 5 represents a day with very light winds and has the least scatter about the X = Y line of the four cases presented. Note that the scatter of the points where W_{vert} is from a quasi-specular echo is about equal to that of the points where W_{vert} is obtained from a turbulence echo and that the bias of the points associated with quasi-specular echoes is only 1 cm/s.

The winds were higher on the days represented by Figures 6-8, the range of W_{vert} associated with turbulent echoes is larger. Even so, the scatter of points about the X = Y line where W_{vert} is from quasi-specular or turbulent echoes is still about the same. However, the long-term $W_{vert} - W_{ew}$ is about 10 cm/s for both turbulence scatter and quasi-specular reflection.

DISCUSSION

The following tentative conclusions can be drawn from the four examples presented:

1. The behavior of the vertical component of wind velocity measured with quasi-specular reflection or with turbulence scatter is not markedly different, either in the hourly median or the daily median ($W_{vert} - W_{ew}$). The similarity of the scatter of $W_{vert} - W_{ew}$ when the vertical beam received a quasi-specular or a turbulence scatter echo puts a limit on the errors in the measurement of W_{vert} due to the tilting of stable layers by gravity waves. This similarity of behavior is also evidence that W_{vert}, measured with either type of echo is the vertical component of that wind velocity in agreement with WATKINS and JAYAWEERA (1985) and RIDDLE and BALSLEY (1985).

2. The daily median $W_{vert} - W_{ew}$ for either type of echo is not more than a few cm/sec.

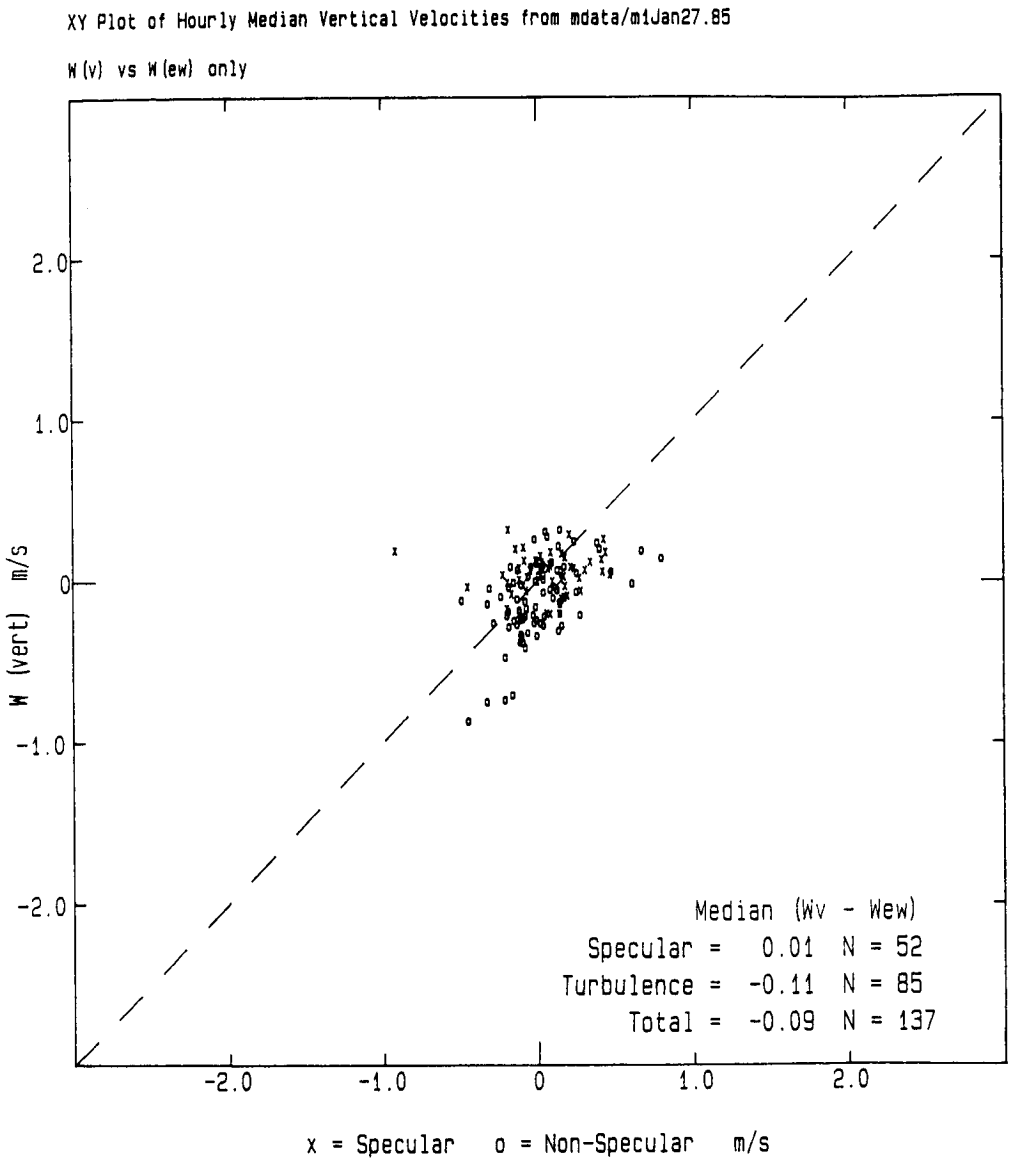

Figure 5. Plot of W_{vert} (vertical axis) vs W_{ew} (horizontal axis) January 27, 1985.

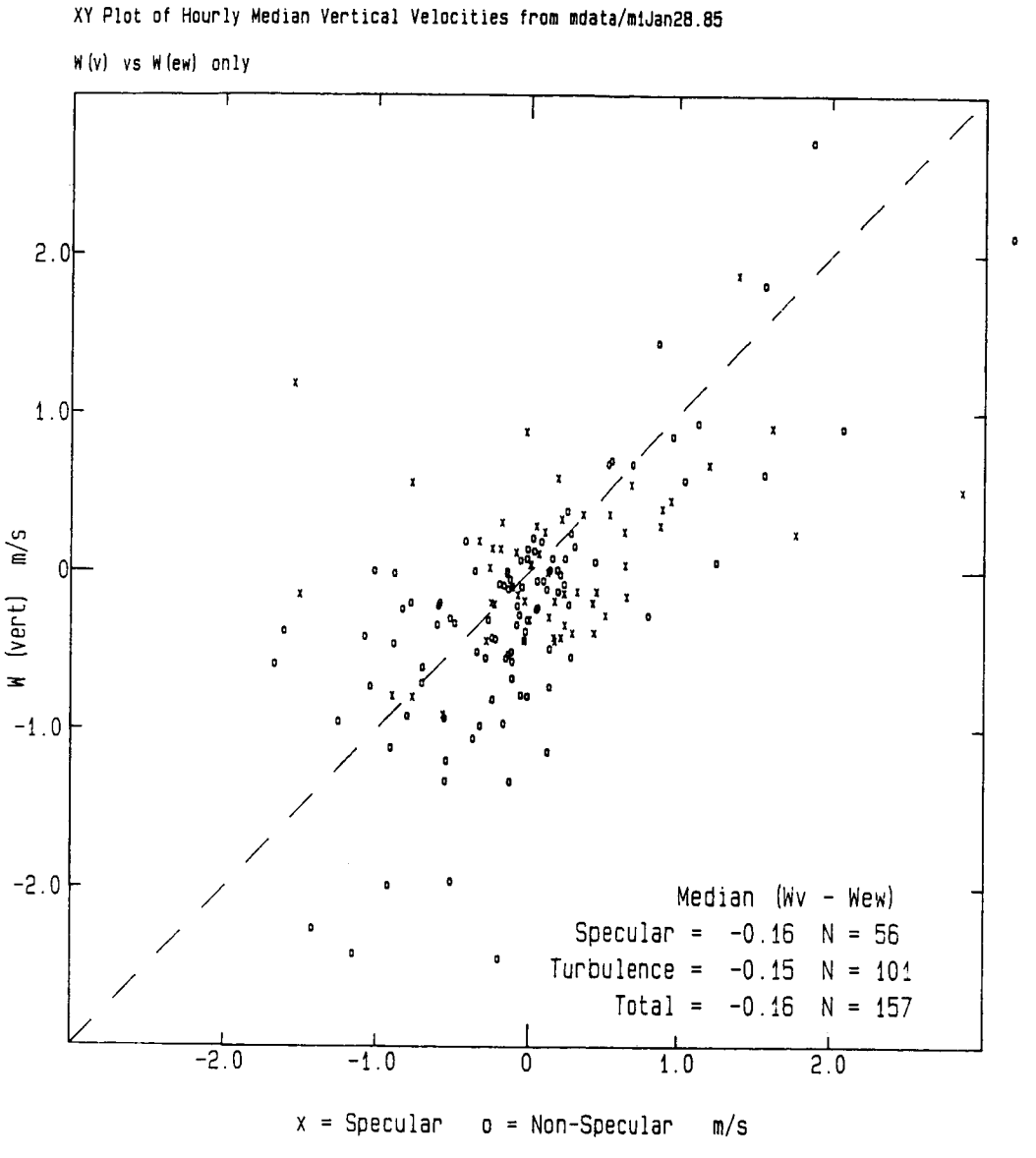

Figure 6. Plot of W_{vert} (vertical axis) vs W_{ew} (horizontal axis) January 28, 1985.

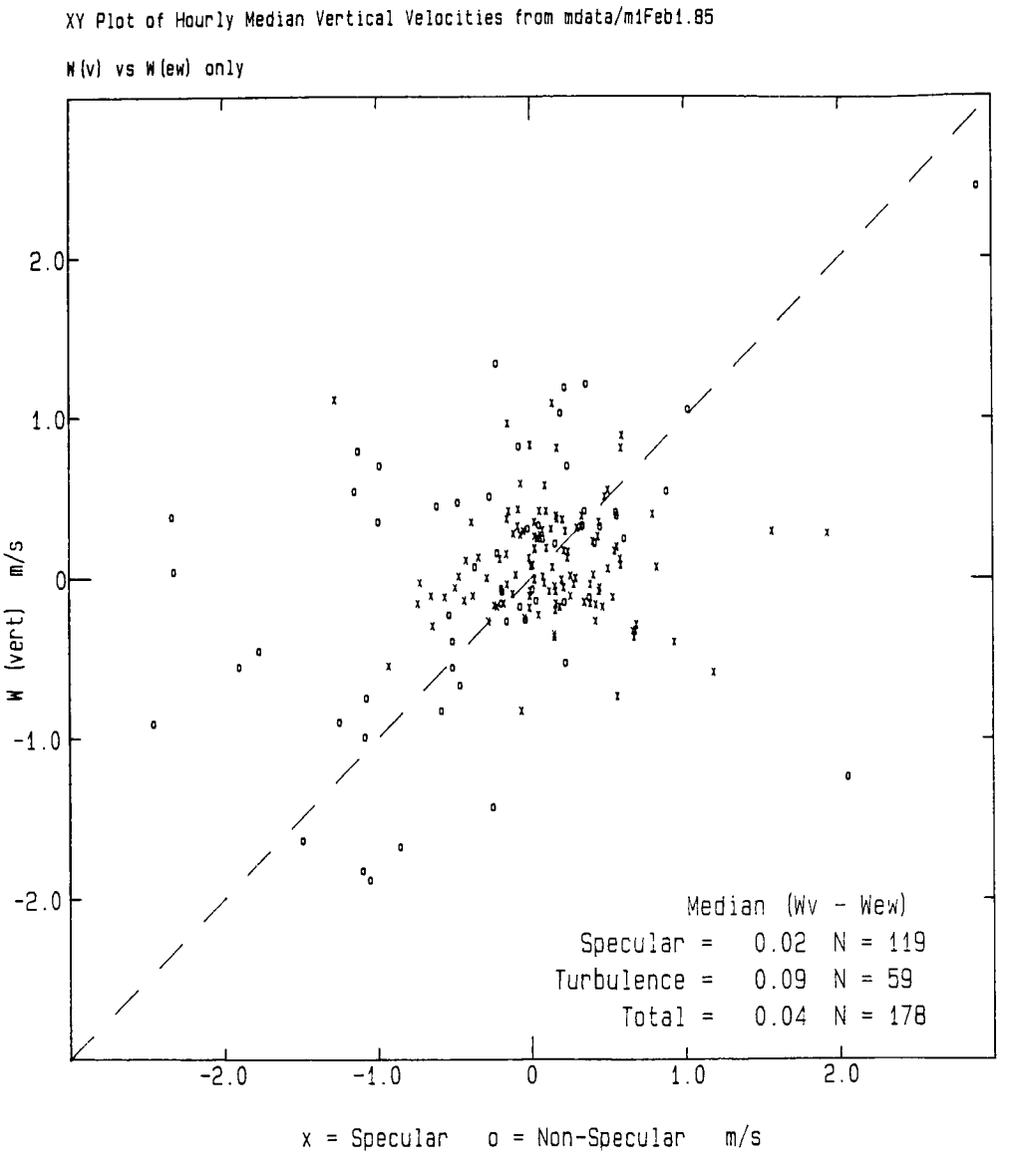

Figure 7. Plot of W_{vert} (vertical axis) vs W_{ew} (horizontal axis) February 1, 1985.

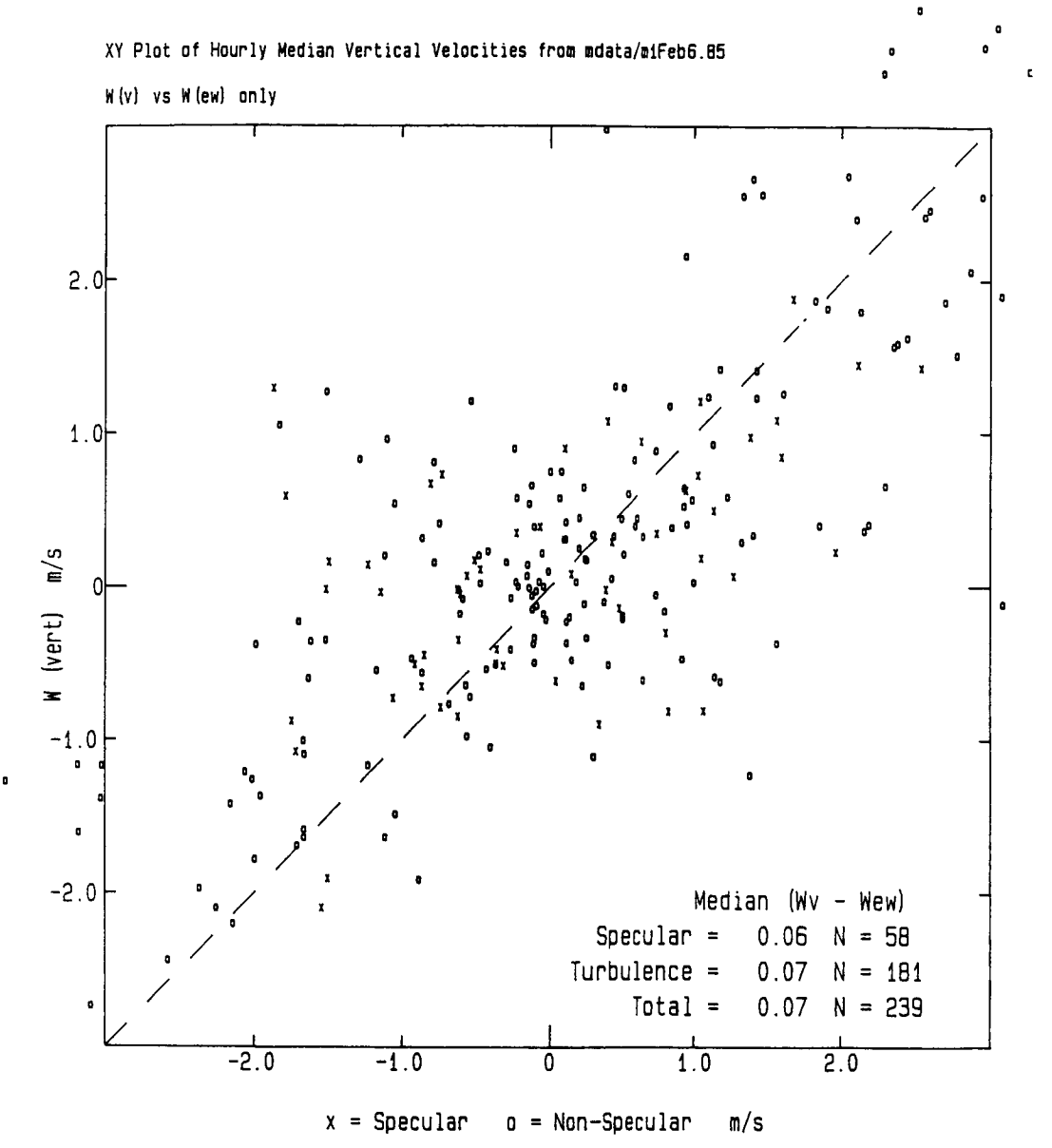

Figure 8. Plot of W_{vert} (vertical axis) vs W_{ew} (horizontal axis) February 6, 1985.

3. Even in the mountain environment, $W_{vert} - W_{ew}$, computed from hourly medians of radial velocity are typically less than $\pm$ 1 m/s. Roughly, the uncertainty in the computation of horizontal components of velocity using hourly medians, but uncorrected by the vertical velocity, would be W cos 15°/sin 15°, or typically less than $\pm$ 4 m/s. The observed scatter of the hourly medians of $W_{vert} - W_{ew}$ could be due to horizontal gradients of vertical velocity (CLARK et al., 1985) and/or by velocity perturbations due to gravity waves.

REFERENCES

Clark, W. L., J. L. Green, and J. M. Warnock (1985), Estimating meteorological wind vector components from monostatic Doppler radar measurements: A case study, Radio Sci., 20, 1207-1213.

Clark, W. L., J. L. GREEN, and J. M. Warnock (1986), Determination of U, V, and W from single Doppler radar radial velocities, this volume.

Ecklund, W. L., K. S. Gage, and A. C. Riddle (1981), Gravity wave activity in vertical wind observed by the Poker Flat MST radar, Geophys. Res. Lett., 8, 285-288.

Gage, K. S., and J. L. Green (1978), Evidence for specular reflection from monostatic VHF radar observations of the stratosphere, Radio Sci., 13, 991-1001.

Green, J. L., J. M. Warnock, W. L. Clark, and T. E. VanZandt (1986), Recent results at the Sunset radar, this volume.

Hooke, W. H., and K. R. Hardy (1975), Further studies of the gravity wave over the eastern seaboard on 18 March 1969, J. Appl. Meteorol., 14, 31-38.

Riddle, A. C., and B. B. Balsley (1985), Comment on "Comparisons of vertical winds measured with the Chatanika and Poker Flat radars, J. Geophys. Res., 90, 8160-8162.

Rottger, J. (1980), Reflection and scattering of VHF radar signals from atmospheric reflection structures, Radio Sci., 15, 259-276.

Rottger, J. (1981), Wind variability in the stratosphere deduced from spaced antenna VHF radar measurements, Proc. 20th Conf. Radar Meteorology, Boston, MA, Am. Meteorol. Soc., 22-29.

VanZandt, T. E., J. L. Green, K. S. Gage, and W. L. Clark (1978), Vertical profiles of refractivity turbulence structure constant: comparison of observations by the Sunset radar with a new theoretical model, Radio Sci., 13, 819-829.

Vincent, R. A., and I. M. Reid (1983), HF Doppler measurements of mesospheric gravity wave momentum fluxes, J. Atmos. Sci., 40, 1321-1333.

Watkins, B. J., and K. Jayaweera (1985), Comparisons of vertical winds measured with the Chatanika and Poker Flat radars, J. Geophys. Res., 90, 8143-8148.

4.1.3 METHODS FOR VERIFYING THE ACCURACY OF WIND PROFILES

R. G. Strauch

NOAA/ERL/WPL
Boulder, CO 80303

Most of the verification tests of the accuracy of winds measured by UHF or VHF radars have been made by comparing the radar data with radiosonde-measured winds. The results usually "show general agreement" and differences are attributed to the "lack of temporal and spatial simultaneity." There have not been extensive or routine comparisons of radar-measured winds with radiosondes or other wind measurements. One of the reasons that routine radiosonde/radar comparisons have not been made is that the agreement that is obtained depends on the particular wind field that is being observed. This is also true for comparisons with other wind measurements such as those obtained by lasers because the instruments are measuring the winds in fundamentally different ways. For example, the Doppler radar and Doppler lidar do not measure the mean radial velocity of the atmosphere in the resolution volume, but rather measure the reflectivity-weighted average of the radial velocity. This is ignored when the measured radial velocities are converted to horizontal winds. The reflectivity weighting depends on the distribution of refractive turbulence for the clear-air radar and depends on the distribution of aerosols for the lidar. Also, the resolution volumes are usually very different. Another problem in making comparisons is the lack of a standard or truth. Winds measured by radiosonde are often regarded as the true wind; however, in tests where two radiosonde packages were flown from the same balloon, the vector winds measured by the two trackers had rms differences of 3.1 m/s (HOEHNE, 1980). Winds measured by radar or lidar will have much better precision. Therefore, comparisons of radar-measured winds have been made with several types of measurements not only to verify radar data but also to seek a satisfactory comparison method.

Three of the comparisons that have been made with Colorado Profiler radars are summarized below:

Radar/Radiosonde

The 915-MHz radar wind profiler at Denver's Stapleton Airport is located adjacent to the radiosonde launch site of the National Weather Service. Hourly averaged winds measured by the radar can be compared with the twice-daily radiosonde winds. Figure 1 illustrates a comparison that "shows general agreement." Note that in this case the 915-MHz radar did not have enough sensitivity to measure the winds in the core of the jet and that above the jet the radiosonde track was lost. If random cases are examined, poor agreement can also result. However, if the time-height cross section of radar-measured winds shows spatial and temporal changes such as illustrated in Figure 2, poor agreement should be expected since the instruments would be observing very different wind fields. Data from radar and radiosondes are available for two years, and these comparisons are continuing.

Radar/Lidar/Radiosonde

In March 1984, a series of comparisons were made with an infrared lidar (10.6 micrometer wavelength), the 915-MHz radar, and radiosondes. The lidar can measure winds with fixed telescope pointing, the same as the radar, or it can do 360-degree VAD (velocity-azimuth-display) scans. Figure 3 illustrates radar/lidar comparisons. Note that the data are plotted as radial velocities at 75-degree elevation angle. Radar and lidar data are from 10-minute

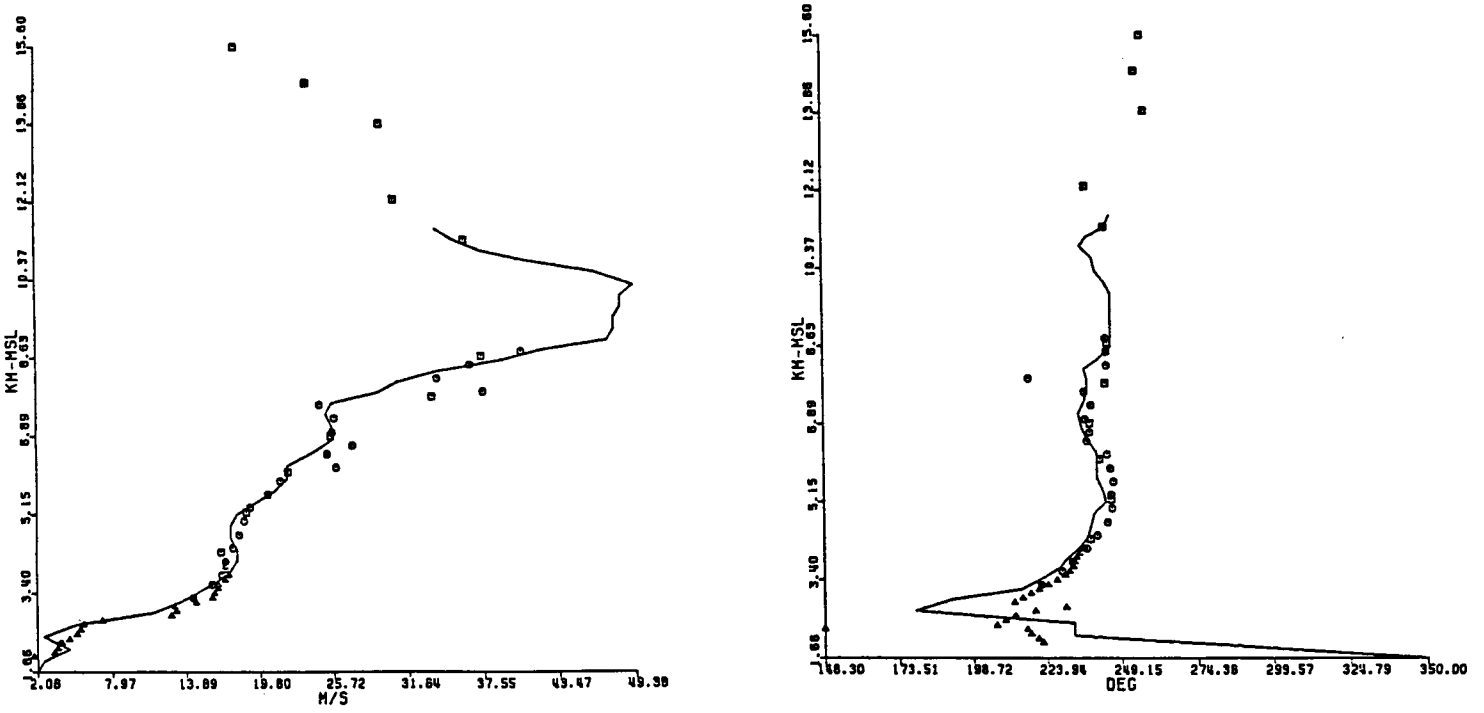

Figure 1. Comparison of radiosonde-measured wind speed (left) and direction (right) with 915-MHz profiler for 12 Z on April 1, 1984. Radiosonde data rate shown in solid lines, 9-μs pulse width profiler data are squares, 3-μs data are circles, and 1-μs data are triangles. Data obtained at the National Weather Service Forecast Office, Denver, Colorado.

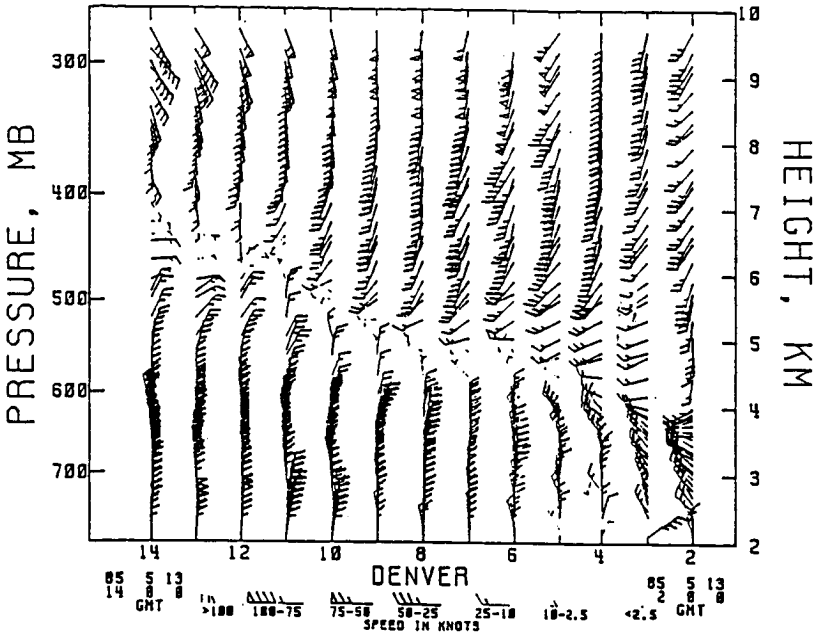

Figure 2. Example of wind profile obtained with 914-MHz radar during frontal passage.

averages. The results of these comparisons (LAWRENCE et al., 1985) show rms differences of about 3 m/s for horizontal wind comparisons for both lidar/radiosonde and lidar/radar. The radar and lidar data sometimes show changes in horizontal wind component speed of several meters per second between 10-min averaging periods.

Radar/Radar

A brief radar/radar comparison of wind measurements was made at Platteville (STRAUCH et al., 1983) using the 50-MHz radar and a 3-cm wavelength meteorological Doppler radar during precipitation. This comparison showed "good agreement." Since January 1985, there have been two profilers colocated at Platteville; a 50-MHz and a 405-MHz system. Both operate in the same modes and measure hourly-averaged winds. In one comparison, shown in Figure 4, the rms difference of horizontal wind components measured at 6.8 km MSL was about 1 m/s for a 5-day period. In general, the comparisons "show good agreement", but the data from the 405-MHz radar are much noisier than from all other profilers. This is believed to be caused by antenna sidelobes, and more of these comparisons will be made after the antenna performance is improved.

There are other comparisons that could be made to attempt to quantify the accuracy of radar wind profiles. Some of these are:

Radar/Aircraft

Routine comparisons of radar-measured winds and winds measured by commercial wide-body jet aircraft equipped with the Aircraft Communications and Reporting System (ACARS) could be made. These aircraft have inertial navigation systems and can derive wind data along the flight track when the

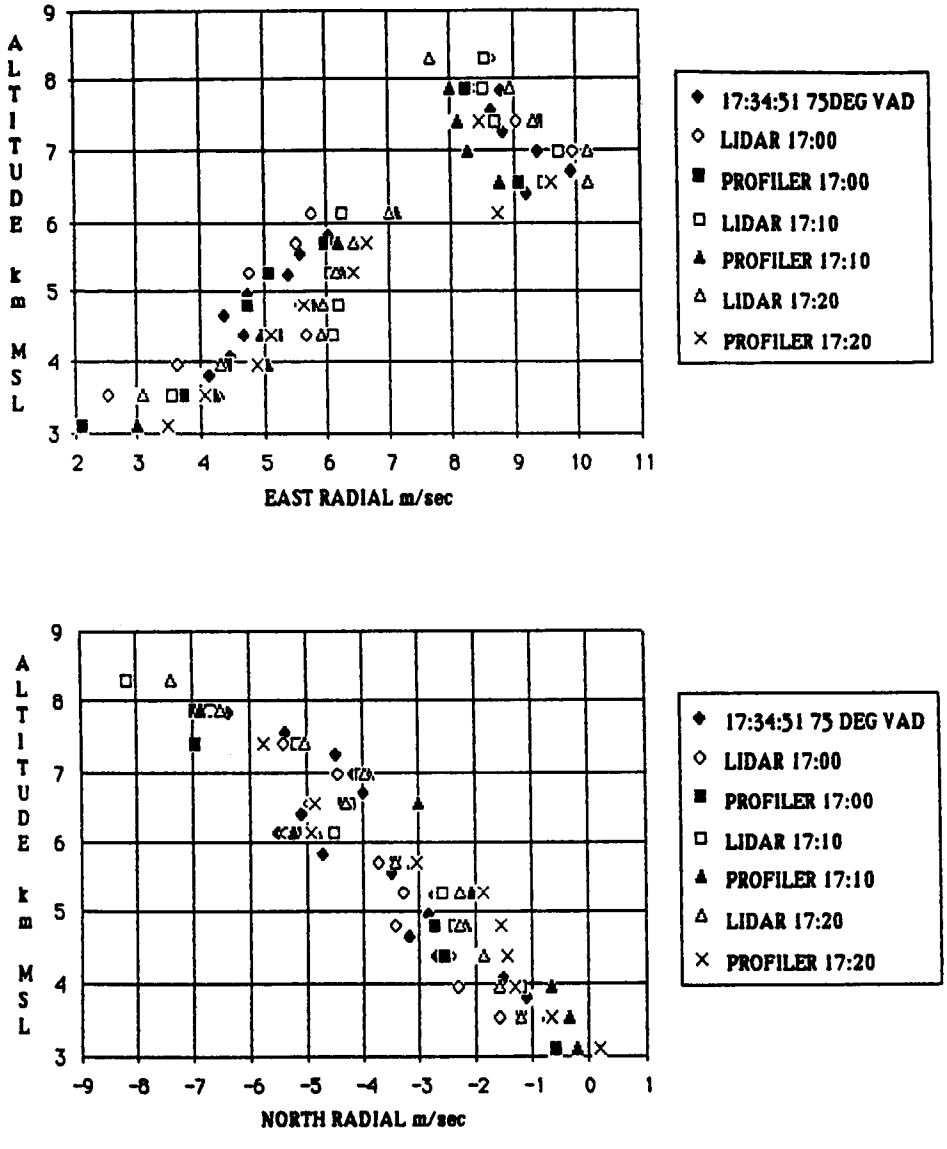

Figure 3. Lidar and 915-MHz profiler radial velocity profiles for 1700-1730 MST on April 12, 1984. Upper: east, 75° elevation radial; Lower: north, 75° elevation radial. Also plotted are lidar VAD data (75° elevation).

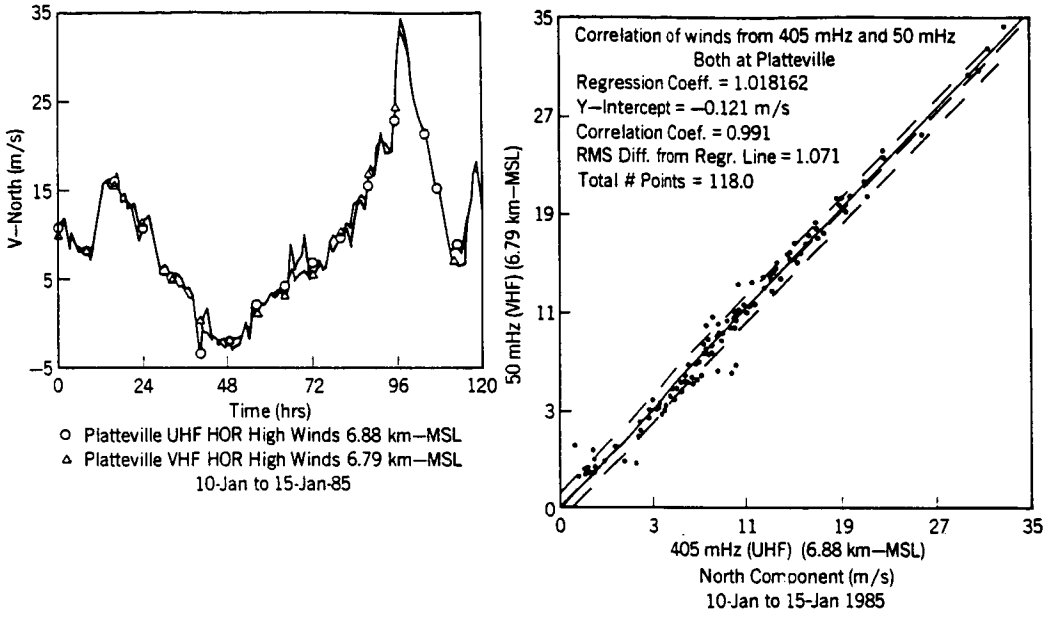

Figure 4. Comparison of north wind component measured with colocated 405-MHz and 50-MHz profilers. Left: 5-day time series of measured values. Right: Scatter plot of measured values.

track is a straight line at constant altitude. These data have not been used for profiler comparisons; they are a potential source of data at altitudes where wind speed is usually high. The aircraft-measured winds may be accurate enough to calibrate the profiler or check the pointing angles of fixed-beam profiles. Research aircraft could also be used for comparison but systematic comparisons would be too costly.

Radar/Meteorological Inference

Wind data from a network of radar wind profilers can be used to calculate divergence and vorticity; a case study was performed by ZAMORA and SHAPIRO (1984), and these calculations were "in agreement" with divergence and vorticity calculated from the radiosonde network. A comparison of winds or quantities derived from wind data obtained by a network with radiosonde data may yield a better accuracy determination than comparisons of individual profiles because the differences in temporal and spatial averaging will be less important when averaging over large areas. Data from a radar network could also be tested for accuracy by initializing models with current radar-measured winds and comparing model predictions with later data. This type of comparison should be tried in simple terrain (such as Eastern Colorado, where two 50-MHz profilers are collecting data routinely) and in simple flow regimes.

Radar/Scanning Radar

A fully scannable clear-air radar measuring wind profiles with VAD analysis at various elevation angles may be the best standard available for radar wind data. It would be especially valuable for calibrating fixed beam systems that use temporal integration rather than spatial integration to obtain representativeness and whose actual pointing angles are difficult to measure.

The antenna pointing angles of a scanning system can be checked using the sun as a source. The scanning system would operate at UHF to keep antenna size manageable and so there would be no pointing uncertainty due to aspect sensitivity. The effects of vertical motion and divergence on radar-measured winds could be assessed. Plans are being made to convert a relatively low-power 405-MHz radar to a scanning system that should be able to measure winds in the clear air to 7-10 km. It is hoped that such a radar would provide data that would be accepted as "true" wind data because it would have temporal resolution of about 5 min and height resolutions of less than 100 m as well as continuous scanning. In addition to calibration of other profilers, such a system would be a mesoscale wind profiler with many potential applications as a stand-alone (as opposed to part of a network) wind profiler.

REFERENCES

Hoehne, W. E. (1980), Precision of National Weather Service upper air measurements, NOAA Tech. Memo. NWS T&ED-16, 23 pp.

Lawrence, T. R., B. F. Weber, M. J. Post, R. M. Hardesty, R. A. Richter, N. L. Abshire, and F. F. Hall (1985), A comparison of Doppler lidar, rawinsonde, and 915 MHz UHF wind profiler measurements of tropospheric winds, NOAA Tech. Memo., in press.

Strauch, R. G., M. T. Decker, and D. C. Hogg (1983), Automated profiling of the troposphere, J. Aircraft, 20, 359-362.

Zamora, R. J., and M. A. Shapiro (1984), Diagnostic divergence and vorticity calculations using a network of mesoscale wind profilers, Preprints 10th Conf. Weather Forecasting, Clearwater Beach, FL, Am. Meteorol. Soc., 386-391.

4.2.1 A COMPARISON OF THUNDERSTORM REFLECTIVITIES MEASURED AT VHF AND UHF

M. F. Larsen

Department of Physics and Astronomy
Clemson University
Clemson, SC 29631

J. Rottger*

Arecibo Observatory
P. O. Box 995
Arecibo, PR 00613

INTRODUCTION

In this paper, we compare observations of thunderstorms made with two radars operating at different wavelengths of 70 cm and 5.67 m. The first set of observations was made with the UHF radar at the Arecibo Observatory in Puerto Rico, and the second set was made with the Max-Planck-Institut fur Aeronomie VHF radar in the Harz Mountains in West Germany. Both sets of observations show large echo strengths in the convective region above the -10°C isotherm. At UHF, precipitation echoes dominate. At VHF, there appears to be a contribution from both the precipitation echoes and the normal echoes due to scatter from turbulent variations in the refractive index.

A number of simple theories can be used to calculate the relative contributions of radar scatter from "clear air" and from precipitation in a cloudy atmosphere as a function of frequency (see, e.g., BATTAN, 1973). The theoretical predictions indicate a wavelength to the -4 power law dependence for scatter from raindrops. GOSSARD and STRAUCH (1981) have labeled this "incoherent scatter", and the scatter from turbulent variations in the refractive index has been called coherent Bragg scatter. The latter is expected to vary as the wavelength to the 1/3 power. Additionally, strong Fresnel scatter or reflection due to refractive index stratification has been found at VHF (e.g., ROTTGER, 1980b). However, the exact wavelength dependence of the reflective process is not known. The few detailed studies of the scatter from clouds at lower frequencies such as UHF and VHF have shown the echo strengths to be larger than expected, based on the theoretical predictions. Examples of such observations are given by SMITH (1964), NAITO and ATLAS (1966), CHERNIKOV (1968), GAGE et al. (1978), and GREEN et al. (1978). The most detailed discussion of the problem has been given by GOSSARD (1979) and GOSSARD and STRAUCH (1981).

Some of the earlier explanations of the enhanced reflectivities dealt with a possible organization of the precipitation on a scale comparable to half the radar wavelength due to turbulent motions within the cloud. Thus, the reflected radar signal would have both a coherent and an incoherent component. GOSSARD (1979) used results from a numerical cloud model developed by CLARK and HALL (1979) to improve the estimates of the dielectric fluctuations caused by water vapor and raindrop spectrum variations within the cloud. He concluded that, for reasonable values of the various parameters, organization of the precipitation by turbulent motions could not account for the observations. However, the variations of the thermodynamic variables and the coupling to the water vapor densities through nonlinear dynamics could produce significantly

*On leave from the Max-Planck-Institut fur Aeronomie, Katlenburg-Lindau, West Germany.

enhanced cloud reflectivities, although the calculated enhancements were still too small to explain the observations.

GOSSARD and STRAUCH (1981) used experimental data from an FM-CW radar to study the contributions from "incoherent scatter" and "Bragg scatter" in winter clouds in Colorado. Their results showed no significant departure from the classical predictions, but they could not conclude anything about the stronger summertime convective storms. Also, they suggested that some of the enhancements in reflectivity that have been reported in the literature could be associated with entrainment and mixing of dry air near the edges of the cloud.

So little data exists and, with the exception of the work by GOSSARD (1979), little has been done to improve the theory of scattering from clouds at long wavelengths. Since the theory of scattering from clouds at long wavelengths is uncertain, it is particularly important to have as much observational data as possible taken with different instruments. In this article, we will present data from two separate thunderstorm observations made in the Summer of 1978 and in the Fall of 1979. The first experiment was carried out with the SOUSY VHF radar located in the Harz Mountains in West Germany and operating at a frequency of 53.5 MHz. The second experiment was carried out with the 430-MHz Arecibo Observatory radar located in Puerto Rico. Although the observations were made in different parts of the world, in different climates, with different radars operating at different frequencies, there are significant similarities. Also, this comparison of the scatter at wavelengths of 70 cm and 5.67 m from cumulus clouds is the only such comparison of which we are aware.

THE SOUSY VHF RADAR OBSERVATIONS

The SOUSY VHF radar is operated by the Max-Planck-Institut fur Aeronomie and is located in the Harz Mountains near Bad Lauterberg. The radar frequency corresponds to a wavelength of 5.67 m, and the nominal height resolution is 150 m (see, e.g., ROTTGER, 1980a). The radar was operated during the early part of June 1978, when the flow over western Europe was characterized by a stable, anticyclonic air mass. On June 1 and 2, air mass thunderstorms developed, and some were reported near the radar site. In the evening of June 2, 1978, data were obtained after 1851 GMT, and, for almost two hours, a thunderstorm was immediately over or near the radar's location. ROTTGER (1980a,b) has described the experiment in greater detail.

The vertical velocities measured by the vertically pointing radar for the period from 1851 GMT until 2040 GMT on June 2, 1978, are summarized in Figure 1 (local Middle European Time is GMT minus one hour). The shaded areas indicate upward velocities, and the contour intervals are 1 m/s. The dark, solid bars show the times and ranges at which radar echoes from lightning were detected. A detailed discussion of these echoes is outside the scope of this paper, but we assume that they are likely due to scattering from the ionized lightning channel, although Bragg scattering from acoustic waves may occur, too. The lower part of the figure shows the measured mean pressure changes at the site and a subjective estimate of the rainfall intensity as a function of time. The thunderstorm symbol indicates the presence of lightning, and the open circle shows a period of clear sky overhead.

In Figure 2 we show the mean quasi-vertical velocity w, the echo power P and the rms velocity fluctuations σ_w during the final period from 2011-2041 GMT. The effective reflectivity, due to scattering from turbulent refractivity variations and partial reflection from coherent discontinuities in the refractivity, is proportional to the power P multiplied by the square of the range. It is normally a measure of the temperature and humidity variations in the radar volume. Note that an uplift of the reflectivity pattern from

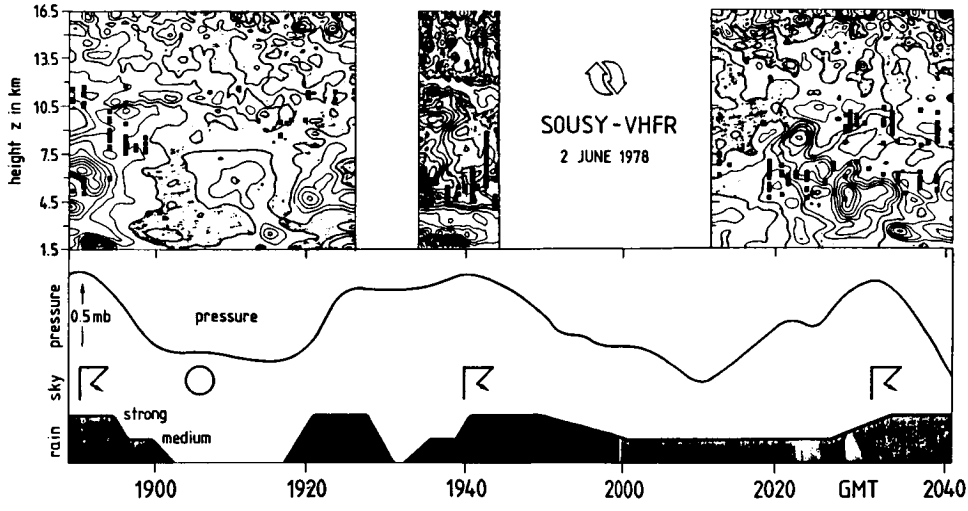

Figure 1.

about 7.5 to 10.5 km occurs within a 10-minute period at the beginning of the period shown in the figure. The reflectivity pattern then remains nearly stationary in height after about 2025 GMT. The behavior of the echoes is consistent with the vertical development of the thundercloud until it reached the height of the tropopause at 10.5 km, if we assume that the gray-shaded region represents the thundercloud region. Two indications support this assumption: (1) the high reflectivity band above 10.5 km at 2011 GMT presumably is the radar-detected tropopause (e.g., ROTTGER, 1980b), and (2) lightning echoes, which originate within the cloud, are detected only within the gray-shaded region. The final uplift of the high reflectivity regions in the tropopause level is connected with mean upward velocities of some meters per second. The strongest turbulence, viz., regions of large rms fluctuations in velocity, occurs in and above the regions of strong upward velocities.

A more detailed analysis of the Doppler spectra shows that, in addition to the relatively small upward velocities, sometimes large downward velocities occur simultaneously. Figure 3 shows 12 consecutive vertical velocity profiles obtained at 2-minute intervals with the SOUSY VHF radar. Actually, the figure represents gray-scale plots of the Doppler spectra as a function of range gate. The darker impressions indicate stronger signal strengths. The spectra for each range gate are normalized to their peak value. Thus, the extent to which the noise is suppressed is an indication of the signal-to-noise ratio.

Each profile shows a small fluctuating vertical wind component with an amplitude no greater than a few m/s over the altitude range from 3.0 to 12.0 km. However, before 1900 GMT, while the thunderstorm is above the radar, there are secondary peaks in the Doppler spectra between 2.5 and 9.0-km altitude. The secondary maxima have associated velocities between a few m/s at the upper end of the altitude range and 10-12 m/s at the lower end. The power associated with the secondary echoes has a maximum value of more than 10 dB above the noise level and is comparable in magnitude to the "clear air" or "small velocity" echoes which are seen to persist after the cloud has passed out of the radar beam. Around 7.5 km altitude at 1851 GMT, the secondary peak is even stronger than the small velocity part of the spectrum, as shown by its suppression resulting from the normalization. The height range where the secondary echoes occur is above the -20°C isotherm as determined from the

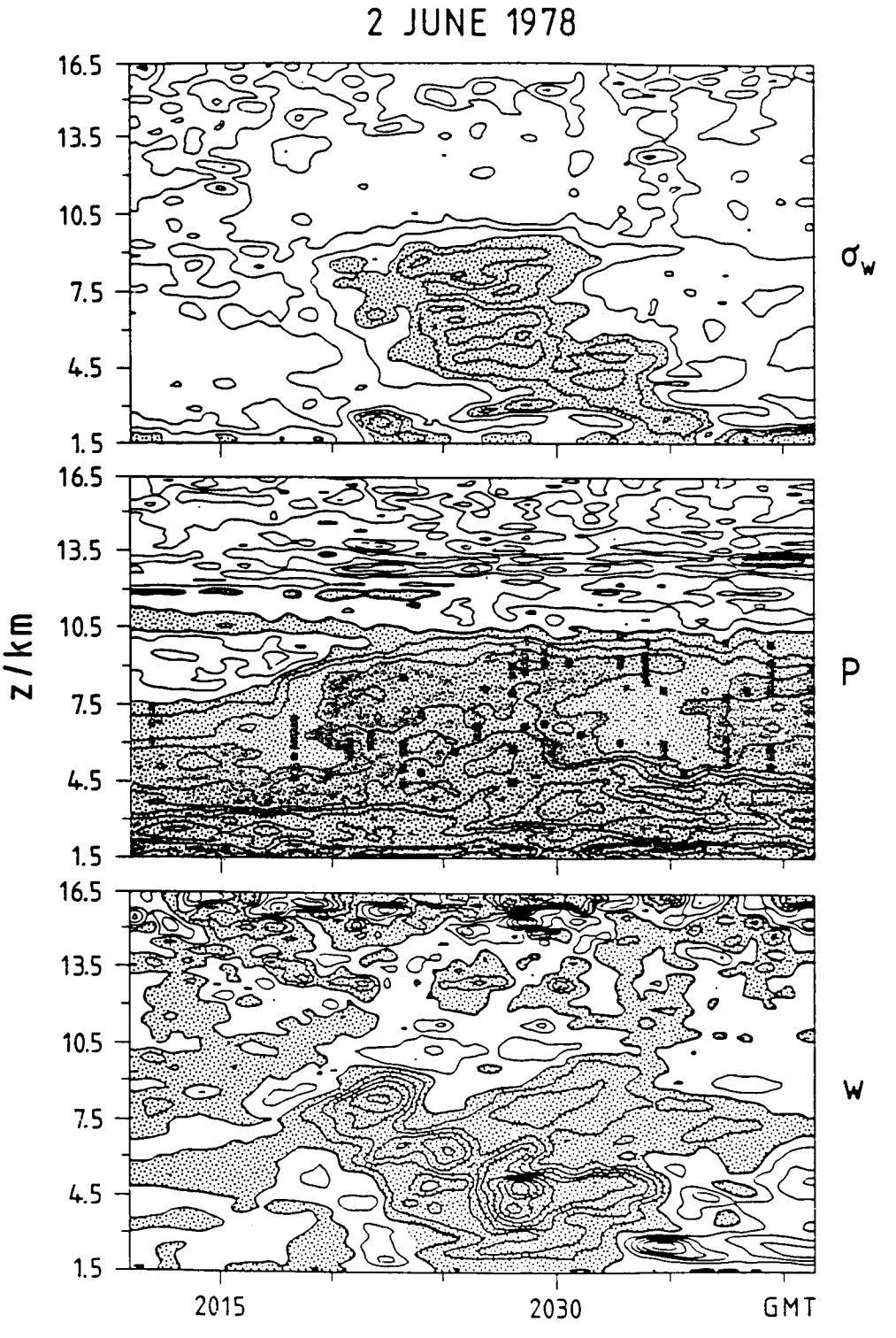

Figure 2.

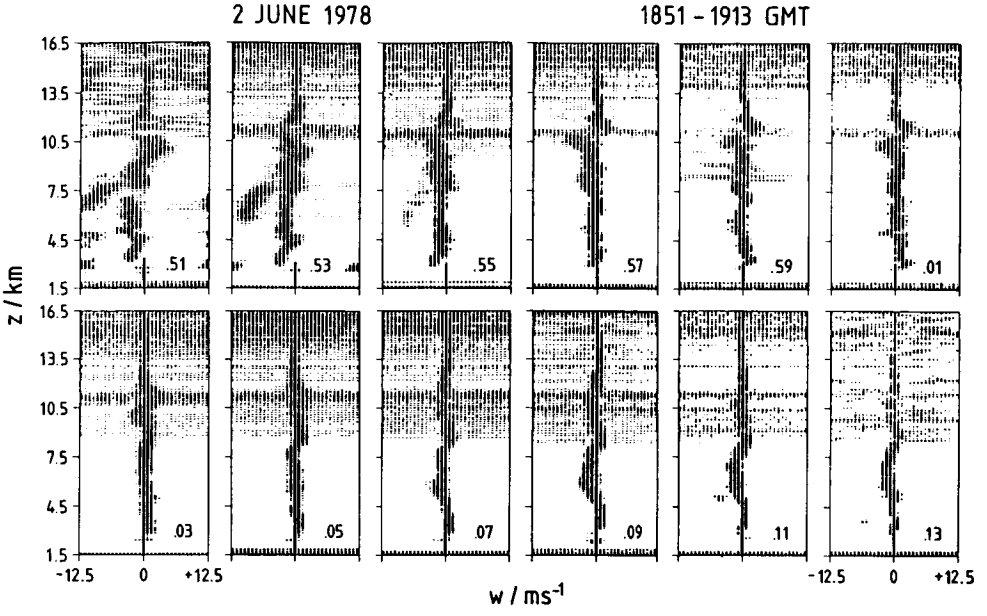

Figure 3.

Hannover radiosonde data which were taken some 100 km northwest of the radar site at 1200 GMT.

Double peaked spectra of VHF radar echoes from a large cumulus cloud were also reported by GREEN et al. (1978). They found it difficult to interpret these double peaks, although they tentatively concluded that an updraft and a downdraft existed simultaneously within the radar volume. They interpreted the secondary echo as being from precipitation but found that the measured reflectivities were too large by an order of magnitude.

430-MHz THUNDERSTORM OBSERVATIONS AT ARECIBO

The experiment at Arecibo was carried out in September of 1979 using the 430-MHz radar at the Arecibo Observatory. The radar frequency corresponds to a wavelength of 70 cm. The radar is steerable within an angular range less than 20° off vertical, but during the experiment, the beam was pointed vertically during the entire observation period. At the beginning of the experiment, the intertropical convergence zone (ITCZ) was located unusually far north. A wave disturbance in the easterly flow passed over the island on September 13 and 14, 1979, and organized the convection that developed over the island due to the strong diurnal heating cycle. On September 14, there was thunderstorm activity over the radar from 1430 AST until 1750 AST. LARSEN et al. (1982) have described the experiment and some of the earlier results in greater detail.

The radar reflectivities are shown in Figure 4 for the period from 1430 to 1730 AST. No renormalization of the power for range-square dependence is necessary since the near-field (Fresnel region) for the Arecibo 430-MHz radar extends out to more than 100 km altitude. The Arecibo 430-MHz radar thus illuminates in the troposphere and stratosphere, a region with a horizontal diameter equal to the 305-m diameter of the dish antenna. As in Figure 2, Figure 4 clearly shows the cross section of a cumulus cloud, including the

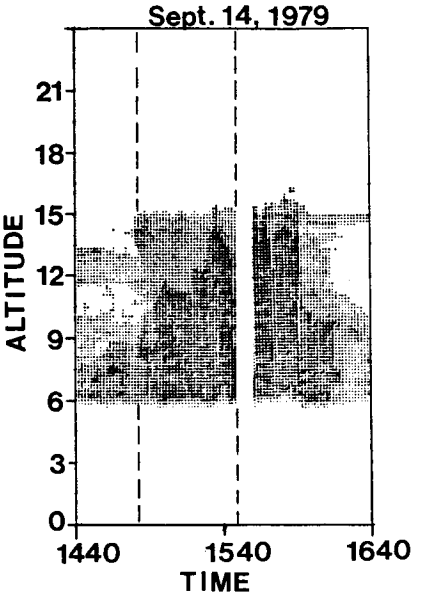

Figure 4.

anvil near the tropopause at the end of the afternoon. It is unusual to have such a long-lived thunderstorm, but in this case the combined effects of the easterly wave, the local topography, and the heating contrast between the land and the ocean must have produced favorable conditions for maintaining the cloud in a nearly stationary position. Care has to be taken in interpreting the data because the radar was not scanning during the experiment. Therefore, Figure 4 shows effects due to both advection of the cloud over the radar and the temporal evolution of the cloud in the course of the afternoon, just as in Figure 2.

Figure 5 shows a sample of five consecutive profiles of the vertical velocities measured with the radar. The vertical and horizontal axes are the same as in Figure 3, but the power is shown in contours rather than as a gray-scale plot. The contour interval is 3 dB. The echoes in the troposphere are very broad, and "x's" have been used to indicate the locations of the maxima in the power spectra. Typically, the echoes in the troposphere would have approximately the same width as the echoes seen in the region above the tropopause near 15 km.

The vertical velocity profiles observed at Arecibo once the cloud was overhead are very similar to the vertical profiles for the "precipitation" echoes observed with the SOUSY VHF radar. The echoes have small velocities near the tropopause and become more negative toward lower altitudes. In this case, the downward velocities attain magnitudes as large as 8 m/s. Note that around 7-8 km the measured Doppler shift is so large that the velocities become aliased and appear as large positive velocities. Data cannot be obtained below an altitude of 5.7 km due to the receiver protection system for the 430-MHz radar. Therefore, we do not know if the downward velocities become larger at lower altitudes.

In the Arecibo data set, there is no evidence of a "low velocity" signal from the "clear air", as there is in the SOUSY VHF radar data taken at a longer

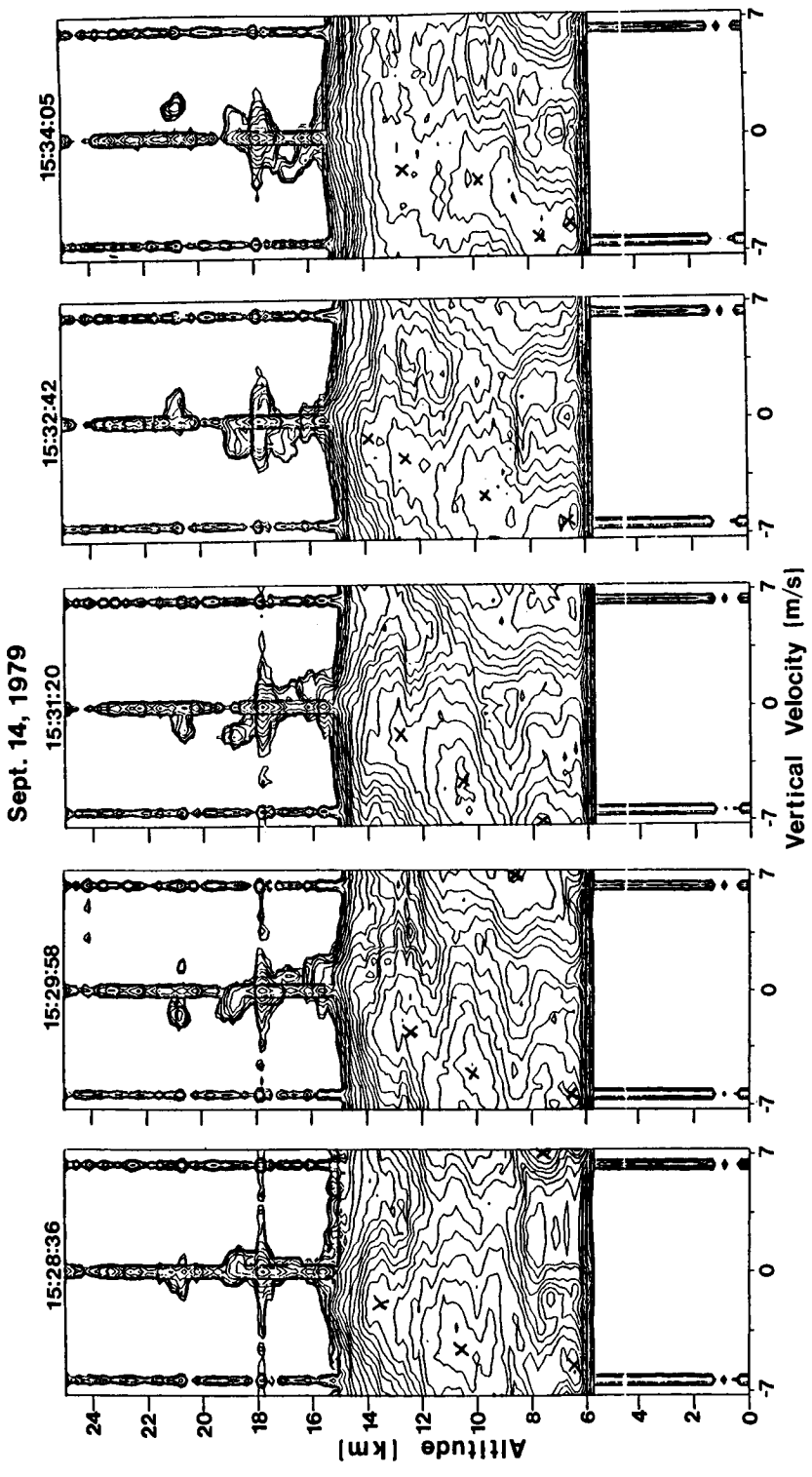

Figure 5.

wavelength. We have examined the Doppler spectra from the UHF radar in detail, and there is no evidence of a double peak. Of course, that may not be surprising since the echo strength of the signals shown in Figure 5 are of the order of 60 dB. The difference in the signal strength just above the tropopause near 15 km and the signals in the cloud just below the tropopause is approximately 30 dB at UHF but only 10 dB at VHF. The signal strength increases further by another 30 dB before it attains maximum values near 10-km altitude. The radiosonde ascent from San Juan, located 80 km east-northeast from the Arecibo radar, showed that the atmosphere was conditionally unstable from ground level to the height of the tropopause, and the lowest height where data were obtained with the radar corresponded to a temperature of -10°C. The temperature decreased further to -20°C at 400 mb or 7.6-km altitude. Therefore, we do not expect much liquid precipitation or liquid cloud droplets in the height range of the radar measurements.

Figure 4 shows that the echoes attain their largest magnitude near the center of the cloud and taper off at the edges. Therefore, the enhancements cannot be due to large refractivity gradients created by mixing of dry and cloudy air near the outside of the cloud. The largest magnitudes occur in what is typically the updraft region of the cloud, the right half of Figure 4, while somewhat less intense echoes occur in the region usually associated with downdrafts, the left half of Figure 4. The same is also true for the VHF observations as shown in the middle frame of Figure 2.

GRAVITY WAVES GENERATED BY THE STORMS

Both the SOUSY VHF radar observations and the Arecibo observations show that gravity waves were generated by the convection once the upward development reached the height of the transition from the unstable lapse rate in the troposphere to the stable lapse rates in the lower stratosphere (ROTTGER, 1980b; LARSEN et al., 1982). The gravity-wave motions are evident in the sample profiles shown in Figures 3 and 5. In Figure 5, the downward phase progression of the waves can be seen in the altitude range from 15 to 22 km. The downward phase progression implies upward group velocity for a packet of gravity waves. Figure 1 also shows some evidence of downward phase progression in the altitude range between 10 and 13 km as can be seen in the tilt of the height/time contours of the vertical velocities.

DISCUSSION

In all, there are a number of similarities between the two data sets in spite of the differences in the conditions and locations used for the observations. Both radars detect a "precipitation" echo that shows vertical velocities close to zero near the tropopause and increasing negative velocities at lower heights. The VHF radar also detects the clear-air component of the vertical motion. Finally, both sets of radar observations showed that gravity waves were generated in the lower stratosphere in connection with the cumulus convection.

REFERENCES

Atlas, D. (1964), Advances in radar meteorology, in Advances in Geophysics, 10, 393-478.

Battan, L. J. (1973), Radar Observation of the Atmosphere, University of Chicago, 324 pp.

Clark, T. L., and W. D. Hall (1979), A numerical experiment on stochastic condensation theory, J. Atmos. Sci., 36, 470-483.

Chernikov, A. A. (1968), Radio-wave scattering in clouds and the radar equation, Paper presented at the Third All-Union Conference on Radar Meteorology, Moscow.

Gage, K. S., J. L. Green, and T. E. VanZandt (1978), Application of the VHF pulsed Doppler radar to cloud physics research, Proc. Conf. on Cloud Physics and Atmospheric Electricity, Am. Meteorol. Soc., Boston, MA.

Gossard, E. E. (1979), A fresh look at the radar reflectivity of clouds, Radio Sci., 14, 1089-1097.

Gossard, E. E., and R. G. Strauch (1981), The refractive index spectra within clouds from forward-scatter radar observations, J. Appl. Meteorol., 20, 170-183.

Green, J. L., R. H. Winkler, J. M. Warnock, W. L. Clark K. S. Gage, and T. E. VanZandt (1978), Observations of enhanced clear air reflectivity associated with convective clouds, paper presented at the 18th Conference on Radar Meteorology, Am. Meteorol. Soc., Boston, MA.

Larsen, M. F., W. E. Swartz, and R. F. Woodman (1982), Gravity-wave generation by thunderstorms observed with a vertically-pointing 430 MHz radar, Geophys. Res. Lett., 9, 571-574.

Naito, K., and D. Atlas (1966), On microwave scatter by partially coherent clouds, paper presented at the 12th Weather Radar Conference, Am. Meteorol. Soc., Boston, MA.

Rottger, J. (1980a), Development of refractivity structures during anticyclonic weather conditions, paper presented at the 19th Conference on Radar Meteorology, Am. Meteorol. Soc., Boston, MA.

Rottger, J. (1980b), Structure and dynamics of the stratosphere and mesosphere revealed by VHF radar investigations, Pure Appl. Geophys., 118, 494-527.

Smith, R. L. (1964), Scattering of microwaves by cloud droplets, paper presented at the 11th Weather Radar Conference, Am. Meteorol. Soc., Boston, MA.

4.2.2 UHF AND VHF RADAR OBSERVATIONS OF THUNDERSTORMS

D. N. Holden, C. W. Ulbrich, M. F. Larsen

Department of Physics and Astronomy
Clemson University
Clemson, SC 29634

J. Rottger, H. M. Ierkic
Arecibo Observatory
P. O. Box 995
Arecibo, PR 00612

W. Swartz
School of Electrical Engineering
Cornell University
Ithaca, NY 14853

INTRODUCTION

A study of thunderstorms was made in the Summer of 1985 with the 430-MHz and 50-MHz radars at the Arecibo Observatory in Puerto Rico. Both radars use the 300-meter dish, which gives a beam width of less than 2 degrees even at these long wavelengths. Though the radars are steerable, only vertical beams were used in this experiment. The height resolution was 300 and 150 meters for the UHF and the VHF, respectively. Lightning echoes, as well as returns from precipitation and clear-air turbulence were detected with both wavelengths. Two tipping bucket rain gauges, an anemometer, wind vane, and electric field change meter provided additional data to complement the regular meteorological balloon soundings taken at San Juan, some 70 kilometers to the east.

Large increases in the returned power were found to be coincident with increasing downward vertical velocities at UHF (Figure 1), whereas at VHF the total power returned was relatively constant during the life of a storm. We attribute this to the fact that the VHF is more sensitive to scattering from the turbulence-induced inhomogeneities in the refractive index and less sensitive to scatter from precipitation particles. On occasion, the shape of the Doppler spectra was observed to change with the occurrence of a lightning discharge in the pulse volume. Though the total power and mean reflectivity weighted Doppler velocity changed little during these events, the power in Doppler frequency bins near that corresponding to the updraft did increase substantially within a fraction of a second after a discharge was detected in the beam. This suggests to us some interaction between precipitation and lightning.

THE EXPERIMENT

During the past year at the Arecibo Observatory, a 46.8-MHz transmitter and receiver was installed which illuminates the 300-meter dish. The peak power available is of the order of 50 kilowatts, with a maximum duty cycle of 2%, and a minimum detectable signal around minus 110 dBm. The feed is located 2.1 degrees inward from the 430-MHz feed. Some of the first data taken with the new system were of the tropical thunderstorms that form over the island in the summer months.

The Doppler spectra at VHF show much of the structure of the thunderclouds. Most of the received power is assumed to be from the scattering processes associated with turbulence, which manifests itself as a very large increase in the variance of the Doppler spectrum. This is indicated in Figure

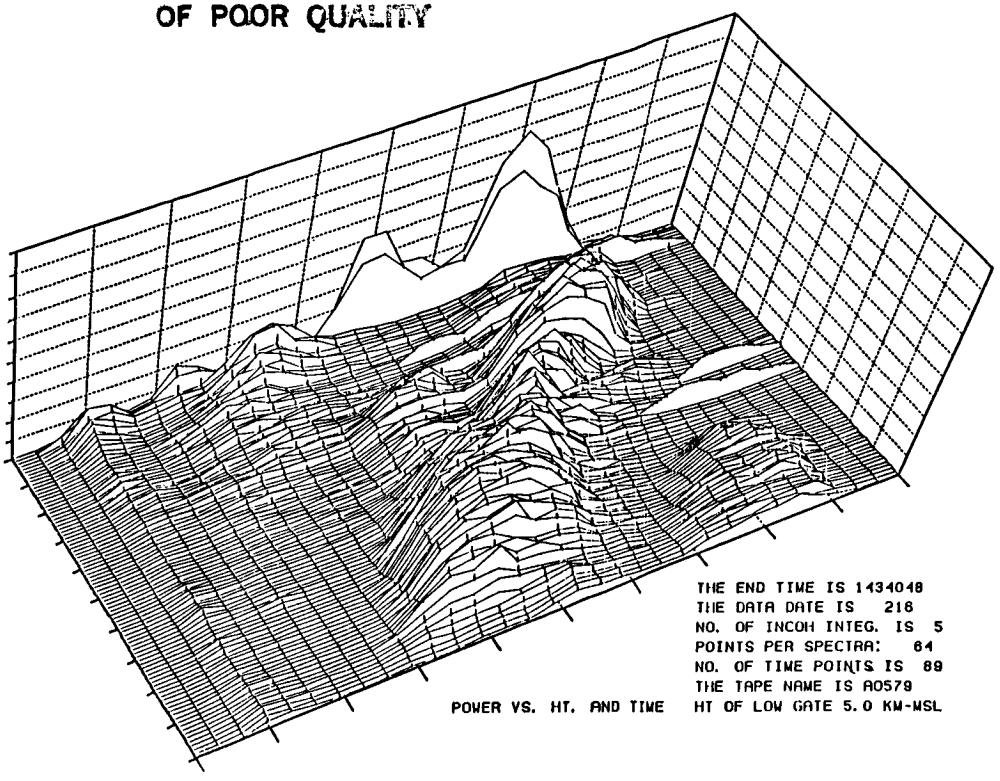

Figure 1. A three-dimensional representation of the zeroth moment (Z direction) of UHF Doppler spectra. Slant range (in this case, height) increases toward the upper right, time increases toward the lower right.

2 where the lower gates have returns in them from a thundercloud, where the upper gates do not. Some of the transient features that we observed in the spectra indicate the presence of precipitation and occasionally, lightning. The scattering process from lightning is not fully understood, since an enhanced echo during a discharge could conceivably originate from a number of sources. One of these is the scatter from the ionized plasma channel itself, and another might be the scatter from the intense gradients in refractive index that surely must exist as a result of the shock wave that is produced by the flash.

During some of the campaign, the 430-MHz radar was also operated. Though the two systems were never operated simultaneously (indeed, with the 2.1 degree separation the two beams do not share the same pulse volume), some comparison of the features of the spectra at the two different wavelengths can be made. The most conspicuous difference between the observations at the two frequencies is the effect of the presence of precipitation in the beam. Only during periods of intense rain does a significant contribution to the echo at VHF appear; the returned power is increased by the precipitation less than 5 or 10 dB. In fact, the presence of precipitation in the pulse volume does not guarantee that the power returned will be greater than when the precipitation is not present. This is shown in Figure 4 when a comparison of the power in gates 56 through 67 is made with the power in gates 71 through 80. At UHF, the

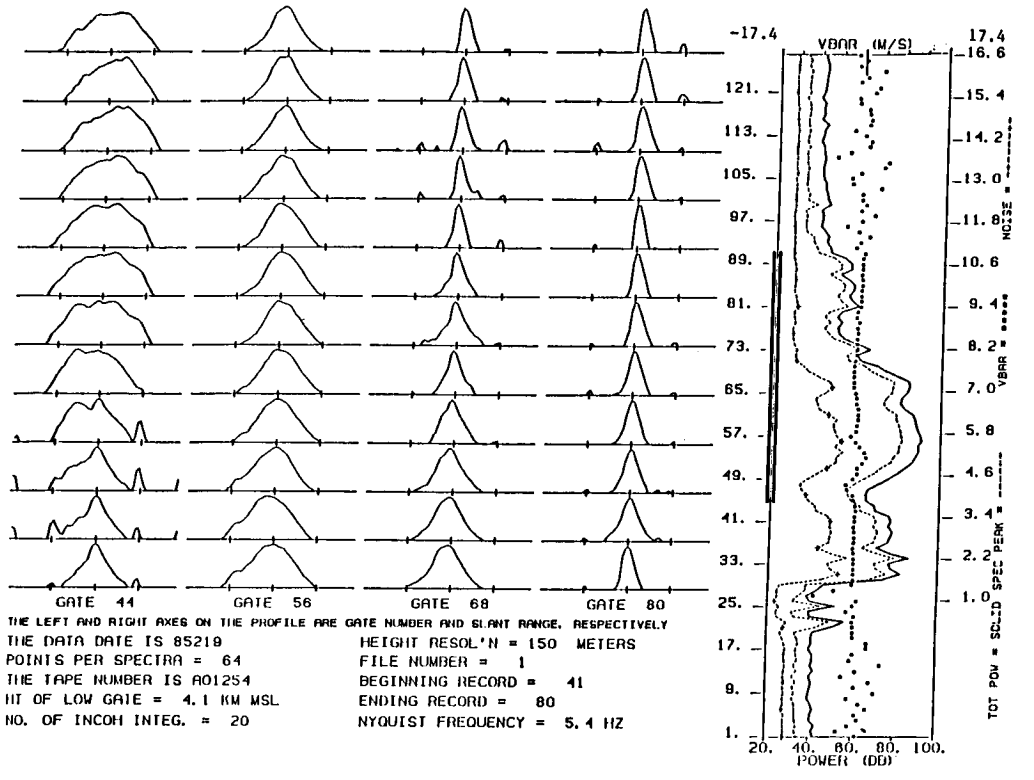

Figure 2. VHF Doppler spectra integrated for two minutes, with spectra plotted for gates 44 through 91 and a height profile of mean velocity, total power, spectral peak, and noise level for 128 gates. Positive Doppler velocity (toward the radar) is to the right of center, each spectra is scaled to its own peak and noise level. Note the large variance in the lower gates as compared with the upper ones.

situation is quite different, there are large changes in the reflectivity (greater than 20 dB) that occur in time intervals of the order of a few minutes. These changes are almost invariably associated with downward vertical velocities that is indicative of precipitation (i.e., velocities around 5 meters per second). The variance of the spectra at both frequencies is seen to increase significantly with the onset of convective activity, sometimes as much as a factor of four or so. The transient echoes associated with lightning are also quite different from one frequency to the other. At UHF, the returns usually appear at Doppler frequencies that are consistent with the vertical air motions, and show a variance that is not atypical of that found in a thunderstorm environment. This implies that the principal scattering mechanism is that of scattering from the lightning channel itself (which is assumed to move with the mean wind). At VHF, lightning in the beam often completely flattens the spectra, as though there is a feature present that has an extremely high Doppler shift and proportional width. This might be consistent with the radar detecting the acoustic wave (thunder) which would have a Doppler velocity of the order of 300 meters per second. Of course, this large shift would be aliased many times around the 5 Hertz Nyquist frequency of the system. Another explanation is simply receiver saturation, though there is some evidence that this is not the case.

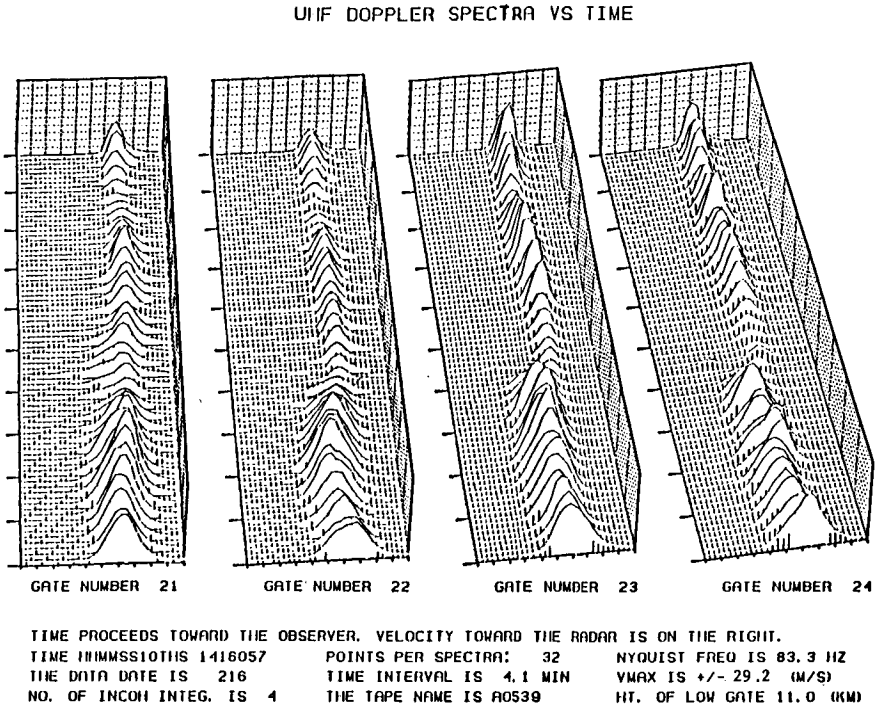

Figure 3. Doppler spectra plotted as a function of time at UHF for range gates 21 through 24. The distinct change in the character of the spectra, about halfway through the sequence is coincident with a lightning flash observed in the beam.

The shorter sampling time of the UHF radar allows a very detailed look at any interaction between the hydrometeors in the clouds and lightning. Occasionally, when lightning is detected in the beam, there is a significant alteration of the Doppler spectra that occurs shortly after the discharge, as is shown in Figure 3. The mean reflectivity weighted Doppler velocity does not change appreciably, nor does the total power. There are, however, substantial increases in reflectivity that occur in certain frequency bins. If the velocity that the lightning echo appears in can be assumed to be the velocity of the air motion, then the increases that are observed happen in frequencies that correspond to small downward velocities relative to the wind field. This can be interpreted in two ways: one, a reorientation of the scatterers as a result of the electric field change that accompanies the lightning, or a growth of the very small cloud particles to larger sizes. It is the latter of the two explanations that is the most plausible, since the changes in the spectra are more or less permanent, that is, of the order of tens of seconds. If there was a simple reorientation of the particles, the random wind field would rearrange them in a time that would be on the order of the time to independence which, in a thundercloud, is less than a second.

The presence of precipitation in the Doppler spectra at VHF can provide much information about the cloud microphysics if the precipitation peak is sufficiently separated from the clear-air peak (see Figure 4). In this case, the clear-air part of the spectra can be approximated (by a Gaussian, say)

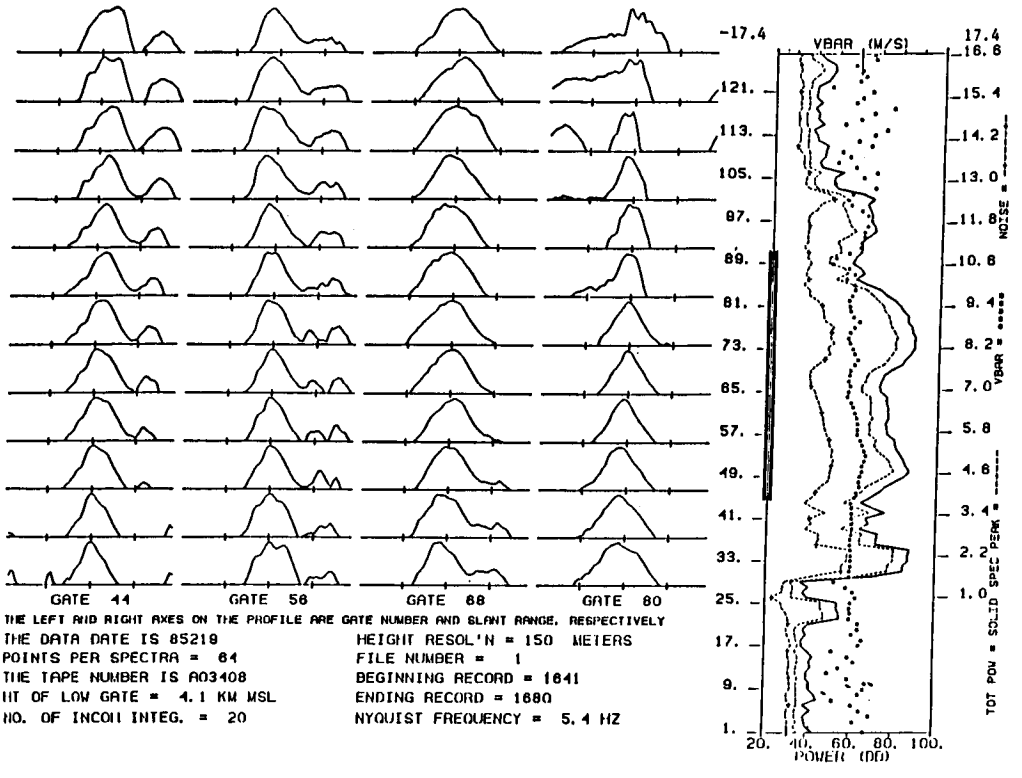

Figure 4. Same parameters as in Figure 2. Here, the smaller peaks that appear to the right of the main peak are the result of scattering from intense (> 50 mm/hr) precipitation.

which, when subtracted from the total spectra, leaves just the contribution due to the precipitation. Subtracting the clear-air velocity now leaves the fall velocity of the drops in still air, then through some terminal velocity-diameter relation, the drop size distribution can then be derived from the spectra.

The new VHF system has good sensitivity, which should make it a valuable addition to the other frequencies that are available at the Arecibo facility. The near proximity of the 430-MHz feed immediately suggests that dual wavelength experiments could be performed, unfortunately, that is not the case, unless large-scale features or long time scales are to be investigated. Even though there is only 2.1 degrees separation between the two beams, with the tremendous inertia that the receiver platform has, it would take about one minute to swing the feed this angular distance. In a convective environment, this is entirely too long as the entire pulse volume can be exchanged in less than 10 seconds during thunderstorms. The construction of a VHF feed that is concentric with the 430-MHz feed would make the Arecibo facility truly unique. Given that an absolute calibration was available for both systems, dual wavelength methods could then be used to study a variety of phenomena: turbulence, drop size distributions, and other effects. In the meantime, more experiments done with the new system will increase its reliability and versatility.

4.3.1 COMPARISON OF MEDIUM FREQUENCY PULSED RADAR INTERFEROMETER AND CORRELATION ANALYSIS WINDS. 1.

C. E. Meek, I. M. Reid, and A. H. Manson

Institute of Space and Atmospheric Studies
University of Saskatchewan
Saskatoon, Canada S7NOW0

INTRODUCTION

In principle, the interferometer analysis determines the radial velocity and direction of single scatterers provided that each has a sufficiently different Doppler frequency to permit separation by spectral analysis. In fact, scatterers will not have constant radial velocity, and their Doppler frequencies as well as their directions will be modulated by their horizontal motion. Thus, there is a tradeoff between the poorer resolution but less "smeared" scatterers on shorter records and the higher resolution (longer) records.

Three or more non-collinear scatterers are sufficient to determine the wind.

EXPERIMENTAL APPARATUS

Figure 1 shows the antenna arrays used, N-S linear is transmitted and E-W linear is received. The recording system, designed by D. G. Stephenson (GREGORY and STEPHENSON, 1972), records raw (8 bit) data simultaneously for 2 channels at 24 height gates and sends it directly to an incremental tape drive. This permits a maximum transmitter pulse rate of 15 Hz, which gives a final sample separation at each antenna of 0.2 sec. At this rate, there is one pulse dropped every 12 sec (8640 bytes) while a block gap is written on tape. Data can be recorded for up to 8 hr (1 tape) in this fashion.

The in-phase (I) and quadrature (Q) outputs of the coherent receiver are 5° in error; this will result in a weak ($\sim$-27dB) sidelobe at the negative Doppler frequency of any signal and is not expected to affect the present results.

ANALYSIS

The data to be discussed consist of 3.6-min lengths starting every 5 min. The I and Q amplitude sequences for each antenna are first tapered along 10% of their length at each end by a cosine function to reduce sidelobes, and then Fourier transformed (1024 points). The cross spectra (which are not smoothed) for pairs of antennas yield the phase differences, $\Delta\phi$, to be used in angle of arrival. These are corrected for cycling delays caused by the recording technique of sampling each antenna in rotation. Since there are only 3 receiving antennas, there is no over-determination of phase, and the only basis left for selecting single scatterers is by peaks in the power spectra. The criteria for selecting Doppler frequencies are: that all antennas should show a local peak in the power spectrum, and that the average (dB) power of the selected peak should be at least 5 dB greater than the average power near the Nyquist frequency, and within 30 dB of the power of the strongest selected peak.

The phase differences at the selected frequencies are then corrected for unequal antenna cable lengths, and an attempt to correct for phase folding is done. Phase folding occurs beyond a real zenith angle of about 30° (depending on azimuth) due to the 1-lambda spacing of the receiver array, and must be

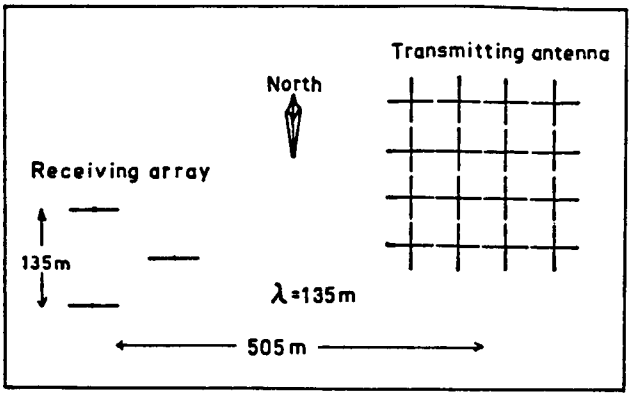

Figure 1. Receiving and transmitting arrays.

considered because of the transmitter antenna sidelobes at 45°; it will affect both the calculated zenith and azimuth angles. The correction procedure is to check whether the three $\Delta\phi$ add to zero -- if they do not, then the $\Delta\phi$ with the maximum absolute value is modified by 360°; if the resulting sum is still non-zero, the peak is rejected. This method is not foolproof, since scattering at very large zenith angles can fold two of the $\Delta\phi$ and look immediately acceptable. The only real solution is closer antenna spacing, and the use of loop antennas to reduce the subsequent increase in coupling.

DATA

A sample record is shown in Figure 2. The left side shows power spectra for the three antennas and selected peaks are marked at the bottom (originally 3 colours). The right side plots the direction (zenith angle is log scale with origin = 1) and the horizontal component of velocity calculated on the assumption that the real vertical component is negligible. Figure 3 shows relative power versus zenith angle. The number of cases are printed on the plot. Also shown is the theoretical transmitter beam pattern (one way) for the N-S plane. Phase folding is probably responsible for the partial filling of the theoretical null in this pattern; little difference was seen when the azimuths were divided into two parts, one looking towards the sidelobes and the other between them.

FULL CORRELATION ANALYSIS

Data were averaged in threes (giving $t = 0.6$ sec) before performing lagged complex correlations. The magnitudes of the correlations were used to calculate apparent (from just the time lags of the peak correlation) and true (using, in addition, the width of the mean auto and the magnitudes of the peak cross correlations) velocities. The mean vertical velocity is found from the slope of the autocorrelation phase near zero lag. The correlations for the data used in Figure 2 are shown in Figure 4.

VELOCITY FROM INDIVIDUAL "SCATTERERS"

This is found by a least squares fit of a 3-D or 2-D (horizontal) velocity vector to the data, which minimizes the squared error in radial velocity. The squared error is first weighted by the power of the Doppler peak relative to that of the largest peak power in each record. In practice, the resulting

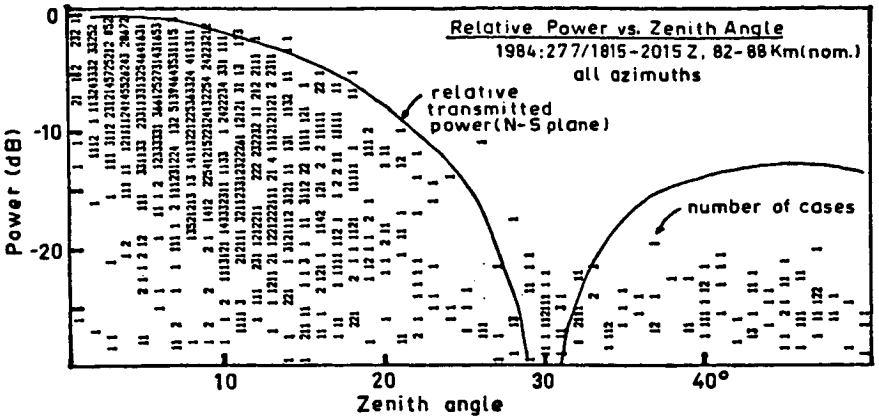

Figure 2. Power (relative to the maximum selected peak in each record) versus calculated zenith angle for a 2 hr period (24 records).

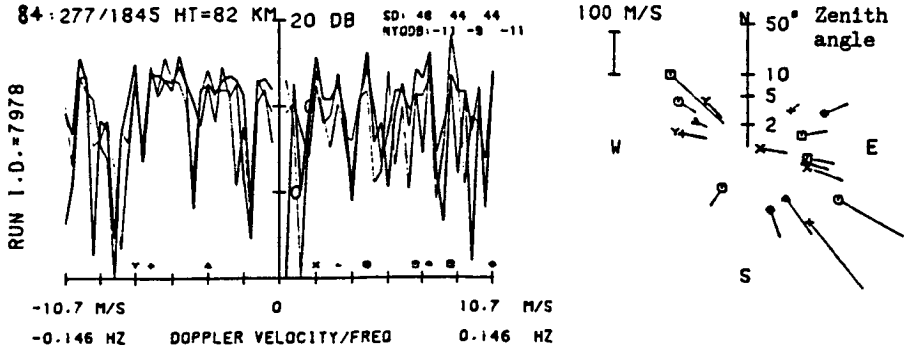

Figure 3. Spectra for 3 antennas shown over a small frequency range (full range is ± 2.5 Hz); symbols indicate chosen peaks and appear on the scatterer location plot at the right as well, where inferred horizontal velocity is shown as a straight line emanating from the scatterer symbol.

vector was found to be relatively independent of the actual weighting used. A lower zenith limit of 5° was used to reduce error due to inaccurate cable length corrections, and an upper limit of 15 to avoid cases of phase folding (a zenith angle of 50° can fold back to 22°). In addition, an upper limit of 40 m/s was placed on the radial velocity -- this also acts as a power limit, since spectra peak near zero frequency.

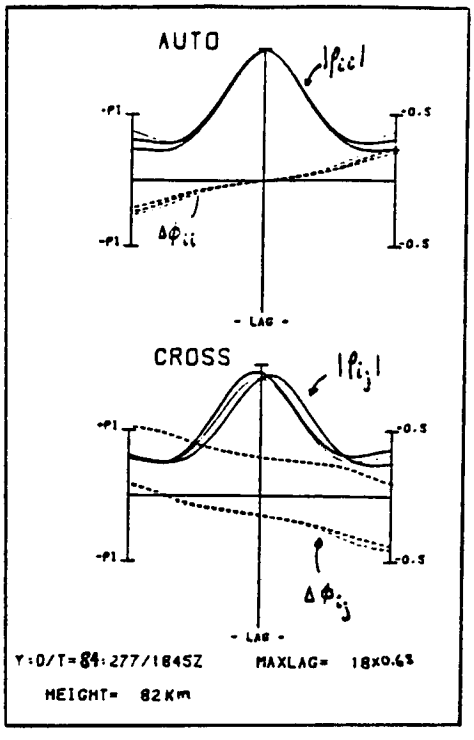

Figure 4. Auto and cross correlations for the record shown in Figure 3.

VELOCITY COMPARISON

Table 1 lists the velocities for the record shown in Figures 2 and 4.

TABLE 1

Comparison of velocities for 1 record (82 km, 1984: 277/1845Z).

	speed (m/s)	direction (E of N)	vertical (m/s)
interferometer analysis (12 Doppler peaks)			
3-D	58	132	1.6
2-D	56	123	
correlation analysis			
apparent	45	123	0.4
true	32	145	

The mean velocities for 1 hour of data (12 records) are shown in Figure 5; most records have correlation Vz values, fewer have apparent, and fewer still, true velocities. The interferometer value was found by one fit to all the individual scatterers found in the hour. Because the height variation for constant range over 5°-15° zenith is within the height resolution of the system

(3 km), no adjustment was made to get real height. Also shown are the mean values (9 km resolution) from the real-time analysis (non-coherent) system.

DISCUSSION

Figure 5 shows that the "apparent" speed agrees with the interferometer value, but the "true" velocity is about half the latter. If it can be shown that the chosen Doppler peaks represent actual single localized scattering regions, then the "true" velocity is in error. This cannot be shown with just one record, because a peak in the spectra can be translated either as a single scatterer, where the $\Delta\phi$ represent the angle of arrival and the Doppler frequency defines the radial velocity, or alternately as a Fourier component of a rigid pattern, where the $\Delta\phi$ represent the wavelength and propagation direction, and the Doppler frequency is related to the phase speed of the "wave". The latter concept gives the "2-D" velocity mentioned previously if it is assumed that the "wave" is a frozen-in component of a rigid pattern - viz. its calculated velocity is only a component of (and thus, in general, smaller than) the real horizontal velocity.

In theory, the use of a larger receiving array does not help to resolve this ambiguity; however, it does increase the degrees of freedom used in the peak selection (effectively a coherence criterion).

Another situation in which peaks may be mistaken for single scatterers is when signals due to several real scatterers overlap in the same frequency bin, either simultaneously or sequentially in one record. Figure 6 shows contours of constant Doppler frequency in space, assuming a constant horizontal velocity. Scatterers positioned anywhere on one contour will have the same radial velocity/Doppler frequency and their radial velocity varies linearly with time. (The plot has assumed constant range; constant height, which is more realistic, bends the contours near the ends -- about 5% change in χ at 15° zenith.)

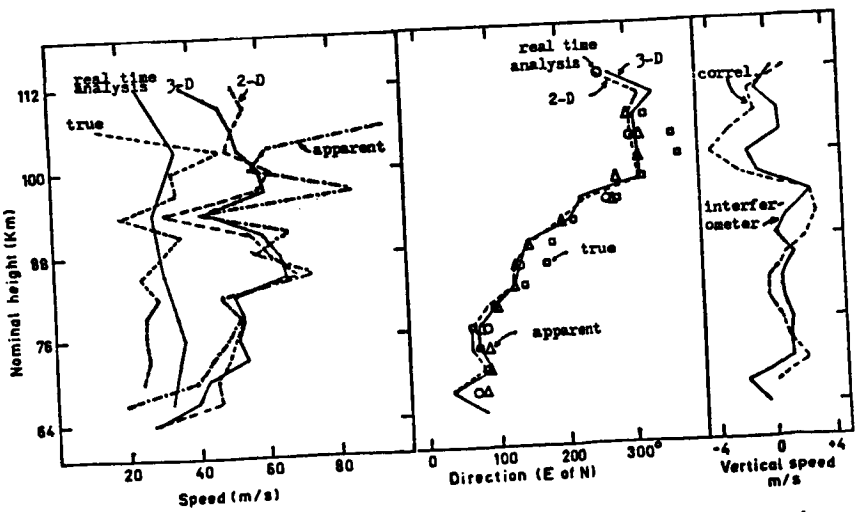

Figure 5. Comparison of interferometer and correlation analysis (apparent and true) horizontal speed and direction and vertical speed over one hour (84:277/1815-2015 GMT). Also shown are the mean winds for the real-time wind system.

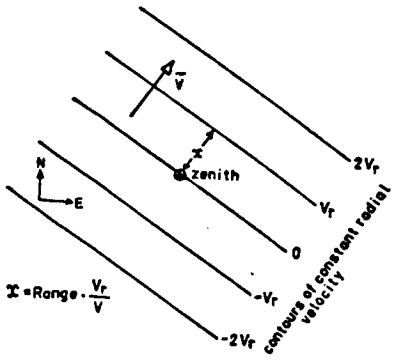

Figure 6. Contours of constant radial velocity as a function of horizontal distance from the zenith.

A simple numerical model shows that the sum of signals due to any set of scatterers (random phase and constant radial velocity over the "record length") placed along one of these contours results in a calculated scatterer located somewhere on the same contour; so there should be no bias in the resulting velocity due to lack of frequency resolution. Also, the composite scatterer, if tracked, moves with the same velocity.

Cases where two or more scatterers "scan" across one frequency bin at different times during a record are more difficult to analyze. Some local Doppler peaks will result just because the spectrum is not smooth. A more complicated model is required to see the effects. It appears that the positions of calculated scatterers would be unrelated to those of the real ones.

Finally, it is interesting to note that the vertical velocities shown in Figure 5 from the correlation method seem to have a smoother height profile that those from the individual Doppler peaks. Correlation techniques are more computationally efficient, and may even produce a more satisfactory value of Vz.

CONCLUSION

From these limited experimental data, it appears that the velocity found from the combined interferometer peaks agrees well with the "apparent velocity" from correlation methods, but the "true velocity" is a factor of 2 smaller. This difference might be resolved by searching for "scatterers" showing regular movement between adjacent records, and this is the subject of the accompanying paper.

REFERENCE

Gregory, J. B., and D. G. Stephenson (1972), High altitude winds from radio reflections, Canadian Research and Development, March/April.

4.3.2 COMPARISON OF MEDIUM FREQUENCY PULSED RADAR INTERFEROMETER AND CORRELATION ANALYSIS WINDS. 2.

C. E. Meek, I. M. Reid, and A. H. Manson

Institute of Space and Atmospheric Studies
University of Saskatchewan
Saskatoon, Canada S7N0W0

INTRODUCTION

The preceding paper compared the mean instantaneous velocity of a group of scatterers with those found from correlation methods and concluded that it agreed well with the apparent velocity (which assumes a rigid isometric diffraction pattern on the ground). In order to test whether the chosen Doppler peaks represent localized scatterers in motion, as opposed to some sort of integrated composite, an attempt has been made to determine the change in position of single "scatterers" over a series of sequential records.

From Figure 6, in Paper 1, it can be seen that single scatterers moving with a constant horizontal velocity have the property that their Doppler frequency/radial velocity varies linearly with time, and has the same slope no matter where the scatterer is physically (this assumes constant range rather than constant height, but is a good approximation near the zenith). Also, assuming isotropic scatter, the power should be roughly constant, apart from transmitter antenna beam width considerations.

EXPERIMENT AND ANALYSIS

This experiment, unlike Paper 1, employs a four-antenna system (Figure 1) which has 1 degree of freedom in phase. Due to equipment limitations N-S linear transmission and E-W linear reception are used. The Doppler frequency peak selection criteria are that at least two of the four power spectra should have a local peak, and that the normalized phase discrepancy,

$$N\phi D = \left| \sum_{i=1}^{3} (\phi_i - \phi_4) \right| / \sum_{i=1}^{3} |\phi_i - \phi_4|$$

should be less than 0.3. An relative power criterion similar to that of Paper 1 is used. Since there are four antennas, the basic time step is 4/15 sec. The record length is 256 points (approx. 68 sec).

EXPERIMENTAL DATA

The raw data consist of half-hour lengths of complex amplitudes in which the receiver gain setting is constant at a given height (i.e., range gate). The records are spaced by 72 sec, giving $\sim$22 records per run. After scatterers have been identified, they are collected in height (rather than range) bins and plotted. Because different ranges, as originally measured, may have different gains, the power is defined to be the average peak power relative to the maximum spectral power in the original spectra. Plots are made of the position of the scatterers in each nominal height bin (which may include several range gates).

Figure 2 is the only example found so far in which moving "scatterers" can be perceived. The dashed line separates scatterers with +ve and -ve radial velocity. Also shown on this diagram are the vector displacements expected between records from the simultaneous 3-D and 2-D (horizontal) velocity vector fit to all scatterers in the half-hour, and that found from the real-time wind system ("true"). [The sense of in-phase (I) and quadrature (Q) signals was determined from this figure, and this is the easiest way because reversing I

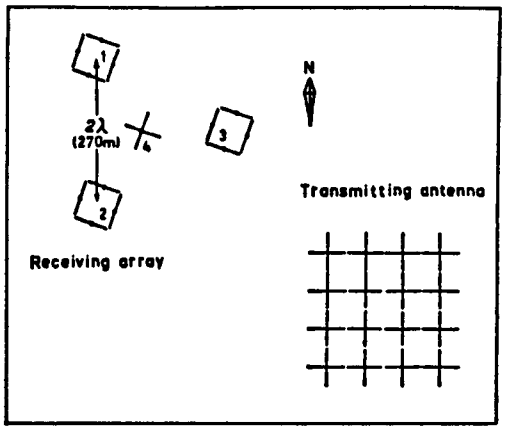

Figure 1. Transmitting antenna and 4 antenna receiving array.

and Q flips the scatterer azimuths by 180° but also changes the sign of the radial velocity; so the horizontal velocity is unaffected.]

The letters A, B, C,.....,L show the positions of scatterers in successive records, and the size indicates their strength (∿8 dB full range). The two sequences of interest are A-B-C and E-F- -H(although there are two possible candidates for H in the latter). The position of C is uncertain because it is very near the zenith, and thus more affected by small phase errors in the system. Table 1 lists the characteristics of these particular scatterers.

With only one such example, speculation is easy; for example, suppose that the signal is not from an isolated point scatterer, but is a moving reflection point on a scattering layer perturbed by a wave. This would explain why the two sequences follow almost the same path. The period of the wave (the time between "B" and "F") is then 4 x 72 sec (= 5 min), and the wavelength can be estimated from the horizontal speed (∿53 m/s, found from "A" assuming that the radial velocity is totally due to the horizontal phase velocity of the wave) to be 15 km. The fact that the direction doesn't agree with that of the "wind" also suggests a wave. Missing elements of sequences may be a result of a patchy scattering layer, which is moving with the background wind.

This is a very simple model, one would actually expect the reflection point to move relative to the wave as it passes over; but these complications will be left for future work.

Figure 3 shows a case in which the scattering seems to be coming from the same location (E-region heights) for the full half-hour. A stable wave perturbation in a "sheet of tin" could produce this effect provided that the ground pattern wavelength, λ_ω, was of the order of several times the array spacing, D, and the ground phase speed, V_ω, sufficient to give a non-zero Doppler frequency in the spectrum. Approximate values for these are given by:

$$\lambda_\omega \simeq \frac{D}{\sin(\text{zenith})} \quad ; \quad V_\omega = f_D \lambda_\omega$$

where f_D is the Doppler frequency; however, in this case, there should also be a peak with the opposite Doppler frequency 180° away in azimuth. Another

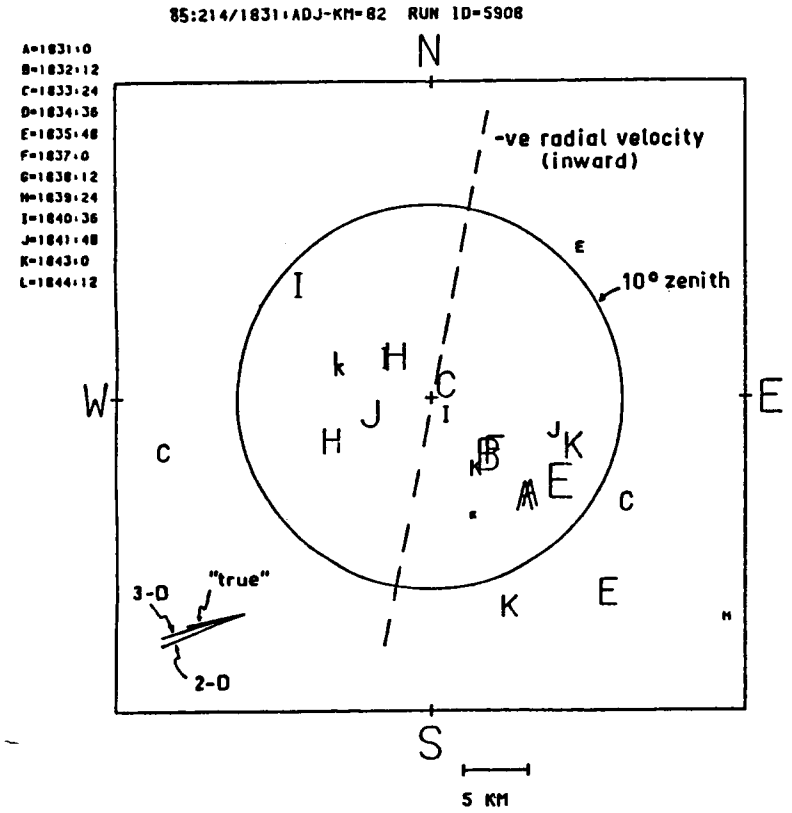

Figure 2. Scatter location over a series of short records, separate letters represent selected Doppler peaks, "+" is the zenith, 5 km distance scale is shown at the bottom. Expected displacements per record for 3 different wind estimates are shown at the bottom left corner.

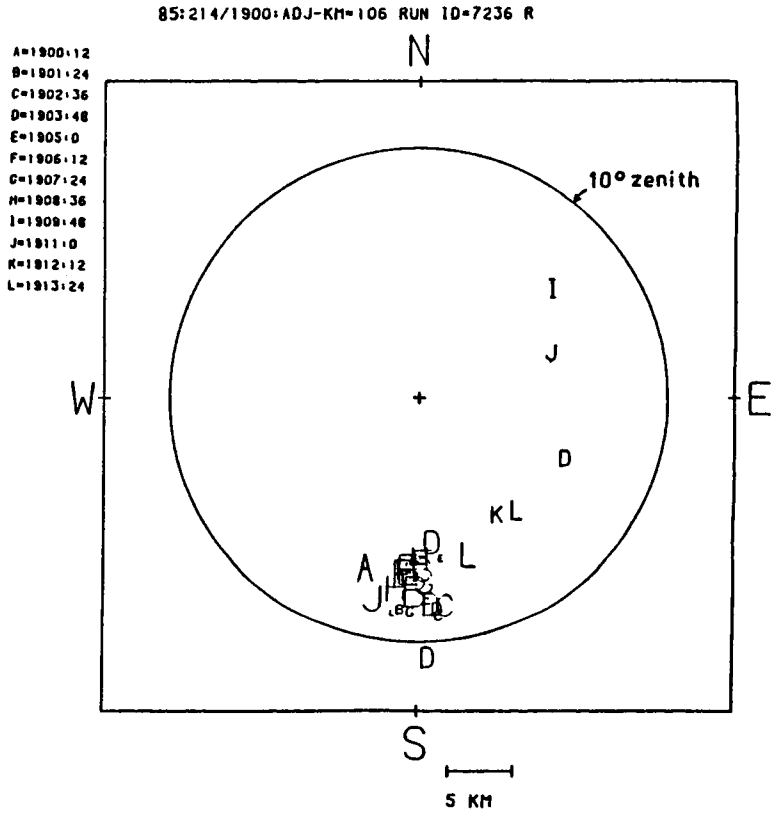

Figure 3. An example of a series of records in which the scatterers seem to be stationary in space and time. The radial velocities in the group are all outwards (see text).

TABLE 1

Calculated powers and positions of the selected Doppler peaks plotted in Figure 2 (all from the 82 km height gate). "Norm." is the normalization factor from the mean power in the original raw amplitudes. "Pmax" is the maximum spectral power (after normalization) in any single antenna spectrum, "Pwr" is the mean power (over all antennas) at the selected Doppler frequency. NϕD is the approximate normalized phase discrepancy.

Time	Plotted symbol	Norm. (dB)	Pmax (dB)	Pwr (dB)	V-rad (m/s)	Zenith (deg.)	Azimuth (Deg E of N)	NϕD
1831:00	A	41.6	-3.2	-4.8	-6.92	7.3	135.5	0.15
	A			-5.4	-5.93	7.4	133.2	0.15
1832:12	B	43.7	1.7	1.0	-1.98	4.3	134.3	0.05
1833:24	C	38.2	-0.2	-1.8	-0.99	1.1	49.5	0.05
1834.36	D							
1835:48	E	42.9	-1.8	-2.6	-8.90	8.3	122.3	0.15
1837:00	F	42.2	-1.1	-2.9	-3.96	4.4	128.9	0.15
1838:12	G							
1839:24	H	41.0	-1.4	-2.6	0.99	2.9	-38.5	0.05
	H			-3.8	6.92	5.7	-112.7	0.25

possibility is a tilted totally reflecting layer (about 7° tilt), but this cannot explain the non-zero Doppler frequency (median = $\sim$ 5 m/s); the scatter location should either move $\sim$ 3 km horizontally every record, or move out of the height gate radially within $\sim$ 10 min, and it does neither. A gradual electron density change below the height of reflection would create a Doppler shift, but it requires a very large change (which would also affect the reflection height) to get 5 m/s.

Something like a large-scale distortion of the atmosphere which "high lights" individual scatterers by focussing or tilting them as they pass through at the background wind speed is required to explain these data -- the scatterers are moving, but they are only seen in one direction.

CONCLUSIONS

The lack of success in tracking individual scatterers seems to suggest a short lifetime (as found by JONES, 1984). If this is the case, then the present experiment is not able to resolve the difference found between the correlation analysis "true" velocity and the interferometer value. On the other hand, it appears that the interferometer may be of some use in tracking waves.

4.3.3 MESOSPHERIC WIND MEASUREMENTS USING A MEDIUM-FREQUENCY IMAGING DOPPLER INTERFEROMETER

G. W. Adams

Center for Atmospheric and Space Sciences
Utah State University
Logan, Utah 84322

and

J. W. Brosnahan

Tycho Technology, Inc.
P. O. Box 1716
Boulder, Colorado 80306

This paper presents some wind results from a medium-frequency radar operated as an imaging Doppler interferometer. We used ten independent antennas, together with the mesospheric wind motions, so that we could Doppler-sort and then echo-locate individual scattering points. We determined the three-dimensional location and radial velocity of each discrete scattering point. Mean winds were then determined by a least squares fit to the radial velocities of the ensemble of scatterers.

Figure 1 shows a two-dimensional map of the scattering surface at 85 km, with the radial velocity indicated for each scattering point (Δ's have phase-decreasing Doppler; +'s have phase-increasing Doppler). Notice that most of the points in the northern half of the sky are approaching the radar, while those in the southern half of the sky are going away, consistent with a southward-directed mean (and mainly horizontal) flow as indicated by the wind clock. Notice also that there is considerable structure in the radial-velocity display, particularly near the zenith. We show below that the vertical velocity shows a 6-minute period consistent with the local Brunt-Vaisala period.

Figures 2 and 3 show several altitude profiles of the direction and horizontal components of the wind, spaced approximately every 30 minutes. Notice the spiral behavior of the direction vector, indicating a vertical wavelength of 40 km (if we ignore the results below 65 km). The component profiles give results that seem physically plausible and seem to have sensible time histories.

The remaining figures show a variety of vertical velocities at 2-minute resolution (1 minute on; 1 minute off). Figure 4 shows a 28-minute time history of the 80-km vertical velocity. The vertical velocity is seen to be periodic, with a period of about 6 minutes. Notice also that the oscillation appears well-centered about zero, even though there is a 30 m/sec eastward wind and a 5 m/sec southward wind. This tends to support our analysis that the method used here is immune to many of the difficulties associated with beam-forming techniques, in particular, contamination of the vertical component by the combination of horizontal winds, finite beam widths, and off-vertical scattering.

Figures 5 and 6 show the time histories at 66 and 86 km, respectively. The vertical velocity at 66 km shows a 20-minute periodicity (less neatly sinusoidal than Figure 4), while the 86-km plot is less regular yet. Both the 66-km and the 86-km results appear, as did the 80-km curve, to be centered around zero, with no obvious upward or downward bias in the results, in spite

of a 20 m/sec northward component at 66 km. (Both horizontal components are close to zero at 86 km.) These results are generally promising. Considerable improvement could be effected with more appropriate processing algorithms, which we hope to implement soon.

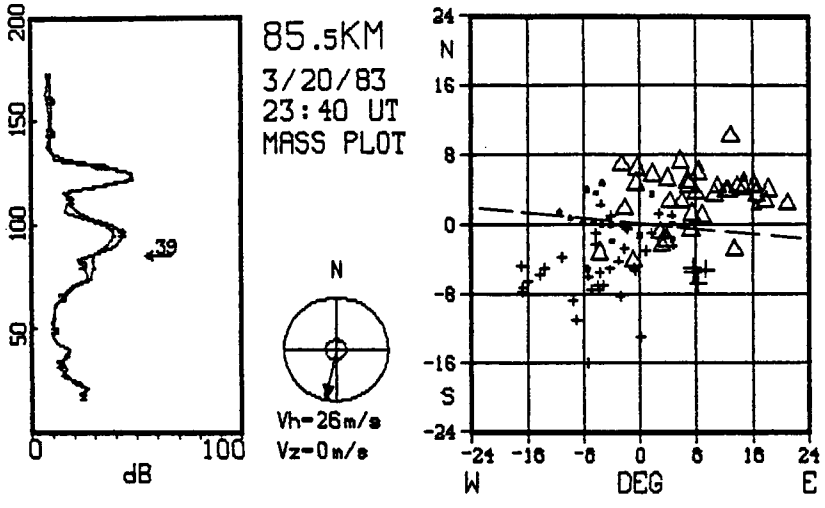

Figure 1.

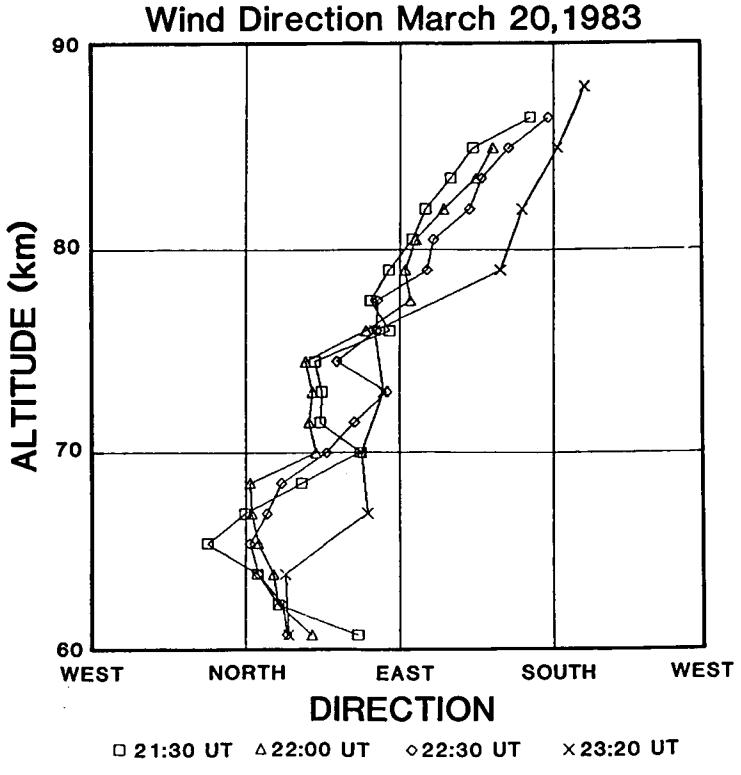

Figure 2.

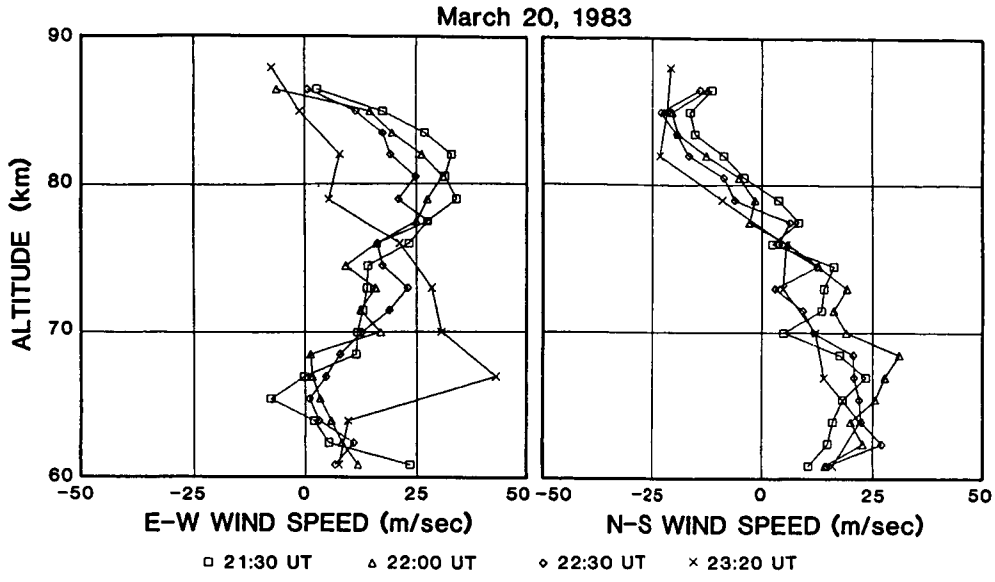

Figure 3.

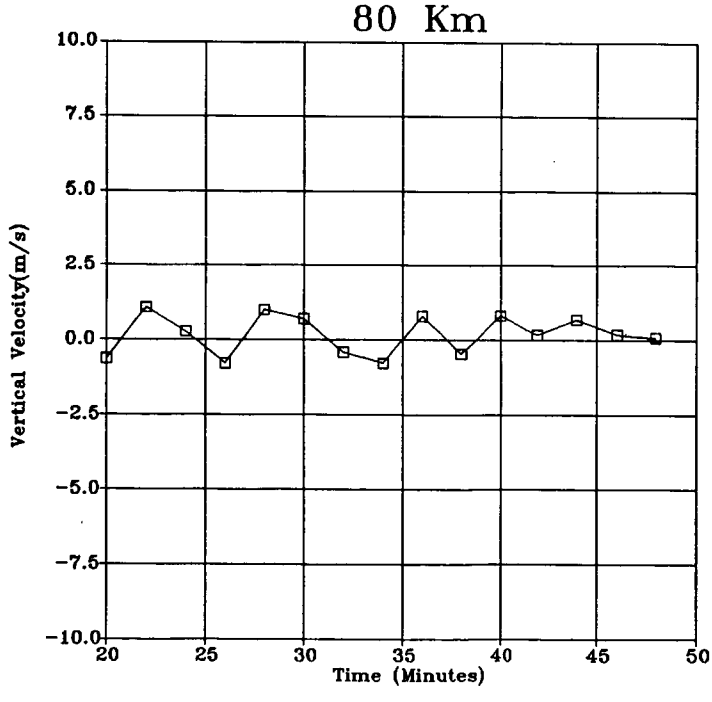

Figure 4.

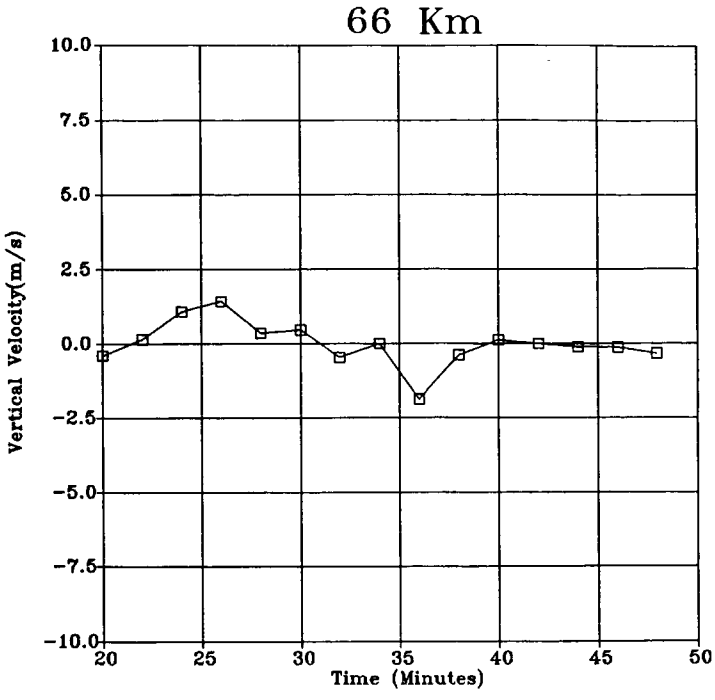

Figure 5.

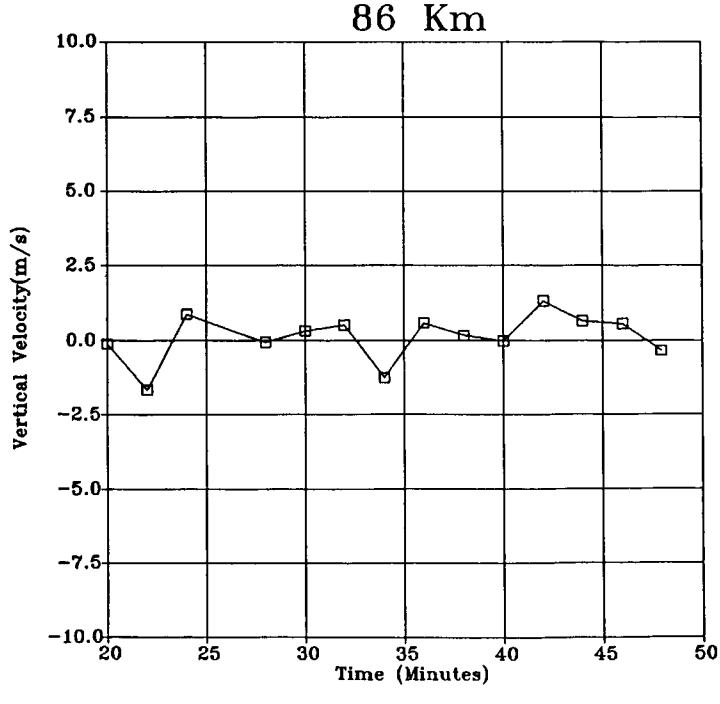

Figure 6.

4.3.4 COMPARISON OF REFLECTIVITY AND WIND PROFILES MEASURED ON 46.8 MHz AND 430 MHz AT THE ARECIBO OBSERVATORY

Jurgen Rottger*

Arecibo Observatory
P. O. Box 995
Arecibo, Puerto Rico

First comparisons of troposphere and stratosphere radar experiments at UHF and VHF were done at the Arecibo Observatory in April 1980 with the 430 MHz radar and the 46.8-MHz radar. Comparisons of echo power, i.e., non-range corrected reflectivity, were described by ROTTGER et al. (1981). Taking into account differences in the average transmitter power, bandwidth, aperture illumination and sky noise temperature as well as near field correction and wavelength dependence of the scattering model, it was found that the average signals (at 12° zenith angle) at VHF were by about 10 dB stronger than at UHF. This was explained by a diffuse reflection process, favoring the longer wavelengths.

A more detailed comparison of signal power/reflectivity profiles at UHF and VHF is shown in Figure 1 (left diagram). The UHF operations and analysis were made by M. Sulzer and T. Sato, using the 430-MHz transmitter with 150 kW average power. The VHF operations were with the transportable SOUSY VHF radar with 160 W average power (e.g., ROTTGER et al., 1981). The profiles in Figure 1 are shifted with respect to each other along the abscissa, to obtain a best fit of the average profiles. The absolute power difference, thus, cannot be read from the graph. The variation of power with altitude is fairly well correlated on both frequencies. The fact that power peaks occur at about the same altitudes on both frequencies indicates that the same (turbulence) layers were seen. However, the peak-to-peak power fluctuations are smaller on VHF than on UHF. The UHF radar, because of its higher power aperture product, yields echoes up to larger heights, although the VHF radar pointed closer to the zenith (ZE = 6.5° on VHF, ZE = 12° on UHF).

In Figure 1 (right hand diagram), we compare the velocity profiles measured on both frequencies with the Doppler beam swinging mode. On VHF, the antenna pointed at 6.5°, and at 12°, on UHF. In general, the velocity profiles (only the zonal component u was measured on both frequencies) are equivalent. The VHF profile, however, shows more fluctuations with height than the UHF profile, although the latter was recorded with 150 m resolution instead of 300 m resolution on VHF. We have to compare carefully the analysis routines used on both frequencies to come to a final conclusion on this difference. However, we also may regard this as an effect of diffuse reflection at VHF which causes non-Gaussian Doppler spectra with superimposed spikes.

More detailed comparisons of 430-MHz and 46.8-MHz radar experiments will now be possible at the Arecibo Observatory (see ROTTGER et al., 1986, and HOLDEN et al., 1986), with the same data-acquisition and analysis routines.

---

*On leave from Max-Planck-Institut fur Aeronomie, Katlenburg-Lindau, West Germany.

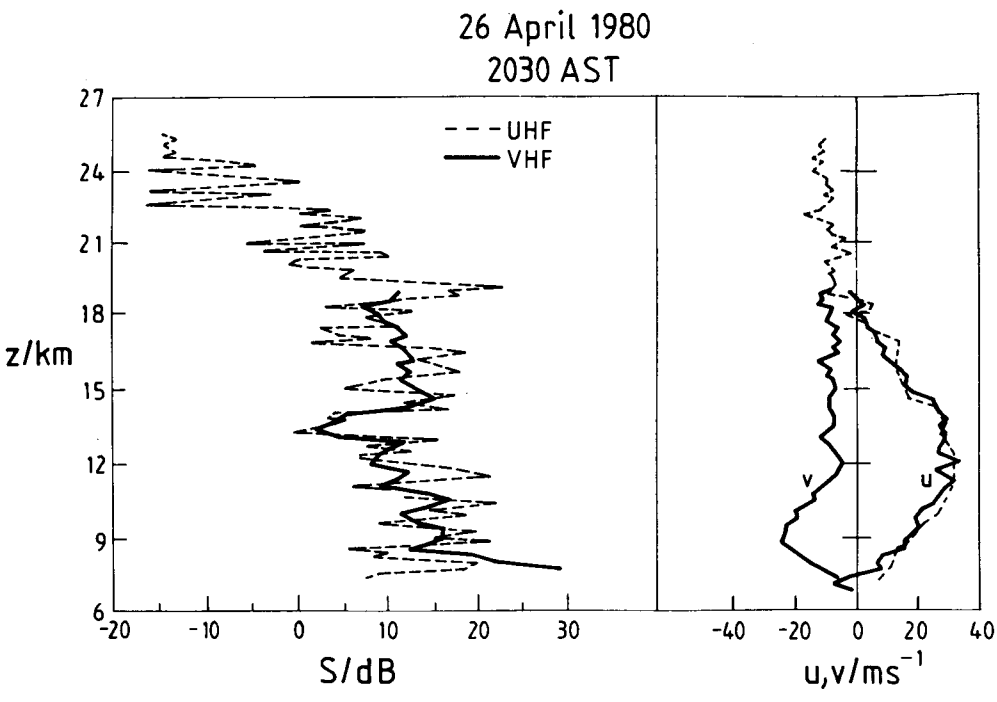

Figure 1. Profiles of relative power measured at UHF and VHF (left-hand diagram), and profiles of meridional (v) and zonal (u) wind velocities (right-hand diagram), the latter measured at UHF and VHF.

REFERENCES

Holden, D. N., C. W. Ulbrich, M. F. Larsen, J. Rottger, H. M. Ierkic, and W. Swartz (1986), UHF and VHF Radar observations of thunderstorms, this volume.

Rottger, J., P. Czechowsky, and G. Schmidt (1981), First low-power VHF radar observations of tropospheric, stratospheric and mesospheric winds and turbulence at the Arecibo Observatory, J. Atmos. Terr. Phys., 43, 789-800.

Rottger, J., H. M. Ierkic, R. K. Zimmerman, and J. Hagen (1986), Investigations of the lower and middle atmosphere at the Arecibo Observatory and a description of the new VHF radar project, this volume.

5.0 MST RADAR NETWORKS AND CAMPAIGNS: SESSION SUMMARY AND RECOMMENDATIONS

Jurgen Rottger*

Arecibo Observatory
Box 995
Arecibo, Puerto Rico

The session dealt with discussions of scientific reasons for campaigns and networks, as there are for instance: the determination of sources of propagation and dissipation of atmospheric disturbances and waves. Also measurements of different parameters with different methods and instruments, particularly the use of radars operating at different frequencies, was felt to be very useful. Special campaigns for comparison of different methods using the same sort of instruments or complementary instruments, e.g., radar and radiometers, were also deemed to be of special interest. Suitable combinations of instruments could be: MST radars, incoherent-scatter radars, low- and medium-frequency (partial reflection) radars, meteorological radars, acoustic sounders, microbarographs, radiosondes, radiometers, multifrequency MST radars, lidars, satellites, rockets, balloons, aircrafts and gliders.

Some dominant campaigns in which MST radar were or will be included in addition to many other instruments, are: ALPEX (Europe), COLDFRONTS (Australia), FRONTS, GALE, MAP/WINE, MAC/SINE, MAC/EPSILON, MESOGERS, PRESTORM, TOGA, STATE and WAGS. Two networks are presently in operation: Colorado Wind profiler and Penn State University Network.

A new idea of tutorial projects was brought up, since it was felt that exchange of experience and mutual training of researchers and operators of radar science and those of meteorological science would be most essential. It was particularly suggested that during any such experiments, project or campaign scientists of both these disciplines should cooperate as closely as possible.

Another way to improve mutual understanding of problems and to facilitate interpretation of radar results and the atmosphere phenomena would be to hold training courses, schools or seminars. It was strongly recommended by the workshop participants to work on plans for preparing and holding such courses to train meteorologists and radar scientists and v.v. Particularly the experience gained and the comprehensive material collected during the three workshops on technical and scientific aspects of MST radar would be a very useful basis for such courses.

---

*On leave from Max-PlancK-Institut fur Aeronomie, Katlenburg-Lindau, West Germany.

5.1.1 AN ANALYSIS AT MESOSPHERIC COHERENT-SCATTER POWER ENHANCEMENTS DURING SOLAR FLARE EVENTS

J. Parker and S. A. Bowhill

Department of Electrical and Computer Engineering
University of Illinois
Urbana, IL 61801

ABSTRACT

Solar flares produce increases in coherent-scatter power from the mesosphere due to the increase in free electrons produced by X-ray photoionization. Thirteen such power enhancements have been observed at Urbana. When such an enhancement occurs at an altitude containing a turbulent layer with constant strength, we may estimate the relative enhancement of electron density from the enhancement in power. Such estimates of enhanced electron density are compared with estimates of the X-ray photoionization at that altitude, deduced from geostationary satellite measurements. It is found that possible types ion-chemical reaction scheme may be distinguished, and the nonflare ion-pair production function may be estimated. The type of ion-chemical scheme and the nonflare ion-production function are shown to depend on the solar zenith angle.

INTRODUCTION

It has, of course, been known for some time that solar flares produce an increase in ionization in the D region. This flare-time enhancement in ionization results in an increase in coherent scattered power which has been assumed to account for an exceptionally full set of good mesospheric velocity measurements during the event of April 11, 1978, 0800 CST at Urbana (MILLER et al., 1978), and also measured directly for the event of January 5, 1981, at 1218 AST at Arecibo (ROTTGER, 1983).

However, the processes linking the solar X-ray enhancement to the coherent-scatter power increase involve many unknowns. Photoionization by X-rays may be considered as the driving function of a set of ion-chemical reactions which finally determines the electron-density profile; this profile must then be advected by turbulence to produce the scattered power. Many details of these processes can only be deduced indirectly.

This paper describes how models of these processes may be constructed which account for some of the features of the power enhancements observed during solar flares. Early work along these lines may be found in PARKER and BOWHILL (1984).

COHERENT SCATTER DEPENDENCE ON ELECTRON DENSITY

The radar scattering cross section is proportioned to the mean-square fluctuation of the retractive index η. At VHF:

$$\eta^2 = 1 - Ne^2/\varepsilon_o m\omega^2$$

where N is the electron concentration, e and m the charge and mass of the electron, ε_o the permitivity of free space, and ω the angular frequency of the impinging wave. The right-hand term is small compared to unity, ε_o fluctuations in η and N are proportional. Further, if the electron concentration increases in a scattering volume by a constant factor, the mean-square fluctua-

tion in electron density ΔN^2 due to turbulence will be

$$\langle \Delta N^2 \rangle \propto (N')^2 \propto N^2$$

where N' is the vertical gradient of the electron density N. Thus, the scattered power P is proportional to N^2 within time-scales where the turbulence is characterized by constant mean-squared statistics. (This assumes no time-lag due to turbulent advection; we shall demonstrate below that this holds at least some of the time.

Finally, when we divide the flare-time scattered power P at a given altitude by the pre-flare power P_o we obtain

$$P/P_o = (N_o + \Delta N)^2/N_o^2$$

which implies

$$\Delta N/N_o = \sqrt{P/P_o} - 1$$

D-REGION FLARE EFFECTS OBSERVED AT URBANA

Table 1 displays features of 13 solar flare events which produced enhanced scatter, the enhancement shown for the altitude range 60-75 km. The sizes of the peak X-ray fluxes from two detectors on the GOES II satellite are shown for comparison. No correlation of X-ray event size and coherent-scatter power enhancement is evident. This is probably due to the wide variability of turbulent strength and the nonflare ion-production rate from one flare event to another. This suggests the need for a more sophisticated analysis.

MODELS RELATING SOLAR X-RAYS AND ELECTRON DENSITY

Given the GOES II X-ray measurements, we may calculate the X-ray ion-pair production rate q_x at a given altitude as follows. First, we must estimate the X-ray spectrum from the two data points provided by the GOES detectors at each time. This may be done by assuming a power law spectral form:

$$\Phi_\infty = A\lambda^B$$

(see for example ROWE et al., 1970) and solving for A and B based on the wavelength response characteristics of the X-ray detectors (published in DONNELLY, 1977).

This form of the X-ray intensity $\Phi_\infty(\lambda)$ is used to calculate the desired ion-pair production function q_x according to Chapman theory. Constants necessary for this calculation are the average air absorption cross sections $\sigma_a(\lambda)$ and the ionization efficiencies for X-rays $\eta(\lambda)$ from BANKS and KOCKERTS (1973), and the scale height H and average air density M from the US STANDARD ATMOSPHERE (1976).

The relationship between q (= $q_o + q_x$) and N is particularly unclear in the lower D region. If we assume overall charge neutrality, an unchanged ratio of negative ions and positive ions, and unchanged proportions of the recombining species, we may derive the following (MITRA, 1974):

$$q = \alpha N^2$$

where the constant of proportionality α is called the effective recombination coefficient (call this Case A). MITRA (1974) also proposes (Case B)

$$q = \beta N$$

Table 1. X-ray flare events producing measurable coherent-scatter radar power enhancements at Urbana between April 1978 and December 1983.

yr mo da cst	SID	Hα	pk flux x 10^{-5}w/m^2 0.1-0.8nm	0.05-0.4nm	61.5-75 km pk CS power dB above P_o
78 04 11 0820	3+	NA	20	3.5	7.7
80 05 21 1510	3	3B	14	3.2	29.8
80 05 28 1354	2+	2B	12	2.0	3.5
80 11 13 1324	2+	1N	4.2	0.7	11.2
80 11 14 1239	2+	1B	2.4	0.4	13.8
81 01 27 0947	2	1B	4.6	1.3	6.1
81 05 05 0809	3	3B	12	3.3	2.8
81 08 03 1425	2+	1N	7.1	1.8	10.1
81 10 14 1111	2+	1B	30	11	7.4
82 03 31 1626	2+	NA	7.5	1.7	4.9
82 06 02 0953	3+	NA	10	2.9	17.4
83 08 13 1215	1	2B	5.2	0.9	3.7
83 08 21 1159	1	2B	2.2	0.3	6.8

as a possible relationship, given other conditions. Both relationships require chemical equilibrium, which may or may not hold during a flare. If not, the relationship is far more complicated, but a model by THOMAS et al. (1973) predicts delays in the lower D region between peak q and peak N of up to 14 minutes, increasing with decreasing altitude (Case D).

DISTINGUISHING CHEMICAL SCHEME TYPES AND ESTIMATING NONFLARE ION-PAIR PRODUCTION

To distinguish between these three possibilities (and possibly others) at a given altitude we may assume each possiblity in turn, compare q_x at each time with $\Delta N/N0$ from the coherent-scatter data, and find the best fit. To simplify this comparison, note that Case A implies $P \propto q$, so that we may estimate q_x/q_o as

$$q_x/q_o = P/P_o - 1$$

For Case B, q and N are proportional, so that

$$q_x/q_o = \sqrt{P/P_o} - 1$$

If we make two plots, one for each of these estimates of q_x/q_o against the same values at q_x from the satellite data, the result would be a line of unit slope only for that case which is correct. If the points of the initial

part of the flare (ascending) do not lie along the same path as those of the decay phase of the flare, we may have Case D, or possibly a time lag due to turbulent advection.

The result of this technique is shown in Figure 1, for the flare of November 14, 1980, and the scattered power from 70.5 km. The plot of upper left shows a close fit to a line, but not of unit slope. The plot of upper right shows a fairly close fit to a line of slope 1. We may conclude $q = BN$, and more: note that the intercept of this line with the $\log (q_x/q_o) = 0$ line implies that when $q_x = q_o$, $\log (q_x) = 0.3$. Thus we may estimate $q_o = 0.5$ cm^{-3} s^{-1}. The lower plot shows the log scattered power and the estimate of q_x based on the satellite data. The coincidence of the peaks of these curves validates the chemical equilibrium hypothesis, and demonstrates that there is no lag due to turbulent advection.

COMBINED RESULTS FOR SEVERAL FLARES

Figure 2 shows the type of power enhancement found for each altitude for each of seven flare events, arranged in order of decreasing solar zenith angle. The symbol E represents extremely large enhancements (some as much as 30 dB) which cannot be accounted for by this model. Also, note that the altitudes showing no response seem to proliferate downward with increasing solar zenith angle. This is not what Chapman theory predicts for ionization, and so possibly indicates a variability in existence of turbulent layers. Some events, particularly at high zenith angles, show delays (Case D), with delay increasing with decreasing altitude. Note, however, that a delay may be either a chemical or turbulent mixing effect.

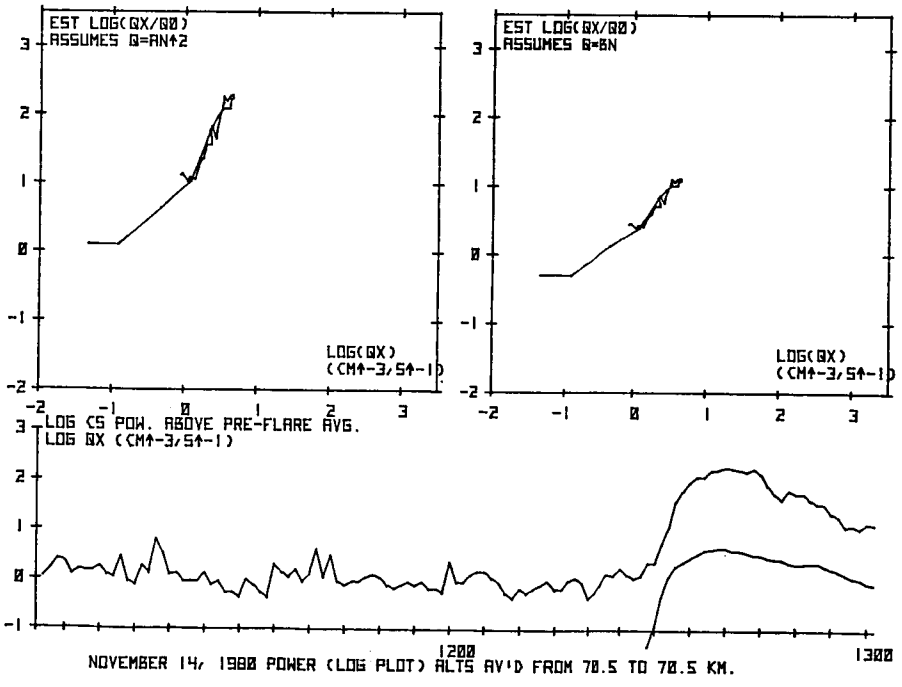

Figure 1. Flare-time scattered power enhancement and estimated electron production rate q_x due to flare X-rays at 70.5 km for the November 14, 1980 event.

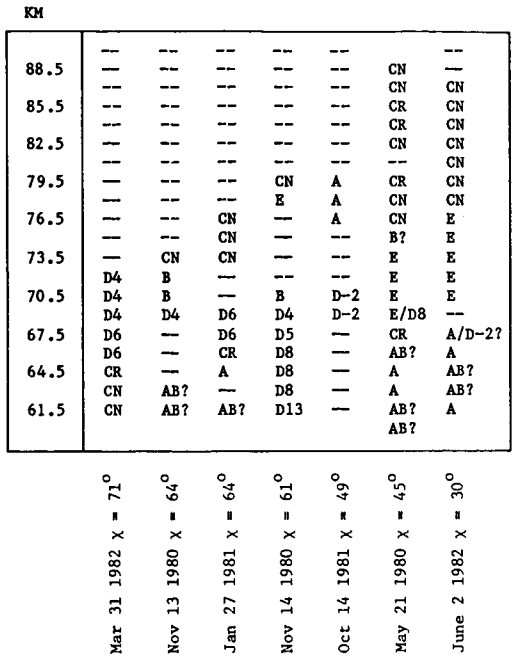

Figure 2. Types of response at each mesospheric altitude for each flare: A) $q = \alpha N^2$. B) $q = \beta N$. AB?) Probably A or B, but plots are ambiguous. D#) Delayed effect, with peak power following q by # minutes. E) Extreme response, power increase greater than cases A or B. CN) Coincident flare-time power response, but unable to fit to A or B model due to comparable nonflare fluctuations in power at that altitude. CR) Coincident response well above nonflare base power, but unable to fit to A or B models due to large fluctuations on the order of the one minute sample time. --) no detectable response.

Figure 3 shows estimates of q_o made by this technique. When the interpretation was unclear between Case A and Case B, but equilibrium seems to hold, a dashed horizontal line indicates the range of possible q_o estimates. Note that the estimates for q_o fall into two clusters, corresponding to small and large zenith angles. Also, the values of q_o for large zenith angle are smaller, as expected. Also, q_o generally increases with altitude for a given flare effect, also as expected. We may conclude that the estimate of q_o has some degree of reliability, although its absolute accuracy is not estimated here.

DISCUSSION AND CONCLUSION

By using models for the uncertain links between the causal X-ray emissions and the coherent-scatter power enhancements, we have gained insights into features which are not otherwise clear. Often one model fits the data better than others, and so we are able to choose between some features of ion-chemical schemes. When no existing model fits the data, as with the extreme power enhancements shown in Figure 3, it is unclear which part of the analysis should be modified: an extreme enhancement may be due to an unknown ion-chemical scheme, or may be due instead to some unknown condition which allows P to increase faster than N^2. This suggests further research.

C-5

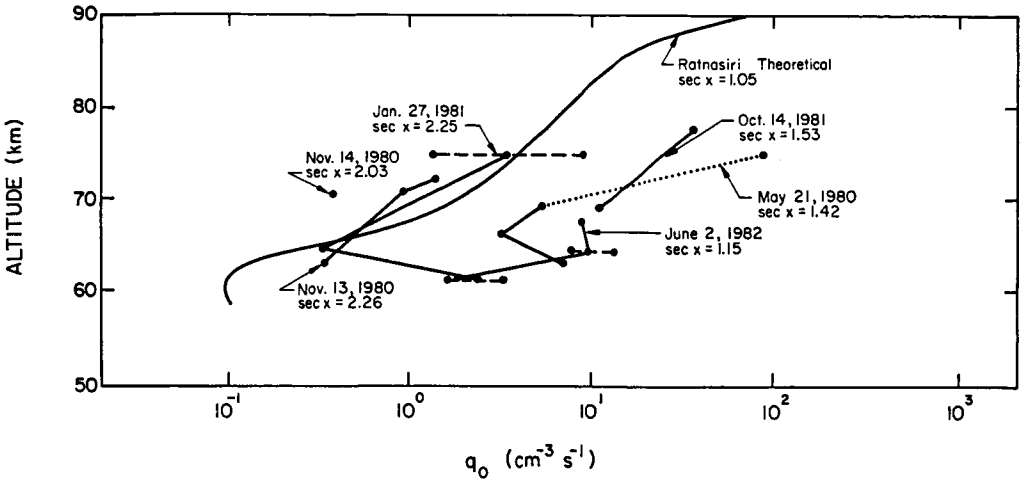

Figure 3. Estimates of q_o made by finding intercept of log (q_x) vs log (q_x/q_o) plots with line log (q_x) $\equiv$ 0 for each altitude and flare event which shows type A ($q = \alpha N^2$) or type B ($q = \beta N$) response. Horizontal dashed lines represent the span between the type A estimate at q_o and type B estimate at q_o at altitudes where the choice between type A and type B is ambiguous. The estimate of q_o by RATNASIRI and SECHRIST (1975) is reproduced for comparison.

Only altitudes with steady turbulent layers produce useful data, so altitude gaps are inevitable. However, the coherent-scatter radar technique compares favorably with earlier methods of observing changes in N during solar flare, such as partial reflection and wave interaction. The temporal and spatial resolution are excellent for the coherent-scatter technique, and the relative changes in N may be measured accurately.

ACKNOWLEDGMENT

The work described in this paper was supported in part by the National Aeronautics and Space Administration under grant NSG 7506.

REFERENCES

Banks, P. M. and G. Kockarts (1973), Aeronomy, Part A, Academic Press, New York.

Donnelly, R. F. (1977), Solar X-ray measurements from SMS-1, SMS-2, and GOES-1 information for data users, NOAA Technical Memorandum ERL SEL-48.

Miller, K. L., S. A. Bowhill, K. P. Gibbs and I. D. Countryman (1978), First measurements of mesospheric vertical velocities by VHF radar at temperate latitudes, Geophys. Res. Lett., 5, 939-942.

Mitra, A. P. (1974), Ionospheric effects of solar flares, Reidel Publishing Co., Dordrecht-Holland.

Parker, J. W. and S. A. Bowhill (1984), Observations of solar-flare ionization in the mesosphere using coherent-scatter radar, Adv. Space Res., 4, 171-174.

Ratnasiri, P. A. J., and C. F. Sechrist Jr. (1975), An investigation of the solar zenith angle variation of D-region ionization, Aeron. Rep., 67, Elec. Eng. Dep., Univ. Il., Urbana, Il.

Rottger, J. (1983), Origin of refractive index fluctuations in the mesosphere as opposed to the stratosphere and troposphere, Handbook for MAP, Vol. 9, SCOSTEP Secretariat, Dep. Elec. Computer Eng., Univ. IL., Urbana-Champaign, 143-144.

Rowe, J. N., A. J. Ferraro, H. S. Lee, R. W. Kreplin, and A. P. Mitra (1970), Observations of electron density during a solar flare, J. Atmosph. Terr. Phys., 32, 1609-1614.

Thomas, L., P. M. Gondhalekar, and M. R. Bowman (1973), The influence of negative-ion changes in the D-region during sudden ionospheric disturbances, J. Atmosph. Terr. Phys., 35, 385-395.

U. S. Standard Atmosphere, 1976, NOAA, NASA, USAF, U. S. Government Printing Office, Washington.

5.1.2 SCIENTIFIC REASONS FOR A NETWORK OF ST RADARS AND COOPERATIVE CAMPAIGNS

M. Petitdidier

CRPE
4 Avenue de Neptune
94107 Saint Maur des Fosses Cedex, France

M. Crochet

LSEET
639 Boulevard des Armaris
83100 Toulon, France

INTRODUCTION

Due to their capabilities of measuring wind profiles in the troposphere and stratosphere with a good time and height resolution whatever are the weather conditions, ST radars are well adapted to carry out atmospheric research in many fields as well as to fulfill the meteorological forecasting needs. That explains the development, all over the world, of such instruments.

The examples presented in this paper came from previous and future national or international campaigns planned in France. The VHF ST radar (Provence) from the LSEET participated in ALPEX 82, FRONTS 84 and MESO-GERS 84, and a network of ST radars will take part in the FRONTS 87 campaign.

ST RADAR NETWORK AND SCIENTIFIC CAMPAIGNS

Most of the scientific goals, which may be studied by ST radars, have been already mentioned (LARSEN, 1983; ROPER, 1983; FRITTS et al., 1984; GELLER, 1984). We may note:

-Even if a network of ST radars can operate by itself for dynamical studies, complementary data are usually necessary for most scientific investigations (radio soundings, microbarographs, precipitation radar, satellite images...). Most of them are available but generally not obtained at the same time or location.

-Even if one radar can contribute usefully to a campaign (cf FRONTS 84, MESO-GERS 84), a minimum of 3 radars is required for most of the spatio-temporal investigations (horizontal extent and variations of the phenomena, wave directional spectrum...).

So, the main difference between a research ST network working by itself and integrated in a specific campaign is essentially the duration of the experiment and the kind and number of instruments involved and working simultaneously.

Table 1 gives a list of some scientific topics which may be studied during specific campaigns involving the participation of other instruments in order to get a global and detailed view of the phenomena under study. In the next section, some examples of such campaigns are given.

These different topics impose the working characteristics of the ST radars and their relative position and spacing in the network. The time resolution is fixed by the expected time scales of the phenomena under study and the height resolution by their spatial scales and by the thickness of the turbulent layers (10 - 300 m). In connection with sodars for boundary layer observations, the lower altitude explored by the ST radar has to be less than 400 m; in connection with balloons for stratospheric observations, the upper altitude has to be higher than 12-15 km. The spacing of the radars acts as a filter in the

TABLE 1

	Boundary Layer	Free Atmosphere	Middle Atmosphere
Dynamics of precipitating clouds	- Fair weather cloud birth - Dynamical properties of the clouds - Relation between turbulence and radiation at the top of the clouds		
Fronts	- Dynamical behaviour of the frontal flow - Mesoscale instability mechanisms and relationship with the precipitation processes - Waves and turbulence in the frontal zone - Boundary layer modification after precipitations		- Gravity waves - Interaction wave - turbulence
Deep Convection		- Convective burst and associated waves - Dynamical environment - Initiation conditions : mesoscale forcing.. - Convection dynamics - Waves and turbulence	
Mesoscale Flow	- Breeze phenomena (sea, valley..) - Nocturnal jets - Thermoconvective vortices		
Jet Stream Physics		- Waves and turbulence - Jet streaks	
Tropopause Dynamics and Topography		- Altitude, Foliation, Break, Stratospheric intrusion - Troposphere - Stratosphere exchange	
Stratospheric Turbulence			- Spatio-temporal structure of turbulence - interaction wave - turbulence

horizontal scales involved. In ALPEX 82, for small horizontal scale (50 km) studies the spacing was about 5 km, in FRONTS 87 for mesoscale studies, it will be about 100 km.

PREVIOUS EXPERIMENTS

In France, some experience has been acquired during the last 3 years concerning the integration of ST radar in scientific campaigns.

(1) During ALPEX 1982, 3 ST radars operated in the vertical mode in the Rhone Delta (ECKLUND et al., 1983) as a result of a collaborative effort between the Aeronomy Laboratory from NOAA and the LSEET (Toulon - France). The main objective of the ST radar experiment was the study of short scale gravity waves from vertical velocity measurements. These observations could also contribute to the ALPEX objectives on Genova gulf cyclogenesis (BRUN et al., 1985a) and local winds.

From this experiment, CARTER et al. (1984, 1985) determined the horizontal wavelength, the phase velocity and the propagation direction of waves. Some conclusions concerning this network are listed:

-The coherence between radar sites was very good while the coherence between heights separated by more than 2 km was generally quite poor. That does not permit a reasonable calculation of vertical wavelengths.

-With radar spacing of roughly 5 km, waves with horizontal wavelengths less than 10 km could be aliased and appear to have longer wavelengths. Since most observed waves had measured wavelengths around 10-20 km, it is possible that some of these are aliased.

-The fact that only vertical observations were made, limited the waves that could be detected to periods less than about 2 hr due to the weakness of the vertical wind induced by the waves of greater periods.

(2) During FRONTS 84, in the southwest of France, a ST radar was operating in the vertical mode during 2 months in coordination with other instruments (RONSARD cm radar, RABELAIS mm radar, balloons, airplane, radiosoundings, meteorological ground network,...). The observations have been focused in fronts and related phenomena, especially gravity waves, tropopause breaks and coordinated observations of clouds and their surroundings by different techniques.

Among all these instruments only the ST radar is able to provide continuously wind profiles with a good height and time resolution whatever the weather conditions (clouds or clear air, precipitation or not). In the experiment FRONTS 84, the ST radar has been useful:

-Inside the storm, to extend the other radar observations at altitudes higher than the ones observed with the precipitation radars;

-Outside the storm, to determine continuously the dynamical field and its perturbations as a function of time and altitude;

-Due to the capability of VHF radar to get large echoes from the tropopause level, to observe the behavior of the tropopause, its breaks... and to locate the breaks relative to the fronts (LARSEN and ROTTGER, 1982).

Sometimes, waves associated with a front have been detected. As an example, on June 3, 1985, a wave of about 40 min period is observed during several hours (BRUN, personal communication).

The comparison between these different sets of data has just begun.

(3) During MESO-GERS 84, with general objectives related to the boundary layer studies and orographic effects, the ST radar was operating in the vertical mode down to the altitude of 1.2 km to complement and extend sodar observations.

The main studies which will be carried out with the sodars and ST radar concern gravity waves and the relationship between surface stress and convergence or divergence effects associated with mesoscale systems. Particularly, with ST radar, it is possible to point out if the energy is propagating upward or downward and also to observe the entrainment effect associated with an inversion layer when it takes place at an altitude too high for sodars.

As the upper limit of the boundary layer has a diurnal variation and also varies with meteorological perturbations in the altitude range of 0.5 to 1 km, it will be suitable for a ST radar to be able to observe at least down to 400 m.

In this campaign, various interesting events occurred: "Hortense" hurricane, different kinds of frontal systems and fair weather conditions. ST radar data are needed to interpret them in a more complete way. This variety of phenomena is a good opportunity to estimate the contribution of ST radar to boundary layer physics.

(4) In 1984, two campaigns involving balloon experiments and ST radars took place. In the first one, which involved the 430-MHz radar of Arecibo, the payload consisted of a thermistor and a sonic anemometer (THOMAS et al., 1985, 1986). In the second experiment, which involved the VHF ST radar from LSEET during FRONTS 84, the payload consisted of a thermistor and an ionic anemometer (DALAUDIER et al., 1985, 1986).

In these cooperative experiments, the radar observations give the temporal variation of wind profiles and turbulent layers while balloon measurements provide the fine structure of wind and temperature profiles. These simultaneous in situ and remote experiments are important for a better description of the dynamical and thermal structure of the atmosphere (DALAUDIER et al., 1985, 1986; THOMAS et al., 1985, 1986) and also for a better understanding of the physical mechanisms producing the clear-air radar echoes (DALAUDIER et al., 1985, 1986).

(5) In conclusion, the preliminary results already obtained show the interest of ST radar in cooperative campaigns for a better understanding of some meteorological problems. Each of these experiments has been very instructive but none was really satisfactory: only the vertical wind was measured, only one radar was working during FRONTS 84 and MESO-GERS 84, and during ALPEX 82 the Rhone delta was not always documented by other techniques. Then taking into account all of these arguments, the use of ST radar will be optimized in other campaigns. A more comprehensive experiment is planned in 1987 with a network of 3 ST radars operating both on the vertical and horizontal components of the wind.

A PLANNED EXPERIMENT - FRONTS 87

FRONTS 87 is a French - U.K. campaign which will take place in France and U.K. on both sides of the Channel from October to December 1987. Its scientific goal is the study of active cold fronts in a nearly flat zone. The objectives are:

-To acquire mesoscale data sets concerning dynamics, thermodynamics and microphysics. The network of ST radars with a spacing of about 100 km will provide wind vector profiles, the altitude of the tropopause, the mesoscale flow, its horizontal gradient and divergence or convergence;

-To acquire continuous data sets in order to get the three-dimensional structure of the front and its environment under some stationary assumptions.

The instruments participating in this campaign will be: ground-based meteorological networks, radiosondes at 3-hr intervals, aircraft dropsondes to produce profiles of temperature, humidity and wind, aircraft in situ observations equipped to carry out dynamical, thermodynamical and microphysical measurements, cm and mm radars, Doppler acoustic radars, lidar...and also images from Meteosat and NOAA satellites.

The network of ST radars is one of the first priority of this experiment. For this purpose and future scientific campaigns, a network of ST radars are under study (PETITDIDIER et al., 1986).

CONCLUSION

These examples point out an evolution in the use of ST radars for dynamical studies. At first, they have been working by themselves with the adjunction of radiosonde data. Then networks have been built or under study and have been used to get horizontal parameters. From now, it appears that ST radar networks will be naturally included in cooperative campaigns. Only national or international scientific campaigns are able to conduct simultaneously all the experiments necessary to obtain an overview of a specific topic.

REFERENCES

Brun, E., M. Crochet, S. V. Venkateswaran, B. B. Balsley, and W. Ecklund (1985a), ST radar observations of Genoa gulf cyclone during ALPEX, submitted to J. Clim. Appl. Meteorol.

Carter, D. A., B. B. Balsley, W. L. Ecklund, M. Crochet, A. C. Riddle, and R. Garello (1984), Tropospheric gravity waves observed by three closely spaced ST radars, Handbook for MAP, Vol. 14, 219-228, SCOSTEP Secretariat, Dep. Elec. Computer Eng., Univ. Ill, Urbana-Champaign.

Carter, D. A., B. B. Balsley, W. Ecklund, M. Crochet, A. C. Riddle, and R. Garello (1985), Tropospheric gravity waves observed by three closely spaced ST radars, Handbook for MAP, Vol. 18, 260-263, SCOSTEP Secretariat, Dep. Elec. Computer Eng., Univ. Ill, Urbana-Champaign.

Dalaudier, F., J. Barat, F. Bertin, E. Brun, M. Crochet, and F. Cuq (1985), Comparison between ST radar and in situ measurements, Proc. 7th ESA Symp. European Rocket and Balloon Programmes, 247-251.

Dalaudier, F., J. Barat, F. Bertin, E. Brun, M. Crochet, and F. Cuq (1986), Comparison between ST radar and in situ measurements, this volume.

Ecklund, W. L., B. B. Balsley, D. A. Carter, A. C. Riddle, M. Crochet, and R. Garello (1983), Observations of vertical motions in the troposphere and lower stratosphere using three closely spaced ST radars, Edmonton, Atlanta - Canada, to be published in Radio Sci.

Fritts, D. C., M. A. Geller, B. B. Balsley, M. L. Chanin, I. Hirota, J. R. Holton, S. Kato, R. S. Lindzen, M. R. Schoeberl, R. A. Vincent, and R. F. Woodman (1984), Research status and recommendations from the Alaska Workshop on gravity waves and turbulence in the middle atmosphere - Fairbanks, Alaska, Bull. Am. Meteorol. Soc. 65, 149-159.

Geller, M. A. (1984), Meteorological and aeronomical requirements for MST radar network, Handbook for MAP, Vol. 14, 1-4, SCOSTEP Secretariat, Dep. Elec. Computer Eng., Univ. Ill, Urbana-Champaign.

Larsen, M. F. (1983), The MST radar technique: Requirements for operational weather forecasting, Handbook for MAP, Vol. 9, 3-11.

Larsen, M. F. and J. Rottger (1982), VHF and UHF Doppler radars as tools for synoptic research, Bull. Am. Meteorol. Soc., 63, 996-1007.

Petitdidier M., V. Klaus, F. Baudin, M. Crochet, G. Penazzi, and P. Quinty (1986), The INSU and DMN networks of ST radars, this volume.

Roper, R. G. (1983), Meteorological and dynamical requirements for MST radar networks, Handbook for MAP, Vol. 9, 1-2, SCOSTEP Secretariat, Dep. Elec. Computer Eng., Univ. Ill, Urbana-Champaign.

Thomas, B. F., F. Bertin, M. Petitdidier, H. Teitelbaum, and R. F. Woodman (1985), Simultaneous fine structure observation of wind and temperature profiles by the Arecibo 430 MHz radar and in situ measurements, Proc. 7th ESA Symp. European Rocket and Balloon Programmes, 381-384.

Thomas, D., F. Bertin, M. Petitdidier, H. Teitelbaum, and R. F. Woodman (1986), Simultaneous fine structure observation of wind and temperature profiles by the Arecibo 430 MHz radar and in situ measurements, this volume.

6.0 PROGRESS IN EXISTING AND PLANNED MST RADARS

T. E. VanZandt

National Oceanic and Space Administration
325 Broadway
Boulder, CO 80303

The papers presented in this session describe radar systems using two different wind-measuring techniques: the partial-reflection drift technique and the MST (or Doppler beam-swinging) radar technique.

The partial-reflection drift technique, first implemented by FRASER (1965), has been shown to work in the troposphere and lower stratosphere and in the mesosphere and lower thermosphere, at frequencies from about 2 to 50 MHz. In practice, however, it is regularly used only in the mesosphere and lower thermosphere at frequencies near 2 MHz. The advantages of this technique include relatively small operating costs and 24-hour operation above about 80 km.

The MST radar technique was independently invented at least three times, by Woodman in 1970 in Peru using a 6-m radar (WOODMAN and GUILLEN, 1974), by Dobson in 1969 in the U.S. using a 10.7-cm radar (DOBSON, 1970), and by Browning and coworkers in 1971 in the U.K. also using a 10.7-cm radar (BROWNING et al., 1972). As far as I know, all of the radars described in this session derive from the pioneering work of Woodman. The early S-band systems were not operated for long, perhaps because of high operating costs. Almost all recent S- and UHF-band systems have utilized radars developed for other purposes in order to avoid the high cost of S- and UHF-band antennas. The only exceptions are the Wave Propagation Laboratory 915-MHz radar at Denver and their 405-MHz system under development for operational use (see the paper by STRAUCH).

The advantages of the MST radar technique are: good spatial resolution, relatively large zenith angle, and consequent simple geometrical interpretation of the signal. The disadvantages are the converse of the advantages of the partial-reflection drift technique.

Since the last MST Radar Workshop in May 1984, several new radars have come into operation, at Penn State, Christmas Island, Chung-li, and Arecibo (VHF), other radars have been augmented, and the planning of several other systems has materially progressed. We look forward to hearing about these developments.

REFERENCES

Browning, K. A., J. R. Starr, and A. J. Whyman (1972), Measurements of air motion in regions of clear air turbulence using high-power Doppler radar, Nature, 239, 267-269.

Dobson, E. B. (1970), Doppler radar measurements of mean wind variations in the clear atmosphere, Preprint Vol., 14th Radar Meteorol. Conf., 69-72.

Fraser, G. J. (1965), The measurement of atmospheric winds at altitudes of 64-120 km using ground-based radio equipment, J. Atmos. Terr. Phys., 22, 217.

Woodman, R. F., and A. Guillen (1974), Radar observations of winds and turbulence in the stratosphere and mesosphere, J. Atmos. Sci., 31, 493-505.

6.1 RECENT RESULTS AT THE SUNSET RADAR

J. L. Green, J. M. Warnock, W. L. Clark, and T. E. VanZandt

Aeronomy Laboratory
NOAA
Boulder, CO 80303

The Sunset radar is a VHF, pulsed Doppler (ST) radar located in a narrow canyon near the Sunset townsite 15 km west of Boulder, CO. This facility is operated by the Aeronomy Laboratory, ERL, NOAA, exclusively for meteorological research and the development of the MST and ST radar technique. A description of this facility can be found in GREEN (1983) and GREEN et al. (1984).

In January-February, 1985, as in the previous year, the Sunset radar was used to measure winds as a part of a multisensor study of aircraft safety sponsored by the Federal Aviation Administration. The FAA will use this broad data set, in part, to evaluate the response of altimeters used on commercial aircraft to mountain lee waves.

A technical report, WARNOCK and VANZANDT (1985), has been prepared to facilitate the use of a statistical turbulence model (VANZANDT et al., 1978). This report contains complete FORTRAN listings of the model and instructions for calculating profiles of C_n^2 from routine National Weather Service rawindsonde data.

The Sunset radar is being used to test new equipment and operating concepts to be used in the proposed Flatland radar. Since both the existing system and the proposed system are similar and modular in design, a new subsystem under development can be substituted with a minimum of inconvenience. For example, a new Transmit/Receive switch was developed by imbedding it in the Sunset system, whose operating characteristics are well known. (GREEN and ECKLUND, 1986).

RECENT PUBLICATIONS

Clark, W. L., J. L. Green, and J. M. Warnock, 1985, Estimating meteorological wind vector components from monostatic Doppler radar measurements: A case study, Radio Sci., 20, 1207-1213.

Clark, W. L., J. L. Green, and J. M. Warnock, Determination of U, V, and W from single Doppler radar radial velocities, this volume.

Green, J. L., and K. S. Gage, 1985, A re-examination of the range resolution dependence of specular echoes by a VHF radar, 1985, Radio Sci., 20, 1001-1005.

Green, J. L., and W. L. Ecklund, An improved T/R technique for MST and ST radars, this volume.

Green, J. L., J. M. Warnock, W. L. Clark, and G. D. Nastrom, A comparison of vertical velocities measured by a VHF radar with specular and non-specular echoes, this volume.

Green, J. L., G.D. Nastrom, K. S. Gage, and T. E. VanZandt, The proposed Flatland radar, this volume.

Green, J. L., An example of scaling MST Doppler spectra using median spectra, spectral smoothing, and velocity tracing, this volume.

Nastrom, G. D., and J. L. Green, Preliminary estimates of vertical momentum flux, this volume.

Warnock, J. M., and T. E. VanZandt, A statistical model to estimate refractivity turbulence structure constant C_n^2 in the free atmosphere, 1985, NOAA/ERL/Aeronomy Lab. Tech. Note.

Warnock, J. M., and T. E. VanZandt, A statistical model to estimate refractivity turbulence structure constant C_n^2 in the free atmosphere, 1985, this volume.

Warnock, J. M., and T. E. VanZandt, A statistical model to estimate refractivity turbulence structure constant C_n^2 in the free atmosphere, to appear in Preprint Vol., Seventh Symposium on Turbulence and Diffusion, Nov. 12-15, 1985, Boulder, CO, 156-159.

REFERENCES

Green, J. L. (1983), Characteristics of Sunset Radar, Handbook for MAP, 9, SCOSTEP Secretariat, Dep. Elec. Eng., Univ. IL, Urbana, IL, 320-324.

Green, J. L., and W. L. Ecklund (1986), An improved T/R technique for MST and ST radars, this volume.

Green J. L., J. M. Warnock, and W. L. Clark (1984), Recent results at the Sunset radar, Handbook for MAP, 14, SCOSTEP Secretariat, Dep. Elec. Eng., Univ. IL, Urbana, IL, 321-323.

VanZandt, T. E., J. L. Green, K. S. Gage, and W. L. Clark (1978), Vertical profiles of refractivity turbulence structure constant: comparison of observations by the Sunset radar with a new theoretical model, Radio Sci., 13, 819-821.

Warnock, J. M., and T. E. VanZandt (1985), A statistical model to estimate refractivity turbulence structure constant C_n^2 in the free atmosphere, NOAA/ERL/Aeronomy Lab. Tech. Note.

6.2 THE PROPOSED FLATLAND RADAR

J. L. Green, K. S. Gage, T. E. VanZandt,

Aeronomy Laboratory
Boulder, CO 80303

and

G. D. Nastrom

Control Data Corp
Minneapolis, MN 55440

INTRODUCTION

The Aeronomy Laboratory of NOAA has proposed to the National Science Foundation to construct a VHF ST radar near Urbana, Illinois for meteorological research. For the reasons given below, this site has been selected because it is located in flat terrain far from mountains.

An effort will be made to involve faculty members from university departments of meteorology and atmospheric sciences in experiments with this radar. It is believed that the combination of the Aeronomy Laboratory's experience with this type of radar, the meteorological expertise of the university faculty members and the meteorological consulting experience of Control Data Corp will be very productive in the further development of this technique as a meteorological tool. A university, private industry, and government effort is envisioned.

A wide range of experimental studies can be made at this radar as can be seen in the diverse subject matter covered in this Workshop on the Technical and Scientific Aspects of MST Radar. However, only three of the proposed experiments are emphasized here as examples.

DESCRIPTION OF RADAR

The Flatland radar will be a flexible ST radar configured for meteorological research. Its characteristics are summarized in Table 1. Continuous, unattended operation is anticipated. As this is a fourth or fifth generation radar, many features that have been found to be desirable in previous research will be incorporated in its construction. For example, its receiving system is designed to have a dynamic range of 100 dB to maintain linearity over the wide range of reflectivities encountered by an ST radar, and will be calibrated against a standard. The array antenna of the Flatland radar will be electronically steerable in the east-west and north-south vertical planes. It is anticipated that initial operation will be with five antenna beam positions as shown in Figure 1. This configuration has been tested at the Sunset radar and found to have many advantages. Velocities measured with redundant beam positions can be compared as in CLARK et al. (1983) or GREEN et al. (1986). The use of redundant beam positions has been found to be crucial to the interpretation of ST radar data near convective storms and will provide a better spatial average of both reflectivity and velocity. The rapid electronic steering of the radar antenna will allow 10 s (one Doppler spectrum per range gate) of data to be accumulated on each of the five beam positions each minute. These spectra will be saved in the on-line computer memory and at the end of a five-minute period, median spectra for each range gate and each direction will be recorded on magnetic tape (RASTOGI, 1984; GREEN, 1986). This rapid scan will prevent the aliasing of most gravity-wave modulation of radial velocity since the Nyquist period will be 2.5 min. This data-acquisition scheme is shown in Figure 2.

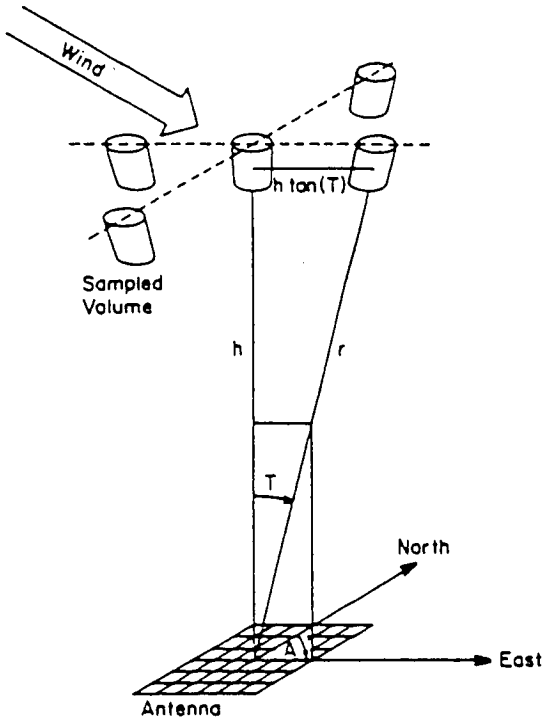

Figure 1. Location of beam positions. The relative location of the radar volumes at an arbitrary altitude corresponding to five radar antenna beam positions.

	TIME						
Antenna Pos	0	1	2	3	4	5	minutes
Vertical	x	x	x	x	x	x	calculate
15° North	x	x	x	x	x	x	median
15° South	x	x	x	x	x	x	spectra
15° East	x	x	x	x	x	x	and
15° West	x	x	x	x	x	x	record

Figure 2. Aquisition of data (one cycle) at the end of the observation cycle the median spectra for each range gate of every antenna position is individually calculated.

THE MEASUREMENT OF SYNOPTIC-SCALE VERTICAL VELOCITIES

One of the many experiments that can be performed with the Flatland radar is the measurement of the small vertical velocities associated with synoptic-scale meteorology. This velocity is the atmospheric variable most closely linked with weather, except perhaps moisture, yet it has been almost impossible to measure it directly. The Flatland radar, sited in very flat terrain, offers an opportunity to measure vertical velocity directly and continuously.

In a recent study (NASTROM, 1984), it was found that the time-averaged vertical motion over the Platteville, Colorado ST radar compared favorably with the computed synoptic-scale vertical velocity under certain synoptic conditions: when the prevailing winds were from the west, across the Rocky Mountains, the meteorological noise was too large to prevent computing a mean vertical velocity with sufficiently small statistical uncertainty, or else standing lee waves made the radar site unrepresentative of the large geographical area of the synoptic-scale system. In either case, it was a signal-to-noise problem induced by the mountains. A similar situation was found in the ALPEX data from Southern France (CARTER et al., 1984), i.e., when the winds were off the sea, the measured and computed vertical velocities agreed favorably, but when the winds were across the mountains, the agreement was poor or uncertain. Thus, we can conclude that at ST radar stations near the mountains, the synoptic-scale vertical velocity can be measured only under restricted conditions. These statistics suggest that it is probable that such a measurement can be made at the proposed Flatland radar which would be situated in very flat terrain far from mountains. As mentioned above, the proposed radar will also be capable of measuring the horizontal components of wind in the troposphere and lower stratosphere which can be used to sense the synoptic-scale systems.

COMPARISONS WITH THE URBANA RADAR

The Aeronomy Laboratory of the University of Illinois operates the Urbana radar. This radar, with its large power-aperture product, has made many observations in the stratosphere and mesosphere (ROYRVIK and GOSS, 1983). It is anticipated that the specialized meteorological measurements by the proposed Flatland would be compared to those of the Urbana radar in a study of troposphere-stratosphere-mesosphere coupling as in BOWHILL and GNANALINGAM (1986).

EXPERIMENTS IN COOPERATION WITH THE CHILL RADAR

A large Doppler microwave radar, the CHILL radar is located a few km from the site of the proposed Flatland radar (MUELLER and SILHA, 1978). This radar is operated by the Illinois State Water Survey. Since this microwave radar can measure the location and velocity of hydrometeors and the VHF ST radar can measure clear (or cloudy) air velocities, simultaneous observations by these two radars of stratiform or convective weather systems would provide unique and valuable meteorological information.

ADDITIONAL STUDIES

The radar data set recorded for the synoptic-scale vertical velocity experiment in a geographical region free from orographic effects would also be useful for studies of clear-air turbulence (VANZANDT, 1983; NASTROM, 1984), gravity waves (VANZANDT, 1986), transport of momentum by gravity waves (NASTROM and GREEN, 1986) tropopause morphology (VANZANDT and VINCENT, 1983; GAGE et

al., 1984) and tropopause height (GAGE and GREEN, 1982). This continuous data set could be used for the compositing of synoptic and mesoscale systems under various synoptic conditions. There is an intriguing possibility of estimating the thermal structure of the atmosphere from a combination of radar wind velocity and satellite radiance measurements (GAL-CHEN, 1986).

An effort will be made to attract experimenters with a wide range of meteorological sensors to special observational periods held at least once a year. Many of the additional capabilities inherent in the design of the proposed radar (variable altitude resolution, additional antenna positions, and real-time access to profiles of wind velocity and tropopause altitude) can be used, as required, in support of these experiments.

TABLE 1

Characteristics of the Flatland Radar

Location	South of Urbana, IL
Frequency	40.475 MHz
Wavelength	7.41 m
Antenna	
Type	Two collocated arrays of coaxial, collinear dipoles
Size	60 m x 60 m
Feed	Tapered to reduce sidelobes
Steerability (initial)	Five preset beam positions Vertical, 15° from the vertical to the north, south, east and west
Transmitter	
Peak power	100 kW
Average power	2 kW
Range Resolution	Variable 150 m to 2.4 km
Operation	Continuously sequence through 5 antenna positions.

REFERENCES

Bowhill, S. A., and S. Gnanalingam (1986), Gravity waves in severe weather, this volume.

Carter, D. A., B. B. Balsley, W. L. Ecklund, M. Crochet, A. C. Riddle, and R. Garello (1984), Tropospheric gravity waves observed by three closely spaced ST radars, Handbook for MAP, 14, SCOSTEP Secretariat, Dep. Elec. Computer Eng., Univ. IL, Urbana, IL, 219-228.

Clark, W. L., J. L. Green, and J. M. Warnock (1983), Estimating unbiased velocity components from MST/ST radar measurements: a case study, Handbook for MAP 9, SCOSTEP Secretariat, Dep. Elec. Computer Eng., Univ. IL, Urbana, IL 210-214.

Gage, K. S., W. L. Ecklund, and B. B. Balsley (1984), A modified scattering model for the parameterization of Fresnel returns, Handbook for MAP, 14, SCOSTEP Secretariat, Dep. Elec. Computer Eng., Univ. IL, Urbana, IL, 88-97.

Gage, K. S., and J. L. Green (1982), An objective method for the determination of tropopause height from VHF radar observations, J. Appl. Meteorol., 21, 1159-1163.

Gal-Chen, T. (1986), A theory for the retrievals of virtual temperature from winds, radiances and the equations of fluid dynamics, this volume.

Green, J. L. (1986), An example of scaling MST Doppler spectra using median spectra, spectral smoothing and velocity tracing, this volume.

Green, J. L., J. M. Warnock, W. L. Clark, and G. D. Nastrom (1986), A comparison of vertical velocities measured by a VHF radar with specular and nonspecular echoes, this volume.

Mueller, E. A., and E. J. Silha (1978), Unique features of the CHILL radar system, Preprints 18th Conf. on Radar Meteorology, Atlanta, GA, American Meteorology Society, 381-382.

Nastrom, G. D. (1984), Synoptic scale dynamics with vertical velocity, Handbook for MAP, 14, SCOSTEP Secretariat, Dep. Elec. Computer Eng., Univ. IL, Urbana, IL, 62-68.

Nastrom, G. D., and J. L. Green (1986), Preliminary estimates of vertical momentum flux, this volume.

Rastogi, P. K. (1984), Criteria and algorithms for spectrum parameterization of MST signals, Handbook for MAP, 14, SCOSTEP Secretariat, Dep. Elec. Computer Eng., Univ. IL, Urbana, IL, 289-293.

Royrvik, O., and L. D. Goss (1983), The Urbana MST radar, capabilities and limitations, Handbook for MAP, 9, SCOSTEP Secretariat, Dep. Elec. Computer Eng., Univ. IL, Urbana, IL, 346-356.

VanZandt, T. E. (1983), Existence of a persistent background of turbulence, Handbook for MAP, 9, SCOSTEP Secretariat, Dep. Elec. Computer Eng., Univ. IL, Urbana, IL, 256-261.

VanZandt, T. E. (1986), A model for gravity wave spectra observed by Doppler sounding systems, this volume.

VanZandt, T. E., and R. A. Vincent (1983), Is Fresnel reflectivity due to low frequency boyancy waves? Handbook for MAP, 9, SCOSTEP Secretariat, Dep. Elec. Eng., Univ. IL, Urbana, IL, 78-80.

6.3 CURRENT STATUS OF THE POKER FLAT MST RADAR

B. B. Balsley

Aeronomy Laboratory
National Oceanic and Atmospheric Administration
Boulder, CO 80303

An earlier brief report on the status of the Poker Flat, Alaska, MST radar appeared last year in MAP Handbook 14. The purpose of the present note is to bring that report up to date.

The Poker Flat MST radar ceased normal operations in April 1985, following more than six years of almost continuous data taking. Analyses of these data have already yielded over ninety research papers, five Ph.D and two MSc. dissertations.

The radar is now being configured to measure gravity-wave momentum flux in the troposphere, lower stratosphere, upper mesosphere, and lower thermosphere. The major change to the system involves modifying the antenna array to enable both (orthogonal) oblique beams to be automatically steered. GWMF data will be obtained on pairs of vertically symmetric beams in the manner described by VINCENT and REID (1983). Current funding is sufficient to complete this modification and to operate in this new mode until Fall 1986.

An additional effort is underway to prepare an archive of the existing six-year Poker Flat data set. This archive, when complete, will be transferred to the National Center for Atmospheric Research (NCAR) for use by anyone in the scientific community.

REFERENCES

Vincent, R. A., and I. M. Reid (1983), HF Doppler measurements of mesospheric gravity wave momentum fluxes, J. Atmos. Sci., 40, 1321-1333.

6.4 CONTINUOUS WIND MEASUREMENT IN THE TROPICAL PACIFIC USING VHF RADARS

B. B. Balsley, W. L. Ecklund, and D. A. Carter

Aeronomy Laboratory
National Oceanic and Atmospheric Administration
Boulder, CO 80303

VHF Radar Wind Profilers are being installed on two tropical Pacific islands to continuously monitor winds aloft for many years. The islands are:

Ponape, East Caroline Islands (158°E, 7°N)

Christmas Island, Republic of Kiribati (157°W, 2°N)

One purpose of this experiment is to study wind fluctuations on time scales between minutes and days, to determine the longitudinal character of these fluctuations, and to examine their relationship to climate variability. A second purpose of the experiment (Christmas Island only) is to provide six-hourly wind profiles via satellite to the scientific community for Project TOGA (Tropical Ocean Global Atmosphere).

The Ponape wind profiler has been operating for fourteen months using only a vertically directed antenna. A multibeam system will be installed later this year.

The Christmas Island radar has just been installed and will be placed in full operation soon. This system will have three antenna beam positions, and will continuously measure the total wind vector. It will be the first wind profiler to provide satellite-transmitted data to a data dissemination center.

Both systems will operate in the low VHF band ($\simeq$ 50 MHz), have 100 m x 100 m COCO antenna arrays, and have a peak transmitted pulse power $\simeq$ 30-50 kW.

6.5 RECENT PROGRESS IN THE URBANA MST RADAR

S. A. Bowhill

Aeronomy Laboratory
Department of Electrical and Computer Engineering
University of Illinois
Urbana, IL 61801

Since the 1984 Workshop, several improvements have been put into effect at the Urbana radar, which operates at 40.92 MHz with a peak power of about 1.2 MW into a 100 x 120 m phased array antenna.

A new accelerated data-acquisition system has been put into operation (BOWHILL and RENNIER, 1986). This permits continuous data acquisition at 60 altitudes from 10 to 90 km, and has also improved the efficiency of the receiving system by a factor of two.

A new beam-steering system has been installed (BOWHILL and MEREWETHER, 1986) which now allows rapid switching between two beams, thereby giving both components of the wind velocity. These beam directions have been calibrated against radiosonde calculations.

The new transmit/receive switch described at the 1984 Workshop (YU, 1984) has been assembled and is in course of installation in the radar.

With these changes, the radar is in regular operation for two hours every day around local noon gathering stratospheric and mesospheric data. Special campaigns are mounted in addition under severe weather conditions.

REFERENCES

Bowhill, S. A., and K. O. Merewether (1986), Beam steering system, this volume.

Bowhill, S. A., and A. D. Rennier (1986), An accelerated FORTH data-acquisition system, this volume.

Yu, B. (1984), T/R switch design for short-range measurements, Handbook for MAP, 14, 251-252, SCOSTEP Secretariat, Dep. Elec. Computer Eng., Univ. IL, Urbana, IL.

6.6 COLORADO WIND PROFILERS

R. G. Strauch

NOAA/ERL/WPL
Boulder, CO 80303

The Wave Propagation Laboratory (WPL) has operated a network of wind profiling radars in Colorado for several years. The current configuration of this network is shown in Figure 1. The 50-MHz profilers at Fleming and Flagler are two-beam systems with 50 m x 50 m collinear-coaxial antenna arrays that are phased to generate pointing angles 15 degrees off zenith toward the north and east. An identical system was installed near Norman, OK in May, 1985. The 915-MHz radar at Denver is a three-beam system. In addition to the same pointing angles that the 50-MHz systems have, this radar has a zenith-pointing position to correct for the effects of vertical velocity on the data obtained with off zenith pointing, particularly in stratiform precipitation. This antenna is an offset paraboloid with three offset feeds. The 50-MHz system at Platteville is also a three-beam system (with the same pointing positions as the 915-MHz system) with 100 m x 100 m collinear-coaxial antenna arrays. The 405-MHz profiler is a two-beam system; the antenna is a phased array with Yagi-Uda elements. The 405-MHz radar started operating in January, 1985. All radars operate continuously and unattended to supply hourly-averaged wind profiles to a central computer in Boulder in real time. A complete description of the radars and their data processing is given by STRAUCH et al. (1984).

During the past year several hardware and software changes have been made to improve reliability. Lightning protection was added on the primary power at the input to the equipment housing and lightning protection (surge suppression) was placed on the telephone lines and computer-telephone data lines. An annoying problem of restart after extended power fail was solved by adding a remote computer reset; previously, the on-site computer had to be reset manually after some power fail events.

We plan to continue to operate this research network to provide wind profiles for operational (NWS and FAA) and research meteorologists and to continue to evaluate the performance of various wavelength systems. Some of the changes that are planned are as follows:

1. The 405-MHz radar will be replaced with a more sensitive radar whose characteristics approximate those of a planned 30-station network to be installed in the central US late in this decade. The antenna will have 5-beam pointing positions.
2. The 50-MHz off-zenith pointing antennas at Platteville will be replaced and a switching system will be added so that four beam-pointing positions will be available.
3. We are studying what hardware changes would be needed to add a high resolution (chirp pulse) mode to the 915-MHz radar. This mode would be used to examine the reflectivity structure of radar scattering at 4- to 10-km altitude with 15-m resolution.
4. A collinear-coaxial element will be evaluated at 405 MHz. If the characteristics are suitable a full antenna array will be built.
5. A transportable 405-MHz system with a fully steerable 6-m diameter antenna is being considered. One of the uses of such a system would be to calibrate fixed beam systems.
6. The Denver and Platteville data are sent to the central computer on dedicated telephone lines; the other sites use dial-up transmission. The data handling will be modified so that Doppler spectra or spectral moments can be transmitted on the dedicated lines and archived by the central computer.

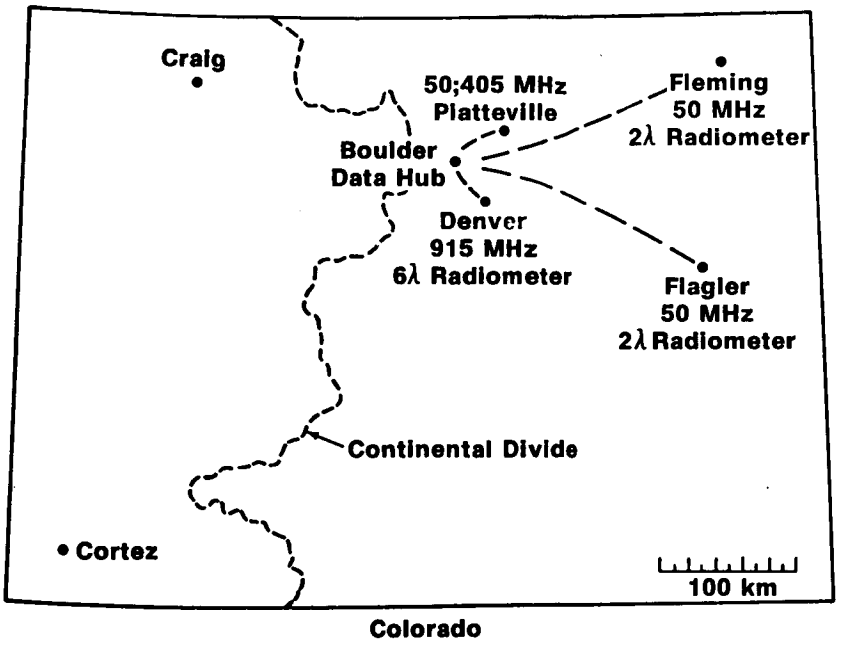

Figure 1. The Colorado wind profiling network.

REFERENCE

Strauch, R. G., D. A. Merritt, K. P. Moran, K. B. Earnshaw, and D. van de Kamp (1984), The Colorado wind profiling network, J. Atmos. Oceanic Tech., 1, 37-49.

6.7 WIND PROFILER DEMONSTRATION SYSTEM

R. B. Chadwick

NOAA/ERL/WPL
325 Broadway
Boulder, CO 80303

The National Oceanic and Atmospheric Administration (NOAA) has started procurement of a 30-station demonstration network of Doppler radar wind profilers to be deployed in the central United States by 1989. Present plans call for twenty-four 405-MHz radars and six 50-MHz radars. The purposes of this demonstration network are: 1) to assess the impact of a large wind profiler network on meteorological forecasting; 2) to test wind profiler hardware designed especially for commercial production and widespread deployment; 3) to provide wind data for research programs involving weather phenomena in the central United States.

The radars will be designed and built by industry under a competitive procurement process. The first step in the procurement is the purchase of two 405-MHz prototype radars and a request for proposals was issued on August 27, 1985. Contract award is expected by March 1986, with delivery of two prototype radars by October 1987. Installation of production models should begin by mid-1988 and be completed by mid-1989.

The radars will operate continuously and unattended with a 6-minute data cycle. During this cycle spectral moment estimates will be made for two range resolution modes on each of three antenna pointing positions. These data will be sent to a central hub computer on land lines. In addition, hourly averaged wind profiles will be calculated and transmitted to the hub computer using the GOES satellite. The Profiler antenna pointing positions will be toward zenith, and about 15 degrees off-zenith in orthogonal planes. From this, East, North, and vertical wind components can be determined. The hub computer will ingest data from the demonstration profiler network and from other research profiler systems. Wind profiles will be calculated, checked for temporal and spatial consistency, broadcast to authorized users, and archived. An important part of the program is the assessment of the data and hardware performance, and will be conducted by the National Weather Service (NWS).

The radars are required to have a mean-time-between-failure of six months. They will have modular construction so that maintenance can be performed by field replacement of defective modules. The data messages will include thorough system status checks. Automatic restart after power fail, lightning protection, and other features needed for operational radars are required. Radar parameters for the 405-MHz units are listed below. Certain specific items such as the type of antenna and type of transmitter are left to the contractor to decide. Also the contractor is to decide the details of the transmitted signal waveform.

Required Antenna Parameters

Number of beams	3
Beam elevation angles	1 @ 90°, 2 @ 75°
Beam switching speed	$\leq$ 0.4 s
On-axis gain	> 32 dBi
3 dB beam width	< 5°
Antenna sidelobes (ref. to on-axis gain)	
$\theta \geq 45°$	< -20 dB
$45° > \theta > 5°$	< -25 dB
$5° > \theta$	< -40 dB

Required Transmitter-Receiver Parameters

	High Mode	Low Mode
Frequency	405.25	405.25 MHz
Bandwidth	0.2	0.8 MHz
Operating noise temperature	235	235 K
Pulse width	6 2/3	1 2/3 μs
Average transmitted power	1500	375 W
Pulse repetition period	153 1/3	100 μs
First gate	7.5	0.5 km
Last gate	16.25	9.25 km
Number of range gates	36	36
Range resolution	1000	250 m
Range gate spacing	250	250 m
Max horizontal velocity (component)	90	60 m/s
First range ambiguity	183	120 km

6.8 REMOTE TEMPERATURE PROFILING IN THE TROPOSPHERE AND STRATOSPHERE BY THE RADIO-ACOUSTIC SOUNDING TECHNIQUE

Nobuo Matuura, Yoshihisa Masuda, and Hisao Inuki

Radio Research Laboratory
Koganei-shi, Tokyo 184, Japan

The application of radar to study of the atmospheric phenomena is carried out by receiving echoes from precipitation and atmospheric inhomogeneities or structure caused by turbulence and atmospheric gravity waves. A somewhat different kind of radar application is the radio-acoustic sounding technique as presented here, in which Doppler frequency shift of radar echoes returned from the atmospheric spherical wave structure, in association with travelling acoustic pulse transmitted from the ground, is detected to give the speed of sound, and hence the atmospheric temperature, as function of altitude.

The experiment presented here aims at temperature measurement in the troposphere and stratosphere by the radio-acoustic sounding technique with the Radio-Acoustic Sounding System (RASS) consisting of the MU Radar, completed in November 1984, at Shigaraki, Shiga, Japan, by the Radio Atmospheric Science Center of Kyoto University (peak power 1 MW, radio frequency 46.5 MHz) and a movable high-power acoustic transmitter provided by Radio Research Laboratory (acoustic power 100 W, acoustic frequency around 100 Hz variable).

Two basic conditions to be satisfied for receiving echoes by RASS in an efficient power are the following: one is the Bragg condition with respect to the radio wavelength λ_r (= 6.45 m) and the acoustic wavelength λ_a, i.e., $\lambda_r = 2\lambda_a$, and the other is the perpendicularity between the radar beam and the acoustic wave front. The Bragg condition can be kept from failure owing to height variation of the acoustic wavelength arising from temperature variation, by sweeping the acoustic frequency from pulse to pulse. The latter condition, which is influenced by the atmospheric wind, can be kept partly by changing the direction of the radar beam and partly by changing location of the acoustic transmitter.

Successful experiments were carried out in March 1985, and August 1985, of remote temperature profiling in the troposphere and stratosphere, attaining with the maximum measurement altitude of about 20 km beyond the tropopause in the August experiment.

6.9 THE PENN STATE DOPPLER NETWORK PROGRESS REPORT

S. R. Williams and R. Peters

The Pennsylvania State University
Department of Meteorology
University Park, PA 16802

At the Second Workshop on Technical Aspects of MST Radar, the software and hardware implementation for the PSU network was discussed (THOMSON, 1984). Delayed delivery of RF equipment and signal processing components resulted in modification of our original timetable. It was determined that the best approach for implementing the second VHF radar would be when the first VHF radar was in reliable and unattended operation. In Table 1, a short summary of the specifications for the three radars is shown. Experiences, plans and improvements for the PSU network are summarized below.

A. VHF1 50-MHz 2/3 beam radar located 15 km south of State College, PA

1) This system became fully operational June 27, 1985. The sole reason for system failures since the onset has been ac outages which are prevalent in this area. Battery back-up and computer-controlled auto-restart of the transmitters (microprocessor controlled) has circumvented this problem.

2) Initial performance statistics done by FRISCH et al., WPL on August 1985 data, indicate very good performance by VHF1. On Beam #1, the next to last range gate (16.8 km MSL) was able to make a wind measurement 99% of the time, while Beam #2 was able to measure the wind at this height 85% of the time. The difference between these two beams is either a bad element or a loss in relay switches in Beam #2 or a noise source in one of the sidelobes. Samples of radar data from VHF1 are shown in Figures 1 and 2.

3) Future changes on VHF1 will be the implementation of a vertical beam. One of the antennas will be phased switched in order to orient the beam to vertical. Software and hardware are in hand, but will not be utilized until our 2nd unit VHF2 is operational.

B. VHF2 50-MHz 2/3 beam radar to be located in NW Pennsylvania near Clarion, PA

1) The process of site location and acquisition is underway for an identical 50-MHz system. This site will be the 2nd point on an equilateral triangle positioned over west central Pennsylvania.

2) All hardware and software components have been delivered. Expected initial turn-on of VHF2 is early 1986.

C. UHF1 portable 440-MHz 2/3 beam radar to be initially located in SW Pennsylvania near Somerset, PA

1) This system is ready for installation pending the delivery of the RF components purchased from Tycho Technology, Inc.

2) Site selection for UHF1 will commence as soon as VHF2 is operational.

Table 1 Specifications for Penn State ST radars

Item	VHF1 and VHF2	UHF1
Type	Pulsed Doppler	Pulsed Doppler
Location	1: S of State College 2: NW of Dubois	SW of Johnstown
Frequency	1: 49.80 MHz 2: 49.92 MHz	405 MHz
Bandwidth	300, 100 KHz	1 MHz, 300 kHz, 70 kHz
Peak Power	30 kW	30 kW
Pulsewidth	3.67, 9.67 μsec	1, 4, 16 μsec
Antenna:		
Type	Phased Array CoCo	64 7-element Yagis
Dimensions	50 m x 50 m	8 m x 8 m
Angle(s)	75° and 90°	75°
On Site Computer	Data General Eclipse	Date General Eclipse
On Site Processing at PW =	3.67 μs or 9.67 μs	1, 4, 16 μs
Time Domain Aver.	≈ 400 or ≈ 125	112, 70, 35
Spectral Aver.	8 or 16	16, 32, 64
Max. Radial Vel.	+ 15.7 m/s or + 19.6 m/s	18.25 m/s
Spectral Vel. Resol.	0.49 m/s or 0.31 m/s	0.29 m/s
Height Spacing	290 m or 870 m	100, 300, 800 m

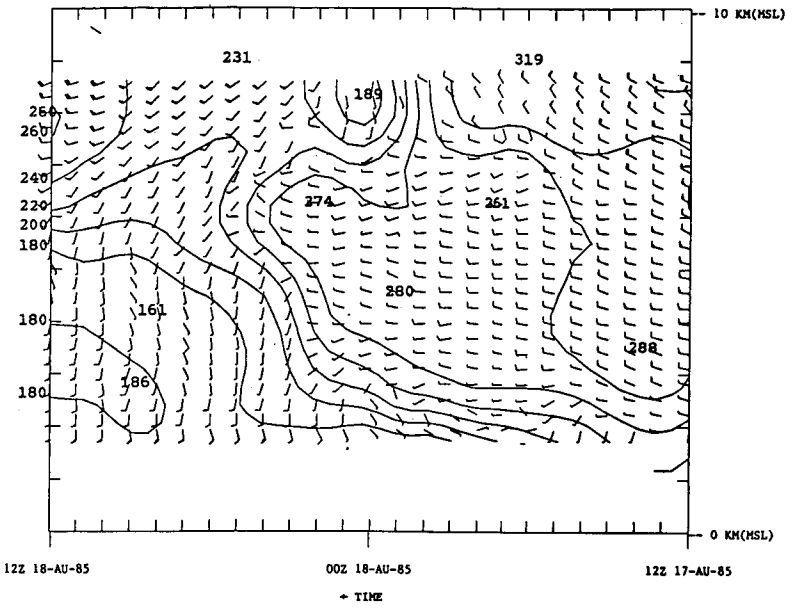

Figure 1.

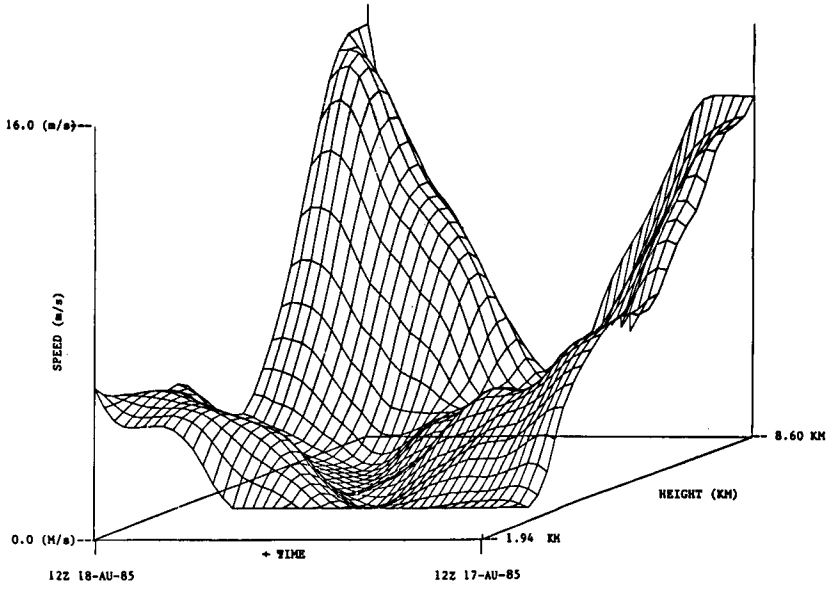

Figure 2.

6.10 THE ADELAIDE MF PARTIAL-REFLECTION RADAR AND VHF ST RADAR: A PROGRESS REPORT

R. A. Vincent

Physics Department
University of Adelaide
Adelaide, South Australia 5001

THE MF PARTIAL-REFLECTION RADAR

The MF partial-reflection radar has been running continuously since November 1983, with data being analysed in real time. The spaced antenna technique has been used routinely to produce a climatology of the mean circulation, atmospheric tides and gravity waves. Since the beginning of 1985, the system has also been used as a Doppler radar to measure the spectral widths of the mesospheric echoes. This has enabled the turbulence dissipation rates to be determined by the technique discussed by HOCKING (1983). Also, since January 1985, observations of gravity-wave momentum fluxes, $u'w'$ and $v'w'$ have made for a period of about 4 days each a month with the dual-beam technique described by VINCENT and REID (1982).

THE ST RADAR

The ST radar, which operates at a frequency of 54.1 MHz and is located adjacent to the MF radar, has been used for a number of investigations of the lower atmosphere. In particular, it was operated in the spaced antenna mode to measure winds in November 1984, in conjunction with a large cooperative campaign organized to study the propagation of cold fronts across SE Australia. Observations have also been carried out in collaboration with the Australian Bureau of Meteorology into the structure of the more intense and deeper cold fronts which occur in late winter. The vertical, as well as the horizontal, winds have been studied. There is good agreement between the upward velocities observed prior to the passage of the fronts (up to 0.2 ms^{-1}) and the magnitudes calculated from the convergence of air into the front.

From the start of 1985, Doppler beam-swinging measurements have also been undertaken to measure the upward flux of horizontal momentum. As the beam can be steered only in the EW plane, this restricts the observations to the $u'w'$ fluxes. After testing several pointing angles, a basic angle of 11 has been used.

The radar system is being continually upgraded. Solid-state transmitters are being installed in order to increase the mean power by a factor of about 50. The transmitters are very efficient (60%) and compact. To make full use of the high duty factors available (up to 20%), a complementary phase coding scheme is being implemented.

REFERENCES

Hocking, W. K. (1983), On the extraction of atmospheric turbulence parameters from radar backscatter Doppler spectra I, Theory, J. Atmos. Terr. Phys., 45, 89-102.

Vincent, R. A., and I. M. Reid (1982), HF Doppler measurements gravity-wave momentum fluxes, J. Atmos. Sci., 40, 1321-1333.

6.11 THE PROUST RADAR

F. Bertin, M. Glass, R. Ney, M. Petitdidier

CRPE
4 Avenue de Neptune
94107 Saint Maur des Fosses Cedex, France

The ST radar called PROUST (Prototype de Radar pour l'Observation en UHF de la Stratosphere et de la Troposphere) is located at Saint Santin (44°39'N; 2°12'E, altitude: 351 m) in the southwestern part of France, a place devoted to the ionospheric incoherent-scatter radar transmitter facility. It works at 935 MHz using the same klystron and antenna as the incoherent-scatter radar. The use of this equipment for ST work has required some important modifications of the transmitting system and the development of receiving, data processing and acquisition devices. This work has been planned in several stages. In the first stage (1984, 1985), the radar worked in a bistatic mode with a height resolution of 600 m and a time resolution of 46 s. The main characteristics of the radar is given in Table 1.

TABLE 1

Frequency	935 MHz
Allotted bandwidth	± 5 MHz
Pulse peak power	140 kW
Transmitting Antenna	2000 m^2 (Near field)
Receiving Antenna (Parabolic)	95 m^2
Pulse length	4 µs
Pulse repetition frequency	156.2 µs
Number of gates	32

As the angle between the transmitting and receiving directions is 1°, the vertical wind is mainly measured. In any case, an estimation of the horizontal wind contribution may be obtained through radiosonde data. Two campaigns were carried out and their main results are given by BERTIN et al. (1985).

In 1985, the phase stability of the transmitter-receiver set has been improved and the coding and decoding system, which leads to a 30-m height resolution, implemented (PETITDIDIER et al., 1985a). Table 2 gives the specifications of this "magnifier" mode.

TABLE 2

Pulse width	4 µs
Number of subpulses	20
Subpulse width	200 ns
Code	Quasi-complementary
Coherent integration number	128
Coherent integration time	20 ms
FFT	256 points
Spectral resolution	3.1 cm/s
Maximal vertical velocity	± 4 m/s

In a first step, only 32 gates out of the 640 decoded ones, are recorded in order not to modify the data recording device. These 32 gates are constituted by 4 groups of 8 gates in succession which may be located anywhere in the range of altitude. In September 1985, all the equipment was tested at Saint Santin. A calibration was carried out and showed that, with a spectral wind resolution of 0.8 cm/s and an amplitude of the artificial dopplerized signal 50 dB below the maximum value detectable, it is possible to detect a wind of about

2 cm/s. During the campaign, only very weak C_n^2 (10^{-18} at 2 km) were observed due to the stability of the weather.

FUTURE DEVELOPMENTS

Spectrum Computation On-line. So far, only the real and imaginary time series are recorded on magnetic tapes and the spectra are computed off-line. The next step is the computation in real time of spectra using the Texas Instruments TMS 320 signal processor and a FFT algorithm. The implementation of this device is under tests and the first campaign is planned at the beginning of 1986.

Monostatic Mode. As shown in Figure 1 and confirmed by experiments, in the bistatic mode the energy budget of the system, klystron and antenna, does not allow observation of echoes above 9 km. But in the monostatic mode, it should allow stratospheric observations. The next step, planned for 1986, will be to transmit and receive on the large antenna.

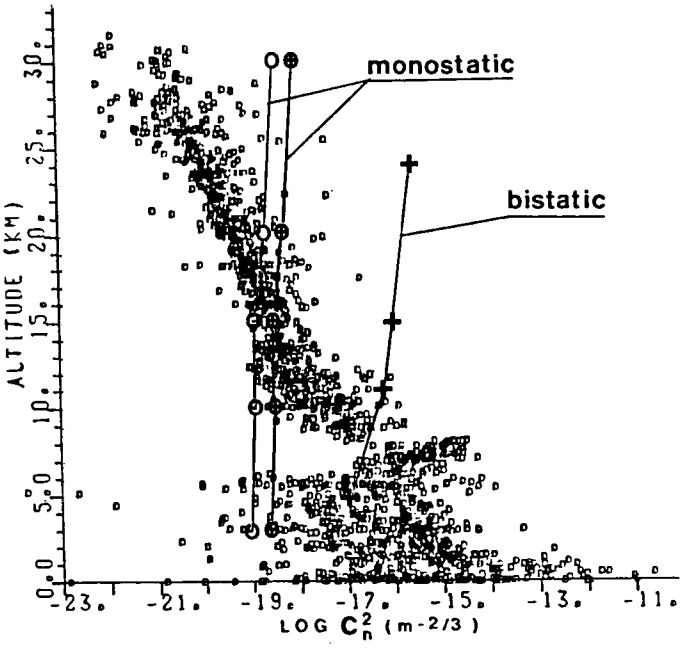

Figure 1. Variation of C_n^2 as a function of altitude using the model of VANZANDT et al. (1978) and 105 rawinsonde data from Bordeaux (France) from PETITDIDIER et al. (1985b). The curves O--O and +--+ indicate the minimum of C detectable as a function of altitude in monostatic and bistatic mode, respectively, for a peak power of 140 kW, and the curve -- in monostatic mode for 50 kW peak power.

REFERENCES

Bertin, F., A. Cremieu, M. Glass, M. Massebeuf, M. Petitdidier (1986), Proust Radar, first results, this issue.

Petitdidier, M., A. Desautez, M. Glass, and G. Penazzi (1985a), A decoder for a 30-m height resolution ST radar, Radio Sci., 20, 1141-1145.

Petitdidier, M., V. Klaus, F. Baudin, M. Crochet, G. Penazzi, P. Quinty (1985b), Radars ST: Reseau de recherche et Reseau operationnel, Symposium on Meteorol. Observ. and inst.

VanZandt, T. E., J. L. Green, K. S. Gage, and W. L. Clark (1978), Vertical profiles of refractivity turbulence structure constant: Comparison of observations by Sunset Radar with a new theoretical model, Radio Sci., 13, 819-829.

6.12 THE PROVENCE ST RADAR

M. Crochet

Laboratoire de Sondages Electromagnetiques
CNRS/Universite de Toulon
83100 Toulon, France

INTRODUCTION

Since the ALPEX Campaign in 1982, when 3 ST radars have been operating in Camarque as a cooperative effort of the Aeronomy Laboratory of NOAA, CO and the LSEET from Toulon, a 50-MHz VHF ST radar has been developed, improved and operated during different experiments.

OPERATING CHARACTERISTICS

- Successive frequencies: 48.85 MHz, 47.8 MHz, 45 MHz
- RF pulse width : 1, 2, 4, 16 μs
- Peak power : 50 kW
- Antenna : 3 x 60 x 60 m^2 coco antennas
- Minimum range : 1 km

MAIN OBJECTIVES

- Physics of the measurement by ST radar by coordinated experiments with other instruments (balloons, lidar, sodar, cm and mm radars, scidar).
- Investigation of gravity waves with ST radar networks and coordinated experiments (Fronts 84 - Fronts 87).
- Investigation of mistral and jet stream.

PRELIMINARY RESULTS

- Gravity waves studies during "ALPEX 82"
- Jet stream and jet streaks "PROVENCE 84"
- Gravity wave studies during "FRONTS 84"
- ST radar - CAT balloons comparisons "MAI 84"
- Multifrequency radar comparisons "FRONTS 84"

FUTURE EXPERIMENTS

- Jet stream and mistral investigations from 2 stations in the south of France.
- Gravity waves and Fronts studies with 3 ST radars during the cooperative experiment "FRONTS 87".
- Multifrequency investigations
- Site comparisons in the south of France

6.13 THE INSU* AND DMN** NETWORK OF ST RADARS

M. Petitdidier[2], V. Klaus[1], F. Baudin[3], M. Crochet[5], G. Penazzi[4], and P. Quinty[1]

[1]CNRM - 42 Avenue Gustave Coriolis - 31057 Toulouse Cedex - France
[2]CRPE - 4 Avenue de Neptune - 94107 Saint Maur des Fosses Cedex - France
[3]CRPE - 38-40 Avenue de General Leclerc - 92131 Issy les Moulineaux - France
[4]INSU - 4 Avenue de Neptune - 94107 Saint Maur des Fosses Cedex - France
[5]LSEET - 639 Boulevard des Armaris - 83100 Toulon - France

Due to their capabilities of measuring wind profiles in the troposphere and stratosphere with a good time and height resolution, ST radars are well adapted to carry out atmospheric research in many fields as well as to fulfill the meteorological forecasting needs. In France, a VHF (Provence - CROCHET, 1985) and a UHF (Proust - BERTIN et al., 1985) ST radar are working for research purposes and two networks are projected (PETITDIDIER et al., 1985).

The INSU Network (3 radars) has been proposed by scientists working in tropospheric and stratospheric physics and will be devoted to research in connection with other instruments (meteorological radar, lidar, rawinsonde, balloon...). The spacing between the radars and their relative locations will depend on the topic under study. In the same way, the time resolution is imposed by the expected time scales of the studied phenomena and the height resolution by their spatial scales and by the estimated thickness of the turbulent layers (10 - 300 m). As these radars will work during simultaneous measurement campaigns, as ALPEX 82 or FRONTS 84, they must be transportable. Table 1 summarizes the main characteristics of such radars.

The DMN network has been proposed in order to equip the French meteorological station network with ST radars. Basically, its specifications are determined by the requirements of the World Weather Watch as it concerns the time and height resolution as well as the range of altitudes. Table 1 gives the main characteristics of such radars. However, measurements of other parameters, available for ST radars as vertical wind and the altitude of the tropopause, or high time resolution data may not be completely excluded as they are interesting for meteorological research and could be used in future weather prediction (GAGE and SCHLATTER, 1984).

TABLE 1

	Research	Meteorology
Minimum altitude	300 m	300 m
Maximum altitude	12 - 15 km	20 km
Height resolution	150 - 300 m	600 m up to 12 - 13 km 1 measure every 50 mb 2 km at 12 km 4 km at 20 km
Wind component	vertical	
		horizontal
	horizontal	
Time resolution	several minutes	1 h
Tropopause altitude	yes	--

*INSU: Institut National des Sciences de l'Univers
**DMN: Direction de la Meteorologie Nationale

In order to carry out these 2 projects simultaneously, the different institutions involved have coordinated their technical and financial investments for a better efficiency. The first stage is the realization of a prototype fulfilling the specifications of the 2 projects. This radar is under study and should take part in the experiment "Fronts 87".

REFERENCES

Bertin F., A. Cremieu, M. Glass, M. Massebeuf, and M. Petitdidier (1985), The PROUST Radar, this volume.

Crochet, M. (1985), The Provence ST radar, this volume.

Gage, K. S., and T. W. Schlatter (1984), VHF/UHF Radar and its application in nowcasting, The Nowcasting II Symp.

Petitdidier, M., V. Klaus, F. Baudin, M. Crochet, G. Penazzi, and P. Quinty (1985), Radars ST: Reseau de recherche et Reseau operationnel, Symposium on Meteorological Observations and Instruments.

6.14 INVESTIGATIONS OF THE LOWER AND MIDDLE ATMOSPHERE AT THE ARECIBO OBSERVATORY AND A DESCRIPTION OF THE NEW VHF RADAR PROJECT

J. Rottger*, H. M. Ierkic, R. K. Zimmerman, and J. Hagen

Arecibo Observatory
P.O. Box 995
Arecibo, Puerto Rico

INTRODUCTION

The atmospheric science research at the Arecibo Observatory, particularly the research of the lower and middle atmosphere, is performed by means of (active) radar methods and (passive) optical methods. The active methods utilize the 430-MHz radar (e.g., WOODMAN, 1980a; TSUDA et al., 1985), which is normally used for incoherent scatter investigations of the ionosphere (including the D region/mesosphere, e.g., MATHEWS, 1985), the S-band radar on 2380 MHz (e.g., WOODMAN, 1980b), which is normally used for investigations of planets and asteroids, the bistatic HF radar (GONZALES and WOODMAN, 1984), which is normally used as heating facility to modify the ionosphere, and a newly constructed VHF radar. The applications of the 430-MHz radar, the S-band radar and the HF radar were described by WOODMAN (1983). The VHF radar was particularly designed as an MST radar, although it also can be used for heating diagnostics. The VHF radar development was based on earlier experiences with a VHF radar system transported temporarily to the Observatory (e.g., ROTTGER et al., 1981), and will be described in more detail in this report.

The passive methods performed at the Observatory include measurements of the mesopause temperature by observing the rotational emissions from OH-bands (e.g., TEPLEY, 1985). The feasibility to use a lidar system to investigate the lower and middle atmosphere at the Arecibo Observatory is presently being studied. It would provide a valuable complement to the existing radars to measure temperature and trace constituent profiles.

Besides the present VHF radar, which is operated with the 1000-ft dish as antenna, an additional VHF system has been proposed. The proposal, submitted to the National Science Foundation, has been suspended, however. Such a stand-alone facility could operate continuously without interrupting other experiments carried out at the Observatory. The implementation of this system would be based on the presently existing radar transmitter and receiver. It could be set up in a valley close to the Observatory using a separate antenna system and should have an average power-aperture product of about 5.10^7 Wm^2, as well as a stand-alone radar control and data acquisition unit.

The scientific goals for such a system are presented elsewhere in this proceedings (ROTTGER et al., 1986). It is foreseen that continuous investigations of the neutral atmosphere in the tropical/subtropical zone of Puerto Rico will encompass such topics as: hurricanes and tropical storms, waves in the easterlies, quasi-inertial waves, tides and short-period gravity waves and their generation mechanisms such as shears in the subtropical jet stream and deep penetrative convection, momentum flux from the troposphere to the mesosphere due to gravity waves, kinetic energy spectra due to waves or turbulence, and land-sea breeze, lee waves and local convection. For the investigation of almost all of these processes, the island of Puerto Rico is a preferred site, and an ancillary VHF radar system should be built near the Arecibo Observatory to conduct such observations.

---

*On leave from Max-Planck-Institut fur Aeronomie, Katlenburg-Lindau, West Germany.

THE AO VHF RADAR

The new Arecibo Observatory VHF radar operates on 46.8 MHz with a 50 kW (peak) transmitter made by Tycho Technology Inc. The system uses the 1000-ft reflector with a newly designed feed antenna. The existing radar control and data-acquisition system is used in addition to additional control and monitor instrumentation which was particularly developed for the 46.8-MHz radar. The average power-aperture product is 4.10^7 Wm^2. The system is set up in two locally separated units: the radar control, signal detection, data-acquisition and monitor instruments are on the ground in the control room building. The transmitter and receiver frontends are located on the antenna platform 130 m above the dish in carriage house 1, to which the feed antenna is mounted. Whereas the carriage house part of the system is permanently configurated, experimenters have to set up for every experiment the different instruments needed in the control room.

ANTENNA

The 46.8-MHz feed presently is a twin 2-element antenna which is located on the downhill side of carriage house 1. Figure 1 shows the arrangement of the feed antenna on the platform. Its driven elements are 9.3 m below the paraxial surface and their center is at 5.3 m distance from the closely neighboring 430-MHz line feed. The clearance of 5.3 m was found to be sufficient for negligible coupling with the 46.8-MHz feed. The 46.8 MHz is outside the caustic of the 430 MHz as well as the closest feed of carriage house 2 (1667 MHz). The impedance and radiation pattern of the 46.8-MHz feed was obtained by computer modeling, proving that the coupling with the nearby feeds is negligible to the impedance. However, influence to the radiation pattern could occur. The 5.3-m distance provides sufficient mechanical clearance to the surrounding guy wires.

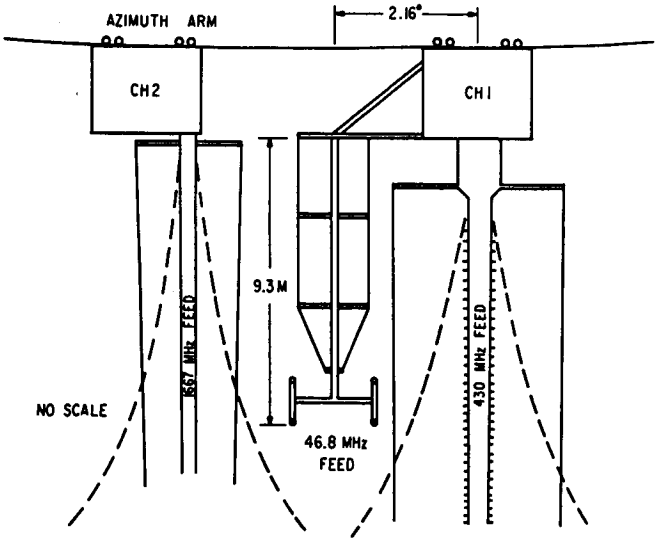

Figure 1. Schematic view (not to scale) of the carriage houses CH1 and CH2 with the 430-MHz, the new 46.8-MHz and the 1667-MHz feed. The dashed lines give the caustics of the two line feeds.

The height of 9.3 m below the paraxial surface was also obtained by computer modeling a point-feed above a spherical reflector. It was optimized to obtain maximum system gain for the chosen twin-Yagi feed antenna. The dimensions of the twin-feed antenna were designed to provide an elliptical illumination pattern of the spherical dish reflector (Figure 2a). The half-power beam width in the E-plane is 78° and in the H-plane, 62°. Since for pointing, the zenith angle is changed in the H-plane, spillover is minimized and the gain is kept almost constant out to maximum zenith angles of $\approx$ 17.81°. The selected illumination pattern and the height of 9.3 m below the paraxial surface corresponds to a (theoretically deduced) effective aperture of 43000 m^2, equivalent to 41-dB gain or 1.8° half power beam width. The effective aperture of 43000 m^2 is very close to the maximum aperture of 45000 m^2 which can be achieved with a 46.8-MHz point feed. The phase center of the twin feed is 2.16° downhill of the center of the 430-MHz line feed. This permits pointing the 46.8-MHz beam to zenith angles from -2.16° to + $\approx$ 17.84°, including the zenith direction. The twin feed was designed such that radiation in the horizontal direction would be minimized. The VSWR of the feed (with balun) is better than 1.22 within the band 45.8 MHz to 47.1 MHz. Since the return loss of the feed antenna is greater than 10 dB within the frequency range $\pm$ 5 MHz off the center frequency, it can also be used for offset frequency receiving (plasma line measurements for heating experiments). Although the absolute sensitivity of the 46.8-MHz antenna system could not yet be measured (because of interference problems and preferred radar operation), a drift scan indicated a beam width of 1.8° (see Figure 2b). The system sensitivity, estimated from the preliminary drift scan is expected to be larger than 10K/Jy. However, more correct pointing beam pattern and sensitivity calibrations have still to be performed to investigate pattern distortions due to coupling.

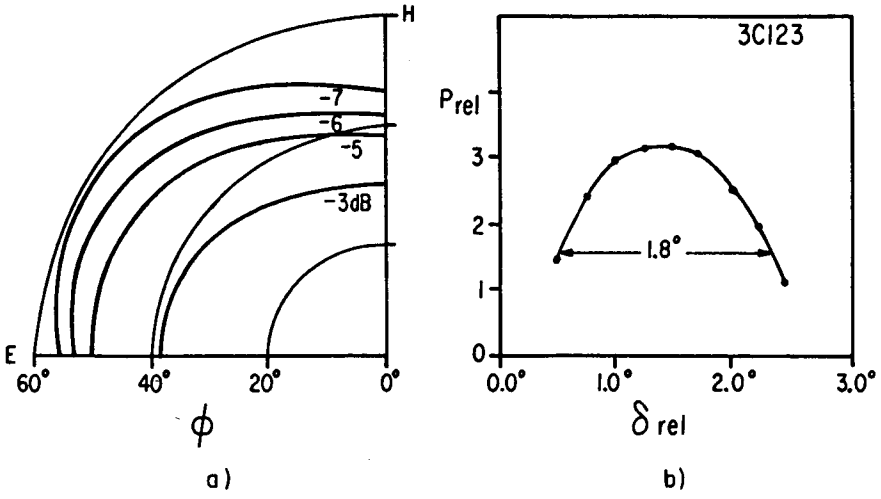

Figure 2. a) Illumination pattern of the spherical 1000 ft dish by the 46.8-MHz point feed. ϕ is the zenith angle, the 60° circles denotes the rim of the dish. H and E denote the H- and E-plane of the feed, which is moved in zenith angle in the H-plane. b) Relative power (P_{rel} = 3 corresponds to approximately 3000 k) measured by a drift scan through the radio source 3C123. This yields a preliminary half power beam width of 1.8° of the 46.8-MHz antenna system.

The method to determine the optimal parameters of the 46.8-MHz antenna system is described in more detail in this proceedings by IERKIC et al. (1986).

TRANSMITTER-RECEIVER

Figure 3 shows the setup of the transmitter/receiver unit which is located in carriage house 1. Essential additions to standard MST radar systems are the calibration noise injection into the receiver frontend, and the digital data link which allows to transmit the HV power supply and final amplifier status as well as the measured forward and reverse transmitter power values down to the control room. The nominal transmitter peak power is 50 kW at 2% duty cycle. The rise and fall times of the total transmitter system are 0.4 µs which allow proper use of pulses as short as 1 µs. The decoupling attenuation of the T/R switch (transmit-receive switch) and the pin diode SPST switch is 50 dB and their insertion loss is 2 dB. This will be improved by changing the pin diode switch which presently courses the main contribution of 1.8 dB to this loss. The noise figure of the receiver frontend is better than 0.5 dB on 46.8 MHz, it is increased by 0.5 dB at 4.30 MHz and 53.3 MHz. The calibration noise injection is presently set to 1690 K.

The received 46.8-MHz signal is amplified and sent to the control room via a 600-m long coaxial cable. All control and monitor signals are sent via other cables between the control room and carriage house.

RADAR CONTROL AND DATA PROCESSING

Figure 4 shows a block diagram of the instruments in the control and computer room. Two phase-coherent signals on 23.4 MHz and 70.2 MHz are used to

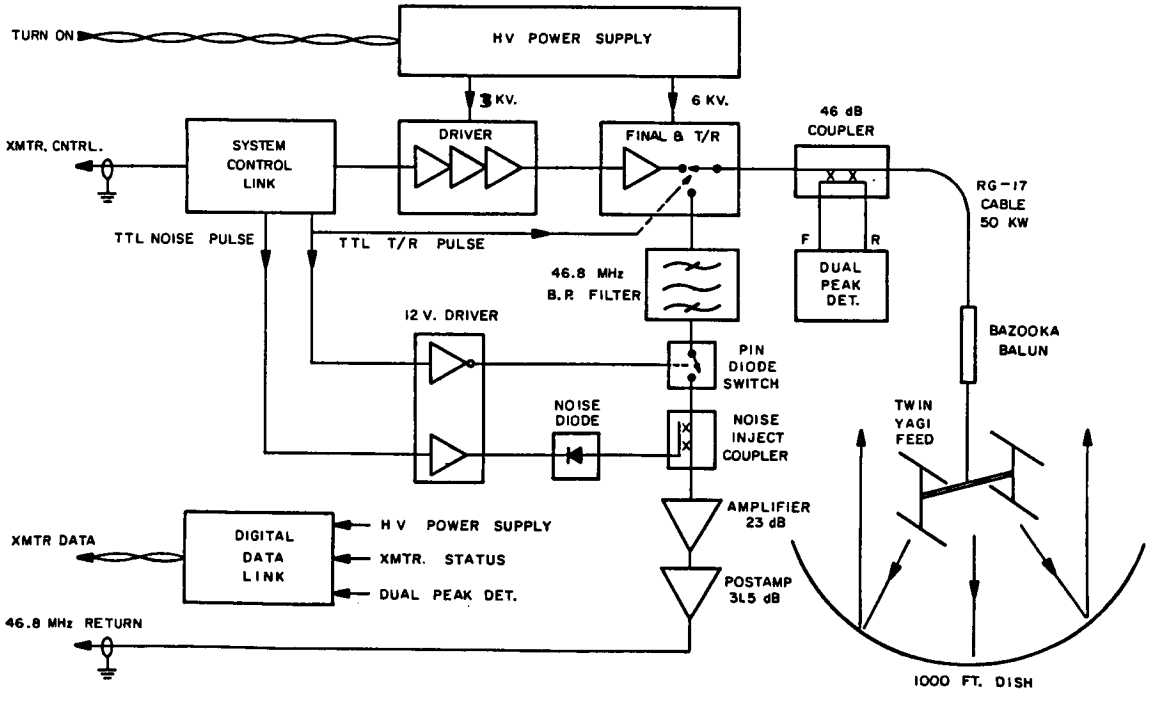

Figure 3. Instruments of the AO VHF radar located in the carriage house 1 on the platform.

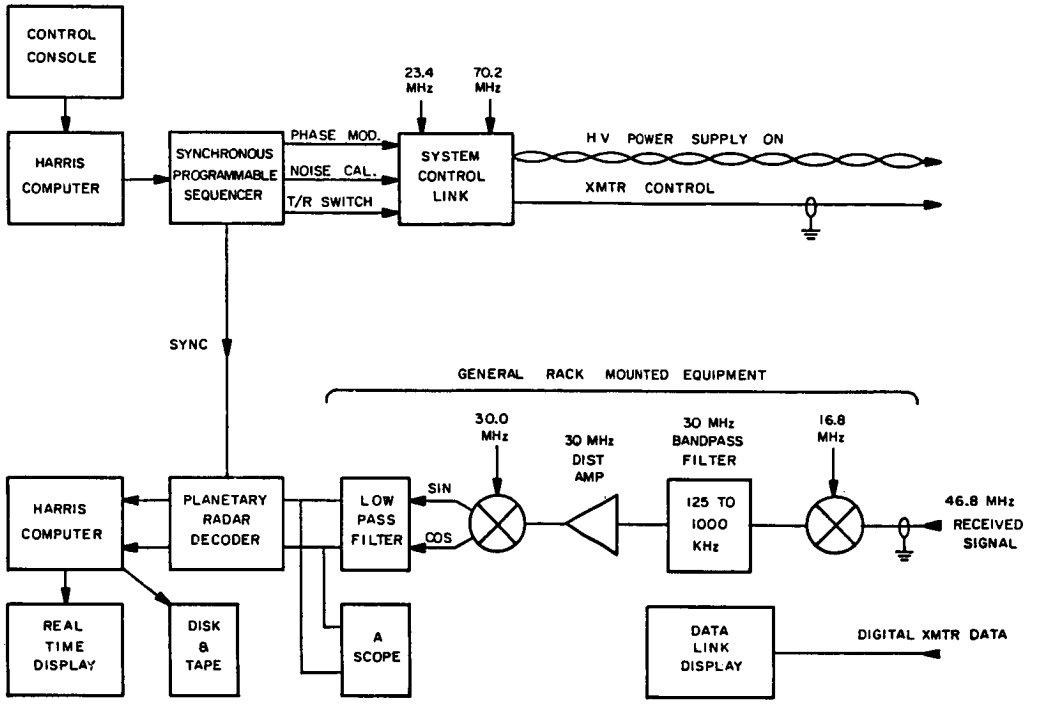

Figure 4. Instruments located in the control- and computer-room on the ground.

transmit the control signals (T/R switch, phase modulation, and receiver noise calibration) via a coaxial cable to the carriage house. These three control pulses are generated in the Synchronous Programmable Sequencer (radar controller), which is in turn controlled by the Harris 100 computer. Single pulse and any choices of complementary codes with interpulse phase flips (instrumental dc-elimination can be used). The RF pulse is derived from a combination of the noise calibration and T/R switch pulses. The pulses are checked in a hardware unit to see if limits of duty cycle (2% RF, 5% T/R) or pulse length (200 μs) are exceeded. The 70.2-MHz signal carries the noise calibration and the phase modulated RF pulse, and the 23.4-MHz signal carries the T/R pulse. These signals are mixed in the system control link (Figure 3) to yield the 46.8-MHz radar pulse.

The received 46.8-MHz signal is converted to the standard 30-MHz intermediate frequency and further to baseband. The planetary radar decoder is used for analog-to-digital conversion (10 bit), on-line decoding and coherent integration (max. 32 interpulse periods) of the quadrature signal. The output (a string of 16 bits selected from the 20-bit accumulator of the planetary decoder) of complex raw data for 2 x 256 range gates is fed to the Harris 100 computer, where it can be further coherently intergrated if desired. From the Harris 100 computer, the data are dumped on disk or tape (presently 1600 bpi, later to be changed to 6250 bpi). Also a real-time display of spectra, mean Doppler and power profiles will be provided.

Presently, only the raw data are dumped, since these are regarded more suitable than power spectra for system performance checks and some special

experiments. Power spectra could be computed on-line by using the array processor. This procedure would become necessary when also the 430-MHz radar will be used with the same radar control and acquisition software or for longer runs with the VHF radar to save tape.

FIRST RESULTS OF THE AO VHF RADAR

System definition and equipment development started in November 1984, (only the transmitter was purchased and further existing hardware was used), it was immediately followed by development of radar control and data-acquisition software utilizing the new Harris operating system, VOS, instead of the earlier DMS. Detailed tests of hardware and software took place in the second quarter of 1985, and first atmospheric echoes were recorded on tape on July 26, 1985.

Figure 5 shows a quick-look display (we acknowledge the software preparation done by D. N. Holden during his stay at the Observatory as a summer

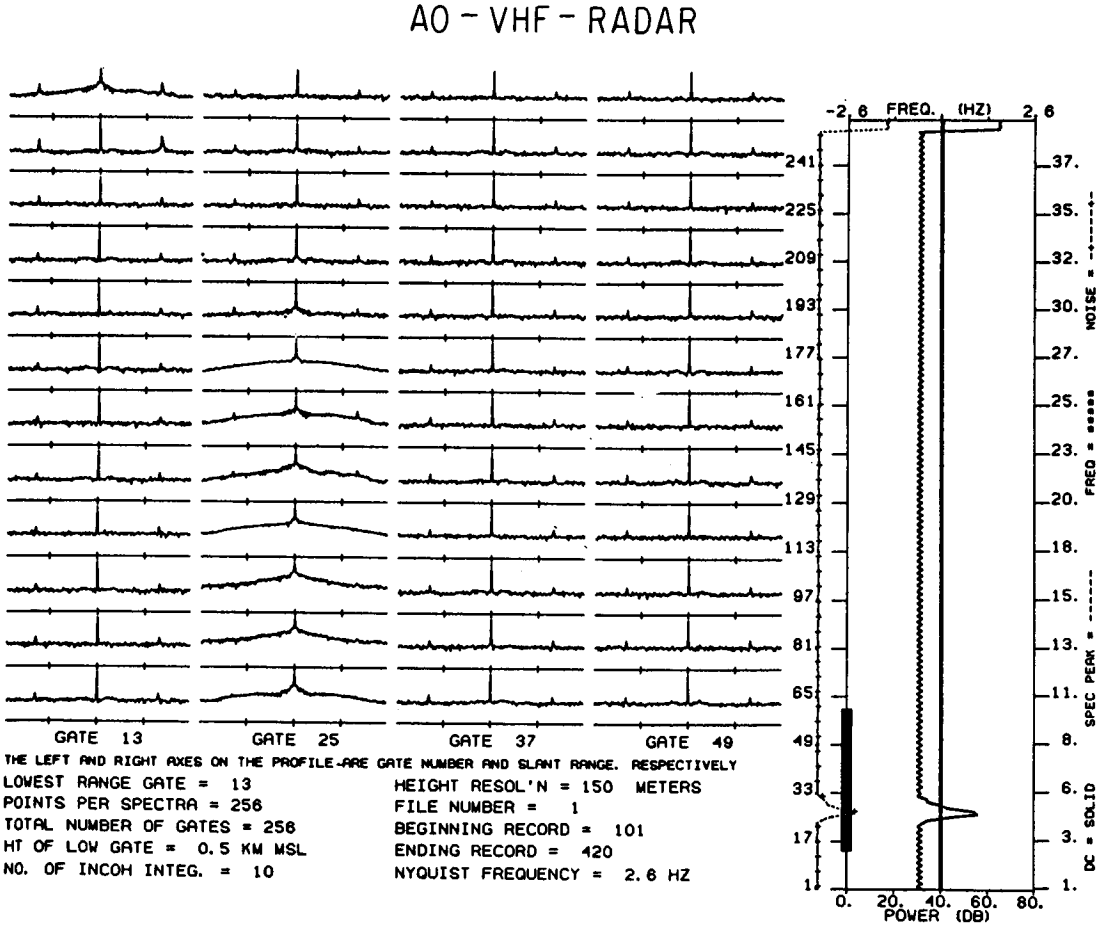

Figure 5. Sample of a real-time quick look plot of the AO VHF radar, displaying 48 normalized logarithmic spectra, and power profiles of dc - component, spectral peak, and noise as well as Doppler frequency of spectral peak. These spectra and profiles are showing results of a test run to check the system performance.

student), which is designed to monitor the data quality and later shall be attached to the system for real-time monitoring. It permits display of 48 normalized spectra of selected range gates and the total power profiles of the dc component, the spectral peak and the noise as well as the Doppler frequency of the highest spectral peak outside zero frequency. The display of Figure 5 presents results of a test series to measure the encoding/decoding properties and the spectral purity of the system. At gate 25, it shows the decoded (4 bit) transmitter pulse. These results prove the acceptable quality of the system, although improvements are desirable (e.g., suppression of code sidelobes). In particular, the graphs of Figure 5 indicate the sidebands of the transmitter pulse are more than 52 dB down at frequencies larger than 2.10^{-2} Hz. We regard this as an essential requirement because the system, due to the elevated feed antenna, intrinsically suffers from strong ground clutter. This would drastically hamper the data analysis if it were to spread out from zero Doppler shift.

Figure 6 shows a few sample spectra which indicate that the Doppler spread of the ground clutter on 46.8 MHz is apparently much less pronounced than that on 430 MHz (see SATO and WOODMAN (1980), who explained the spreading on 430 MHz due to fading by propagation effects). This evidence can be more directly seen in the profile of Figure 7, which proves that the difference between dc power and the (non-zero frequency) spectral peak is always larger than 40 dB. However, the absolute power of the ground clutter is severely large. Particularly in the lower ranges out to about 4-5 km, we will have some difficulties to avoid receiver saturation and to separate ground clutter from normal atmosphere echoes.

It also has to be mentioned here that the noise level frequently increases drastically due to interference in the radar band. We have partly identified the type of interference (spread-spectrum and narrow-band communication). It

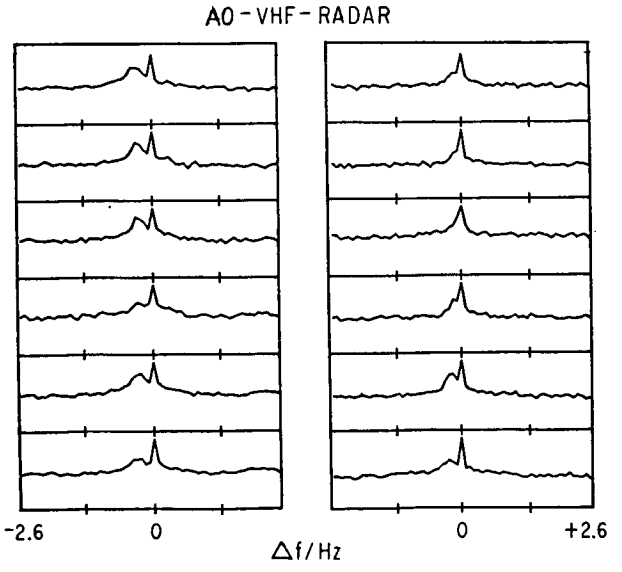

Figure 6. Selected spectra of tropospheric ranges obtained with vertical beam. Note that the power spectra are logarithmic and normalized to the maximum power in each range gate. The total power range changes between 60 dB and 90 dB.

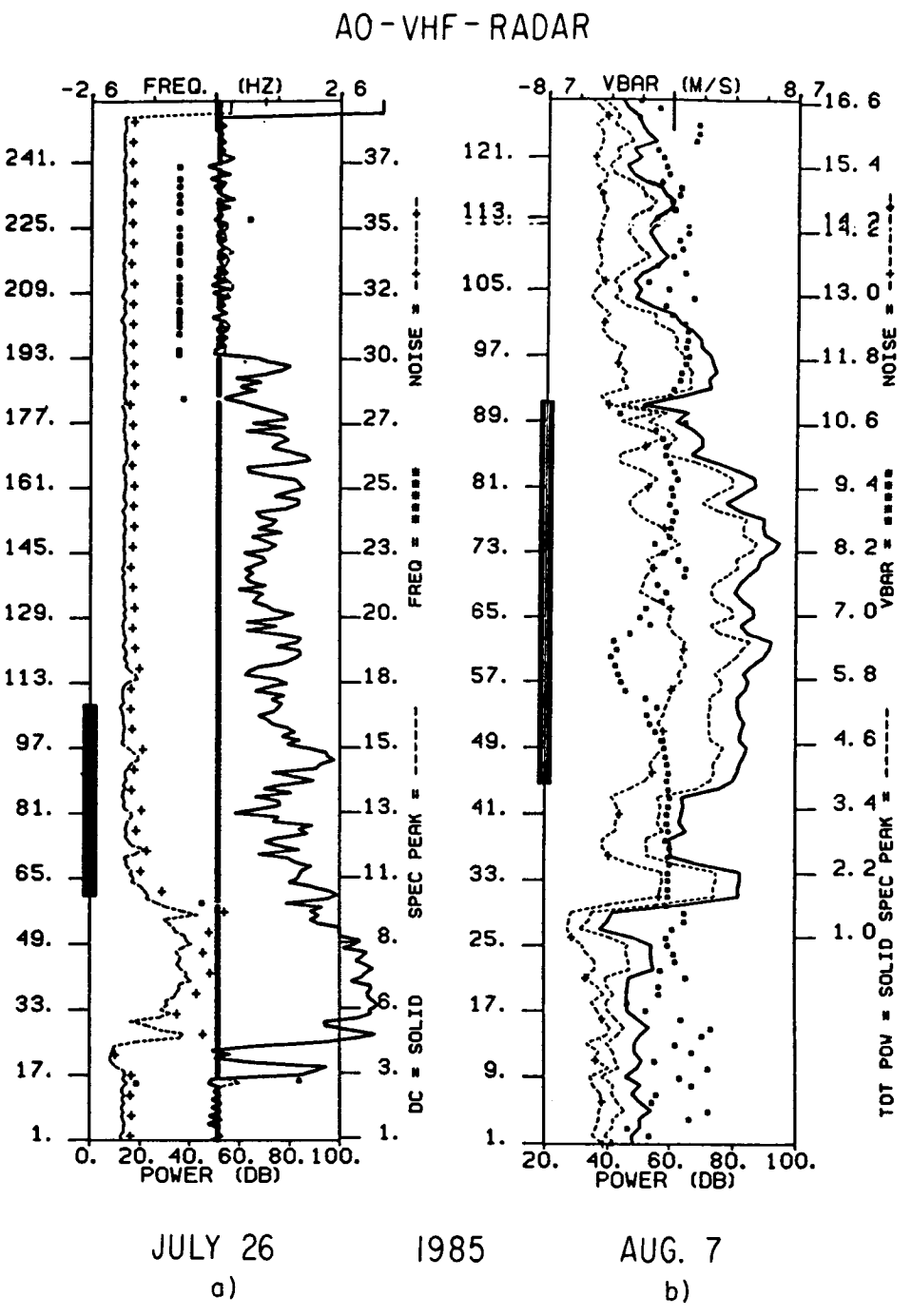

Figure 7. a) Quick look profiles of powers and Doppler frequency. b) Profiles of power (total and peak of signal and noise power) and mean vertical velocity (VBAR) measured during the passage of a convective cloud. The right-hand side scale gives the altitude, whereas the left-hand scale gives range gate number.

appears impossible to eliminate this kind of interference with the presently used antenna setup. Only operation during noninterference hours or the use of a shielded phased array (at least for reception) would solve this problem. The latter solution was envisioned as phase 1 of the stand-alone VHF radar system which has been proposed to NSF.

Figure 7b shows profiles of more elaborate parameters, total power, spectral peak, mean velocity and noise, which were obtained (due courtesy of Larsen, Holden and Ulbrich) during the first application of the new VHF radar in experiments proposed by visiting scientists. The atmospheric echo power in this case was abnormally high because the echoes were from convective clouds. During this experiment HOLDEN et al. (1986) also used the 430-MHz radar with single pulse, and the results should be found elsewhere in this proceedings.

SUMMARY AND OUTLOOK

In addition to continuing use of the 430-MHz and 2380-MHz radars to study waves and turbulence with improved data taking programs and higher range resolution (on 430 MHz), we anticipate increased use of the 46.8-MHz radar. Besides improving this radar to make it more user-friendly, two further feeds are planned to allow fast beam steering, particularly to study in a better way gravity waves and turbulence and their interaction with the background wind.

Several experiments with the 46.8-MHz radar are presently being conducted have been proposed, or are scheduled: the measurement of momentum flux due to gravity waves (Woodman, Cornish, Ierkic, Rottger), measurements of wave number spectra of tropospheric stratospheric and mesospheric velocities (VanZandt, Rottger, Ierkic, Mathews, Ying), determination of the influence of the Doppler effect on frequency spectra of tropospheric, stratospheric, mesospheric velocities (Liu, Scheffler, Franke, Rottger, Ierkic, Mathews, Ying), range-Doppler study of shear instabilities in the MST region using fine-resolution techniques at Arecibo (Rastogi, Rottger, Ierkic), changes in cloud-droplet spectra associated with lightning (Larsen, Holden, Ulbrich), and further investigations of the scattering/reflection mechanism of 46.8-MHz radar echoes from the tropical troposphere and stratosphere (Rottger, Ierkic). It is foreseen, on the other hand, that strong attempts will continue to obtain funds for installing and operating a stand-alone 50-MHz radar facility for MST studies at the Arecibo Observatory.

ACKNOWLEDGEMENT

We acknowledge the helpful cooperation and support of the electronics, maintenance and computer department of the Arecibo Observatory/NAIC. We are particularly indebted to Aixa Ramirez, Jose Vives, Ron Tower, Barry Paine and Dan Holden for working on parts of the project. The National Astronomy and Ionosphere Center, Arecibo Observatory, is operated by Cornell University under contract with the National Science Foundation.

REFERENCES

Gonzales, C. A., and R. F. Woodman (1984), Pulse compression techniques with application to HF probing of the mesosphere, Radio Sci., 19, 871-877.

Holden, D. N., C. W. Ulbrich, M. F. Larsen, J. Rottger, H. M. Ierkic, and W. Swartz, UHF and VHF radar observations of thunderstorms, this volume.

Ierkic, H. M., J. Rottger, J. Hagen, and R. K. Zimmerman (1986), Method to determine the optimal parameters of the Arecibo 46.8-MHz antenna system, this volume.

Mathews, J. D. (1985), Incoherent scatter radar probing of the 60-100 km atmosphere and ionosphere, Manuscript, Case Western Reserve University, Cleveland, Ohio.

Rottger, J., P. Czechowsky, and G. Schmidt (1981), First low-power VHF radar observations of tropospheric, stratospheric and mesospheric winds and turbulence at the Arecibo Observatory, J. Atmos. Terr. Phys., 43, 789-800.

Rottger, J., M. F. Larsen, H. M. Ierkic, and T. Hagfors (1986), Need for a subtropical wind profiling system, this volume.

Sato, T., and R. F. Woodman (1980), Spectral parameter estimation of CAT radar echoes in the presence of fading clutter, Preprints 19th Conf. Radar Meteorol., Am. Meteorol. Soc., 568-574.

Tepley, C. (1985), Airglow News Reports, Arecibo Observatory, Puerto Rico.

Tsuda, T., K. Hirose, and S. Kato (1985), Some findings on correlation between the stratospheric echo power and the wind shear observed by the Arecibo UHF radar, Manuscript, Kyoto University, Japan.

Woodman, R. F. (1980a), High-altitude resolution stratospheric measurements with the Arecibo 430-MHz radar, Radio Sci., 15, 417-422.

Woodman, R. F. (1980b), High-altitude-resolution stratospheric measurements with the Arecibo 2380 MHz radar, Radio Sci., 15, 423-430.

6.15 THE FIRST OPERATION AND RESULTS OF THE CHUNG-LI VHF RADAR

J. K. Chao, F. S. Kuo, Y. S. Chu, I. J. Fu

National Central University
Chung-Li, Republic of China

J. Rottger

Arecibo Observatory
Box 995
Arecibo, Puerto Rico

C. H. Liu

Department of Electrical and Computer Engineering
University of Illinois
Urbana, IL

It was decided that the Chung-Li VHF radar would be used in dual-mode operation, applying Doppler beam-swinging as well as the spaced-antenna-drift method. The original plans of this radar were discussed by BROSNAHAN et al. (1983). The total system was developed and constructed by Tycho Technology Inc. in Boulder, CO, under supervision of the Department of Atmospheric Science of the National Central University in Chung-Li, and the National Science Council of the Republic of China, advised by an international advisory committee. In May 1985, the radar was set up at the campus of the National Central University in Chung-Li and the first echoes were recorded on May 29, 1985.

The design of the radar was based on a proposal by ROTTGER (1981) to use three phase-coherent transmitters feeding three separate antenna modules with vertical beams; each can be used as the three receiving antennas of the spaced-antenna-drift and interferometer method (see Table 1). In the Doppler beam-swinging mode, either of the three antennas can be steered independently to five directions (vertical, 12° off-vertical to north, south, east or west) or all three antenna modules can be steered into the same direction. Three antenna modules of 64 four-element Yagis are used (see Figure 1), which are set up in a T-shape. The total aperture is about 2500 m^2. Three transmitters (Tycho MST-50-TX-3), each with a peak power of 50 kW, can be operated at a duty cycle of 2% and shortest pulse length of 1 μs. The final power-aperture product should be close to 10^7 Wm^2. Each transmitter has its own transmit/receive switch, from which the received signals are fed to three independent receiver ADC and preintegrator channels. The ADCs can be set optionally to 8, 10 or 12 bits accuracy. The preintegration is done in a new high speed signal processor (BROSNAHAN and WOODARD, 1984) and it allows coherent additions up to 32 bits. Through a multichannel bus, the coherently integrated raw data for up to 400 range gates are transferred to a Codata 3300 computer from where they are dumped on tape (Cipher F880 tape drive). The Codata computer with the preintegration signal processor can be used later for on-line decoding and/or further data processing. The radar control is performed by a system synchronizer (Tycho MST-50-1APC) which generates also complementary codes (up to 16 bits) and controls the antenna beam steering. The raw data on tape are analysed with the CYBER-720 and the VAX 11/750 computers at the University campus. The latter computer is used also for image processing of power and velocity plots (e.g., ROTTGER et al., 1986). More technical details of the Chung-Li VHF radar will be presented elsewhere by BROSNAHAN et al.

During the first system tests, the radar was operated with one vertically beaming antenna module, one transmitter and one receiver channel. Single pulse operation with shortest pulse length of 1 μs was tested at a duty cycle up to

Table 1.

Chung-Li VHF Radar

National Central University, Chung-Li, R.O.C.

Dual-Mode: Doppler beam swinging and spaced-antenna at 52.0 MHz

3 transmitters, each 50 kW (peak),
1 μs shortest pulse (compl. code),
2% duty cycle,
phase coherent.

3 antenna modules
of 64 four-element Yagis each,
$\sim$ 2500 m^2 total effective aperture,
vertical and four off-vertical directions.

3 independent receiver -- and preprocessor channels
(max 400 range gates each)

1 system synchronizer,
Codata computer
Cipher tape drive

(transmitters, receivers, antennas, system synchronizer and preprocessor made by Tycho Technology, Inc.)

1%. It was shown during the acceptance tests that this system configuration, comprising less than 1/10 of the final system sensitivity, is suitable for quite a variety of experiments, although improvements of the system performance are necessary, such as elimination of some digital noise, receiver saturation at short ranges and occasional data transfer failures, besides the addition of antenna beam steering. Using the vertical beam, ground clutter was not a problem, although the facility is built on a flat area sloping into a large valley with many buildings and power lines. Also, high mountains at about 20 km distance did not show up as strong clutter. Part of the time, interference was encountered and echoes from aircraft spoiled some range gates for a small fraction of time.

Figure 2 shows some first spectra of tropospheric signals detected with the vertically beaming Chung-Li VHF radar. The ground clutter was obtained from a longer time series and was subtracted before the spectra were computed. Range gate KH=6 corresponds to 3-km altitude, the range gate separation is 300 m, thus, range gate 25 is at 8.7 km. The spectra are normalized which can be seen by the noise level varying from gate to gate. They show the well known features of narrow and broad spectrum width due to dominance of scattering or partial reflection. Figure 3a shows the distribution of signal plus noise power as a function of height. Due to receiver transition effects (causing an attenuation out to delays of 40 μs ($\simeq$ 6 km range)), the absolute power at the lower heights is incorrect. However, a layered structure is clearly noticed.

A first physical result, which we regard as a new finding, is the lack of an enhanced echo from the tropopause (the enhanced power in the upper range

ORIGINAL PAGE IS
OF POOR QUALITY

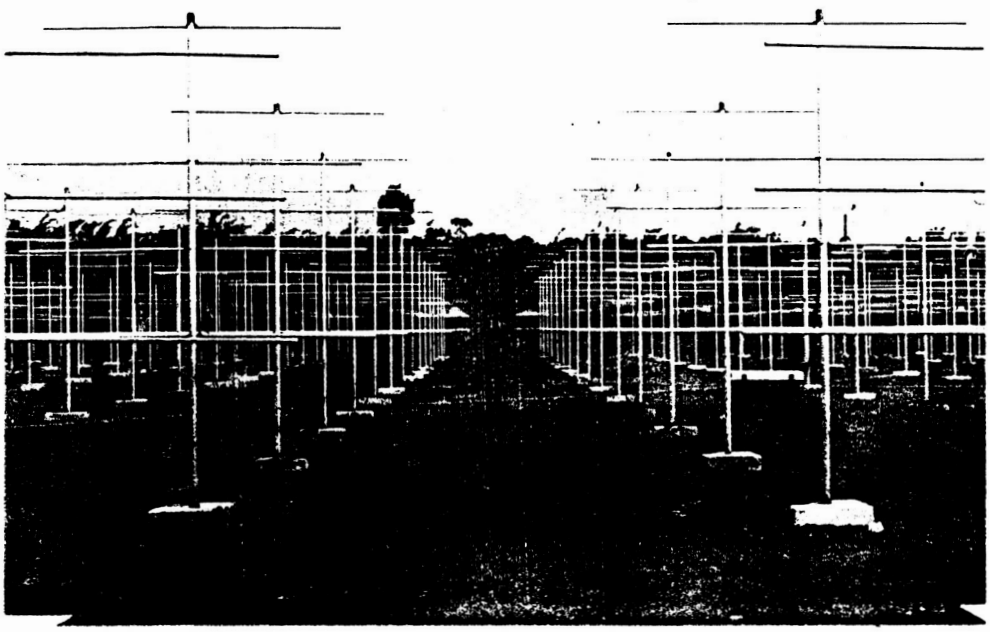

Figure 1. Part of the antenna field of the Chung-Li VHF radar, consisting of 192 four-element Yagi antennas.

gate 40 is due to preprocessor or data transfer problems. The tropopause height was between 12 km and 13 km, but no echo was seen at these altitudes. This evidence was checked also with other pulse schemes. FUKAO (personal communication, 1985) reported an analysis of MU-radar observations where he apparently did not find such clear indications of the tropopause as seen in mid- and high-latitude observations (e.g., ROTTGER, 1981). The latitude of the MU-radar (35°N) and of the Chung-Li radar (25°N) are in the region of the tropopause break separating the tropical and midlatitude tropopause. Since the tropopause is dissimilar here as compared to higher latitudes, we would expect its characteristics with respect to VHF radar reflectivities to be quite different. This may be a possible reason why we did not see the enhanced tropopause echo with the Chung-Li VHF radar.

In Figure 3b, the distribution of radial velocity is displayed. Single velocity data were deduced (after ground clutter and instrumental dc-elimination) from 4 sec averages of the first lag of the complex autocorrelation function. The distributions in Figure 3b cluster around zero velocity with rms variations of about 10 cm s^{-1}. The mean radial (vertical) velocity is close to zero, as expected, and it increases continuously in the upper troposphere up to 10 cm s^{-1} at 11 km altitude. Analysis of the velocity time series indicates that part of the velocity variation is due to short-period gravity waves. Above range gate 34, the velocity estimates are random, which is expected because the signal had disappeared in the noise.

We regard our first tests and observations as well as the results of the preliminary analyses to prove the relevance and applicability of the Chung-Li VHF radar. It will comprise another essential tool to study the subtropical atmosphere.

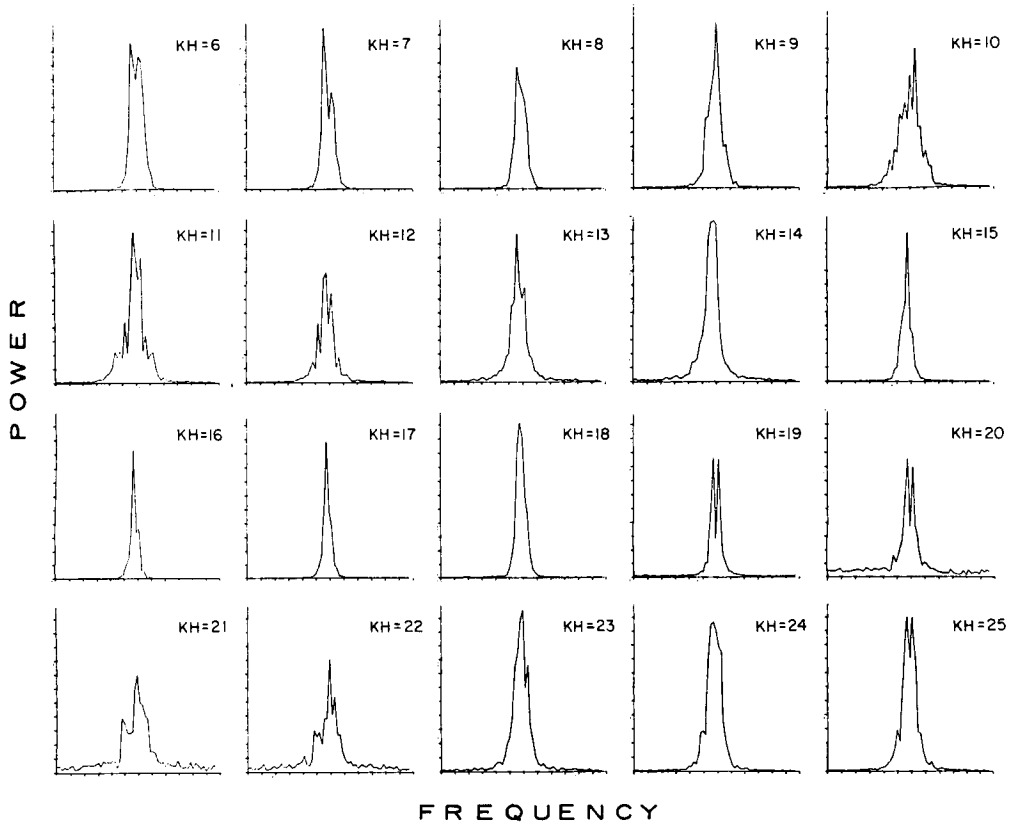

Figure 2. Normalized spectra of tropospheric returns with vertical beam. KH = 6 corresponds to 3 km altitude and the range gate separation is 300 m.

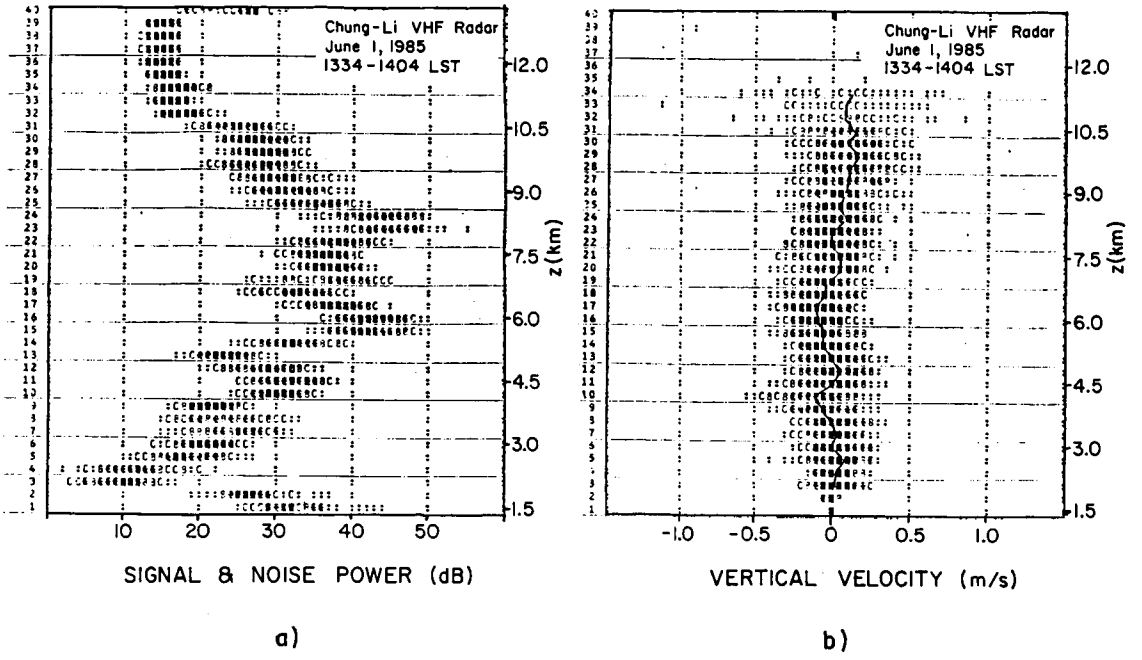

Figure 3. Distributions of a) signal plus noise power, b) radial (vertical) velocity.

ACKNOWLEDGEMENT

Two of us, C. H. Liu and J. Rottger, appreciated very much the outstanding hospitality and cooperation experienced during their stay at the National Central University.

REFERENCES

Brosnahan, J. W., J. K. Chao, and J. Rottger (1983), Chung-Li Taiwan Dual-Mode VHF Radar, Handbook for MAP, 9, 383-386.

Brosnahan, J. W., and D. M. Woodard (1984), A high-speed digital signal processor for atmospheric data, Handbook for MAP, 14, 280-284.

Rottger, J. (1981), The capabilities of VHF radars for meteorological observations, ESA-SP-165, (Proc. Nowcasting Symposium, Hamburg 1981), 143-148.

Rottger, J., I. J. Fu, F. S. Kuo, C. H. Liu, and J. K. Chao (1986), On the use of colour reflectivity plots to monitor the structure of the troposphere and stratosphere, this volume.

6.16 PROGRESS IN THE MF RADAR SYSTEM AT SASKATOON

C. E. Meek and A. H. Manson

Physics Department
University of Saskatchewan
Saskatoon, Canada S7N0W0

INTRODUCTION

Two improvements have been made to the radar system in the last year, one is the addition of O/X mode capability to the full antenna array used in the real-time wind system, and the other is the development of a coherent receiver -- a temporary arrangement until a fully engineered model is completed.

X-mode should be useful in reducing interference at night, and should also increase signal strength since the reflection coefficient is greater than O-mode and its absorption minimal. It was found that running O-mode in daytime resulted in a loss in data at lower heights, probably because of the reduced reflection coefficient, so the system was set to choose between linear N-S and X-mode (transmission is fixed linear N-S), alternating between X and linear every 5 min at night with a separate set of gains maintained and updated for each mode. Preliminary results (1 month) show negligible difference between the two, based on the number of wind values obtained. The reasons for this are still under investigation; possibly there are enough ionospheric absorption events to reduce the effectiveness of X-mode at this location.

The addition of a coherent receiver significantly expands the experimental capabilities of the system in terms of phase measurement for interferometer experiments (two papers in this proceedings), and coherent integration for extending the useful height range of the spaced antenna system downward. Also, it allows measurement of mean Doppler shift which can be used to determine vertical velocities. One such system has already been set up.

REAL-TIME Vz SYSTEM

Figure 1 shows a schematic diagram of the system. The transmitter antenna is also used for reception, resulting in a theoretical half beam width (3 dB) of 10°. Normal operation employs 4-point coherent integration (at 32 heights) giving a final Δt of 0.533 sec before accumulating autocorrelations (32-point integration can be done with a slight increase in Δt). Full 8-bit multiplication is used. Present selection criteria are fading rate (width of autocorrelation) and phase curvature near zero lag. It can be shown that the slope of the phase at zero lag is a weighted average of the radial velocity of the separate scatterers. A reasonable estimate of vertical velocity, Vz, should be obtained if scatterers are uniformly distributed in azimuth over the number of records averaged. At present, the records are 4.5 min long; this is not a system limit but is necessary so that the gain-height pattern, which is only set once for a record, can follow signal strength variations. Records can be almost as short as required -- a run of 90-sec records with 32-point integration has been done (but the number of heights analysed by the C64 has to be reduced for very short records). Figure 2 shows an example of hourly mean data from the system. At 85 km, data are a little erratic because it is one of the heights (every fourth) where a gain change is made when necessary.

COHERENT REAL-TIME WIND SYSTEM

Figure 3 shows a schematic of the proposed system. The maximum transmitter pulse rate is 60 Hz, which allows 32-point coherent integration when there is a receiver for each antenna. More importantly, the new receivers

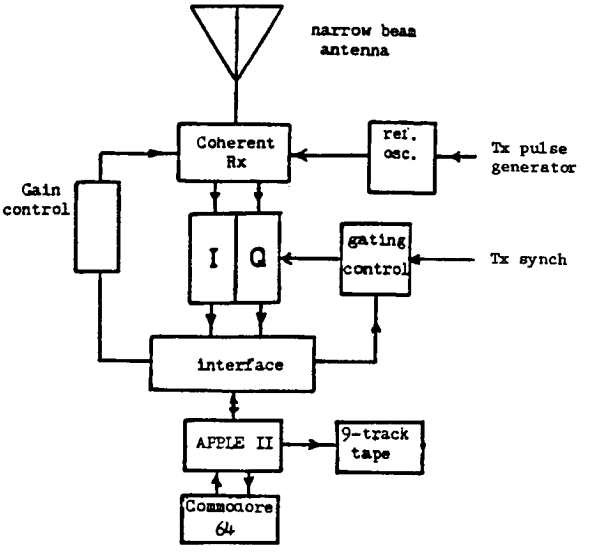

Figure 1. Schematic diagram of the real-time Vz system.

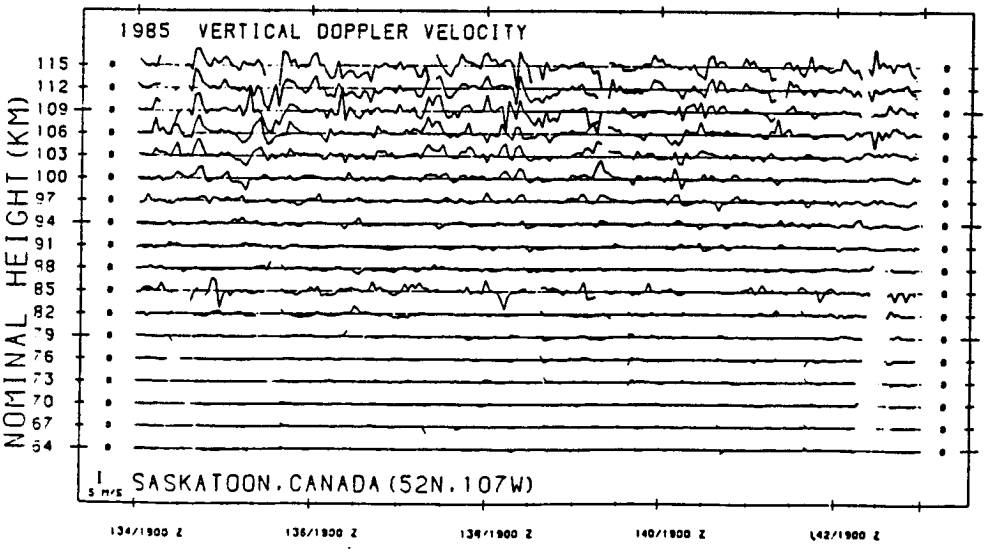

Figure 2. An example of hourly mean Vz data (from 4.5 min records).

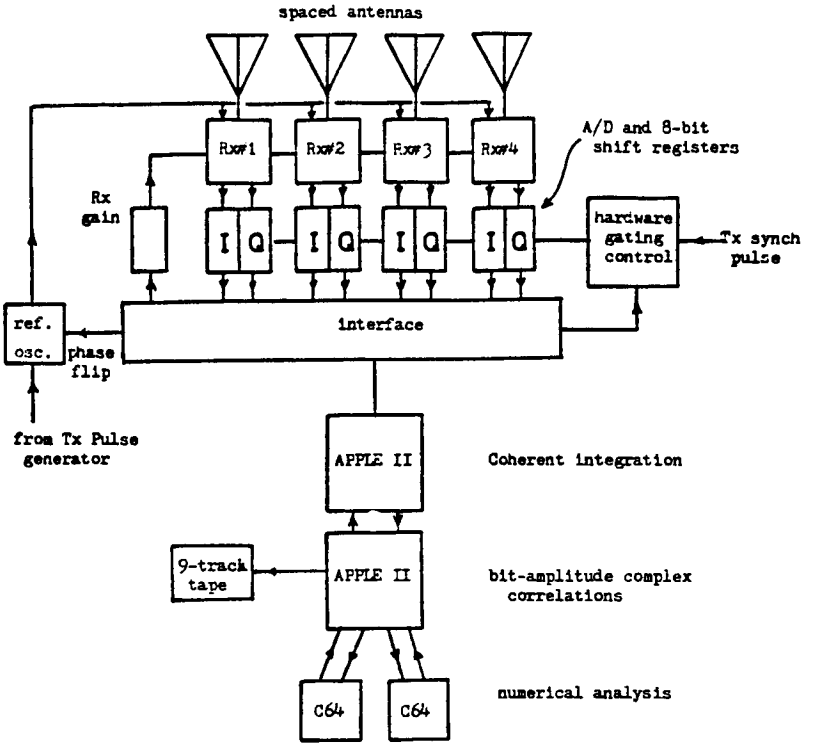

Figure 3. Schematic diagram of the proposed coherent real-time wind system.

will be able to change gain very rapidly, so that the best gain can be set for each height gate. (The present receiver gain control precedes the IF filter, and results in filter "ringing" with some loss of data at the height after a gain change; consequently the gain is set for groups of 4 heights, which means that only one height in four has optimum gain.)

Coherent integration will be done in software with a phase-flip system to remove dc offset, and the sign bit of the result kept to represent the amplitude -- giving an instantaneous conversion to binary sequences. A second microcomputer, probably an Apple, which appears to be marginally fast enough, will do the required auto- and cross correlations. Numerical analysis will probably require two Commodore 64s.

Figure 4 compares complex amplitude and complex bit amplitude correlations for one height. Three-point coherent integration was used. There is some minor degradation of the correlations when using bit amplitudes.

FABRY-PEROT INTERFEROMETER

The Institute has recently procured a new scanning Fabry-Perot system from D. Rees (U.K.); this operates under computer control, and partial real-time processing is incorporated. Filters including 630 nm (F region), 558 nm (F, E region) and OH bands (upper middle atmosphere) may be used, leading to atmospheric temperatures and winds. Special cooperative experiments with the MF radar are already planned to try to locate the height of the green-line emission; and using the OH data, relate thermal winds to temperatures, and gravity-wave effects to data from the radar "GRAVNET" system.

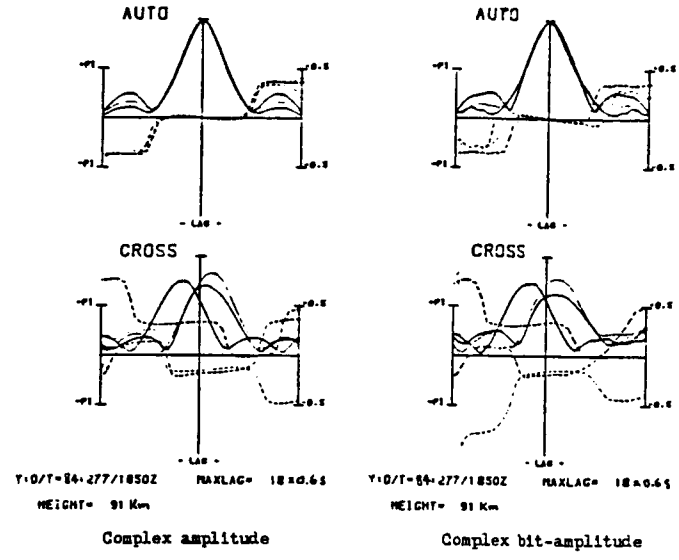

Complex amplitude

Complex bit-amplitude

Figure 4. Comparison between amplitude (8-bit) and single-bit correlations.

6.17 STATUS OF MENTOR, BRIGHTON, AND MAPSTAR RADARS

G. W. Adams

Center for Atmospheric and Space Sciences
Utah State University
Logan, Utah 84322

MENTOR

MENTOR (Meteor Echoes; No Transmitter, Only Receivers) is a proposal to measure meteor winds by receiving pulses scattered out of ST radar beams by meteor trails. One virtue of this approach is that an ST radar network becomes also a mesospheric wind network with the addition of a single passive site. A proposal to build a MENTOR receiver and field it initially in Colorado is pending with the Air Force Office of Scientific Research.

BRIGHTON

The Brighton, Colorado, (Boot Lake) field site was home for the NOAA/NSF HF radar (a digital ionosonde) and the 2.66-MHz imaging Doppler interferometer, which was an enhancement of the HF Radar. The field site has been dismantled. The HF Radar is now at the Los Alamos National Laboratory.

MAPSTAR RADAR

AFOSR/AFGL is conducting a four-year study of mesospheric wave effects by measuring infrared (vibrational OH) emissions and medium-frequency radar scattering. A new radar is being constructed; it differs from the Boot Lake system primarily as follows:

	New Radar	Boot Lake Radar
Frequency:	2 MHz	2.66 MHz
Power:	150 kW	50 kW
Deployment:	Portable	Permanent

6.18 PROPOSED UK VHF RADAR

A. J. Hall

Rutherford-Appleton Laboratory
Chilton, Didcot, Oxon, UK

Progress towards the establishment of an MST radar in the UK has continued at a low level because of the resources presently available.

Certain components including an antenna phasing control network, digital pulse shaping and some preprocessing logic are being developed in anticipation of full funding from April 1986, onwards.

A frequency of 46.5 MHz, within a UK reserved military band, has been agreed with the authorities for use on a noninterference basis.

The site in South Wales referred to in a previous report, MAP Handbook 14, 1984, pp 356, is now required for at least a further three years by the present holder for work incompatible with a VHF radar. Since we cannot accept this delay, another site, much nearer to Aberystwyth, is being considered. The radar equipment will be housed initially in a transportable container to speed up the installation process.

6.19 SYSTEM ASPECTS OF THE INDIAN MST RADAR FACILITY

G. Viswanathan

Indian Space Research Organization
Bangalore, India

One of the major objectives of the Indian Middle Atmosphere Programme is to investigate the motions of the middle atmosphere on temporal and spatial scales and the interaction between the three height regions of the middle atmosphere viz., mesosphere, stratosphere and troposphere. Realizing the fact that radar technique has proved to be a very powerful tool for the study of earth's atmosphere, the Indian Middle Atmosphere Programme (IMAP) has recommended establishing a MST radar as a national facility for atmospheric research. The major landmarks in this endeavour to setup the MST radar as a national facility are as follows:

The first major step was the constitution of a National Committee on MST Radar in July 1981, by the Chairman of the Advisory Committee for Space Sciences (ADCOS) of the Department of Space. User scientists from different national laboratories like the Physical Research Laboratory, Ahmedabad; National Physical Laboratory, New Delhi; and Space Physics Laboratory, Trivandrum; the different Indian universities involved in atmospheric research, as well as engineers with experience in design and development of radar systems, drawn from the Department of Space, the Department of Electronics, Tata Institute of Fundamental Research, Bombay, and public sector industries like the Electronics Corporation of India, Hyderabad and Bharat Electronics Limited, Bangalore, participated in the deliberations of this National Committee. The Committee submitted its report in early 1982, generating the user requirements and identifying the major specifications for the subsystems for the Indian MST radar.

Based on this, the Chairman of ISRO and the Secretary, Department of Space, made a decision in middle 1982 to entrust the overall responsibility for the design, development and commissioning of this radar system to the public sector undertaking M/s. Bharat Electronics Limited. The overall responsibility for establishing this national facility rests with the Department of Space, identified as the Nodal Agency with financial contributions coming from different departments of the Government of India, like the Department of Electronics, the Department of Science and Technology, and the Council of Scientific and Industrial Research, etc.

The Chairman of ADCOS constituted a committee in the middle of 1982 for site selection. This had representation from the user scientists, the Frequency Management Office of the Department of Space and M/s. Bharat Electronics Limited. The Site Selection Committee, after considering various locations, recommended a site near the temple town of Tirupathi in the state of Andhra Pradesh. Some of the important considerations which formed the basis for this selection are the following: 1) proximity to a university or a national scientific laboratory, 2) remoteness to industrial activity, 3) availability of natural shielding, and 4) moderate separation from the geomagnetic equator, so that the facility could be used to study the ionosphere at the same time and not get saturated by the equatorial electrojet.

The toughest challenge in trying to establish the MST radar as a national facility in India continues to be the frequency and siting clearance. Out of th six candidate sites surveyed by the Site Selection Committee, five have to be rejected in view of possible interference to existing VHF communication facilities, radio astronomy groups or military installations. After considerable deliberation by inter-agency groups, the WPC, a wing of the

Ministry of Communications (connected with frequency clearance), Government of India, have tentatively sanctioned the operating frequency of 53 MHz with an operating bandwidth of 1 MHz (3 dB) with severe restrictions on the type of emission and spectrum usage.

The siting clearance is still awaited as there is an objection from the point of view of possible interference to the international air traffic overflying the chosen site. Based on this objection, a second site at Tirupathi has been studied. Once the siting clearance is obtained, work on the facility is expected to start in full swing.

Table I gives the salient features and the important system level parameters for the Indian MST radar facility.

It is also contemplated to establish a SODAR at the MST site for the investigation of 0 to 5 km height range in detail, and a lidar to cover the stratosphere region. Plans also exist for using the MST system with its large power aperture product for the study of the ionosphere in the incoherent backscatter mode. Figure 1 gives a simplified block diagram of the Indian MST radar. Figure 2 gives an artist's impression of the proposed MST site showing the antenna array and the control building. Figure 3 shows a subarray feeding network.

It can be concluded that when this facility is fully established, it will provide valuable data on the middle atmosphere over lower latitudes in the Indian Ocean region, not only for Indian scientists, but for atmospheric scientists all over the world who are interested in global modelling of the middle atmosphere.

Table I

Indian MST radar system specifications

Type of system	:	Pulse Doppler
Operating frequency	:	53 MHz
Operating bandwidth	:	1 MHz
Power aperture product	:	$\simeq 7 \times 10^8$ wm^2
SUB SYSTEMS:		
ANTENNA:		
Type	:	coaxial collinear/Yagi
Gain	:	36 dB (Min)
Beam width	:	$3° \pm 0.3°$
Beam switching	:	(a) zenith (b) $\pm$ 20° E-W from zenith (c) $\pm$ 20° N-S from zenith (d) $\simeq$ 12° due north from zenith
Pointing accuracy	:	$\pm$ 0.1° for zenith beam TBD for other beams
Sidelobe level	:	15 dB below main lobe (design goal 20 dB)
Maximum tolerable Antenna gain towards the horizon	:	+ 1 dB
Additional null	:	additional null at 12° north during normal MST operation

Null depth	:	40 dB
Polarization	:	2 orthogonal polarizations

ADDITIONAL REQUIREMENTS:

1) The antenna system should be capable of being used separately either in ST mode or MST mode.
2) The antenna system should have provision for time delay compensation when excited with coded waveforms to avoid code smearing on the antenna axis.
3) Provision to use antenna in SA mode at a later stage.

TRANSMITTER		
Configuration	:	(a) 24 modules of ≃ 100 kW each are combined to generate a peak power of 2.5 MW and average power of 60 kW for the radar. Specifications of individual module is enumerated below. (b) Pulse width and PRF will be selected such that the averaged power is maintained at ≤ 60 kW.
Peak power	:	100 kW ± 10%
Average power	:	2.5 kW ± 10%
Duty ratio	:	2.5%
Bandwidth	:	1 MHz
Pulse width & wave form	:	
(a) Uncoded	:	1, 2, 4, 8, 16, 32, 64, 128 μsec
(b) Coded	:	16 μsec 32 μsec Complementary code using ± π phase modulation (BPSK) with subpulse length of 1 μsec
PRF	:	62.5, 125, 250, 500, 1K, 2K, 4K, 8K PPS selectable
Spurious signal output	:	2nd and 3rd harmonics and spurious output should be 60 dB below fundamental
T/R switch isolation	:	50 dB (design goal 60 dB)
Limited input to Rx	:	+ 13 dBm
RECEIVER SYSTEM	:	
Preamplifier	:	
Frequency	:	53 MHz
Bandwidth	:	5 MHz ± 10%
Noise figure	:	3 dB or better
Gain	:	20 dB ± 1 dB
Maximum input signal handling without saturation	:	+ 4 dBm
Overload recovery	:	7 μsec
RECEIVER	:	
IF	:	30 MHz
Local oscillator	:	Frequency to suit 53 MHz carrier using USB or LSB

Total gain	:	110 dB (Min)
Dynamic range	:	70 dB (Min)
Deviation of linearity over the 70 dB dynamic range	:	$\pm$ 1 dB
IF bandwidth (3 dB)	:	1 MHz
Video bandwidth	:	$\frac{1.2}{\text{pulse width}}$
I & Q video amplitude	:	$\pm$ 2 V P P
VSWR	:	1.5:1
Local oscillator stability	:	
(1) Short term	:	1×10^{10} (for 15 min)
(2) Long term	:	1×10^{9} (for 36 hrs)

SIGNAL PROCESSING :
The signal processing system consists of:

(1) The system synchronizer unit which generates all the baseband waveforms for waveform generation, triggering, gating and clock generating and timing under the control of the overall system control.
(2) Data acquisition unit which digitizes I & Q channel outputs, performs coherent integration, decoding, sweep integration, FF transform and velocity estimation.
(3) System controller & data processor unit which controls all the subsystems based on the system operating modes selected, coordinates the data acquisition, processing, real-time display, recording and generation of hard copy outputs.

The important specifications of these three units are listed below:

SYSTEM SYNCHRONIZER UNIT	:	
PRF	:	62.5, 125, 250, 500, 1000, 2000, 4000, 8000, PPS (selectable)
Range gates	:	150 m, 300 m, 600 m, 1.2 km, 2.4 km, 4.8 km (selectable)
Basic clock	:	10 MHz
DATA ACQUISITION UNIT	:	
Type of A/D converter	:	Flash converter
Sampling rate	:	2 MHz
Data resolution	:	12 bits (desirable) 10 bits (essential)
Analog input	:	$\pm$ 2 volts
Number of range slots for FF transform	:	64 maximum
Number of points for spectral estimation	:	64, 128, 256, 512
Maximum velocity	:	12 (11.75) m/sec or 24 (23.5) m/sec or 47 m/sec (selectable)
Velocity resolution	:	0.182 or 0.09 m/sec (selectable)
Spectrum integration period	:	Selectable from 5 sec to 10 min in suitable steps

Type of signal processor : Dedicated FFT processor

SYSTEM CONTROLLER :
Functions:

(1) Mode control for all subsystems like transmitter, receiver and signal processor
(2) Antenna control, for beam position, polarization, etc.
(3) Data display, storage and archiving and hard copy generation.

Type of computer	:	General purpose minicomputer based on 16-bit μprocessor chip.
Operating system	:	Real-time operating system, with multitasking feature
Peripherals and storage devices	:	(1) CRT terminals with colour graphic capability (2) Hard copy device for terminal (3) Graphic printer (4) Magnetic tape drives (5) Floppy disk drives (6) Winchester hard disk drives.
Power supply	:	400 V 3 ϕ ac 50 Hz

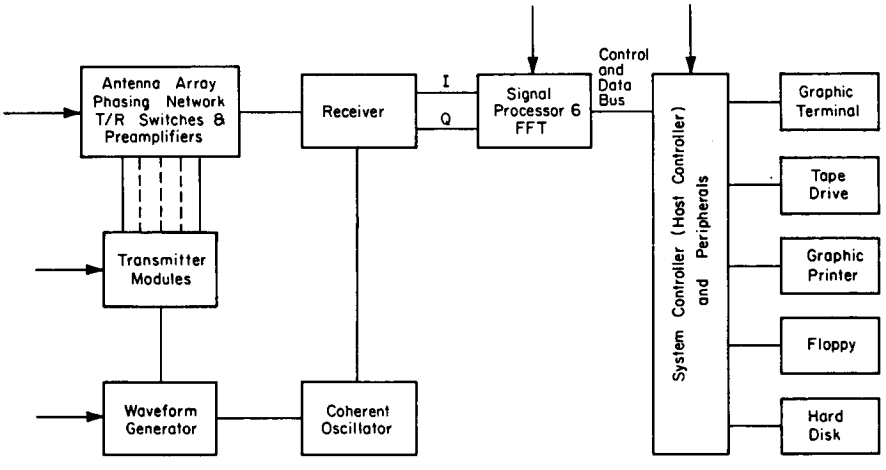

Figure 1. Simplified block diagram: Indian MST radar.

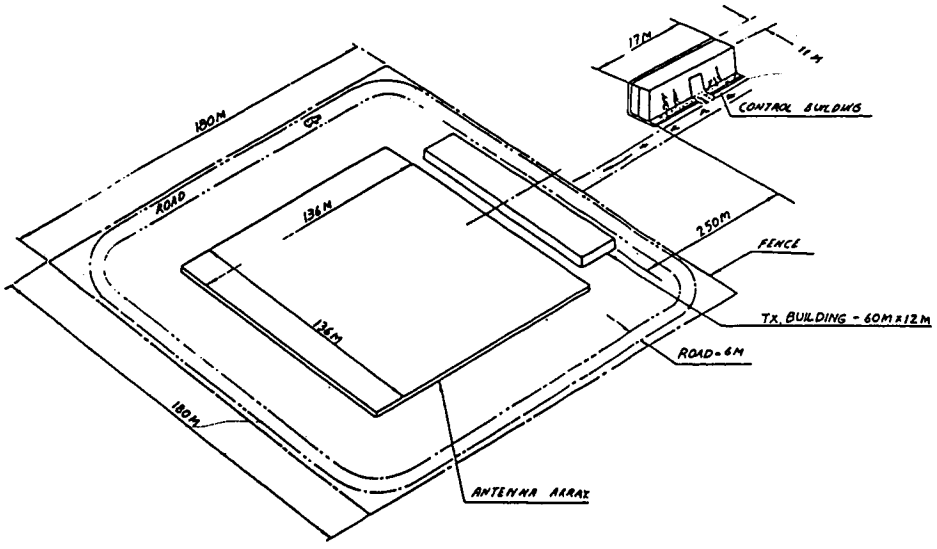

Figure 2. View of antenna site and equipment buildings for MST radar.

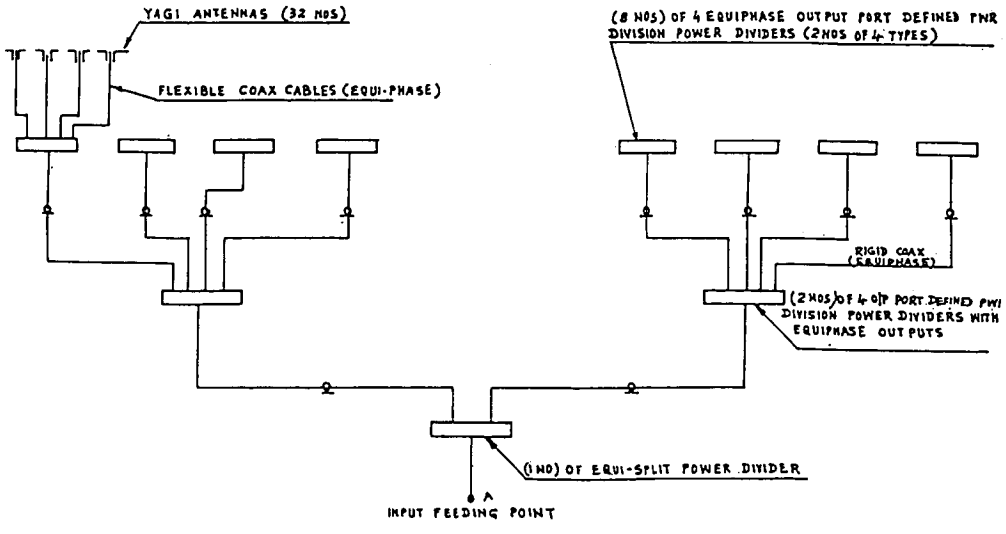

Figure 3. Subarray feeding network.

6.20 HISCAT

- A PROPOSED NEW SCATTER FACILITY IN NORTHERN SCANDINAVIA -

R. Bostrom and B. Thide

Uppsala Ionospheric Observatory
S-755 90 Uppsala, Sweden

ABSTRACT

It is proposed that a new versatile ionospheric and atmospheric scatter radar be constructed in northern Scandinavia through a multinational collaborative effort. The new facility, tentatively named HISCAT (High frequency, High power, High latitude, Heating and Ionospheric Scatter facility), should be used for scientific investigations of: the physics of the neutral (middle) atmosphere; fundamental plasma phenomena, natural or artificially induced in the ionosphere; electrodynamic conditions at high altitudes above the auroral region and in the polar cap ionosphere; plasma waves in the solar atmosphere (if technically feasible).

The system should thus be able to operate as a MST radar, a so-called ionospheric modification ("heating") facility, incoherent-scatter radar, coherent-scatter radar, and solar radar. It would complement the existing facilities EISCAT, Heating, STARE, SOUSY, and ESRANGE also located in northern Scandinavia and should be operated in close coordination with these.

Basically, the new facility should be a device that can operate simultaneously on several frequencies in the frequency range 5-50 MHz not covered by other instruments. It should comprise: powerful transmitters, capable of delivering a total average power of several megawatts; an advanced phased antenna array of high gain (30-40 dB) forming one or two steerable and well collimated beams; an advanced data collection and analysis system.

It is proposed that the facility be located out on the ESRANGE field to facilitate real coordination with sounding rocket experiments, minimize interference, and obtain a suitable geometry for coordinated experiments with EISCAT.

7.0 PHASED-ARRAY DESIGN FOR MST AND ST RADARS

W. L. Ecklund

Aeronomy Laboratory
NOAA
Boulder, CO 80303

INTRODUCTION

All of the existing radar systems fully dedicated to clear-air radar studies use some type of phased-array antenna. The aim of this session is to communicate developments in array design and application. The suggested subtopics for this session are listed below along with a brief discussion of each subject.

BEAM-STEERING TECHNIQUES INCLUDING FEED NETWORKS AND PHASE SHIFTERS

Clear-air radars built to date have varying degrees of beam-steering flexibility, depending on the planned research goals (and the available funding). The simplest clear-air radar arrays use fixed beams (hard wired), and the most complex use computer-controlled phase shifters that can steer the beam to any position within 20 to 30 degrees of the zenith in a few microseconds. In general, increased beam-steering flexibility requires more complicated feed networks with additional phase-shifting hardware and associated control and testing circuitry.

SIDELOBE CONTROL, GROUND-CLUTTER SUPPRESSION AND LOW ALTITUDE COVERAGE

Sidelobe reduction in clear-air radar arrays is important for two major reasons. First, if the atmospheric reflectivity is very nonuniform horizontally, unwanted echoes from regions of high reflectivity in the sidelobes may override the wanted echoes from the main lobe of the array. Specular reflections from stable layers and scattering from isolated rainclouds are examples of regions with high reflectivity that may cause problems. The second reason that sidelobe reduction is important involves clutter from nonatmospheric targets. Echoes from airplanes, cars and the sea surface may override the atmospheric echo. In addition, the Doppler shifts from these objects may be nearly the same as the Doppler shifts from the wanted atmospheric targets making it difficult to filter out the unwanted clutter. Ground clutter may also be so strong that it overdrives the receiver at fixed ranges. The above problems suggest that at least under some circumstances it may be important to reduce the antenna array sidelobes.

The goal of most of the clear-air radars built to date has been to get useful data from the highest possible altitudes. However, for some applications (particularly wind profiling) continuous measurements from the ground upward are desired. Most clear-air radars operating in the lower VHF band do not obtain data below several km. It would be very useful if this lower altitude coverage could be extended downward. Reasons why these radars do not work at lower altitudes are not very well established at this time but may include the following problems: leakage of frequency-coherent energy from the transmitter after the pulse (turn-off problem); reflection of energy within the array with an intensity that overdrives the receiver for a finite time; reflection of energy from the nearby ground (ground clutter) that overdrives the receiver.

ARRAYS WITH INTEGRATED RADIATING ELEMENTS AND FEED NETWORKS

Most clear-air radar antenna arrays use a large number of radiating elements. This means that the feed network is generally complex, consisting of at least one feed cable per element. This approach makes it possible to steer the beam to a large number of positions, since the phase of each element can be controlled separately. However, if only limited or no beam steering is required, the antenna system can be simplified by using designs that physically integrate the radiating elements and the feed network. These designs are generally either traveling wave or resonant structures. The traveling wave structures have the property that beam position is controlled by the operating frequency. Beam steering by frequency scanning or stepping might be attractive for some clear-air radar applications. However, since most radars operate at a single, fixed frequency, the resonant structures seem to be most applicable for clear-air radar use. The Franklin and coaxial-collinear arrays are examples of structures that drive a number of radiating elements end-to-end from a single feed point. The grid or chain array is a structure that allows a large square array to be driven from a single feed point.

ANALYSIS OF THE COAXIAL-COLLINEAR ANTENNA

The earliest clear-air radar experiments were conducted at the Jicamarca Radar Observatory in Peru. This radar uses coaxial-collinear elements made of rigid metal tubes and rods with the inner and outer conductors interchanged at half-wavelength intervals. Antennas using the same design but made of ordinary flexible coaxial cable have been widely used in clear-air radar arrays for the past 10 years. In spite of their widespread use (and usefulness), a number of questions still remain about how these antennas work and whether or not the design could be further optimized. Several studies of the coaxial-collinear antenna are currently in progress and the results from these studies may lead to improved designs in the future.

USE OF ARRAYS WITH MULTIPLE BEAMS

The usual way to form multiple beams with an array antenna is to use phase shifters in the feed network to form one beam at a time. There is currently some debate about how many beams are required to adequately describe the wind and wave fields in the atmosphere. A practical problem of using too many beams is that for dwell times of a minute or more (required to get adequate sensitivity) the cycle time around a large number of positions is so long that short period wave activity cannot be measured. One way to overcome this problem is to use an interferometer array to form a number of beams simultaneously. If the wind field is fairly uniform over the beams, the Doppler shifted echoes from each beam are separated in frequency and can be uniquely identified. This approach can be used for special studies when the reduced sensitivity is not a problem and when simultaneous measurements of velocity and signal to noise are required on a number of separate beams.

ARRAY MEASUREMENT AND TESTING

It is difficult to measure the antenna patterns of large area array antennas because the near field often extends to altitudes that cannot be reached by airplanes. Even in those cases when airplanes can be used to map the patterns, it is difficult to know or control the position of the airplane with sufficient accuracy. Most array patterns have been measured by using satellite beacons or cosmic radio sources. Radiating elements in the array can also be probed for relative phase and amplitude, and the resulting measurements can be used to compute the antenna patterns. The important pattern parameters are beam position, beam width and sidelobe levels. It is desirable to know the sidelobe levels over the entire hemisphere, since in some antenna designs unwanted high level sidelobes can occur far from the main beam.

7.1.1 THE NOAA TOGA ANTENNA ARRAY

W. L. Ecklund, D. A. Carter and B. B. Balsley

Aeronomy Laboratory
NOAA
Boulder, CO 80303

NOAA's Aeronomy Laboratory has recently installed a 100 by 100 meter array antenna with limited beam steering on Christmas Island as part of the TOGA (Tropical Ocean and Global Atmosphere) program. In this report, we describe the array and the associated beam steering and indicating hardware. The array consists of center-fed 48-dipole coaxial-collinear antenna strings. Thirty-two of these strings are installed parallel to each other at one-half wavelength spacing to make a 100 by 100 meter array. A second set of 32 antenna strings are physically superimposed perpendicular to the first set to form the other polarization. The TOGA antenna strings are aligned north-south and east-west geographic.

Figure 1 shows the feed network for the TOGA array. Each string of 48 dipoles is indicated at the top of the figure by numbered open circles. The antenna strings are fed in a repeating pattern of 8 (a spacing of 4 wavelengths) by equal lengths of transmission line. Antenna strings 1, 9, 17 and 25 are fed through phase shift module 1 in the field box. Strings 2, 10, 18, and 26 are fed by module 2, etc. In this way, only 7 phase shift modules provide 5 usable beam positions (vertical, and 15 or 30 degrees east and west of the zenith). In the initial TOGA installation, one polarization is switched between vertical and 15 degrees east of zenith. The other polarization is hard-wired to 15 degrees north of zenith, but a second field box can be installed later to provide steering in the north-south direction as well. A coaxial SPDT vacuum relay selects either the east-west or north-south array.

Each basic phase shift module consists of 2 SPDT vacuum relays mounted in a block with clamp fixtures to attach 2 fixed lengths of RG-213 coaxial cable. Seven of these basic modules allow any 2 of 5 beam positions to be selected. Addition of a second module set in series (in the same field box) provides 4 positions. One set of cables in the seven modules and the fixed cable shown in Figure 1 are cut for identical phase shifts to form the vertical beam. The 15-degree east beam is formed by switching in a second set of cables in modules 1 through 7 that are longer than the vertical set by progressive one-eighth wavelength increments.

The phase shift modules and the polarization switch are driven via a multiconductor cable by the beam selector-indicator box located in the equipment shelter at the edge of the array. Beam positions can be selected by computer control or by manual control from either the shelter or the field box located in the center of the array. Beam positions and possible vacuum relay faults are indicated by logic circuitry located in the field box. The position of each SPDT vacuum relay is monitored by checking continuity of the transmission line center conductor through the 2 or 4 SPDT relays in each module and the polarization switch to the shorted quarter-wavelength stub shown in Figure 1. This position information is decoded, indicated in the field box and equipment shelter, and compared with the selected position. Any discrepancies (indicating a relay problem) are indicated by fault lights. The beam position and fault lights are read and logged by the system computer.

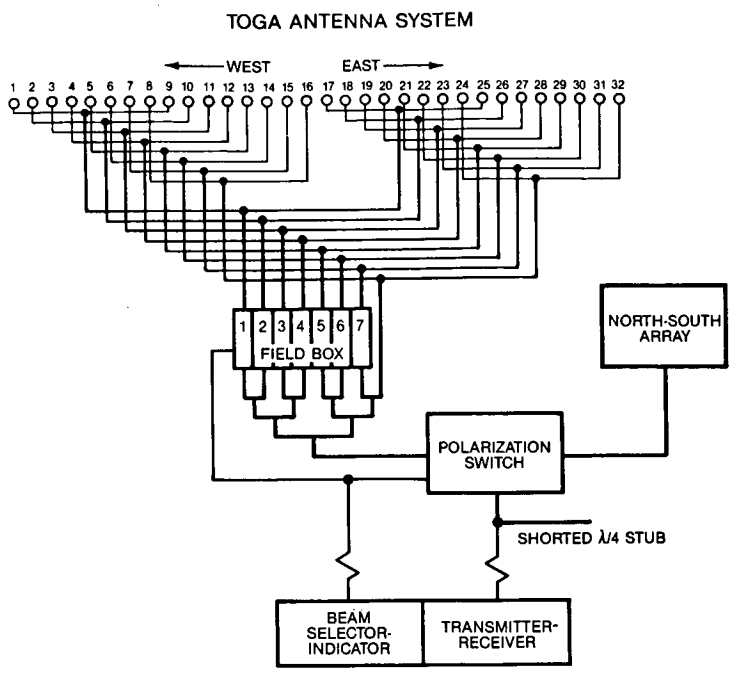
TOGA ANTENNA SYSTEM
WEST
EAST
1 2 3 4 5 6 7 8 9 10 11 12 13 14 15 16 17 18 19 20 21 22 23 24 25 26 27 28 29 30 31 32
1 2 3 4 5 6 7
FIELD BOX
NORTH-SOUTH ARRAY
POLARIZATION SWITCH
SHORTED λ/4 STUB
BEAM SELECTOR-INDICATOR
TRANSMITTER-RECEIVER

Figure 1.

7.1.2 BEAM STEERING SYSTEM

S. A. Bowhill and K. O. Merewether

Department of Electrical and Computer Engineering
University of Illinois
Urbana, IL 61801

This paper describes a simple technique for steering the beam of a multimodule phased-array MST radar antenna. The Urbana radar antenna consists of six modules, each having 14 elements in the northwest direction and 12 elements in the northeast direction. The antenna is constructed on a ground plane tilted 1.61 deg from horizontal in the southeasterly direction. This has made it possible to measure horizontal velocity in the southeasterly direction by averaging the line-of-sight velocity over a 1-hr period to minimize gravity-wave contamination.

It is clearly desirable to be able to point the antenna in multiple directions, so as to derive all components of the horizontal velocity. This has been done on an experimental basis by adding parallel-wire line to the feed for the southwest module pair, and subtracting it from the northeast pair, thereby achieving a southward tilt of the antenna, and conversely to achieve a northeast tilt.

The calculated E-plane (i.e., northwest) patterns of Figure 1 show the extent of beam degradation for slewing angles of up to 4 deg. The beam can be steered 2 deg or perhaps 3 deg without serious degradation of the pattern (remembering that the sidelobes are reduced by an equal factor during transmitting and receiving). The scheme shown in Figure 2 was therefore devised. The incoming power is connected to a rotor with two silver-plated copper brushes in contact with a stator consisting of two semicircular silver-plated copper strips, spaced so as to match the antenna impedance. The northeast and southwest module pairs are connected to the ends of the stator, while the center module pair is connected to the rotor.

With the rotor in the central position, all three module pairs are fed in phase. If the rotor is turned to one side, the phase of the energy for one end module pair is increased, and for the other is decreased, thereby steering the antenna beam away from the broadside direction. The rotor is motor-driven, and the stopping points are located by microswitches running on a cam.

It is proved possible to steer the beam through most of the available range without adversely affecting the VSWR seen from the transmitter. No problems have arisen from burning of the contacts. The entire assembly is surrounded by a water-proof plastic enclosure.

Calibrating the antenna direction can be accomplished by observing radio sources, though there are an inadequate number to cover all directions. An easier way is to measure the direction and magnitude of stratospheric winds with the radar, and compare the results with radiosonde observations. When this was done for the broadside direction of the Urbana antenna, a zenith angle of 1.13 deg was found rather than the theoretical value of 1.61 deg based on land surveys and phase measurements. We believe that the discrepancy arises from aspect sensitivity of the stratospheric echoes.

For various assumed values of the aspect sensitivity in dB/deg, and the calculated antenna pattern, it is possible to calculate the effective pointing angle of the antenna, defined as that angle which would give an identical location for the centroid of the power spectrum if aspect sensitivity were absent. The results for the Urbana antenna are shown in Table 1. The apparent

Figure 1. E-plane field strength plots for various pointing directions of the antenna.

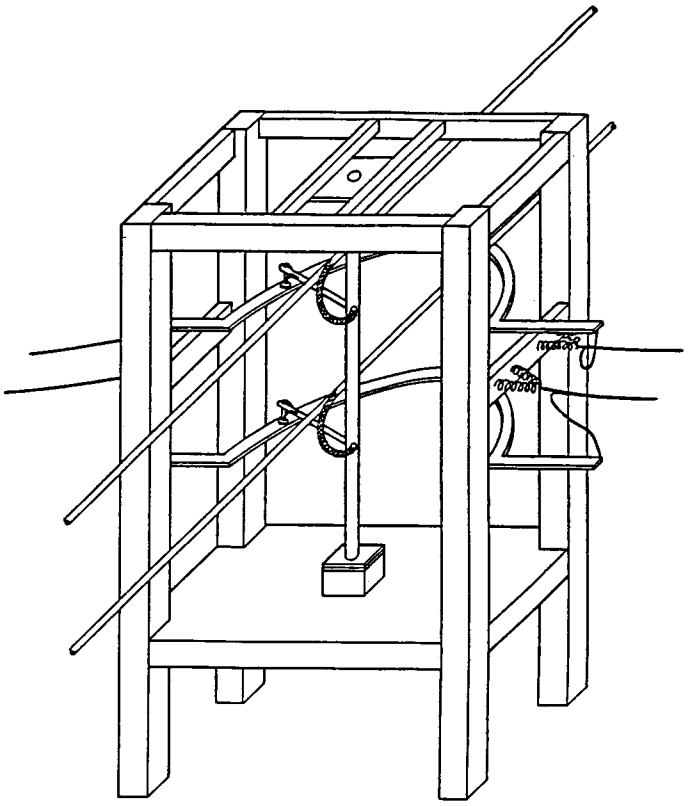

Figure 2. Sketch of the phasing device for the Urbana MST radar antenna.

Table 1

Aspect Sensitivity dB/deg	Apparent zenith angle deg
0	1.610
0.2	1.534
0.4	1.461
0.6	1.391
0.8	1.323
1.0	1.258
1.2	1.196
1.4	1.137
1.6	1.081
1.8	1.027
2.0	0.976
2.2	0.928
2.4	0.882
2.6	0.838
2.8	0.797
3.0	0.758

pointing angle of 1.13 deg corresponds to an aspect sensitivity of about 1.4 dB/deg, in agreement with measurements using steerable antennas. This calibration procedure was repeated for 2 off-axis pointing directions, and the results are shown in Figure 3. The spread of the points is primarily due to geographic separation of the radiosonde station, Peoria, from the Urbana radar.

Using averaged apparent steering directions, eastward and northward winds were calculated for special radar runs simultaneous with 14 balloon launches at Peoria and results are presented in Table 2. Overall, agreement is quite good, with the differences perhaps due to spatial separation between the sites.

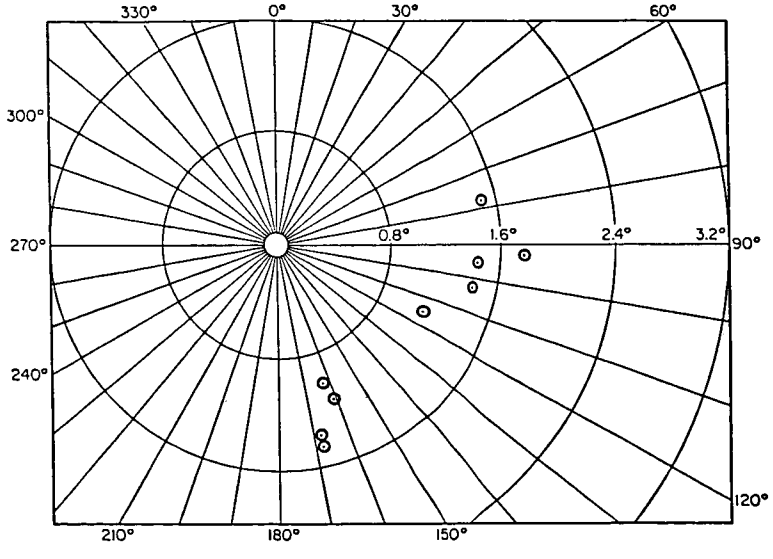

Figure 3. Derived pointing directions for the Urbana array.

Table 2

Derived wind components at Urbana
using two antenna pointing directions.
Theta1 = 18.63 Phi1= 1.3580
Theta2 = 72.96 Phi2= 1.2084

12 KM		13.5 KM		15 KM		16.5 KM		18 KM	
URBANA	RAWIN	URBANA	RAWIN	URBANA	RAWIN	URBANA	RAWIN	URBANA	RAWIN
-.5873	-1.446	1.5808	1.0404	2.8033	1.4338	2.3258	3.3039	2.3131	.15253
11.125	17.339	13.539	19.462	14.356	14.519	12.766	12.593	10.103	8.7386
5.5465	2.5889	3.5606	.53753	2.8057	-.5222	2.1243	-.2309	3.8776	3.9760
24.164	22.038	21.892	21.383	18.765	17.092	14.875	12.847	9.9010	6.6173
-2.198	2.8252	-2.257	-.1694	.08998	-3.100	-.9411	-.3125	-1.154	-2.915
19.799	17.837	18.216	16.459	14.176	13.231	9.5989	9.2747	5.4083	4.8515
5.7387	5.4837	4.2904	-.4858	3.9420	-.2071	3.8307	-1.925	1.4106	-1.619
31.344	37.774	27.477	15.632	22.764	10.407	17.886	10.199	11.754	7.0154
15.674	17.164	12.025	2.0885	8.2250	2.1394	3.4321	1.7042	1.4943	-.1256
15.383	18.790	15.417	14.126	13.891	10.065	7.9296	8.5212	7.4322	3.5978
4.2922	4.3600	1.9227	-2.027	-.1922	-.4517	-1.961	-.0696	-2.951	-3.140
19.845	17.474	17.599	14.317	13.369	9.7595	9.4240	9.7397	7.3270	7.0525
-2.397	-.0249	-1.770	.99704	-2.905	-2.734	-4.350	-2.185	-3.555	-2.491
6.8860	8.4099	9.1101	11.948	9.6625	11.365	7.8260	8.9984	5.2935	4.4955
-3.817	-6.986	-4.930	-7.927	-6.513	-4.134	-4.205	-3.159	-2.846	-4.901
1.3133	1.3707	2.2294	5.4140	2.4217	6.1854	3.2352	4.6962	2.5401	2.83
-8.342	-11.82	-7.964	-11.41	-5.263	-6.792	-3.824	-5.471	-2.110	-2.613
1.0480	2.1902	1.9593	5.6119	4.3792	5.5951	4.7528	5.9317	5.7361	6.1581
-12.10	-11.10	-12.09	-9.506	-9.781	-7.917	-7.884	-6.163	-4.251	-3.703
-1.076	-2.895	.45044	7.2896	3.7955	7.4039	4.8583	6.6538	3.2644	1.8060
-11.49	-12.62	-11.89	-8.592	-10.02	-5.854	-7.837	-2.884	-4.609	-6.105
4.8336	9.0953	4.7323	10.229	5.1024	9.8518	4.2017	7.1716	5.3166	3.8154
-7.397	-14.67	-9.865	-8.368	-10.04	-5.991	-4.389	-6.240	-5.249	-4.971
7.4801	4.2345	8.1176	11.085	6.2928	10.673	5.2882	4.3031	3.4041	4.4764
-22.60	-15.88	-20.50	-10.44	-8.912	-1.524	-.5903	-1.152	-3.218	-5.137
28.369	23.326	24.408	19.578	20.483	14.168	16.244	14.714	9.1429	7.0708
-2.867	2.0799	-1.886	-4.536	.16551	-.9604	-1.210	-6.753	-1.443	-.3137
27.989	39.555	32.225	24.645	26.251	26.192	20.176	16.631	13.200	3.5863

7.1.3 DETERMINATION OF U, V, AND W FROM SINGLE STATION DOPPLER RADAR RADIAL VELOCITIES

W. L. Clark, J. L. Green, and J. M. Warnock

Aeronomy Laboratory
National Oceanic and Atmospheric Administration
Boulder, CO 80303

INTRODUCTION

The ST/MST clear-air Doppler radar, or wind profiler, is becoming an important tool in observational meteorology because of its capability to remotely observe dynamic parameters of the atmosphere. However, there are difficulties, which have long been recognized in work with precipitation sensitive Doppler radars, in transforming the observed radial velocities into meteorological wind components. As WALDTEUFEL and CORBIN (1979) put it "... the problem lies in the fact that one would like to know as much as possible about the wind vector field, whereas a single-Doppler radar yields only one wind component, the radial. Every attempt to gain some knowledge of the vector field, therefore, must compound the data field with additional hypotheses or simplifications." In this paper, we review how this problem has been treated in the past, and recast some of the analysis to a form more suited to the high elevation angle, fixed beam ST radar profiling techniques. We then examine the diagnostic abilities of a number of fixed beam configurations with reference to a linear wind field. The results, in conjunction with other work which treats problems such as the effects of finite sample volumes in the presence of nonhomogeneous atmospheric reflectivity (e.g., KOSCIELNY et al., 1984), have implications important to the design of both individual MST/ST radars and MST/ST radar networks.

BACKGROUND

The use of pulse Doppler radar to measure horizontal winds seems to have been first suggested in the literature by PROBERT-JONES (1960) in connection with a 3-cm precipitation sensitive system. LHERMITTE and ATLAS (1961) suggested the VAD (velocity azimuth display) method of retrieving the mean horizontal velocity from radial velocity data taken in horizontal circles centered along the vertical of the radar site. CATON (1963) and BROWNING and WEXLER (1968) confined the analysis to a horizontal plane to deduce mean convergence, stretching and shearing deformation as well as the mean horizontal velocities from VAD observations. All of these authors treated only the stratiform situation, where $\partial w/\partial x = \partial w/\partial y = 0.0$.

EASTERBROOK (1975) examined the processing of data in a conical sector, wherein values are estimated at a point not centered on the radar. In this case, although five parameters of the wind field can be extracted, the mean horizontal velocity is contaminated by vorticity and cannot be independently determined.

The papers by WOODMAN and GUILLEN (1974) describing results using the Jicamarca incoherent-scatter radar, and GREEN et al. (1975) describing the results from the prototype VHF ST wind profiling radar at Sunset, Colorado, mark the arrival in the literature of VHF clear-air Doppler radars as important wind profile measurement tools. These radars are generally fixed-multibeam systems, utilizing large elevation angles consistent with wind height-profiling through the troposphere and into the lower stratosphere, as opposed to the conventional meteorological radars, which usually have a single rotating beam, and utilize low zenith angles consistent with measuring winds at low heights.

Because precipitation sensitive Doppler radars work under conditions of relatively high signal to noise, a practical radar may utilize a rotatable dish antenna. Then it is natural to apply data-redundant least squares techniques taking advantage of the easily produced circular symmetry, such as the VAD technique (BROWNING and WEXLER, 1969). Although clear-air Doppler radars must work with the much poorer signal-to-noise ratio provided by echoes from irregularities in the refractive index of the air itself, special high performance clear-air radars are able to create sufficient power-aperture by using very high power to allow use of a rotatable dish antenna. Under these conditions, VAD techniques can be used in clear air, as demonstrated by PETERSON and BALSLEY (1979). They used the Chatanika 23 cm Doppler radar to compare the accuracy of VAD, VED (velocity elevation display), and direct vertical probing in measuring w, the vertical wind component. They found direct measurement with the vertical beam superior to the other two methods.

With typical ST radars, however, the power-aperture requirements couple with economic considerations to dictate large, immobile antennas for economical systems. It is not practical to steer these antennas by physically moving them, and though electronic beam steering methods are available (GREEN et al., 1984, CLARK and GREEN, 1984, FUKAO et al., 1985), they have not yet been generally applied. Thus, each beam position is expensive to implement, so that economical ST systems are designed to obtain the minimum amount of data to measure the wind components with as little bias as possible.

CLARK et al. (1985) show the significant bias reduction obtained in u, v estimates over mountainous terrain obtained by adding a vertical beam to measure w. It will be apparent from the next section that the addition of additional beams can reduce the bias even further when stratiform conditions prevail. However, as discovered in the previous work with precipitation sensitive radars, it is not possible to eliminate bias completely with single-Doppler radar techniques. The following discussion will try to clarify the nature of this bias, and serve as an aid in design of economical ST radar systems.

THE GENERAL SCALING EQUATION FOR A LINEAR WIND FIELD

We adopt the usual Cartesian coordinate system x, y, z, representing distances to the east, north and zenith, respectively, with origin at the center of the radar antenna (Figure 1). The primary assumption applied to the wind field is linearity in the region about (x_o, y_o, z_o), the point in space at which the flow parameters are to be determined. The vector distance to a measuring volume from the antenna is defined as

$$\vec{r} = x\hat{i} + y\hat{j} + z\hat{k}$$

where $\hat{i}$, $\hat{j}$, and $\hat{k}$ are the usual unit vectors. The wind vector at $\vec{r}$ is

$$\vec{v} = u\hat{i} + v\hat{j} + w\hat{k}$$

where it is assumed

$$\begin{aligned} u &= u_o + (x-x_o)u_x + (y-y_o)u_y + (z-z_o)u_z \\ v &= v_o + (x-x_o)v_x + (y-y_o)v_y + (z-z_o)v_z \\ w &= w_o + (x-x_o)w_x + (y-y_o)w_y + (z-z_o)w_z \end{aligned} \qquad (1)$$

The x, y, z subscripts denote partial differentiation (e.g., $u_x = \partial u/\partial x$); u_o, v_o, and w_o are the primary parameters we wish to measure, being the values of u, v, and w at the point (x_o, y_o, z_o).

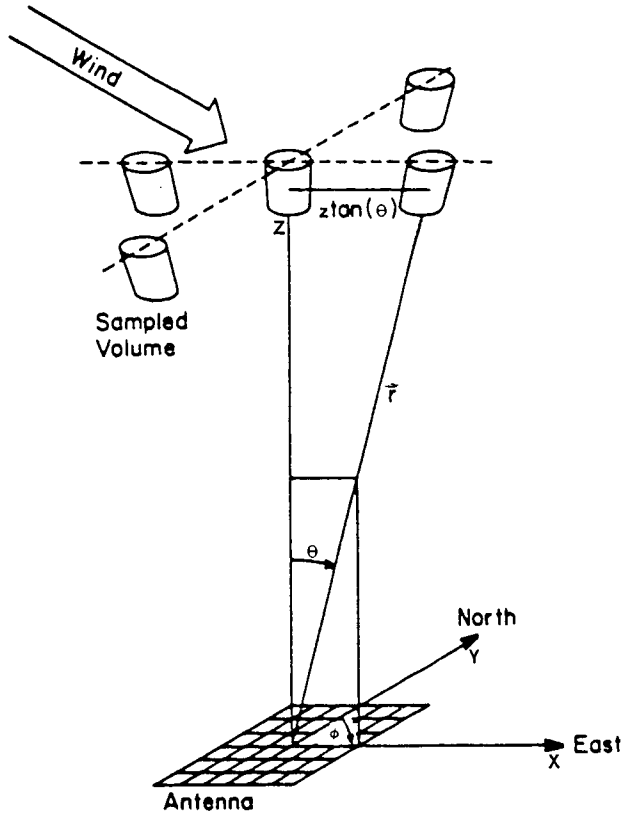

Figure 1.

Often at this point in the analysis, a transformation to polar coordinates convenient to the operation of a radar is made. Instead, we will stay in Cartesian coordinates to facilitate the analysis. If we intend to make measurements of wind velocity at points (x_o, y_o, z_o) for large ranges not centered on the radar antenna, it would be necessary to consider the curvature of the earth (DOVIAK and ZRNIC, 1984, p 261). Here we confine analysis to profile measurement directly above the antenna, where z is identical to height.

The mean radial velocity v_r observed within a sample volume at a given $\vec{r}$ is related to the wind vector $\vec{v}$ there by the dot product

$$rv_r = \vec{v}\cdot\vec{r} = ux + vy + wz \tag{2}$$

Inserting the linear flow relations of equation (1) into equation (2), we get the general relation relating the parameters of the linear wind field, which we would like to measure, to the observed v_r's:

$$\begin{aligned} rv_r = {} & (u_o + u_x(x-x_o) + u_y(y-y_o) + u_z(z-z_o))x \\ & + (v_o + v_x(x-x_o) + v_y(y-y_o) + v_z(z-z_o))y \\ & + (w_o + w_x(x-x_o) + w_y(y-y_o) + w_z(z-z_o))z \end{aligned} \tag{3}$$

Equation (3) is an arrangement of the general scaling equation convenient for developing sample location strategies. Much of the rest of the paper is concerned with describing some of these strategies. First, however, we will examine a second arrangement of the scaling equation in which general characteristics of solution are more apparent:

$$\begin{aligned} rv_r = {} & x[u_o - u_x x_o - u_y y_o - u_z z_o] \\ & + y[v_o - v_x x_o - v_y y_o - v_z z_o] \\ & + z[w_o - w_x x_o - w_y y_o - w_z z_o] \\ & + x^2[u_x] \\ & + y^2[v_y] \\ & + z^2[w_z] \\ & + xy[u_y + v_x] \\ & + xz[u_z + w_x] \\ & + yz[v_z + w_y] \end{aligned} \tag{4}$$

This is a linear equation with nine parameters (the quantities in brackets), which may be solved from simultaneous observation of v_r at nine spatially independent locations. Of these nine parameters, only three correspond directly to the twelve parameters that specify the linear wind field. The other six are couples of these parameters, so that, in general, only linear combinations may be found. Specifically, solution of equation (4) for any given position (x_o, y_o, z_o) provides: 1) the parameters necessary to describe the divergence of the flow $\nabla \cdot \vec{v} = [u_x] + [v_y] + [w_z]$; 2) the additional three parameters $[u_y + v_x]$, $[u_z + w_x]$, and $[v_z + w_y]$ necessary to specify the deformation of the flow; and 3) parameters containing u_o, v_o, and w_o coupled inextricably with spatial derivatives.

PROFILING: MEASUREMENT OF THE WIND FIELD ALONG THE VERTICAL

In volumes directly above the radar we have that $x_o = y_o = 0.0$, so equation (3) becomes

$$\begin{aligned} rv_r = {} & x[u_o + xu_x + yu_y + (z-z_o)u_z] \\ & + y[v_o + xv_x + yv_y + (z-z_o)v_z] \\ & + z[w_o + xw_x + yw_y + (z-z_o)w_z] \end{aligned} \tag{5}$$

Once again, this equation may be rearranged to give

$$\begin{aligned} rv_r = {} & x[u_o - z_o u_z] \\ & + y[v_o - z_o v_z] \\ & + z[w_o - z_o w_z] \\ & + x^2[u_x] \\ & + y^2[v_y] \end{aligned} \tag{6}$$

$$+ z^2[w_z]$$

$$+ xy[u_y + v_x]$$

$$+ xz[u_z + w_x]$$

$$+ yz[v_z + w_y]$$

where the bracketed terms represent the nine parameters that may be evaluated. The difference between this equation and equation (4) is the disappearance of all but the vertical shear terms from the first three parameters, leaving u_o, v_o, and w_o coupled only to u_z, v_z, and w_z, respectively. From the last two terms we see that when the stratiform condition is present (i.e., w_x and w_y may be neglected), u_z and v_z may be evaluated, thus allowing unbiased solution for u_o and v_o.

VERTICAL BEAM MEASUREMENT OF w_o and w_z

Measurements made with a vertically pointing beam are particularly simple to analyze, since they only contain information on two of the linear flow parameters: w_o and w_z. Inspection of the scaling equation with $x = y = 0$ shows that the observed v_r is identically w_o, the vertical velocity component at height z_o. Furthermore, the values of v_r observed at two closely spaced heights, z_o and z_1, yield w_z, so that

$$w_o = v_{ro}$$

$$w_1 = v_{r1} \tag{7}$$

and

$$w_z = \frac{v_{ro} - v_{r1}}{z_o - z_1}$$

Thus a vertically directed beam allows unbiased determination of w_o and w_z in the presence of linear flow.

OBLIQUE BEAMS

Assuming that w_o and w_z have been determined using a vertically pointing beam, we may treat these values as knowns and move them to the left side of the equation. It is then convenient to define the quantity V_r as

$$V_r = rv_r - z[w_o - z_o w_z] - z^2 w_z$$

which contains only known quantities. Then we can write equation (6) as

$$V_r = x[u_o - z_o u_z]$$

$$+ y[v_o - z_o v_z]$$

$$+ x^2[u_x]$$

$$+ y^2[v_y] \tag{8}$$

$$+ xy[u_y + v_x]$$

$$+ xz[u_z + w_x]$$

$$+ yz[v_z + w_y]$$

This is the general overhead scaling equation when the vertical velocity and vertical velocity shear are known or negligible. It has seven parameters, requiring seven spatially independent observations for solution.

ORTHOGONAL VERTICAL PLANES

If measurement of the deformation of the flow is not required we can require all beams to be either in the xz or yz vertical plane. Then either $y = 0$ or $x = 0$ for all beams, so that the fifth term of equation (8) disappears. Under these conditions, equation (8) divides into two independent equations. For $y = 0$

$$\frac{V_r}{x} = [u_o + z_o u_z] + x[u_x] + z[u_z + w_x] \tag{9}$$

and for $x = 0$

$$\frac{V_r}{y} = [v_o + z_o w_y] + y[v_y] + z[v_z + w_y]$$

In each plane, we now have three unknown parameters, requiring three spatially independent observations for solution. Thus, considering both planes and the two vertical beam observations used to evaluate V_r, eight independent observations are needed altogether when using orthogonal vertical planes. This does not mean we need eight different beams, since observations may be independent if they are separated in range along a beam. This technique will be considered in the next section.

SINGLE BEAM ANALYSIS

It would be very efficient if equation (9) could be solved by utilizing observations in three sample volumes along a single beam. However, such a scheme cannot lead to complete solution since z and x are not independent, being related by

$$z = x \operatorname{ctn}\theta$$

where θ is the zenith angle of the beam. For example, in the xz plane substituting for z using this relation yields

$$V_r = x[u_o - z_o u_z] + x^2[u_x + \operatorname{ctn}\theta\,(u_z + w_x)] \tag{10}$$

The number of parameters is thus reduced to two. While u_o is still biased by $z_o u_z$, the stratiform approximation no longer allows solution for u_z, which is now coupled to both u_o and u_x. Thus, neither u_o nor $\vec{\nabla}\cdot\vec{v}$ may be measured in unbiased form in the presence of u_z.

CONSTANT HEIGHT ANALYSIS

Starting again with equation (5), the vertical shear terms may be eliminated if we require that all observations be for $z = z_o$ (i.e., constant height analysis), giving

$$rv_r = x[u_o + xu_x + yu_y] + y[v_o + xv_x + yv_y] + z_o[w_o + xw_x + yw_y] \quad (11)$$

Gathering like terms

$$rv_r = z_o[w_o] + x[u_o + z_o w_x] + x^2[u_x] + xy[u_y + v_x] + y[v_o + z_o w_y] + y^2[v_y] \quad (12)$$

This is a linear equation with six unknowns. The bias to u_o and v_o is now the $z_o w_x$ and $z_o w_y$ terms, respectively, so that once again the stratiform approximation allows solution for u_o and v_o.

USE OF THE VERTICAL BEAM

It is easy to see that for a vertically pointing beam (i.e., $x = y = o$),

$$v_r = w_o \quad (13)$$

Thus, w_o is measured directly, with no bias.

USE OF ORTHOGONAL VERTICAL PLANES

Restricting beam positions such that either $x = 0$ or $y = 0$ splits equation (12) into two independent equations.

$$rv_r - z_o w_o = x[u_o + z_o w_x] + x^2[u_x] \quad (14)$$

and

$$rv_r - z_o w_o = y[v_o + z_o w_y] + y^2[v_y]$$

Thus, two beams in the xz plane plus two beams in the yz plane plus a vertical beam yield $[w_o]$, $[u_o + z_o w_x]$, $[v_o + z_o w_y]$, $[u_x]$, and $[v_y]$.

DISCUSSION AND CONCLUSIONS

The ability of ST radars to measure vertical velocity is unmatched at the present time by any other technique. It is straightforward and without bias, even if the linear wind field assumption is poor. Only under fiscal restraints of the most severe kind, or for very special purposes, should this beam be left out of ST radar systems, since this parameter is not only of general interest, but is necessary to remove bias from u and v measurements (CLARK et al., 1985).

The key parameters to uncoupling terms in the scaling equations are w_x and w_y. Whenever the stratiform condition, which states that these two parameters are negligible, is satisfied, a five-beam ST radar may determine unbiased (with reference to a linear wind field) values of u, v, and w for sample volumes directly above the radar. Furthermore, the divergence and partial deformation of the flow may be determined.

Three-beam systems can determine w and w_z, but are unable to obtain u and v wind components uncontaminated by vertical sheer terms, even when the stratiform condition is satisfied.

REFERENCES

Browning, K. A., and R. Wexler (1968), The determination of kinematic properties of a wind field using Doppler radar, J. Meteorol, 7, 105-113.

Caton, P. G. (1963), The measurement of wind and convergence by Doppler radar, Preprints, Tenth Weather Radar Conf., Washington, DC, Am. Meteorol. Soc., 290-296.

Clark, W. L., and J. L. Green (1984), Practicality of electronic beam steering for MST/ST radars, Handbook for MAP, 14, 253-256.

Clark, W. L., J. L. Green, and J. M. Warnock (1985), Estimating meteorological wind vector components from monostatic Doppler radar measurements: a case study, Radio Sci., 20, 1207-1213.

Doviak, R. J., and D. S. Zrnic (1984), Doppler Radar and Weather Observations, Academic Press, 458 pp.

Easterbrook, C. C. (1975), Estimating horizontal wind fields by two dimensional curve fitting of single Doppler radar measurements, Preprints, 16th Radar Meteorology Conf., Houston, Am. Meteorol. Soc., 214-219.

Fukao, S., T. Sato, T. Tsuda, S. Kato, K. Wakasugi, T. Makkihira (1985), The MU radar with an active phased array system: 1. Antenna and power amplifiers, Radio Sci., 20, 1155-1168.

Green, J. L., J. M. Warnock, R. H. Winkler, and T. E. VanZandt (1975), Studies of winds in the upper troposphere with a sensitive VHF radar, Geophys. Res. Lett., 2, 19-21.

Green, J. L., J. M. Warnock, W. L. Clark, F. J. Eggert, and K. J. Ruth (1984), Modification to the Sunset radar to provide antenna beam steering, Preprint 20th Conf. on Radar Meteorology, 1981, Boston, MA.

Koscielny, A. J., R. J. Doviak, and D. S. Zrnic (1984), An evaluation of the accuracy of some radar wind profiling techniques, J. Atmos. and Ocean Tech., 1, 309-320.

Lhermitte, R. M., and D. Atlas (1961), Precipitation motion...by pulse Doppler, Preprints, Ninth Weather Radar Conf., Kansas City, Am. Meteorol. Soc., 218-223.

Peterson, V. L., and B. B. Balsley (1979), Clear Doppler radar measurements of the vertical component of wind velocity in the troposphere and stratosphere, Geophys. Res. Lett., 6, 933-936.

Probert-Jones, R. (1960), Meteorological use of pulse Doppler radar, Nature, 186, 271-273.

Waldteufel, P., and H. Corbin (1979), On the analysis of single-Doppler radar data, J. Appl. Meteorol., 18, 532-542.

Woodman, R. F., and A. Guillen (1974), Radar observations of winds and turbulence in the stratosphere and mesosphere, J. Atmos. Sci., 31, 493-505.

7.1.4 A 405-MHz, 5-BEAM PHASED ARRAY ANTENNA

Daniel C. Law

NOAA
Wave Propagation Laboratory
Boulder, CO 80303

The Wave Propagation Laboratory has completed the design and construction of a phased array antenna for use at 405.25 MHz for atmospheric wind profiling. The steering geometry of the sequentially switched beam is shown in Figure 1.

The Yagi-Uda antenna elements are arranged on a square grid whose axes are 45° with respect to the cardinal directions. For a given steering angle this allows an element spacing $\sqrt{2}$ larger than that required for a broadside steered array. This feature helps minimize element interaction and reduces the number of elements required to populate a given aperture. This geometry is shown in Figure 2.

By constraining the phase difference between rows of identically phased elements to an even, integral submultiple of 360°, symmetries appear in the phasing maps which reduce the switching hardware. In this design, for example, the element spacing, X of Figure 2, is .91 λ and $\Delta\phi$ is 60° resulting in an oblique beam direction of 15° from vertical. Only 15 RF coaxial transfer switches are used to synthesize the required 18 phase combinations for north, east, south, and west steering. These 18 signals are labeled A through R in Figure 3.

The vertical beam is generated by switching around the four beam circuitry of Figure 3 resulting in identical phasing on all of the elements. Requiring 36 RF coaxial SPDT switches, the vertical beam alone is more expensive than the four cardinal beams.

After the 18 signals are synthesized they are split and distributed about the array while maintaining proper phasing because of the symmetries. Uneven power splitter/combiners are used for amplitude tapering. A schematic of the whole antenna is shown in Figure 4, and a map of the quasi-circular array in Figure 5 shows the placement of seven each of the 18 phases for a total of 126 elements. The antenna characteristics are listed in Table 1.

Computer simulations were employed in the design process. Antenna patterns from the simulations are shown for the north and vertical directions in Figure 6. Antenna pattern measurements by aircraft are planned to verify the performance.

A NOAA Technical Memorandum detailing the design and computer techniques is planned for 1986.

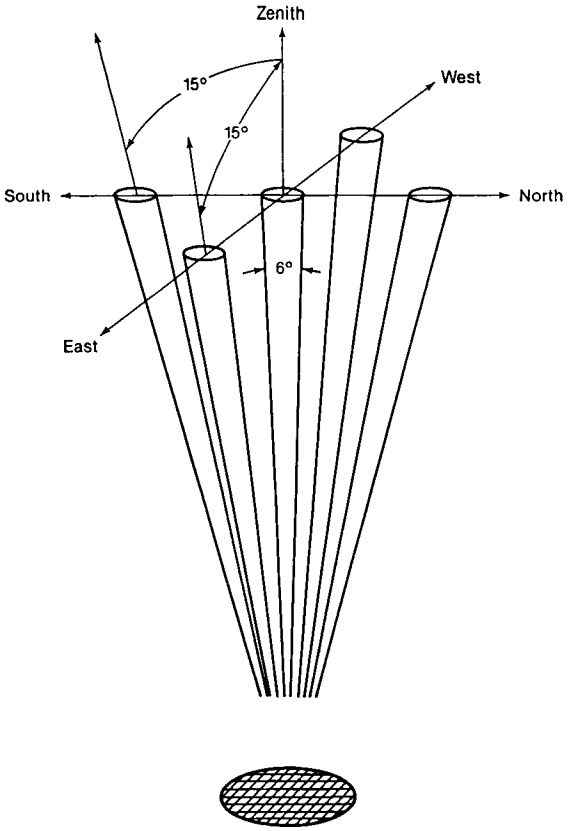

Figure 1.

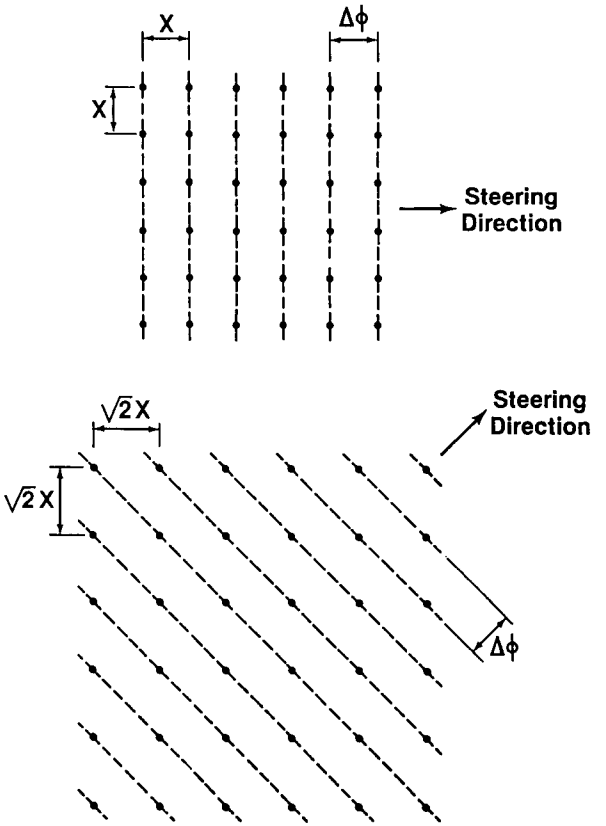

Figure 2.

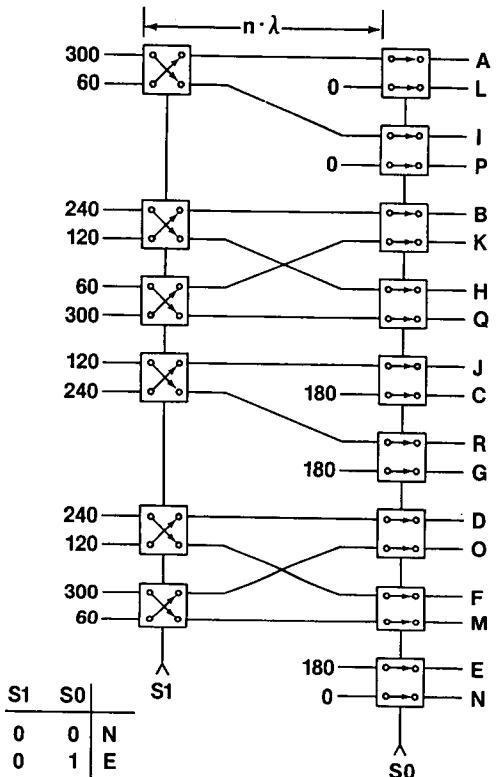

4 BEAM SWITCHING
(SOUTH PHASING POSITIONS)

Figure 3.

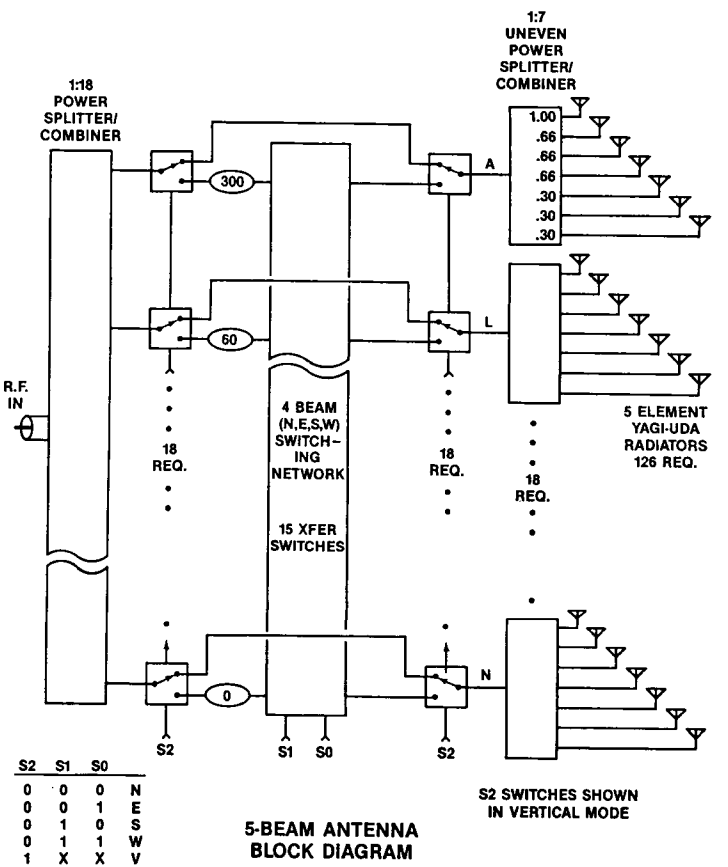

5-BEAM ANTENNA
BLOCK DIAGRAM

Figure 4.

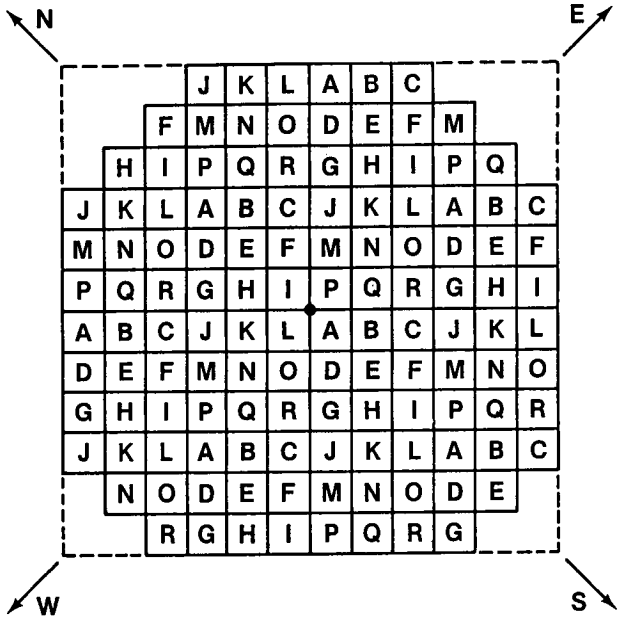

Figure 5.

Table 1

405-MHz phased array antenna

Number of steering directions:	5
Oblique beam directions:	4
Azimuth:	0°, 90°, 180°, 270°
Elevation:	75°
Gain:	30 dBi
One-way 3 dB beam width:	6°
Effective aperture:	44 m^2
Peak power:	60,000 W
Average power:	6,000 W
Technology:	126 5-element Yagi-Uda radiators
	51 RF coaxial switches with indicators
	1 1:18 high power reactive splitter/combiner
	18 1:7 uneven reactive splitter/combiners
	low loss foam distribution cables

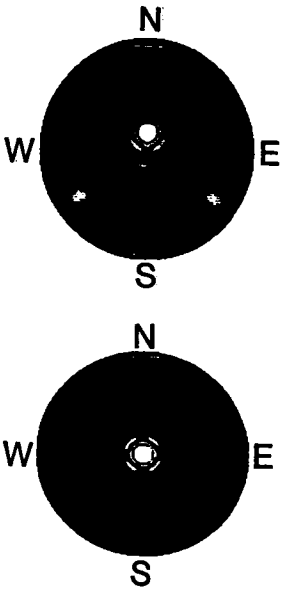

Figure 6.

7.2.1 LOW-ALTITUDE COVERAGE OF ST RADARS

W. L. Ecklund

Aeronomy Laboratory
NOAA
Boulder, CO 80303

Clear-air ST radars are now widely used for atmospheric research and wind profiling. Most attention to date has been directed toward extending the altitude coverage of these radars as high as possible. It is also desirable to extend the coverage as low as possible, but low altitude coverage has not received much attention (probably because it is not very glamorous). Any improvement in the low altitude coverage of existing wind profiling radars would be useful. In this note, we list the approximate lower limits of some existing ST radars, and then briefly speculate on what establishes these limits.

Table 1 lists the low altitude coverage (height above ground) of a number of different radars. The values for the WPL (NOAA-Wave Propagation Lab) radars were obtained from STRAUCH (private communication). The table shows that the 915-MHz radar has the best low altitude performance. The 50-MHz radars show a fairly wide range of low altitude coverage depending on antenna size, pulse width and transmitter configuration. The 800-meter coverage in France was obtained by using the driver stage of the transmitter (peak power about 3 kW) instead of the final stage (peak power about 40 kW). Tests in France showed that the minimum system range was about 500 meters when transmitting into a dummy load. The receiver in the Liberal, Kansas, 50-MHz radar was saturated out to a range of about 2000 meters when transmitting 40 kW peak power pulses into the antenna.

The results from France suggest that decreasing the peak power might improve low altitude performance. It is clear that system recovery time is increased when the transmitter is switched from a dummy load to the antenna. This may be due to internal reflections in the antenna or to intense nearby ground clutter. It is suspected that internal reflections may be the problem, since the low altitude coverage of the Liberal, Kansas, radar (100 by 100 meter antenna) is poorer than the coverage of the Colorado network radars (50 by 50 meter antennas). System recovery time has also been observed to be limited by significant amounts of nearly coherent energy leaking from the transmitter into the receiver after the main transmitter pulse is turned off. This problem might be solved by using a better TR/ATR switch or by using a transmitter with a significantly wider bandwidth.

Table 1

Radar location (organization)	Freq. (MHz)	Antenna (m^2)	Pulse width (microsec.)	Low alt. (always)	Coverage (m) (sometimes)
Denver, CO (WPL)	915	100	1	300	200
Liberal, KS (AL)	50	10,000	2,4	-	2100
Colorado (WPL)	50	2500	3	1700	1400
France (LSEET)	48	2500	1	-	800

7.2.2 FURTHER CONSIDERATIONS REGARDING ANTENNA LAYOUT FOR THE UK MST RADAR

A. J. Hall and J. D. Gilbert

Rutherford-Appleton Laboratory
Chilton, Didcot, Oxon, UK

In the original description of the proposed UK MST radar, MAP Handbook 9, pp 387-397, an arrangement for powering 100 antenna subarrays from 10 transmitter modules was described having octantal symmetry. The arrangement permitted a very approximate radial power tapering for sidelobe suppression with no waste of available RF pulse power.

It has been appreciated since then that a better focussing may be achieved in the receive mode by any of several different arrangements without reducing the effectiveness of the transmission scheme.

One such connection scheme is shown in Figure 1. By tailoring the contributions of signal from the elements within approximate concentric circles, Figure 2, a more acceptable approach to a Dolph-Tchebycheff tapering may be achieved in the receive mode.

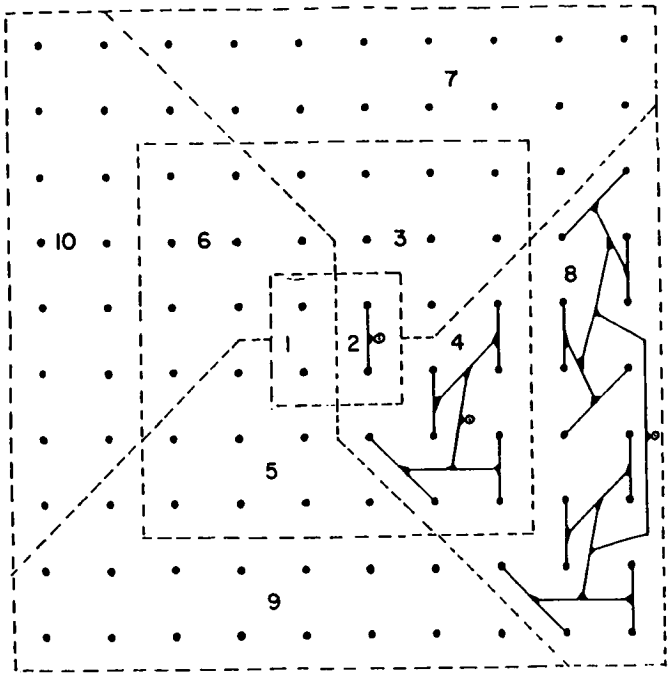

Figure 1. Plan of 10 x 10 array of quads (4 yagis) each numbered region powered from one transmitter amplifier unit.

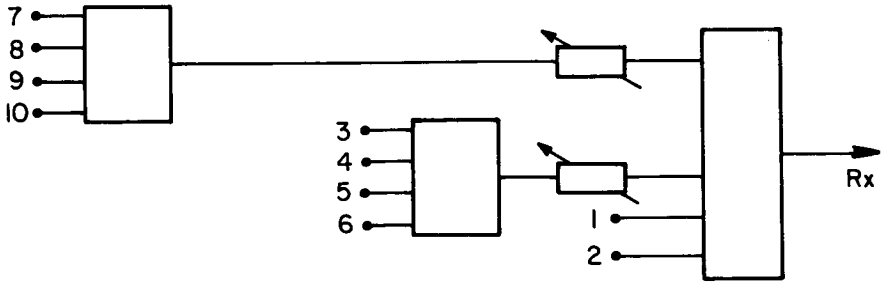

Figure 2.

7.3.1 THE GRID ARRAY ANTENNA

W. L. Ecklund

Aeronomy Laboratory
NOAA
Boulder, CO 80303

The purpose of this note is to call attention to the grid array as a possible useful antenna design for UHF clear-air radars. This type of antenna integrates radiating elements and the feed network into a single structure so that a fairly large array can be driven from a single feed point. TIURI et al. (1974) described the chain antenna and parallel strings of chain antennas that they called grid antennas. Their designs were fed at one end and terminated at the other so that the beam was scanned along the chain as the frequency was varied. They built and tested a 635-MHz grid array using this traveling wave design. A more extensive analysis of the grid antenna is given by CONTI et al. (1981). They used the array as a resonant (broadside) radiating structure at fixed frequency. In addition, they devised a way to taper the array illumination for sidelobe reduction.

Figure 1 has been adapted from CONTI et al. (1981) to demonstrate the basic principle of the grid array. Conductors are arranged above a ground plane in a repeating, staggered array of connected rectangles. Each rectangular element is approximately one by one-half wavelength in size. The arrows in Figure 1 show the currents on the conductors at resonance. Note that the vertical elements are all in phase, and that the currents on the horizontal conductors reverse at one-half wavelength intervals. This causes the vertical field components to add and the horizontal components to cancel, forming a vertically polarized beam in the far field. The grid array shown in Figure 1 can be expanded in both vertical and horizontal directions about the feed point by adding additional rectangular conductors. The array illumination can be tapered by making the central conductors larger (lower impedance) than those near the edges.

The grid array antenna would seem to be useful for UHF clear-air radar applications where a single broadside beam is required. The design eliminates the feed network and would provide a thin, panel-like antenna that could be easily built and transported.

REFERENCES

Conti, R., J. Toth, T. Dowling, and J. Weiss (1981), The wire grid microstrip antenna, IEEE Trans. Antennas Propagat., AP-29, 157-166.

Tiuri, M., S. Tallgrist, and S. Urpo (1974), Chain antenna, Int. IEEE/AP-S Symp. Dig., 274-277.

7.4.1 SIMULTANEOUS MULTIBEAM SOUNDING OF WIND AND TURBULENCE

E. Brun and M. Crochet

LSEET
Toulon 83100, FRANCE

and

W. L. Ecklund

NOAA
Boulder, CO 80303

INTRODUCTION

Most clear-air radars use an antenna with either a few fixed beam positions or one that can be steered to a number of beam positions, one position at a time. For spatial studies of parameters that can change rapidly, such as C_n^2 (related to turbulence) or wind fields influenced by short-period waves, these conventional radars may be severely limited. The problem is that the fixed-beam radars do not cover enough positions and the steerable radars may not be able to cover the entire field of interest in a short enough time period. In this report, we present preliminary results from a brief experiment that suggests a way to overcome some of these space-time problems in clear-air radar research.

In September 1984, a typical clear-air radar antenna located in France was modified in a simple way to produce a number of beams simultaneously. In the following paragraphs, we describe the radar, the modifications and the resulting beam patterns. We then show spectra obtained with the multibeam array and present some results on the spatial variations of reflectivity. Finally, we summarize both the positive and negative aspects of using a multibeam antenna array for clear-air radar studies.

EXPERIMENTAL ARRANGEMENT

A 47.8-MHz clear-air radar (Provence) was installed at Termes d'Armagnac (West of Toulouse) as part of a coordinated experiment called Fronts 84. The radar used a 50 by 50 meter antenna comprised of 16 strings of coaxial-collinear antennas and phase shifters, so that the beam could be directed either vertically or 15 degrees east of the zenith. The 16 strings of antennas were spaced one-half wavelength apart, and groups of 4 adjacent antennas were fed by separate branch networks and phase shifter sets that were in turn fed by the main 4 to 1 branch and phase shifter set. In this way, antennas 1 to 4, 5 to 8, 9 to 12 and 13 to 16 were fed by separate branches.

In this experiment, the connectorized feed lines were changed so that the main 4 to 1 network and phase shifters fed only 4 selected strings of antennas out of a total of 16. For a spacing of 2 wavelengths between strings, we connected antennas 1, 5, 9 and 13, and for a spacing of 2.5 wavelengths, we used antennas 1, 6, 11 and 16. Figure 1 shows the calculated multibeam antenna patterns for 3 of the arrangements. The top pattern is for a spacing of 2 wavelengths with all four antennas in phase, and the middle pattern is also for a 2-wavelength spacing but with a progressive phase shift between antennas (the same phase shift that is used to form the 15-degree east beam in the full array). The bottom pattern is for a 2.5 wavelength spacing with all antennas in phase.

EXAMPLES OF MULTIBEAM DOPPLER SPECTRA

The data presented here were obtained over a one-day period (9 to 10 September, 1984). The radar was operated with all 3 beam configurations shown in Figure 1, and representative Doppler power spectra from each configuration are shown in Figure 2. The wind was blowing from the west during this period, and the spectral peaks due to each antenna beam are clear in the spectra displayed in Figure 2. These spectra were obtained at different times and heights, and the radial velocity scales are not the same on all three spectra. Note that the largest peak in each spectrum has been set to full scale. The point we want to make with Figure 2 is that if one has knowledge of the wind profile in the plane of the beams it is possible to identify the Doppler shift, spectral width and echo power associated with each beam by the relative position of each peak on the Doppler spectrum. The wind profile can be obtained from the oblique beam of the full array or by some other method such as balloon sounding.

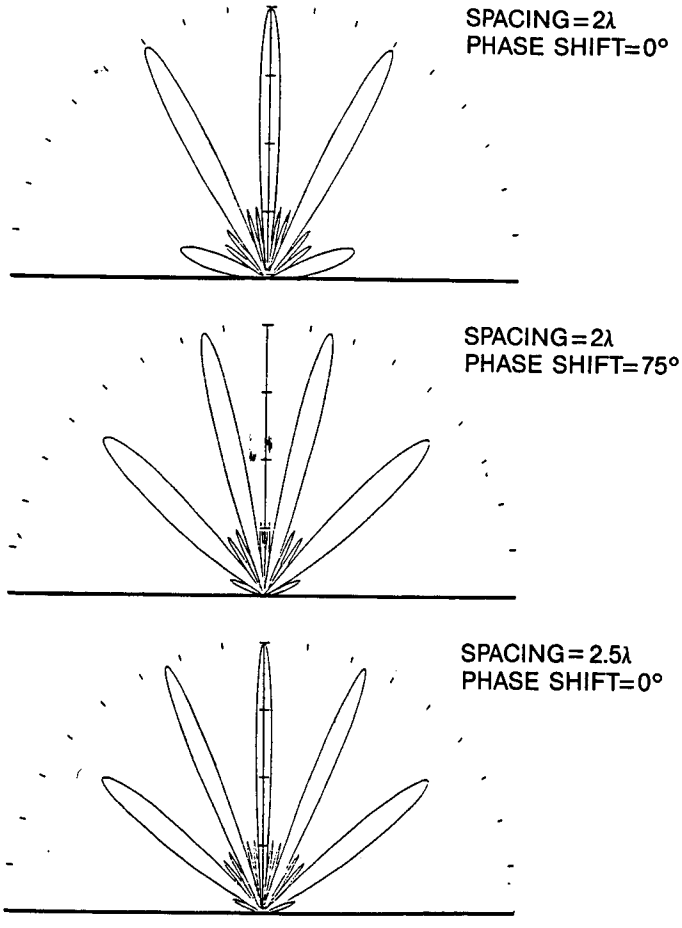

Figure 1.

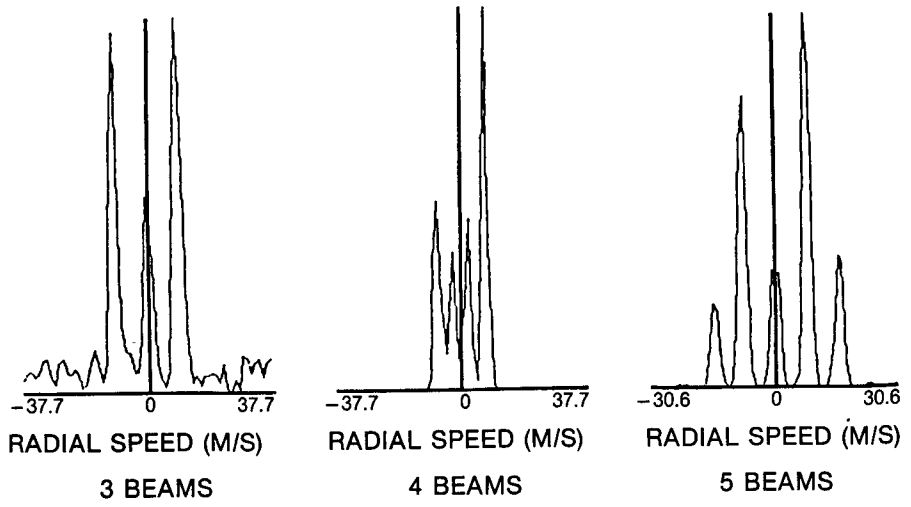

Figure 2.

EXAMPLES OF SPATIAL VARIATIONS IN ECHO POWER

For most of the short experimental period, we used the 5-beam configuration shown at the bottom of Figure 1. In Figure 3, we show a sample spectrum obtained with this arrangement. The peaks in the spectrum have been labeled 1 through 5. Peaks 1 and 5 are from the symmetrical antenna beams with zenith angles of about 52 degrees and peaks 2 and 4 are from the symmetrical beams with zenith angles of about 23 degrees. Peak 3 corresponds to the vertical beam.

Figure 4 shows a set of 3 spectra obtained over a 17-minute period that demonstrate large differences in the relative echo power observed in peaks 1 and 5 (peaks 2, 3, and 4 are just visible in the spectrum taken at 7:45 UT). Since the spectra were obtained from a range of 7 km, peaks 1 and 5 correspond to scattering volumes at a height of about 4.3 km and with a spacing of about 11 km horizontally (peak 5 to the west, peak 1 to the east). In the first spectrum at 7:28 UT, peak 5 is larger than peak 1 by a factor of about 5 in power, at 7:43 UT peak 5 is smaller than peak 1 by a factor of 5 and at 7:45 UT peak 5 is slightly larger than peak 1. These differences in echo power at two regions separated by about 11 km horizontally are very dynamic, suggesting a good deal of spatial structure in the related turbulence refractivity structure constant (C_n^2).

The spatial variations of echo power in 2 sets of symmetrical beams are displayed as a function of time for a 12-hour period in Figure 5. The ratio of echo power from peaks 1 and 5 is shown in the top plot, and the ratio of peaks 2 and 4 (Figure 3) is shown at the bottom. Ratios smaller than 1 have been inverted and assigned negative values. Peaks 2 and 4 correspond to scattering volumes at a height of about 6.4 km, separated by a horizontal distance of about 5.4 km. Peaks 1 and 5 correspond to volumes at about 4.3-km altitude, separated by about 11 km. Since the scattering volumes in the upper and lower plots are not at the same heights, we do not expect to see similarities in the 2 ratios due to patterns of enhanced C_n^2 moving across the beams. We note, however, that both ratios range from nearly plus to minus 10 showing that the relative echo power in each pair of symmetrical beams varies by a factor of 100 (20 dB) during the 12-hour period.

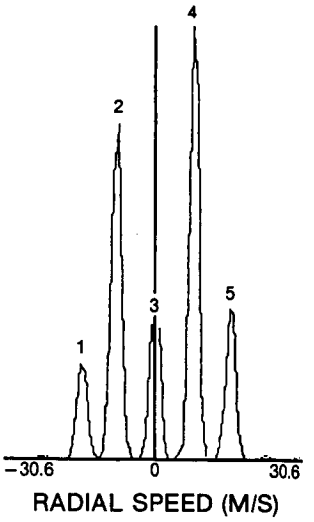

Figure 3.

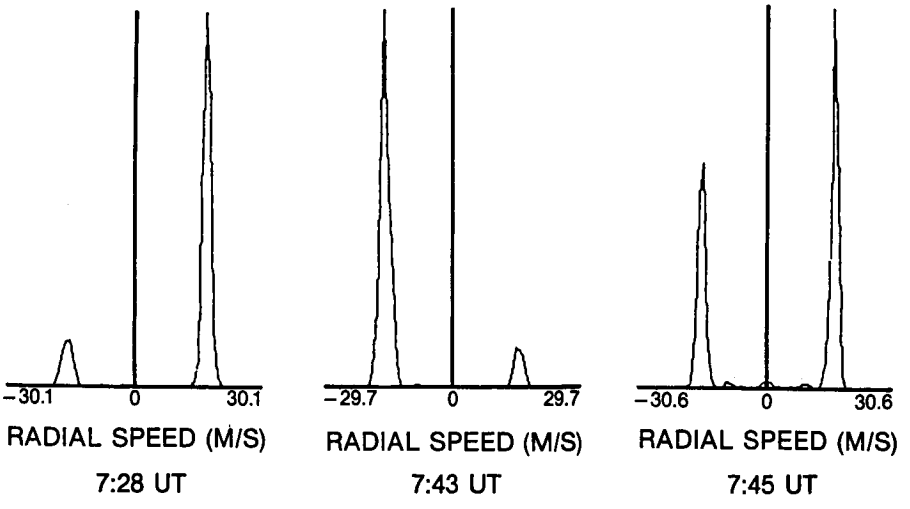

Figure 4.

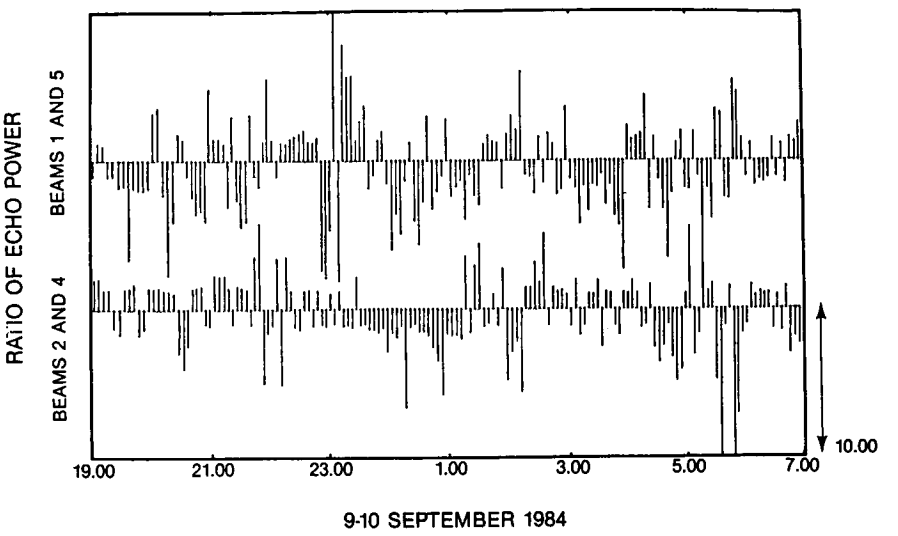

Figure 5.

EXAMPLES OF HEIGHT VARIATIONS IN ECHO POWER

In addition to the dynamic horizontal differences in echo power just presented, the multibeam radar also shows interesting differences in echo power on the different beams as a function of altitude. Figure 6 shows power spectra as a function of range taken with the 3-beam antenna. The central peak is from the vertical beam and the peaks on either side are from the symmetrical beams with zenith angles of about 30 degrees (see Figure 1). Note that the relative echo power in the vertical and oblique beams changes markedly as a function of height. At a range of 2.8 km, the oblique peaks dominate the vertical peak and at 5.2 km the opposite is true. This simultaneous comparison of vertical and oblique reflectivities can be used to infer the relative contributions of specular reflection and turbulent scatter as a function of height. The oblique peaks in Figure 6 correspond to heights lower than the range shown on the ordinate because of the slant range correction required for the 30-degree zenith angles of the oblique beams.

Figure 7 shows power spectra as a function of range taken on the 4-beam antenna. The spectra on the left were taken with a transmitted pulse length of 16 microseconds (2.4 km range resolution) and the spectra on the right were taken with 1-microsecond pulses (150 m resolution). Note that the 4 spectral peaks corresponding to the 4 beams are clearly evident at the lower heights in the left panel, but in the right panel the peaks are intermittent with height. This seems to indicate that the observed scattering is due to relatively thin layers of enhanced reflectivity. Since the spectra in the right panel of Figure 7 were taken with 150-meter resolution but are displayed at only 600-meter range intervals, it is not possible to trace the differences in the peaks at the inherent 150-meter resolution as a function of height. This example does, however, demonstrate the possibility of using the multibeam system to explore reflectivity structure with good height resolution.

SUMMARY

In this report, we have shown some preliminary results from a clear-air radar modified to operate with simultaneous multiple antenna beams. We think

this approach has promise for special studies of turbulence and waves that require good spatial and temporal coverage. The technique should be ideal for momentum flux measurements. If one of the multiple beams is directed vertically, it is possible to compare both echo power and radial velocity on vertical and oblique beams at the same time. We have shown how an existing full array can be simply modified to provide multiple beams. It should also be pointed out that if the wind in the plane of the beams can be obtained by some other method, the multibeam antenna can be very simple, consisting of only a few antenna strings. This antenna would be inexpensive and easy to transport and install. Addition of a second set of antennas perpendicular to the first set would give up to 4 simultaneous azimuths if 2 transmitters were employed. In addition, the relatively low elevation angles of some of the symmetrical beams provide lower altitude coverage than is available from the normal, nearly vertical beams (but with poorer altitude resolution).

A major disadvantage of the multibeam array for clear-air radar use is the reduced sensitivity due to the decreased antenna collecting area. A simple antenna, such as the one used in this experiment, would probably limit the height coverage of most ST radars to the lower troposphere. Another problem is the requirement to know the wind in the plane of the antenna beams. It might also be difficult to uniquely assign all of the spectral peaks to their corresponding antenna beams if the wind field changes rapidly with height. The last problem is that multibeam data reduction is complicated by the fact that different peaks in a spectrum taken at a fixed range correspond to different heights depending on the corresponding multibeam zenith angles.

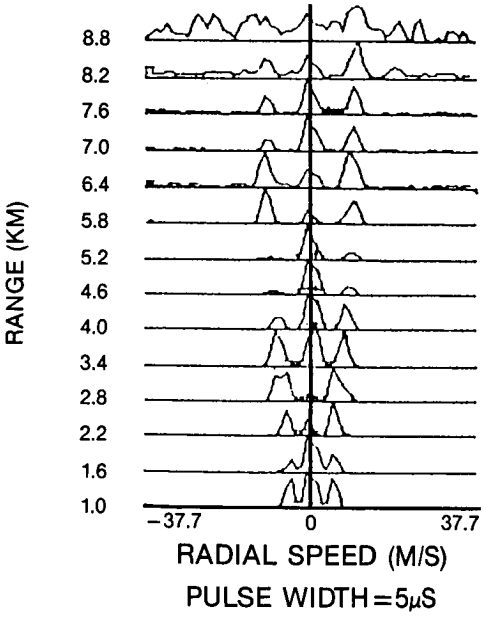

Figure 6.

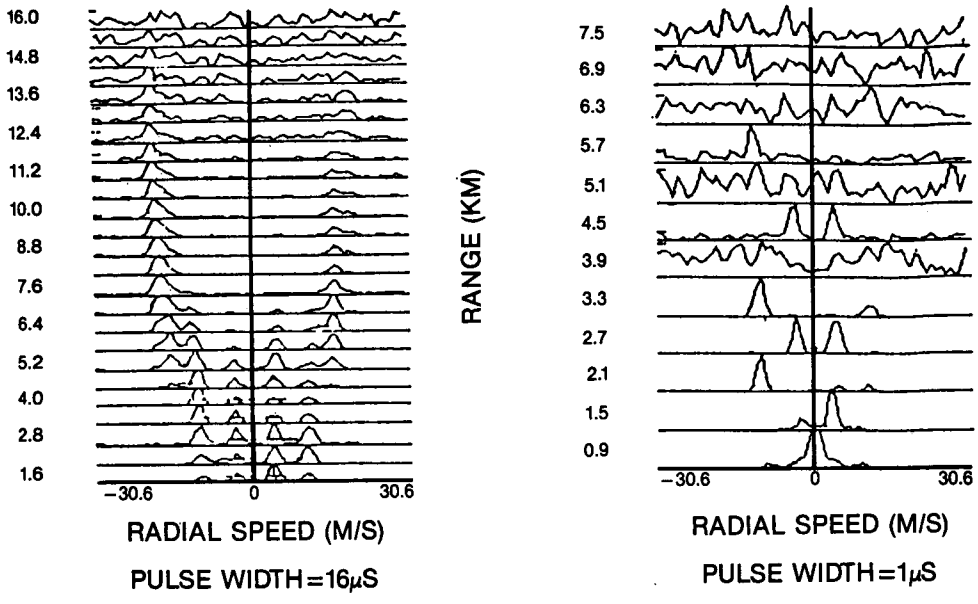
16.0
14.8
13.6
12.4
11.2
10.0
8.8
7.6
6.4
5.2
4.0
2.8
1.6
−30.6
0
30.6
RADIAL SPEED (M/S)
PULSE WIDTH=16μS
RANGE (KM)
7.5
6.9
6.3
5.7
5.1
4.5
3.9
3.3
2.7
2.1
1.5
0.9
−30.6
0
30.6
RADIAL SPEED (M/S)
PULSE WIDTH=1μS

Figure 7.

7.5.1 MEASUREMENTS OF ANTENNA POLAR DIAGRAMS AND EFFICIENCIES USING A PHASE-SWITCHED INTERFEROMETER

R. A. Vincent, B. Candy, and B. H. Briggs

Physics Department
University of Adelaide
Adelaide, South Australia 5001

It is desirable for many reasons to know antenna polar patterns and efficiencies accurately. In the past, calibration measurements have been made using balloons and aircraft and more recently satellites. These techniques are usually very expensive. We show that under certain circumstances it is possible to use a simpler and inexpensive technique by connecting together the antenna under test with another antenna (not necessarily the same) to form a phase-switched interferometer as first described by RYLE (1952).

For two antennas separated by a distance d in the EW direction and with respective amplitude polar patterns of the form $E_1(\theta)$ and $E_2(\theta)$, the interference pattern is given by

$$P(0) = k_1 k_2 E_1(\theta) E_2(\theta) \cos(\pi d/\lambda) \quad (1)$$

Here k_1 and k_2 are constants determined by preamplifier gains and cable losses. If a point radio source drifts through the center of the beams then the envelope of the interference pattern is determined by the combined polar patterns of the antennas; if one antenna is much larger than the other then $P(\theta)$ is essentially determined by the larger antenna and its pattern can be so measured and compared with the theoretical pattern. We have applied this technique to measurements of the polar diagram of the co-co transmitting array (dimensions of $16\lambda \times 16\lambda$) used with the Adelaide VHF radar (BRIGGS et al., 1984). The second antenna was one of the yagi receiving arrays ($4\lambda \times 4\lambda$).

What does not so far appear to have been recognized is that this technique can also be used to measure the effective area and hence the efficiency, of arrays. This is because $E(\theta)$ is proportional to $\sqrt{A}$, where A is the effective area such that the received power can be written

$$P_{12} = k_1 k_2 (A_1 A_2)^{1/2} \quad (2)$$

Suppose that the first antenna is replaced by a third antenna of known area e.g., a dipole located $\lambda/4$ above a perfect ground, then

$$P_{23} = k_1 k_2 (A_3 A_2)^{1/2} \quad (3)$$

The ratio of (2) to (3) gives the ratio of the areas for antennas 1 and 3 in terms of the ratio of the measured interferometer powers. In principle, this technique is very simple. It does require a suitable radio source which gives measurable powers when using small antennas (e.g., dipoles) and since dipoles have broad patterns, radio sources with similar right ascensions but different declinations to the primary source can be a problem. These problems can partly be overcome by filtering the interference pattern. Measurements of the efficiencies of the Adelaide antennas are in progress.

REFERENCES

Briggs, B. H., B. Candy, W. G. Elford, W. K. Hocking, P. T. May, and R. A. Vincent (1984). The Adelaide VHF radar -- capabilities and future plans, Handbook for MAP, 14, 357-359.

Ryle, M. (1952), A new radio interferometer and its application to the observation of weak radio stars, Proc. Roy. Soc. London A 211, 351-375.

7.5.2 USE OF THE SUN TO DETERMINE POINTING OF ST RADAR BEAMS

A. C. Riddle

Cooperative Institute for Research in Environmental Sciences
University of Colorado
Boulder, CO 80309

Verification of the beam-pointing direction for ST radars is a technically difficult problem. Consequently it is not usually done. For measurement of horizontal winds, the lack of precise knowledge of the beam-pointing direction is usually of little consequence as any errors cause only a small uncertainty in the measured velocity. However, instantaneous vertical velocities are typically more than an order of magnitude less than horizontal velocities and average vertical velocities are more than two orders of magnitude less than average horizontal velocities. Hence even small pointing errors ($< 10^{-2}$ radian) for vertical beams can result in large errors due to contamination by horizontal winds. Experimental confirmation of pointing accuracy using the measured winds is difficult but has been achieved where horizontal and vertical winds are measured at the same site (BALSLEY and RIDDLE, 1984; RIDDLE and BALSLEY, 1985).

Sited at Ponape, Federated States of Micronesia, is a ST radar with only a vertical beam. However, because of the equatorial location (+ 7°N) the sun passes through the beam for a few days twice a year. The passage of the sun through the beam in April 1985 was used to determine the pointing of the beam. The analysis below suggests that the beam is within 11 arc min (.003 radian) of vertical. Already this is a useful confirmation of verticality. Improvement of the measurement by a factor of 3 or 4 should be easily achieved and will be very useful for equatorial ST radars. It should be noted that this measurement refers only to the receive beam. For radar operation the effective beam is a combination of the transmit and receive beam.

The ST radar at Ponape operates at 50 MHz and collects spectral data about every 80 seconds. From each set of spectra an estimate of the background noise can be obtained. For the days of solar passage through the beam, 2 hrs of noise values were computed. The 40 minutes of data at each end of the computed interval were used to remove any linear trend in the noise values. The center 40 minutes contained the solar transit which caused a maximum of 3-dB enhancement. The noise fluctuations were about 0.5 dB.

By fitting a Gaussian enhancement to each of 13 days of noise data, 13 estimates of the effective beam longitude were obtained (Figure 1a). The difference between the effective longitude and the site longitude is an estimate of the off-vertical pointing angle. The average estimate was 7 arc min with a formal error from the dispersion of individual values of 5 arc min. The whole data set was also fitted by a two-dimensional Gaussian (Figure 1b) to produce both effective longitude and effective latitude estimates. For this fit, the longitude error was 5 arc min and latitude error 11 arc min. A formal value for the error of the pointing-angle estimate was obtained by repeating the fitting process after adding more noise to the data and amounted to 2 arc min.

The actual determinations of the effective longitude and latitude of the beam are given in Table 1. The formal errors in determining the off-vertical pointing angle are only a lower bound to the errors because no account has been taken of systematic errors. Consequently, we prefer to use the actual estimated off-vertical angles as an estimate of the accuracy of our beam pointing. The largest of these estimates was 11 arc min.

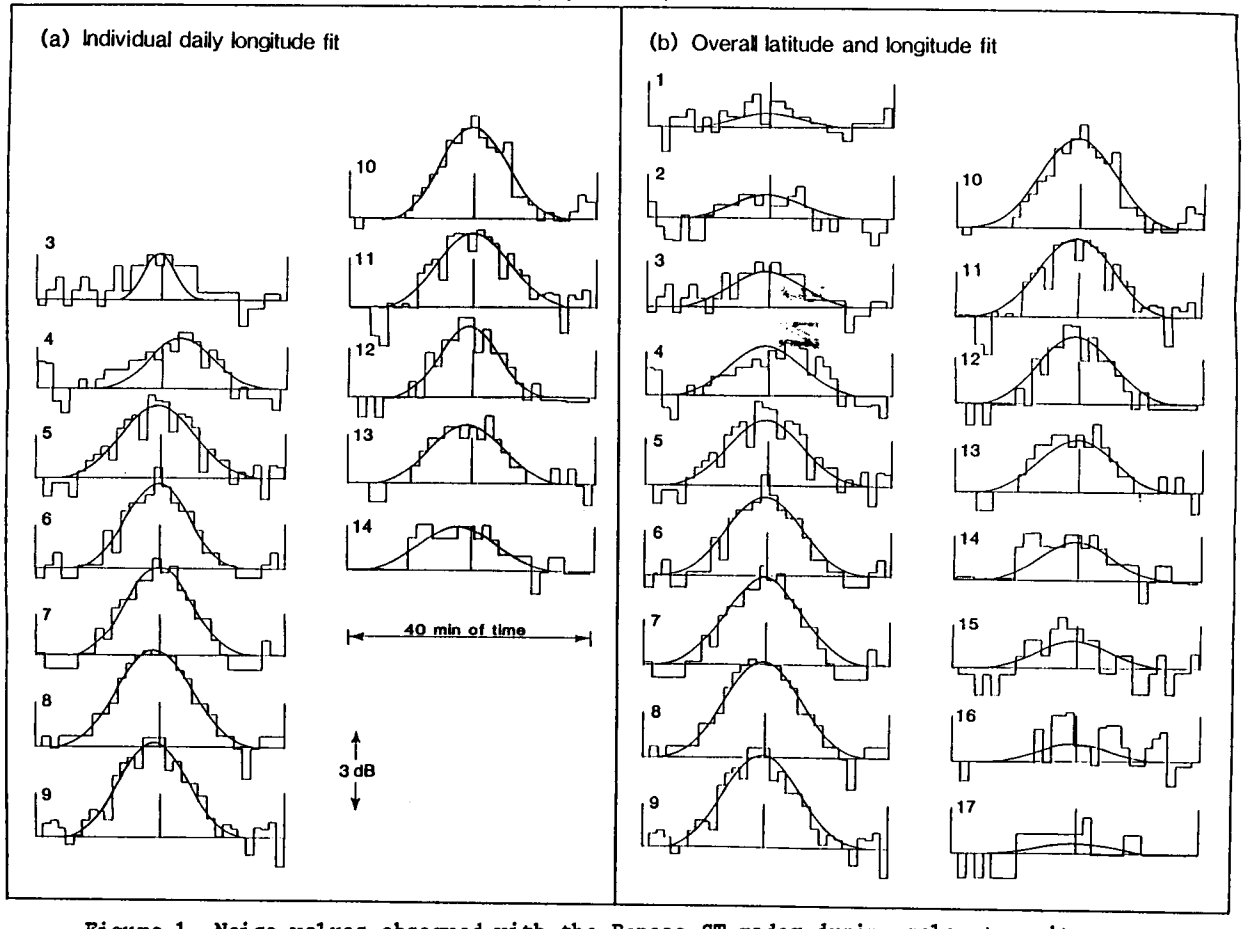

Figure 1. Noise values observed with the Ponape ST radar during solar transits of April 1985. a) The data are fitted each day to a separate 1-dimensional Gaussian model. b) The data as a whole are fitted by a 2-dimensional Gaussian model. The number on each plot is the observing date.

TABLE 1

April 1985 positions determinations

	Longitude	Latitude
Ponape site	158° 11.5'	6° 57.4'
Individual fit	158° 4.2 ± 5'	--
Overall fit	158° 6.8 ± 2'	7° 8.9 + 2'

In passing, it should be noted that the fitting process also determined a half power width for the beam of 3.2°. The expected width for a uniform aperture is 3.1°, so the fitting process also confirms that a fairly uniform aperture illumination has been achieved.

The main source of error in this pointing-angle estimation procedure is currently the high level of fluctuation of the noise values compared to the enhancement of noise due to the sun. In addition to its direct contribution the fluctuations also mask other effects described below. It is a very simple matter to reprogram our observations at Ponape to more closely emulate a radio astronomy receiver rather than a radar receiver. By reprogramming, we expect to be able to reduce noise fluctuation to well below 0.1 dB while enhancing the time resolution. We should then see clearly several other potential sources of error.

The noise level in the data is almost entirely due to the radio sky and varies during 24 hours by about 3 dB. The linear trend removal described above removes some of this variation. With lower noise fluctuations a better removal of the variation would be possible. The noise level also fluctuates from day to day due to varying atmospheric attenuation (mainly in the ionosphere) and receiver gain variations. These variations would also be easier to recognize and remove with lower noise fluctuations. Another potential error source is the inherent assumption that the 50-MHz sun is symmetric about the solar center. However, during this observing period there were no substantial active regions on the sun and no major flares. Hence we do not anticipate any problems from this cause, even at the arc minute level. Even in more active phases of the solar cycle there is not likely to be a major problem. GRAF et al. (1971) have analyzed the radio centroid at 9.1-cm wavelength over several years. They suggest rms centroid displacements of several arc minutes. However, at 50 MHz the quiet sun (the stable symmetric component) is much hotter (5×10^5 K vs 2×10^4 K) and the slowly varying component (associated with the moving active regions) less intense (2×10^6 K vs 10^7 K). Hence the centroid variations should be reduced to negligible values. Errors due to solar meter wavelength radio bursts should also be easier to detect with lower noise fluctuations.

REFERENCES

Balsley, B. B., and A. C. Riddle (1984), Monthly mean values of mesospheric wind field over Poker Flat, Alaska, J. Atmos. Sci., 41, 2368.

Graf, W., R. N. Bracewell, J. H. Denter, and J. S. Rutherford (1971), The sun as a test source for boresight calibration of microwave antennas, IEEE Trans. Antennas Propagat., AP-19, 606.

Riddle, A. C., and B. B. Balsley (1985), Comments on 'Comparisons of vertical winds measured with the Chatanika and Poker Flat radars', by B. J. Watkins and K. Jayaweera, J. Geophys. Res., 90, 8160.

Addendum

Data from the September 1985 transit have been received. The sun was discernable on 15 days of data. Those days were subject to the same analysis as for April 1985, and the mean of the individual fits for longitude was 158° 11.3'. An overall fit gave 158° 7.6'.

The September 1985 analysis revealed a timing error in the April 1985 longitude fits. To correct that error 5.4' must be added to the fitted longitudes in Table 1, making those fits even better.

The final 4 days of the September 1985 transmit were obtained using the radio astronomy mode of observation described in the text. The expected reduction of noise to better than 0.1 dB was achieved.

7.6.1 MONITORING OF THE MU RADAR ANTENNA PATTERN BY SATELLITE OHZORA (EXOS-C)

Toru Sato[1], Yasuhiro Inooka[1], Shoichiro Fukao[2], and Susumu Kato[1]

[1]Radio Atmospheric Science Center
Kyoto University
Uji 611, Japan
[2]Department of Electrical Engineering
Kotot University
Kyoto 606, Japan

INTRODUCTION

As the first attempt among MST type radars, the MU radar features an active phased array system (KATO et al., 1984; FUKAO et al., 1985a,b). Unlike the conventional large VHF radars, in which output power of a large vacuum tube is distributed to individual antenna elements, each of 475 solid-state power amplifiers feeds each antenna element. This system configuration enables very fast beam steering as well as various flexible operations by dividing the antenna into independent subarrays, because phase shift and signal division/combination are performed at a low signal level using electronic devices under control of a computer network. The antenna beam direction can be switched within 10 μsec to any direction within the zenith angle of 30°.

Since a precise phase alignment of each element is crucial to realize the excellent performance of this system, careful calibration of the output phase of each power amplifier and antenna element has been carried out. However, it is necessary to confirm the total performance by measuring the radiation pattern of the whole array from distant places where the antenna far field condition is satisfied.

Among various aircrafts which may be used for this purpose, e.g., airplanes, helicopters or balloons, artificial satellites have an advantage of being able to make a long-term monitoring with the same system. An antenna pattern monitoring system for the MU radar has been developed using the scientific satellite OHZORA (EXOS-C) which was launched on February 14, 1984. OHZORA has an almost circular orbit with the apogee of 815 km, perigee of 350 km and a high inclination of 74.6°, which are quite suitable for the purpose of monitoring.

A receiver named MUM (MU radar antenna Monitor) on board the satellite measures a CW signal of 100-400 watts transmitted from the MU radar. The received signal strength is transferred to the tracking station (Kagoshima Space Center of ISAS; KSC) through a telemetry channel. The overall antenna pattern is synthesized by integrating the data over many passes with different zenithal and azimuthal angles.

PRINCIPLE OF THE MEASUREMENT

The received signal strength is affected not only by the transmitting antenna pattern, but also by height and attitude of the satellite, the receiving antenna pattern and its radiation impedance. In order to remove these factors, a small omnidirectional reference antenna is installed at the MU radar site, which transmits a CW signal of a frequency of 50 kHz offset from the MU radar frequency. The level of this reference signal is compared with the MU radar signal on the satellite, and the MU radar antenna pattern is determined as the relative gain to that of the reference antenna. A turnstile antenna with a ground plane in a grid structure of 5 m x 5 m is located as the reference antenna on the top of the control building of the MU radar. Figure 1 illustrates the scheme of the measurement.

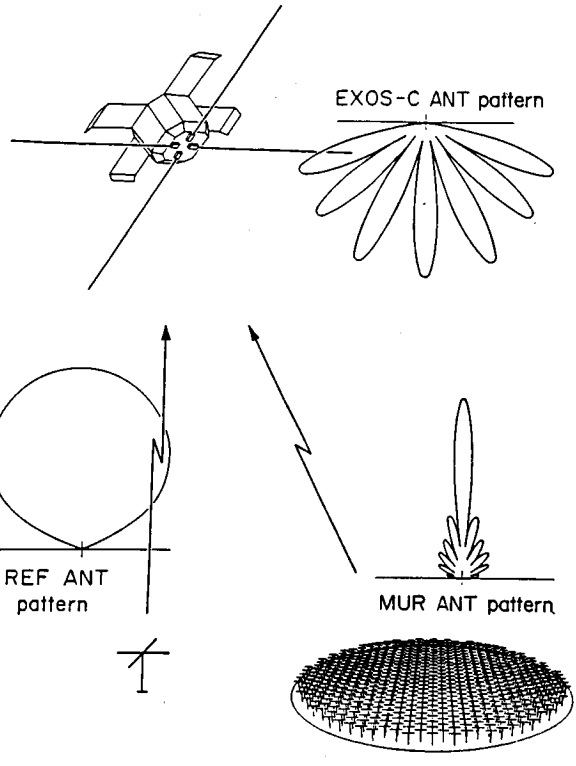

Figure 1. Principle of the MU radar antenna pattern measurement.

A pair of long wire dipole antennas of 40 m tip-to-tip installed for another physical instrument is utilized as the receiving antenna of MUM. As the length of this antenna corresponds to 6-wave dipoles at the frequency of the MU radar, the receiving antenna pattern becomes quite complicated. Also, the range of the satellite from the MU radar site varies from about 300 to 3000 km. In order to adapt to the expected wide dynamic range of the received signal due to these effects, an automatic gain control (AGC) is applied relative to the reference signal level.

The angular velocity of the satellite seen from the MU radar is 1.5°/sec at most, which is fairly slow considering the main beam width of 3.6° of the MU radar antenna. Therefore, a received-signal sampling rate of 100 msec is sufficient to make a detailed measurement of the antenna pattern. Since a sampling rate of as fast as 2 msec is available for the data processing unit of OHZORA, the MU radar antenna beam can be pointed up to about 10 different directions switched periodically during one pass of the satellite, still allowing for several contiguous samples in each beam direction. Figure 2 schematically shows this sequence.

RESULTS

In the example shown below, the MU radar antenna beam is pointed to 6 directions switched every 15.2 msec alternately when the satellite passes above the antenna. Among these directions, five directions are pointed to different

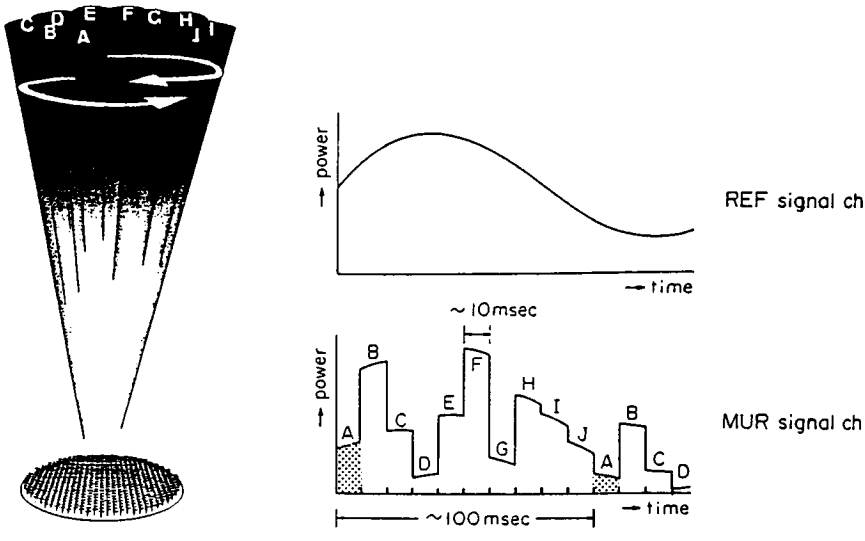

Figure 2. Schematic diagram of the temporal variation of the received signal levels. The antenna beam switched in a sequence of A, B, C,...J in this example. In practice, one of these beam direction (A) is used as a timing marker by shutting down the transmitter.

points on the expected path of the satellite, and the transmitter is shut down for the period of the remaining direction. This shut-down period is used as a timing marker to distinguish different beam directions in the off-line data analysis.

Figure 3 shows an example of unprocessed data of such measurement. The horizontal line around 150 digit is the reference signal level. Figure 4 gives the theoretical (thin line) and measured (thick line) relative gains of the MU radar antenna over the reference antenna for one of these five directions separated from the data in Figure 3. Since the reference antenna has almost constant gain of 6-8 dB for the elevation angles shown in this figure, this figure is regarded as the directivity pattern of the MU radar antenna if the above-mentioned gain of the reference antenna is added.

This figure shows that both main beam direction and gain agree very well with the theoretical ones, indicating that both the MU radar and the MUM system are working properly.

The sidelobe levels, on the other hand, shows some discrepancy of $\sim$5 dB between the theoretical and measured patterns, although the positions of sidelobes agree fairly well down to low elevation sidelobes. The consistent offset in the gain throughout the sidelobe region seems to suggest that a slightly larger random phase error might remain in the individual power amplifiers and/or antenna elements of the MU radar, which are inseparably related in radars with an active phased array system. Apparently more detailed and continuous monitoring of the radiation pattern, as well as careful calibration of individual amplifiers and antennas, is necessary in order to establish the performance of this system.

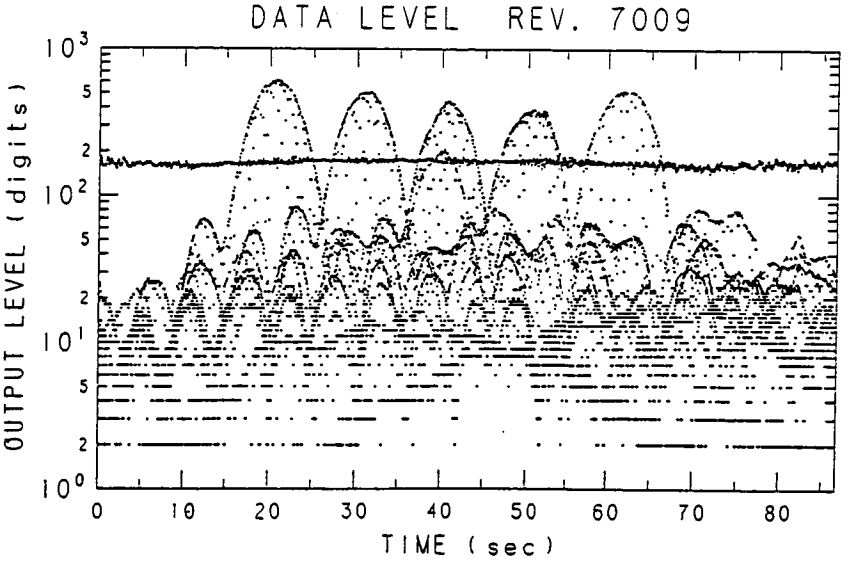

Figure 3. An example of unprocessed data which contains 5 different beam directions.

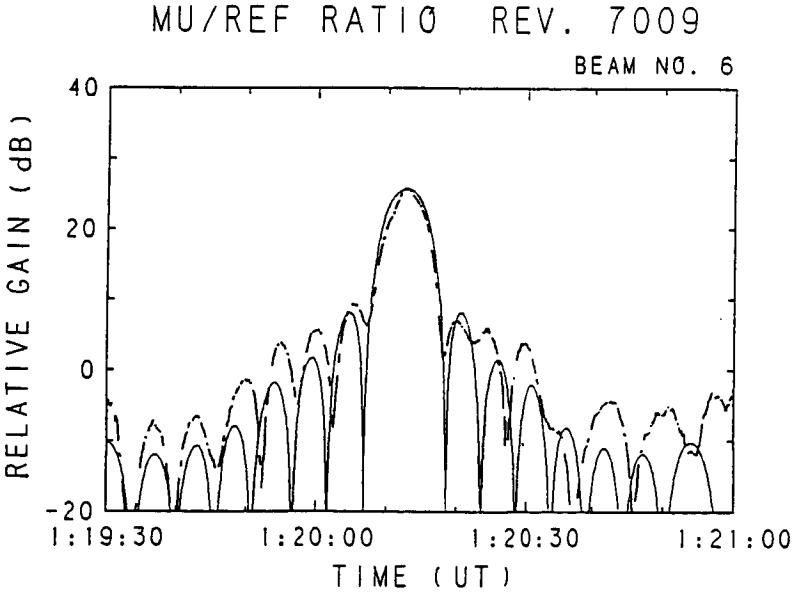

Figure 4. An example of the MU radar antenna pattern measured by MUM (thick line), and the corresponding theoretical antenna pattern (thin line).

REFERENCES

Kato, S., T. Ogawa, T. Tusda, and T. Sato (1984), The middle and upper atmosphere radar: first results using a partial system, Radio Sci., 19, 1475- 1484.

Fukao, S., T. Sato, T. Tsuda, S. Kato, K. Wakasugi, and T. Makihira (1985a), The MU radar with an active phased array system, 1, Antenna and power amplifiers, Radio Sci., 20, 1155-1168.

Fukao, S., T. Tsuda, T. Sato, S. Kato, K. Wakasugi, and T. Makihira (1985b), The MU radar with an active phased array system, 2, In-house equipment, Radio Sci., 20, 1169-1176.

7.6.2 APPLICATION OF A PORTABLE DISK-TYPE ANTENNA FOR ST RADAR STUDIES

D. C. Fritts and B. J. Watkins

Geophysical Institute
University of Alaska
Fairbanks, Alaska 99775-0800

The Geophysical Institute of the University of Alaska is presently developing a portable radar for studies of mean, wave, and turbulence motions in the troposphere and lower stratosphere. A unique aspect of this system, relative to other portable ST radars, is that we will be using a dish antenna. This is possible because of the frequency at which the system will operate, 219 MHz, and due to a unique antenna design, which will permit smaller segments of the antenna to be used for applications away from our primary operating facility.

The primary dish will have a diameter of 150 ft and a feed-point height of 100 ft, where we will locate five Yagis to form five separate beams. The dish will be constructed in concentric rings, each 20 ft wide, with support provided by an aluminum radial rib structure. This will permit dish diameters in 40 ft increments for use in portable applications.

Using the full antenna, the beamwidth will be 2°, with one beam vertical and two beams in each of two orthogonal planes at 15° off vertical to permit detailed gravity-wave structure, momentum flux, and turbulence studies.

The radar will be computer driven, have an array processor for initial data processing, and a peak power of 50 kW. We anticipate a resolution of better than 100 m and a useful height range of 1 - 12+ km.

7.6.3 METHOD TO DETERMINE THE OPTIMAL PARAMETERS OF THE ARECIBE 46.8-MHz ANTENNA SYSTEM

H. M. Ierkic, J. Rottger, J. B. Hagen, and R. K. Zimmerman

Arecibo Observatory
P.O. Box 995
Arecibo, Puerto Rico

INTRODUCTION

The spherical reflector at the Arecibo Observatory (AO) offers great advantages for the design of simple and inexpensive high performance steerable antennas at VHF. Light and small feeds have the added benefit that they can be quickly installed in the Arecibo platform causing almost no interruption to other experiments that may be in progress. Acceptable (primary) antennas are, for example, dipoles with reflectors, Yagis, loops etc. It is important to evaluate the performance of any given feed including the effects of the spherical reflector. In this paper, we will emphasize the optimization of two parameters, namely, the distance below the focal point of the reflector and the beam width of a 'point' feed. For the actual design of the feed at 46.8 MHz at the AO we had other requirements (e.g., best performance possible over a 10 MHz bandwidth around the carrier frequency for application in ionospheric modification experiments) independent of MST work. Details on the antenna mounting constraints and a comprehensive description of the new VHF radar can be found in ROTTGER et al. (1986).

DESIGN OF (PRIMARY) ARRAY

Numerical simulation codes were used to facilitate the exhaustive evaluation of the characteristics of the primary feeds, thus facilitating their design. The Numerical Electromagnetic Code (BURKE AND POGIO, 1981) obtains the solution of integral field equations that describe the currents flowing over wires and surfaces that the user has specified. The description of the program and the limitations that the approximations, implicit in the algorithms, create can be found in the reference above.

We modelled several types of feeds and decided on a simple dipole with a reflector. To minimize spillover out of the surface of the reflector by the illuminating feed after installation (for large zenith angles) and also to somewhat improve against clutter from the horizon, we decided to form an array of two feeds side by side separated by about half a wavelength. We call this array a twin Yagi feed. The numerical simulation provided us with the radiation pattern in the E and H planes and the impedance. The dimensions deemed appropriate are 3.8 m for the reflectors, 3.1 m for the driven elements with a separation of 1.5 m and with a radius for all the elements of 1.33 cm. The two antennas composing the array are separated by 3.2 m and fed with a parallel transmission of 100 Ω impedance. The radar system requires 50 Ω for optimum matching.

We summarize the performance of the array in the following table.

Table 1

F (MHz)	Gain (DB)	Beam width E	Beam width H	Impedance (Ω)
42	8.1	75.2	53.1	54 - i37
45	7.8	75.7	57.6	45 - i19
47	7.6	77.7	61.3	43 - i4
49	7.5	79.2	62.0	44 + i11
52	7.4	79.3	61.0	56 + i38

The actual environment where the array is installed in the platform includes the AO 430-MHz line feed. Care was taken to locate the array far enough (out of the Caustic region of influence of the line feed) to avoid interference (ROTTGER et al., 1986). Almost no perturbation of the array performance was found theoretically by modelling the AO feed with a set of wires.

PERFORMANCE OF (PRIMARY) ARRAY WITH THE AO SPHERICAL REFLECTOR

The problem of finding the gain of an antenna in front of a spherical reflector has been treated by many workers; we follow closely the development by CONDON (1969). To simplify the algebra, we assume that the (primary) array main lobe is rotationally symmetric and thus can be characterized by one angle only. This approximation simplifies the algebra and is enough for our purposes.

The far field due to the electric field distribution over an aperture can be written as

$$E(\phi) = 1/\lambda^2 \int_{\text{aperture}} E(x,y) \exp\left(\frac{i2\pi\chi\sin\phi}{\lambda}\right) dx\, dy \qquad (1)$$

where

$E(x,y)$ = electric field on the plane immediately above the reflector surface.

χ = path length difference
ϕ = zenith angle

We rewrite this equation in terms of polar coordinates (Figure 1) to take advantage of the rotational symmetry of the radiation pattern,

$$G(\phi) = \left|\frac{2\pi}{\lambda^2} \int_0^{rm} E(r)\, J_o\left(\frac{2\pi r}{\lambda}\sin\phi\right) \cos\frac{2\pi\epsilon}{\lambda}\, rdr\right|^2 \qquad (2)$$

$$+ \left|\frac{2\pi}{\lambda 2} \int_0^{rm} E(r)\, J_o\left(\frac{2\pi r}{\lambda}\sin\phi\right) \sin\frac{2\pi\epsilon}{\lambda}\, rdr\right|^2$$

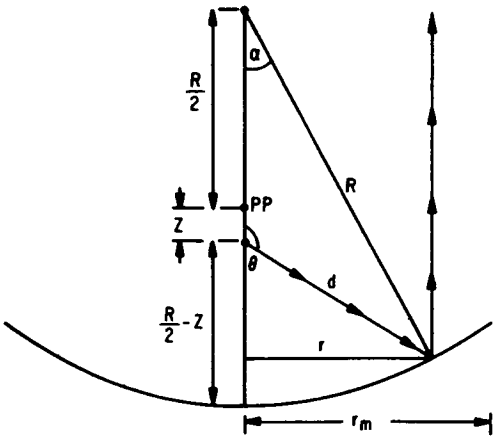

Figure 1. Geometry involved in the computation of the antenna gain (adapted from CONDON, 1969).

where

$\varepsilon(r)$ = path length error of array reflected from a sphere.
r_m = radius of the aperture of the reflecting surface.

Equation (2) can be readily evaluated once the primary antenna pattern is specified since the rest of the quantities depend only on the geometry. Following CONDON (1969), we have assumed that the primary pattern can be fitted with a cosine square type of function. This simplification makes it possible to characterize an antenna by its beam width alone.

Using this procedure, we have computed the values of antenna aperture shown in Table 2 for several beam widths and distances z to the paraxial surface. Note from this table that for the array previously discussed with an average beam width of about 70°, the maximum aperture is 43000 m^2 when z = 9.3 m. The radiation diagram corresponding to this antenna is shown in Figure 2. The half-power beam width (found from the figure) is 1.6° with a sidelobe 2.6° off axis suppressed by about 17 dB. For comparison, the figure also shows the diagram for the array in front of a parabolic reflector.

CONCLUSIONS AND FUTURE DEVELOPMENTS

A straightforward procedure has been proposed to design and install simple antennas in the AO platform facing the spherical reflector.

Further work will include relaxation of some of the constraints used in this note (e.g., rotational symmetry, cosine square primary pattern, etc.). We are also planning to design antennas that will allow us to monitor the same scattering volume at two frequencies (i.e., concentrical to the 430-MHz line feed).

Table 2

Antenna aperture (x $10^{-4} m^2$)
Beam width (degrees)

F =	47.0 MHZ										
Z/HPBW	50.0	55.00	60.00	65.00	70.00	75.00	80.00	85.00	90.00	95.00	100.00
0.5	2.60	2.53	2.21	1.96	1.75	1.57	1.41	1.28	1.17	1.07	0.98
0.8	2.64	2.60	2.29	2.03	1.80	1.62	1.45	1.32	1.20	1.10	1.01
1.0	2.68	2.67	2.37	2.09	1.86	1.67	1.50	1.36	1.23	1.13	1.04
1.3	2.71	2.73	2.45	2.16	1.93	1.72	1.55	1.40	1.27	1.16	1.07
1.5	2.75	2.80	2.53	2.24	1.99	1.78	1.60	1.45	1.32	1.20	1.10
1.8	2.78	2.86	2.61	2.31	2.06	1.84	1.66	1.50	1.36	1.25	1.15
2.0	2.81	2.93	2.70	2.39	2.13	1.91	1.72	1.56	1.42	1.29	1.19
2.3	2.83	2.99	2.78	2.47	2.21	1.98	1.78	1.62	1.47	1.35	1.24
2.5	2.86	3.04	2.86	2.55	2.28	2.05	1.85	1.68	1.53	1.40	1.29
2.8	2.88	3.10	2.95	2.64	2.36	2.13	1.93	1.75	1.60	1.47	1.35
3.0	2.90	3.15	3.03	2.72	2.45	2.21	2.00	1.82	1.67	1.53	1.41
3.3	2.91	3.20	3.11	2.81	2.53	2.29	2.08	1.90	1.74	1.61	1.48
3.5	2.93	3.24	3.19	2.90	2.62	2.38	2.17	1.99	1.82	1.68	1.56
3.8	2.93	3.28	3.27	2.98	2.71	2.47	2.26	2.07	1.91	1.76	1.64
4.0	2.94	3.32	3.34	3.07	2.81	2.57	2.36	2.17	2.00	1.85	1.72
4.3	2.95	3.35	3.41	3.16	2.90	2.67	2.45	2.26	2.09	1.94	1.81
4.5	2.95	3.38	3.48	3.25	3.00	2.77	2.56	2.37	2.19	2.04	1.90
4.8	2.94	3.40	3.54	3.33	3.10	2.87	2.66	2.47	2.30	2.14	2.00
5.0	2.94	3.42	3.60	3.42	3.19	2.97	2.77	2.58	2.40	2.24	2.10
5.3	2.93	3.44	3.66	3.50	3.29	3.08	2.88	2.69	2.51	2.35	2.21
5.5	2.92	3.45	3.70	3.58	3.39	3.19	2.99	2.80	2.63	2.46	2.31
5.8	2.91	3.45	3.75	3.66	3.48	3.29	3.10	2.92	2.74	2.58	2.43
6.0	2.89	3.45	3.79	3.73	3.57	3.40	3.21	3.03	2.86	2.69	2.54
6.3	2.87	3.45	3.82	3.80	3.66	3.50	3.33	3.15	2.98	2.81	2.66
6.5	2.85	3.44	3.84	3.86	3.75	3.60	3.44	3.27	3.09	2.93	2.77
6.8	2.83	3.43	3.86	3.92	3.84	3.70	3.55	3.38	3.21	3.05	2.89
7.0	2.80	3.41	3.88	3.97	3.92	3.80	3.66	3.50	3.33	3.16	3.00
7.3	2.77	3.38	3.88	4.02	3.99	3.89	3.76	3.61	3.44	3.28	3.12
7.5	2.74	3.36	3.88	4.06	4.06	3.98	3.86	3.71	3.56	3.39	3.23
7.8	2.71	3.32	3.87	4.09	4.12	4.06	3.96	3.82	3.66	3.50	3.34
8.0	2.68	3.29	3.85	4.12	4.18	4.14	4.05	3.92	3.77	3.61	3.45
8.3	2.64	3.25	3.83	4.13	4.22	4.21	4.13	4.01	3.86	3.71	3.55
8.5	2.60	3.20	3.80	4.14	4.26	4.27	4.21	4.10	3.96	3.81	3.65
8.8	2.56	3.15	3.77	4.14	4.29	4.32	4.27	4.17	4.04	3.89	3.74
9.0	2.51	3.10	3.72	4.13	4.32	4.37	4.33	4.24	4.12	3.98	3.82
9.3	2.47	3.05	3.67	4.12	4.33	4.40	4.39	4.31	4.19	4.05	3.90
9.5	2.42	2.99	3.61	4.09	4.33	4.43	4.43	4.36	4.25	4.11	3.97
9.8	2.38	2.93	3.55	4.05	4.32	4.44	4.46	4.40	4.30	4.17	4.02
10.0	2.33	2.86	3.48	4.01	4.31	4.45	4.48	4.43	4.34	4.21	4.07
10.3	2.28	2.79	3.41	3.95	4.28	4.44	4.48	4.45	4.36	4.25	4.11
10.5	2.23	2.73	3.33	3.89	4.24	4.42	4.48	4.46	4.38	4.27	4.14
10.8	2.18	2.65	3.24	3.82	4.19	4.39	4.46	4.45	4.38	4.28	4.15
11.0	2.13	2.58	3.15	3.74	4.13	4.35	4.44	4.44	4.38	4.28	4.16
11.3	2.07	2.50	3.06	3.65	4.06	4.29	4.40	4.41	4.36	4.27	4.15
11.5	2.02	2.43	2.96	3.56	3.98	4.23	4.34	4.36	4.32	4.24	4.13
11.8	1.97	2.35	2.86	3.45	3.89	4.15	4.25	4.31	4.28	4.20	4.10
12.0	1.91	2.27	2.76	3.34	3.79	4.07	4.20	4.24	4.22	4.15	4.06
12.3	1.86	2.19	2.66	3.23	3.69	3.97	4.12	4.17	4.15	4.09	4.00
12.5	1.80	2.11	2.55	3.11	3.57	3.86	4.02	4.08	4.07	4.02	3.93
12.8	1.75	2.03	2.44	2.98	3.45	3.74	3.91	3.98	3.98	3.93	3.85
13.0	1.69	1.95	2.33	2.85	3.32	3.62	3.79	3.87	3.87	3.84	3.77
13.3	1.64	1.87	2.22	2.72	3.18	3.48	3.66	3.75	3.76	3.73	3.67
13.5	1.59	1.79	2.11	2.59	3.04	3.34	3.53	3.62	3.64	3.62	3.56
13.8	1.53	1.72	2.00	2.45	2.89	3.20	3.38	3.48	3.51	3.49	3.44
14.0	1.48	1.64	1.89	2.31	2.74	3.04	3.23	3.33	3.37	3.36	3.32

z (meters)

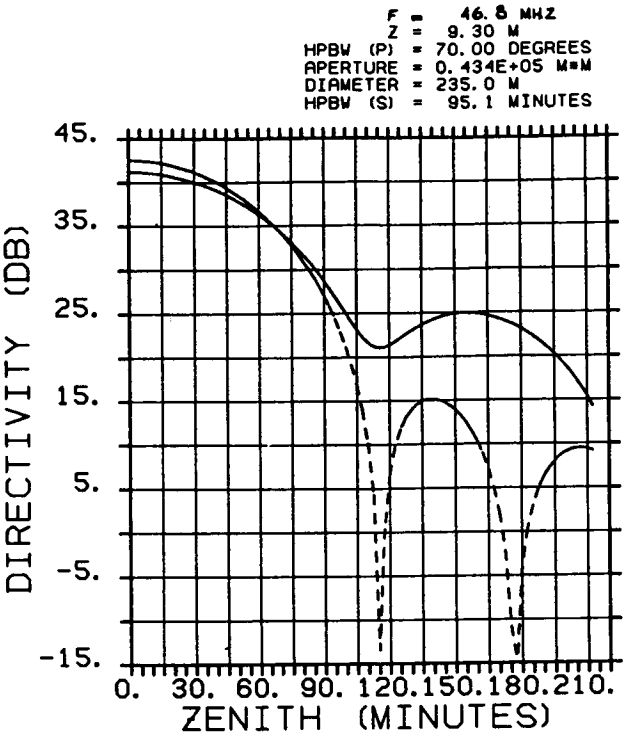

Figure 2. Radiation pattern for AO array in front of spherical reflector (solid line) and parabolic reflector (dashed line). Primary beam width is 70° and distance z from paraxial surface 9.3 meters.

REFERENCES

Burke, G. J., and A. J. Pogio (1981), Numerical electromagnetic code, Lawrence Livermore Laboratory, Technical Document 116, 1-3.

Condon, J. J. (1969), Theory of point fed spherical reflectors, Cornell-Sydney University Astronomy Center, CSUAC 182.

Rottger, J., H. M. Ierkic, R. K. Zimmerman, and J. B. Hagen (1986), Investigations of the lower and middle atmosphere at the Arecibo Observatory and a description of the new VHF radar project, this volume.

7.7.1 THE ELIMINATION OF A CLASS OF PSEUDO ECHOES BY AN IMPROVED T/R SWITCH TECHNIQUE

J. L. Green and W. L. Ecklund

Aeronomy Laboratory, NOAA
325 S. Broadway
Boulder, CO 80303

INTRODUCTION

In the session on "Design of Radar Transmitters and Transmit-Receive Switches" of the Workshop on the Technical Aspects of MST Radar, Urbana, IL, May, 1984, it became evident from the discussion that a class of pseudo echoes had been observed in the Doppler spectra from a number of ST and MST radars. This class of pseudo echoes can be characterized as being occasional, variable, and usually located on these spectra near zero Doppler shift. These pseudo echoes have also been observed to gradually change apparent Doppler shift with altitude and time. It was also reported during this session that these pseudo echoes are most intense at the very closest radar ranges, but as shown in Figure 1, can be seen occasionally as high as the tropopause when the echoes from the atmosphere are especially weak. As shown in Figure 1, these echoes can usually be easily recognized and edited from the radar records. Also, it is often possible to eliminate them by careful adjustment of the radar.

Because these pseudo echoes occur only occasionally and are easily recognized, they have not seriously degraded the usefulness of ST or MST radars, but rather can be typified as a nuisance.

LABORATORY SIMULATION

One of us, W. L. Ecklund, studied this problem by means of a laboratory simulation. In this simulation, a ST radar was configured using actual radar components (high power transmitter, transmit-receive switch and radar receiver) with a 50-ohm resistor (dummy load) as a substitute for the radar antenna (ECKLUND, 1983; JOHNSTON et al., 1976). By using this resistor in place of the antenna, the reception of radar echoes was, of course, precluded. A schematic drawing of this simulation is shown in Figure 2.

The pseudo echo was successfully duplicated in this laboratory study and found to be due to "ringing" (damped oscillations) of the high quality resonant circuits in the final stage of the radar transmitter. This is a very reasonable explanation. For the benefit of readers unfamiliar with radio frequency engineering, the term Q, or the quality factor of resonant circuits is introduced,

$$Q = \text{(energy stored)} / \text{(energy dissipated), per cycle.}$$

It is obvious that Q is related to the number of cycles which a resonant circuit will ring after excitation is removed. It is customary in the construction of high power radar transmitters to use resonant circuits with intrinsic Qs of several thousand to minimize the heating of the circuit components by their internal dissipation of radio frequency power.

During the short period of time when the radar transmitter is delivering the radar pulse to the antenna, the Q of these circuits is typically no more than 10 because the flow of radio frequency power to the antenna represents a dissipation of energy. But, a few microseconds after the radio frequency radar pulse is terminated, the transmit-receive switch connects the receiver to the antenna. This switch also simultaneously disconnects the transmitter, whose

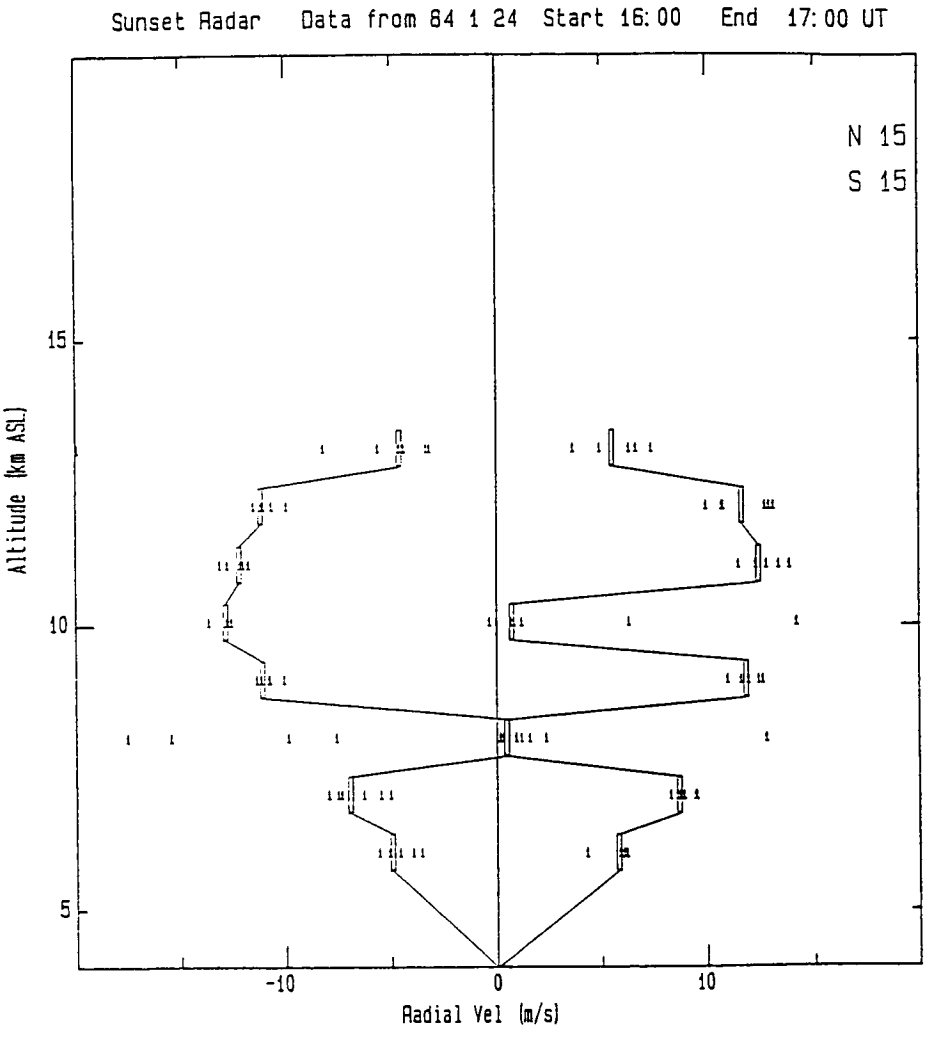

Figure 1. Example of pseudo echoes in a Sunset radar plot of radial velocity. The velocities on the left are from an antenna beam directed 15° from the vertical towards the north while the velocities on the right are from an antenna beam 15° from the vertical towards the south. The median velocities at each altitude are denoted by the small rectangles connected by lines. At altitudes of 8 km and 10 km, note the pseudo echoes near zero velocity that have captured the medians.

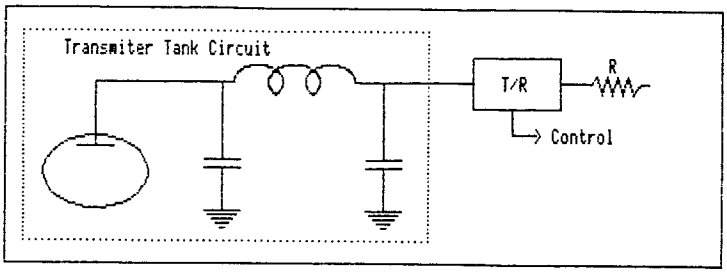

Figure 2. Schematic of laboratory simulation of a ST or MST radar used to study origin of pseudo radar echoes. Except for the antenna, which has been replaced with a high power resistor (dummy load), the components are from an operating ST radar.

circuitry reverts to its intrinsic high value of Q -- hence the ringing and the pseudo echo. It is clear from these laboratory experiments that the pseudo echoes in question are caused by the leakage of the ringing of the transmitter circuits into the extremely sensitive radar receivers. Much of the variability in frequency, intensity and damping rate of these psuedo echoes that has been observed with operating ST and MST radars, can now be explained as the tuning or detuning of these high-Q circuits by changes in the operating temperature of the transmitting equipment.

SOLUTIONS

In the light of the foregoing laboratory experiments, it is probable that this type of pseudo echo has not been observed with radars using transmit-receive switches based on 3 dB hybrid circuits as shown in Figure 3, a schematic drawing of the transmit-receive switch circuit used at the SOUSY radar (CZECHOWSKY et al., 1983). In this type of device, as the receiver is connected to the antenna, the transmitter is simultaneously switched from the antenna to a dummy load, rather than being left connected to an open circuit. By our reasoning, the provision of an alternate load for the transmitter during the receiving portion of the radar cycle, prevents the Q of the output circuit of the transmitter from rising to its intrinsic value, thereby allowing ringing and the associated pseudo echoes.

One of us, J. L. Green, made use of the information gained from the laboratory simulation described above, to redesign the transmit-receive switch at the Sunset radar (GREEN, 1983). As is shown in Figure 4, the isolation of the receiver from the transmitter provided by this switch was increased by approximately 50 dB with the incorporation of an extra section. Even this was not sufficient to eliminate the occasional pseudo echo from the lowest altitude range gates (probably because of direct radiation from the transmitter to the radar antenna) so additionally, the length of the coaxial line from the switch to the transmitter was adjusted so that as the transmitter was disconnected from the antenna, the intrinsic resonance of its output circuit and the coaxial line was changed to a frequency far outside the pass band of the radar receiver. These two modifications to the Sunset radar have effectively eliminated the pseudo echoes. An example of a radar record free from these echoes is shown in Figure 5.

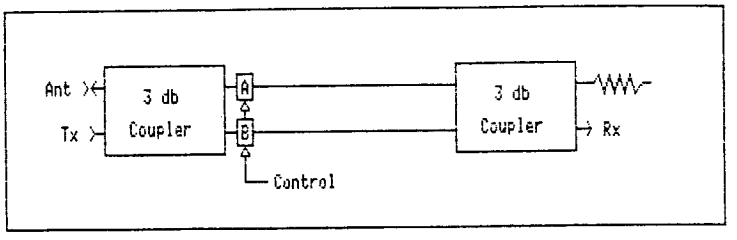

Figure 3. Schematic of SOUSY radar transmit-receive switch as noted in the text, after the emission of the radar pulse, as this circuitry connects the receiver to the antenna, it simultaneously connects the transmitter to a dummy load. Any ringing of the transmitter circuits is therefore quickly damped.

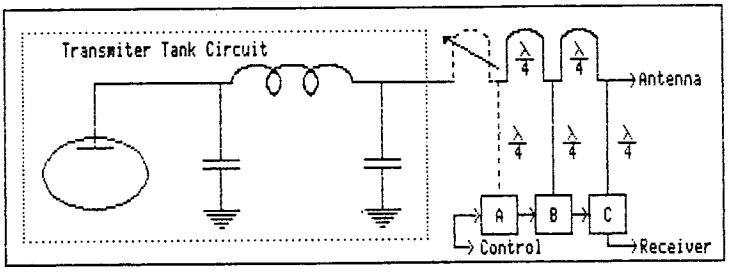

Figure 4. Schematic of improvements of sunset radar transmit-receive switch. The control voltage to the PIN diode switches A, B and C, alternately connects the transmitter and disconnects the receiver to the antenna or vice versa. The new section added in this modification is drawn with dashed lines.

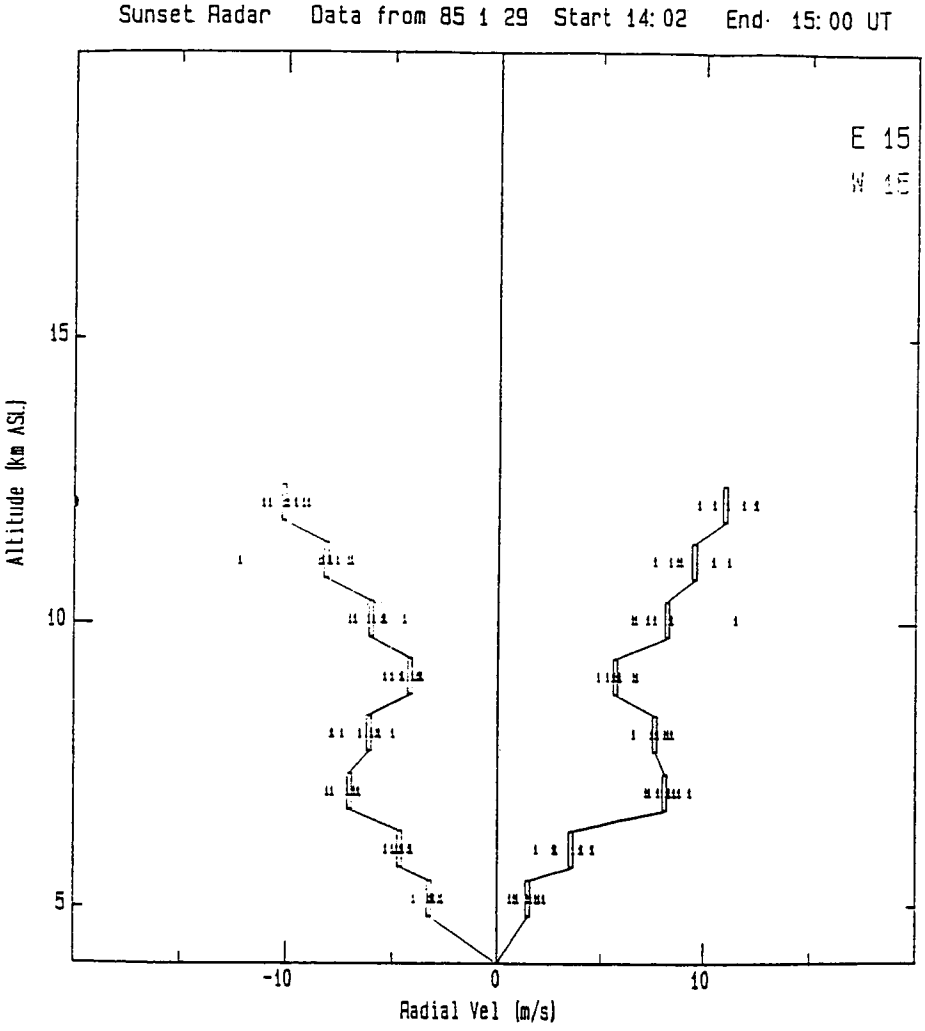

Figure 5. Example of a Sunset radar plot of radial velocities with no pseudo echoes evident. The velocities on the left are from an antenna beam directed 15° from the vertical towards the west while the velocities on the right are from an antenna beam 15° from the vertical towards the east. The median velocities at each altitude are denoted by the small rectangles connected by lines.

CONCLUSION

We have described an annoying class of pseudo echoes that evidently occur occasionally in a number of ST radars and located the origin of these signals in the output circuitry of the radar transmitter. We have also suggested two methods for their elimination.

REFERENCES

Czechowsky, P., G. Schmidt, and R. Ruster (1983), The mobile SOUSY Doppler radar -- technical design and first results, Handbook for MAP, 9, SCOSTEP Secretariat, Dep. Elec. Eng., Univ. IL, Urbana, IL, 433-446.

Ecklund, W. L. (1983), Design considerations for high-power VHF radar transceivers -- T/R switch design, Handbook for MAP, 9, SCOSTEP Secretariat, Dep. Elec. Eng., Univ. IL, Urbana, IL, 431-432.

Green, J. L. (1983), Characteristics of Sunset radar, Handbook for MAP, 9, SCOSTEP Secretariat, Dep. Elec. Eng., Univ. IL, Urbana, IL, 320-324.

Johnston, P. E., W. L. Ecklund, and R. A. Greenwald (1976), A VHF transmitter and system synchronizer for use in a portable Doppler radar system, NOAA Technical Report ERL 358-AL, 11, U.S. Government Printing Office, Washington, D.C. 20402.

8.0 AN OVERVIEW OF DATA ACQUISITION, SIGNAL CODING AND DATA ANALYSIS TECHNIQUES FOR MST RADARS

P. K. Rastogi

Electrical Engineering and Applied Physics Department
Case Western Reserve University
Cleveland, Ohio 44106

INTRODUCTION

In this paper, I will attempt to give an overview of the data-acquisition, signal-processing, and data-analysis techniques that are currently in use with high-power MST and ST radars. Many of the topics discussed here have also been the subject of papers presented at the two previous MAP Workshops on MST Radars, and have been reviewed by RASTOGI (1983) and FARLEY (1984). This review supplements, and hopefully augments, the work discussed in these papers. An additional useful reference is the comprehensive review of the MST technique by ROTTGER (1984).

We begin with a general description of data-acquisition and signal-processing operations and attempt to characterize these on the basis of their disparate time scales. Then signal-coding techniques, a brief description of frequently used codes, and their limitations are discussed, and finally, several aspects of statistical data-processing such as signal statistics, power-spectrum and autocovariance analysis, outlier-removal techniques, etc. are discussed.

DATA-ACQUISITION AND SIGNAL-PROCESSING OPERATIONS

It is interesting to note that although all the signal-processing operations in MST radars are carried out in time, these operations can be conveniently divided into three different categories on the basis of their time scales as shown in Figure 1.

The operations that proceed most rapidly, at scales of the order of a μsec, take place along the T_z axis. Time measured along this axis scales directly to radar range z through $z = 0.5\ cT_z$. The total span of the T_z axis is of the order of 1 msec corresponding to a maximum range of 150 km. The operations along this axis include transmitter pulse shaping, receiver impulse response, range gating, signal coding, and decoding. Each point along this axis represents a complex sample, with an in-phase and a quadrature component, corresponding to a range cell. The samples are usually digitized to an accuracy of 8-12 bits. The time-resolution along the T_z axis should correspond to the most rapid modulation imposed on the transmitted pulse, and the duration of the receiver impulse response should be closely matched to it. In the simplest MST radar experiments this resolution is the duration of the transmitted pulse, typically 10 μsec. In coded-pulse experiments, the scale along the T_z axis corresponds to the duration of a code element, typically 1 μ sec. The only operation that proceeds more rapidly than the time-scale along the T_z axis is that of analog to digital (A/D) conversion of the received signal. For using signal coding, not only should the A/D converters be fast with a conversion time of only a fraction of a μsec, they should also be linear over a wide dynamic range (about 60 dB) that includes low-level noise as well as the strong ground clutter and interference.

The time scale along the T_Y axis is measured in units of the interpulse period (IPP), that is typically of the order of a msec, and it extends for times of the order of 10-100 sec. For each channel or range cell, a digitized complex sample is obtained every IPP. The operations along the T_Y axis

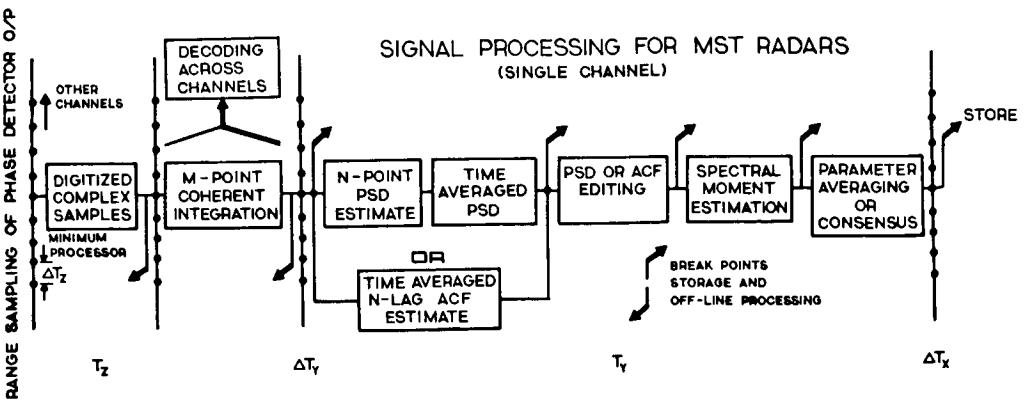

Figure 1. Signal-processing operations in MST radars can be decomposed on the basis of three different time scales as shown above. The specific operations that proceed at these time scales are shown in the boxes. In some cases, decoding is carried out after coherent integration.

include coherent integration of the digitized complex samples, estimation of averaged power spectral density (PSD) of the integrated samples, automated editing of the spectral estimates, and finally estimation of the basic spectral-moment parameters. An equivalent amount of information can be obtained through autocovariance function (ACF) of the coherently integrated samples.

In most MST radar experiments, the received signals have a small bandwidth with fading times of the order of 0.1 sec. A sufficiently large number M of digitized complex samples can therefore be added together, thus resulting in a substantial reduction in data rate. When a coding scheme is used during transmission, the operation of signal decoding can often be relegated until after coherent integration for slowly fading signals, with a remarkable saving in computational effort. For a linear system, the operations of coherent integration and decoding are commutable. The estimation of PSD or ACF of the received signal is carried out on finite blocks (of length N) of coherently integrated samples. Usually some time-averaging of these estimates is desirable. Estimates of averaged spectra for all the channels are supposed to be available at the far end of T_Y axis, at intervals of the order of 0.1 to 1 min. The final operations along the T_Y axis involve spectral editing and spectral-moment estimation. The averaged PSD estimates often are contaminated with undesired signatures due to ground clutter, aircraft echoes, and ducted returns. Algorithms for removing the effect of these signatures tend to be ad-hoc in nature and are often implemented in post-processing. Algorithms for obtaining low-order spectral moments of the averaged PSD estimates vary in their sophistication from evaluation by definition, to rigorous least-square fits to idealized spectral shapes.

The time-scale along the T_X axis is of the order of 1 min. The operations carried out along this axis can be classified under statistical data analysis. These operations include post-processing of averaged PSD estimates to obtain time-series of physical parameters for all range cells and for all antenna pointing directions.

Even though all of the signal-processing operations mentioned above have become reasonably standardized, the details of their implementation differ

considerably from one radar to another. Figure 2 shows the sequence in which these operations are usually carried out. An important decision in the overall organization of these operations pertains to their division into real-time (or on-line) and off-line (or post-) processing. Processing in real time requires synchronization of all the data acquisition, housekeeping, and processing modules -- usually through access to additional fast processors. The data input rate to a real-time processor is typically 0.5 Mbyte/sec for a 256-channel radar. If the processor obtains averaged 128-point spectra for all channels in the form of 4-byte integers at intervals of 1-min, then the data output rate is only about 131 kbyte/min. To provide this near 250-fold reduction in data rate, the processor needs the ability to carry out over a million multiplications per sec. The numbers on which the processor operates are, of course, irretrievably lost and the processing scheme is relatively inflexible. A 'minimum processor' on the other hand would merely transfer raw data samples to a storage medium, relegating the major computational tasks to an off-line processor for a later time. Off-line processing allows the experimenter total flexibility in examining and reducing the data. There is, however, a serious limitation in terms of storage requirements. Due to the very high data-input rates, a standard 9-track, 2400; 1600 bpi tape can accommodate only 1-2 min worth of raw data samples. Most MST radars tend to make a compromise between these two extremes, depending on the available storage and real-time processing facilities.

Figure 2 shows several other breakpoints for dividing up the processing effort into real-time and off-line. At the breakpoint chosen, the partially processed data are transferred to a storage medium. The most common breakpoints are either after coherent integration (before or after decoding), or

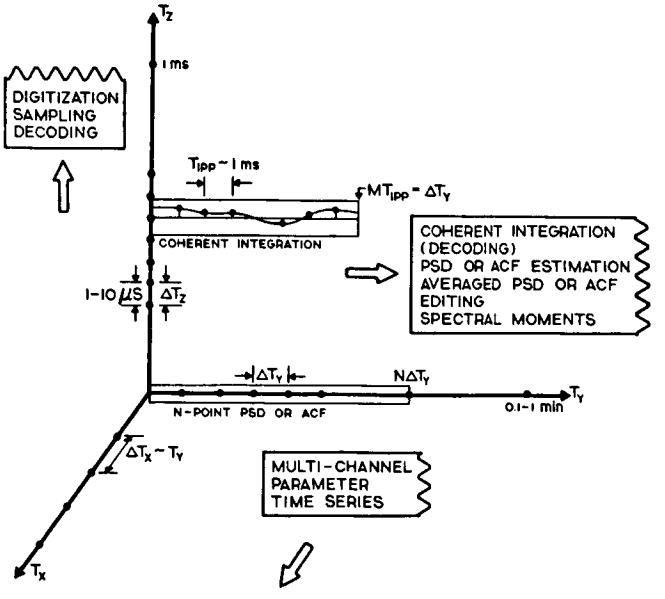

Figure 2. Sequence of signal-processing operations for a single channel is shown above. Sampling and digitization of phase-detector output provides a time sequence of complex samples for each channel. Decoding is carried out across channels. Oblique arrows show possible breakpoints for on-line and off-line processing. PSD estimation may be replaced by an equivalent ACF estimation.

after averaged PSD estimates have been formed. Editing of averaged PSD estimates and spectral-moment estimation is invariably carried out off-line. When the alternative method of obtaining spectral moments through the ACF estimates is followed, it can be very simply implemented in on-line processing. It suffers from a serious limitation, however, that no subsequent correction can be applied for external interference.

Some form of display routines are essential for monitoring the progress of experiments. When PSD estimation is not carried out in real time, ACF estimation for a small number of time lags can still be implemented on-line to provide a display of the low-order moments for a few representative ranges. At MST radar installations with more sophisticated processing and display facilities, it is usual to display averaged PSD estimates for all ranges. Such displays allow experimenters to take crucial real-time decisions.

In the simplest data-acquisition schemes, the input data stream is directed to a memory buffer. Data acquisition is halted once the buffer is full, and at the same time the processor starts working on the numbers in the buffer and updates the processed results. Such single-buffer schemes are simple to implement, but work with only a fraction of raw data that could be handled with improved data-acquisition schemes. Most data-acquisition systems have a direct memory access (DMA) channel, which permits transfer of data to a memory buffer. As long as the DMA channel and the processor do not share the same memory buffer at the same time, data transfer and processing can proceed concurrently. The DMA channel can interrupt the processor but the converse is not true. If sufficient memory is available, then data-throughput can be increased by adopting a dual-buffer scheme in which two data-acquisition and processing paths are maintained in parallel, all the way from input to output. One buffer is processed while the other is being replenished, and vice versa There is a trade-off between available memory, processor speed and data throughput. This permits the use of one or several slow-processors in a multibuffer scheme. With the declining cost of microprocessors and large-scale memory chips, such schemes have become a viable alternative to large, dedicated processors for MST radar applications.

In large processors that allow several programs to run concurrently at different priorities, on-line processing tasks can be broken up into modules in such a way that time-critical operations, e.g., range gating and digitization, PSD of ACF estimation etc., run at the highest priorities. Operations such as display can be run on a very low priority. To ensure proper synchronization of these operations, a high-speed processor or an auxiliary parallel processor is usually required.

SIGNAL CODING AND DECODING

The atmosphere behaves as a diffused random medium for radio waves. The objectives of radar experiments are to probe it with as fine a range solution as possible, and to measure its velocity precisely. To attain a fine range resolution, the radar must send an infinitely narrow pulse. For precise velocity measurements, it must send a pure sinusoidal waveform. The two objectives are clearly contradictory. For a slowly moving medium, a compromise is effected by sending a modulated pulse train in which pulse duration is T_t PRI is T_p, and the duration of pulse train is T_D. In this scheme, often called the single-pulse technique, the range resolution is $0.5\ cT_t$ and the radial velocity resolution is $c/2f_0T_D$, for a radar frequency f_0. This is a standard mode of operation for many MST radars.

An obvious way to improve the range resolution, i.e., to decrease it, is to reduce the pulse duration. This is actually the approach followed in a few

tropospheric radar experiments, but it has the following disadvantage. Since practical transmitters have both a peak power and an average power limitation, sending narrow pulses at a given PRI reduces the average power that in turn degrades the received signal power and detectability of Doppler shifts. Since the range is aliased beyond 0.5 cT_p, the PRI cannot be very much reduced below about 1 msec.

An alternative method is to transmit a broad pulse, but to modulate the phase of the radio frequency carrier in accordance with a code. Successive parts of the scattering volume are now illuminated with different phases, but this can be undone through an inverse operation called decoding on the received signal. To provide a fine range resolution, a phase code should have an almost impulse-like ACF. The decoding operation then merely involves correlating the received signal with a delayed replica of the code. For two-level or binary phase codes, the decoding operation can be implemented without actual multiplications, using additions only. For this reason, and because of technical limitations in applying multi-level phase modulation to radar transmitters, binary phase codes have been widely used in MST radar experiments.

A binary phase code is simply a sequence of 0's and 1's (or + and -), where a 0 or + denotes a reference phase and a 1 or -, a phase shift of 180 deg. The time T_B corresponding to the duration of a 1 or 0 is called a baud or baud length, a term derived from telegraphy. The code length can be expressed either in bauds or in time units. Phase codes that achieve an impulse-like autocorrelation function provide a range resolution of the order of 0.5 cT_B, corresponding to the baud length. Some examples of the most commonly used binary phase codes are given below.

Barker codes. These codes are known for several lengths $n \leq 13$. The value of autocorrelation function is n at zero lag, but 0 or 1 at all non-zero lags. This code is useful when the scattered signal has a large bandwidth or a large Doppler shift, e.g., in D-region incoherent-scatter experiments (where these codes were first applied), and low-elevation ST experiments. The codes for several values of n are given below (GOLOMB and SCHOLTZ, 1965).

n = 1	+	1
n = 2	++	2
n = 3	++ -	2,1
n = 4	+++ -	3,1
n = 5	+++ - +	3,1,1
n = 7	+++ -- + -	3,2,1,1
n = 11	+++ --- + -- + -	3,3,1,2,1,1
n = 13	+++++ -- ++ - + - +	5,2,2,1,1,1,1

Complementary code pairs and sets. These codes form pairs, or more generally sets, with a very interesting property. The autocorrelation functions for the individual codes have sidelobes that exactly cancel each other upon addition. For complementary codes of length n, the sum of the two autocorrelation functions is 2n at zero lag and zero at all other lags. This behavior is near ideal. In order that perfect sidelobe cancellation may occur, it is imperative that the scattering medium should remain unchanged during illumination by the two codes in the pair, i.e., over at least two p.r.i.'s. In the most commonly used form of MST radar experiments, this happens to be true for several (tens to hundreds) p.r.i.'s. An interesting application of linear system theory provides a great saving in computations required for decoding complementary code pairs. If the signals corresponding to each code are separately and coherently integrated, then decoding can be done after coherent integration. Several complementary code pairs, adapted from RABINER and GOLD (1975), are given below.

n = 2	++
	+ −
n = 4	+++ −
	++ − +
n = 8	+++ − ++ − +
	+++ −−− + −
n = 16	+++ − ++ − ++++ −−− + −
	+++ − ++ − + −−− +++ − +
n = 32	+++ − ++ − ++++ −−− + − +++ − ++ − + −−− +++ − +
	+++ − ++ − ++++ −−− + −−−− + −− + − +++ −−− + −

The basic property of complementary code pairs, that the sidelobes in their ACFs cancel each other when the ACFs are added, can be extended to sets of codes. In his original paper, GOLAY (1961), discusses methods of forming complementary code sets from code pairs of lengths $n = 2^k$ as well as for a few other values of n. SARWATE (1983, 1984) discusses methods of forming feedback shift-register sequences with complementary property. For integer values of k, 2^k sequences of length 2^k-1 exist. For MST radar applications, complementary code sets for $n \leq 6$ should be useful. In using such code sets, some of the simplicity of decoding with complementary code pairs is lost since it is no longer possible to use coherent integration due to limitations on fading time of signals, and on the number of separate memory buffers that can be maintained. Use of fast pulse-by-pulse decoders becomes essential in this case.

Quasi-Complementary Code Sets. For a baud length T_B μsec, the transmitter should have a nominal bandwidth of $(1/T_B)$ MHz. For this finite bandwidth of the transmitter, abrupt phase transitions required for ideal phase codes cannot be faithfully reproduced. A desired phase relation may only be attained after many cycles of the carrier have elapsed. For this reason, the ideal performance of binary phase codes is rarely achieved, even if the signals returned from the atmosphere remain perfectly coherent. It is feasible to carry out a selective Brute-Force search for code sets that are quasi-complementary at a specified ACF sidelobe level. An exhaustive search of this kind is impossible even for short code lengths, e.g., 32 (SULZER and WOODMAN, 1984). When the ACFs for the entire code sets are added together, the sidelobes are at a finite though small level. The sidelobe levels tend to become randomized and even smaller when quasi-complementary code sets are used with a transmitter of finite bandwidth $1/T_B$ for probing a slowly fluctuating medium.

An empirical search for quasi-complementary code sets has been made by SULZER and WOODMAN (1984). The search was made through 0.7 billion codes of length 32 using about 350 hr of computations on an array processor connected to a host minicomputer, to first screen about 300 codes with acceptable sidelobe properties. From these a set of 48 codes was selected to give an acceptable collective sidelobe performance. In actual tests, the performance of this code set was indeed found to be superior to a complementary code pair.

Due to their inherent complexity, the use of sophisticated coding and decoding schemes is likely to be limited to only a few research facilities, most notably the Arecibo Observatory where a planetary radar decoder has been available for MST work. With the development of alternative decoding hardware (SULZER and WOODMAN, 1983; PETITDIDIER et al., 1985) it is certain that these schemes will find wider application.

Two additional limitations of coding schemes should be stressed at this point. The first one pertains to ground-clutter performance. Since a wide transmitted pulse is used, the average transmitter power in coded-pulse experiments is frequently larger than without signal coding. The ground-

clutter problem thus becomes more severe at larger ranges. The second limitation pertains to the length of the code. Since decoding is implemented as a correlation in range, a total number of range cells corresponding to the code length is wasted. In a 256-channel experiments using a 32-baud code, only 224 channels are available after decoding. Long codes are therefore not very useful for standard monostatic radar experiments. They are, however, quite useful for bistatic experiments.

ASPECTS OF STATISTICAL SIGNAL AND DATA ANALYSIS

In this section, we consider aspects of signal and data analysis with application to MST radars.

Signal statistics. In recent years, two distinct scattering mechanisms have been identified, viz. volume scattering from refractivity fluctuations and specular reflections from sharp refractivity gradients. Evidence for these mechanisms comes from observations of aspect sensitivity and spectral characteristics of scattered signals. An alternative method of discriminating between the two mechanisms is on the basis of signal statistics, in terms of their moments, probability density function, and higher-order spectra. Since the emphasis in most MST radar experiments is to obtain the PSD or ACF of the signals, there is very little direct information available on their statistics. The necessary observations for this type of analysis can be obtained by using the 'minimum processor' mentioned earlier for a small number of range cells.

PSD and ACF estimation. The PSD of the received signals is estimated as their time averaged periodogram using the discrete Fourier transform (DFT) methods. Essentially, a block of n coherently integrated complex samples is transformed, and the squared magnitude of the transform is averaged in time. The averaged PSD estimate thus obtained gives only a distorted and aliased estimate of the ACF when Fourier transformed. The direct ACF estimates obtained by an averaged lagged-product method do not have this restriction and are clearly superior. The DFT method, despite its serious drawback, has become the standard procedure for estimating the PSD. The PSD estimates can be improved by padding the sample block with n zeros and transforming the resulting 2n points at a time.

Data smoothing and outliers. Radar data are frequently contaminated with data points of dubious validity. Visual inspection of almost any time series will show a few points that clearly do not belong. Such points are usually called outliers. Manual editing of outliers is impractical for large data sets. Direct averaging of data points is likely to yield a biased and even meaningless average. The following procedures based on median and order statistics reduce the effect of outliers on averages.

The median of a given data set is a more realistic indicator of its average than the mean. For a long data sequence, a 7-point running median (e.g.) performs better smoothing than a 7-point running mean and is robust with respect to outliers. Mean is obtained as a linear combination of data points, whereas median does not possess any such properties. When some smoothing is to be performed on data contaminated with outliers, a very acceptable smoothing procedure is to consider a block of n data points, sort them in ascending order, discard x% of the highest and lowest values and average over the remaining points. It is necessary to sort out only a few highest and lowest values. This scheme discriminates between data points and outliers on the basis of their magnitudes. If more is known of outlier statistics, better algorithms can be devised. No rejection scheme can be perfect, however, for some good data points may be rejected and some outliers may be accepted. A good scheme will tend to minimize these errors.

Data-analysis techniques based on median and order statistics provide a quantitative basis for handling noisy data. Recently, these methods have been successfully applied to editing and analysis of ST spectra at Millstone Hill. D-region incoherent-scatter data from Arecibo (GERMAN, 1985; YING, 1985), and power-law analysis of mesoscale winds from Poker Flat (BEMRA, 1985). Potential MST applications include improved interference rejection algorithms for spectral moment estimation, and improved filtering schemes for automated analysis of large data sets.

ACKNOWLEDGEMENT

This work was supported under NSF Grant ATM-8313153.

REFERENCES

Bemra, R. S. (1985), Study of gravity waves at 5-min to 5-day periods in the troposphere and stratosphere using the Poker Flat MST radar, M.S. Thesis, EEAP Dep., Case Western Reserve University.

Farley, D. T. (1984), Overview of on-line data processing for MST radars, Handbook for MAP, 14, edited by S. A. Bowhill and B. Edwards, SCOSTEP Secretariat, Dep. Elec. Computer Eng., Univ. IL, Urbana-Champaign, 262-267.

German, M. J. (1985), Interference detection and correction while performing ionospheric studies with an incoherent-scatter radar, M.S. thesis, EEAP Dep., Case Western Reserve University.

Golay, M. J. E. (1961), Complementary series, IRE Trans. Inf. Th., IT-7, 82-87.

Golomb, S. W., and R. A. Sholtz (1965), Generalized Barker sequences, IEEE Trans. Inf. Th., IT-11, 533-537.

Petitdidier, M., A. Desautez, M. Glass, and G. Penazzi (1985), A decoder for a 30-m height resolution ST radar, Radio Sci., 20, 1141-1145.

Rabiner, L. R., and B. Gold (1975), Theory and Application of Digital Signal Processing, Prentice-Hall.

Rastogi, P. K. (1983), Data processing techniques used with MST radars: a review, Handbook for MAP 9, edited by S. A. Bowhill and B. Edwards, SCOSTEP Secretariat, Dep. Elec. Computer Eng., Univ. IL, Urbana-Champaign, 477-488.

Rottger, J. (1984), The MST radar technique, Handbook for MAP, 13, SCOSTEP Secretariat, Dep. Elec. Computer Eng., Univ. IL, Urbana-Champaign, 187-232.

Sarwate, D. V. (1983), Sets of complementary sequences, Electronics Lett., 19, 711-712.

Sarwate, D. V. (1984), Construction of complementary code sequence sets, Handbook for MAP, 14, edited by S. A. Bowhill and B. Edwards, SCOSTEP Secretariat, Dep. Elec. Computer Eng., Univ. IL, Urbana-Champaign, 276-277.

Sulzer, M. P., and R. F. Woodman (1983), Decoding: codes and hardware implementation, Handbook for MAP, 9, edited by S. A. Bowhill and B. Edwards, SCOSTEP Secretariat, Dep. Elec. Computer Eng., Univ. IL, Urbana-Champaign, 489-495.

Sulzer, M. P., and R. F. Woodman (1984), Quasi-complementary codes: a new technique for MST radar sounding, Radio Sci., 19, 337-344.

Ying, W. P. (1985), Analysis of the D-region incoherent scatter ion line power spectra, M.S. Thesis, EEAP Dep., Case Western Reserve University.

SUMMARY

The keynote paper on this topic reviewed salient aspects of data acquisition, use of phase codes and decoding techniques, estimation of ACF and PSD, and data-processing methods used in MST radar probing of the atmosphere. Additional papers on this topic focussed on three important areas. These papers were followed by brief invited reviews of points that would be generally useful but are often overlooked.

CODING AND OTHER TECHNIQUES FOR IMPROVING RANGE RESOLUTION

SULZER and WOODMAN described a practical approach for implementing optimum codes for which decoding is done through "inverse" codes that correct for non-ideal behavior of high-power transmitters.

STITT and BOWHILL presented a frequency-hopping scheme within the coherence time of signals, that provides improved range resolution. This technique is equivalent to a digital frequency chirp within the signal coherence time, and is potentially useful for very slowly fading signals e.g., in HF radar experiments.

HARDWARE DEVELOPMENTS

STITT and JOHNSON described a variable frequency local oscillator, using computer controlled phase-lock loops, for de-chirping in the frequency-hopping scheme mentioned above.

BOWHILL and RENNIER described an inexpensive but versatile data-taking system using an Apple microcomputer and Forth language. This system is used in ST experiments with the Urbana radar to obtain spectral moments in real time and to display velocities up to 29 km altitude. The system cost is about $5000.

CARTER et al. described an inexpensive preprocessor and pulse-generator card for coherent integration.

DATA PROCESSING

ROTTGER described a matched-filter algorithm for enhancing signal spectra. GREEN, YING et al., and BOWHILL discussed the application of median and related statistics for spectral and data editing. GREEN described the use of a 3-spectra median statistic, with smoothing and peak tracking, for reducing the effect of interference echoes. YING et al. presented methods based on median and percentiles for forming templates that are effective in rejecting interference in routine processing of D-region incoherent-scatter spectra. BOWHILL described a three-point median filtering algorithm due to Tukey, and discussed its effectiveness in removing single outliers.

INVITED DISCUSSIONS

ROTTGER described an on-line technique for removing the instrumental dc effects in which the phase of transmitted pulse is alternately switched between 0 and 180 deg, and the receiver output corresponding to the latter is inverted in sign. When the receiver output for successive pulses is accumulated, it is virtually devoid of instrumental dc effects. This method has been in use at Jicamarca for almost 25 years and deserves the attention of groups designing new MST radars.

SATO summarized the distortions introduced in the PSD estimates through the method of averaged periodograms using the DFT algorithms. These distortions are introduced through the aliasing of the ACF, and are most significant in the presence of a very slowly fading near dc component. The effect of these distortions is frequently apparent in UHF radar spectra contaminated by slowly fading and slightly Doppler-shifted strong ground clutter. These distortions also become very important in the analysis of meso-scale wind fluctuations with a power-law spectrum.

WOODMAN commented on the computational and SNR advantages of using coding and decoding techniques in MST radar experiments, especially when the operations of decoding and coherent integration can be commuted with little extra storage, e.g., with the use of complementary code pairs.

CONCLUDING REMARKS

It appears that an awareness of signal-processing and data analysis methods that have been developed through research use of MST radars over the last 15 years would be of benefit to groups currently involved in designing and constructing new radars. Most of the on-line signal processing tasks can be implemented inexpensively through modules using microprocessors and signal-processing chips. Median and related filtering schemes provide an effective means for automated editing of radar spectra and derived parameters contaminated with interference or other outliers. These schemes deserve further examination.

8.1.1 OPTIMUM CODING TECHNIQUES FOR MST RADARS

Michael P. Sulzer

Arecibo Observatory
Box 995
Arecibo, Puerto Rico

and

Ronald F. Woodman

Instituto Geofisico del Peru
Apartado 3747
Lima, Peru

INTRODUCTION

The optimum coding technique for MST radars is that which gives the lowest possible sidelobes in practice and can be implemented without too much computing power. Coding techniques are described in FARLEY (1985). The best technique, in theory, is the complementary code pair. Coherent integration can be used to reduce the size of the data set, and so the amount of computation is not excessive. The sidelobes are zero in theory, but when errors induced by imperfections in the modulation of the transmitter are significant, the quasi-complementary set gives better results (SULZER and WOODMAN, 1984). However, this technique requires an extraordinary amount of computation. We discuss here a technique mentioned briefly in FARLEY (1985), but not fully developed and in general use. This is decoding by means of a filter which is not matched to the transmitted waveform, in order to reduce sidelobes below the level obtained with a matched filter. This is the first part of the technique discussed here; the second part consists of measuring the transmitted waveform and using it as the basis for the decoding filter, thus reducing errors due to imperfections in the transmitter. There are two limitations to this technique. The first is a small loss in signal-to-noise ratio, which usually is not significant. The second problem is related to incomplete information received at the lowest ranges. Appendix A shows a technique for handling this problem. Finally, we show that the use of complementary codes on transmission and non-matched decoding gives the lowest possible sidelobe level and the minimum loss in SNR due to the mismatch.

THE CODING-DECODING PROCESS

A model of the coding-decoding process starts with a square pulse of length t_p where t_p corresponds to the desired range resolution and the square pulse is described by $h_{sq}(t)$, since the pulse may be thought of as the response of a filter to an impulse, and thus is identified by the impulse response of this filter. This square pulse is what we would like to transmit if we had sufficient peak power. If no coding is done, the received signal is passed through a matched filter and is given by

$$s(t) = h_{sq}(t)*h_{sq}(-t) \tag{1}$$

The impulse response of the matched filter is just the flip of that of the transmitted signal, or in the frequency domain, the amplitude responses are the same and the phases are additive inverses.

If we use a phase code, then

$$s(t) = h_{sq}(t)*h_c(t)*h_{sq}(-t)*h_{dc}(t) \tag{2}$$

$h_c(t)$ is the impulse response of the coding filter. For a binary phase code $h_c(t)$ is a sequence of positive and negative impulses. For normal decoding $h_{dc}(t)$ is the flip of $h_c(t)$. For a perfect code $h_c(t)*h_c(-t)$ is an impulse. Imperfect codes will give sidelobes.

Consider the function $h_{dcp}(t)$ for an arbitrary code such that

$$h_c(t)*h_{dcp}(t) = [\text{impulse}] \tag{3}$$

This is the decoding function which eliminates all sidelobes. It exists for most codes, and it is calculated from the Fourier transform of $h_c(t)$:

$$H_c(f) = A_c(f)e^{j[\text{phi}(f)]} \tag{4}$$

Then the impulse response of the decoding filter with no sidelobes is

$$h_{dcp}(t) = F^{-1}[(1/A_c(f))e^{j[-\text{phi}(f)]}] \tag{5}$$

As long as $A_c(f)$ has no zeros the inverse exists. The perfect code has $A_c(f)$ equal to a constant, and requires no amplitude correction at all. For good codes, the amplitude function is nearly constant and thus, the inverse exists and varies little as a function of frequency. The effect of the inverse amplitude filter is to pass more random noise than in normal decoding. This is one cost of eliminating the sidelobes, one that is a function of how good the code is. With a good code such as the 13-bit Barker code, the loss in signal to noise ratio is about .25 dB, hardly significant. A randomly selected code might lose several dB. A second problem is that $h_{dcp}(t)$ is infinitely long and thus can never be used exactly for deconvolution. Sometimes this does not matter, and there are techniques for minimizing the effect when it is important that sidelobes be kept very small at very close ranges.

EXPERIMENTAL RESULTS

The results of various types of decoding are shown in Figures 1 through 4. These consist of the transmitted 430-MHz signal and the received signal covering a total time period of 256 microsec. The transmitted signal was the output of a probe in the waveguide; the received signal consisted of ground clutter and atmospheric scatter. The figures show power versus range, and it is the ground clutter which is the dominant signal. The two signals were added at the i.f. (30 MHz) level and thus passed through a common 500-kHz Gaussian filter. The transmitter was coded with a 13-baud Barker code with 2 microsec baud length. The sampling rate was also 2 microsec. The response of the sampled transmitted waveform to the decoding process is called the system function, since it shows the response of the receiver and decoder to a very narrow target.

Figure 1 shows the power versus range obtained when the transmitted and received signals are decoded with the Barker code. The main lobe of the decoded transmitter signal is broadened by the 500-kHz. Gaussian filter and sidelobes are visible both before and after the main lobe. The sidelobes before the main lobe are very close to the expected -22 dB level. The sidelobes following the main lobe are quite different. We shall not discuss the generating mechanism of these sidelobes except to say that both finite bandwidth and nonlinearities are involved, since physical filters can only affect the signal at later times.

Figure 2 shows the same data decoded with the inverse of the Barker code. The sidelobes to the left of the main lobe have been considerably reduced, since the sidelobes due to the code have been removed, while those that are

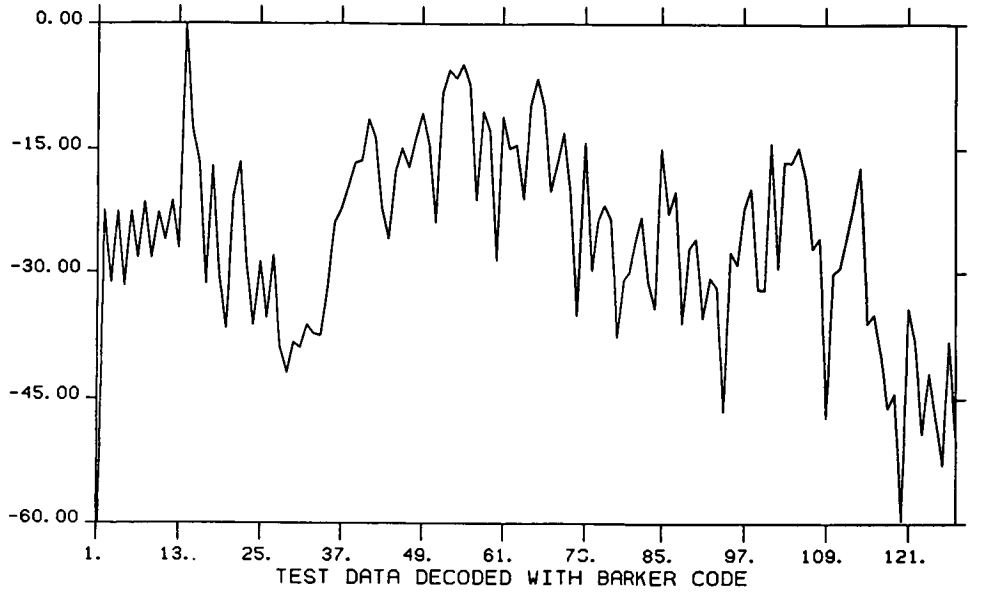

Figure 1.

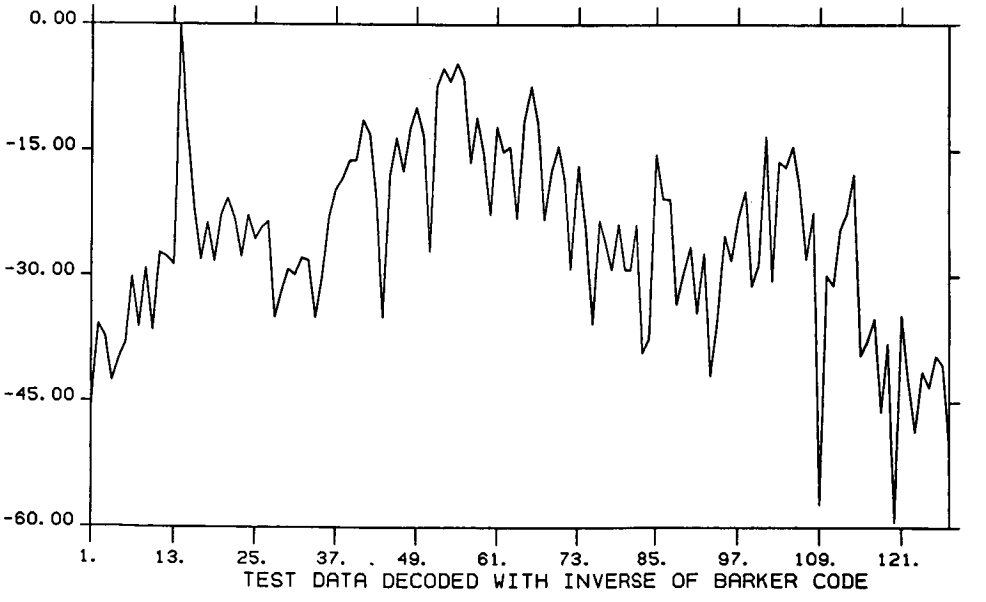

Figure 2.

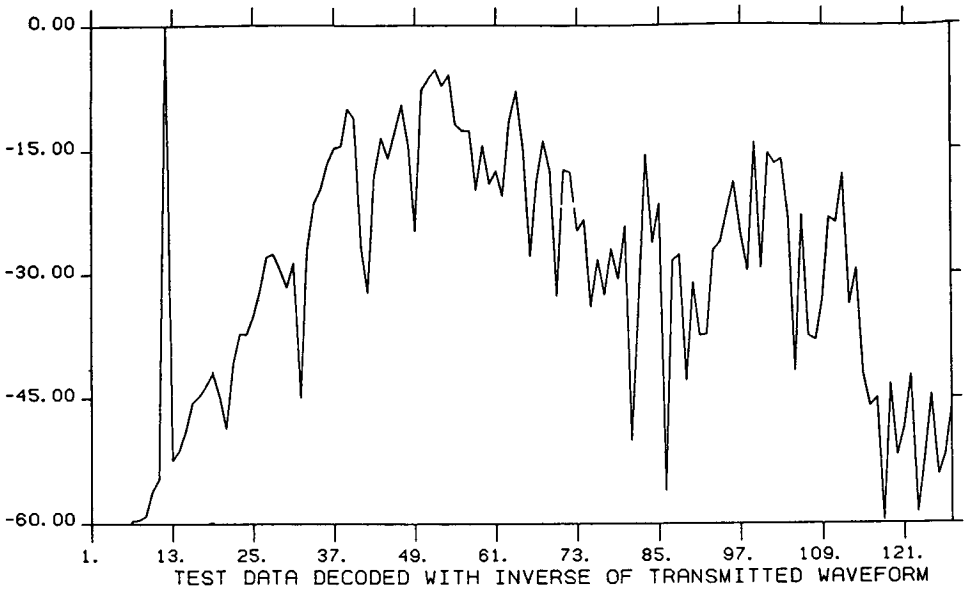

Figure 3.

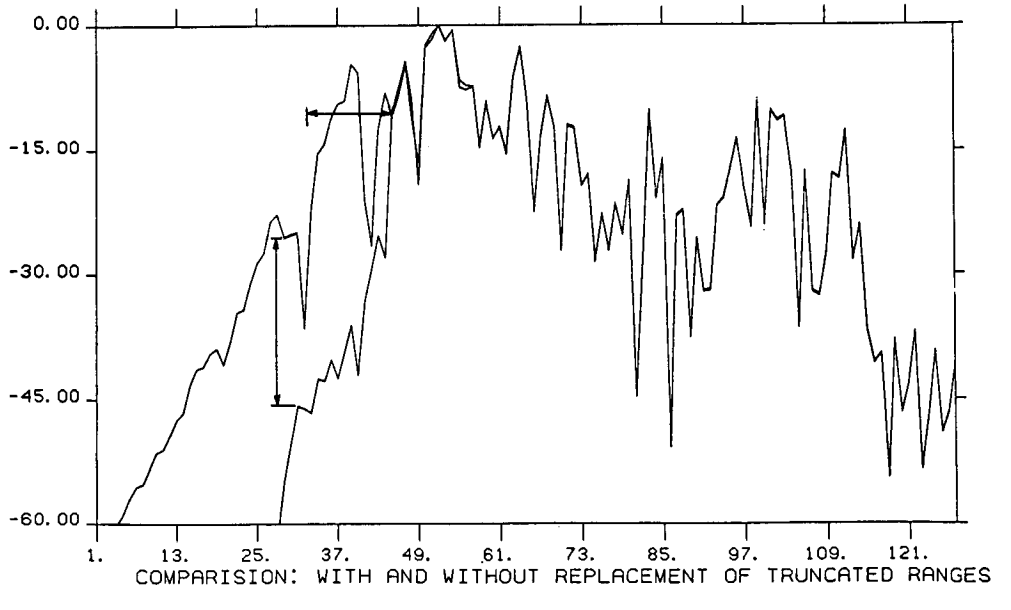

Figure 4.

left are from imperfections in the transmitted waveform. In the forward direction, the sidelobes are not significantly changed since the dominant effect already was the imperfections. The gap between the transmitted and received signals has been partly filled with signal. This has happened because the first range gates of the received signal contain signal from ranges which are truncated by the receiver cutoff. Complete decoding is impossible with either the Barker code or its inverse, but the inverse of the code gives worse response in this respect because the convolving waveform is longer than the code. A comparison of the first two figures reveals some reduction in sidelobe level near the end of the sampled period.

Figure 3 shows the same data decoded with the inverse of the transmitted waveform. Sidelobes are of course completely removed from the transmitted signal. The remaining signal at these delays is due to leakage of the truncated signal to lower altitudes. The range of the leakage has increased due to the increased length of the inverse code. The effect of the Gaussian filter has also been removed, and some signal-to-noise ratio has been lost in doing this. Square pulse matched filters should be used, and then the data will have the ideal triangular shape which is achieved when using a Gaussian filter only by some increase in noise. Finally, the decrease in sidelobes is evident near the end of the sampled time period.

As mentioned before, the leakage due to the truncation of the lower ranges can be reduced. The technique for doing this is explained in detail in Appendix A; briefly, the normal decoding method is used to find the signals at the lower ranges, with sidelobes, of course. The signals from the truncated ranges can then be subtracted away to an accuracy determined by the sidelobe level. The nonmatched decoding technique is used with the result that the range nearest the truncated ranges has leakage about equal to the sidelobe level of the normal decoding method, but the sidelobe levels decrease quickly with increasing range. Figure 4 shows a comparison of the decoding with and without removal of the truncated ranges. The differences in the leakage levels in the direction of decreasing range are similar to the differences expected in the other direction. Using the subtraction technique reduces the leakage by about 20 dB in the lower ranges and it becomes completely insignificant within one pulse width.

PRACTICAL USES OF THE TECHNIQUE

The complementary code pair provides very low sidelobes in many practical circumstances. Two cases where it does not are:

1) When the coherence time is short compared to twice the interpulse period. This is usually the case with incoherent scatter.

2) When transmitter modulation errors are significant.

As long as the coherence time is longer than the pulse length, we can take any good code and gain a substantial reduction in sidelobes with this technique.

If transmitter modulation errors are a problem but the coherence time is long, then we can use a modification of the technique. The complementary codes are used to modulate the transmitter in the normal way. What is transmitted is somewhat in error, and when we decode, we choose $h_{dc}(t)$ for each complementary code such that the sidelobes of the complementary code are achieved. In other words, we do not try to get rid of the sidelobes, but merely make them what they would have been in the absence of the transmitter errors. As long as transmitter errors are small, this involves a very small correction to the spectral amplitude function, and hence causes no noticeable loss in signal-

to-noise ratio. When the returns from the complementary pair are added, there will be no sidelobes. Since the correction is very small, truncation errors will also be very small.

REFERENCES

Farley, D. T., On-line data processing techniques for MST radars, Radio Sci., 20, 1177-1184.

Sulzer, M. P., and R. F. Woodman (1984), Quasi-complementary codes: a new technique for MST radar sounding, Radio Sci., 19, 337-344.

Appendix A

Reducing the Effect of Truncated Ranges

The problem with the truncated ranges that affects the technique described in this paper occurs because given an infinite decoding waveform, the extent of leakage of a range for which the signal is incomplete is infinite. The solution to the problem depends upon the fact that with normal decoding, only those heights that are truncated are affected. The explanation of these two statements requires a detailed examination of the coded waveform.

Figure A1 shows how this waveform can be broken into its component parts. Figure A1a shows the radar signal before decoding. No signal is received to the left of the vertical line because of the receiver cutoff. Figures A1b and A1c show returns from two ranges. When the returns from these two ranges and also from all other ranges are added the signal of Figure A1a is obtained. The signal of Figure A1c is completely to the right of the heavy vertical line, and this means that we have all the information from that range. On the other hand, the signal of Figure 2b is partly to the left of the vertical line, and thus we have only a part of the information from this range. This range is referred to as a truncated range.

Figure A1d shows the waveform used in normal decoding in a position for decoding the lowest nontruncated range. Sidelobes from the truncated ranges are decoded normally, and the lack of information to the left of the vertical line does not affect the decoding of nontruncated ranges. Figure A1e shows the inverse of the Barker code placed in position to decode the same lowest nontruncated range. This waveform extends to the left of the vertical line and thus requires all the information from the truncated ranges in order to reject them completely.

In order to reduce this effect, we decode the first n-1 untruncated ranges using normal decoding (n is the length of the code). This waveform contains normal sidelobes from the truncated ranges below and the untruncated ranges above. We recode this signal, which means convolving with the code. Both the wanted signal and the unwanted sidelobes are convolved with the code and thus look like coded signals. Next, we replace the first n-1 numbers in the original coded signal with zeros; this is the first n-1 samples to the right of the vertical line in Figure A1a. Then, we add to this the recoded waveform from the last step. Finally, inverse decoding is performed on the composite waveform. In the lower ranges, we get sidelobe levels about the same as with normal decoding, but the sidelobes go to zero very quickly as the range increases.

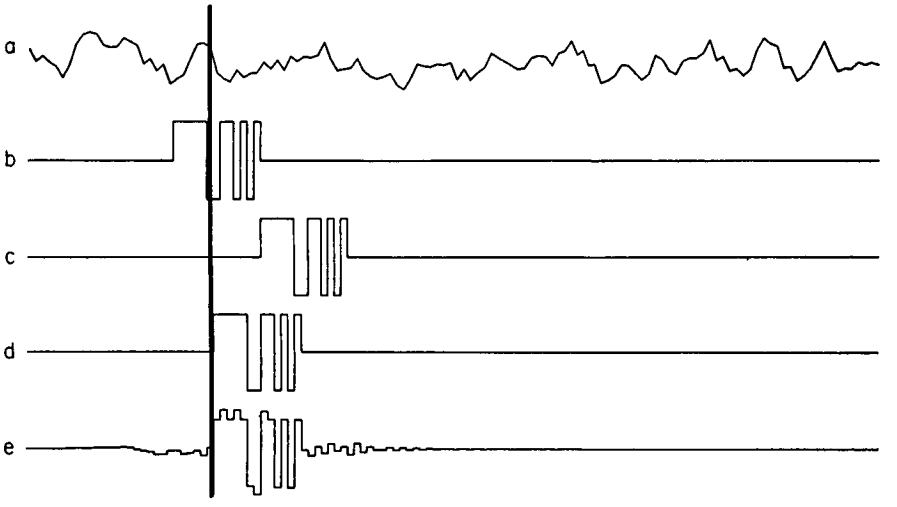

Figure A1.

8.1.2 IMPROVING RANGE RESOLUTION WITH A FREQUENCY-HOPPING TECHNIQUE

G. R. Stitt and S. A. Bowhill

Aeronomy Laboratory
Department of Electrical and Computer Engineering
University of Illinois
Urbana, Illinois 61801

INTRODUCTION

Range resolution of a conventional pulsed Doppler radar is determined by the scattering volume defined by the transmitted pulse shape p(z). To increase the resolution, the length of the pulse must be reduced. Reducing the pulse length, however, also reduces the transmitted power and hence the signal-to-noise ratio unless the peak power capability of the transmitter is greatly increased, which is a very expensive process. Improved range resolution may also be attained through the use of various pulse-coding methods, but such methods are sometimes difficult to implement from a hardware standpoint. The "frequency-hopping" (F-H) technique to be described increases the range resolution of pulsed Doppler MST radar without the need for extensive modifications to the radar transmitter. This technique consists of sending a repeated sequence of pulses, each pulse in the sequence being transmitted at a unique radio frequency that is under the control of a microcomputer.

All of the radar parameters in the following discussion, such as pulsewidth and Inter Pulse Period (IPP), apply to the F-H system being developed for the Urbana radar.

ANALYSIS OF SYSTEM

Figure 1 shows one way of representing the pulse train sent by the radar transmitter. Since the wavelength of each pulse differs from that of its neighbors by about one centimeter, it is to be expected that echoes from a turbulent scatterer will differ slightly from each other in phase. Taking advantage of these phase differences constitutes the crux of the frequency-hopping technique.

The frequency sequence applied to consecutive transmitter pulses is also shown in the pulse pattern diagram of Figure 2. For example, at time $t = 0$, a pulse is sent at frequency ω_o; at time $t = \tau$, a pulse is sent at frequency $\omega_o + \Delta\omega$, and so forth. At time $t = 16\tau$, the pattern repeats itself. The range of frequencies covered by the pattern is 750 kHz, with contiguous frequencies separated by 50 kHz. Notice that the sawtooth waveform of Figure 2 repeats itself three times every 1/8 s. The present Urbana coherent scatter system integrates samples for 1/8 s. Hence, by integrating samples corresponding to three of the waveforms in Figure 2, the F-H system possesses a coherently integrated sample length identical to that of the present coherent scatter system. It must be realized, however, that only samples taken at the same frequency may be coherently summed. Consequently, each 1/8-second coherently integrated F-H sample actually consists of 16 subsamples, with each subsample comprised of three individual samples at the same frequency added together.

Consider the situation that the atmosphere contains only a single infinitely thin, mirror type scatterer located somewhere within the range gate z_o, and moving with a constant velocity v_d throughout the collection of a 1/8-second coherently integrated data sample. In this case, nonzero samples are obtained only for range gate z_o. Consider also the following sample sequence x(n):

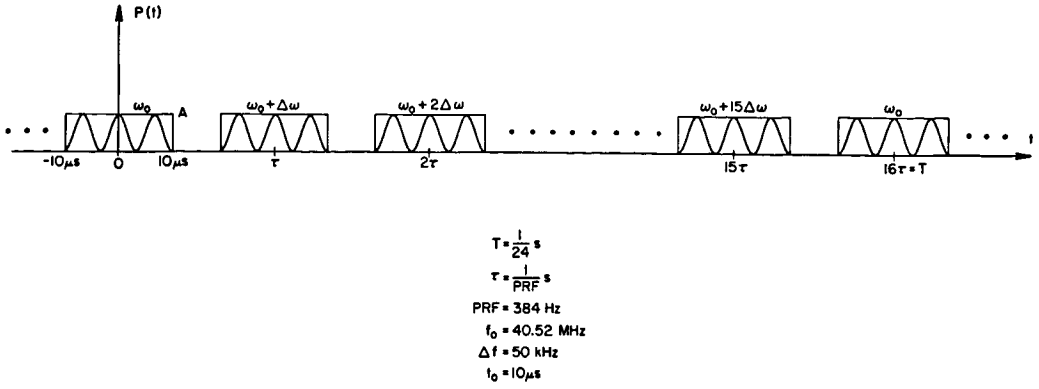

Figure 1. Pulse train sent by the radar.

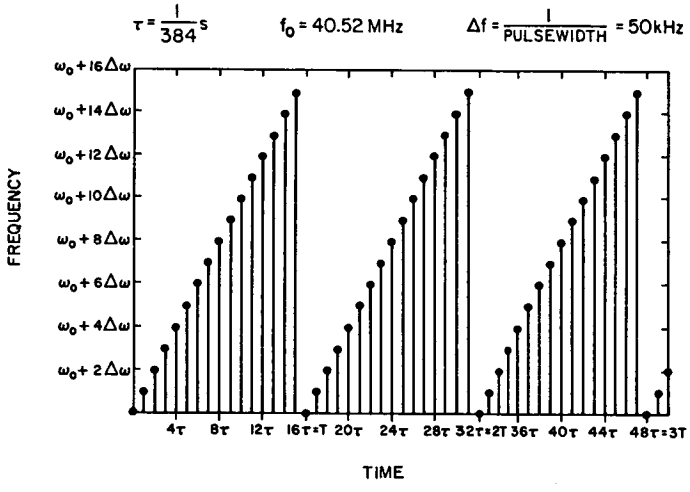

Figure 2. Time vs. frequency pulse pattern of the F-H system.

$$x(n) = B_n e^{j\phi_n} \qquad (1)$$

where n = 0, 1, 2, ..., 47. x(n) is the sequence that results from sampling the radar returns caused by the reflection of the transmitted pulse train shown in Figure 1 from the mirror scatterer. Notice that the index of x(n) takes on the values 0-47. Hence, x(n) consists of all the individual samples contained in a single 1/8-second coherently integrated F-H sample. B_n is the magnitude of sample n, and ϕ_n is the phase.

The mirror scatterer is a delta function in range space; that is, as a function of z. Consequently, its Fourier transform is a constant for all values of wave number k. Since radar pulses are scattered by fluctuations in the index of refraction with a nonzero Fourier component equal to one-half

the radar wavelength in the direction of propagation of the pulse, the ideal mirror scatterer reflects radar pulses at all frequencies equally well. As a result, all samples of the sequence x(n) have the same magnitude, and equation (1) may be rewritten as

$$x(n) = Be^{j\phi_n} \tag{2}$$

In order to consider the phase ϕ_n of the samples of the sequence x(n), it is convenient to make the following definitions. Let

$\tau = 1/384$ s
$f_o = 40.52$ MHz
$\Delta f = 50$ kHz
v_d = the velocity of the scatterer
Δz = the distance, at time t = 0, at which the scatterer is located above or below z_o. Δz must satisfy the relation $|\Delta z| \leq 1.5$ km
λ_n = the wavelength of the nth radar pulse
f_n = the frequency of the nth radar pulse
$= f_o + (n)_{16}\,\Delta f$
z_n = the height of the scatterer when it reflects the nth radar pulse
$\approx z_o + \Delta z + v_d\, n\tau$
$(n)_{16}$ = n mod 16

With these definitions, ϕ_n may be written as

$$\phi_n = \frac{4\pi}{\lambda_n} z_n$$

$$= \frac{4\pi}{C}\left[f_o z_o + f_o \Delta z + f_o v_d n\tau + (n)_{16}\Delta f z_o + (n)_{16}\Delta f(\Delta z + v_d n\tau)\right] \tag{3}$$

Substituting the above result for ϕ_n into equation (2) yields

$$x_n = B\exp\{j\frac{4\pi}{C}[f_o z_o + f_o \Delta z + f_o v_d n\tau + (n)_{16}\Delta f z_o + (n)_{16}\Delta f(\Delta z + v_d n\tau)]\}$$

Let us define the constant α as

$$\alpha = \frac{4\pi}{C}(f_o z_o + f_o \Delta z)$$

Using this definition, and noting the property

$$\exp\{j\frac{4\pi}{C}[(n)_{16}\Delta f z_o]\} = 1$$

the expression for x(n) may be written as

$$x(n) = Be^{j\alpha}\exp\{j\frac{4\pi}{C}[f_o v_d n\tau + (n)_{16}\Delta f(\Delta z + v_d n\tau)]\} \tag{4}$$

Recall that in each 1/8-second coherently integrated F-H sample, individual samples at the same frequency are to be coherently summed. So if y(n) is the 16-point sequence that results from adding individual samples at the same frequency, then

$$y(n) = \sum_{m=0}^{2} x(16m+n)$$

$$\approx 3B \exp\{j\frac{4\pi}{C}[f_o z_o + \Delta z(f_o + n\Delta f) + v_d(16\tau + n\tau)(f_o + n\Delta f)]\} \quad (5)$$

where n = 0, 1,..., 15. Notice that since the index of the sequence y(n) has a maximum value of 15, the clumsy modular notation has been dropped.

The third phase term in equation (5) results in a systematic error in the range estimation of the scatterer, due to the velocity of the scatterer itself. However, this effect is of concern only if the third phase term is approximately the same size as the second, which is due to the actual position of the scatterer. In order to gain an idea of the scatterer velocity that is necessary for this to occur, the two terms may be set equal.

$$v_d = \frac{\Delta z}{16\tau + n\tau}$$

Substituting the worst case values $\Delta z = 200$m, n = 15 into the equation above, it becomes clear that the scatterer must be moving with a velocity of at least $v_d = 2500$ m/s in order for the two terms to be about equal. Hence, for all practical purposes, the third phase term of equation (5) may be ignored.

Recalling the definition of α, a constant D may be defined as $D = 3B \exp(j\alpha)$. Using this definition and the equation

$$\frac{4\pi}{C}(n\Delta f \Delta z) = \frac{n\pi\Delta z}{8d_o}$$

where $d_o = 187.5$ m, equation (5) may be rewritten as

$$y(n) = D \exp(j\frac{n\pi\Delta z}{8d_o}) \quad (6)$$

where n = 0, 1, ..., 15.

Equation (6) reveals the form of the individual samples in a single 1/8-second coherently integrated F-H sample, assuming a single mirror-type scatterer located somewhere within the range gate z_o. As anticipated, each sample has the same magnitude, and there is a phase difference from one sample to the next. This intersample phase difference is in fact linear, and its size depends upon the distance Δz of the scatterer from the center of the scattering volume (z_o).

To take advantage of the linear intersample phase shift present in the sequence y(n) of equation (6), it is possible to simply calculate the DFT of the sequence. Figure 3 shows graphs of the sequence Y(p) resulting from the DFT of y(n), assuming different values for Δz. It is clear that as Δz becomes more positive, the intersample phase shift in (6) becomes larger, and the central peak of Y(p) moves up the graph. Conversely, as Δz becomes more and more negative, the central peak of Y(p) wraps around to the top of the graph, and begins to move down it.

When a 1/8-second coherently integrated F-H sample is obtained from the atmosphere for range gate z_o, the value of Δz is of course not known. It is made clear by the graphs of Figure 3, however, that by taking the DFT of the individual samples within the coherently integrated sample, it is possible to deduce the position of the scatterer Δz within the scattering volume by the position of the central peak of Y(p). This fact is the basis for the improved range resolution offered by the frequency-hopping technique.

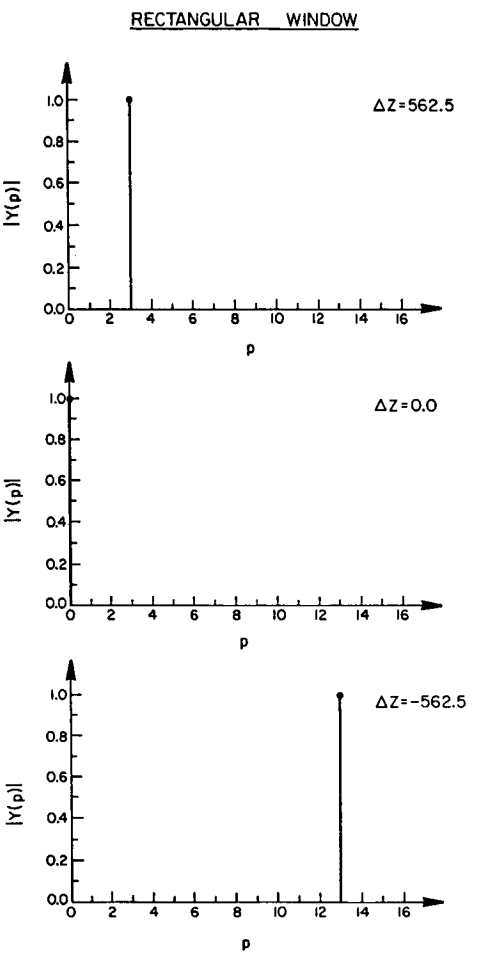

Figure 3. Y(p) for different values of Δz.

A more complex analysis involving the convolution of the pulse train in Figure 1 with scatterers present in the atmosphere, and taking into account the coherent detection scheme employed by the Urbana radar, has also been performed; it yields results similar to those obtained using the more intuitive approach outlined above.

COMPLICATIONS IN ANALYSIS

All of the values of Δz assumed in the graphs of Figure 3 are integer multiples of d_o = 187.5 m. d_o is the basic range resolution of the frequency-hopping system; integer multiples of d_o may therefore be termed "subrange" gates of the system. Hence, all of the scatterers in the graphs of Figure 3 are assumed to fall exactly in the middle of a subrange gate. This pleasant situation is unlikely to be duplicated in the real atmosphere. Figures 4(a) and 5(a) show graphs of Y(p) plotted in semilog form for more arbitrary values of Δz. A scatterer is shown starting in the middle of the third subrange gate, and gradually moving downward until it reaches the point

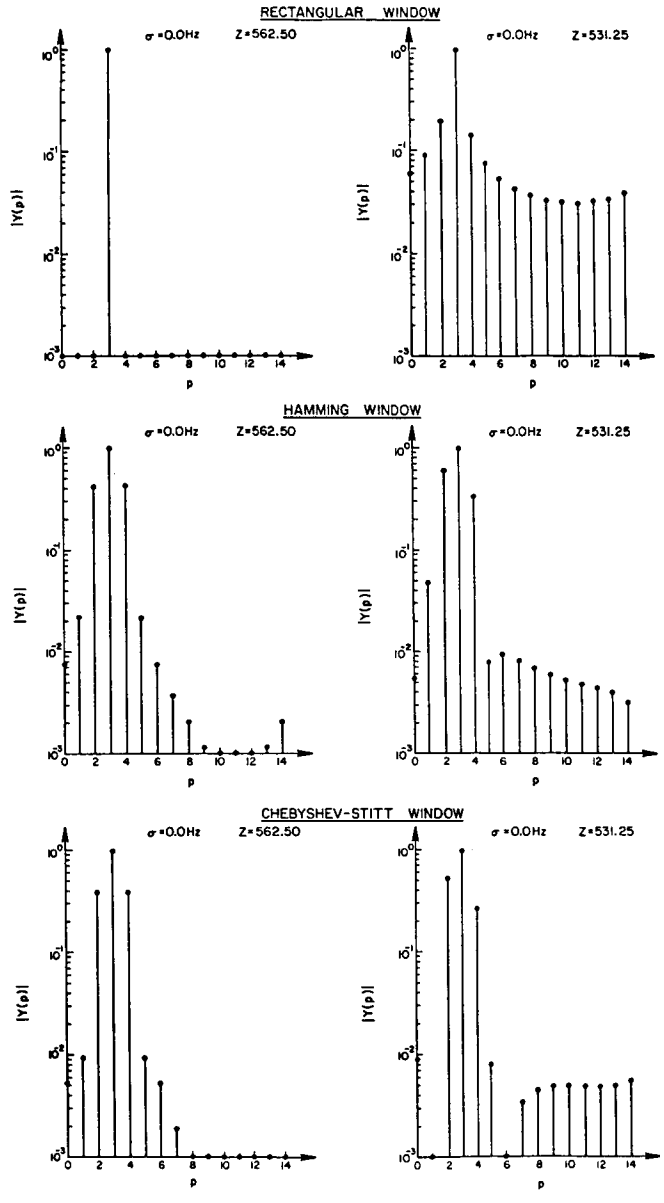

Figure 4. Effects of different windows.

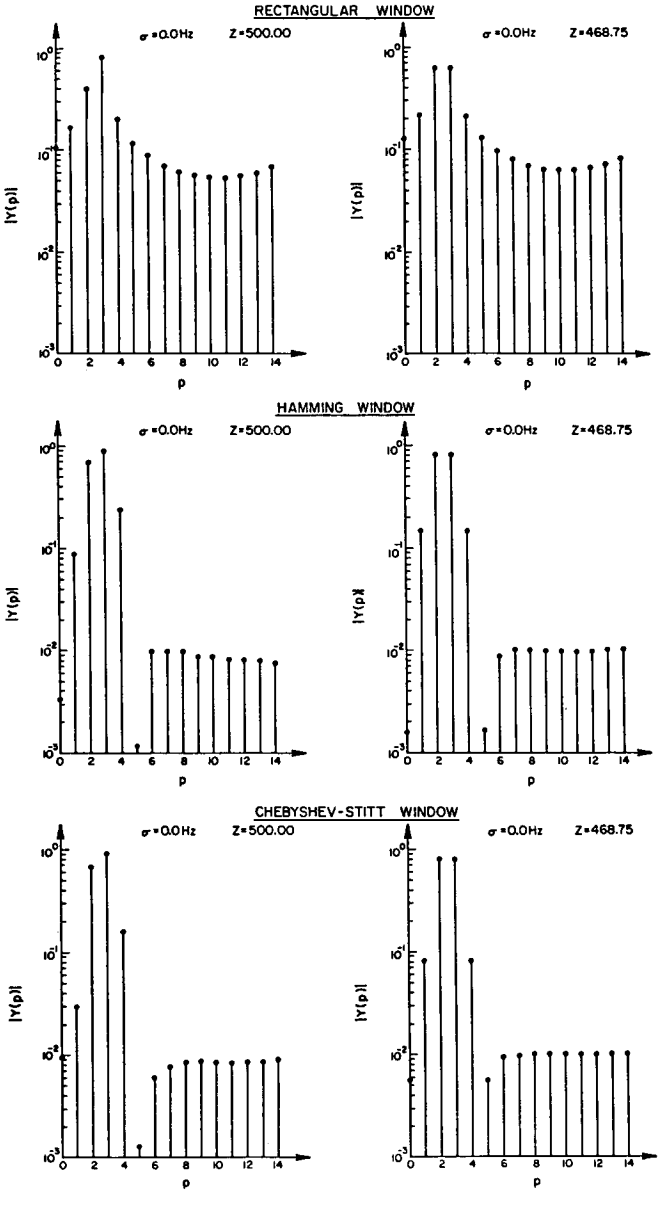

Figure 5. Effects of different windows.

halfway between the second and third subrange gates. The central peak of Y(p) remains in the correct position, but it is now accompanied by undesirable sidelobes in the subrange gates that should be zero.

The sidelobes present in the graphs of Figures 4(a) and 5(a) are due to the fact that the sequence y(n) of equation (6) is unwindowed; or, to be more precise, a rectangular window has been applied. To reduce the sidelobes, a window having more gently rounded edges may be used. In other words, we may derive a new sequence y(n), having more desirable transform properties, from the old sequence y(n) as follows

$$y(n) = Dn \exp(j\frac{n\pi\Delta z}{8d_o}) \tag{7}$$

where $D_n = w(n)D$, and w(n) is a windowing sequence of length 16.

Figures 4(b) and 5(b) show the effects of selecting a Hamming window sequence for w(n). A useful reduction in sidelobe level has been achieved, at the cost of a slight increase in the width of the main peak, or lobe, of the sequence Y(p).

Although the standard Hamming window quite effectively reduces the sidelobes of Y(p), the unusual form of the sequence y(n) in equation (7) makes possible a somewhat more clever approach. Since the weighting sequence D_n in (7) is arbitrary, it is possible to specify that D_n must be symmetric about its center. In this case, it may be shown that the DFT of y(n) can be written as

$$Y(\psi) = \sum_{n=0}^{\frac{N}{2}-1} An \cos[(2n+1)\frac{\psi}{2}] \tag{8}$$

where
$$A_n = A_{-(n+1)}$$
$$= D_{n+N/2}$$
$$\psi = \pi(p - N/2\,\Delta z/d_o)/8$$
$$N = 16$$

Since a relationship exists between A_n and D_n, if values can be found for A_n, then the values of the weighting coefficients D_n will be known. One way of finding appropriate values for A_n is by solving the equation

$$Y(\psi) = T_7(x)$$

where $T_7(x)$ = a seventh order Chebyshev polynomial (9)
$x = a \cos(\psi/2)$
a = an arbitrary constant

$T_7(x)$ is a polynomial consisting of terms of the form $[a \cos(\psi/2)]^k$, where k is an odd, positive integer. On the other hand, $Y(\psi)$ is a polynomial consisting of terms of the form $\cos(p\,\psi/2)$, where p is also an odd, positive integer. In order to solve equation (9), then, trigonometric identities must be used to reduce terms of the form $[a \cos(\psi/2)]^k$ into terms of the form $\cos(p\,\psi/2)$. This can be a very tedious process. Fortunately, operations of this kind are tabulated in books on antenna engineering (see, e.g, JASIK, 1961).

Figures 4(c) and 5(c) show the results of applying a window of this type to the sequence of equation (7). Although these results appear very similar to those obtained using a standard Hamming window, the sidelobe levels and

mainlobe width have in fact been slightly reduced. A window of this type should be optimal in the sense of giving the narrowest possible main lobe for a specified sidelobe level, or vice versa. The main lobe width may be varied by adjusting the value of the arbitrary constant a. In generating the graphs of Figures 4(c) and 5(c), the value of a was chosen so that the sidelobe level is approximately 40 dB below the main lobe peak.

The Urbana radar normally employs a 20μs pulse, so that range gates are separated by 3.0 km intervals. When the F-H technique is employed, however, such range gate spacing can cause range-aliasing problems. In particular, when a scatterer is located at the boundary of two range gates, it becomes impossible to determine its correct position. By oversampling at 1.5 km intervals, it is possible to construct an unaliased vertical profile by throwing out the subrange gates at the edges of each range gate, then fitting the remaining subrange gates together in a manner analogous to the "overlap-save" algorithm used to perform large DFTs (see, e.g., OPPENHEIM and SCHAFER 1975).

SUMMARY OF DATA ANALYSIS PROCEDURE

At this point, a fairly thorough discussion has been given of the manner in which a single 1/8-second coherently integrated F-H sample might be processed. No mention has been made, however, of the way in which an entire minutes' worth of data for a single range gate is to be processed. Figure 6 shows one way of representing such a block of data. In order to understand the graph in this figure, it is perhaps easiest to make the following set of definitions:

$x(m,n)$ = a two-dimensional data sequence containing one minutes' worth of F-H data for a single range gate. Each column consists of a single 1/8-second coherently integrated F-H sample.

M = the number of 1/8-second coherently integrated samples in one minute of data.

N = the number of frequencies at which the F-H system operates. This number is 16 for the present system.

$t' = 1/8$ s.

mt' = the time at which the mth column is collected.

$f_o+n\Delta f$ = the transmitting frequency corresponding to the nth element of a column.

Assume that the range gate corresponding to the data of Figure 6 contains only one scatterer. Suppose that the one-dimensional DFT of the first column in Figure 6 is calculated. Earlier discussions suggest that only one element (or perhaps two) of the resulting column is essentially nonzero. Precisely which element is nonzero depends, of course, on the position of the scatterer within the scattering volume. Now suppose that the one-dimensional DFTs of all of the columns in Figure 6 are taken. After the completion of these operations, only one row of the resulting graph is essentially nonzero. The position of that row may be used to determine the position of the scatterer within the scattering volume. By taking the one-dimensional autocorrelation function of the nonzero row, the usual parameters of velocity, power, and correlation time may be derived for the single scatterer.

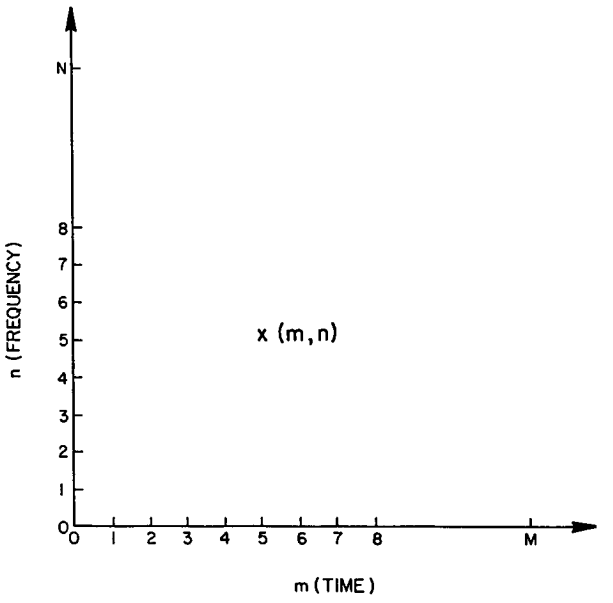

Figure 6. Representation for one minute of data in a single range gate of the F-H system.

Thus, a one-minute block of data, such as that represented in Figure 6, may be processed in five steps:

(1) Each column of the two-dimensional sequence is windowed using a Chebyshev window of the type discussed earlier.

(2) Each column of the sequence is transformed using a one-dimensional DFT.

(3) Undesired rows are thrown out using the overlap-save algorithm discussed earlier.

(4) The one-dimensional autocorrelation function of each of the remaining rows is found.

(5) The usual velocity, power, and correlation time parameters are derived for each row.

ACKNOWLEDGEMENT

The research described in this paper was supported by the National Aeronautics and Space Administration under Grant NSG 7506.

REFERENCES

Jasik, H. (1961), Editor, Antenna Engineering Handbook, Mcgraw-Hill, NY.

Oppenheim, A. V. and R. W. Schafer (1975), Digital Signal Processing, Prentice-Hall, NJ.

8.2.1 A VARIABLE-FREQUENCY LOCAL OSCILLATOR FOR THE FREQUENCY-HOPPING TECHNIQUE

G. R. Stitt and L. J. Johnson

Aeronomy Laboratory
Department of Electrical and Computer Engineering
University of Illinois
Urbana, IL 61801

The frequency-hopping technique described elsewhere (STITT and BOWHILL, this volume) requires the use of a local oscillator whose output frequency may be rapidly and accurately changed by a fixed frequency increment. Such a device, capable of producing 16 different frequencies separated by 50 kHz over the range 35.02-35.77 MHz, has been build for the Urbana MST radar facility. The following paragraphs describe the design and construction of this device, which is illustrated by the block diagram of Figure 1.

A 5.00 MHz crystal oscillator provides a reference source for the synthe sizer. The oscillator output is divided by 100 to provide a precise 50 kHz input to the 16 separate NE564 Phae-Locked-Loops (PLLs). Each PLL, though locked to the same master oscillator, is set to run continually at its own unique frequency. Although the use of a battery of 16 PLLs may seem a bit extravagant, the NE564 chips employed are very inexpensive, and this approach avoids the problems with capture range and settling time that may occur when a single PLL is used to generate multiple frequencies.

A frequency synthesizer consisting of 16 separate oscillators connected to an analog multiplexer was also considered. Unfortunately, this brute force approach is quite expensive, as it requires the use of high quality oscillators. This is due to the sensitivity of the frequency-hopping technique to random variations in the operating frequencies of the oscillators; if these frequencies deviate by more than a few Hertz from their desired values, the frequency-hopping method simply does not work. The use of 16 separate PLLs, each locked to the same reference oscillator, helps to minimize this problem.

Returning to Figure 1, it may be seen that the local oscillator frequency generated at any given time is determined by the 16-to-1-line multiplexes. When the radar is operated in the frequency-hopping mode, this multiplexes is controlled through a parallel port by an Apple II+ microcomputer. A switch allows control of the multiplexer to transferred to a row of rocket switches on the front panel of the device. In this way, the local oscillator frequency may be fixed at a chosen value when the radar is operated in a more conventional mode.

The output frequency range of the synthesizer is beyond the maximum operating frequency of the NE564 PLL. Consequently, it is necessary to mix the PLL outputs with that of a 40.02 MHz oscillator in order to obtain the desired output frequencies. Since it is difficult to mix a squarewave due to the higher order harmonics present, the PLL outputs are filtered with a low-pass elliptic filter to ensure an approximately sinusoidal waveform before being mixed. The mixer output is then bandpass filtered in order to eliminate the undesirable harmonics produced by the mixing operation. Finally, the resulting signal is amplified by a pair of MWA 120 wideband hybrid amplifiers.

The frequency synthesizer illustrated in Figure 1 physically consists of 10 printed circuit boards inserted into a card cage. Eight of these boards, labeled PLL in Figure 1, contains two PLL circuits apiece. These cards are all identical except for the frequencies the individual PLLS are set to run at. One board (labeled FSO) contains the multiplexer and 5.00 MHz reference

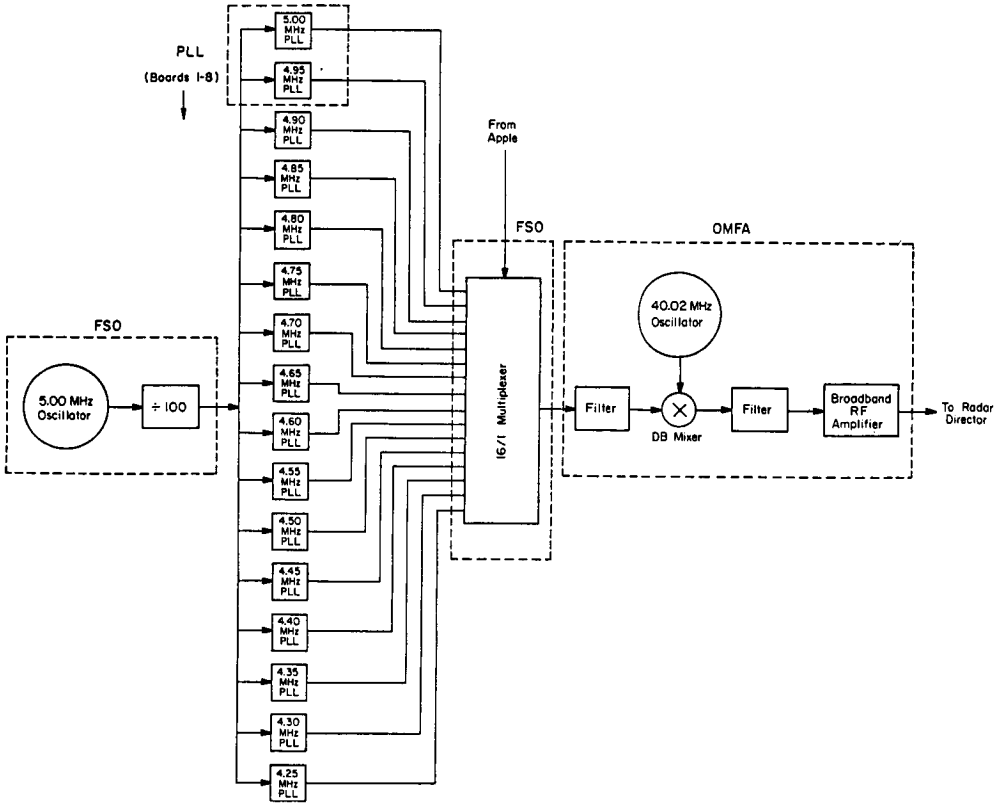

Figure 1. Implementation of the frequency synthesizer.

oscillator. The remaining board (labeled OMFA) contains the 40.02 MHz oscillator, mixer, filters, and amplifiers. The modular construction used for this synthesizer should simplify maintenance, and make it easier to change operating frequencies should that prove desirable in the future.

Figures 2 and 3 show spectrum analyser displays corresponding to the 35.77 MHz output of the frequency generator. Figure 2 indicates that there are no significant frequency components present other than those near the desired frequency. Figure 3, which expands the central peak in Figure 2, reveals that there are undesirable frequency components located $\pm$ 50 kHz and $\pm$ 100 kHz away from the 35.77 MHz component. These undesirable components, whose amplitudes are approximately 23 dB below the central peak, are apparently caused by the phase comparator section of the NE564 chip. If they prove troublesome, it will be necessary to use a different type of PLL.

ACKNOWLEDGEMENT

The research described in this paper was supported by the National Aeronautics and Space Administration under Grant NSG 7506.

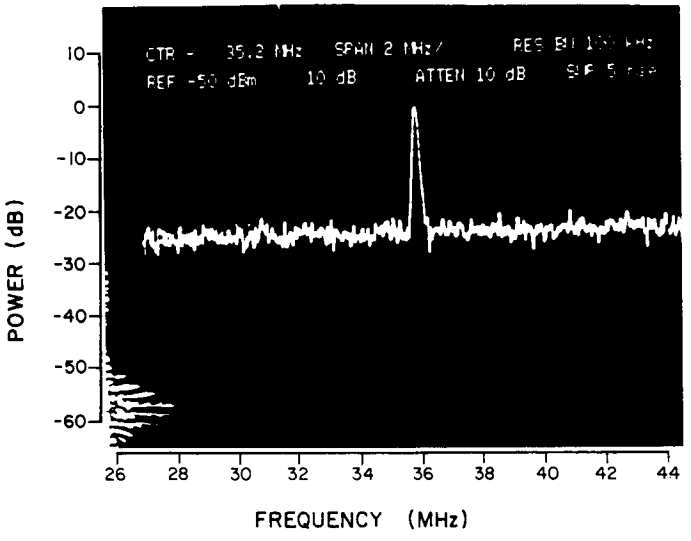

Figure 2. Spectrum analyser display of synthesizer output. Main peak is at 35.77 MHz. Vertical scale is 10 dB/ division, horizontal scale is 2 MHz/division.

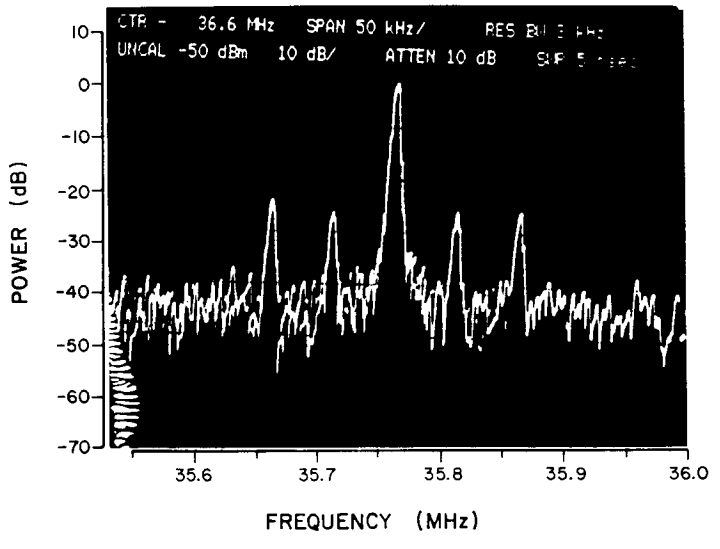

Figure 3. Same as Figure 2, except that the horizontal scale is 50 kHz/division.

8.2.2 AN ACCELERATED FORTH DATA-ACQUISITION SYSTEM

S. A. Bowhill and A. D. Rennier

Department of Electrical and Computer Engineering
University of Illinois
Urbana, Illinois 61801

A new data acquisition system was put into operation at Urbana in August 1984. It uses a standard Apple II microcomputer with 48 k RAM and a standard 5 1/4 inch floppy disk. Design criteria for the system includes the following:

1. Acquire two 8-bit data bytes each 10 microseconds for 60 altitudes, compared with 20, previously.
2. Coherently integrate real and imaginary components for 50 pulses (1/8 sec)
3. Display coherently integrated samples in real time
4. Perform complex autocorrelation each minute
5. Write correlation data to floppy disk each minute
6. Display height profiles of power and Doppler frequency each minute while data are being written to disk
7. Accommodate 1 hour's data on each side of floppy disk.
8. Perform the above for as many altitudes as possible

The system was implemented using fig-FORTH, a threaded interpretive language which permits easy interfacing to machine code. The throughput of this system is better by a factor of 6 than the PDP-15 minicomputer system previously used, and in addition has the real-time display feature and provides the data in much more convenient form. The improved performance is due to the following features:

1. FORTH uses a zero-address pseudo-machine with an integer stack and integer arithmetic
2. An accelerator board raises the Apple clock frequency to 3.6 MHz
3. I/O and coherently integration routines were written in machine code and interrupt driven
4. Two A/D converters were used in tandem for the real and imaginary components
5. The Apple II permits direct screen access for the real-time display
6. The quarter-square algorithm was used for multiplication

Figure 1 shows the improved performance obtained from the new system in the stratosphere. Velocity data can be obtained to 28.5 km altitude.

Complete documentation of the software (RENNIER and BOWHILL, 1985) is available from the University of Illinois, together with compiled system disk and complete source code.

REFERENCE

Rennier, A. D., and S. A. Bowhill (1985), FORTH system for coherent-scatter radar data acquisition and processing, Aeron. Rep. 115, Aeron. Lab., Dept. Elec. Computer Eng., Univ. IL, Urbana-Champaign.

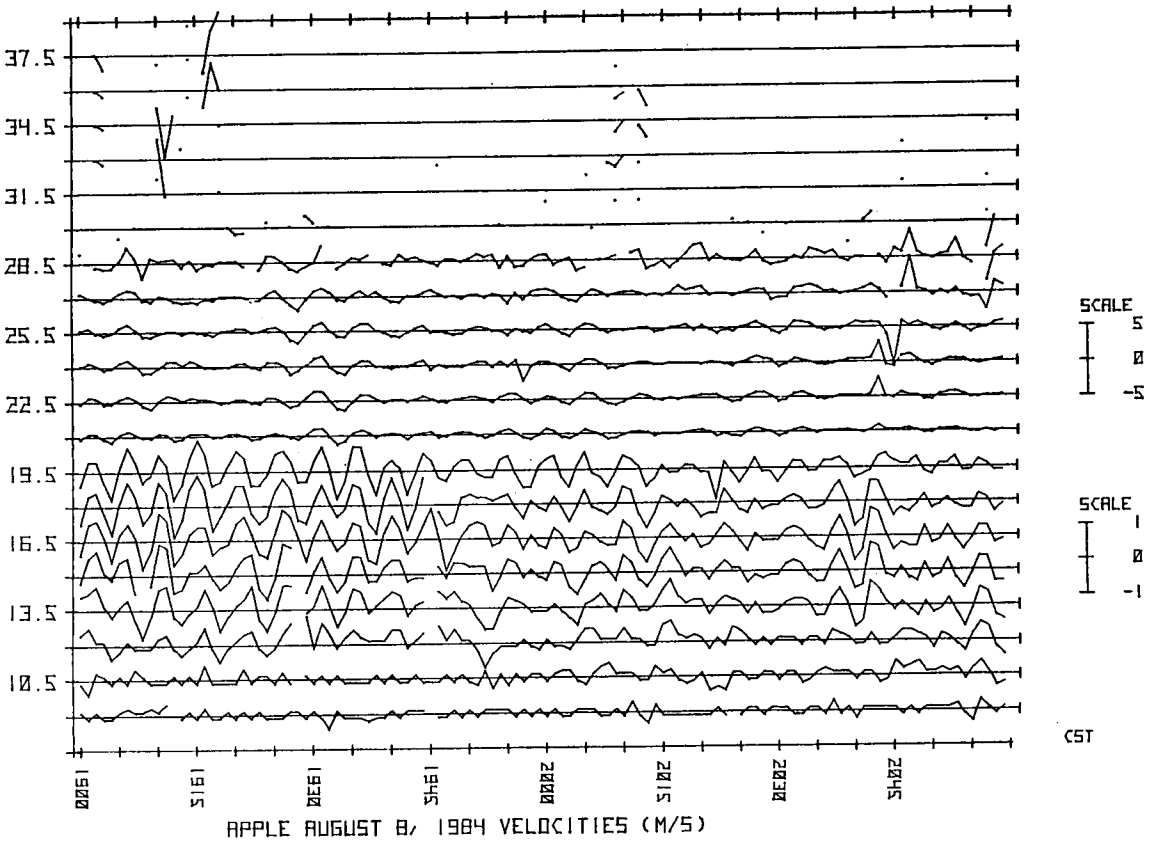

Figure 1. Recent stratospheric line-of-sight velocities showing improved sensitivity. Note the scale change above 19.5 km from 1 to 5 m/s per vertical division.

8.3.1 A SINGLE-BOARD PREPROCESSOR AND PULSE GENERATOR

D. A. Carter, A. E. Ayers, and R. P. Schneider

Aeronomy Laboratory
National Oceanic and Atmospheric Administration
Boulder, CO 80303

The Aeronomy Laboratory of NOAA has designed and built a single-board, programmable radar controller for use with VHF ST radars. The controller consists of a coherent integrator preprocessor and a radar pulse generator, both described here, as well as interfaces to an antenna beam switch and a receiver bandwidth switch. The controller occupies a single slot in a Data General Nova or Eclipse computer. The integrator and pulse generator take advantage of high density, dual-port FIFO chips such as the 512 x 9 MOSTEK MK 4501. These FIFOs have separate input and output ports and independent read and write cycles with cycle times of less than 200 ns, making them very fast and easy to interface.

A simple block diagram of the coherent integrator is shown in Figure 1. At the completion of each ADC conversion, the 8-bit data from each receiver channel is latched into a register. The two channels are alternately placed at one input of the 16-bit adder. During the first interpulse period (IPP) the other input to the adder is set to zero and the data word is written directly into the FIFO. During successive IPPs, the data words are read from the FIFO, added to the incoming data from the corresponding range gate and rewritten to the FIFO. After the desired number of coherent additions have been completed, the data read from the FIFO is sent to the computer via the DMA channel, while the incoming data are being added to zero, beginning the cycle again. When a specified number of coherently averaged points for each range gate have been sent to the computer, the device is done and can interrupt the computer program. A status register, read from software, indicates errors such as adder overflow, FIFO overflow, and missed data points.

The integrator is designed to handle inputs from one receiver (2 channels) with 1 sec sample spacing. The timing could probably be adjusted for 500 ns samples, and additional receivers could be processed without any hardware modification by using one integrator board for each receiver. The design could also be altered to multiplex more channels onto a single board, but the maximum sampling rate would consequently be reduced.

The pulse generator is based on controllers designed by R. F. Woodman for the Arecibo and SOUSY radars using a "recirculating memory" scheme. Figure 2 shows the basic circuitry of the Aeronomy Laboratory device. The output lines of the pulse generator are the TR switch control pulse, the transmitter (Tx) logic pulse, and the sample gates. The state of each line changes according to the state of a specified bit of the FIFO memory as the data words are sequentially latched into an output register. The remaining bits of the FIFO word represent the number of 1-μsec clock cycles for that particular state to be held on the output latch. When that number is counted down to zero, a READ pulse is created and the next FIFO word is read into the output latch and the counter. The last word in the sequence is indicated by setting one bit (LAST) which creates a retransmit (RETRANS) signal. The retransmit function of the FIFO nondestructively resets the internal read pointer so that the data may be reread from the beginning.

The FIFO is loaded with the proper pulse sequence by a software DATA OUT (DOB) command and may be read back by a DATA IN (DIB) instruction. Once a START command is executed, the pulse generator will run continuously without further computer intervention. It can be stopped without destroying the FIFO

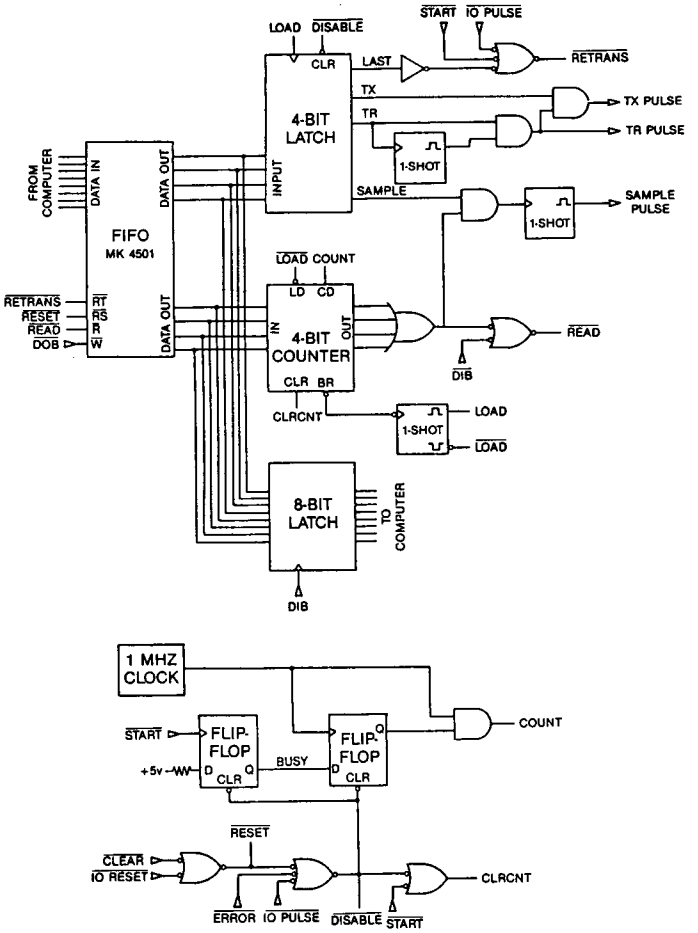

Figure 1. Coherent integrator block diagram.

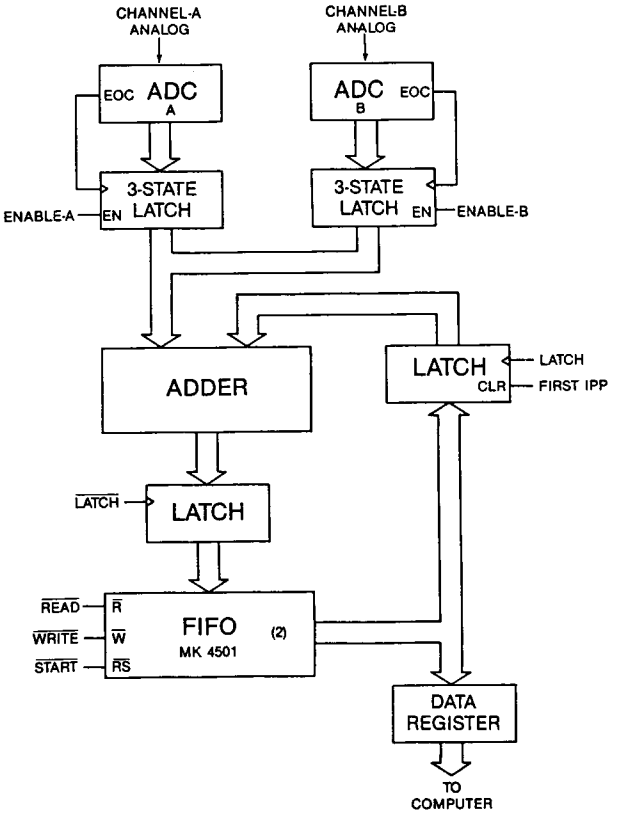

Figure 2. Radar pulse generator.

contents by a software IOPULSE command. A software CLEAR or hardware IORESET will reset the internal read and write pointers for rewriting the FIFO contents.

A number of safety features are built into the hardware. The TR pulse is gated with a fixed-length pulse to prevent the TR from accidently being turned on too long. The Tx pulse is allowed on only while the TR pulse is on. Any command that halts the pulse generator also clears the output lines. The ninth bit of the FIFO is used for parity. If a parity error is detected after a FIFO read cycle, the pulse generator is stopped and the computer program is interrupted.

In the pulse generator actually built, two FIFOs are used in parallel so that 8 lines are available for pulse signals and 8 lines for counting. Two of the additional signal lines are set up for Tx pulse coding. Coherent integration of the coded returns can be done in the preprocessor part of the board, but the decoding must be done in software.

The Aeronomy Laboratory has built three of these preprocessor/pulse generator devices. They each occupy about half of an MDB Systems I/O board, the other half being used by the vendor-supplied interfacing to the Data General I/O bus. One such board was used during the 1985 PRE-STORM program and others will be installed in Pacific Ocean ST radars on Ponape and Christmas Island. Compared to previous systems that used software coherent integration and manually controlled pulse generator boxes, this design offers great advantages in speed, flexibility, and radar efficiency.

8.3.2 A MICROPROGRAMMABLE RADAR CONTROLLER

by

Daniel C. Law

NOAA/ERL
Wave Propagation Laboratory
Boulder, CO 80303

The Wave Propagation Laboratory has completed the design and construction of a microprogrammable radar controller for atmospheric wind profiling. Unlike some radar controllers using state machines or hardwired logic for radar timing, this design is a high speed programmable sequencer with signal processing resources. A block diagram of the device is shown in Figure 1.

The device is a single 8 1/2" x 10 1/2" printed circuit board and consists of three main subsections: 1) the host computer interface, 2) the microprogram sequencer, and 3) the signal processing circuitry.

HOST INTERFACE

The host computer bus chosen for this design is the Digital Equipment Corporation Q-Bus supported by DEC's 11/23, 11/73, and MicroVAX computers.

The radar interface control/status register (RICSR) allows control of the radar controller from the host. The RF control/status register (RFCSR) allows the host to control the operation and check the status of up to seven external RF devices such as the receiver/exciter, the antenna controller, the pulse amplifier, etc.

MICROPROGRAM SEQUENCER

An Advanced Micro Devices 2910A microprogram sequencer determines the address for the microprogram memory. Such features as an internal loop counter, a 9-word deep stack for microsubroutines, and condition testing allows efficient microcoding for radar control and signal processing. The microprogram memory is 2048 words deep by 64 bits wide. Most of the bits in the microword control the microprogram sequencer and the signal processor but eight of these bits are sent out for high speed radar timing signals such as Transmit, T/R, Receiver Blank, A/D Sample, Pulse Coding, etc. Since the sequencer runs at 10 MHz, these signals are all controllable with 100 nanosecond resolution. The clock source may either be an on-board crystal oscillator or a 10-MHz external reference oscillator such as the master oscillator in a phase locked receiver design.

SIGNAL PROCESSING

In-phase (I) and Quadrature (Q) digital data are sequentially processed using a high speed 16 x 16 bit multiplier-accumulator and a 2048-word deep by 32-bit wide accumulation memory.

If simple time-domain averaging is desired, the coefficient/scaling memory contains a fixed scale factor which, when multiplied by each incoming sample and accumulated without truncation, results in a properly scaled value in the most significant 16 bits of the accumulation memory at the end of the time-domain averaging period.

A weighted average may be implemented by multiplying each incoming sample by a weighting value from the coefficient/scaling memory along with the

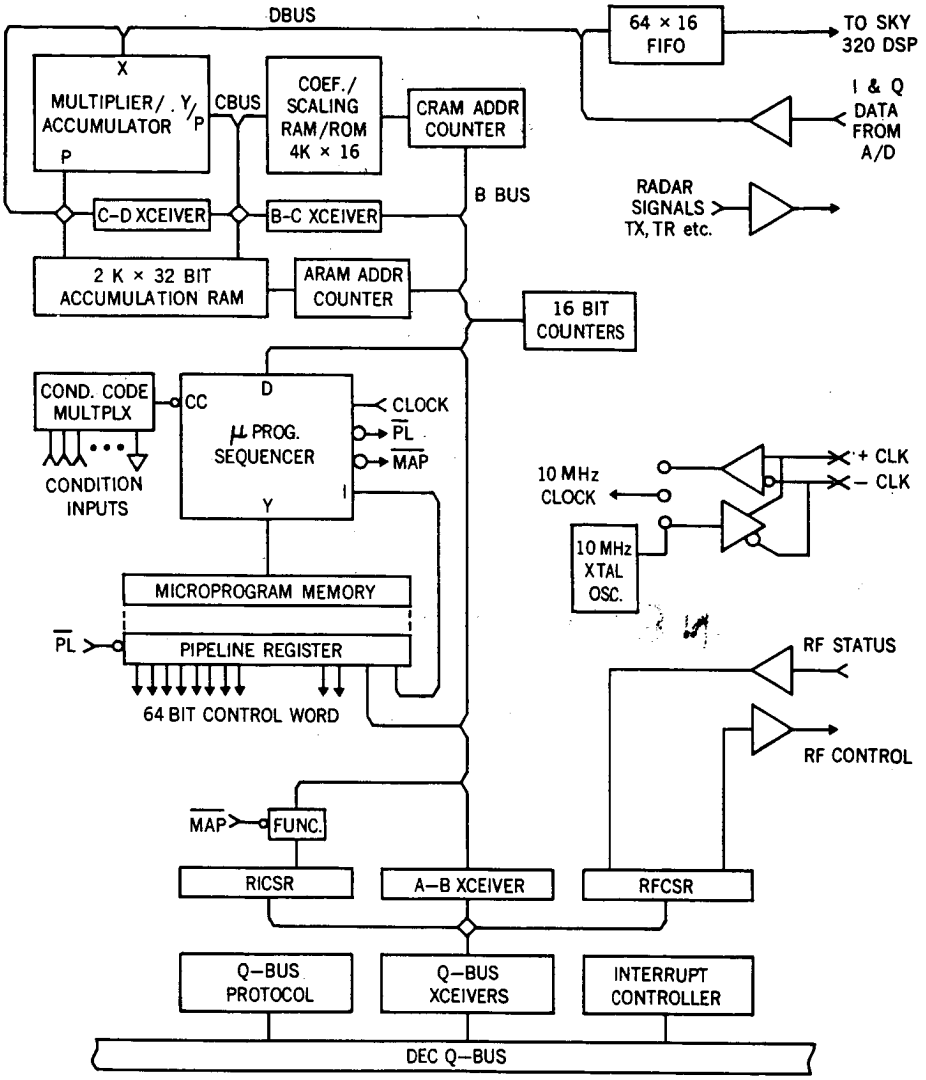

RADAR CONTROLLER
BLOCK DIAGRAM

Figure 1.

accumulation. This is a digital transverse low pass filter and has been used to help reject RF interference and moving targets.

After the averaging process, the data are sent out of the device via the First In-First Out memory to a commercially available digital signal processing board. The SKY320, manufactured by Sky Computers, Inc., sorts the data, performs dc removal, performs the fast Fourier transform, and the windows the spectra. The SKY320 is programmed to process 128 point complex time series from 36 range gates and is operating at one-third its maximum throughput capacity.

Data are then retrieved from the SKY320 by the host computer which performs spectral moment calculation, wind calculations, etc.

This configuration results in real-time operation (100% dwell time) without the use of expensive array processors or high speed memory.

MICROCODE DEVELOPMENT

Microcode is written on the host machine using commercial meta assembler software. An auxiliary writable control-store board substitutes for the Radar Controller microprogram memory during development. Programmable Read Only Memory is then loaded with the developed microcode and is used as the microprogram memory for a fixed number of radar parameters.

A NOAA Technical Memorandum detailing the design and microprogramming of the device is planned for 1986.

8.4.1 THE APPLICATION OF MATCHED-FILTER ANALYSIS TO DEDUCE A BEST ESTIMATE OF MEAN DOPPLER VELOCITY

Jurgen Rottger*

Arecibo Observatory
P.O. Box 995
Puerto Rico

Several methods are usually applied in MST radar data analysis to estimate mean Doppler velocity and spectrum width, such as the computation of moments from spectra or autocorrelation functions or the nonlinear least-squares fit. We present here another approach which is based on a best matched filter estimate.

Having computed the power spectrum P(f) of radar data, we use P(-f) as a best estimate to compute the autocovariance function

$$\rho_f(\Delta F) = \sum_{-f_N}^{+f_N} P(f - \Delta f) \cdot P(-f) \qquad (1)$$

ρ_f has a maximum at exactly twice the mean frequency of P(f). The advantage of this technique is that it is less sensitive to unsymmetrical and spiky spectra, and it eliminates aliasing. It also allows to better estimate the spectral width. The amplitude of ρ_f is a measure of the unsymmetry or spikyness of the spectra P(f).

Figure 1 shows examples of P(f), computed from the complex autocorrelation function (ACF) and the corresponding covariance function ρ_f of incoherent scatter data. This method has recently also been successfully applied to mesospheric VHF radar signals (Figure 2).

*On leave from Max-Planck-Institut fur Aeronomie, Katlenburg-Lindau, West Germany.

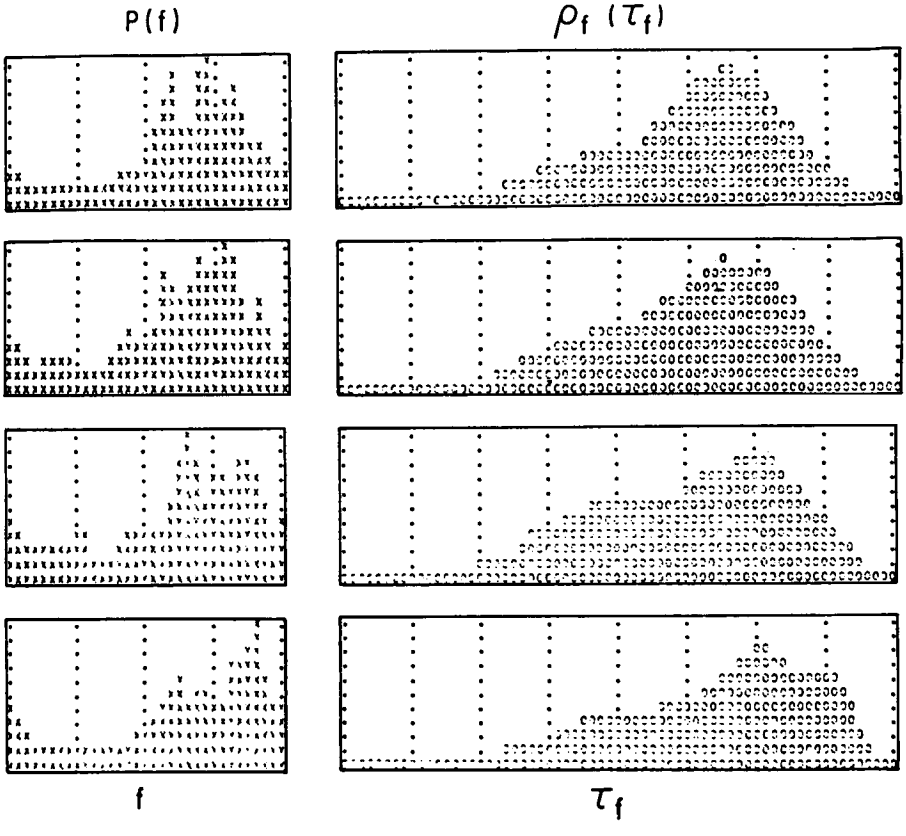

Figure 1. The right-hand diagrams show 10-min averages of the real and imaginary part of the autocorrelation function of incoherent-scatter signals from 75 km and 95 km altitude, measured with the EISCAT UHF radar (ROTTGER, 1984). The corresponding power spectra are shown in the upper left-hand diagram. The lower left-hand diagram shows the auto-covariance functions computed from equation (1). The location of their maxima at $\tau_{f_{max}}$ divided by two gives the mean Doppler frequency of the power spectrum.

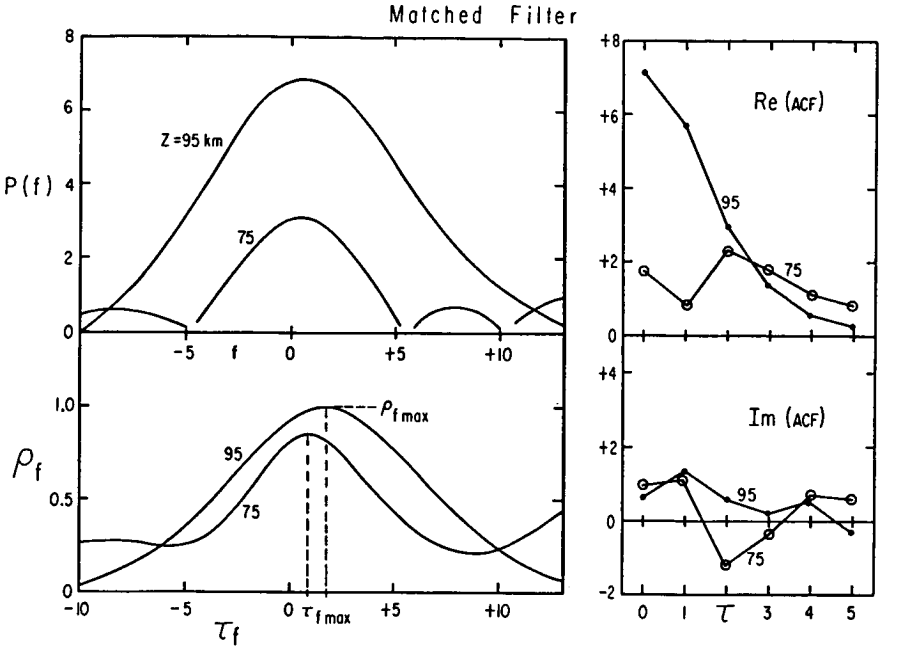

Figure 2. Power spectra (1-min averages) and corresponding autocovariance functions of mesospheric VHF radar echoes, measured at the Arecibo Observatory. The deduced Doppler frequencies were used to compute gravity-wave spectra and mean wind profiles (see ROTTGER, 1985a,b).

REFERENCES

Rottger, J. (1984), Further developments of EISCAT as an MST radar, Handbook for MAP, 14, 309-318.

Rottger, J. (1985a), The relation of gravity waves and turbulence in the mesosphere, Handbook for MAP, this volume.

Rottger, J. (1985b), The use of the experimentally deduced Brunt-Vaisala Frequency and turbulent velocity fluctuations to estimate the eddy diffusion coefficient, Handbook for MAP, this volume.

8.4.2 AN EXAMPLE OF SCALING MST DOPPLER SPECTRA USING MEDIAN SPECTRA, SPECTRAL SMOOTHING, AND VELOCITY TRACING

J. L. Green

Aeronomy Laboratory
NOAA
Boulder, CO 80303

INTRODUCTION

Although automatic, computer scaling methods appeared at the start of the MST radar technique, there is a continuing need for scaling algorithms that perform editing functions and, if possible, increase the sensitivity of radar by post processing. The scaling method presented here is an adaptation of the method of scaling MST Doppler spectra presented by RASTOGI (1984), to the particular problems encountered at the Sunset radar. It also uses elements from ZRNIC (1979), CLARK and CARTER (1980), CARTER et al. (1980), and WOODMAN (1983).

A brief overview of this method is as follows: a median spectrum is calculated from several sequential spectra; the median noise value is subtracted from this derived spectrum; the median spectrum is smoothed; the detection/nondetection decision is made by comparing the smoothed spectrum to the variance of the smoothed noise; and if a signal is detected, then the half-power points of the smoothed echo spectrum are used to place limits on the evaluation of the first two moments of the unsmoothed median spectrum. In all of the above steps, the algorithm is guided by tracing the expected velocity range upward from the lowest range as far as is possible.

There is evidence that the radar echo power from the troposphere and stratosphere is log-normally distributed (NASTROM, 1985). This means that the use of a point-by-point median of several Doppler spectra is more appropriate than the point-by-point arithmetic mean employed by a number of ST and MST radar groups. The median technique has the added advantage of rejecting transient interference.

To accurately obtain the integral of the echo spectrum for the determination of echo power, the noise must be subtracted from the echo spectrum. This has been a problem to the author, and perhaps others, because if a mean value of the noise is calculated, frequently a large spectral component from noise or interference can cause an unacceptable error. This problem can be reduced, if not practically eliminated by using instead, the median value of the noise.

Smoothing the Doppler spectra in frequency (or radial velocity) increases the signal-to-noise ratio of the radar echo and thus enhances the detectability of weak echo. However, the selection of the smoothing function and its width is important since the detectability is maximum when the smoothing function "matches" the echo spectrum.

The increases sensitivity provided by smoothing the Doppler spectrum before detection also increases the probability of detecting a noise peak not associated with the radar echo. The probability of false detection can be reduced by tracing the velocity from the lowest ranges upwards. At each successive altitude a search for a radar echo can be conducted over a spectral range based on "a reasonable shear" (RASTOGI, 1984).

IMPLEMENTATION OF SCALING ALGORITHM

Figure 1 is an example of this adapted scaling method. The top three panels are Doppler spectra at a particular altitude and antenna beam position from three sequential records. These three spectra are transformed into the median spectrum in the bottom panel by finding the median of each corresponding spectral point. Note that the strong echo from an aircraft on the right side of the 3rd panel has been eliminated from the median spectrum. Also, the median value of the noise has been subtracted from each point of the median spectrum.

Referring again to Figure 1, the spectrum in the 4th panel was obtained by smoothing the median spectrum in the 5th panel with an 11-point Gaussian function. This function and its width were selected empirically as being an approximation of a typical ST radar echo spectrum. The echo spectrum has been obviously enhanced by the smoothing. The algorithm searched for this echo spectrum over a Doppler range centered on the velocity detected at the next lowest range. Limits, L_1 and L_2, were then located at the half-power points of the envelope of the yet untested smoothed signal spectrum. In this case, the smoothed echo was determined to be valid because it was located within the search range, and because its integral from L_1 to L_2 exceeded the integral of the variance of the smoothed spectrum over the same interval by a factor T. T is an arbitrary threshold, discussed below.

Finally, the integral, center and width of the signal spectrum was obtained from the median spectrum in the bottom panel of Figure 3, by the methods used in CLARK and CARTER (1980), but using L_1 and L_2 as limits to the required integrations. The signal integral, center and width can obviously be transformed into the echo power, radial velocity and velocity width. It is suspected, but not yet proven, that the use of the unsmoothed median spectrum in the evaluation of these moments results in greater accuracy.

DISCUSSION

About 1200 individual Doppler spectra from the Sunset radar have been studied using the technique described here. It has been found that the variance of the spectral noise tends to decrease with the square root of the number of spectra used in computing the median spectrum, as expected for an arithmetic average. Because of the large array storage now available in small computers, it is practical to calculate median spectra as a means of on-line compaction of data at a radar site.

As mentioned, the smoothing function and its width should be selected to match the radar echo. At the Sunset radar the Doppler width of echoes varies over a factor of 50:1. The development of an adaptive function is required for the maximum enhancement of weak signal detection.

The selection of the detection threshold requires some consideration. In Figure 2, the two curves, P_t and P_f explore the consequences of the hypothesis that the probability of detecting an actual echo varies as $(S/N)^{1/2}$ and the probability of detecting a false echo as $(S/N)^{-1/2}$. The point at which the two curves intersect represents an equal probability of true and false detection. There are obviously costs associated with setting T too high or too low. One approach is to choose T so that $P_f/P_t < 1/2$ and then employing some further method of automatic editing such as a random sample consensus (STRAUCH, 1983) or the comparison of velocity measurements with redundant antenna positions (CLARK et al., 1983).

Sunset Radar Doppler Spectra (Lin) from 84-1-25 Plotted 1985 09 25 15:51:35

17:08:45 FileNo = 16 Az = 180.0 Zn = 15.0 Alt No = 13 Alt = 17.0
17:10:06 FileNo = 16 Az = 180.0 Zn = 15.0 Alt No = 13 Alt = 17.0
17:11:26 FileNo = 16 Az = 180.0 Zn = 15.0 Alt No = 13 Alt = 17.0

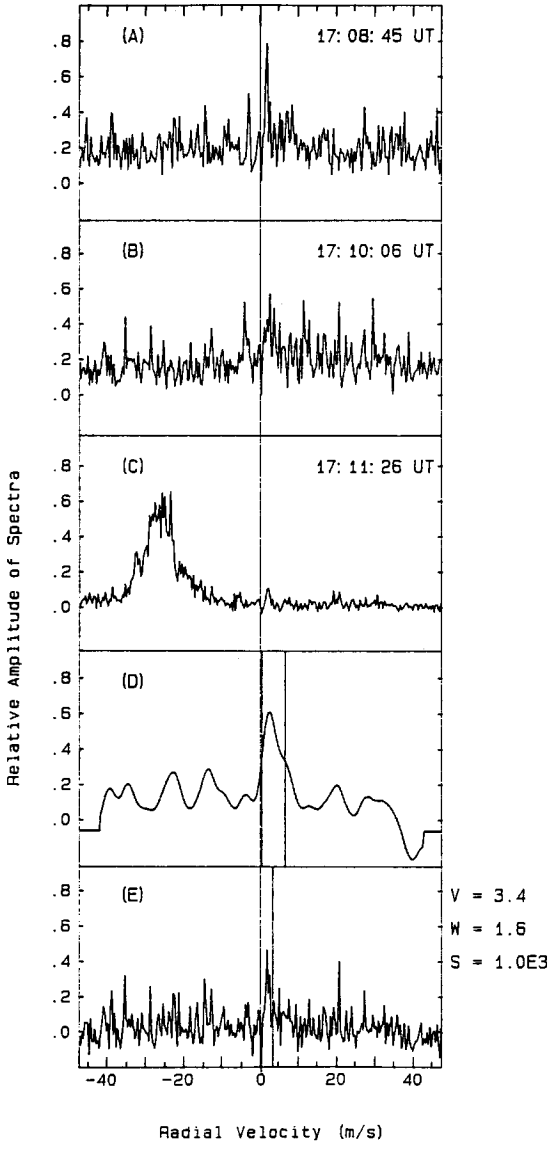

Figure 1. Example of scaling method showing intermediate steps.

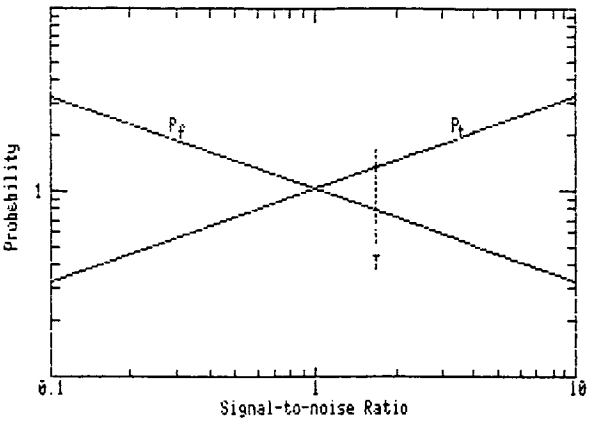

Figure 2. Hypothetical probability of true detection P_t and false detection, P_f. T is an arbitrary threshold.

ACKNOWLEDGEMENTS

Appreciation is expressed for helpful discussions on this subject with D. A. Carter, W. L. Clark, W. L. Ecklund, and Dr. T. E. VanZandt.

REFERENCES

Carter, D. A., B. B. Balsley, and W. L. Ecklund (1980), The Poker Flat MST radar: signal analysis and data processing techniques with examples, Proc. AMS 19th Conf. on Radar Meteorology.

Clark, W. L., and D. A. Carter (1980), Real-time scaling of atmospheric parameters from radars using the MST technique, Proc. AMS 19th Conf. on Radar Meteorology.

Clark, W. L., J. L. Green, and J. M. Warnock (1983), Estimating unbiased velocity components from MST/ST radar measurements: a case study, Urbana, IL, Handbook for MAP, 9, SCOSTEP Secretariat, Dep. Elec. Computer Eng., Univ. IL, Urbana, IL, 210-214.

Nastrom, G. D. (1985), Private communication.

Rastogi, P. K. (1984), Criteria and algorithms for spectrum parameterization of MST signals, Handbook for MAP, 14, SCOSTEP Secretariat, Dep. Elec. Computer Eng., Univ. IL, Urbana, IL, 289-293.

Strauch, R. G. (1983), Data analysis techniques: signal processing, Handbook for MAP, 9, SCOSTEP Secretariat, Dep. Elec. Computer Eng., Univ. IL, Urbana, IL, 548-562.

Woodman, R. F. (1983), Spectral moment estimation in MST radars, Handbook for MAP, 9, SCOSTEP Secretariat, Dep. Elec. Computer Eng., Univ. IL, Urbana IL, 528-531.

Zrnic, D. S. (1979), Estimation of spectral moments for weather echoes, IEEE Trans. Geosci. Elec., GE-17, 113-128.

8.5.1 INTERFERENCE DETECTION AND CORRECTION APPLIED TO INCOHERENT-SCATTER RADAR POWER SPECTRUM MEASUREMENT

W. P. Ying*, J. D. Mathews, and P. K. Rastogi

Electrical Engineering and Applied Physics
Case Western Reserve University
Cleveland, Ohio 44106

ABSTRACT

A median filter based interference detection and correction technique is evaluated and the method applied to the Arecibo incoherent-scatter radar D-region ionospheric power spectrum is discussed. The method can be extended to other kinds of data when the statistics involved in the process are still valid.

INTRODUCTION

The expression for the D-region ionosphere incoherent-scatter radar (ISR) power spectrum has been a well-known quantity (DOUGHERTY and FARLEY, 1963; TANENBAUM, 1968; MATHEWS, 1978, 1984a), from which more physical parameters can be inferred (MATHEWS, 1984b) than if the power profile measurement is carried out alone. However, a real-time power spectrum measurement was not possible until the computer power advanced so that an efficient fast Fourier transform can be realized into the array processor. Tepley (TEPLEY et al., 1981) first reported a successful experiment of D-region power spectrum using the 430-MHz ISR at Arecibo. Although the collision-dominated power spectrum shape can be seen easily from the raw data, interference can be a serious problem which sometimes even overwhelms the spectrum totally.

Several interference removal techniques have been devised, among them the commonly used method to model a theoretical data set, and then divide the experimental data with the theoretical data to obtain a 'flat', 'noise-like' data sequence which then allows easier detection and removal of outliers from the data. Another useful method is to form two complementary data sets by summing and subtracting the experimental data with the theoretical data, and then sum two complementary data sets to get rid of the outliers (RASTOGI, private communication). In both of these approaches, the performance depends totally on how accurately the theoretical data resembles the true data, i.e., a good a priori knowledge of the real data is required, but this condition is seldom met.

The method we bring out here, which is named the Template Process, is based on the concept of median filtering (RASTOGI, 1983). Even though we applied this method to the D-region power spectrum, it is independent of the shape of the data and no prior knowledge is necessary, therefore is suitable to process other kinds of power spectra as long as the statistical properties of the data can be described by the assumptions that we made to form this method. Consequently, it is a good practice to treat the following discussion as a generalized idea and we use the D-region power spectrum only as an example.

TEMPLATE PROCESS -- METHODOLOGY

Median Filtering. A time integrating method (or time averaging) can enhance the estimate of the return signal by increasing the signal-to-noise ratio. But this applies only to the additive Gaussian noise channel. If other

*Presently at Arecibo Observatory, Arecibo, Puerto Rico 00613

signals, like interference, are involved in the integrating process, then the estimate is biased due to this non-Gaussian signal.

If one sorts the data sequence of interest (either in an ascending or descending order), the middle point, which is called the median is approximately the same as the mean value (theoretically they are the same, if it is a continuous infintely long Gaussian process) for signals from additive Gaussian noise channels. Furthermore, it gives a better estimate of the true mean even with interference involved.

Median filtering is, in a sense, a process that, if a finite number of data pass through the filter, the output will be the median value of the sequence. For an interference-contaminated Gaussian signal, the median filtering is superior to the direct averaging since the latter one no longer gives a good estimate, whereas the former one gives a more reasonable estimate of the true mean.

Interference can occur at any time, at any place, and in any form in the power spectrum data, a good process should be able to not only pin-point the interference but also correct it. An idea derived from the median filtering technique eventually leads to the solution of this problem. The process is described as follows.

Each spectral point in a power spectrum can be regarded as a random variable and the corresponding value is chosen from the parent population (this should refer to the infinite long sample space, but later on, we also use this terminology to designate the finite length sample space only for convenience). For a stationary process, and if no interference intervened, each parent population is Gaussian and has its own expectation value and variance. These expectation values then constitute the ideal or expected spectrum. Furthermore, if ergodicity applies here, each parent population can be generated by an infinite number of measurements in time. A three-dimensional probability density function of the D-region power spectrum from one height is shown in Figure 1 which explains this situation when the parent populations can be obtained and the process is stationary.

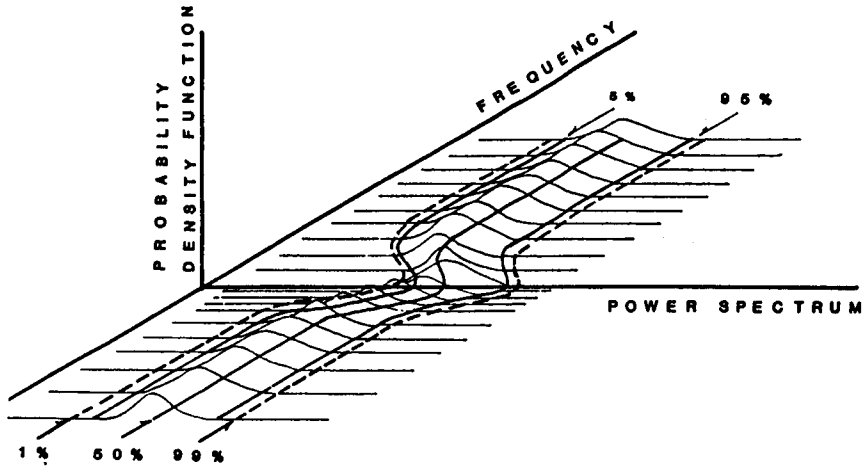

Figure 1. Three-dimensional diagram of the probability density function for each power spectrum point. Median value (50%), original template value (5%, 95%) and final template value (1%, 99%) are shown, respectively.

To form a statistically meaningful parent population in order to form a 'reasonable' median point, one has to include a large enough data set. In the case of D-region power spectrum measurement, the diurnal variation of the D region prohibits the time span to be too long, but one can incorporate the data from the neighboring heights within the same scale height, therefore, decreasing the number of the data in time to make the stationarity valid in the analysis.

Once a valid population for each spectral point of the power spectrum in question is formed, one can use the median filter technique and apply to each population created for each spectral point, then a series of median values, which is close to true mean, for every spectral point is obtained, this series of spectral points forms the median filtered power spectrum. But to carry out the template process, more information is needed in addition to the 'median' power spectrum during the median filtering process.

Template Formation. When the median filtering is carried out on a Gaussian-distributed data sequence, the middle point of this sequence is assigned as the median and that should be very close to the mean even if interference is present. In addition to the median, two extra outputs are obtained from the median filter. They are the values of the i^{th} point (i is less than N/2, the median point) and the (N-ith) point and serves as auxiliary observation points of this data sequence for the template process. Here, N is the number of the sample points for each parent population and i is a number to be decided on next.

Obviously, the amplitude of interference should be always larger than the power spectrum itself. This is simply because the power spectrum data have no negative value and if the interference is smaller, then it will be hidden in the spectrum, so that no comparison can be made to this mixed signal whether it is interference or a real signal. If the median does point to the true mean of this data sequence and since the lower part of the power spectrum is almost not influenced by the interference, the lower margin value along with the median, bear very important information about the true statistics of this data sequence.

For example, if N is chosen as 100, then the values of the 51st point (or 50th point, since N is even in this case) is approximately the mean value of this Gaussian data sequence and if i is chosen as 5, then from the table (the table of the standard normal distribution function, LINDGREN, 1960), it is known that the 5th point stands for 1.645 standard deviation away from the mean. Since the Gaussian distribution is symmetric to the mean, one can use this information to set up a tolerance level. For instance, to cover 99% Gaussian data (2.33 times standard deviation), by taking the difference between the median value and lower 5% margin times 2.33/1.645 and adding the difference to the median value, the upper margin is formed. Consequently, all other spectral data outside these two margins can be treated as interference. Note that the interference may be included with greater chance if the 95th data point is used as the upper margin.

To be able to store and recreate these margins efficiently, a standard least-square Lorentzian fit was applied (the D-region power spectrum has the shape of Lorentzian distribution, see MATHEWS, 1984a,b; YING, 1985) to both the lower margin and the 'median' spectra and stores only four coefficients for each fit. Since almost no interference occurs at median and lower margin spectra (notice that this is the primary assumption we made to the template process), the Lorentzian fit gave out coefficients corresponding to the wanted signals, and when the templates are needed, these two 'fitted' power spectrum margins are used to decide the appropriate size of the template in order to detect and correct the interfered spectrum.

This is called template process only because this selecting procedure is just like putting a template onto the pdf-spectrum plot, as shown in Figure 1, and only those points within the template are selected. The template is shown as the region within two dashed lines in Figure 1. By using this template, the interferences not only can be detected but also can be modified in a sense that the good data and bad data are isolated in a single spectrum and then the good data can be processed instead of throwing out the whole spectrum.

Baseline Adjustment. One of the advantages of forming the templates is that the templates can be used to any spectrum within the 'height-time' windows that were used to generate the valid sample space for the median filtering process to remove the contaminated spectral points. But since the template formation process is done in a semi-stationary state because of the span in time and height baseline shift might exist throughout the experiment. Therefore, a proper baseline readjustment may be needed for certain spectra in order to have a proper 'cutoff' by the templates.

This is done by sorting the spectrum and assuming the median point is not interfered, then uses both the position and the value of the median point as references and aligns the center (average) of the two margin spectra at the corresponding position to this median point, consequently this spectrum should be positioned properly within the two margins of the template, and the proper 'cutoff' can be formed.

APPLICATION TO ARECIBO D-REGION POWER SPECTRUM

The power spectrum data that we are dealing with here were taken during a sequence of three and half days experiment from January 3 to 6 of 1981, at Arecibo, Puerto Rico. The basis of the experiment uses a 52 microsec 13-baud Barker coded pulse with 1 millisec interpulse period, which yields an effective height resolution of 0.6 km and 1 kHz bandwidth. For every 256 samples from the same height, a power spectrum was formed, results in a 3.9-Hz frequency resolution. A total of 63 heights spectra records were formed for each time designation.

The template formation process is carried out by using a 'window' of 20 records in time and 5 heights. This corresponds to a window that covers a time span of approximately one and a half hours, and 3 km height (note that 3 km height window is smaller than the nominal scale height of the D region which is around 5 km, therefore stationarity in height for the median filtering process can be secured). Since there are 63 heights, the highest process window includes height numbers from 59-63, overlaps with the next lower one, i.e., it shares the spectrum data of height numbers 59 and 60 with the second highest process window. The final template process on this experiment comprises 51 time spans, 13 different heights and thus 663 windows.

Figure 2 demonstrates a complete template formation process using the window from 11:46 to 13:13 of January 4, 1981, and height window 11 which comprises the actual height number from 51 to 55 and is about 89 km to 92 km in altitude. Figure 2a shows the actual spectra within the window with slight interference effect, each spectrum is populated into the plot and consequently there are 25600 spectral points in this figure. The interference can be seen from the upper part of the plot only; therefore, the lower part of the spectral points has reliable statistical significance. Figure 2b shows the median filtered result with the median spectrum and lower 5% spectrum superimposed onto the scattered spectral points. Apparently, the median spectrum is around the center as we expected. Figure 2c is based on Figure 2b with the fitted results displayed for the median and lower 5% spectrum. These two fitted spectra are used to form the two margins for the final template which is shown in Figure 2d as two dashed lines. 1% selection range was used in this case.

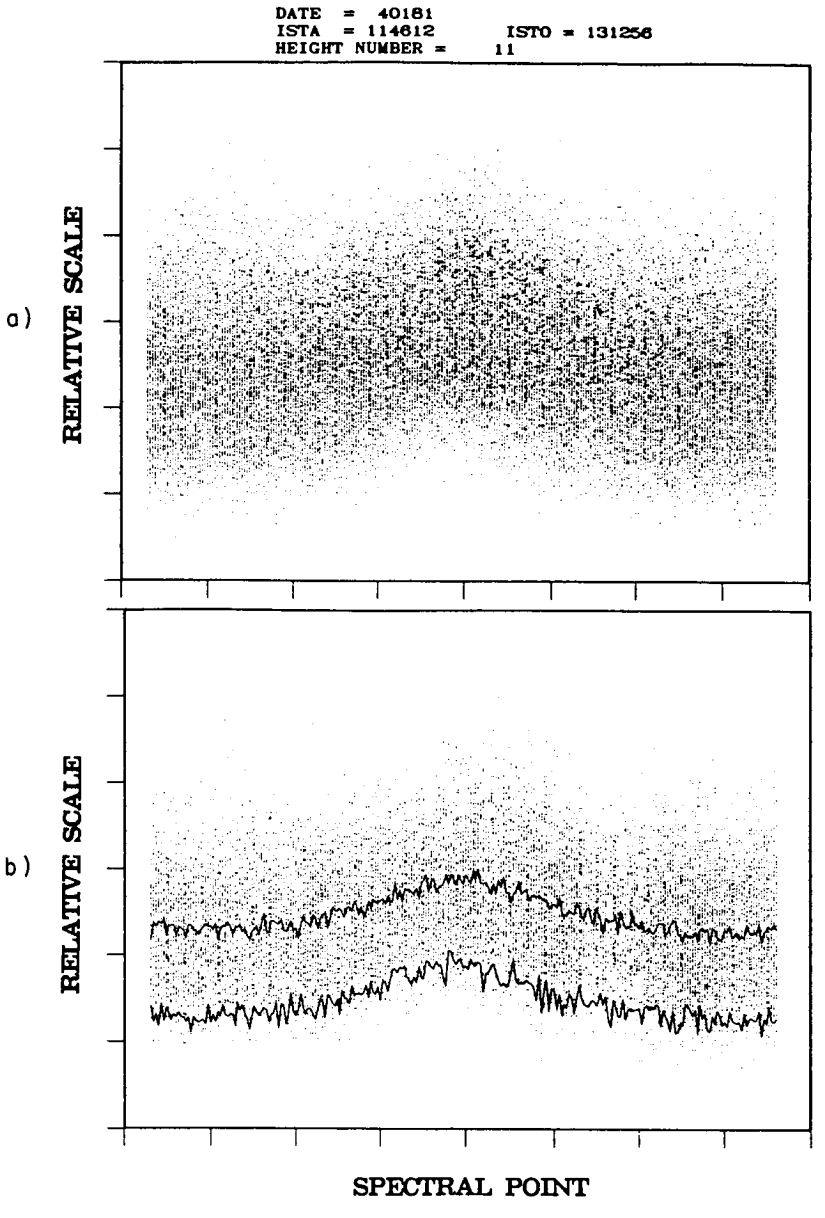

Figure 2. Demonstration of the template formation process for the time-height window from 11:46 to 13:13 January 4, 1981, in time and 89 km to 92 km in height. This is a slight interference contaminated case.
X axis represents spectral points from 1 to 256,
Y axis represents relative amplitude for all spectra.
(a). Spectral population of the specific window. There are 100 spectra within the window, altogether, 25600 data are present in this plot.
(b). Median filtering result of the specific window. The higher solid line represents the median spectrum, the lower solid line represents the 5% spectrum, the background is the spectral population.

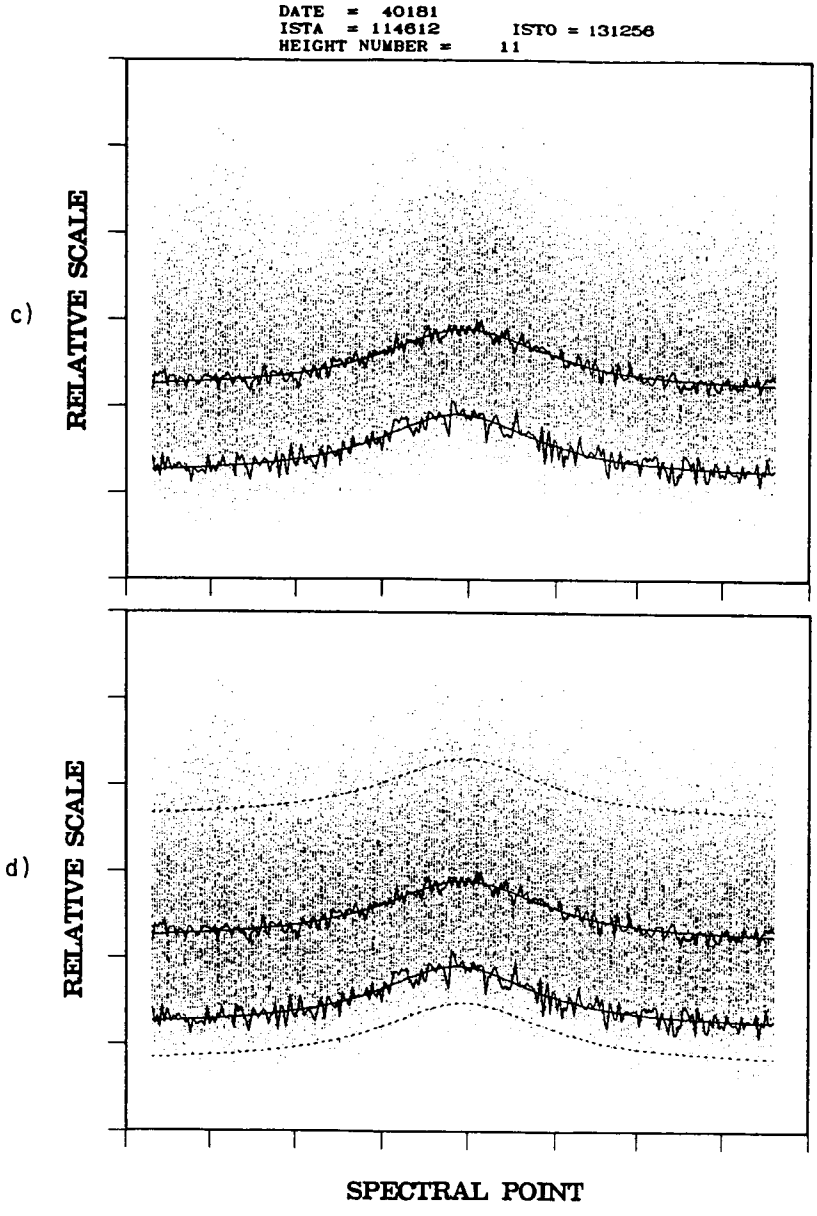

(c). Fitted result of the two median filtered spectra, which are represented by two 'smoothed' solid curves. (d). The final templates formed by two margins shown in dashed lines. The template formed by two margins can be enlarged or reduced depending on how strictly the selection criterion is enforced. In this case, 1% selection is used.

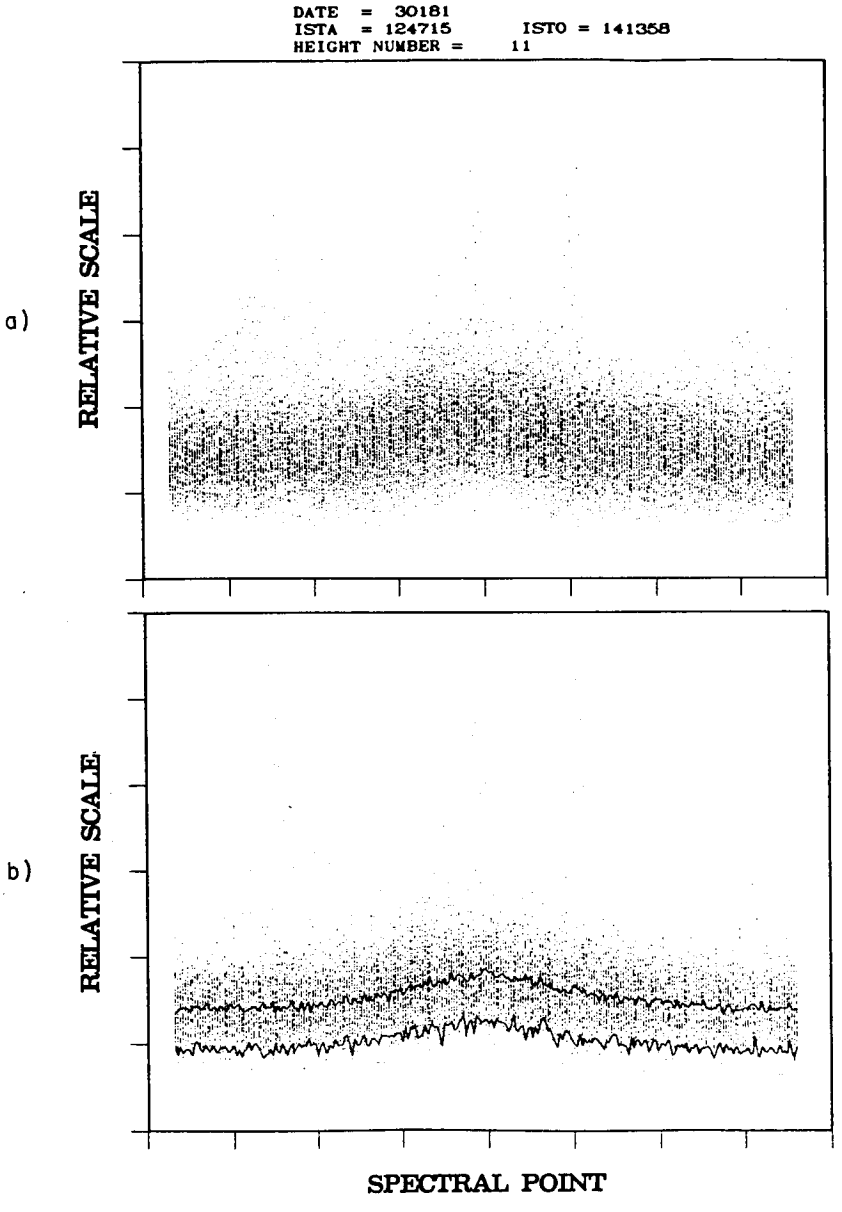

Figure 3. Demonstration of the template formation process for the time-height window from 12:47 to 14:14 January 3, 1981, in time and 89 km to 92 km in height. This is a severe interference contaminated case.
X axis represents spectral points from 1 to 256,
Y axis represents relative amplitude for all spectra.
(a). Spectral population of the specific window. There are 100 spectra within the window, altogether, 25600 data are present in this plot. Interferences can be easily seen from the upper part of this plot.
(b). Median filtering result of the specific window. The higher solid line represents the median spectrum, the lower solid line represents the 5% spectrum, the background is the spectral population.

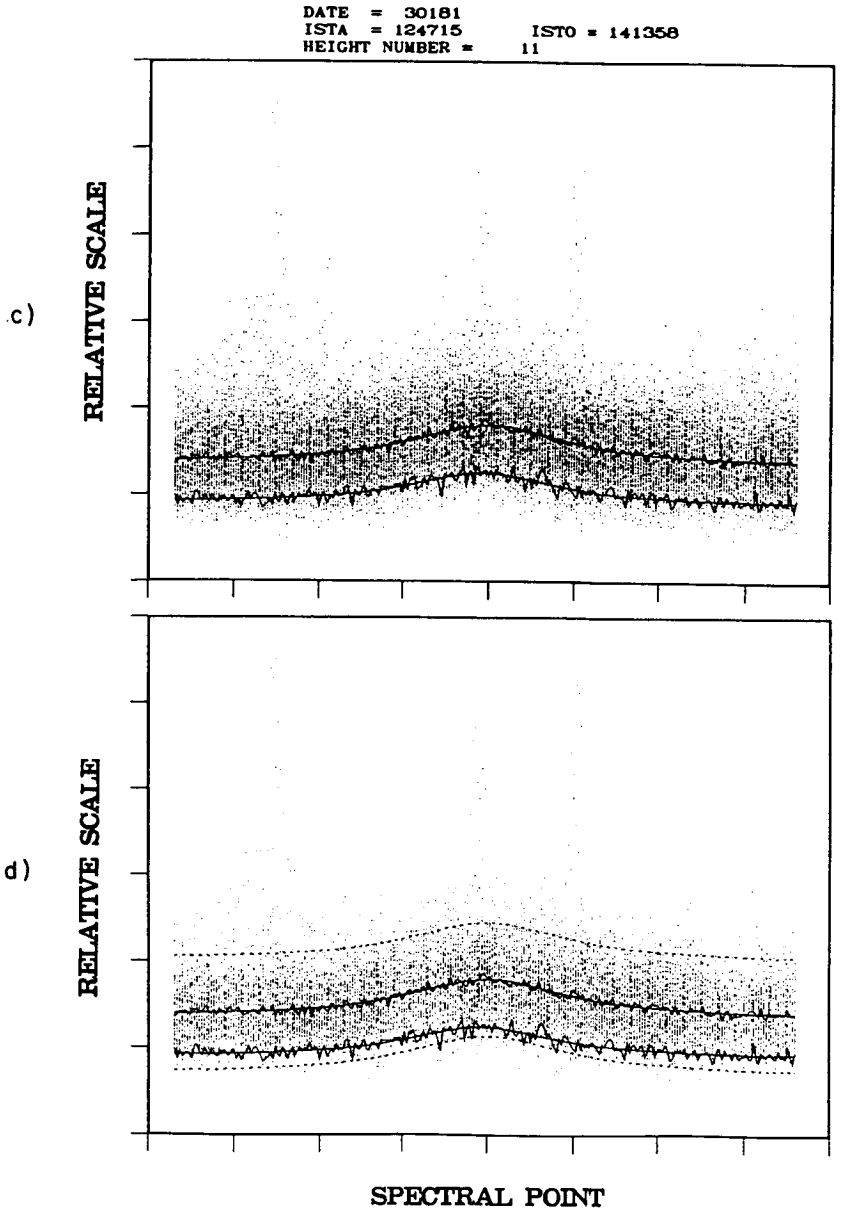

(c). Fitted result of the two median filtered spectra, which are represented by two 'smoothed' solid curves. (d). The final templates formed by two margins shown in dashed lines. The template formed by two margins can be enlarged or reduced depending on how strict the selection criterion is enforced. For this 1% selection template, one can see how effectively the interferences can be detected and removed.

Figure 3 shows another template process for a window with severely interfered spectrum involved. The time is from 12:47 to 14:14 of January 3, 1981, the height window is the same as in Figure 2. Figure 3a shows such spectra with highly peaked interferences existing in the upper part of the window, but again the lower part of the window shows no evidence of 'outliers'. Figure 3b shows the median filtering process results and two more fitted spectra of both median spectrum and 5% spectrum are included in Figure 3c. Finally, Figure 3d reveals that the final template again successfully rejects the outliers and the remaining spectral points bear good statistics so that a further averaging and Lorentz fit can be applied.

SUMMARY

We have reported an almost universal interference detection and removal scheme which has been applied to the Arecibo D region power spectrum measurement to demonstrate the effectiveness of this method. The scheme comprises three major parts, each of them depends heavily on the stationarity of the process and the interference contaminating condition of the data.

The first part is the median filtering process which finds the median and 5% power spectrum from a collection of the spectra for which stationarity is assumed. Then the template is derived from the fitted median and lower margin spectrum. In this stage, and that not more than half of the spectra are contaminated is the major assumption here, so that both the median and lower margin spectrum can be assured to have the valid statistical meaning. The last process is to readjust the template to a proper position when performing the interference removal process, so that even though a slight nonstationarity exists during the template formation, a proper cutoff can be formed.

Another important idea has to be pointed out here is that, when further averaging is required of these interference-free spectra in order to gain the signal-to-noise ratio, one has to carry the template detection information along, so that a statistical weighting can be applied to each spectral point (YING, 1985) (for instance, the fewer points averaged together, the less statistical significance can be made to this averaged point). This is especially true when a further least-square fitting process is required, because the least-square fit depends on the statistics of each individual point that is fitted to.

ACKNOWLEDGEMENT

We wish to thank the staff of the Arecibo Observatory for their assistance, especially to Dr. M. P. Sulzer for sparing his time to evaluate this paper.

This work was supported by the National Science Foundation Atmospheric Sciences Division Grant ATM82-13619 to Case Western Reserve University. The Arecibo Observatory of the National Astronomy and Ionosphere Center is operated by Cornell University under contract with the National Science Foundation.

REFERENCES

Dougherty, J. P., and D. T. Farley (1963), A theory of incoherent scattering of radio waves by a plasma, 3, Scattering in a partly ionoized gas, J. Geophys. Res., 68, 5473.

Lindgren, B. W. (1960), Statistical Theory, The Macmillian Company.

Mathews, J. D. (1978), The effect of negative ions on collision--dominated Thomson scattering, J. Geophys. Res., 83, 505.

Mathews, J. D. (1984a), Incoherent scatter radar as a tool for studying the ionospheric D region, J. Atmos. Terr. Phys., 46, 975.

Mathews, J. D. (1984b), Incoherent scatter radar probing of the 60-100 km atm, Submitted to IEEE Trans. on Geo-science & Remote Sensing.

Rastogi, P. K. (1983), Data processing techniques used with MST radar: a review, unpublished paper, Handbook for MAP, 9, 477.

Tanenbaum, B. S. (1968), Continuum theory of Thomson scattering, Phys. Rev., 171, 215.

Tepley, C. A., J. D. Mathews, and S. Ganguly (1981), Incoherent scatter radar studies of Mesospheric temperatures and collision frequencies at Arecibo, J. Geophys. Res., 86, 11330.

Ying, W. P. (1985), Analysis of the ionospheric ion line power spectra, M.S. thesis, Case Western Reserve University, Cleveland.

8.5.2 THE TUKEY ALGORITHM FOR ENHANCING MST RADAR DATA

S. A. Bowhill

Aeronomy Laboratory
Department of Electrical and Computer Engineering
University of Illinois
Urbana, Illinois 61801

One of the most troublesome features in MST velocity measurements is the determination of unwanted scatterers whose velocity is different from that of the surrounding atmosphere. Aircraft seen in the sidelobes of the antenna are the principal problem.

Because coherent integration essentially eliminates echoes with line-of-sight velocities greater than 10 or 20 m/s, aircraft are seen only when their flight path is almost perpendicular to the line-of-sight. Then, they give large returns whose velocities may be positive or negative, and certainly different from that of the surrounding air. These "glitches" in the minute-by-minute velocity records are quite troublesome in that they may distort the statistics of the velocity. Table 1 illustrates a simulation where a fairly smooth velocity profile was generated by applying a 20-point moving average to a sequence of random values whose standard deviation is unity. Standard deviation of those points should be .224. The lines A on Table 1 show sample standard deviations of 20 sequences of 60 points generated in this way and represent hourly data. The mean standard deviation is .216, reasonably close to the theoretical value. The considerable variation in these hourly standard deviations illustrates the problems in trying to determine accurate statistics on a time series such as this.

Lines B represent standard deviations of the simulated hourly data with randomly added 1-minute glitches, each having a standard deviation of unity (or about 4.5 x the time series standard deviation). The probability that a glitch will appear in a given minute of data varies from .01 to 0.3. Mean standard deviations for the glitched data are as high as .520 for a glitch probability of 0.3.

An objective way is therefore needed to remove sporadic points of this kind. For this purpose, the Tukey algorithm is appropriate and has some advantages over averaging.

The Tukey algorithm, applied to a data array, uses for each data point the median of it and the two points surrounding it. If the three points form a monotonically increasing or decreasing sequence, the original point is copied without change. However, if the central data point is remote from the other two, it is replaced by whichever of the two surrounding points is closest in value.

In Table 1, lines C and D show the results of applying the Tukey algorithm to the original and to the glitched data. As can be seen, almost all of the glitches are successfully removed by the use of the Tukey algorithm, and even the original data are not much affected as far as standard deviation is concerned.

The greatest effect of the Tukey algorithm is on data where the successive points are uncorrelated. Table 2 shows the results of applying the Tukey algorithm to five samples of a 1000-element random array with population standard deviation unity. Its standard deviation is reduced by a factor of approximately .687, so serious errors can be produced by applying the algorithm to such data.

TABLE 1

Glitch probability	Velocity	Standard Deviations x 1000					Mean
0.01	A	174	158	217	179	254	197
	B	192	158	217	179	333	216
	C	171	159	205	178	249	192
	D	172	159	205	178	251	193
0.03	A	367	237	212	201	183	240
	B	367	345	222	272	184	278
	C	365	230	207	188	180	234
	D	365	231	209	189	181	235
0.1	A	238	194	274	202	196	221
	B	268	332	377	328	303	322
	C	235	189	267	199	199	218
	D	236	188	262	233	197	223
0.3	A	206	175	143	271	150	189
	B	527	536	474	563	501	520
	C	193	172	142	271	143	184
	D	213	207	188	282	144	207

A is simulated wind, theoretical standard deviation = .224
B is A with added glitches, each with s.d. = 1
C is A smoothed with Tukey algorithm
D is B smoothed with Tukey algorithm

TABLE 2

Effect of Tukey algorithm on 1000-element random array of theoretical standard deviation unity.

Sample No.	Standard Deviations Random Array	Tukeyed array	Ratio
1	1.0110	0.6952	0.6876
2	0.9731	0.6751	0.6938
3	1.0049	0.6845	0.6812
4	1.0019	0.6954	0.6941
5	0.9946	0.6755	0.6792

Average ratio = 0.6872 $\pm$ .0005

Table 3 shows another simulation in which 1000-element arrays were generated with Gaussian correlation functions, with E-folding times of 0, 0.7, 1.4, and 3.1 min. Lines A represent the correlation function or the original winds and lines B represent the correlation functions after Tukey smoothing. Acceptable results are found of the correlation times of 1.4 min or more.

The Tukey algorithm has been successfully used in smoothing stratosphere MST velocity data (BOWHILL and GNANALINGAM, this volume) and the results were found to be of good quality.

TABLE 3

Correlation time (min)	Velocity	Correlation x 1000 vs Lag (min) 0	1	2	3	4	5	6	7
0	A	1000	-26	44	10				
	B	1000	542	325	43				
0.7	A	1000	679	200	37	37	31		
	B	1000	766	394	145	58	37		
1.4	A	1000	812	433	162	62	24	-14	
	B	1000	838	523	248	106	44	1	
3.1	A	1000	907	679	420	254	83	17	-5
	B	1000	915	707	463	256	116	38	0

A is simulated wind, Gaussian autocorrelation
B is A smoothed with Tukey algorithm

9.1.1 ON THE USE OF COLOUR REFLECTIVITY PLOTS TO MONITOR THE STRUCTURE OF THE TROPOSPHERE AND STRATOSPHERE

J. Rottger

Arecibo Observatory
Arecibo, Puerto Rico

I. J. Fu, F. S. Kuo

National Central University
Chung-Li, Republic of China

C. H. Liu

Department of Electrical and Computer Engineering
University of Illinois
Urbana, IL

and

J. K. Chao

National Central University
Chung-Li, Republic of China

The radar reflectivity, defined as the range-squared corrected power of VHF radar echoes, can be used to monitor and study the temporal development of inversion layers, frontal boundaries and convective turbulence. These observations as well as possible conclusions were discussed in more detail for instance by GAGE and GREEN (1979), ROTTGER (1979), and LARSEN and ROTTGER (1982, 1985). Also, the development of convective turbulence can be observed (ROTTGER, 1980). Such measurements can most conveniently be done with VHF radars operating with vertical beams.

From typical features of upward (cold front) or downward (warm front) motion of reflectivity structures, the advection/convection of cold and warm air can be predicted. Whereas, inversion layers, the tropopause and frontal zones evolve as fairly stratified, stable and often thin laminated structures on the height-time-reflectivity plots, convective turbulence is clearly characterized by upwelling, nonstratified structures.

High resolution colour plots appear to be useful to trace and to study the life history of these structures, particularly their persistency, descent and ascent. These displays allow an immediate determination of the tropopause height as well as the determination of the tropopause structure (e.g., highly stratified, split into multiple layers, fairly dissolved, or indications of potential temperature gradient deduced from reflectivity magnitude, etc.). The life history of warm fronts, cold fronts, and occlusions can be traced, and these reflectivity plots allow detection of even very weak events which cannot be seen in the traditional meteorological data sets. The life history of convective turbulence, particularly evolving from the planetary boundary layer, can be tracked quite easily. Its development into strong convection reaching the middle troposphere can be followed and predicted.

In a cooperative project of the Max-Planck-Institut-fur Aeronomie, the University of Illinois and the National Central University in Chung-Li, data taken with the SOUSY-VHF-Radar (ROTTGER, 1980) were analyzed in terms of reflectivity and further processed with the VAX 11/750 image processor of the Centre for Remote Sensing and Space Physics of the National Central University.

Figure 1 shows two examples of black-white copies of colour height-time-reflectivity plots. The abscissa is time, covering 6 hours for each plot, and the ordinate is altitude from 1.5 km to 16.5 km MSL. Whereas, gray-shade or contour plots and also these black-white copies can only barely cope with the large dynamic range of 60 dB of the reflectivity throughout the troposphere and lower stratosphere, but the colour plots indicate a lot of interesting fine structure as well as allow an immediate detection, tracing and interpretation of relevant structures.

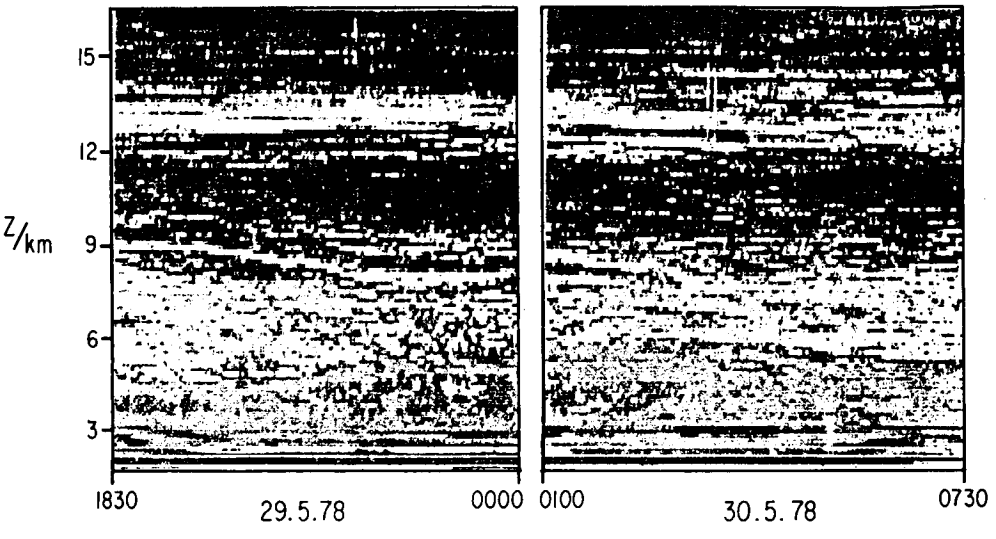

Figure 1. Copies of colour prints of height-time-reflectivity plots obtained by image processing of VHF radar reflectivity, measured with vertical beam and 150 m height resolution. Time coverage is 2 x 6 hours, and altitude coverage from 1.5 to 16.5 km.

REFERENCES

Gage, K. S., and J. L. Green (1979), Tropopause detection by partial specular reflections using VHF radars, Science, 203, 1238-1240.

Larsen, M. F., and J. Rottger (1982), VHF and UHF Doppler radars as tools for synoptic research, Bull. Am. Meteorol. Soc., 63, 996-1008.

Larsen, M. F., and J. Rottger (1985), Observations of frontal zone and tropopause structures with a VHF radar and radiosondes, Radio Sci., 20, 1223-1232.

Rottger, J. (1979), VHF radar observations of a frontal passage, J. Appl. Meteorol., 18, 85-91.

Rottger, J. (1980), Development of refractivity structure during anticyclonic weather conditions, Preprint 19th Conf. Radar Meteorol., Am. Meteorol. Soc., 593-598.

9.1.2 DATA COMMUNICATIONS AND MONITOR FOR THE PENN STATE UNIVERSITY PROFILER NETWORK

Robert M. Peters

Department of Meteorology
The Pennsylvania State University
University Park, PA 16802

The profiler network to be installed by the Department of Meteorology at Penn State University (THOMSON et al., 1984) utilizes a microcomputer for network monitoring and control. When completed, the network will consist of two VHF and one UHF wind profiling Doppler radars. Additional measurement systems to be added to the network include temperature and humidity profiling radiometers, sodar for boundary layer wind profiling and selected surface-based baseline systems.

Experience gained at Penn State has shown that reliable unattended operation of automated instrumentation systems has been best achieved when the data base and communications/monitor functions are handled by separate computer systems. The data base, which is generally available to many student and faculty users, is incorporated on a large multiuser system with many other data types, sources and applications. The "port" to the large system, the communications controller, is a dedicated microcomputer optimized for failsafe and unattended operation. This approach frees the operation of the network from depending upon the use of a particular large, and usually maintenance intensive, system as the data base. The communications controller serves as a temporary archive if the on-line data base system is not available. The microcomputer controller is also cost effective. Capital costs, maintenance fees, and factors such as uninterruptable power supplies are small in comparison to those for "mini-mainframe" systems. Thus, if need be, the microcomputer can be considered a disposable and replacable component.

Alarms on the network monitor provide an indication of network component malfunctions. This is accomplished by monitoring data quality and transmitter electronic parameters. A large color graphics display driven by the microcomputer network controller also provides selected profiler output and status indicators.

Each wind profiler within the Penn State network is currently using the software and signal processing hardware developed by the NOAA/ERL Wave Propagation Laboratory (STRAUCH et al., 1984). Several new features not currently available on the earlier prototype systems are also available. The transmitters (Tycho Technology, Inc.) include an internal microprocessor control system. Each transmitter is linked via a serial line to the local radar control minicomputer. This link provides the capability for complete monitoring and control of the transmitters. The sodar systems, which are designed around a microcomputer, will also be linked to the local radar minicomputer. Uninterruptable power sources are only used with the radar control computer, the radar signal processor and the radar site modem. Thus, automatic and controlled restart of the transmitters is an essential feature in the radar control software given the temporary but regular power outages which occur on the service lines during thunderstorms.

Remote diagnostic capabilities are also being implemented in the Penn State network. It will be possible to remotely analyze many specific malfunctions of the transmitters or signal processor. Persons interested in specific technical details of any of these systems should contact the author here or at Penn State.

REFERENCES

Thomson, D., C. Fairall, and R. Peters (1984), Network ST radar and related measurements at Penn State University: a progress report, Handbook for MAP, Vol. 14, SCOSTEP Secretariat, Dep. Elec. Computer Eng., Univ. IL, 350-355.

Strauch, R., K. Earnshaw, D. Merritt, K. Moran, and D. Van de Kamp (1984), Performance of the Colorado wind-profiling network, Handbook for MAP, Vol. 14, SCOSTEP Secretariat, Dep. Elec. Computer Eng., Univ. IL, 38-48.

9.1.3 ARCHIVAL OF POKER FLAT MST RADAR DATA

A. C. Riddle

Cooperative Institute for Research in the Environmental Sciences
University of Colorado
Boulder, CO 80309

B. B. Balsley and K. S. Gage

Aeronomy Laboratory
National Oceanic and Atmospheric Administration
Boulder, CO 80303

The Poker Flat MST radar has operated almost continually from early 1979 to early 1985. The data recorded during that time resides on some 1100 magnetic tapes. A second (compressed) data set containing only the derived parameters of velocity, width and signal to noise of the primary echo at each height, plus the noise on each spectra, occupies another 250 tapes. While the processing to generate the compressed data set does correct some known errors (such as incorrectly recorded dates or records taken when the transmitters were off) no attempt has been made to identify or remove spurious echoes. When the data are analyzed at the Aeronomy Laboratory, we have programs which can remove many types of spurious data and the knowledge to avoid analysis of data for which the problems cannot currently be rectified.

However, other users of the data set, a rapidly increasing group, do not have the advantage of insider knowledge or availability of programs to help them sort out the good data from the bad. Because the Poker Flat data set is such a unique and valuable resource, we are proposing to archive the data in forms more useful for analysis.

The archived data set would contain only the parameters for significant echoes with contamination from airplanes, unwanted ionospheric returns, frequency aliased Doppler signals and other sources removed. An example of the improvement already achievable is shown by comparisons between Figures 1 and 2. Figure 1 is a contaminated data set plotted with a program which removes only a few of the more easily detected contaminants. Figure 2 shows the same data plotted with a program having a more advanced contamination elimination facility. The improvement in reducing contamination while selecting more significant echoes is obvious. The archived set should be as good or better than that shown in Figure 2 and may occupy only 25-50 tapes.

For many users, data at time intervals of an order of one minute is not required. For their purposes, average data at half or one hour intervals would suffice. Data in that form will also be archived and the total data set may fit on only 1 or 2 tapes.

The archived tapes, together with documentation, will be available through the National Center for Atmospheric Research. From the persons at this meeting, or reading this paper, we solicit suggestions as to format for the archived data and preferred intervals for time averaged data. Testing of procedures to produce the archive quality data will commence soon and the complete data set is expected to be available within 2 to 3 years.

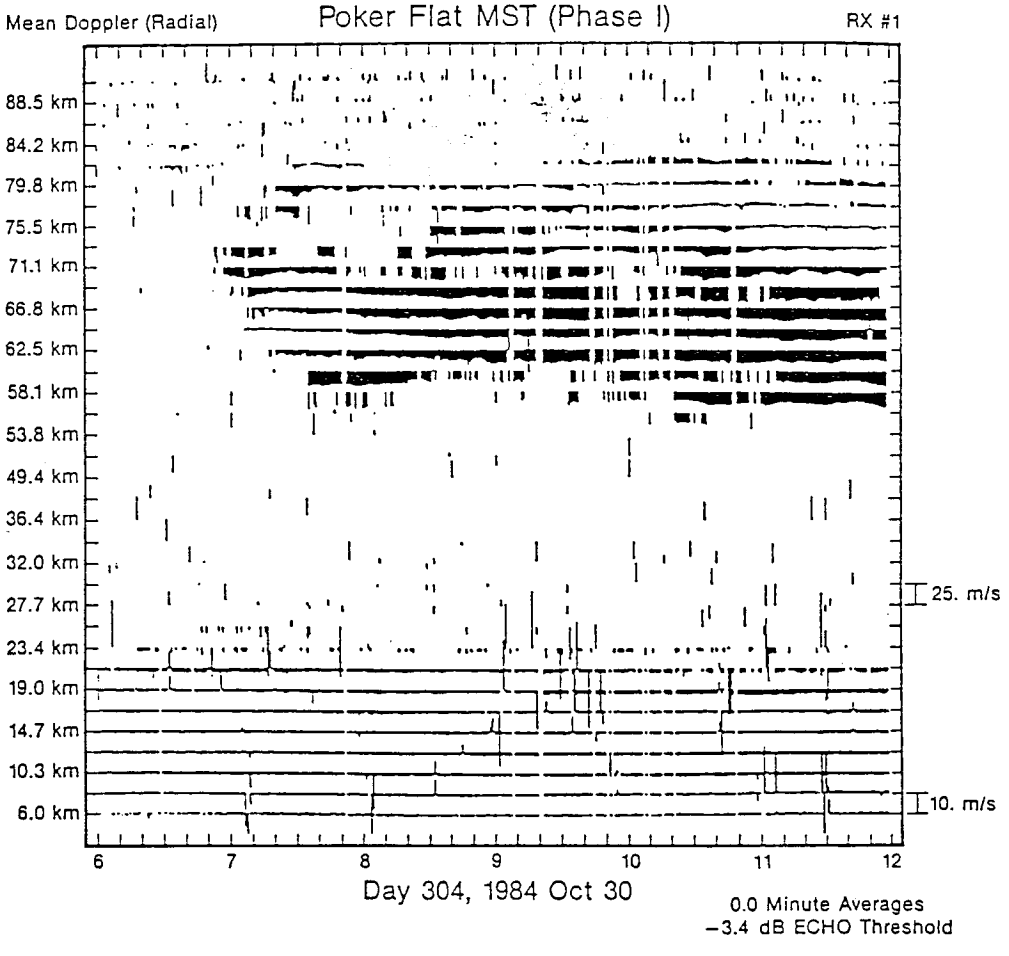

Figure 1. A fairly typical sample of Doppler velocities observed on Day 304, October 30, 1984, plotted by the "quick-look" program. Large contaminating velocities caused by airplanes, etc. can be seen at lower altitudes. Sporadic echoes above 80 km are due to meteors.

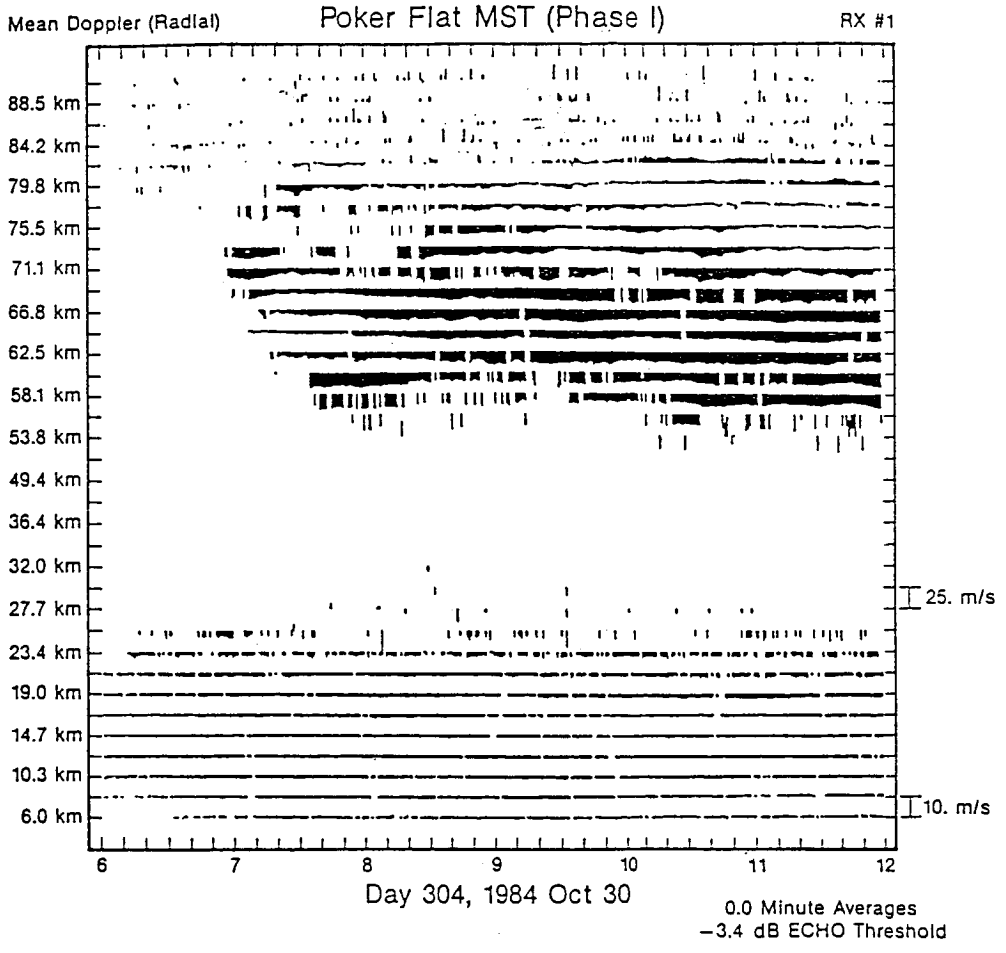

Figure 2. The same data set as Figure 1 subjected to some quality control. Data at adjacent heights and times were compared to obtain consensus. Airplane associated noise spikes have been removed and the data are now noticeably cleaner. In addition, the effective threshold signal-to-noise ratio is lower, which yields considerably more usable data at 23.4 km. In the mesosphere, the data quality and quantity is also improved. Other forms of interference remain. To eliminate these, more sophisticated quality-control strategies need to be developed.

9.2.1 REPORT FROM MSTRAC

P. K. Rastogi

Electrical Engineering and Applied Physics Department
Case Western Reserve University
Cleveland, Ohio 44106

At the first Workshop on Technical Aspects of MST Radar, the MST Radar Coordination (MSTRAC) Group was initiated to serve as a forum for data-exchange, and to coordinate and foster other activities related to MST radars. During its first year the group was jointly chaired by Dr. B. B. Balsley and Dr. S. K. Avery. Through their efforts, a small group of users was identified to which sample data tapes were furnished by several participating observatories. In their report, at the end of the first year (AVERY and BALSLEY, 1984), it was noted that the response from the observatories had not been overly enthusiastic and though it was possible to identify several potentially useful areas (e.g., data catalogs, data format and possibly radar frequency allocation), it was necessary to reassess the program. The current chairman assumed responsibility during summer, 1984.

During October, 1984, a questionnaire was mailed to about 15 scientists who either managed an MST radar facility or had close collaboration with one. The purpose of the questionnaire was to assess the level of interest in providing data for an interim data repository or data base and in other related activities. Of the 9 questionnaires returned, only about half were from groups already involved in dissemeniating data to other users or from groups that planned to do so once their facilities became operational. In subsequent discussions with several of the respondents, it became clear that the principal reasons for the tepid response were the lack of resources or shortage of trained personnel, frequently both. Also, most of the facilities are already directly involved with user(s), who naturally seem to share in the burden of developing programs, documentation and data analysis schemes. Few respondents have expressed an interest in participating in discussions on data-exchange formats, and frequency allocation for MST radars. Due to the limited response, however, it is uncertain whether a discussion on these topics would be of any genuine interest to the MST radar community at large.

Some of the facilities (e.g., Poker Flat) are currently in the process of establishing their own data base. Dr. A. D. Richmond has been managing the Incoherent-Scatter Data Base (ISDB) at NCAR and has expressed a willingness to extend this data base to incorporate a part of MST radar data. Since ISDB already has an established format shared with several incoherent-scatter radar facilities, it would be desirable to adhere to this format and provide a complete documentation with tapes.

During the last year, no further requests have been received from the user community for additional MST radar data.

In the opinion of this chairman, it is necessary to reassess the need for MSTRAC and to clearly define a role in which it can be of service to the MST radar community.

REFERENCE

Avery, S. K., and B. B. Balsley (1984), Data base management -- MSTRAC, Handbook for MAP, 14, edited by S. A. Bowhill and B. Edwards, 300-301, SCOSTEP Secretariat, Department Electrical and Computer Engineering, University of Illinois, Urbana-Champaign, IL.

9.2.2 MST DATA EXCHANGE TRHOUGH THE NCAR INCOHERENT-SCATTER RADAR DATA BASE

A. D. Richmond

HAO/NCAR
P.O. Box 3000
Boulder, CO 80307

One means of making MST data more easily accessible for scientific research by the general scientific community is through a centralized data base. Such a data base can be designed to readily provide information on data availability and quality, and to provide copies of data from any radar in a common format to the user.

The ionospheric incoherent-scatter radar community has established a centralized data base at NCAR that may serve not only as a model for a possible MST data base, but also as a catalyst for getting an MST data base started. Some key elements of the NCAR data base are:

Data are processed to yield geophysical parameters (e.g., velocities instead of Doppler shifts) by the radar organizations before being sent to NCAR;
Emphasis is on data for which measurement and analysis techniques have become well-understood and relatively routine;
All radar organizations use a common format for sending data;
NCAR catalogues the data and prepares summary information files;
NCAR provides data copies to users upon request;
NCAR assists users when possible with documentation and software, and helps place users in contact with appropriate persons at radar organizations for further information;
Users are required to offer co-authorship on publications to data providers;
Costs are largely borne by each respective institution with minimum transfers of funds. (NSF-supported radars are supposed to have funds included in their contracts to cover costs of participation in the data base).

The NCAR data base can include MST data in this same framework with relatively little extra effort. We are willing to handle MST data on a limited basis in order to permit assessment of community interest and in order to provide some experience with a centralized data base for MST data. If sufficient interest develops, NSF support could be sought for a full-scale MST data base, either at NCAR or elsewhere. Data from the Poker Flat radar are already under consideration for inclusion in the NCAR data base.

One important requirement is a common data format. The format currently used for incoherent-scatter data is quite flexible, and in fact was designed with the thought in mind of having it usable for data from other types of instruments. A brief description of this format is appended. The MST community may find this format acceptable, or may wish to design a more specialized format.

NCAR's data base tape format

All words are 16-bit, 2's complement integers.

Physical Record

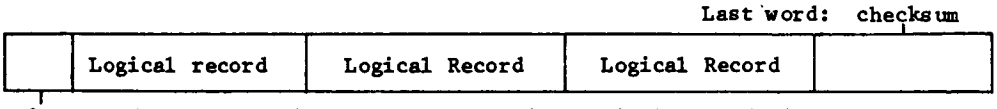

First word: total number of words in this physical record, including this word and checksum.

Each physical record contains an integral number of logical records.

Logical Record (Data Record)

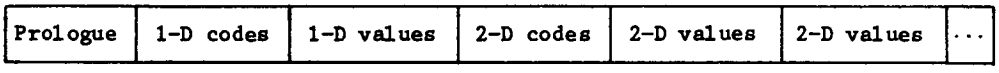

		Length
Or:	Prologue	LPROL
	1-D codes	JPAR
	1-D values	JPAR
	2-D codes	MPAR
NROW rows	2-D values	MPAR
	2-D values	MPAR
	.	.
	.	.
	.	.

PROLOGUE

WORD NUMBER	NAME	DESCRIPTION
1	LTOT	Number of 16-bit words in this record, including this one
2	KREC	Kind of record (1002 for data record in this format)
3	KINST	Instrument code
4	KINDAT	Kind-of-data code, pointing to documentation on analysis procedure used
5	IBYR	Beginning year for data in this record
6	IBDT	Beginning month/day (MMDD)
7	IBHM	Beginning hour/min (HHMM)
8	IBCS	Beginning centisecond
9	IEYR	Ending year
10	IEDT	Ending date
11	IEHM	Ending hour/min
12	IECS	Ending centisecond
13	LPROL	Length of this prologue (at least 16)
14	JPAR	Number of single-valued parameters (0 permissible)
15	MPAR	Number of multiple-valued parameters (0 permissible)
16	NROW	Number of entries for each multiple-valued parameters (0 permissible)

SAMPLE PARAMETER CODES

Code	Description	Designator		Units
10	YEAR (UNIVERSAL TIME)	YEAR	1.	UT
20	MONTH/DAY (UNIVERSAL TIME)	MMDD	1.	UT
21	DAY NUMBER OF YEAR (UNIVERSAL TIME)	DAY #	1.	UT
30	HOUR/MIN (UNIVERSAL TIME)	HHMM	1.	UT
34	TIME PAST 0000 UT	HR > 0000UT	1.E-03	HOUR
60	INTEGRATION TIME FOR THESE DATA	INTEGRATN T	1.	S
70	SAMPLING INTERVAL (TIME BETWEEN SAMPLS)	SAMPL NTRVL	1.	S
110	ALTITUDE (HEIGHT)	ALTITUDE	1.	KM
111	ADDITIONAL INCREMENT TO ALTITUDE	ADDITNL HT	1.E-01	M
115	ALTITUDE AVERAGING INTERVAL	AVGNG DEL H	1.	KM
116	ADDITIONAL INCREMENT TO HT AVGNG INTRVL	ADDITNL D H	1.E-01	M
120	RANGE	RANGE	1.	KM
121	ADDITIONAL INCREMENT TO RANGE	ADDITNL RNG	1.E-01	M
125	WIDTH OF RANGE GATE	RANGE GATE	1.	KM
126	ADDITIONAL INCREMENT TO RNGE GATE WIDTH	ADDITNL R G	1.E-01	M
130	MEAN AZIMUTH ANGLE (0 = GEOG N, 90 = EAST)	AZ ANGLE	1.E-02	DEG
140	ELEVATION ANGLE (0 = HORIZONTAL, 90 = VERT)	EL ANGLE	1.E-02	DEG
402	PULSE LENGTH	PULSE LEN	1.E-06	SEC
412	LOG10 SIGNAL TO NOISE RATIO	LG10(SNR)	1.E-03	
486	PEAK POWER	PEAK POWER	1.	KW
490	TRANSMITTED FREQUENCY	XMITTED FRQ	1.E+05	HZ
492	RECEIVED DOPPLER FREQUENCY OFFSET	R DPLR OFST	1.	HZ
494	RECEIVER BANDWIDTH	RCVR BANDWD	1.	KHZ
496	RECEIVER DELAY TIME	RCVR DLAY T	1.E-06	SEC
830	LOG10 (NUTRL ATM MASS DENSITY IN KG/M3)	LG10(M DEN)	1.E-03	
910	NEUTRAL ATMOSPHER LOG10(PRESSURE IN PA)	LG10(PRES)	1.E-03	
920	PRESSURE SCALE HEIGHT	PRES SCL HT	1.E+01	M
1010	SKEW ANGLE DEFININ GEOG UNIT VECTRS:1-3	ROT ANGL-GG	1.E-02	DEG
1410	NEUTRAL WIND IN DIRECTION 1	VN1	1.	M/S
1420	NEUTRAL WIND IN DIRECTION 2	VN2	1.	M/S
1430	NEUTRAL WIND IN DIRECTION 3	VN3	1.	M/S

Codes for error values are the negative of the corresponding parameter code, e.g. -1410 is the code for the error in the measured neutral wind in direction 1.

Missing data values are entered as -32767.

The angle given under code 1010 gives the rotation of direction 1 from eastward and of direction 2 from northward. Direction 3 is upward.

9.2.3 SUMMARY

A. D. Richmond

HAO/NCAR
P.O. Box 3000
Boulder, CO 80307

The first three papers presented information on some data management procedures used at different radars. An issue was brought up in the last two talks concerning data exchange. The MSTRAC chairman, Dr. P. K. Rastogi, noted that several impediments exist to data exchange, notably the lack of time and resources needed to prepare and transfer data. Although Richmond noted that NCAR could handle archiving and sending data copies to interested users, it was not clear that this alone would be sufficient to provide for an active data exchange.

AUTHOR INDEX

ATTENDEES

G. W. Adams, Utah State University, Logan, UT
S. A. Bowhill, University of Illinois, Urbana, IL
W. Birkmeyer, Arecibo Observatory, Arecibo, PR
J. Brosnahan, TYCHO Technology Inc., Boulder, CO
E. Brun, LSEET, Toulon, France
R. Burnside, Arecibo Observatory, Arecibo, PR
W. L. Clark, NOAA, Boulder, CO
T. S. Dennis, Clemson University, Clemson, SC
E. M. Dewan, OPA/AFGL, Hanscom AFB, MA
W. L. Ecklund, NOAA, Boulder, CO
B. Edwards, University of Illinois, Urbana, IL
D. C. Fritts, University of Alaska, Fairbanks, AK
I. J. Fu, National Central University, Taiwan, ROC
T. Galchen, University of Oklahoma, Norman, Oklahoma
R. B. Good, AFGL, Hanscom AFB, MA
J. L. Green, NOAA, Boulder, CO
T. Hagfors, NAIC/Arecibo Observatory, Arecibo, PR
A. J. Hall, Rutherford Appleton Lab, Chilton, UK
D. N. Holden, Clemson University, Clemson, SC
H. M. Ierkic, Arecibo Observatory, Arecibo, PR
B. Isham, NAIC, Ithaca, NY
E. Kessler, National Severe Storm Lab, Norman, Oklahoma
V. Klaus, C.N.R.M., France
M. F. Larsen, Clemson, University, Clemson, SC
C. H. Liu, University of Illinois, Urbana, IL
R. D. McPherson, NOAA, Washington, DC
C. E. Meek, University of Saskatchewan, Saskatoon, Canada
A. P. Mitra, National Physical Lab, India
G. D. Nastrom, Control Data Corporation, Minneapolis, MN
R. M. Peters, Pennsylvania State University, University Park, PA
M. Petitdidier, CRPE, Saint Maur des Fosses Cedex, France
P. K. Rastogi, Case Western Reserve University, Cleveland, OH
A. D. Richmond, HAO/NCAR, Boulder, CO
A. C. Riddle, NOAA, Boulder, CO
J. Rottger, Arecibo Observatory, Arecibo, PR
T. Sato, Kyoto University, Japan
F. Six, Arecibo Observatory, Arecibo, PR
R. E. Smith, Marshall Space Flight Center, Huntsville, AL
S. A. Smith, CIRES, Boulder, CO
T. L. Smith, PROFS/NOAA, Boulder, CO
R. G. Strauch, NOAA, Boulder, CO
M. Sulzer, Arecibo Observatory, Arecibo, PR
C. Tepley, Arecibo Observatory, Arecibo, PR
B. Thide, Uppsala Ionospheric Observatory, Sweden
T. E. VanZandt, NOAA, Boulder, CO
R. A. Vincent, University of Adelaide, Adelaide, South Australia
K. Wakasugi, Kyoto Institute of Technology, Japan
J. Weinstock, NOAA/ERL, Boulder, CO
S. R. Williams, Pennsylvania State University, University Park, PA
R. F. Woodman, Instituto Geofisico, Peru
W. P. Ying, Arecibo Observatory, Arecibo, PR
R. K. Zimmerman, Arecibo Observatory, Arecibo, PR
E. J. Zipser, NCAR, Boulder, CO

☆U.S. GOVERNMENT PRINTING OFFICE: 1986-159-708/50518

CUMULATIVE LISTING FOR THE MAP HANDBOOK

Volume	Contents	Date of Publication
1	National Plans, PMP-1 Report, PMP-2 Report, PMP-3 Report, Approved MAP Projects	June 1981
2	Symposium on Middle Atmosphere Dynamics and Transport (Extended Abstracts)	June 1981
3	PMP-5 Report, MSG-1 Report, MSG-2 Report, MSG-3 Report, Antarctic Middle Atmosphere Project (AMA), EXOS-C Scientific Observations, WMO Report No. 5, Updated Chapter 2 of MAP Planning Document, Condensed Minutes of MAPSC Meetings	November 1981
4	Proceedings of MAP Assembly held in Edinburgh, 14-15 August 1981, Condensed Minutes of MAP Steering Committee Meetings held in Edinburgh, Proceedings of MAP Open Meeting held in Hamburg, 19 August 1981	April 1982
5	A Catalogue of Dynamic Parameters Describing the Variability of the Middle Stratosphere during the Northern Winters	May 1982
6	MAP Directory	November 1982
7	Acronyms, Condensed Minutes of MAP Steering Committee Meetings, Ottawa, May 1982, MAP Project Reports, National Reports, Committee Reports, PMP and MSG Reports, Workshop Reports, Announcements and Corrigendum	December 1982
8	MAP Project Reports: DYNAMICS, GLOBUS, and SSIM, MSG-7 Report, National Reports: Czechoslovakia, USA	July 1983
9	Papers presented at the URSI/SCOSTEP Workshop on Technical Aspects of MST Radar, May 23-27, 1983, Urbana	December 1983
10	Papers presented at the International Symposium on Ground-Based Studies of the Middle Atmosphere, May 9-13, 1983, Schwerin, German Democratic Republic	May 1984
11	Condensed Miuntes of the MAP Steering Committee Meetings held in Hamburg 13-14 August 1983, Research Recommendations for Increased US Participation in the Middle Atmosphere Program, GRATMAP Project Report, MAP Study Group MSG-7 Report	June 1984
12	Coordinated Study of the Behavior of the Middle Atmosphere in Winter (PMP-1) Workshops	July 1984
13	Ground-Based Techniques	November 1984
14	Papers presented at the URSI/SCOSTEP Workshop on Technical Aspects of MST Radar, May 22-25, 1984, Urbana	December 1984
15	Balloon Techniques	June 1985
16	Atmospheric Structure and its Variation in the Region 20 to 120 km: Draft of a New Reference Middle Atmosphere	July 1985
17	Condensed Minutes of MAP Steering Committee Meeting, Condensed Miuntes of MAP Assembly, MAP Projects and Study Group Reports, National Reports	August 1985
18	Papers presented at MAP Symposium, November 26-30, 1984, Kyoto (Extended Abstracts)	December 1985
19	Rocket Techniques	March 1986
20	Papers presented at the URSI/SCOSTEP Workshop on Technical and Scientific Aspects of MST Radar, October 21-25, 1985, Aguadilla, Puerto Rico	June 1986

THIRD WORKSHOP ON TECHNICAL AND SCIENTIFIC ASPECTS
OF MST RADAR

Session Topics